STRONG MICROWAVES: SOURCES AND APPLICATIONS

2009

Volume 2

STRONG MICROWAVES:
SOURCES
AND APPLICATIONS

PROCEEDINGS
OF THE VII INTERNATIONAL WORKSHOP

Nizhny Novgorod, 27 July – 2 August 2008

Edited by
A. G. Litvak

In two volumes
Volume 2

Edited by decision of the Editorial
and Publishing Board of the IAP RAS

CURRENT DRIVE AND PLASMA HEATING BY MICROWAVES IN NUCLEAR FUSION DEVICES

PROGRESS TOWARDS FULL FEEDBACK CONTROL
OF MHD INSTABILITIES ON TEXTOR

E. Westerhof[1], M. R. de Baar[1], B. A. Hennen[1], J. W. Oosterbeek[2],
W. A. Bongers[1], A. Bürger[2], E. M. M. Demarteau[4], S. B. Korsholm[3],
S. K. Nielsen[3], P. Nuij[4], D. J. Thoen[1], M. Steinbuch[4], and the TEXTOR-Team

[1] FOM-Institute for Plasma Physics Rijnhuizen,* Association EURATOM-FOM,
Trilateral Euregio Cluster, Nieuwegein, The Netherlands, www.rijnhuizen.nl
[2] Institut für Energieforschung – Plasmaphysik, Forschungszentrum Jülich,
Association EURATOM-FZJ, Trilateral Euregio Cluster, 52425 Jülich, Germany
[3] Association Euratom - Risø DTU, Risø National Laboratory for Sustainable Energy,
Technical University of Denmark, DK-4000 Roskilde, Denmark
[4] Dep. Mechanical Engineering, Technical University Eindhoven,
P.O. Box 513, 5600 MB Eindhoven, The Netherlands

The TEXTOR ECRH system is being prepared to come to full feedback control of MHD instabilities. The mechanics of the ECRH launcher has been characterized. On this basis a dedicated controller has been designed and tested on a mock-up of the actual launcher. An ECE diagnostic observing the plasma along the ECRH wave beam line has been taken into operation, which will greatly simplify the alignment of the ECRH power deposition with MHD modes. Algorithms are described to obtain the required information on mode location and phase from available signals.

1. Introduction

High power microwaves in the electron cyclotron range of frequencies are being used for heating and non-inductive current drive in fusion plasmas. The possibility to focus the high power microwave beam, and the resonant power coupling to the plasma at the electron cyclotron resonance or a harmonic allow to heat and to drive current very locally inside the plasma. Moreover, the easy coupling from flexible mirror antennas allows the localization of the heating and current drive at any particular location inside the plasma. These unique properties of electron cyclotron resonant heating (ECRH) and current drive (ECCD) make them into ideal tools for the manipulation of plasma stability. Several plasma instabilities depend sensitively on the local current density and pressure profiles.

ECRH and ECCD have been applied successfully for the suppression of (neoclassical) tearing modes (N)TMs [1–3], and for the control of sawteeth [4–6]. Up to now, these experiments have been mostly performed in feedforward: the plasma parameters and the ECRH/ECCD launcher settings are preprogrammed to achieve the desired localization of the heating or current drive to induce the desired effect.

The challenge for future energy producing fusion reactors is to achieve such control under active feedback. Thus, viable feedback control strategies will have to be developed and tested in current experiments as well as in the international

experimental tokamak reactor ITER [7]. In fact, NTM and sawtooth control are among the main tasks for the ITER ECRH systems [8]. Such active control requires of course the proper sensors and actuators. In the present context, the actuator is provided by the ECRH or ECCD. Sensors are required to detect and localize on the one hand the instability – the resonant surface on which the magnetic island created by the NTM resides, or the sawtooth inversion radius – and on the other hand the effect of the heating or current drive. Such sensors are provided, for example, by electron cyclotron emission (ECE) providing information on the temperature fluctuation associated with rotating magnetic islands or sawtooth relaxation oscillations, or by Mirnov coils detecting the associated magnetic perturbations outside the plasma. The heating and current drive profiles could be calculated knowing the launching mirror settings and the plasma equilibrium.

In general, sensors and actuators will be located at different positions around the tokamak. Moreover, the signal carrying the information on the plasma properties to the actuator may travel along entirely different trajectories as the high power microwaves from the actuator. As a consequence, full knowledge of the plasma equilibrium will generally be required to link the information from the sensors to the proper settings of the actuator, i.e. the steering of the ECRH/ECCD to the appropriate location. A straightforward solution to this problem would be to use the same sight line for both the actuator (ECRH/ECCD) as well as the sensor (ECE) as first proposed in reference [9].

This paper describes a number of key elements of the feedback control loop based on this same sight line principle as it is being implemented on TEXTOR [10]. The possibility to trigger tearing modes by the application of well controlled perturbation fields from the dynamic ergodic divertor (DED) [11] make TEXTOR ideally suited for this type of experiments. An overview of the entire control loop is presented in Section 2. Next, the control of the mechanical launcher is discussed. On the basis of a detailed analysis of the mechanical properties of the launcher an optimized controller is derived. Section 4 then describes the ECE diagnostic mounted in the ECRH/ECCD high power transmission line and viewing the plasma along the same optical path as traveled by the high power ECRH/ECCD [12]. The key element of this diagnostic is the frequency selective coupler separating the backward propagating low power ECE from the forward propagating high power ECRH/ECCD. First measurements obtained with this in-transmission-line ECE diagnostic are presented. Section 5 describes methods for real time analysis of the ECE signals in order to determine the location and phase of a tearing mode. The final section provides a summary and outlook.

2. Feedback control loop for MHD instability control

The generic feedback loop for the control of MHD instabilities consists of the following elements as sketched in Fig. 1 [13]. At the centre of the loop one has the plasma itself. It may evolve into an unstable state with either a large, ro-

tating magnetic island formed by a tearing mode or showing sawtooth relaxation oscillations of the core. The plasma is observed by diagnostics in order to measure the relevant plasma parameters. In the system as being prepared on TEXTOR, these diagnostics include a six channel ECE radiometer viewing the plasma through the ECRH / ECCD transmission line and a selected Mirnov coil. The in-transmission-line ECE system is described in detail in Section 4. When necessary, additional diagnostic signals can be added. The next steps in the control loop are the data acquisition, the data processing of the diagnostic signals, and the central controller. The final outputs of these steps are the desired settings for the ECRH / ECCD: namely, the proper launching angles and the required gyrotron power to achieve the desired effect. In Section 5, a number of these real time signal processing techniques is discussed. The next block contains the steering of the actuator, i.e. the ECRH / ECCD, in terms of the mechanical launcher steering to achieve the requested injection angles – this is the subject of the next Section – and the gyrotron control to obtain the requested power. The loop is then closed by the response of the plasma to the input from the actuator: i.e. its response the local ECRH / ECCD.
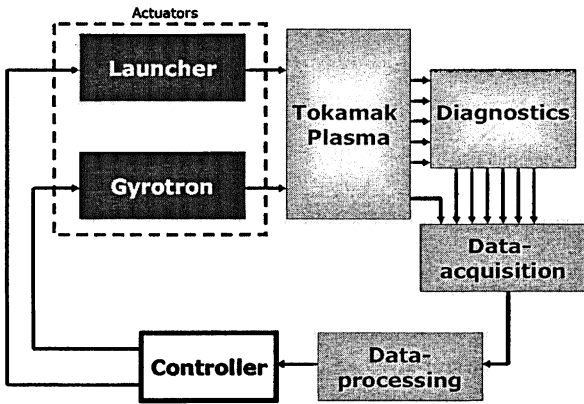

Fig. 1. Schematic overview of a generic closed loop control system for the control of MHD instabilities by ECRH / ECCD (adapted from Ref. [13]).

Models are being developed for each element in the control loop [13]. The models are kept as simple as possible while retaining the essential dynamical properties of each of the elements. For example, in case of tearing mode feedback control, the evolution of the associated magnetic island width is described by the generalized Rutherford equation [1], including terms describing the effects from the perturbation field from the DED, as well as from the application of ECRH or ECCD. All models are integrated in a Simulink™ environment, which allows the testing of different control strategies before implementation in the real system.

3. Mechanical launcher control

In TEXTOR the high power microwaves for ECRH/ECCD are launched into the plasma from a final focusing mirror that can be actuated in two rotational degrees of freedom [14]. In the horizontal plane the injection angle (rotation, ϕ) can be varied from $-45°$ to $+45°$, where $0°$ corresponds to injection along the major radial direction of the torus. This allows injection from virtually counter-tangential to co-tangential with respect the magnetic axis of the plasma. Non-inductive current drive requires a finite rotation angle, where a negative rotation results in co-ECCD. In the vertical plane the injection angle (elevation, θ) can be varied from $-30°$ to $+30°$, which allows covering the entire poloidal cross section on the high field side. The two degrees of freedom are actuated by push-and-pull rods which are driven by AC permanent magnet synchronous spindle motors equipped with servo amplifiers and high resolution encoders. The design of the launcher is sketched in Fig. 2 [14].
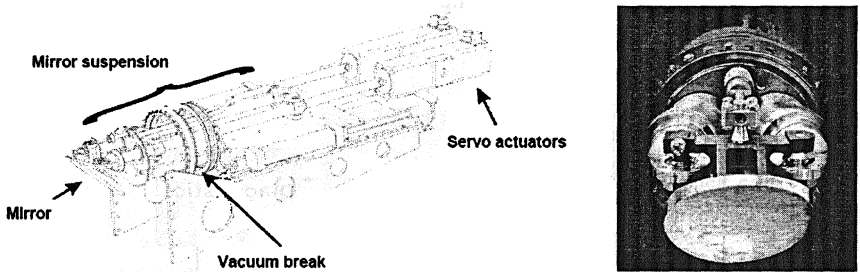

Fig. 2. A schematic view of the TEXTOR ECRH launcher (left) and a picture (right) showing the in vessel mirror with bearings (adapted from Ref. [14]).

Since any misaligned ECRH could result in undesired destabilization of a mode, no power will be deposited during the period of time between occurrence of an island and the moment at which actual alignment is achieved. Accordingly, the island is allowed to grow further without stabilization. Minimization of the actual time needed to achieve alignment is therefore required. For TEXTOR, reasonable estimates of the growth rate of a magnetic island result in a desired angular mirror rotation in the poloidal plane of $10°$ in 100 ms, with a desired positioning accuracy of $1°$.

In order to assure flexible, fast and accurate positioning of the ECRH / ECCD beam, the dynamics of the launcher have been analyzed experimentally using frequency response measurement techniques. A detailed account of these experiments is given in Ref. [15]. The frequency response measurements allow the extraction of transfer function estimates. These estimates can be exploited to derive and optimize controllers for the system, within the physical limitations.

The procedure resulted in a feedback controller consisting of a standard proportional integral derivative (PID) controller, a lead/lag filter and a low-pass fil-

ter. In simulations, the stability robustness and performance of the feedback controlled system was verified. The controller was then implemented in real-time control experiments on a mock-up of the actual launcher system, which has been built to offer a test-bed for controller design and optimization. Figure 3 shows the set-point trajectory for one of these experiments [13].
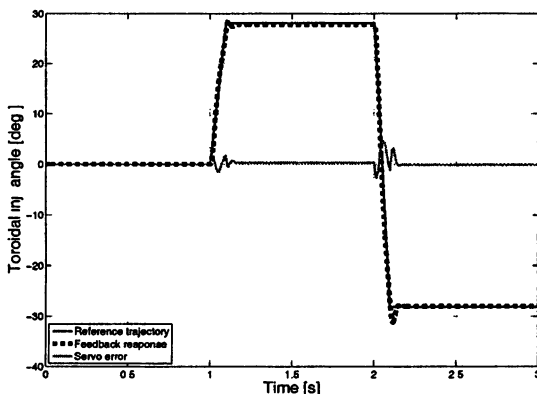

Fig. 3. Performance of a controller for the mechanical launcher [13]. The figure shows the set point or reference trajectory, the achieved trajectory and servo error for a real-time feedback control implementation on the mock-up launcher test facility.

The feedback response, measured by the encoders of the servo actuators, is shown along with the achieved servo error. The rotation angle of the launcher mirror in the toroidal plane has been calculated from the encoder signal. The mirror is swept from +28° to 28° within 100 ms. During the acceleration phase, the servo error increases to 6° at maximum. The designed controller damps the oscillations caused by this sudden acceleration ramp. A maximum steady-state error of 0.6° is achieved within 200 ms after the start of the sweep. Comparable performance can be achieved for mirror rotations in the poloidal plane.

4. In-transmission-line ECE

One of the problems of real-time control is the precise (radial and poloidal) localization of the island. This is required for the control of the ECRH / ECCD power deposition with an accuracy of 1 to 2 cm with respect to the mode resonant surface and the proper phasing of a possible ECRH / ECCD power modulation such that the power is only injected when the O-point phase of the island is in view of the ECRH / ECCD launcher. For this purpose, a dedicated ECE diagnostic has been developed on TEXTOR, which views the plasma along the identical line of sight as traced by the injected ECRH / ECCD microwave beam [9, 12]. The advantage of this diagnostic is that a complicated reconstruction of the plasma equilibrium is not needed. Moreover, geometrical optics effects like diffrac-

tion can be neglected as they will be the same for the sensor signal and the actuator ECRH / ECCD beam. This method implies that the ECE signal (in the order of a few nW) needs to be separated from the high power ECCD beam (in the order of 1 MW). Also, the reflection of the back reflected stray radiation (of the order of 100 W) into the radiometer has to be reduced to an acceptable level.

On TEXTOR this problem is solved by choosing the ECE signal frequency slightly different from the high power ECRH / ECCD frequency and employing a sharp frequency filter to block out the high power signal from the diagnostic signal. For this purpose a Fabry-Perot interference filter has been developed. The filter is based on a quartz plate placed under an angle of 22.5° in the ECW transmission line [12]. The plate is made resonant at the gyrotron frequency and anti-resonant at selected ECE frequencies with a periodicity of 3 GHz which determines the channel separation of the radiometer. The transmission of the ECCD-beam is optimized to 95% whilst the reflection of the backward stray radiation is minimized to 0.2%. The maxima in the reflected signal, determining the signal strength of the ECE signal diverted out of the beam line, yield a 37% reflection coefficient. At the resonant frequency the power absorption of the plate is 5%. The diagnostic ECE signal is subsequently passed through a second quartz plate placed under 22.5° in order to further reduce stray gyrotron radiation. A focusing mirror shapes the microwave beam into the antenna pattern of the corrugated receiving horn of the radiometer. The design of the optical system is sketched in Fig. 4.
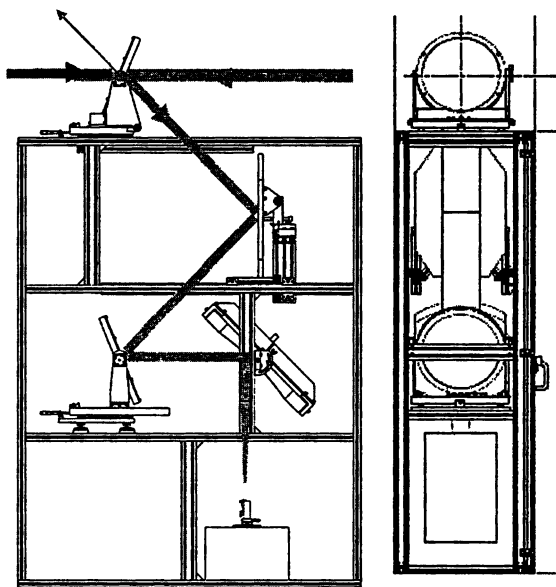

Fig. 4. Design of the optical system separating the ECE from the plasma (the radiation coming from the right) from the high power ECRH beam going to the right. The thick lines indicate the trajectories of the microwaves. © Ref. [12]

Before entering the radiometer, a −80 dB, 140 GHz notch filter with a bandwidth of 100 MHz serves as a third attenuation step of stray gyrotron radiation. In addition, a pin-switch protects the radiometer from spurious modes produced by the gyrotron during switch-on and switch-off at frequencies that differ from the 140 GHz and are therefore not blocked by the notch filter. The ECE spectrum is monitored in a frequency band of 132 to 148 GHz, which under normal TEXTOR operating conditions covers about 1/3 of the plasma cross-section on the high field side.

The first measurements obtained with the novel in-transmission-line ECE diagnostic during ECRH clearly demonstrate the potential of identifying various structures in the ECE spectrum, like sawtooth inversion and rotating magnetic islands [12]. A sample of such measurements is shown in Fig. 5. In some cases strong perturbations in the measured signals are observed during combined ECE and ECRH / ECCD. In the presence of an island a very high power level saturates the channel at 138.5 GHz during a particular phase of the mode. This phase typically lasts 10% to 20% of the mode period. During saturation the power level is so large that the radiometer goes into compression, forcing all other channels down. In case the ECRH is launched perpendicularly the ECE measurements are perturbed in a similar way, without clear correlation to MHD activity. The mechanism causing these perturbations, probably from plasma physics origin, is under investigation. Also, methods for the real time removal of these perturbations from the signal are being developed. This should allow use of the in-transmission-line ECE signals for the intended feedback control purposes even in the presence of these perturbations.
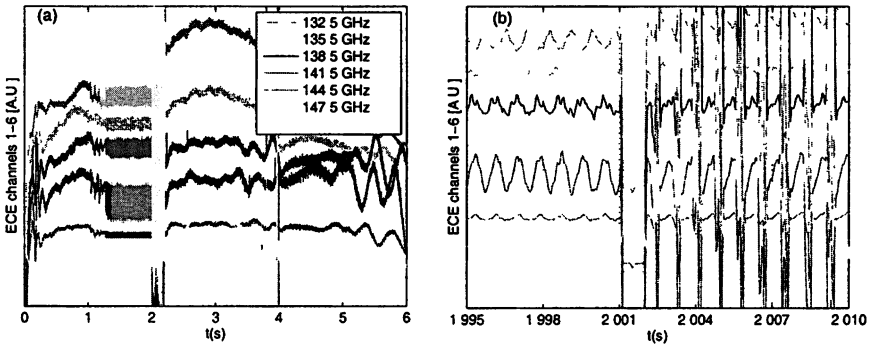

Fig. 5. In-transmission-line ECE measurements as obtained in TEXTOR discharge #107125 (adapted from Ref. [12]): (*a*) shows an overview of the signals during the entire discharge in which 400 kW of ECRH is injected from 2 to 4 s; (*b*) shows the detailed signal around the start time of the ECRH. The phase reversal in the oscillations indicating the position of the magnetic island can clearly identified between the 132.5 GHz and the 138.5 GHz signals. After switch-on of ECRH the signals are strongly perturbed most likely by scattered high power ECRH radiation.

These results motivate the further development and the implementation of similar ECRH / ECCD aligned ECE systems for NTM control in larger fusion machines [16]. A new scheme has been designed for implementation on ASDEX Upgrade (AUG), which is based on waveguides equipped with a fast directional switch (FADIS [17]). A possible further development for ITER is also discussed in [16].

5. Signal processing techniques

The magnetic island parameters are concealed in (noisy) ECE signals. Identification of the control variables from these data requires processing. The control variables are: the radial location, amplitude and phase of an island. The set-points for control of the launcher angles and the gyrotron power can be derived from these variables. Examples of data-processing techniques to extract these control parameters are found in literature [18, 19]. In this section, two algorithms are demonstrated. Their processing time should be minimized, to increase the response time of the overall control loop in a real-time implementation.

5.1. Basic correlation algorithm [13]

The radial location of the O-point of a rotating island can be inferred from ECE data as a phase jump between two adjacent radiometer channels [19]. In order to detect this phase difference, the DC offset should be compensated for. In the presented case, this was achieved by subtracting a running average of 100 data points ($\sim$ 1 ms) from the original signal. The obtained signals $\overline{x}_{i,a}$ and $\overline{x}_{i,b}$, where i indicates the sample number and a, b the channel index, can then be multiplied in pairs to compute the respective correlation factors between different ECE channels. The pair wise multiplication is done over a summation window with length $N = 200$, following

$$C_{a,b}^n \equiv \sum_{i=n-N+1}^n \overline{x}_{i,a}\overline{x}_{i,b} \ .$$

A negative and positive threshold can be defined such that exceeding the negative threshold indicates that the two ECE channels are in anti-phase, i.e. on opposite sides of the resonant surface. Trespassing the positive threshold indicates that the two signals are in phase, i.e. on the same side of the resonant surface. Figure 6 shows the result of an implementation of this algorithm for two line-of-sight ECE time traces. The island induced fluctuations occur at 1.273 s. The time required for the sum to build up and exceed the threshold is representative of the time required to detect the island, e.g. three oscillations of the rotating island. Simultaneous computation of these correlation factors for pairs of radiometer channels results in identification of the radial location of the island.
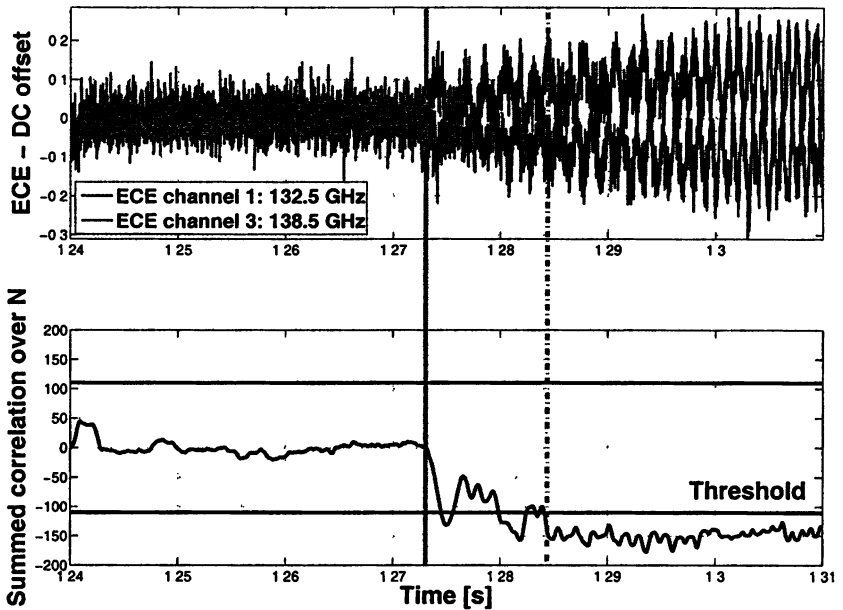
Fig. 6. Electron temperature fluctuations on the in-transmission line ECE channels 1 and 3 for TEXTOR discharge # 107125 (top), and their mutual correlation (bottom). A threshold can be defined below which a positive identification of the island position is achieved. © Ref. [13]

5.2. Mode phase and frequency identification [13]

In addition to this basic algorithm, the instantaneous amplitude, phase and frequency of a signal $x_r(t)$ can be computed using the so-called Hilbert transform [20]. For any real-valued function $x_r(t)$, the analytic signal $x(t) = x_r(t) + i\hat{x}(t) = a(t)e^{i\phi(t)}$ can be constructed, where $x_r(t)$ is the original set of real-valued data, while $\hat{x}(t)$ is the complex conjugate of the original signal, obtained via the Hilbert transform. The imaginary part of the analytic signal $\hat{x}(t)$ is a version of the original real-valued sequence shifted $90°$ in phase. The Hilbert transformed series has the same amplitude and frequency content as the original real data and includes information on the phase of the original signal. The instantaneous amplitude is given by $a(t) = \sqrt{x_r^2 + \hat{x}^2}$, while the phase of the signal reads $\phi(t) = \arctan(\hat{x}/x_r)$. Realizing that the instantaneous frequency of a signal is the time rate of change of the instantaneous phase angle, the instantaneous frequency is simply obtained via $f(t) = d\phi/2\pi dt$.

269

The result of an implementation of this algorithm on line-of-sight ECE time traces is depicted in Fig. 7. Note that the algorithm can be employed to determine the instantaneous frequency of the island and to locate its X- and O-points.
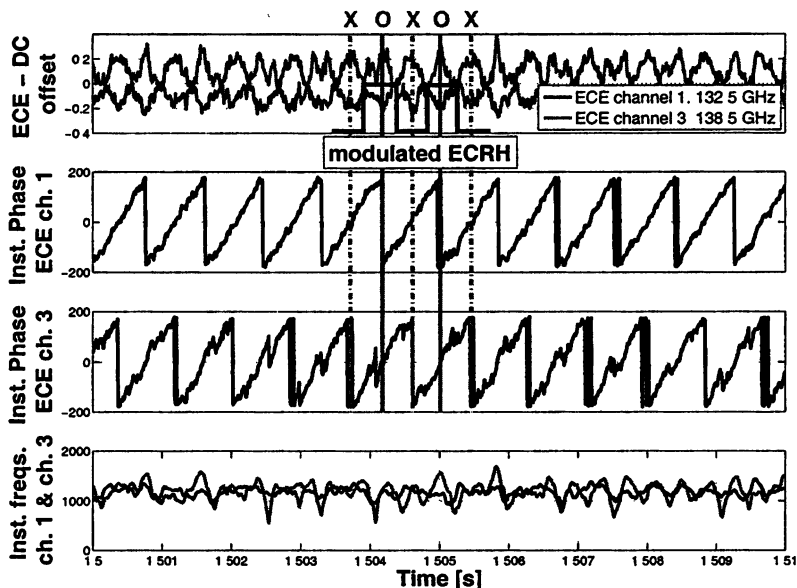

Fig. 7. Electron temperature fluctuations on the line-of-sight ECE channels 1 and 3 for shot # 107125, including their instantaneous phase and frequencies as obtained from a Hilbert transform. This analysis allows a unique identification of the X- and O-point passages in front of the combined ECRH-ECE launcher. © Ref. [13]

This information can effectively be used to construct a set-point trajectory for controlled modulation of the gyrotron power deposition in phase with the periodically rotating center of the magnetic island.

6. Summary and Outlook

In preparation of the full feedback control of instabilities by ECRH or ECCD on the TEXTOR tokamak significant progress has been achieved. A dedicated controller has been developed for the steering of the mechanical ECRH launcher which takes into account the known dynamical properties as obtained from a frequency response analysis of the system [15]. An ECE diagnostic integrated into the ECRH transmission line and viewing the plasma along the same optical path as traveled by the high power ECRH wave beam has been taken into operation [12]. The diagnostic is dedicated to feedback control purposes, as the use of the same sight line as the ECRH allows for a straightforward

270

localization of the ECRH power relative to MHD modes observed in the in-transmission-line ECE diagnostic: no knowledge of the plasma equilibrium nor the actual dispersion of the waves inside the plasma is required, since these are identical for the actuator (ECRH / ECCD) and the sensor (ECE). Measurements have demonstrated the capability to identify the position of magnetic islands or the sawtooth inversion radius. Finally, algorithms to identify the location in the ECE spectrum of a tearing mode and its phase are in place [13]. Further algorithms for determination of the sawtooth period and inversion radius are under development.

Models have been developed for all elements of the control loop. These are now being implemented in a Simulink™ environment, and the necessary control algorithms will be tested. In the next step all these elements will be integrated on the TEXTOR tokamak. With the feedback loop closed, experiments will then be carried out on the control of tearing modes and sawteeth. At the same time CW, wave guide compatible in-transmission line ECE systems are being developed for implementation on larger devices, in particular, AUG and ITER [16].

Acknowledgement

References

1   *La Haye R J* Phys Plasmas **13** (2006) 055501.
2.   *Prater R.* Phys. Plasmas **11** (2004) 2349.
3.   *Westerhof E. et al* Nucl. Fusion **47** (2007) 85.
4   *Angioni C. et al.* Nucl Fusion **43** (2003) 455.
5.   *Mück A. et al.* Plasma Phys. Control Fusion **47** (2005) 1633.
6.   *Westerhof E. et al.* Nucl. Fusion **43** (2003) 1371.
7.   *Hender T C. et al.* Nucl. Fusion **47** (2007) S128.
8.   *Henderson M A et al.* J. Phys.. Conf. Ser. **25** (2005) 143.
9.   *Westerhof E et al.* Proc of the 13th Joint Workshop on ECE and ECH, 17–20 May 2004, edited by A Litvak, Institute of Applied Physics/RAS, Nizhny Novgorod, Russia, 2005, p 357.
10   *Samm U.* Fusion Sci. Technol. **47** (2005) 73.
11   *Finken K H* Fusion Eng. Des. **37** (1997) 337.
12. *Oosterbeek J. W et al.* Rev. Sci. Instrum **79** (2008) 093503.
13. *Hennen B. A. et al.* to be published in Proc 25th Symposium on Fusion Technology (SOFT), Rostock, Germany, 15–19 September 2008, Fus. Eng. Design.
14   *Westerhof E et al.* Fusion Sci. Technol **47** (2005) 108.
15. *Hennen B A. et al* 4th IAEA TM on ECRH Physics and Technology for ITER, Vienna (2007) http://www-naweb iaea.org/napc/physics/meetings/4ECRH.htm
16   *Bongers W A et al* accepted for publication in Fusion Sci Technol. (February 2009).
17   *Kasparek W. et al* Nucl. Fusion **48** 054010 (2008).
18   *Berrino J et al.* IEEE Trans. Nucl. Sci **53** (2006) 1009.
19   *Berrino J et al* Nucl Fusion 45 (2005) 1350.
20   *Vakman D.* IEEE Trans. Signal Processing **44** (1996) 791.

OVERVIEW OF THE ITER ECH&CD SYSTEM

C. Darbos, M. A. Henderson, F. Albajar[1], T. Bigelow[2],
T. Bonicelli[1], R. Chavan[3], G. Denisov[4], R. Heidinger[5],
N. Kobayashi, S. L. Rao[6], D. Rasmussan[2],
G. Saibene[1], K. Sakamoto[7], K. Takahashi[7]

ITER Organization, 13108 St. Paul-lez-Durance, France
[1] Fusion For Energy, C/ Josep Pla 2, Torres Diagonal Litoral-B3, E-08019 Barcelona, Spain
[2] Oak Ridge National Laboratory, 055 Commerce Park,
PO Box 2008, Oak Ridge, TN 37831-6483, USA
[3] Centres des Recherches en Physique des Plasma, EPFL Ecublens,
CH-1015 Lausanne, Switzerland
[4] Institute of Applied Physics, Russian Academy of Sciences,
46 Ulyanov Street, Nizhny Novgorod, 603950 Russia
[5] Association EURATOM-FZK, IMF I, Postfach 3640 D-76021, Karlsruhe, Germany
[6] Institute for Plasma Research, Near Indira Bridge, Bhat, Gandhinagar, 382428, India
[7] Japan Atomic Energy Agency, 801-1 Mukoyama, Naka-shi, Ibaraki 311-0193 Japan

1. Introduction

The EC system is studied for being able to inject 20 MW in the plasma, at a frequency of 170 GHz, for heating and current drive and MHD (Magneto Hydro Dynamics) control. It is composed of HVPS (High Voltage Power Supplies), up to 24 gyrotrons (unit output power between 1MW and 2 MW), transmission lines and 2 types of launchers [1].

These four main subsystems will be in-kind procurements, delivered by 5 parties:

*   Europe is responsible for delivering 8 MW for the H&CD (Heating and Current Drive) gyrotrons, all the HVPS for the 20 MW H&CD injected power and the four upper launchers.
*   India is responsible for procuring the start up system (2 MW 10 s gyrotrons and the corresponding HVPS).
*   Japan is responsible for delivering 8 MW for the H&CD gyrotrons and the equatorial launcher.
*   The Russian Federation is responsible for procuring 8 MW for the H&CD gyrotrons.
*   US are responsible for delivering all the Transmission Lines (TL), from the gyrotrons up to the launchers.

ITER is responsible for the build to print design (for the launchers, both upper and equatorial types) and for defining the functional specifications for the other subsystems, but the responsibility for the installation, the commissioning and the operation of the EC system will be shared between ITER and the Domestic Agencies (DA). Therefore a strong partnership is required to make this system successful, resulting in a full collaboration between all partners.

2. Description of the present EC system

2.1. RF Building

Up to mid 2007, the EC system was supposed to be installed in the Assembly Hall, close to the Tokamak building, but with a major concern on the schedule which was not compatible with the time needed for installing and commissioning all the components, to be on time for the 1st plasma [2]. Indeed, both IC (Ion Cyclotron) and EC sources could not be installed until tokamak assembly was completed. As a result, a new building called RF building was decided to be built, along the Assembly hall on the East side and devoted to IC and EC sources including their HVPS [3]. This building is composed of 3 levels (see Fig. 1):

- The 1st level (or ground floor) where will be located the main HVPS including transformers, the HV distribution.
- The 2nd level (1st floor) where will be installed the BPS (Body Power Supplies) the cathode heating PS and when needed the APS (Anode Power Supplies).
- The 3rd level (2nd floor) where will be located the gyrotrons on a false floor, leaving space for running the TL below, all the cubicles for the auxiliary PS and interlocks/CODAC requirements and a local I&C (Instrumentation and Control) room for local operation. A microwave laboratory will be included near this room. The distance between neighboring gyrotrons has to be optimized, taken into account the stray magnetic field coming from the tokamak and the gyrotrons themselves, and the steel frame structure of the building. At present time, they could be on 5 × 4.8 m grid by staggering the positions of the tubes.
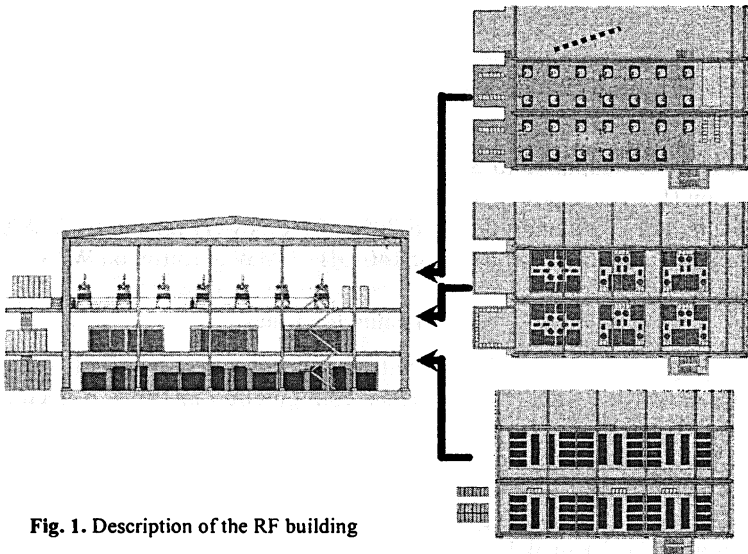

Fig. 1. Description of the RF building

273

The EC system is located in the south side of the RF building, to minimize the stray magnetic field due to the tokamak, whereas the IC system which is not sensitive to the field is located in the north area.

The central area of the building is left empty, or nearly empty at the beginning of the operation of ITER but is suitable for a further upgrade of the EC system, up to 48MW of installed power, assuming 1 MW sources.

2.2. HVPS

One of the option was to have thyristor-based PS, with 1 PS feeding 12 gyrotrons. This option was not compatible with 3 different gyrotrons (provided by 3 different parties). A second option is preferred, a PSM-based system with 1 PS feeding 2 gyrotrons which offers modularity and flexibility, meaning a better availability of the whole EC system for a better reliability of the total power delivered to the plasma. This HVPS concept (see Fig. 2) has then to be capable of supplying cathode voltage for two 1 MW-gyrotrons or one 2 MW-gyrotron in the same time, with independent body voltage and even anode voltage when needed and has to be compatible with fast shutdown.
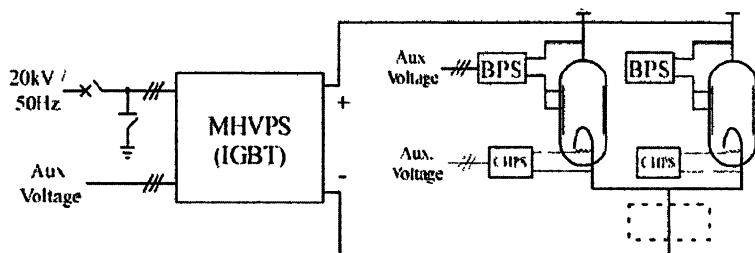

Fig. 2. PSM-based HVPS

It has to be adaptable to 3 gyrotron types and should provide up to 1 kHz modulation (for 100% power modulation) for the main power supply and up to 5 kHz (for partial modulation down to 70% of the power) for the BPS. A similar configuration is successfully used for 140 GHz 1 MW gyrotron on W7X.

2.3. Transmission Lines

The length of the TL increased with the EC system now installed in the RF building, but in the same time, a better configuration allowed to decrease the number of miter bends (from 1 to 5 miter bends less, depending on line), thus optimizing the losses with this new layout (see Fig. 3).

In order to maximize the space around the gyrotrons, they will run under a false floor in the RF building, go through the Assembly hall along the East wall and penetrate the tokamak building through its South wall. But due to the desire
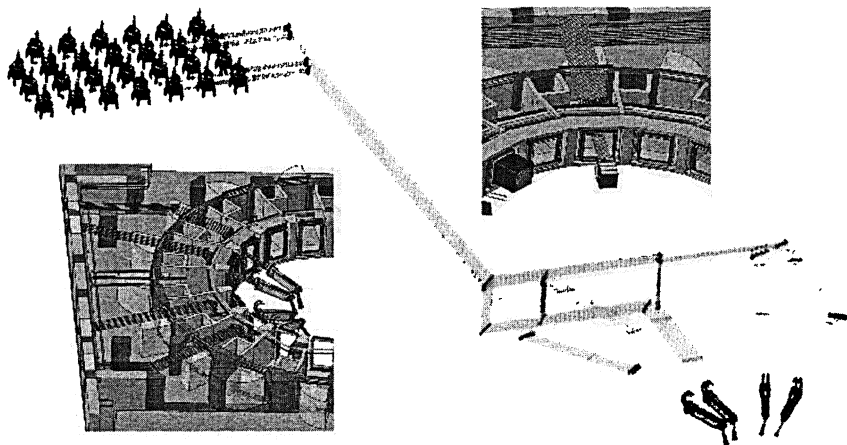
Fig. 3. Layout of the transmission lines

compact layout, some R&D activity is needed, in particular for developing a compact rotary switch, compatible with the 300 mm spacing between 2 adjacent lines, whereas only existing switch are today commercially available with linear actuator. This switch is required to either direct the wave in the equatorial launcher or in an upper launcher.

2.4. Launchers

Two types of launchers are planned to be installed on iter:

- 1 Equatorial Launcher (EL) mainly for heating and current drive, installed in port 14 (see Fig. 4); it will have 24 entries, organized in 3 rows of 8 beams. This launcher has 3 fixed mirrors and 3 steering mirrors in the toroidal direction, based on a mechanical system. The steering range will be $0 < \rho_T \leq 0.45$.

- 4 Upper Launchers (UL) mainly for MHD control (NTM and sawteeth stabilization), installed in ports 12, 13, 15, 16 (see Fig. 5). Each UL will be made of 8 entries, organized in 2 rows of 4 beams. In each launcher, 2 fixed mirrors and 2 steering mirrors in the poloidal direction (a lower one and an upper one) based on a pneumatic mechanism will allow to reach $0.3 < \rho_T \leq 0.86$. Some simplification has been done for the UL, with the decrease of the temperature limit from 240 C° to 200 for baking of main port plug structure, allowing a central single, passively cooled or heated wall instead of a complete double and actively cooled of heated wall.
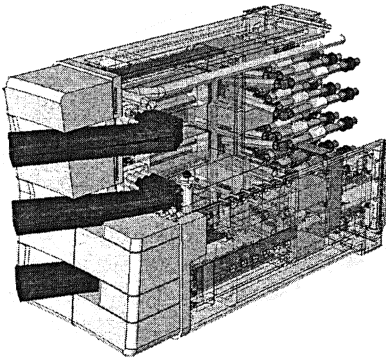
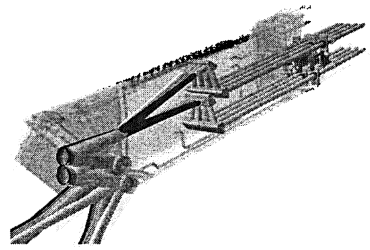275

Fig. 4. Design of the EL   **Fig. 5.** Design of the UL

For both launcher types, the in-situ maintenance of a torus window is now allowed, decreasing the exposure dose rate and avoiding the removal of the launchers in the hot cell for repair [4].

3. Schedule and commissioning

Several PAs (Procurement Arrangements) will have to be signed between IO and the DAs for the in-kind procurements, beginning in 2010 for the gyrotrons and ending in 2011 with the launchers. The launchers being Build to Print (B2P) specification, the detailed design has to be performed, prior to the PA whereas for the other components, only a conceptual validated design is required. The RF building is supposed to be available beginning of 2014, before the delivery of the 1st EC component mid 2014. Then, as soon as all services (including HV and cooling availability) are ready, beginning 2015, the 1st HVPS can be tested and commissioned. Several teams will have to work in the same time, one testing a HVPS in parallel with another one installing and testing a gyrotron (which could be done when one HVPS has been accepted), another one devoted to the installation of the transmission lines etc… Each launcher will have to be tested on ITER site, on a port plug test facility, prior to its installation on the tokamak. These tests will include cold and hot leak detection, baking cycles, but should exclude any high RF power tests, each component and subsystem within the launcher being tested and validated before the assembly. Up to 9 teams may work in the same time, before the completion of all ex-vessel commissioning planned beginning of 2017. The entire EC system may then be commissioned, without plasma, end of 2017 and on time for its commissioning on plasma as soon as a reliable and compatible plasma scenario is available (see Table).

The EC system is not on the critical path for the 1st plasma scheduled mid 2018 and even a 1-year margin still exists.

Main Milestones	Target date
5.2.1a Equatorial Launcher / JA PA	Jan. 2011
5.2.1b Upper Launcher / EU PA	Mar. 2010
5.2.2 Transmission Line / US PA	Apr. 2010
5.2.3 Gyrotron / EU/JA/RF/IN PAs	Sep. 2010
5.2.4 Power Supplies / EU/IN PAs	May 2011
Availability of RF building	Jan. 2014
Arrival of first EC sub-system delivery	June 2014
22kV, cooling availability in RF building (start of commissioning)	Jan. 2015
Arrival of first launcher for testing in port plug TF	Jan. 2015
First testing of PS-gyrotron-TL assembly	Jan. 2016
Completion of all ex-vessel commissioning	Feb. 2017
Completion of all launchers	April 2017
Completion of all gyrotron acceptance tests	July 2017
Completion of all commissioning procedures (without plasma)	Nov. 2017
Completion of all commissioning procedures (with plasma)	D1 + 6 months [1]
EC system ready for routine service	D1 + 9 months [2]

[1] Requires target plasma and diagnostics (such as ECE, magnetics and soft x-ray).
[2] 3 months will be required to analyze the data prior to routine operation.

4. Present issues

4.1. Start up configuration

Due to limited ohmic loop voltage available, ITER will need Electron Cyclotron assisted plasma breakdown. Originally the ITER startup scenario had the plasma initiated from the low field side limiter, the frequency of the breakdown EC system was then chosen to be 127 GHz with a resonance at around 7.2 m. But in the new breakdown scenario, the plasma initiation has moved from the outboard side to a more central location, which reduces the plasma inductance and transformer volt-seconds consumption. Shifting the location of the initial breakdown modifies the requirements of the EC start-up frequency, favoring a higher frequency than the present 127 GHz (see Fig. 6).
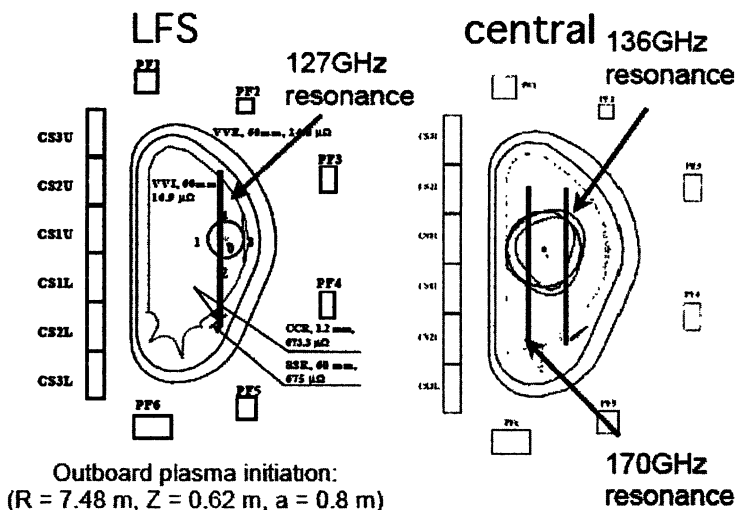
LFS   **central** 136GHz

Outboard plasma initiation:
(R = 7.48 m, Z = 0.62 m, a = 0.8 m)

170GHz resonance

Fig. 6. Start up configuration

The central breakdowns favors a frequency near 140 GHz, while the high field side (HFS) favors a frequency closer to 170 GHz. For the various envisioned breakdown scenarios and taking into consideration that ITER will operate at reduced field strengths, there is no single frequency that can satisfy the coincident location of the resonance and null center. But the breakdown capabilities of the 170 GHz system is actually equivalent or more favorable than the 127 GHz system for the central and high field side null locations. A decrease in the magnetic field moves the resonance inward, shifting the 170 GHz further from the null region, while decreasing the distance to the 127 GHz. This can be compensated by shifting the null region further inward following the resonance. Moreover, at half field strength, the 170 GHz system can be used as second harmonic breakdown (or H&CD applications) by changing the beam polarization [5].

Results on JT-60U, DIII-D and ASDEX-Upgrade have shown that EC breakdown is reliable even without the coincidence of the null and resonance location. It appears that as long as the resonance surface lies within the main vacuum chamber of the plasma, the EC system can provide the free electrons needed for initiating the plasma breakdown [6]. This relaxes considerably the requirements on the choice of the start up frequency. For example the 170 GHz system has either its O1 or X2 resonance in the vacuum chamber for any given choice of magnetic field strengths.

The main requirement is to have the resonance in the plasma chamber for all chosen operating magnetic field strengths. The 170 GHz satisfies this condition as well as provides a resonance in the null region during nominal and half field

operation (see Fig. 7). Therefore, the 170 GHz system is as useful as any other frequency and having dedicated gyrotrons only increases the complications and the cost of the EC system and should be avoided.
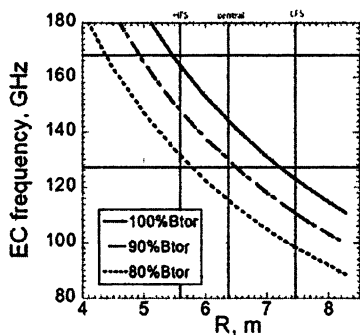

Fig. 7. Resonance of EC beams

4.2. Safety compatibility

Primary confinement system normally consists of 2 windows or of an equivalent system (window + valve + operational valve for diagnostics for instance). A second valve or window is needed to provide confinement and a window is normally preferred; however, for the EC system, the reliability of the EC window needs to be better assessed.

Then, for the EC launchers, the primary confinement will consist of a valve + + window, with an additional valve. The secondary confinement would be the port cell and the N-VDS (Vault Detritiation System) (see Fig. 8).
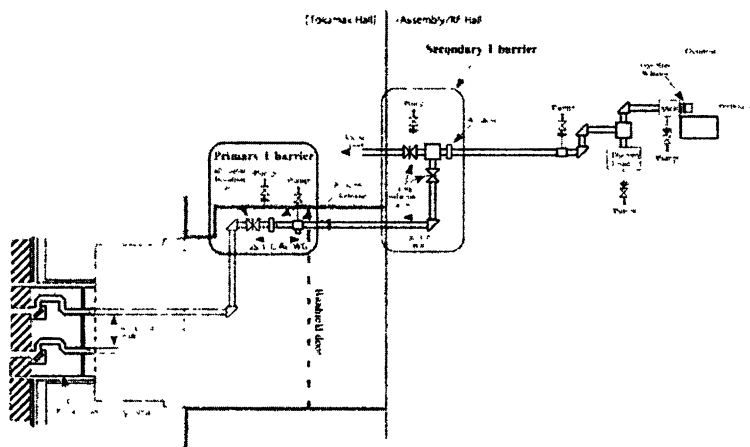

Fig. 8. General layout of the TL including tritium barriers

These components will be ready for the first phase, meaning the Hydrogen phase. For the following DD (Deuterium) and DT (Deuterium-Tritium) phases, to avoid spread of contamination during valve closing (~ 1 s), in case of a window break in a launcher, another window before the gyrotron window is recommended.

4.3. Risk analysis and mitigation strategy

The gyrotrons represents one of the two components presenting any risk to the EC procurement plan. At present time, only one gyrotron (developed by JAEA) has demonstrated a reasonable operating scenario as envisioned for ITER, achieving 170 GHz, 1 MW for 800 s [7]. However, this is only one gyrotron out of the three procurement packages planned for the H&CD system. The gyrotrons procured by RF (developed by GYCOM) already achieved 1 MW for more than 100 s [8], the limitation was due to the HVPS capabilities and the upgrade of the test bed end of this year will allow long pulse operation and demonstration. The most risky delivery is at present time the 2 MW gyrotrons, developed by EU as it is still under study [9]. To mitigate the risk, a conventional gyrotron developed from the existing 140 GHz tube can be developed, with a decision between the two designs to be made early 2010, pending to the 2 MW refurbished prototype results.

Four main critical issues associated with the gyrotron development can be stated:

- Frequency: The frequency needs to be 170 GHz ± 0.25 GHz to ensure all deposition profiles are superimposed in the plasma (requirement for MHD control via the UL).
- Output Power: The output power needs to be 1 MW, if not more. The EC system could benefit from higher power gyrotrons providing more delivered power for a fixed number of transmission lines and launcher entries.
- Pulse length: The gyrotron has to provide power during the flat top of the plasma discharge, specifications assume 3000 s.
- Reliability: The gyrotron must be able to provide the desired output power and pulse length with a very high regularity with encountering internal breakdown that could discontinue the use of that gyrotron for the remaining duration of the pulse.

This issue can become critical if the gyrotron cannot be restarted within the same plasma, in case of an internal breakdown, as it may occur at any time during the pulse length. To reduce the probability of an arc event, the gyrotron conditioning is a first option, which will be used to decrease the number of breakdowns down to an acceptable level. But even with conditioning, as 2 gyrotrons will at least share the same HVPS, in case of an arc, the power corresponding to 2 gyrotrons will be turned off and it becomes essential that within the same plasma, the gyrotron power can be turned on after an arc in a few seconds. It is of course even more important that the gyrotrons are highly reliable in order to optimize the

power coupled to the plasma during operation. Tests are planned to be performed next year in JAEA, using a 170 GHz prototype, to simulate 2 weeks of operation on iter and to study the present reliability and capability of restarting after internal breakdowns.

The second EC subsystem which presents a non negligible risk is the launchers, with a main issue associated to stray radiated power (both for equatorial and upper launchers). First, for both types, cyclic fatigue testing have been successfully performed on steering mechanism components prototypes and risk assessment and mitigation analysis of the millimetre wave systems of both upper and equatorial launchers have been made in a strong collaboration between F4E and JAEA. Low and high power tests are being performed on mock-ups or are under plans, but no full high power tests are envisioned, either on the equatorial or on the upper launcher. This would lead in additional costly R&D, whereas simulation of stray radiation injecting equivalent power in port plug launcher volume could already give pretty accurate results on the overall behaviour of the launchers at full power.

4.4. Interfaces definition

All interfaces are currently identified, some already defined (as for the vacuum vessel). The RF building will be frozen mid 2009, leading to the precise definition of all requirements needed for the EC system, such as the crane, the structural loads for HVPS and gyrotrons taken into account the layout of all subsystems...

Some internal interfaces need to be clarified, such as the use of MOU (Matching Optic Unit) instead of RFCU (Radio Frequency Conditioning Unit) which leads to a swap between the gyrotrons and the TL procurements and simplifies and decreases the cost of the whole EC system.

5. Conclusion

The integration of all the subsystems delivered by the different parties and the interface management of these sub-systems within the EC system and with the ITER auxiliary systems are in progress The EC system is on track for the first plasma on iter, planned mid 2018 at present time. The layout is being revised, progressing toward a more detail design level. Next activities, which already began will consist in resolving all issues associated with the EC system, such as the precise definition of both external and internal interfaces, the revision of the baseline documentation required for the PA signatures for all procurements. But due to the limitation in IO staff size, a strong partnership between IO and the DAs is required, to allow design improvements and to optimize the whole EC system.

In a more or less near future, some issues will have to be clarified, such as the 2 MW compatibility for the transmission line, required for the 2 MW EU

gyrotrons, such as the tritium containment philosophy which will need to be investigated, the feasibility, reliability and utility of CW dual frequency gyrotrons, high power combiners and some others...

References

1. Detailed Design Document 5.2 Electron Cyclotron Heating and Current Drive System.
2. *Henderson M. A. and Saibene G.* Critical interface issues associated with the ITER EC system, Nuclear Fusion 48 (2008) 054017.
3 *Kobayashi N. et al.* Design of Electron Cyclotron Heating and Current Drive System of ITER. Proc of 17th Topical Conf on Radio Frequency Power in Plasmas, Clearwater, Florida, 7–9 May, 2007, 413–416.
4. *Heidinger R. et al* Conceptual design of the ECH upper launcher system for ITER, this conference.
5. *Lloyd B et al.* Plasma Phys. Control, Fusion 38 (1996) 1627.
6. *Jackson G. L. et al* Plasma Initiation and Startup Studies in the DIII-D Tokamak with Second Harmonic Assist, 15th Joint Workshop on ECE and ECRH, 9–14 March, 2008, Yosemite NP, California, USA
7. *Sakamoto K et al.* Achievement of robust high-efficiency 1 MW oscillation in the hard-self-excitation region by a 170 GHz continuous-wave gyrotron, nature physics, v 3, 411–414.
8. *Denisov G. G., Litvak A. G., Myasnikov V. E. et al.* Development in Russia of high-power gyrotrons for fusion, 2008, Nucl. Fusion, 48 054007.
9. *Hogge J -P., Albajar F, Alberti A et al.* The Europian 2 MW, 170 GHz Coaxial Cavity Gyrotron for ITER, in Conference Digest of the 32nd Int. Conf. IRMMW, Sept. 3–7, 2007, Cardiff, UK, 2007, pp. 38–40.

OPERATION EXPERIENCE
WITH THE ASDEX UPGRADE ECRH SYSTEM

F. Leuterer and ASDEX Upgrade ECRH Team

Max Planck Institut für Plasmaphysik, EURATOM Ass., D-85748 Garching, Germany

The ASDEX Upgrade ECRH system works at a frequency of 140 GHz and comprises 4 gyrotrons with 0.5 MW / 2 s each (optionally 0.7 MW / 1 s), and 4 independent transmission lines and launchers. A major problem to be solved was the unfavorable magnetic situation at the place where the gyrotrons are installed. There were three reasons: first the AUG tokamak has an air OH-transformer with a far reaching poloidal magnetic field, second the fields from high current bars in the basement, and third the fields of adjacent cryomagnets. It affected the electron beam deposition in the gyrotron collector and the startup of the oscillation.

Two gyrotrons are fed from one high voltage power supply via a common series modulator. After solving some related problems a fairly reliable and flexible operation was achieved.

The transmission lines are combined quasioptical and corrugated waveguide lines working at normal air pressure. Although the gyrotron output beam passes two phase correcting mirrors to restore a Gaussian beam there are still indications of a non-Gaussian content. The average transmission losses of the lines are 12%.

A study of the performance in the AUG experiments showed that failure of individual gyrotrons was ≈ 5%, but system failure was much more.

Introduction

Construction of the ASDEX Upgrade ECRH system started in summer 1993. It works at a frequency of 140 GHz, corresponding to the second harmonic of the electron cyclotron frequency, and comprises 4 gyrotrons (GYCOM, Russia) with 0.5 MW / 2 s each (optionally 0.7 MW / 1 s) [1], and independent transmission lines and launchers. The system was planned and commissioned in close cooperation between the Institute for Plasmaresearch of the University Stuttgart, Germany, and the Institute of Applied Physics in Nizhny Novgorod, Russia. The first gyrotron of this system was installed in summer 1997, and the installation was completed in spring 2000. Since then two gyrotrons failed and were replaced by similar gyrotrons which were in use in the former W7-AS installation of IPP [2]. Each gyrotron is connected to separate transmission lines equipped with switchable mirrors which allow to direct the microwave beam to a high power load at the line entrance or to a calorimetric load at the end of the line. Thus in the everyday work all gyrotrons can be started up simultaneously, and after a sequence of about ten pulses with increasing rf-energy, ranging from 65 kV / 10 ms to 73.5 kV / 1.6 s, we are ready for participation in tokamak experiments.

However, before reaching this performance we had to overcome some unexpected difficulties which are described in the following sections. First we describe problems with magnetic perturbations to the gyrotron operation, then we describe some observations concerning gyrotron operation and transmission line

alignment, and finally we discuss the performance of the whole system. A more extensive summary about our operating experience can be found in [3].

Magnetic perturbations affecting gyrotron operation

Magnetic fields emanating from the tokamak

An apparently convenient place for the ECRH installation was found close to the tokamak. The distances of the gyrotrons from the tokamak axis are between 14.8 m and 18.8 m, and therefore the transmission lines are only between 20 m and 25 m long. However, since ASDEX Upgrade (AUG) does not have an iron transformer to confine the magnetic flux, there is a far reaching poloidal magnetic field from the tokamak. At the place of the gyrotron which is closest to the tokamak this field can be up to 30 Gs as calculated on the basis of a maximum possible AUG performance with $I_p = 1.6$ MA. This field varies with time, approximately following the current in the ohmic heating transformer coil, and it switches sign during a discharge. The gyrotrons are located such that the cavity is at the level $z = 0$, i.e. at the torus midplane, where we expect a minimum horizontal component of the poloidal field in a double null tokamak configuration. In addition to the tokamak stray magnetic field we have more localized stray magnetic fields, which were ≈ 50 Gs at the level of the cathode, emanating from high current bars feeding the tokamak coils, which are installed in the basement underneath the gyrotrons. The latter fields were screened by a layer of 2 cm of soft iron placed on the floor. Another layer of 1 cm of soft iron was placed on the ceiling of the gyrotron hall with the intention to reduce the horizontal comonent of the stray field. The calculated horizontal component was then ranging from zero at the bottom of the gyrotron hall to ≈ 5 Gs at the top of the collector. This was considered as tolerable. Fig. 1a shows field lines as calculated with the presence of the iron plates, and Fig. 1b shows the variation of the horizontal component along the height of the gyrotron. In experiments up to now we had only about 2/3 of the calculated maximum value of the tokamak stray field, i.e. a horizontal component of ≤ 3.5 Gs.

Although this seems negligible compared to the 5.4 T magnetic field in the cavity region of the gyrotron, it has a strong effect on the electron beam deposition on the collector inner surface. This is sketched in Fig. 2a. An unperturbed hollow beam hits the collector along a horizontal ring. However, with an additional external horizontal magnetic field one side moves up and the other side down. This happens already at small fields of a few Gauss. The vertical component of the stray field moves the deposition further up or down, enhancing the displacement on one side and partly compensating it on the other side.
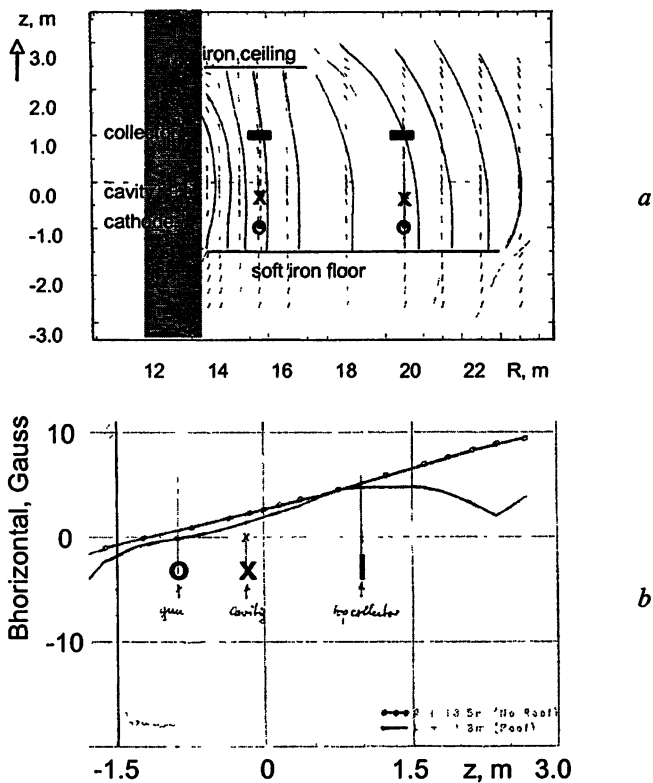
Fig. 1. Magnetic field distribution in the gyrotron hall (*a*),
and vertical component variation along two extreme gyrotron positions (*b*)
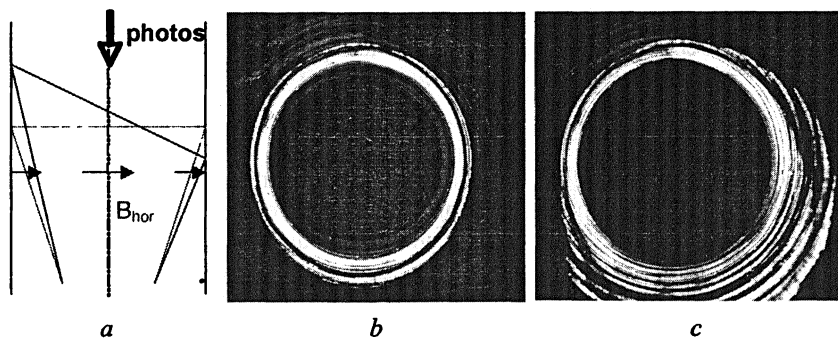

Fig. 2. Scheme of field line distortion due to an external horizontal B-field (*a*)
and electron beam deposition on the collector surface at a constant sweep coil current
of 24 A with (*b*) and without (*c*) an AUG stray magn. field

285

Figs. 2b and 2c show an example recorded with a dummy tube. This is an actual gyrotron where the top of the collector is cut away and replaced by a vacuum window for visual observation. The inner surface of the collector is covered with a fluorescent layer. With a weak electron beam of $\approx$ 1.5 kV / 1 mA the deposition becomes visible. In Fig. 2b and 2c the current in the sweep coil is constant at 24 A and the beam deposition is not yet at the top of the collector. The photo in Fig. 2b shows a view into the dummy tube in absence of a AUG stray field, while in Fig. 2c a stray field is present. On one side the beam is shifted up by $\approx$ 15 cm while on the other side it remained nearly at the same position. Results taken at various constant sweep coil currents are shown in Fig. 3a. This effect was analyzed using a paraxial approximation for the magnetic field near the gyrotron axis together with an approximation for the perturbing magnetic field. The result of this estimate is shown in Fig. 3b and is in agreement with the experimental observations. The gyrotrons were therfore operated with a reduced amplitude of the sweep coil current, such that the electron beam deposition did not hit uncooled collector areas.
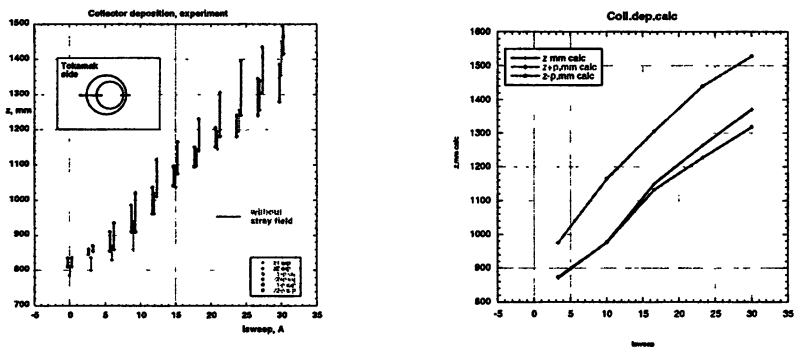
Fig. 3. Experimental and calculated spread of beam deposition in the collector of the dummy tube as a function of sweep coil currnt

Magnetic field from the adjacent cryo-magnet

Another source of magnetic perturbation comes from adjacent cryo-magnets. In the AUG case the distance between the axis of adjacent gyrotrons is 2.8 m, and the magnetic field from the adjacent magnet along the axis of the other gyrotron is $\leq$ 4 Gs, with a horizontal component ranging from -2 Gs near the cathode to $+3$ Gs at the top of the collector. This did lead to a similarly strong deformation of the deposition in the collector as seen in Fig. 4. This perturbation could not be tolerated in addition and therefore two one-turn rectangular shaped compensation coil were attached to the collector to compensate on average the horizontal component of the perturbing field. The design was such that these coils could be

286

driven with the current flowing through the adjacent cryo-magnet. Thus, whenever one magnet was switched on the compensation for the other gyrotron was automatically active [4].
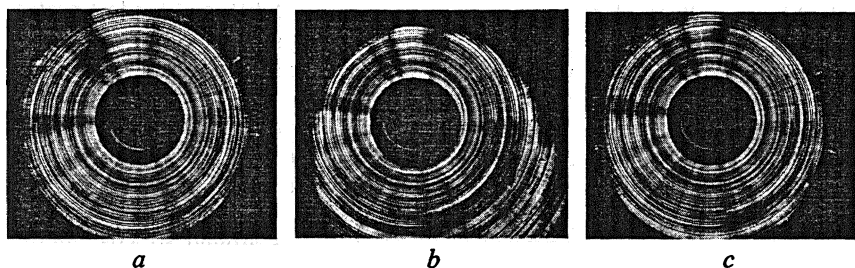

Fig. 4. Electron beam deposition along the collector surface of the dummy tube with a 0 – 28 A sweep coil current: *a*) without, *b*) with an active adjacent cryo-magnet, and *c*) with active adjacent magnet and compensation coil

Effect of perturbing magnetic field on the gyrotron oscillation

Not only the beam deposition in the collector is influenced by the tokamak stray magnetic field, but also the startup of the gyrotron oscillation can be affected. In one of our gyrotrons we observed that in modulated pulses some individual rf-pulses were missing, although high voltage was applied. An example is shown in Fig. 5. This only occured when the gyrotron was operated with AUG pulses, but never in test pulses outside of the AUG program. Simulating vertical perturbation field with cables wound around the oil tank we could confirm that this was due to the vertical component of the stray field. We avoided this effect by setting the gun coil current to a different value.

Calculations of the field line distortion in the gyrotron due to the horizontal component of the AUG poloidal field, as done for Fig. 3, show a displacement of the magnetic axis from the geometrical axis in the cavity by 0.02 mm, which cannot be compensated with the gun coil, but is obviously tolerable.
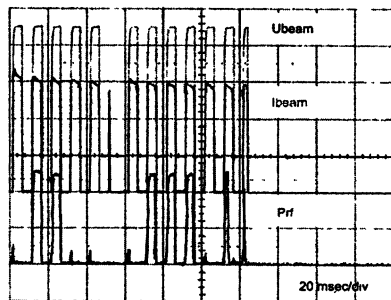

Fig. 5. Missing rf pulses due to hampered gyrotron startup as a consequence of the vertical component of the AUG stray magnetic field

287

Gyrotron operation

In our installation two gyrotrons are fed via one common tetrode modulator. This modulator serves to switch the gyrotrons on and off, to feedback control the applied beam voltage of up to 73.5 kV to a ripple < 0.5 kV, and for fast protection of gyrotrons and transmission lines in cases of arcs (≤ 5 µs). By only partly reducing the beam voltage we can realize step functions in the output power and also a fast modulation with frequencies up to 30 kHz.

The beam current decreases during a 2 s pulse from initially close to 40 A down to ≈ 26 A. Towards the end of a pulse the gyrotron can therefore end up in a cutoff or a mode jump, or it can end up in an electron beam instability. Such an instability shows up in a very noisy current signal, in a decreased output power as seen in Fig. 6a, and in the emission of low frequencies around 30 MHz and its harmonics. In one case it happened that when only one of gyrotrons was connected to the modulator this instability did not occur, but when both gyrotrons were connected it did occur. Apparently the external impedance between cathode and anode is important. Capacitors connected across the cathode–anode gap at the gyrotron did suppress this instability.

a
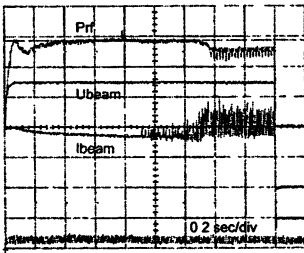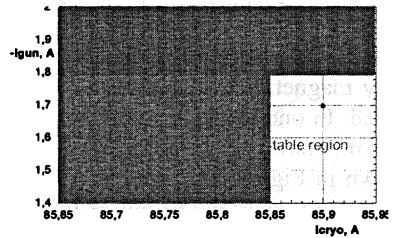
b

Fig. 6. Gyrotron pulse with 1.8 s showing signs of electron beam Instability (*a*), operation limits due to cutoff and beam instability (*b*)
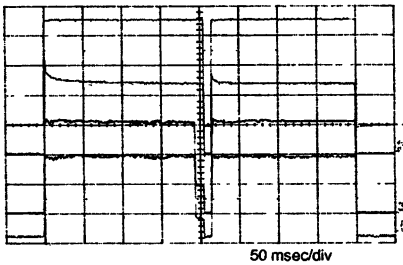

50 msec/div

Fig. 7. Detector signal indicating a cutoff or a mode jump. After 10 ms the high voltage is switched off and on again and the pulse continues regularly

Nevertheless a restricted range of operation remained, Fig. 6b. A cutoff or a mode jump can be detected with a detector monitoring the output power whose signal drops to zero or a much lower level although the applied voltage stays constant. Such a situation should not persist for a long time. In such a case we switch the high voltage off after 10 ms, and after another 10 ms we switch it back on, as in Fig. 7. This not only protects the gyrotron but saves many AUG pulses for physics evaluation.

Transmission lines

The transmission lines have a quasi-optical section followed by a waveguide section operated at normal air pressure [5]. The scheme is shown in Fig. 8. The housing of the quasi-optical section has a great fraction of absorbing walls, paint and concrete, to absorb any side lobes and diffuse radiation leaving the gyrotron in addition to the main beam.
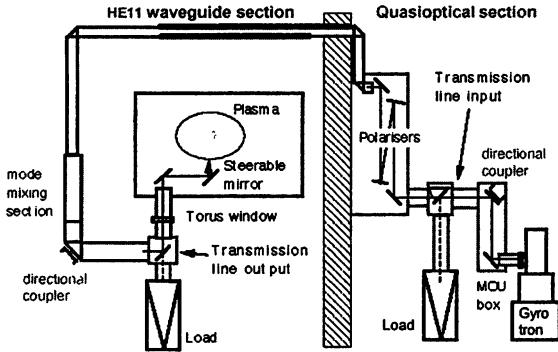

Fig. 8. Transmission line scheme with quasi-optical and waveguide sections, and positions of loads and directional couplers

The first two mirrors after the gyrotron are phase correcting mirrors designed to restore a Gaussian beam [6]. In the second mirror there is also a directional coupler to monitor the output power [7, 8]. They are followed by a switchable mirror to direct the beam into a load, or to let him pass towards two polarizer mirrors designed to allow any elliptical polarisation. Then the beam is focused into an 87 mm I.D. HE11 corrugated waveguide. The alignment is done with the help of thermo-paper at pulse lengths up to 20 ms, or with liquid crystal foils attached to a layer of Eccosorb at pulses up to 2 ms. The latter gives a better indication of the boundary contour of the beam as as seen in Fig. 9. With these in field techniques the beam axis can be determined within ±2 mm.
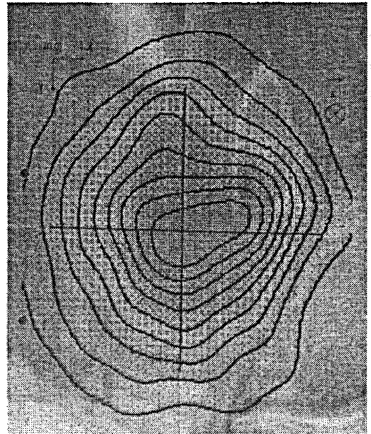

Fig. 9. Photo of a beam pattern on a liquid crystal foil overlayed with the calculated intensity pattern after phase correction

We have numerically studied the impact of misalignment of the phase correcting mirrors on the beam quality [9]. Along the beam a variation of the distance between the two mirrors, which is nominally 716 mm, by ± 20 mm is not critical. But perpendicular to the beam a few millimeters reduce the quality of the beam considerably. For example, shifting the second mirror by 4 mm results in a reduction of the Gaissian beam content from 99.9% to 96.0%, while a displacement of the first mirror by 4 mm leads to a beam with only 91.7% Gaussian content. A few percent of non-Gaussian content can lead to a deformation of the wanted circular intensity contours of the beam. This can actually be seen in Fig. 9 where the liquid crystal plot is overlayed by the calculated intensity contour of the phase corrected beam with 98.5% Gaussian content. In the waveguides such a beam can lead to the excitation of higher order modes.

At the end of the waveguide line there is another switchable mirror to direct the beam either to the plasma or to a calorimetric load. From calorimetric measurements of the power at the entrance and at the end of the transmission lines we determined an average transmission loss of 12% for our 4 lines with ≈ 10 mirrors and mitrebends each. Additional losses of ≈ 7% arise from the BN-torus window and the mirrors in the launching structures.

System performance

Requested by EFDA we provided an overview of the performance of our system in plasma pulses [10]. For this we considered only AUG pulses from May 1998 to May 2006 for which ECRH was requested. Tests into loads are not included. The total number of these pulses was 1806. The number of gyrotrons requested in these pulses was quite different, because either not all gyrotrons were available or because the requested power was low. Included are pulses in nominal and optional regimes, cw pulses as well as modulated pulses.

Of these   862 pulses were successfull as planned

944 did not perform as planned

Among the latter there are

387 pulses where ECRH was not started at all (mainly because the plasma was not properly started)

97 pulses in which ECRH was interrupted by external reasons (like plasma disruptions)

460 pulses in which ECRH was interrupted by reasons within the ECRH system. Many of these were still useful for physics evaluations.

Reasons for system failure were gyrotron problems, transmission line problems, subsystem problems, control system problems, or high voltage problems.

A clearer picture is obtained when we look at the performance of each individual gyrotron as shown in Fig. 10 for one example. The other three gyrotrons behaved similar. Gyrotron failure was only ≈ 5%, whereas system failure was much more.
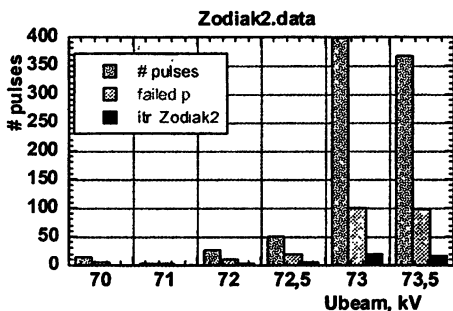
Fig. 10. Summary of pulses at different beam voltages with gyrotron Zodiak 2.
Of ≈ 23% failed pulses only ≈ 5% failures were due to the gyrotron.

Conclusion

Gyrotrons are very sensitive to magnetic perturbations. External magnetic fields perpendicular to the gyrotron axis of a few Gauss only severely distort the deposition of the electron beam in the collector. Great care has therefore to be devoted to the site selection and the site preparation when planning a new ECRH system. In addition, not only a reliable gyrotron performance, but also reliable system performance, with reliable failure detection and identification in the hostile environment of a tokamak and its subsystems, will be a big issue for a system like the one planned for ITER.

References

1   *Myasnikov V. et al.* Proc 3rd Int. Workshop on Strong Microwaves in Plasmas, Nizhny Novgorod 1996, V. II, 577.
2.   *Erckmann V. et al.* Nucl. Fusion 43 (2003) 1313.
3.   *Leuterer F. et al.* to be published in Fusion Science & Technology Jan. 2009
4.   *Leuterer F. et al.* Fus. Eng. Design 53 (2001) 485.
5.   *Tumm M., Kasparek W.* IEEE Trans. Plasma Science PS-30 (2002) 755.
6.   *Chirkov A. et al.* Optics Communications 115 (1995) 449.
7.   *Empacher L. et al.* Proc. 20th Conf. Infrared and Millimeter Waves (1995) 473.
8.   *Foerster W. et al.* Fusion Technology 1994, Elsevier Science B.V. Amsterdam (1995) 485.
9.   *Leuterer F. et al.* Fus. Eng. Design 56–57 (2001) 615
10. EFDA Technology Workprogramme 2006, task TW6-TSL-005.

EVOLUTION OF SMALL-SCALE TURBULENCE AND ANOMALOUS ELECTRON TRANSPORT IN DYNAMIC TOKAMAK EXPERIMENTS

E. Z. Gusakov[1], A. D. Gurchenko[1], D. V. Kouprienko[1], S. Leerink[2],
A. B. Altukhov[1], V. V. Dyachenko[1], L. A. Esipov[1], J. A. Heikkinen[3],
S. I. Lashkul[1], A. Yu. Stepanov[1]

[1] Ioffe Physical-Technical Institute of the RAS, St.-Petersburg, Russia
[2] Euratom-Tekes Association, Helsinki University of Technology, Espoo, Finland
[3] Euratom-Tekes Association, VTT, Espoo, Finland

The results of systematic investigations of the small-scale turbulence performed in dynamic fast current ramp up and lower hybrid (LH) heating experiments at FT-2 tokamak are reported Both frequency and wave number (q) spectra are measured with correlative enhanced scattering diagnostics It is found that during the dynamic discharge the turbulence component identified with the dissipative TEM mode possesses a wide q-spectrum which could be described by universal exponential dependence in the range of 3–4 orders of amplitude characterized by two parameters – the turbulence level and scale length. Both parameters are found to decrease substantially when the shear of the poloidal plasma rotation increases at plasma periphery. Simultaneously suppression of anomalous electron transport is observed in the experiment. On contrary, the q-spectrum of the component, identified with the ETG mode, looks very different from exponential. It is characterized by pronounced maximum at wave number corresponding to the largest ETG instability growth rate. Its behavior, in agreement with the GS2 code predictions, in the dynamic LH heating experiment is correlated with the ratio of electron temperature and density scale lengths, but not with the electron thermal diffusivity.

Introduction

The fine scale drift wave turbulence excited due to the electron temperature gradient (ETG) mode instability well known since 60th [1], is discussed nowadays in theory as a possible candidate for explanation of the anomalous electron energy transport in tokamak plasmas [2–6]. According to theoretical and computational analysis of [2, 3], performed using gyrokinetic approach in flux tube geometry, this turbulence, possessing the shortest wave length in the electron gyroradius range, in contradiction to the quasi linear theory estimations, can cause a substantial heat flux due to formation of streamers at the nonlinear stage of its evolution. In spite of the fact the predictions of different theoretical models not always coincide and have not been checked experimentally yet, the ETG mode turbulence is often used for interpretation of experimental data on anomalous electron transport. The lack of experimental data on the ETG mode turbulence was caused by its extremely small scale, complicating investigation with diagnostic tools currently used in tokamaks. Nevertheless the mentioned theoretical breakthrough have stimulated the development of new experimental techniques based on the microwave back and side scattering which resulted in observation of

Fig. 1. FT-2 poloidal cross section: *1* – movable antennae; *2* – magnetic surface; *3* – UHR. Probing beam: circles – 0 dB; triangles – 1.5 dB; rhombuses – 3 dB power suppression levels.
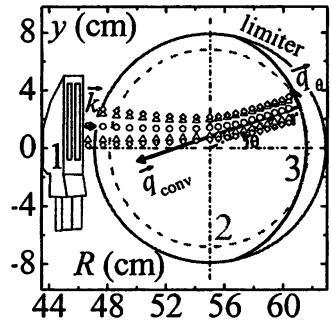
ETG-mode scale fluctuations at measurable level in FT-2, DIII-D and NSTX tokamaks [7–11]. Just recently in dynamic plasma heating experiments on these machines the enhancement of the small-scale turbulence level with growing electron temperature gradient [12–14] and in particular its correlation to the ETG instability threshold excess [12, 14] has been demonstrated allowing identification of the observed turbulence as the ETG mode.

In the present paper we report results of systematic investigations of the small-scale turbulent modes performed in dynamic current ramp up (CRU) and lower hybrid (LH) heating experiments at FT-2 tokamak using the correlative enhanced scattering technique (CES).

The correlative enhanced scattering technique

The enhanced scattering (ES) or the upper hybrid resonance (UHR) backscattering (BS) technique [15] utilizes for local diagnostics of small-scale plasma fluctuations the effect of growth of wave vector and electric field of the probing extraordinary (*X*-mode) wave in the UHR, where condition $f_i^2 = f_{ce}^2(R) + f_{pe}^2(r)$ is fulfilled for the probing frequency f_i (R and r are tokamak major and minor radii, f_{ce} and f_{pe} are electron cyclotron and plasma frequencies, correspondingly). To provide the UHR accessibility in tokamak experiment the probing wave is launched from the high magnetic field side of the torus under conditions when the electron cyclotron resonance layer exists somewhere in a plasma. The ES diagnostics benefits of the probing wave field and radial wave number q_r growth leading to high localization, enhanced sensitivity to submillimetric scales and substantial frequency shift of the backscattered wave due to so called Enhanced Doppler effect [11, 16, 17], associated with a finite projection of the large probing wave vector, perpendicular to the UHR surface, onto the poloidal direction in the point shifted from the equatorial plane by y

$$k_\theta = (2k_{\theta*} + k_r \cos\psi_*)y/y_*. \qquad (1)$$

Here $k_{\theta*}$ is a poloidal wave number out of the UHR at the probing beam axis possessing vertical displacement y_*; ψ_* is the angle between UHR and magnetic surface there.

The probing and back scattering wave's radial wave numbers k_r and k_{sr} grow rapidly in the vicinity of the UHR. Therefore the back scattering Bragg condition ($q_r = k_r + k_{sr} = 2k_r$) could be easily satisfied for small-scale fluctuations in wide q_r range.

According to [15], the ES frequency spectrum $P_{ES}(\Omega)$ is determined by the turbulence spectrum $|n|^2_{q_r,q_\theta,\Omega}$, ES efficiency $S_{ES}(q_r)$, as well as by the antenna beam power distribution on the UHR surface in the vertical direction $F^2 = \exp[-2(y - y_*)^2\rho^{-2}]$ and is given by an integral over poloidal and radial fluctuation wave numbers q_θ and q_r

$$P_{ES}(\Omega) = \int I_{q_r,\Omega}dq_r = \int |n|^2_{q_r,q_\theta,\Omega}\, S_{ES}(q_r)F^2(y)dq_\theta dq_r, \qquad (2)$$

here we also assumed the relation

$$q_\theta = (2k_{\theta*} + q_r\cos\psi_*)y/y_* \qquad (3)$$

between poloidal and radial wave numbers q_θ and q_r of fluctuations contributing to the backscattering in the UHR and vertical displacement y of the point where it happens following from (1) and the BS Bragg condition. The ES technique is only sensitive to fluctuations possessing wavelength smaller than half probing wavelength. The ES efficiency $S_{ES}(q_r)$ shown in Fig. 2 for the FT-2 experiment parameters experiences a sharp maximum at $q_r \approx 2(2\pi f_{ce}/c)(c/V_{Te})^{1/2}$ which corresponds to backscattering in the linear conversion point [15]. A significant drawback of the ES diagnostics in the standard approach [15] is poor q-resolution, which however may be improved using the correlation technique utilizing simultaneous probing by different frequencies and further correlation analysis of the measured signals [18].

Fig. 2. ES efficiency for $T_e = 90$ eV

According to [18], the cross-correlation function (CCF) of two ES signals at probing frequencies f_1 and f_2 is related to the ES spectrum $I_{q_r,\Omega}$ via Fourier transform

$$CCF_\Omega(f_1, f_2) = \int I_{q_r,\Omega} \exp\left\{iq_r\left[(f_1 - f_2)\partial x_{UH}/\partial f\right]\right\}dq_r. \qquad (4)$$

This relation allows inversion and determination of $I_{q_r,\Omega}$ based on experimental data. Moreover, as it was shown in [8], the q_r-spectrum of turbulent fluctuations, as well as their phase velocity may be reconstructed from the CES diagnostics measurement as a result of fitting procedure under natural assumption that the turbulence spectrum is described by expression accounting for the broadening of the drift wave dispersion relation due to nonlinear effects

$$|n|^2_{q_r,q_\theta,\Omega} = \frac{|n|^2_{q_r,q_\theta}\sqrt{\pi}}{\Delta q_\theta}\exp\left[-\left(q_\theta - \frac{\Omega}{V_\theta}\right)^2 \middle/ (\Delta q_\theta)^2\right]. \qquad (5)$$

Two-component ES spectrum investigation in the ohmic discharge

The experiment was performed in ohmic discharge at the FT-2 tokamak possessing major radius $R_0 = 55$ cm and limiter's radius $a = 7.9$ cm, toroidal field 2.2 T, plasma current 32 kA, density $n_e(0) = 3 \cdot 10^{19}$ m^{-3}, electron temperature, measured by multipass Thomson scattering diagnostics, $T_e(0) = 530$ eV. The movable focusing double antennae set, allowing off equatorial plane plasma X-mode probing with the maximal vertical displacement $y_a = \pm 2$ cm was installed at FT-2 at the high magnetic field side [8] (see Fig. 1). The beam radius at the UHR position is $\rho \approx 0.7 \div 0.9$ cm, as calculated using the beam tracing code. Both emitting and receiving antennae are narrow along the toroidal direction and thus produce wide toroidal wave number spectra. The probing is performed in the frequency range $53 \div 72$ GHz at low power level of 20 mW. The coupling of emitting and receiving antennae is less than 40 dB.

In the present experiment the probing wave UHR layer was situated at $r > 4$ cm, where necessary condition for the ETG mode excitation $L_T < 1.25 L_n$ following for the FT-2 parameters from analysis [1, 3] was fulfilled (L_T, L_n are electron temperature and density gradient scale lengths). The corresponding T_e and n_e profiles are shown in Fig. 3. The ES spectra obtained at $y_a = 1.5$ cm for different probing frequencies (UHR positions) are shown in Fig. 4. The ES spectrum is weakly shifted in the electron diamagnetic drift direction and symmetric at the edge, whereas its shift and asymmetry grows, when moving inward. A pronounced "wing" is observable at frequencies less than -2 MHz (HF domain) already at $r = 6$ cm. At $r = 5.6$ cm the second line possessing more than twice higher frequency shift (-2.5 MHz) appears in the spectrum. At $r = 5$ cm its amplitude exceeds the amplitude of the first line. The amplitude of the low frequency (LF) satellite decreases when moving inward the plasma whereas the high frequency (HF) satellite's amplitude increases. (The non-shifted component in spectrum 4 corresponds to direct coupling of emitting and receiving antennae which appears visible at small ES power.) The observation of a doublet in the ES signal is most likely associated with coexistence of two different drift modes in the FT-2 plasma. To check this supposition and to identify modes the q-spectrum of turbulence was investigated by the CES diagnostics [12]. Two signals at close probing frequencies
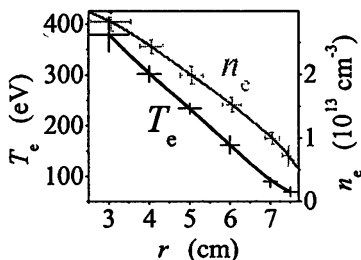

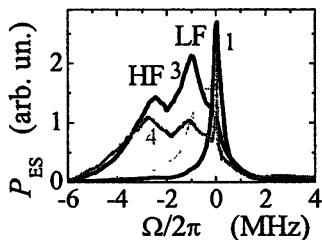**Fig. 3.** Electron density and temperature profiles

Fig. 4. The ES power spectra P_{ES} for $r = 7.9$ cm (*1*), 6 cm (*2*), 5.6 cm (*3*) and $10 P_{ES}$ for 5 cm (*4*)

with difference $|f_2 - f_1| = \{10, 20 \ldots 400\}$ MHz, corresponding to two slightly separated UHR layers in plasma, where the ES by fluctuations with low frequency $\Omega = 2\pi f_\Omega$ occurs, were measured simultaneously using the asymmetric correlation scheme [8]. Probing was performed on the discharge to discharge basis. The data acquisition of the ES si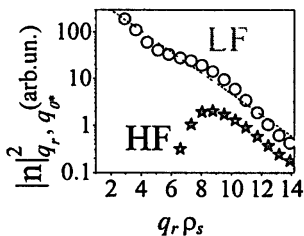gnal for all the discharge duration was performed at 20 MHz clock rate of 12-bit ADC. Frequencies higher than 6 MHz were filtered out. Statistical averaging of the data was performed typically over samples of 0.8 ms duration. The reconstructed q_r-spectra for the LF and HF ES frequency spectrum components are shown in Fig. 5 in semi logarithmic scale. As it is seen, the LF component spectrum is reconstructed in a wide q_r-domain. It is growing towards small wave numbers and may be well fitted by the linear dependence, whereas the HF component spectrum is localized in the high wave number region. It possesses maximum for scales most easily excited by the ETG instability (at $q_r \rho_s = 8$). The reconstructed poloidal velocity of the HF component directed in the electron diamagnetic drift direction is a factor of 2 higher than the LF component velocity ($V_\theta{}^{LF} = 2.7 \pm 0.3$ km/s; $V_\theta{}^{HF} = 5.6 \pm 0.5$ km/s). The poloidal wave numbers corresponding to the LF and HF satellites are $q_\theta{}^{LF} = 23$ cm^{-1} and $q_\theta{}^{HF} = 27$ cm^{-1}. The HF ES signal component radial distribution is different from that of the LF component, as it is seen in Fig. 6 where amplitudes of the LF and HF spectral satellites normalized to the ECE emission level are plotted against minor radius. The HF component is growing towards the centre of discharge whereas the LF component is growing in the opposite direction. The dependence of the HF and LF components on the vertical displacement of the antenna set and therefore, according to (1), on the fluctuation q_θ is also different. As it is seen in Fig. 7, the HF component is rather growing with q_θ, whereas the LF component is definitely decaying.
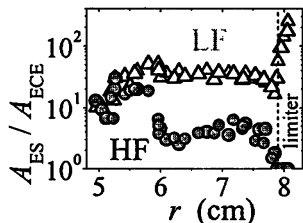
Fig. 5. q_r spectra of LF and HF components

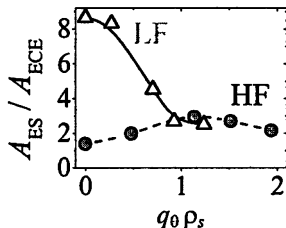**Fig. 6.** Normalized LF and HF component amplitudes versus radius

Fig. 7. q_θ dependence of LF and HF components

The differences in the HF and LF ES signal spectral component behavior were also studied in dynamic LH heating experiment.

A different behavior of the UHR BS spectrum LF and HF components was observed in the LH heating experiment at FT-2, where 180 kW of RF power was launched in plasma at frequency 920 MHz during 6 ms initiating transition to the improved confinement regime [19]. The HF component behavior in these dynamical experiments was sensitive to the variation of n_e and T_e profiles. As it is seen in Fig. 8a, enhancement of the HF component of the ES spectrum during the LH heating pulse at $30 \div 35.7$ ms is only observed for $r < 6.5$ cm when and where the ETG instability condition $L_T < 1.25 \, L_n$ is satisfied (see Fig. 8b). After the RF pulse when the ETG instability condition is definitely violated, the HF component is suppressed all over the observation volume. (The approximate threshold condition $L_T < 1.25 \, L_n$ derived in [1, 3] was confirmed for FT-2 experimental parameters using the GS2 code. See for example in Fig. 8c the comparison of growth rate dependencies on q_θ computed for points A and B shown in Fig. 8b.) This observation provides a final confirmation to the ETG instability origin of the observed HF turbulence component.

Unlike the HF component, the LF part of the ES signal is not directly sensitive to the relative gradient scale lengths variation. As it is seen in Fig. 9, it is rather correlated to the temporal behavior of the effective

Fig. 8. Evolutions of the (a) HF signal power normalized to its OH value; (b) the ratio of L_n and L_{Te}; (c) growth rates and frequencies for linear modes at A and B points. (ρ_i – ion gyroradius)

electron thermal diffusivity χ_e determined from the experimental T_e and n_e profiles with the help of ASTRA transport code. The level of ES signal LF component is decreased simultaneously with χ_e just after the RF power is on. The growth of later at the very edge of plasma preceding the RF pulse termination is also correlated to the growth of the ES signal observed in this region. It is important to note, that as it was shown by CES technique measurements before and after the RF pulse, the typical q_r of LF fluctuations contributing to the ES signal increased during the pulse. Therefore accounting for the growing dependence of ES efficiency on q_r we may conclude that the growth of the LF component of the ES signal corresponds to even stronger increase in the turbulence level. It is interesting that the q_r-spectra of the LF component plotted in semi logarithmic
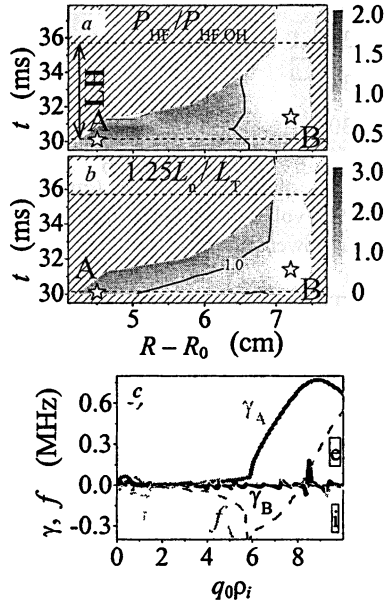
scale both before and after the RF pulse, as the spectrum in Fig. 5, may be well fitted by the linear dependence (see Fig. 10).
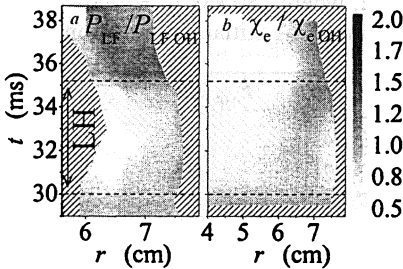

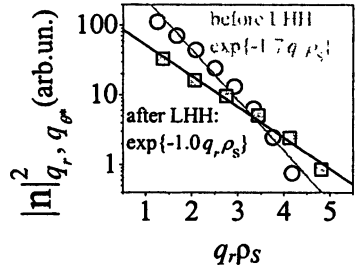**Fig. 9.** Evolution of the normalized (*a*) LF signal power and (*b*) χ_e

Fig. 10. LF q_r-spectra before and after LHH

These universal exponential spectra of the small-scale LF turbulence component are routinely observed at the FT-2. Evolution of their parameters was studied in the CRU experiment leading to improvement of the energy confinement in the electron channel.

Evolution of the exponential turbulence wave number spectra in the CRU experiment

The measurements were carried out in fast CRU experiment (20 MA/s from 22 kA to 32 kA) (Fig. 11). The important feature of this scenario is suppression of anomalous electron transport observed at the current relaxation stage. Namely, investigation of electron and ion temperature, electron density profiles and radiation losses evolution together with ASTRA code modelling allows us to conclude that the effective electron thermal diffusivity coefficient χ_e was suppressed in the discharge at 4÷6 ms after CRU and, in particular, decreased by a factor of 2 at plasma periphery. It should be stressed that the χ_e behaviour there (Fig. 12) is well correlated with the ES signal suppression by 30÷40 %. The level of the ES signal LF component power integrated in [−2 ... +2] MHz frequency band was measured for different UHR radial positions from $r = 5.5$ cm till 7.5 cm. The evolution of obtained profiles normalized to the profile at 29 ms (before CRU) is shown in Fig. 12*b*. (The HF ES signal component "wing" was not pronounced at the plasma edge in the 22 kA discharge.)
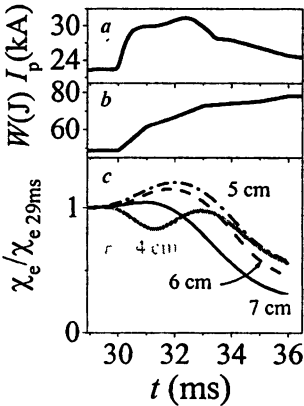

Fig. 11. Dynamics of (*a*) plasma current, (*b*) energy content and (*c*) χ_e
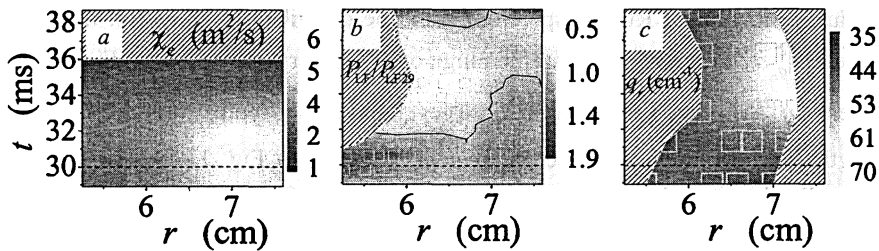
298

Fig. 12. Temporal variation of profiles (a) χ_e, (b) normalized LF signal power (gray squares: measuring points; solid black curves: $P_{LF}/P_{LF}(29\ ms) = 1$), (c) q_r at ES spectrum maximum.

Unfortunately, the ES signal suppression could not be directly interpreted in terms of the density fluctuation level drop, because of the strong ($S_{ES} \sim q_r^3$) dependence of the ES efficiency on the turbulence radial wave number. Nevertheless, investigation of the ES $I_{q_r,\Omega}$ spectrum evolution during the CRU experiment provides additional arguments in favour of the turbulence suppression. Namely, as it is clearly seen from comparison of Fig. 13a and Fig. 13b, the $I_{q_r,\Omega}$ spectrum determined at $r = 6.2$ cm experiences a substantial shift to higher q_r after CRU. The approximation surface $q_r (r, t)$ demonstrating the evolution of q_r values corresponding to ES $I_{q_r,\Omega}$ spectra maximum is shown in Fig. 12c. Since the drop of the ES signal (Fig. 12b) is accompanied by increase of q_r from 40 cm^{-1} till 70 cm^{-1} (Fig. 12c) and thus by strong increase of the ES efficiency, one could conclude that the real drop of the turbulence level was even higher than the ES signal power suppression, observed in the experiment. In addition to the above rough analysis we have also recon-
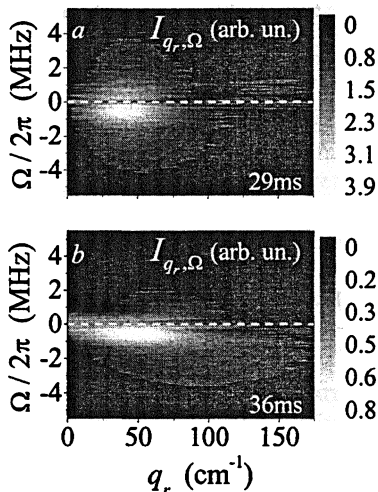
Fig. 13. $I_{q_r,\Omega}$ spectra for (a) 29 and (b) 36 ms in the CRU experiment

structed the turbulence q_r-spectra at different radii and followed their evolution during CRU. The turbulence q_r-spectra were determined for $8 > q_r\rho_i > 0.8$ at a distance 1÷3 cm from the limiter. Plotted in double logarithmic scale (Fig. 14a) they are usually knee-like, suggesting that the turbulence cascading to small scales where damping takes place is measured. However when shown in semi logarithmic scale (circles in Fig. 14b), they fit linear dependence surprisingly well. Moreover, it was found that in the whole range of radii accessible for ES,

299

during 13 ms after CRU the spectrum could be described by universal dependence $|n|^2_{q_r} \sim |n|^2_0 \exp\{-q_r L\}$ in the range of 3–4 orders of amplitude (Fig. 14b), where $|n|^2_0$ is related to the turbulence level and L is a typical turbulence scale length. The evolution of these parameters is shown in Fig. 15, where $|n|^2_0$ is normalized to its value at 29 ms. Both parameters are found to decrease substantially at 2÷6 ms after CRU simultaneously with strong growth of the poloidal plasma rotation velocity gradient in the edge region. Estimated from the ES signal Doppler frequency shift, the later increased from 25 kHz to 190 kHz (Fig. 16a).
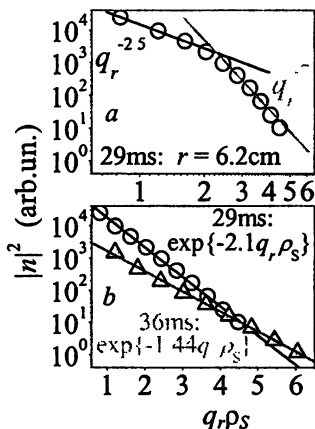
Fig. 14. LF q_r-spectra (a) in double- and (b) semi-logarithmic scale
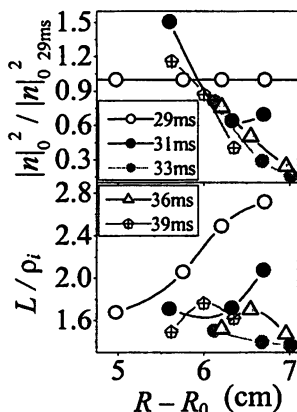
Fig. 15. (a) Turbulence level and (b) spatial scale
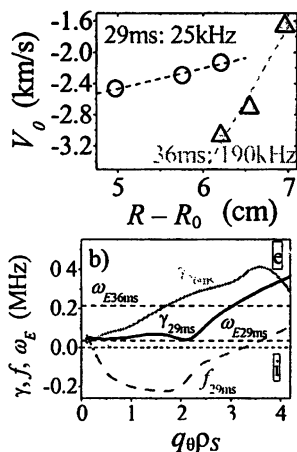
Fig. 16. (a) Poloidal plasma velocity distribution; (b) rotation shear, drift mode growth rate and frequency versus wavenumber

300

To interrelate these two effects the linear mode analysis by GS2 code [20] was performed for FT-2 discharge parameters during the CRU experiment allowing to determine the most unstable mode growth rate γ and to compare it with the poloidal plasma rotation shear ω_E at $r = 6.2$ cm. As it is seen in Fig. 16b, before CRU (29 ms) the condition $\omega_E \leq \gamma$ is fulfilled in all q-range that makes possible the instability excitation. On contrary, during the current relaxation period (36 ms) the opposite condition $\omega_E > \gamma$ definitely holds for turbulence with $q_\theta \rho_i < 1.7$ thus, according to [21], making possible the turbulence suppression at these scales, actually observed in the experiment (Fig. 15a). It should be mentioned that the observed decrease of the turbulence correlation length (Fig. 15b) accompanying its suppression at $\omega_E > \gamma$ is also predicted by [21]. Based on the domain of $q_\theta \rho_i < 2$ where the LF mode was measured and its sensitivity to the plasma rotation shear we conclude that the mode may be identified as a hybrid of the dissipative TEM [22] and ITG mode.

It is important to note that the drift mode frequencies and phase velocities predicted by the GS2 computation for $q_\theta < 15$ cm^{-1} corresponding to the measured range for the LF component in the CRU experiment are much smaller than actually observed. The difference may be attributed to the plasma cross field drift velocity justifying the procedure of plasma velocity shear determination from the Doppler frequency shift of ES signal used in this paper.

Discussing the physical origin of the universal exponential q-spectrum reconstructed for the LF component one should recall that, according to theoretical predictions [23], the q-spectra of drift wave turbulence in tokamak in a wide q-range corresponding to the so called inertial interval between the high growth rate and high dissipation region should obey a power law taking a Kolmogorov-like form, where q-spectrum looks linear in double logarithmic scale: $\lg(|n|_q^2 / |n|_{q_0}^2) = -\alpha \lg(qL)$. Experimental observations carried out in a limited q-range usually confirm this prediction. The measurements specially performed by CO_2 laser scattering in a wide q-range shifted to small scales [24] gave an evidence for a knee-like spectrum composed of two power law spectra with different indexes α. A possible explanation of this observation discussed in [24] is overlapping of the investigated q-range with both inertial interval and turbulence dissipation region. However, as it was shown in [24], when plotted in semi logarithmic scale, the observed spectrum fitted surprisingly well the exponential dependence $\lg(|n|_q^2) \sim -qL$. This intriguing observation performed by CO_2 laser scattering, unfortunately limited in spatial resolution, were appealing for more detailed studies of the small-scale drift turbulence q-spectra by more precise diagnostics. The measurements in the high q_r-range performed in the present paper by the CES technique possessing much better spatial resolution have resulted in confirmation of the exponential spectral law, which is shown to be universal for the LF turbulence component in the FT-2 tokamak plasma. In spite of the fact the

measurements are taken at high q_r not typical for the ITG or TEM mode to which the LF mode may be identified, the parameters of its exponential spectrum (level and characteristic length) are shown to be sensitive to the plasma rotation velocity shear and correlated to the electron transport, as it should be for the mentioned modes [23].

A possible explanation of this unconventional spectrum (not predicted by theory treating the nonlinear interaction of drift modes) may be given in terms of the density fluctuation Fourier transform which is provided by any scattering diagnostics. The small-scale asymptotic of this Fourier transform appears to be visible due to high sensitivity of the CES diagnostics in the small-scale domain. This part of the spectrum may not correspond to the fluctuations participating in the energy transfer in the phase space, nevertheless been sensitive to the parameters of the turbulence.

Conclusions

Summarizing the results of the paper we would like to state that two small-scale modes have been found in the enhanced scattering spectra under conditions when the threshold for the ETG mode instability [1, 3] $L_T < 1.25L_n$ is overcome. The first, identified as the ETG mode, is possessing frequency higher than 2 MHz and radial wave number $q_r \rho_s = 8$ close to the position of the ETG mode growth rate maximum. Its phase velocity is twice as high as for the LF mode and amplitude is growing towards the centre increasing where and when the ETG instability threshold is overcome according to GS2 code, as it is shown in dynamic lower hybrid heating experiment. The second possessing frequency close to 1 MHz is localized at the plasma periphery and probably associated with the small-scale component of the collisional TEM mode. It is found that this turbulence component possesses a wide q-spectrum which could be described by universal exponential dependence in the range of 3–4 orders of amplitude characterized by two parameters – the turbulence level and scale length. Both parameters are found to decrease substantially during the dynamic current ramp up discharge when the shear of the poloidal plasma rotation increases at plasma periphery exceeding the growth rate of drift instability determined with the GS2 code. Simultaneously transition to the improved confinement resulting in suppression of anomalous electron transport is observed in the experiment.

References

1   *Mikhailovskiy A. B* Sov. J Tech. Phys. **37**, 1365 (1967)
2.   *Jenko F , Dorland W , Kotschenreuther M , Rogers B N*. Phys Plasmas **7**, 1904 (2000).

3   *Jenko F , Dorland· W., Hammett G. W.* Phys. Plasmas **8**, 4096 (2001).

4.   *Lin Z et al* Proc. 20 IAEA Conf on Fusion Energy (Vienna) IAEA-CN/TH/8-4 (2004).

5   *Bottino A. et al* Proc. 33 EPS Conference on Plasma Phys. (Rome) ECA 30I, O-3 001 (2006).

6   *Candy J , Waltz R. E* Proc 21 IAEA Conf on Fusion Energy (Chengdu) IAEA-CN/TH/2-1 (2006).

7.   *Gusakov E. Z., Gurchenko A. D., Altukhov A. B et al.* Proc. 32 EPS Conf. on Control. Fusion and Plasma Phys. (Tarragona) ECA 29C, D-4.007 (2005).

8.   *Gusakov E Z , Gurchenko A D., Altukhov A. B. et al.* Plasma Phys. Control Fusion **48**, A371 (2006).

9.   *Rhodes T. L. et al.* Proc. 21 IAEA Conf. on Fusion Energy (Chengdu) IAEA-CN/EX/P4-37 (2006).

10. *Menard J. E. et al.* Proc. 21 IAEA Conf. on Fusion Energy (Chengdu) IAEA-CN/OV2-4 (2006).

11. *Gusakov E. Z., Gurchenko A. D., Altukhov A. B. et al.* Plasma Phys. Control. Fusion **48**, B443 (2006)

12. *Gurchenko A. D., Gusakov E. Z., Altukhov A. B. et al* Nucl. Fusion **47**, 245 (2007)

13. *Rhodes T. L., Peebles W. A., DeBoo J. C. et al.* Plasma Phys Control. Fusion **49**, B183 (2007).

14. *Mazzucato E., Smith D. R., Bell R. E. et al.* Phys. Rev. Lett. **101**, 075001 (2008).

15. *Novik K. M., Piliya A. D.* Plasma Phys. Control. Fusion **35**, 357 (1994).

16   *Bulyiginskiy D. G. et al* Phys. Plasmas **8**, 2224 (2001).

17. *Altukhov A. B , Gurchenko A. D., Gusakov E. Z. et al* Proc 30 EPS Conf. on Control. Fusion and Plasma Phys. (St.-Petersburg) ECA 27A, P-4.170pd (2003).

18. *Gusakov E. Z., Kaganskaya N. M., Kramer M., Selenin V. L.* Plasma Phys. Control. Fusion **42**, 1033 (2000).

19. *Lashkul S. I. et al* Proc. 21 IAEA Conf. on Fusion Energy (Vienna) IAEA/EX/P6-18 (2006)

20. *Kotschenreuther M., Rewoldt G., Tang W. M.* Comp. Phys. Comm. **88**, 128 (1995).

21. *Biglari H., Diamond P. H., Terry P. W.* Phys. Fluids B **2**, 1 (1990)

22. *Connor J. W., Hastie R. H., Helander P., Field A.* Proc. 33 EPS Conf on Plasma Phys. (Rome) ECA 33I, O-3.002 (2006).

23   *Horton W.* Rev. Mod. Phys. **71**, 735 (1999).

24. *Hennequin P. et al* Plasma Phys. Control. Fusion **46**, B121 (2004).

MULTI-FREQUENCY ECRH AT ASDEX UPGRADE

*D. Wagner[1], J. Stober[1], F. Leuterer[1], G. Sips[1], G. Grünwald[1], F. Monaco[1],
M. Münich[1], E. Poli[1], H. Schütz[1], F. Volpe[1], W. Treutterer[1], H. Zohm[1],
T. Franke[1], M. Thumm[2], R. Heidinger[3], G. Gantenbein[2], A. Meier[3],
W. Kasparek[4], C. Lechte[4], A. Litvak[5], G. Denisov[5], A. Chirkov[5],
E. Tai[6], L. Popov[6], V Nichiporenko[6], V. Myasnikov[6], E. Solyanova[6], S. Malygin[6]*

[1]Max Planck Institut für Plasmaphysik, Association EURATOM-IPP,
D-85748 Garching, Germany
Forschungszentrum Karlsruhe, Association EURATOM-FZK,
[2]Institut für Hochleistungsimpuls- und Mikrowellentechnik,
[3]Institut für Materialforschung I, D-76021 Karlsruhe, Germany
[4]Universität Karlsruhe, Institut für Höchstfrequenztechnik und Elektronik,
D-76128 Karlsruhe, Germany
[5]Institut für Plasmaforschung, Universität Stuttgart, D-70569 Stuttgart, Germany
[6]Institute of Applied Physics, RAS, 603600 Nizhny Novgorod, Russia
GYCOM Ltd, 46 Ulyanov St., Nizhny Novgorod, 603155, Russia

Since 2006, the two-frequency GYCOM gyrotron Odissey-2 is in regular operation at the ASDEX Upgrade tokamak. It has an output power of 620 kW and 910 kW at 105 GHz and 140 GHz respectively at a pulse length of 10 s. At 140 GHz the system is a crucial tool for H-mode operation with the fully W-coated inner walls now present in ASDEX Upgrade. The transport in the plasma center is significantly increased by the additional Rf-heating and suppresses the central accumulation of heavy impurities also for moderate values of density and safety factor. At 105 GHz the EC-beam is used as probe for a collective Thomson scattering diagnostic, which uses the launcher of the second unit as a receiver. Fast steerable launchers that will allow for feedback controlled suppression of neoclassical tearing modes in the plasma are installed. The development of the feedback control system is underway. Future gyrotrons will be operated at 4 frequencies between 105 and 140 GHz. These gyrotrons require broadband vacuum windows both at the gyrotron as well as at the torus The gyrotrons can be equipped with a broadband CVD diamond Brewster angle window Since the torus window has to be transparent also for elliptically polarized beams, a double disc CVD diamond window has been installed The distance between the two diamond discs will be controlled remotely within an accuracy of a few μm A method for in-situ low power measurements of the reflection has been tested. The ECRH system will be extended with two more multi-frequency gyrotrons.

Introduction

A single frequency ECRH system at 140 GHz is in operation at the ASDEX Upgrade tokamak since 1996 [1]. The system consists of 4 gyrotrons with an output power of 500 kW each and a pulse length of 2 s. A new ECRH system is currently under construction that will in its final stage deliver a total power of 4 MW with a pulse length of 10 s corresponding to the maximum flat top time of ASDEX Upgrade discharges [2]. An additional feature of the four gyrotrons of the new system is their frequency step tunability allowing operation at both 105 and 140 GHz, corresponding to the resonant frequency of a single disc CVD

304

diamond window [3]. This capability extends the operating space of the ECRH at ASDEX in terms of both magnetic field and deposition radius [4]. A first two-frequency gyrotron is in routine operation since 2006. Its output power is 910 kW at 140 GHz with a beam voltage of $U_c = -56$ kV, a body voltage of +29 kV and a beam current of $I_b = 37$ A. At 105 GHz, 620 kW were achieved with $U_c = -49$ kV, $U_b = +26$ kV and $I_b = 34$ A. The transmission losses at both frequencies are below 10% which is in good agreement with theoretical predictions. They were measured using identical calorimetric loads installed both in the MOU and next to the torus window. There is no problem with arcing in the non-evacuated waveguide transmission line. Arcing occasionally occurred in the mirror box due to dust particles on the mirror surfaces. The gyrotron can be tuned to another frequency within approximately 20 min which corresponds to the time between two ASDEX Upgrade discharges. The broadband gyrotron output window still requires further development. Therefore the next two gyrotrons will also be two-frequency gyrotrons. The fourth gyrotron is planned to be a multi-frequency gyrotron with additional frequencies in between 105 and 140 GHz. For this gyrotron broadband vacuum windows are required both at the gyrotron and at the torus. The launchers of the new system have a poloidal fast steering capability that will allow for a change of the deposition location during the discharge without changing the toroidal magnetic field. The ultimate goal is to have a very flexible system for localized plasma heating and current drive that allows for feedback control of neoclassical tearing modes, pressure profile and transport [5].

Multi-frequency hardware extensions

The transmission of the millimeter waves from the gyrotrons to the torus is mainly through non-evacuated corrugated waveguides with an inner diameter of 87 mm. The total length of the transmission line is approximately 70 m. These waveguides support the low-loss HE_{11} mode over the whole frequency band of the system. Each gyrotron is connected to a quasi-optical matching optics unit (MOU) that conditions the millimeter wave beam such that it can be effectively coupled to the corrugated waveguide. An individual set of two phase correcting mirrors is required for each frequency of a step-tunable gyrotron to convert the gyrotron beam to a fundamental Gaussian beam that guarantees optimum coupling to the HE_{11} mode in the corrugated waveguide. These mirrors also correct the angular mismatch of up to 2° of the different output beams with respect to the optical axis of the MOU and the waveguide input. This angular variation happens only in the plane perpendicular to the gyrotron axis and is due to the different caustic radii of the resonant gyrotron modes. The required space for these mirrors limits the number of applicable frequencies to four. The planned frequencies are 105, 117, 127 and 140 GHz, corresponding to resonant modes of the gyrotron. The phase correcting mirrors are mounted on turntables and are automatically set when the frequency is changed (Fig. 1). The MOU also contains a pair of broad-

305

band polarizer mirrors [6] as well as a short-pulse load for a maximum pulse length of 1 s. Additionally a long-pulse load capable of 1 MW, 10 s can be coupled to each gyrotron beam successively. The gyrotron beam is linearly polarized and thus a broadband Brewster window is possible which is under development. The torus window however has to be transparent for an arbitrary elliptical polarization. Therefore a tunable double disc window was developed and constructed [7]. It takes advantage of Fabry-Perot reflection minima at frequencies where the single discs are not transparent. The reflectivity of the double disc window was measured and compared to theory (Fig. 2). The inter-space between the two discs is evacuated to prevent arcing due to the field enhancement. The evacuation also leads to a slight bending of the discs which is responsible for the frequency shift of the measurement compared to theory (Fig. 2). The measurement was repeated after demounting the disc as well as after bake-out up to 150 °C. To test an in-situ measurement method for the installed double-disc torus window, the beam was launched through 3 m of straight waveguide plus one miter bend. Again, this measurement gave the same result.
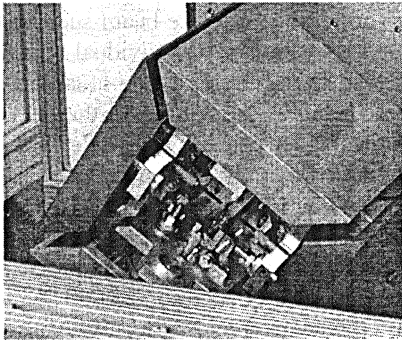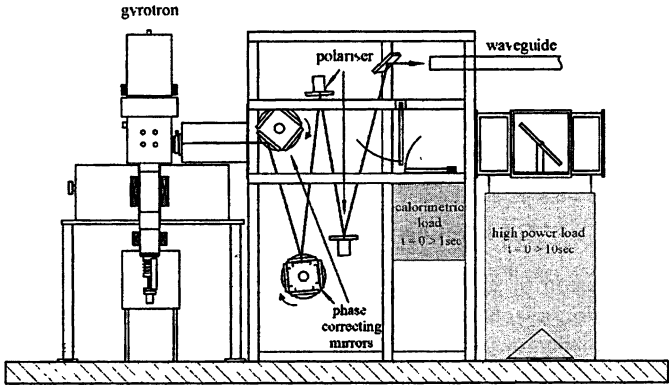

Fig. 1. MOU with phase correcting mirrors
for the multi-frequency gyrotron mounted on turntables

306
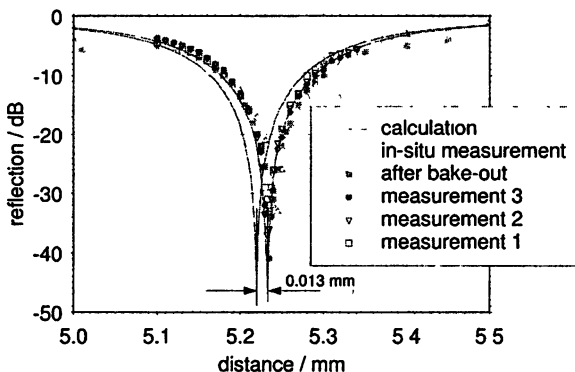
Fig. 2. Measured and calculated reflectivity of the CVD diamond double disc torus window at $f = 117.5$ GHz as a function of the distance between the two discs

Launcher tests

The launcher consists of a fixed focusing mirror and a plane mirror with a fast spindle drive and a push rod. Fast poloidal steering with up to 10°/100 ms has been achieved while the toroidal angle can be set in between pulses by rotating the steerable mirror around its own axis. First plasma experiments were done with pre-programmed launcher movements that were set by the ECRH control system before the discharge. For future feedback controlled operation of the ECRH system it is necessary to leave the control of the poloidal launcher movement during a plasma discharge with the main discharge control system (DCS) of ASDEX Upgrade. Fig. 3 shows the first test of a launcher movement controlled by the DCS. The dashed line shows the desired position as required by the discharge program, the solid line gives the response of the launcher measured at the push rod. As can be seen from Fig. 3 the launcher follows closely the path given by the control signal. The total poloidal angular sweep in this example was 8.5°.

Fig. 3. Poloidal ECRH launcher movement during a plasma discharge controlled by the DCS

307

Experimental results

A. Operation with W-walls

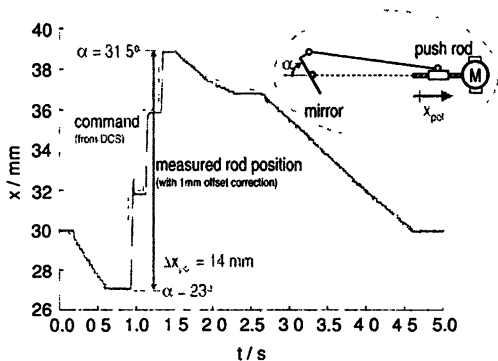Since early 2007 ASDEX Upgrade operates with fully tungsten covered plasma facing components in order to study this material for its use in future fusion reactors, which cannot cope with the high erosion rate and Tritium co-deposition found for carbon walls, which are in use in most of today's fusion experiments. The relative concentration of W in the plasma must be much lower ($< 10^{-4}$) than for C ($< 10^{-2}$) since the radiation losses per ion are much larger. The operation of ASDEX Upgrade since 2007 showed that well confined H-modes can be obtained with pure W surfaces, even without using boronization for wall conditioning [8]. For the pure W-surfaces, i.e. without boronization, stable H-mode operation using only NBI as additional heating requires a high level of gas puff, resulting in moderate pedestal temperatures and high ELM frequency, both favorable for a low rate of W erosion. The usage of central ECRH reduces the central peaking of the tungsten concentration and allows to access higher pedestal temperatures. In Fig. 4 a plasma is shown, which is unstable without central ECRH, due to an uncontrollable increase of the central W concentration and the corresponding core radiation. The deposition of the ECRH is varied to find out how central it has to be to suppress the accumulation of tungsten. On top three different launching conditions are shown as calculated with TORBEAM [9]. Condition A corresponds to the central heating known to suppress accumulation. In a first experiment the fast poloidal mirror of the new system was used to move the ECRH deposition upwards (Fig. 4, middle). At about 5.0 s, corresponding to launching condition B, the tungsten concentration in the plasma center increases and the stored energy drops due to a reduction in core temperature. A cross check of this observation was made using the toroidal magnetic field instead of the poloidal launcher angle to vary the ECRH deposition as shown in Fig. 4, bottom. At 5.5 s the plasma becomes unstable corresponding to launching condition C. In both cases the plasma becomes unstable when the deposition is roughly at the same flux surface (dashed line). This flux surface is in the vicinity of the flux surface for which the safety factor q equals unity. Actually at least two mechanisms seem to cause the effect of the ECRH on the W accumulation which are both still under study using modulation experiments. A clear change in (1,1) MHD activity and sawteeth is seen comparing launching conditions A and B indicating a direct effect of the MHD on the heavy impurities. It is well known that such MHD modes are sensitive to the location of the ECRH with respect to the $q = 1$ surface [10]. If, for launching position B, the ECRH is switched off, the W influx occurs much faster. This indicates that the central ECRH has an additional effect on the impurity transport outside the $q = 1$ surface. This has previously been explained by an increased diffusivity due to an increased turbulence level due to the central heating [11].

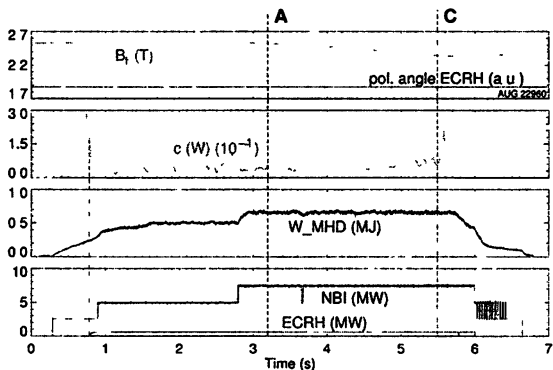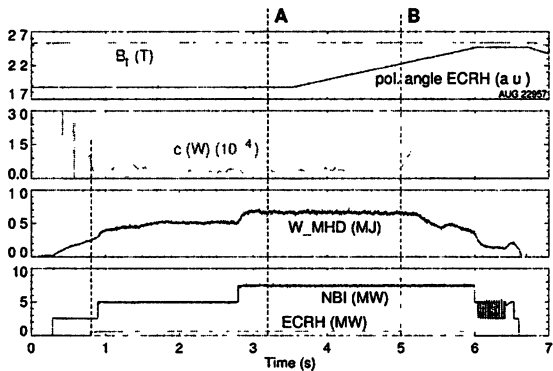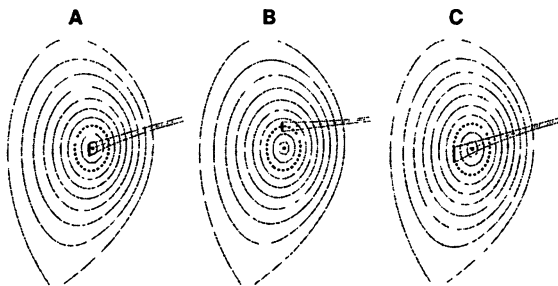**Fig. 4.** Variation of the ECRH deposition in the plasma center. Top: selected launching conditions, corresponding to the dashed time marks in the middle and bottom part. Middle: variation of the poloidal launching angle. Bottom: variation of the toroidal magnetic field. Plasma parameters at 3.2 s: $I_p = 1.0$ MA, $q_{95} = 4.8$, $n/n_{GW} = 0.65$, H98(y, 2) = 0.95. The ECRH power coupled to the plasma is 600 kW.

B. Plasma breakdown

In future machines like ITER the superconductivity of the transformer coil will limit the loop voltage severely. Additionally, most of the flux swing of the transformer will be used to raise the plasma current. The length of the current flat-top can be increased significantly if the plasma conductivity in the ramp-up phase of the discharge can be increased. Therefore the use of ECRH for pre-ionization of the neutral gas and subsequent ECR heating during the current rise phase are discussed for ITER [12]. Several of such scenarios both at 105 and 140 GHz have been successfully tested at ASDEX Upgrade [13]. The one that worked best was at the first harmonic O-mode (O1) with an on-axis magnetic field of 3.2 T using the two-frequency gyrotron at 105 GHz. Fig. 5 shows the corresponding data where the plasma breakdown happened almost immediately, given by the D_α radiation after the ECRH with approximately 400 kW was switched on. The plasma current rise could be controlled such that it was almost linear.

Additionally the second harmonic X-mode scenario [14] has been tested with 140 GHz at 2.2 T, which works as well, but the pre-ionization takes some 10 ms longer as compared to O1. These scenarios are fully in line with the 170 GHz envisaged for the main ECRH system of ITER for full toroidal field (5.2 T, O1) and half toroidal field (2.6 T, X2). This means that the 170 GHz ITER gyrotrons can be used also for plasma breakdown whereas originally a 127.5 GHz startup system consisting of 3 gyrotrons was planned [15].
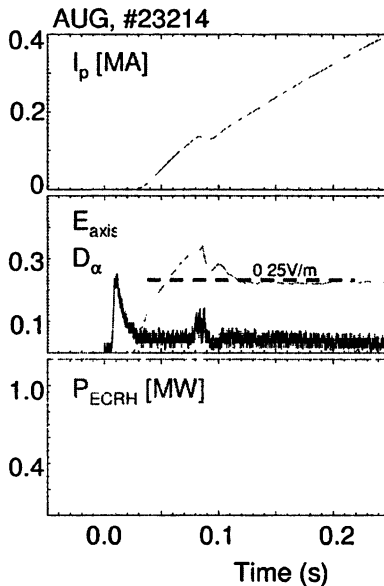

Fig. 5. Plasma breakdown in ASDEX Upgrade using ECRH at 105 GHz, 3 2 T corresponding to first harmonic O-mode

References

1. *Leuterer F. et al* Operation Experience with the ASDEX Upgrade ECRH system, ECE-15.
2. *Wagner D. et al* Present Status of the New Multifrequency ECRH System for ASDEX Upgrade, IEEE Trans Plasma Science **36**, 324–282331, April 2008.
3. *Denisov G G et al.* Development in Russia of high power gyrotrons for Fusion, Nuclear Fusion, **48**, 054007, May 2008.
4. *Zohm H and Thumm M.* On the use of step-tunable gyrotrons in ITER, J of Phys: Conf. Series, **25**, 274–282, May 2005.
5. *Manini A. et al.* Development of a feedback system to control MHD instabilities in ASDEX Upgrade, Fusion Eng. And Design, **82**, 995–1001, October 2007.
6. *Wagner D. and Leuterer F* Broadband Polarizers for High-Power Multi-Frequency ECRH Systems, Int. J. on Infrared and Millimeter Waves, **26**, 163–172, February 2005.
7. *Heidinger R. et al.* Development of high power window prototypes for ECH&CD launchers, Fusion Eng. And Design, **82**, 693–699, October 2007.
8. *Neu R. et al.* Plasma wall interaction and its iplication in an all tungsten divertor tokamak, Plasma Phys. Controll. Fusion, **49**, B49-B70, October 2007.
9. *Poli E. et al.* EC beam tracing in fusion plasmas, Fusion Eng. Design, **53**, 9–21, January 2001.
10. *Manini A. et al.* Proc. 14th Loint Workshop on ECE and ECRH, Santorini, Greece, Heliotopos Conference Ltd., Athens, 2006.
11. *Dux R. et al.* submitted to Journ. Nucl. Materials.
12. ITER Technical Basis 2002, ITER EDA Documentation Series No 24, (Vienna: IAEA)
13. *Sips G* Nuclear Fusion, to be published.
14. *Jackson G. L.* Second harmonic electron cyclotron pre-ionization in the DIII-D tokamak, Nuclear Fusion, **47**, 257–263, March 2007.
15. *Kobayashi N. et al.* Design of Electron Cyclotron Heating and Current Drive System of ITER, Proc. 17th Top Conf. on Radio Freq. Power in Plasmas, AIP Conf. Proc. **933**, 413–416, 2007

IMPROVED CONFINEMENT TRANSITION IN LOWER HYBRID HEATING EXPERIMENT ON FT-2 TOKAMAK

S. I. Lashkul[1], A. B. Altukhov[1], V. V. Bulanin[2], V. V. Dyachenko[1], L. A. Esipov[1], A. D. Gurchenko[1], E. Z. Gusakov[1], M. Yu. Kantor[1], D. V. Kouprienko[1], A. V. Petrov[2], S. V. Shatalin[2], A. Yu. Stepanov[1], E. O. Vekshina[2], A. Yu. Yashin[2]

[1] A. F. Ioffe Physico-Technical Institute, Politekhnicheskaya 26, St.Petersburg, Russia
[2] St. Petersburg State Polytekhnical University, St.Petersburg, Russia

The Lower Hybrid Heating (LHH) scheme is used at FT-2 tokamak to provide ion and electron heating and transition to improved confinement regimes. In the present paper the plasma drift velocity and turbulence level evolution have been studied at RF power level $P_{LHH} \approx 2P_{OH} = 180$ kW using spectroscopic, Langmuir probes as well as Doppler reflectometry and the Upper Hybrid Resonance (UHR) backscattering (BS) techniques. The data measured with these diagnostics were analyzed and compared to each other.

Introduction

The Lower Hybrid Heating (LHH) scheme [1] has been routinely used at FT-2 tokamak to provide ion and electron heating and a transition to improved confinement regimes with Internal Transport Barrier (ITB) at RF power level $90 \div 100$ kW [2]. Recently the possibility of LHH at enhanced power level ($P_{LHH} \approx 2P_{OH} = 180$ kW) resulting in a transition to improved energy confinement regime during RF pulse and in the post heating stage has been demonstrated [3]. The LH heating efficiency of the ion component at the high RF power level remains the same high as at the lower powers.

Experiment

The characteristic features of the FT-2 plasma parameters are the following: $R = 0.55$ m, $a_L = 0.079$ m, $I_{pl} = 22$ kA and $B_t = 2.2$ T. The safety factor $q_L = 6$. For on-axis LHH need the original line-of-sight averaged density $<n_e> = (3,2 \div 3.6) \cdot 10^{19}$ m^{-3} [1]. The RF pulse $P_{LHH} \approx 180$ kW, $\Delta t_{LH} = 5$ ms, $f = 920$ MHz is applied in the middle of a $\Delta t_{pl} = 60$ ms plasma shot. The central ion temperature increases about three times and electron temperature increases about two times, see Fig. 1. Observed relatively fast rise of the central ion temperature $\Delta \tau \sim 1$ ms $< \tau_{Eion}$, seems, can be explained by decrease of the ion energy confined time with LHH start. As shown energy balance simulation for ion
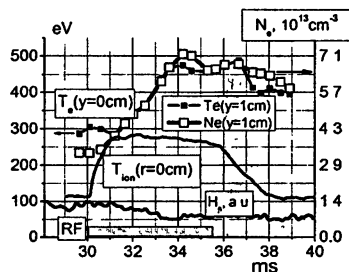

Fig. 1

component, where $\chi_{i,eff}$ is taken in the quasi neoclassical (QNC) approximation [1], the τ_{Eion} decreases with LHH start from 3÷4 ms up to 1÷2 ms and than increases up to 4÷5 ms with ITB formation at 33 ms, when hydrogen line H_β decreases, recall Fig. 1. [The energy balance simulation with QNC approximation is based on propositions that $\chi_{i,eff}$ during LHH experiment $\chi_{i,eff} = \chi_{i,eff}^{neo} \times k$, where

$$\chi_{i,eff}^{neo} = \frac{-\chi_i^{neo} n_i grad T_i + \frac{5}{2}\Gamma T_i}{4\pi^2 Rr\Delta T_i n} \quad \text{and the factor} \quad k = \frac{\chi_{i,eff}(OH)}{\chi_{i,eff}^{neo}(OH)}. \text{ The particle flux } \Gamma,$$

accordingly idea of the [4], has to be determined from the experimental data.]

L-H transition takes place befor/or RF pulse end when the density turbulence suppression are observed in the plasma periphery and SOL [3, 5]. For more detail investigation of these effects the LHH scenario was reproduced in the typical experimental runs (#061505, #053106, #030708), and the evolution of the plasma poloidal rotation and turbulence levels have been studied using spectroscopic, Langmuir probes [2], Doppler reflectometry [6] and the Upper Hybrid Resonance (UHR) Doppler backscattering (BS) techniques [7]. In the present paper the data measured with these diagnostics were analyzed and compared to each other.

Fig. 2 shows plasma parameter versus to Flux Surfaces (FS) radii ρ measured by Neutral Particle Analyzer (NPA) and spectroscopy (T_i), by the laser Thomson scattering (TS) diagnostics, and a 2 mm interferometer. It should be noted that during additional heating a small shift (without any plasma current disruptions) of the plasma column outward along of the major radius R is observed [5]. The shifts of the circular (FS) (in respect to the chamber center due to plasma core controlled shift and Shafranov's FS shifts) resulted from the process of inverting of the density chord profiles have been taken into account in Fig. 2, where the main plasma parameters are presented. The density profiles

Fig. 2. Plasma parameters versus ρ

are in the Fig. 2b. The TS electron temperature data versus ρ is presented in Fig. 2a. The $T_i(\rho)$ profiles and the radiation losses $P_{rad}(\rho)$ measured by scan bolometric technique are presented in Fig. 2c and d, respectively. The experimental data for the ion component demonstrate that during on-axis LHH $T_i(\rho)$ rises with ITB formation at $\rho = 4÷5$ cm (see 32 ms and 34 ms). These data are consistent with the previous observations [2, 3]. In particularly, the central electron temperature increases and remains at the high level for about 5 ms after the RF pulse switch off (recall Fig. 1). This fact at relatively high density level (which is higher that need for LH wave absorption by electron component) permits proposed that elec-
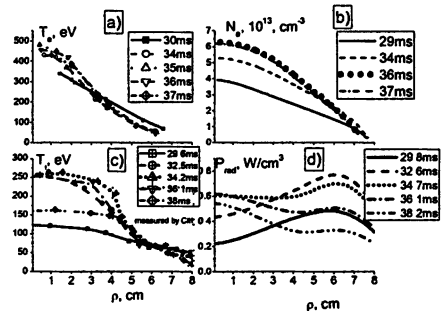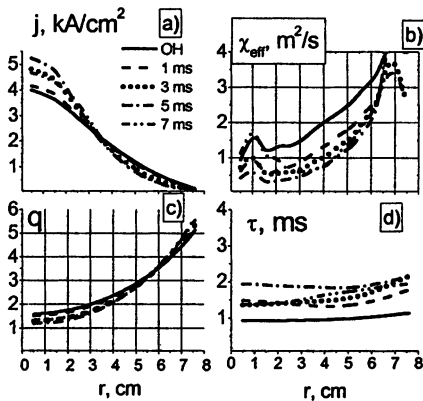
Fig. 3. ASTRA code modeling data.
The timing from the RF pulse start

trons are not heated directly by LH waves [1, 8]. The ASTRA code modeling data, shown in Fig. 3b, indicates that the thermal conductivity of the plasma electron component χ_e decrease, which leads to doubling of the electron energy confined time τ_E towards the end of LHH, see Fig. 3d. Fig. 3a and 3c depict sharpening of the plasma current density $j(\rho)$ and steepening of the safety factor gradient $q(\rho = 4 \div 7.5$ cm). It seems that the central electron temperature rise could be explained by the $j(\rho)$ sharpening and the thermal conductivity decrease.

Evolution of E_r

I. It is well known that a change in the radial electric field E_r can suppress turbulence level (and anomalous transport) by strong $E_r \times B$ poloidal plasma rotation shear ω_s [9]. The $E_r(\rho)$ field and the corresponding poloidal plasma $E_r \times B$ rotation can be measured spectroscopically using the effect of Doppler shift of impurity spectral lines. The CIII (464.7 nm) spectral line emissivity has been analyzed. Spectral measurements in the visible region are made by two monochromators that record fast parameter changes at the periphery of the plasma column [5]. E_r is calculated using the MHD force balance equation (see, e.g., [10]) for the C^{2+} impurity ion. Resulting poloidal ion velocity v_θ is defined as $v_\theta = \nabla_r P_{iz} / Zen_{iz}B_\Phi - E_r / B_\Phi + v_\Phi B_\theta/B_\Phi$, where the first term is due to the diamagnetic drift and the second due to electrostatic drift. The third term with the tor-

Fig. 4. Spectroscopically measured $E_r(\rho)$

oidal velocity v_Φ was neglected because $B_\theta/B_\Phi \approx 0.04$. The results of the $v_\theta^{C2+}(\rho)$ measurements for C^{2+} ion emissivity region (where CIII spectral line is detected) of the plasma column during LHH experiment (#053106) are presented and discussed in detail in the paper [5]. The $E_r(\rho)$ values obtained from 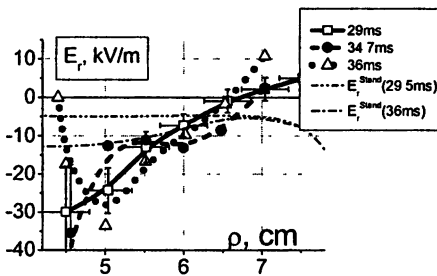the force balance equation are presented in Fig. 4 for three following moments: OH before LH heating (29 ms), before the end of RF pulse (34.7 ms), and 36 ms of the post heating phase. Measurements demonstrate that E_r data are differed from

314

the standard neoclassical values [9] (shown by dash-dot lines). They are larger of E_r^{stan} at the middle radii and smaller at the LCFS vicinity. The higher E_r can be explained by peculiarities of chosen FT-2 regime with high safety factor $q_L \sim 6$. Monte Carlo simulations of the E_r evolution in a low current tokamak FT-2 have shown that E_r can make a spontaneous transition to higher negative value during LHH, if the local Mach number for ions became about (or higher) one [11]. One could propose that a sudden rise of the E_r and its shear ω_s in the region 4÷5 cm could result in the ITB formation observed at the ion temperature profiles $T_i(\rho)$ during LHH (Fig. 2c). In the post heating phase (36 ms), a sharp decrease in the magnitude of E_r in vicinity of 4÷5 cm (crossing of the X axis) is observed. Such a reduction in $E_r(\rho)$ exceeds diagnostic uncertainties and needs additional experimental verification and theoretical analysis. One couldn't eliminate possibility that the radial electric field in vicinity of 4÷5 cm may be significantly modified by magnetic island itself [9, 12].

II. As mentioned above, in the vicinity of the LCFS there are characteristic differences between the spectroscopically measured E_r and E_r^{NEO}. In particular, $E_r(\rho)$ is smaller than E_r^{NEO} and even changes sign near $\rho \sim 6.5$ cm $< a = 7.9$ cm. The correspond-ding poloidal plasma drift velocity profiles of $V_{Er \times B}(\rho)$ are compared with the profiles of the poloidal velocity derived from the Doppler Reflectometry (DR) measurements. In the Doppler reflectometry the rotation velocity is obtained from the Doppler frequency shift of the backscattered radiation under oblique incidence onto the cutoff surface [6, 13]. The actual velocity extracted from the Doppler shift consists of two terms: $V_0 = V_{ph} + V_{E \times B}$, where V_{ph} is the phase velocity of the scattering fluctuation and $V_{E \times B}$ is the plasma drift velocity caused by a radial electric field. If the phase velocity of the density fluctuation is negligible, then the measured V_0 may be interpreted as the $E_r \times B$ drift velocity. The same sum of velocities was estimated in the SOL region by Langmuir probe correlation technique. Fig. 5 depicts the poloidal velocity, measured by the three diagnostics, for the plasma periphery,

Fig. 5

5.5÷8 cm. It is seen that the spectroscopic and DR profiles are close to each other, in particular, for the end of the heating pulse and in the post-heating stage.

It is remarkable that two diagnostics show approximately the same radial location for the point where $V_{E \times B}$ changes its direction. This point is close to the resonance magnetic surface $q = 4$ (recall Fig. 2c), where the radial electric field
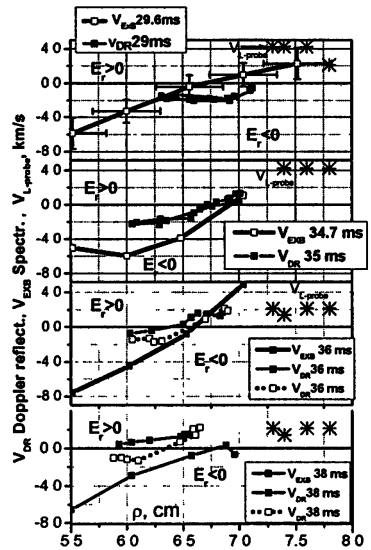
may be significantly modified by the magnetic island itself. Indeed, different MHD behavior is identified by Mirnov probes for slightly different (mentioned above) displacement of the plasma column along the major radius. In this case DR measurements register two slightly different V_θ profiles (fill and empty boxes in Fig. 5). Fill boxes correspond to discharges with strong MHD activities and empty boxes correspond to weak one, which have been observed in the post heating stage (36 ms and 38 ms). The plausible reason of occurrence of rotation in the ion diamagnetic drift direction (recall Fig. 5 at 36 ms and 38 ms) is a change in the electron–ion balance due to the magnetic flux surface distortion caused by MHD activity or/and plasma column displacement along the major radius [14]. Observed differences between the spectroscopic and DR $V_{E \times B}$ profiles are more than diagnostic uncertainties and need further analysis. Langmuir probe-measured poloidal velocities of the fluctuation floating potential data [15] are marked by stars in Fig. 5 for the plasma LCFS vicinity and SOL regions ($r = 7.2 \div 8$ cm). Those data show a good agreement in the region where the diagnostics overlap and can be useful for diagnostics comparison in the future.

Turbulence suppression

It is remarkable, that the drastic fluctuation suppression, measured by DR approximately across all frequencies (fluctuation frequency band $f < 1$ MHz and $k \sim 1 \div 6$ cm^{-1}), is detected slightly before the velocity inversion (Fig. 6). The solid curve Δf gives the temporal behavior of the Doppler frequency shifts. In Fig. 6 f and Δf are presented in the same frequency scales (see left axis). The black doted curve shows the cut-off radius displacement (right axis). The observed suppression of the density fluctuations (33–35 ms) is in good agreement with the Langmuir probe measurements. One can assume that the fluctuation suppression is just near of strong shear of rotation, it is the vicinity of the point where there is velocity inversion (recall Fig. 5 at 35 ms). That agrees with theoretical prediction of plasma turbulence suppression via increasing plasma rotation shear [9].

Fig. 6. Spectrogram of the Doppler reflectometer signal

The UHR Doppler BS diagnostics with X-mode 20 mW power probing in V-band from high magnetic field side with +1.5 cm vertical displacement above the equatorial plane was implemented for investigating the density turbulence dynamics with shorter scales ($\lambda < c / 2\pi f_i$) compared to DR. Scanning the plasma region from $r = 5$ cm to 7.5 cm has shown that two small-scale drift modes are observable on the plasma periphery [7]. The first mode with frequency less than

1.5 MHz is probably associated with the small-scale component of TEM. The second mode with frequency higher than 2 MHz is associated with the ETG mode [16]. In the present experiment, as in the previous (#061505) one [3], both types of turbulence was suppressed during LH-heating. After the RF-pulse the first mode usually grows, in accordance with the peripheral rise of the electron thermal conductivity (recall Fig. 2b), whereas staying suppressed the ETG mode is rather consistent with the gradient scale length of electron temperature and density profiles [16]. Therefore the recent efforts in the regime with Improved Confinement Transition strongly suggest investigating the direct role of the ETG mode on transport through the barrier under conditions when other drift modes are suppressed.

References

1. *Lashkul S. I., Budnikov V. N. et al.* Pl. Phys. Reports, 2001. V. 27, No. 12, pp.1001–1010
2. *Lashkul S. I, Shatalin S. V. et al.* Pl. Phys. Reports, 2006. V. 32, No. 5, pp. 353–362.
3. *Lashkul S. I., Altukhov A. B., Gurchenko A. D. et al.* 21st IAEA FEC, 2006, EX/P6-18.
4. *Rozhansky V. A. and Cendin L. D.* Preprint of LPI, Leningrad, 1986.
5. *Lashkul S. I. et al.* Proc. of the 34th EPS and Pl. Phys. Warsaw,V. 31F, P2.148, (2007).
6. *Bulanin V. V. et al.* Proceed. of Strong Microwaves in Pl. Nizhny Novg. (2002) 398–403.
7. *Gusakov E. Z. et al.* Plasma Phys. Control. Fusion **48**, B443 (2006).
8 *Lashkul S. I., Budnikov V. N. et al.* Pl. Phys. and Cont. Fus. 42(2000), A169–A174.
9. *Rozhansky V.* Pl. Phys. Contr. Fus. 46 (2004) A1–A17.
10. *Field A R., Fussmann G., Hormann J V.* Nucl. Fusion 32 (1992) 1192
11. *Kurki-Suonio T, Heikkinen J. A. and Lashkul S. I.* Phys. of Plas., **14**, 072510 _2007.
12. *Ida K. et al.* Nucl. Fusion 44 (2004) 290–295.
13. *Lashkul S. I et al.* Proc. of the 34th EPS and Pl. Phys. Warsaw, V. 31F, P-2.055 (2007).
14. *Bulanin V. V. et al.* PPCF, 48 (2006) A101–A107.
15. *Shatalin S V et al.* Plasma Physics Reports, 2007, Vol 33, No. 3, pp. 169–178.
16. *Gurchenko A D. et al.* Nucl Fusion 47 (2007) 245–250.

INTERNAL TRANSPORT BARRIER FORMATION DURING SLOW HEAT (COLD) PULSE PROPAGATION IN JT-60U, LHD AND T-10

S. V. Neudatchin[1], N. Hayashi[2], S. Inagaki[3], K. Itoh[3],
Y. Sakamoto[2], T. Takizuka[2], N. Tamura[3]

[1]Nuclear Fusion Institute, RRC "Kurchatov Institute", Moscow Russia
[2]Japan Atomic Energy Agency, Naka Fusion Research Est., Naka, 311-093, Japan
[3]National Institute for Fusion Science, Oroshi-cho 322-6, Toki 509-5292, Japan

Understanding of properties of internal transport barrier (ITB) is of importance for the fusion research of toroidal magnetic confinement. In T-10, ITB has been recognized by means of analyses of heat pulse propagation (HPP) induced by central ECRH-onset and cold pulse propagation (CPP) by off-axis ECRH cut-off in a sawtooth-free plasma created by off-axis ECRH [1–3]. The cold pulses propagate slowly and diffusively with dynamic electron heat diffusivity $\chi_e^{HP} \sim 0.1$ m^2/s. It is known by many years, that in L-mode, $\chi_e^{HP} \approx 2$–$4 \chi_e^{PB}$ (so called "enhanced" HPP). At present, this relationship is usually explained by "critical gradient model". In the present report, we focus at fully opposite cases with $\chi_e^{HP} < \chi_e^{PB}$. For the first time, this case was found in T-10 many years ago [1] and called "self-deceleration of heat wave", or, in a contrast with L-mode, "reduced" HPP. Non-local bifurcations of core transport (at ~30–40 % of minor radius inside and around ITB in a ms timescale) were found in various JT-60U normal and RS plasmas and called ITB-events [4–6]. In RS shots, the ITB-events create very slow electron and ion outward HPP with $\chi_e^{HP} \sim 0.1$ m^2/s, $\chi_i^{HP} \sim 0.14$ m^2/s [5]. The new interpretation of slow inward CPP induced by spasmodic shrinking of the wide zone with low transport formed by large C_8H_8 pellets in LHD is also described. The new method allows one to reconstruct a gradual reduction of $\chi_{e,i}$ (r, t) during slow electron and ion HPP in the cases described above.

Interpretation of the slow pulse propagation

Regarding the perturbations of the heat sources and density, HPP/CPP is analysed using a simplified transport equation for δT_e, as usually (e.g. see [1–4] for detail and references therein):

$$1.5n_e\partial\delta T_e /\partial t = \text{div}(n_e\chi_e^{HP} \nabla\delta T_e) \tag{1}$$

with the various initial and boundary conditions. Important experimentally measured characteristic of the CPP is the index of the relative sharpness of a heat wave (Sh) (see [1–4]):

$$Sh = |(\delta\nabla T_e/\delta T_e)/(\nabla T_{e0}/T_{e0})|. \tag{2}$$

The value of Sh characterizes the sensitivity of the diffusive term ($\chi_e^{HP}\delta\nabla T_e$) to the terms proportional to δT_e such as convective and convective-like terms (electron-ion exchange sources perturbations, dependence of χ_e on T_e, etc.) In the experiments described below, the value of *Sh* exceeds 5, and the role of convective terms is negligible.

Regarding the perturbations of the heat sources, density and convective heat flux, the transport of $\delta T_e\,(r,\,t)$ is described by full equation:

$$1.5 n_e \partial \delta T_e / \partial t = \mathrm{div}(\delta \Gamma_e), \quad \delta \Gamma_e = n_e(\chi_{e0}\nabla\delta T_e + \delta\chi_e(\nabla\delta T_e + \nabla T_{e0})), \qquad (3)$$

where $\delta\Gamma_e$ is the variation of the electron heat flux, χ_{e0} is background power balance electron heat diffusivity, ∇T_{e0} is T_e gradient before HPP, and $\delta\chi_e$ is the variation of power balance electron heat diffusivity during HPP. Comparison of equations (3) and (5) gives follows:

$$n_e\chi_e^{HP}\nabla\delta T_e \approx n_e(\chi_{e0}\nabla\delta T_e + \delta\chi_e(\nabla\delta T_e + \nabla T_{e0})), \qquad (4)$$

since calculations with simplified equation (1) describe experiments rather well [1–4]).The evolution of $\chi_e \equiv \delta\chi_e + \chi_{e0}$ is described by the following expression derived from eq. (4):

$$\chi_e \approx (\chi_e^{HP}\nabla\delta T_e / \nabla T_{e0} + \chi_{e0}) / (1 + \nabla\delta T_e / \nabla T_{e0}). \qquad (5)$$

In T-10, the slow inward CPP (with $\chi_e^{CP} = 0.08$ m^2/s) was induced by turning-off of the 0.5 MW off-axis second harmonic ECRH (0.18 MA / 2.32 T shot, line average density = $1.5 \cdot 10^{19}$/m^3 [2]. Figure 1b represents the evolution of χ_e at $r/a = 0.25$ taken from eq. (5). The value of χ_e falls quickly and $R\nabla T_e/T_e = R/L_{Te}$ reaches critical value in two ms (R/L_{Te} reaches 17 in the end of CPP). The circles shows χ_e values obtained from power balance calculations before CPP (χ_{e0}) and in the end of CPP [2]. The reconstructed decay of χ_e fits well the value of χ_e in the end of CPP.
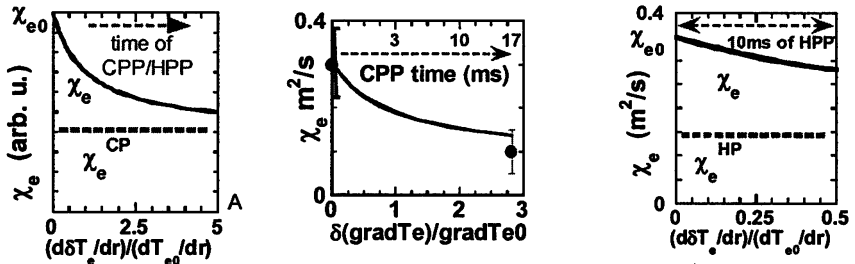
Fig. 1. (a) Dependence of χ_e on $\nabla\delta T_e / \nabla T_{e0}$ (see eq. 5). (b) T-10: Dependence of χ_e on $\nabla\delta T_e / \nabla T_{e0}$ during inward CPP from off-axis ECRH cut-off [2] with $\chi_e^{HP} = 0.08$ m^2/s. (c) T-10: Dependence of χ_e on $\nabla\delta T_e / \nabla T_{e0}$ during outward HPP at $r/a = 0.45$ induced by central ECRH-on at the background created by off-axis ECRH [1].

For the firs time, slow HPP was found in T-10 nearly 20 years ago [1] in the shots with $I_p = 0.38$ MA, $B_t = 3$ T, line averaged density = $4 \cdot 10^{19}$/m^3. Slow outward HPP with $\chi_e^{HP} = 0.14$ m^2/s at $r/a = 0.45$ was created by on-axis ECRH-on (0.4 MW at the first harmonic) imposed on the background sawteeh-free plasmas with 0.9 MW off-axis ECRH started 100 ms earlier. The density profile was constant within 15 ms after central ECRH-on. The time interval of HPP study was limited by 10 ms since the mixture of SXR and ECE data was used in the HPP analysis. Figure 1c shows the reconstructed decay of χ_e during HPP at $r/a = 0.45$ ($\chi_{e0} = 0.35$ m^2/s).

In JT-60U reverse shear experiments [4–5], ITB-events A and C reduces transport and form stronger ITB. Figures 2a–b shows the timetraces of $T_{e,i}$. ITB-event C creates diffusive outward ion and electron HPP with $\chi_e^{HP} \sim 0.1$ m^2/s, $\chi_i^{HP} \sim 0.14$ m^2/s [5]. Figure 2c displays the evolution of toroidal rotation velocity V_t. Figure 3 represents the evolution of χ_e (with two values of χ_{e0}) at $r/a = 0.63$ taken from eq. (5). The initial value of χ_{e0} measured from power balance calculations is known with significant erorbars.
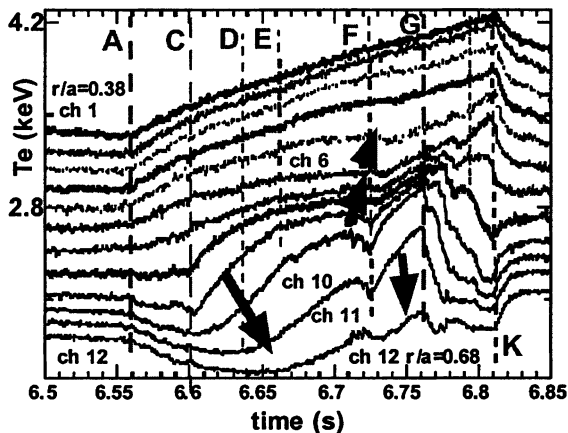
Fig. 2. JT-60U: (a–b) Time-traces of $T_{e,i}$ at ITB-events A, C and outward HPP induced by event C. (c) profiles of toroidal V_t.
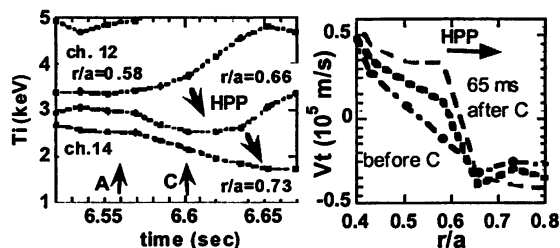
Fig. 3. JT-60U: Timetraces of χ_e at $r/a = 0.63$ for two values of χ_{e0} (power balance errors) taken from eq. (5) and evolution of R/L_{Te} (dotted line).

Nevertheless, the behaviour of $\chi_e(t)$ is similar and final values of χ_e are low even at very high level of $R/L_{Te} = 27$ in the end of HPP. It is worthless to mention that even the low values of $\chi_e = 0.2$–0.3 m^2/s in the end of HPP are still higher compare with the values of $\chi_e^{HP} \sim 0.1$ m^2/s. The evolution of χ_i is similar. The decay of $\chi_{e,i}$ during HPP correlates with the rise of ∇Pi and ∇V_t.

Now we discuss the behavior of eq. (5) in extreme cases. χ_e decreases almost line-

320

arly at small values of $\nabla\delta T_e /\nabla T_{e0}$ since $\chi_e \approx \chi_{e0} - (\chi_{e0} - \chi_e^{HP})\nabla\delta T_e/\nabla T_{e0}$ at $\nabla\delta T_e/\nabla T_{e0} \ll 1$. We used this qualitative explanation of slow HPP during ITB formation earlier [1–4]. The opposite case is the interpretation of HPP/CPP experiments with strongly rising T_e gradients ($\nabla\delta T_e/\nabla T_{e0} \gg 1$) on the heat (cold) wave front. In these cases equation (5) may be rewritten as $\lim_{\nabla\delta T_e/\nabla T_{e0} \to \infty} \chi_e = $ $= \chi_e^{HP}$ (see an obvious limit $\chi_e = \chi_e^{HP}$ in Fig. 1. In this case slow HPP/CPP indeed represents low transport with $\chi_e \approx \chi_e^{HP}$ in the end of HPP.

Non-local reduction of electron heat transport in LHD is observed simultaneously with the evaporation of small C_8H_8 pellets in low-density plasmas with ECRH [7]. In the present paper, new details of slow inward CPP induced by spasmodic shrinking of the wide zone with low transport formed by large C_8H_8 pellets in LHD [8] are described. Evaporation of large TESPEL pellet creates a hollow profile of electron density n_e. After an initial decay, the electron temperature T_e starts to rise rapidly. Later, when the T_e value exceeds the level observed before injection, an abrupt decay of T_e ("event") appears at periphery. The events penetrate gradually deeper and deeper toward the plasma center. We interpret this behaviour as a step-wise shrinking of the zone with strongly reduced transport, which is initially formed by the evaporation of the pellet. Each event creates an inward CPP. The example of slow inward CPP is given in Fig. 4a. The value of

Fig. 4. LHD. (a) Events and inward CPP created by the events. Dotted and bold red traces after time B at ch.9 are calculations of CPP from ch.10 with $\chi_e^{CP} = 0.5$ m²/s (faster compared to the experiment) and $\chi_e^{CP} = 0.15$ m²/s (agrees with the experiment). (b) Variation of $R/L_{Te} \equiv$ $\equiv R\nabla T_e/T_e$ during CPP at ($r/a = 0.77$). (c) Two different solutions of $\chi_e(t)$ at an abstractedly taken radius r_{abstr} (e.g. r_9 in Figure 4a and with fictitious events 0)-III). Fictitious event 0) creates CPP and does not affect instantly the transport in the zone around r_{abstr}. First solution with $\chi_{e0} = \chi_e^{CP}$ and events I), II, III). Second solution with unknown level of χ_{e0} and decrease of $\chi_e(t)$ during CPP after event 0) in accordance with equation (5).

321
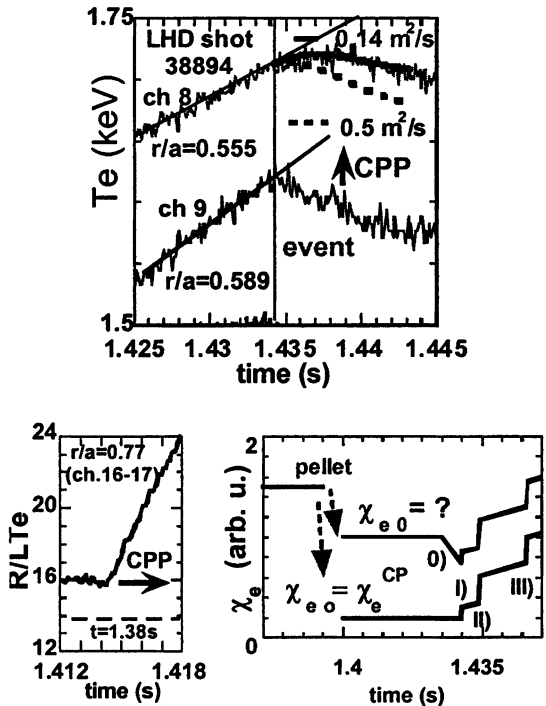
R/L_{Te} rises well (see Fig. 4b). Figure 4c shows two different scenarios of $\chi_e(t)$ after pellet injection at an abstractedly taken radial position r_{abstr}. Fictitious event 0) creates CPP and do not covers zone around r_{abstr}. The first curve is the simplest solution with $\chi_e^{CP} = \chi_{e0}$ and fictitious events I), II), III). It should be underlined that these events are not real ones. Quantity of events varies at the given radius The second curve displays the solution with unknown level of χ_{e0} value described by equation (5) and shown in Fig. 4c. In this case χ_e reduces during CPP created by event 0).

Discussion and conclusions

The heat flux is described by the following expression derived from equation (5):

$$\chi_e \nabla T_e \equiv \chi_e(\nabla T_{e0} + \nabla \delta T_e) \approx \chi_e^{HP}\nabla T_e + (\chi_{e0} - \chi_e^{HP})\nabla T_{e0} \tag{6}$$

or

$$\chi_e \nabla T_e \approx \chi_e^{HP}\nabla T_e + (\chi_{e0} - \chi_e^{HP})\nabla T_{e0}(T_e/T_{e0}) \text{ at } \delta T_e/T_{e0} << \nabla \delta T_e/\nabla T_{e0}. \tag{7}$$

We are not able to choose between equations (6) and (7) since the first term varies much stronger compare with the second term (e.g. in the end of CPP/HPP analyzed above, $\delta T_e/T_{e0} = 0.03\nabla\delta T_e/\nabla T_{e0}$ at JT-60U and $\delta T_e/T_{e0} = 0.07\nabla\delta T_e/\nabla T_{e0}$ at T-10). The second term is convective term and its presence can be explained by the transport caused by global modes or fluctuations with large radial scale. (above $0.2r/a$ in T-10 and $01.r/a$ in JT-60U and LHD).

The new method allows us to reconstruct approximate behaviour of $\chi_{e,i}(r, t)$ during slow electron and ion HPP. Important consequence of eq. (5) is that the value of χ_e remains above the value of χ_e^{HP}. In T-10, the reconstructed decay of χ_e fits well the value of χ_e at the end of CPP (obtained independently from the power balance). The fluctuations level measured by reflectometer [9] falls below the ohmic level in some shots with slow CPP in T-10. In J-60U, the decay of $\chi_{e,i}$ during HPP is accompanied by the rise of ∇Pi and ∇V_t. Depending on measurements available (reflectometer data, Er variation etc), new method brings new possibilities to study physics of ITB formation in time and space.

References

1. *Bagdasarov A A, Vasin N L, Neudachin S. V., Savrukhin P. V.* 1991 (Proc. 15th Int IAEA Conf., Washington, 1990), Vol 1 (IAEA: Vienna, 1991) 523
2. *Neudatchin S V, Kislov A. Ya., Krupin V. A. et al.* 2003 Nucl. Fusion 43 1405.
3. *Neudatchin S V., Inagaki S., Itoh K et al.* 2004 J. Pl. and Fus. Res. Series 6 134.
4. *Neudatchin S. V, Takizuka T et al.* Pl Phys. Contr Fusion 1999 41 L39 and 2001 43 661.
5. *Neudatchin S. V, Takizuka T, Hayashi H. et al.* 2004 Nucl. Fusion 44 945.
6. *Neudatchin S V., Takizuka T, Shirai H.* Proc 18th IAEA Fusion Energy Conf. on Fusion Energy (Sorrento, 2000) (Vienna: IAEA)CR-ROM file EXP5/01.
7. *Tamura N. et al.* 2005 Phys. Plasmas 12 110705.
8. *Neudatchin S V. et al.* SMP-2005 report.
9. *Vershkov V A, Shelukhin D A, Razumova K. A* 30th EPS Conf On Pl. Phys Contr. Fus. (St. Petersburg) P-3.115.

POWERFUL ECH APPLICATION
FOR THE PHYSICAL NATURE INVESTIGATION
OF THE LARGE SCALE PLASMA OSCILLATIONS
AT T-10 TOKAMAK

V. I. Poznyak[1], O. Valensia[2], V. V. Piterskii[1], G. N. Ploskirev[1], E. G. Ploskirev[1]

[1] Russian Research Centre "Kurchatov Institute", Moscow, Russia
[2] People Friendship University, Moscow, Russia

Introduction

The goal of work is analysis of the structure and motion of the large scale modes (so called *MHD* modes) and verification of the hypothesis about kinetic nature of this process. The control amplification of the oscillation amplitudes by the on-axis ECH was used for confident and detail analysis. Three on-axis gyrotrons (140 GHz) and one off-axis (129 GHz) with shifted outer absorption zone are used for this purpose. Power of each gyrotron is $300 \div 350$ kW. The slightly power modulation (~5%, 1st harmonic of frequency ~ 1.8 kHz) is applied for "marking" of oscillations. In such case a strong positive feedback between amplitudes of oscillations and electron temperature manifests, the frequency capture by the external force happens, the relative oscillating amplitudes rise from 10 to 50% [1]. Single and many channel receivers are used for the space structure analysis. ECE in X-mode is received from two antennae trough 90° along torus on low field side and two antennae ±60° on poloidal angles at third section of tokamak. The comparative analysis of ECE in O-mode (1st harmonic) and X-mode (2nd harmonic) from central plasma with high optical density was fulfilled. Intensity of X-mode is determined only by perpendicular electron energy. Intensity of O-mode depends also on longitudinal electron energy. Plasma noise signal (1÷16 GHz) fixing real moment of every internal disruption [2] is applied as "absolute time" monitor.

Experiment

Figure 1 shows ECE signals during ECH in regime: $B_t = 25$ kGs, $I_t = 250$ kA, $N_e = 1.7 \cdot 10^{13}$ cm^{-3}. Magnetic surface $q = 3$ ($r = 28$ cm) lies near current channel boundary (30 cm). Area of the maximal amplitudes is near the plasma center and coincides with ECH absorption zone. Maximum of oscillations displaces with shift of ECH from the center, their amplitudes drop and oscillations disappear when absorption area goes out $q = 1$ zone. The slow changing part of signals (background) inside the $q = 1$ zone decreases as rule to the end of saw-tooth period.

Figure 2 shows spectra of oscillations. Frequencies (measured by X-ECE) decrease after ECH start during ~ 50 ms to their modulating values $f^*{}_m$. Eigen frequencies $f^*{}_{1/1}$ were obtained by the inverse time delay between low and high

field side ECE signals [1] and directly by the magnetic probes oscillations. Eigen frequencies do not depend on electron temperature, density and input power.
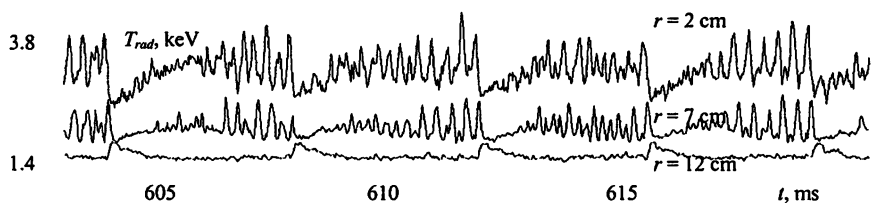
Fig. 1. ECE signals with high level oscillations. $q = 1$ position ~ 8.5 cm
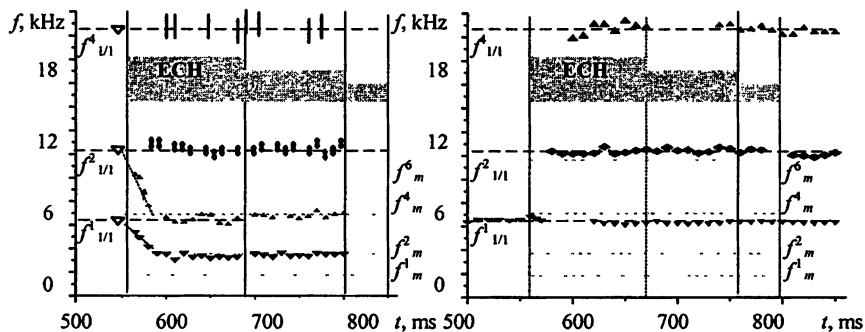
Fig. 2. Spectra of oscillations. *Left* – 2nd X-ECE. *Right* – magnetic probes

Figure 3 shows variation of the ECE profile during oscillations. Area of forced oscillations is limited by $q = 3/2$ zone although $q = 1$ zone is inverse one in disruption according to many channel SXR and ECE. Figure 4 shows the relative amplitudes of ECE and SXR oscillations. SXR distribution has minimum at the center in contradistinction to ECE. This peculiarity is consequence that that this mode in SXR is odd (Fig. 5*a* and *b*). Its "rhythm", which characterizes the motion of disturbance from the external torus side to the internal side and backwards, is 2/4. Interference of SXR oscillations along the chords passing near the center makes them zero. ECE signals have also equal phases at the external or internal sides of torus correspondingly (*c* and *d*). However phases of opposite in space signals are not opposite (*e*). Their motion "rhythm" is 3/4 Besides SXR splashes are wider then ECE splashes on ~ 40÷50 µs.

Fig. 3. Radial distribution of X-ECE: *1* – maximum outside; *2* – maximum inside; *3* – minimal level; *4* – just after internal disruption
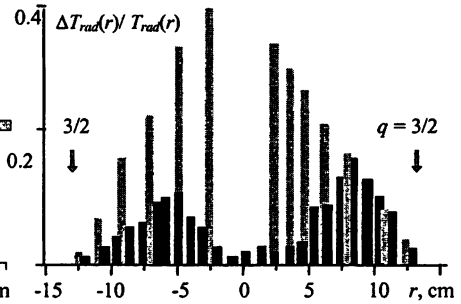
Fig. 4. Radial distribution of relative oscillating amplitudes: black – vertical SXR chamber; X-ECE – measured from low field side. Frequency ~ 3.6 kHz
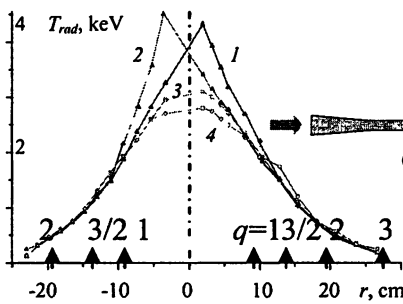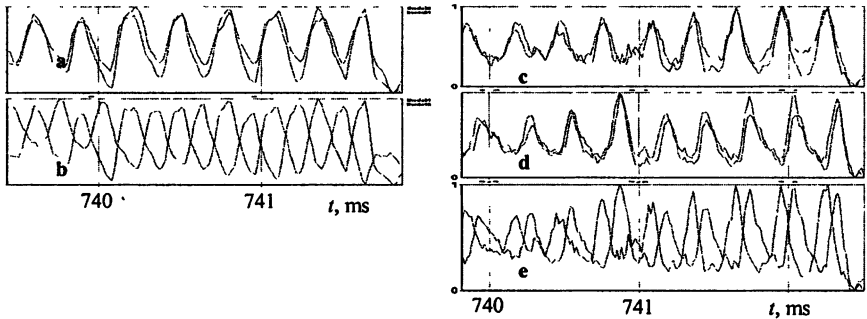

Fig. 5. The phase features of oscillations: *a* – SXR signals along one side radius; *b* – SXR signals from the opposite points of magnetic surface; *c* – ECE from the outer side radius; *d* – ECE from the inner side radius; *e* – ECE from the opposite points of magnetic surface

The analysis of signals from the vertical and horizontal SXR chambers shows that disturbances move in the poloidal direction keeping synchronism along small radius as "spoke of wheel". This effect was checked by two X-ECE signals from different radial positions by oblique antenna (60° in poloidal plane). Such property simplifies the analysis of the disturbance motion in experiment. It is sufficient to investigate ECE signal dynamics only on single magnetic surface.

Figure 6 shows ECE measurements from different points of the poloidal plain at surface $r \sim 5$ cm. Here signals 1, 2, 3 and 4 received from angles 0°, 60°, 300° and 180° correspondingly. Signal 5 (spike of the plasma noise) shows to real time of the internal disruption. Signals 1, 2, and 3 have practically the same depth of modulation whereas the modulation depth of 4th signal is continuously

325

amplified up to the disruption level. Such behavior of signals can not be explained by the pure poloidal disturbance rotation but this is possible – by the intensifying of the oscillating (torsion) motion in the poloidal direction.

Fig. 6. ECE signals from different poloidal points of common magnetic surface

The analysis of disturbance motion in toroidal direction under different levels of input power shows that visible motion at laboratory system changes the direction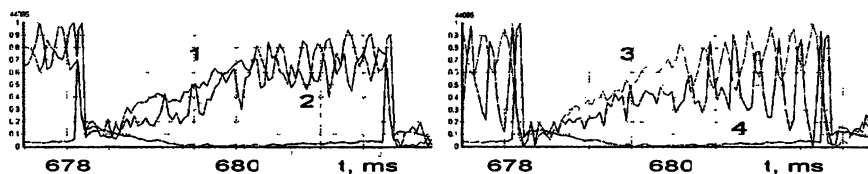 when power is exceeds certain level (~ 200 kW, one gyrotron with diminishing power). Under the growth of EC power (two, three or more gyrotrons) direction of visible motion is kept. In order to reveal the character of the disturbance motion, it should to take into consideration the continuous electric plasma drift of neoclassical kind. Its direction is determined by the electric potential minimum at the plasma center. Observing motion can be explained by the summarizing of the continuous drift motion and the periodical pulsing in opposite direction. The visible motion changes its direction when velocity during pulsing period exceeds continuous one.

The observing peculiarities of the poloidal and toroidal disturbance motion give ground to assume that disturbance accomplishes alternative motion along the magnetic force lines. Such character of motion can be connected with a pulsing of plasma current at area of $m/n = 1/1$ oscillations. In order to check this supposition the ECE measurements in two polarizations in the same time with using of the common antenna and ADC were fulfilled. Optical density for both ECE modes at the central area of column is high and both signals give information about main plasma component. Figure 7 shows the signals receiving from the common point in space (5 cm) inside $q = 1$ zone under low oscillation level. The amplitude variations of both signals are practically equal as it must be when we deal with Maxwellian plasma. However the signals of different polarizations distinguish in phase. Maximum in O-mode outstrips that in X-mode on 40÷50 μs (as difference between X-ECE and SXR) and earlier drops before disruption. Under two gyrotrons X-mode background is saturated, O-mode background decreases. This difference heightens essentially with the following power increase (Fig. 8). Rate of O-mode grows just after disruption excels that of X-mode in three – five times and then slowly decreases.
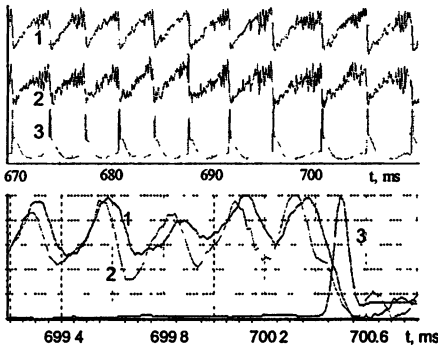
326

Fig. 7. X- (136 GHz) (curve 1), O-mode (68 GHz) (2) and plasma noise (3) signals from "black body" plasma under low level of oscillations (one on-axis gyrotron) in different time scale
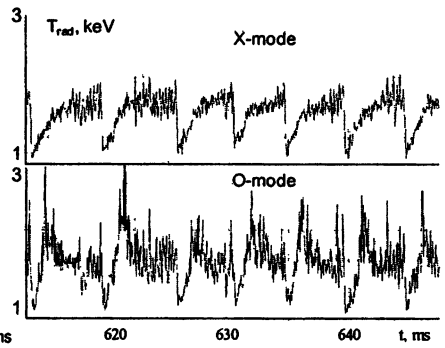
Fig. 8. X-mode and O-mode signals under high level of oscillations (three gyrotrons – two on-axis and one off-axis)

Discussion

Receiving ECE power from plasma with high optical density can be impress as integral of shape $P^x_\omega \sim \int v^2_\perp f(v)d^3v$ for X-mode and for O-mode $P^o_\omega \sim \int v_\perp v_{//} f(v)d^3v$. Differences between integration limits are small under such conditions and integrals can be exchanged by the first approximations: $P^x_\omega \sim <v^2_\perp> \sim <v_\perp><v_\perp>$ and $P^o_\omega \sim <v_\perp v_{//}> \sim <v_\perp><v_{//}>$. According to this evaluation, the variation of perpendicular velocity in acts of pulsing consists of 20÷30%. Variation of longitudinal velocity – 30÷50% is essentially higher in spite of the permanent pumping of perpendicular energy by ECH. The relatively slow changing of longitudinal velocity during every saw-tooth cycle can reach 50÷80%. Evidently the electron distribution "compression" and "widening" in the longitudinal direction with characteristic time of energy over-pumping ~ 45 μs happens in every acts of oscillations. Similar process takes place slowly also during every "saw" cycle. Joint oscillation of O- and X-ECE shows the total energy change during every oscillation period. That is sinusoidal as SXR also. It should to take into account that SXR characterizes namely total energy variations. Different behavior of X-, O-ECE and SXR signals ("rhythm", duration of splashes, phase relations, asymmetry of oscillation distributions) confirms the strong periodical "swinging" of electron velocity vector. The loss of the longitudinal momentum of electrons on the potential plasma waves [3] on the external side of torus and as result the loss of the directional velocity creates the braking effect on motion of "plasma cloud" to the internal side. Phase shifts between O- and X-mode for oscillations on low and high magnetic field sides are

327

opposite. Perpendicular energy in such case strongly rises in consequence of ECH dependence on electron velocities $D^v\!\perp \sim v^2\!\perp/v_{/\!/}$ that explains more deep ECE modulation and considerable exceeding of X-ECE amplitudes above SXR on high magnetic field side. Apparently amount of trapped electrons in this case are significantly increased that drives to saturation of ECH with the power rise. Rhythmic electron distribution "compression" and "widening" in the longitudinal direction can create the plasma current pulsing and as result – the periodical generation of high electric field. Emission spikes of high energy electrons registering by the downshifted O-mode synchronously with oscillations [2] confirm this supposition. Evaluation of the pulsing toroidal electric field can surpass 1 V/cm.

Data show that "temperature" disturbance is not local and occupies all area inside the $q = 3/2$ zone. Position of maximum corresponds to the ECE absorption zone. Disturbances are synchronized along small radius. Their motion is not pure rotating and can be explained as "torsion swinging" along the directions of magnetic force lines under the continuous electric drift of plasma background. In limit of small oscillations, its motion looks like (for observer) as almost pure rotating. In case of strong oscillations, it looks like motion with alternating direction. Electron anisotropy variation and amplitude of "swinging" along force lines essentially depends on the input ECE power in range $0.2 \div 1.2$ MW.

Experimental data show that such terms as "electron temperature" and "classical electric conductivity" by Spitzer can not be used for theoretical description of the global plasma oscillations. The analysis of electron distribution function with taking into account all self-consistent micro (potential plasma waves) and macro fields is necessary. ECE and ECH methods are very fruitful for solution of this problem.

References

1   *Poznyak V. I.* Proc. in 14 ECE Workshop, Santonny, Greece, p 123, 2006.
2.   *Poznyak V. I et al.* Proc. in 10 ECE Workshop, Ameland, the Netherlands, p 155, 1997.
3.   *Poznyak V. I. et al.* Proc. in 15 International Conference on Plasma Physics and Control Fusion, Seville, Spain, Nuclear Fusion, v. 2, p. 169, 1995

FRONT STEERING CONFIGURATION WITH INTERNAL OPTICS FOR THE ECRH ITER UPPER LAUNCHER

A. Moro[1], E. Alessi[1], A. Bruschi[1], S. Cirant[1], R. Chavan[2],
A. Collazos[2], D. Farina[1], M. A. Henderson[3], J. D. Landis[2],
P. Platania[1], E. Poli[4], G. Ramponi[1], G. Saibene[5],
H. Shidara[6], C. Sozzi[1], V. S. Udintsev[2]

[1] Istituto di Fisica del Plasma, CNR-EURATOM-ENEA Association,
20125 Milano, Italy
[2] Centre de Researches en Physique des Plasmas, CRPP-EPFL, Lausanne, Switzerland
[3] ITER, Cadarache Joint Work Site, Saint-Paul-lez-Durance, France
[4] Max-Planck-Institut für Plasmaphysik, EURATOM-Association, Garching, Germany
[5] Fusion for Energy, Barcelona, Spain
[6] University of Tsukuba, Japan

Amongst the possible improvements in the internal optics for the ECRH Upper Launcher of ITER, which is assessed and close to completion, a full quasi-optical design for the launcher has been investigated and here proposed. This option is obtained with the replacement of the mitre bends with free space mirrors and can provide improvements in terms of a reduction of the power density with respect to the mitre bends case, additional flexibility and transmission efficiency, with an overall downgrading of the costs of the launcher. In this work we present the general ideas of this proposal, starting from the present Front Steering (FS) design and following a matching approach from given final beams and positions, in order to minimize impact on design.

Introduction

The physics of the stabilization of Neo-classical Tearing Modes (NTM) in ITER fixes the requirements for the EC Upper Launcher (UL). In particular, stabilization is achieved if the launcher deposits j_{CD} within the magnetic island corresponding to the NTM with a peak value of j_{CD} greater than the local bootstrap current by a factor 1.2.

The build to print stage of the present design of the ECRH Upper Launcher for ITER [1] is straightforward since the stabilization criterion is met for all the locations where NTM are expected to occur. Moreover, latest developments have increased the range including the access to inner regions for sawteeth control as well. Starting from this configuration and from a CRPP proposal we investigated the possibility to replace either one or two of the mitre bends of the launcher by free space mirrors. Motivations of this activity are found in a lower cost with respect to the mitre bends setup and in lower ohmic losses in transmission. Moreover, the exploitation of this solution allowed us to take advantages from some degree of freedom in positioning and choosing the optical properties of additional elements in terms of a lower power density on mirrors and decreased level of astigmatism in the beams injected into the plasma.

Front Steering Extended Physics Launcher (FS-EPL)

The main aims of the ITER ECRH Upper Launcher is to drive current locally in order to stabilize NTMs (which are expected to occur on rational surfaces $q = 3/2$ and $q = 2$) and to deposit EC power near the $q = 1$ rational surface to control sawtooth instability. To meet these requirements, a narrow and peaked driven current profile is necessary, this demanding a large enough steering range and proper focusing for the injected EC beams. The Extended Physics Launcher (EPL-UL) for the upper launcher of ITER is based on a front steering (FS) concept and it represents an upgrade of the FS design of 2006 [1]. In the EPL launcher 2 dedicated steering mirrors are used to launch up to 20 MW of EC power coming from 24 Gyrotron sources ($f = 170$ GHz; $1\div2$ MW each). Power is bunched in four ports, with 8 beams per port divided in two rows (an upper row and a lower one), and using a single steering mirror for each row. A schematic view of the EPL Launcher is shown in Fig. 1.

Optimization studies carried out in terms of poloidal and toroidal injection angles and beam parameters [2] resulting from a constant feedback between beam tracers and designers produced a design that ensures collimated beams with focus in the plasma of ITER and optimal injection angles ($\beta \approx 20°$).
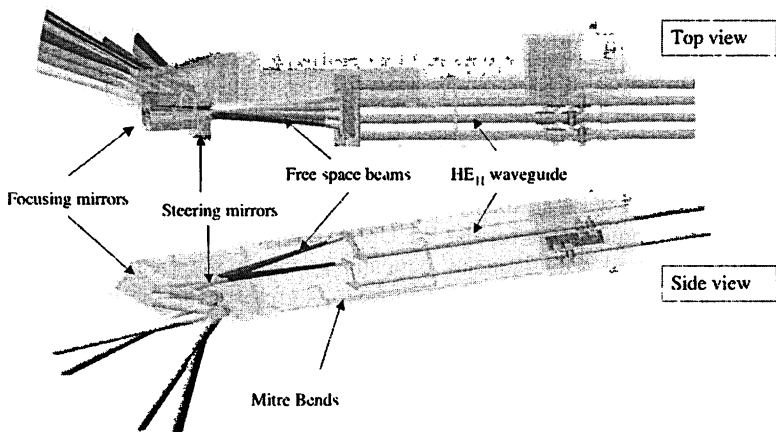
Fig. 1. Schematic views of the EPL in the configuration with mitre bends

The deposition displacement coming from the two steering mirrors is such that beams coming from the upper steering mirror reach inner the NTMs regions and the $q = 1$ surface (in terms of the normalized toroidal magnetic field flux $0.3 \leq \rho_T \leq 0.8$, for a total power deliverable of about 13.3 MW) while the beams injected from the lower steering mirrors access the outer NTMs region ($0.6 \leq \rho_T \leq 0.86$, total power deliverable 13.3 MW). Partial overlapping will be achieved in the range $0.6 \leq \rho_T \leq 0.8$ where the maximum power of 20 MW could be deposited.

The resulting figure of merit for NTM stabilization exceeds the requirements, as shown in Table 1 and in [1]. Even with a possible theoretical reduction of efficiency due to the inclusion of additional physical effects from spatial inhomogeneity and dispersion, included in the quasi-optical model presented in [3], a safety margin on many rational surfaces q and scenarios is still guaranteed in the EPL.

Table 1. NTM stabilization efficiency in the case of the EPL assuming 20 MW of injected power and expected power P_{NTM} to get $\eta_{NTM} = 1.2$ for the different ITER scenarios considered, according to [1]

Scenario	η_{NTM}	P_{NTM} (MW)
2 ($q = 2$)	3.5	6.8
2 ($q = 3/2$)	2.5	9.5
3a ($q = 2$)	2.7	8.9
3a ($q = 3/2$)	1.8	13.2
5 ($q = 2$)	2.1	11.6
5 ($q = 3/2$)	1.9	12.4

A first possibility for improvements in the EPL launcher was studied [4] aiming at the optimization of the driven current density profiles lowering the launching location to get better absorption of the injected power. This analysis showed improvements in the performances but a significant negative impact on cost and schedule for ITER due to the necessary revision of the vessel design, of the port plug structure and of the steering mechanism to cite some. On the contrary, improvements in the internal optics seemed to be more reachable with lower impact the present design, as it will be shown in the following.

Quasi-Optical design improvements on EPL

'The approach followed to design the full quasi-optical (QO) FS launcher consisted in adapting the already developed design with internal mitre bends (MB) with the replacement of the bends with mirrors, without major changes in the blanket shield module (BSM) region, where the final focusing mirrors (FM) and the steering mirrors (SM) and their mechanisms are placed. First, the replacement mirror focal length and the alternative beam path is evaluated using a reference virtual beam for each row. In this way also distances, mirrors positions and preliminary geometry are defined. Successively, quasi-optical elements are detailed and single beamlines are added. Special attention is paid on the resulting beams, in particular regarding launching angles and relative toroidal divergence $\Delta\beta$ of the beams with respect the optimal toroidal injection angle β_{OPT}. Beam tracing calculations [5] are necessary to determine the optimal divergence to get the same deposition location for the different beams launched from different points on the last mirror. Other parameters were kept unchanged with respect to the MB version: the beam spot size on the focusing mirror ($w_{FM} \approx 60$ mm) and the relative spacing between adjacent beam axes on the focusing mirror. The preliminary design is shown in Fig. 2, where the replacement mirrors are named M1

(in front of the waveguide) and M2 (between M1 and FM). The first focusing mirror M1 has a focal length of 793.6 mm to get an output beam waist of 21.0 mm, very close to the one at the former waveguide output.
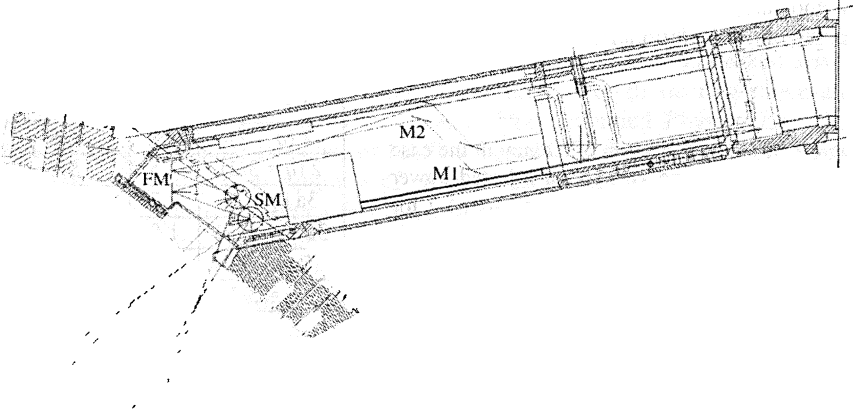

Fig. 2. 2-D schematic view of the new elements of the QO launcher inserted in the port structure

In the approximation valid for nearly circularly polarized beams, the expression

$$P_{DEN} = P_{MB} \frac{\cos \vartheta_{QO} w_{MB}^2}{\cos \vartheta_{MB} w_{QO}^2} \tag{1}$$

can be used to estimate the dependence of the peak power density on incidence angles and beam spot sizes. P_{DEN} and P_{MB} represent the peak power density in the quasi optical case and mitre-bends case respectively, ϑ_{QO} and ϑ_{MB} are the angles of incidence in the two configurations and w_{QO} and w_{MB} the different spot sizes. The circular polarization is considered representative of the one suited for injection at toroidal angles of $\approx 20°$. Substituting the values for the mitre-bends case (from [1]) and using for w_{QO} and ϑ_{QO} the present ones, upper row, we get a reduction of the peak power density on M2 mirror from 4.2 MW/m^2 to about 2.8 MW/m^2.

The mirror M2 is chosen to be flat for convenience: further adjustments to the beam characteristics (including a modification of the astigmatism of the final beams) can be obtained choosing a suitable curvature for its surface. After reflection on M2 mirrors the beams cross in the toroidal and poloidal directions and reach the focusing mirror (here a single mirror is used for each row). The optical properties of the FM and the orientation of the FMs and the corresponding SMs are fixed by the required output beam directions, dimensions and relative spacing. This last requirement is added in order to maintain the already optimized mirrors dimensions in the BSM. Optimum values for beam waists in the plasma ($w_0 = 29$ mm for the USM beam and $w_0 = 21$ mm for the LSM) are reproduced using the 2-D geometrical model for the virtual beamlines (Fig. 2) to define the

FM surfaces. They are chosen as ellipsoids of revolution with parameters $A = 2464.2$ mm, $B = C = 2105.4$ for the upper and $A = 2558.5$ mm, $B = C = 2240.2$) for the lower focusing mirror.

Since the beam incident on the FM is circularly symmetric, reflection produces simple astigmatic beams as a result. Given the mirror orientation and the incidence angle, the propagation of the reference beams is described introducing two effective focal lengths (f_{pol}, f_{tor}) in directions respectively close to the poloidal and toroidal ones. Table 2 shows some of the data of the virtual beamlines of the QO reference design. The beam spot sizes on FMs are in the range $60.5 \div 60.7$ mm for the upper row and $62.0 \div 62.2$ mm for the lower row. A fixed spacing $\Delta y = 44.0$ mm on the FMs was chosen to be the same of the MB design.

Table 2. Beam parameters (in mm) for the virtual beamlines of the QO reference design. Labels in and out refer to input and output parameters with respect to the focusing mirror. Poloidal and toroidal distinction is taken into account for these last parameters.

Virtual beam	w_{0in}	d_{0in}	w_{FM}	f	w_{0out}	d_{0out}
Upper_pol	21	2118.4	60.4	1437	29.0	2740
Upper_tor	21	2118.4	60.4	1141	19.1	1950
Lower_pol	21	2182.5	62.0	1237	21.0	2200
Lower_tor	21	2182.5	62.0	1234	20.9	2190

Mirror orientation is determined to give optimal output angles α_{REF}, β_{REF} for the virtual beams, while toroidal focal length is determined in order to obtain the desired divergence in terms of $\Delta\beta$ for the single beams with respect to β_{REF}. As the rotation of the steering mirror is introduced in terms of the steering angle γ (around mirror rotation axis properly oriented, with steering range $-5.5° < \gamma < +5.5°$), the resulting beam parameters as a function of γ can be determined. In Fig. 3 beam dimensions for the two reference beams in the two astigmatism directions from waveguide termination is presented.
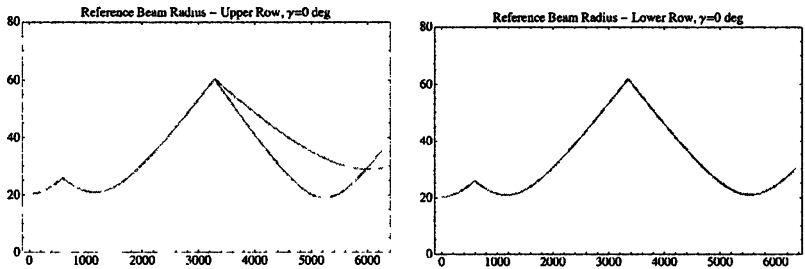

Fig. 3. Beam widths (in vacuum) for the reference beamlines as a function of distance from waveguides towards plasma in the two astigmatism directions. *Left*: Astigmatic beams arise after FM for the upper row. *Right*: Circularity of the beam is preserved after FM for the lower row.

333

Single-beam description

Beam propagation in vacuum within the launcher and towards the plasma was studied independently for each beam of a row. In order to determine precisely the values of the effective focal lengths for each one of the real beams, the relations for reflection from a generic curved surfaces arbitrarily oriented [6] have been applied locally at the beam incidence point. As a result, each beam needs an individual description in terms of waist size and position in the resulting astigmatism directions. Beams are strongly astigmatic in the case of upper row beams and approximately circular for the lower row ones. Astigmatism is not of a generalized type, as expected, and the fixed orientation angle of the spot ellipse in the plane orthogonal to the wave vector k have been evaluated as well.

Regarding the beam spot size orientation after the SM, the ellipse of constant amplitude is found to be oriented close to the poloidal direction (the maximum deviation from the poloidal/toroidal direction is about $|\varphi_W| \approx 14.4°$). Obviously, the more circular the beams are, the less critical the orientation angle is.

The present QO reference design successfully reproduces the good beams of the EPL launcher, in particular in terms of resulting launching angles (with optimal divergence, as shown in Fig. 4), beam dimensions in the absorption region and a reduced astigmatism compared to the Upper beams of the EPL design.

Additionally, peak power density on mirror can be reduced to about 2.8 MW/m^2 in the QO option. In Table 3 and 4 we present the resulting main parameters for the 8 beams of the upper and lower rows as a function of the steering angle γ for the three different possible orientations to give lower, zero and maximum poloidal angle α. It has to be noted that the overall impact on the present design can to be carefully checked only once the QO design (a schematic view of the 3-D analytical model of the reference design is shown in Fig. 5) will be implemented in a CATIA model. The advantage of a greater flexibility resulting from the use of free space mirrors in orientating and shaping the EC beams gives additional margins for corrections or modifications that may be required by physical or mechanical constraints, particularly on the final focusing and steering mirrors.

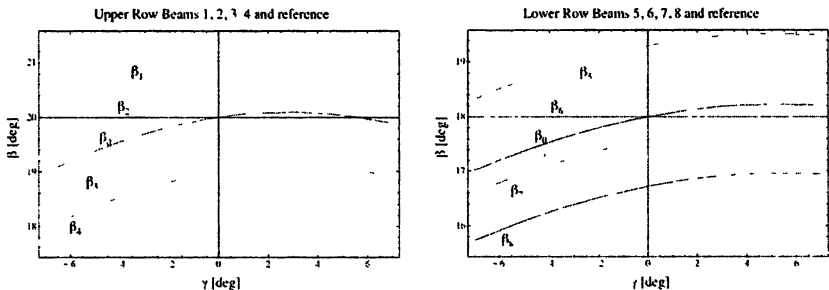**Fig. 4.** Output β as a function of the steering angle γ for the upper row beams (*left*) and lower row beams (*right*). A divergence Δβ[0-2_3] = ±0.3° and Δβ[0-1_4] = ±1° is found for the upper beams, while Δβ[0-6_7] = ±0.4° and Δβ[0-5_8] = ±1.3° appear for the lower beams

Table 3. Output beam parameters for the 4 beams reflected from the USM, for minimum, zero and maximum poloidal angle α (Deg). Beam waists and their locations after USM are in mm.

USM	α	β	w_{0POL}	w_{0TOR}	z_{0POL}	z_{0TOR}
Beam 1 [$\gamma = -5.5°$]	44.6	20.3				
Beam 1 [$\gamma = 0°$]	56.3	21.0	28.9	19.0	2746	1951
Beam 1 [$\gamma = 5.5°$]	68.1	21.0				
Beam 2 [$\gamma = -5.5°$]	44.2	19.6				
Beam 2 [$\gamma = 0°$]	56.1	20.3	29.0	19.1	2739	1950
Beam 2 [$\gamma = 5.5°$]	67.8	20.3				
Beam 3 [$\gamma = -5.5°$]	44.3	18.9				
Beam 3 [$\gamma = 0°$]	55.6	19.7	29.0	19.1	2739	1950
Beam 3 [$\gamma = 5.5°$]	67.6	19.7				
Beam 4 [$\gamma = -5.5°$]	44.1	18.3				
Beam 4 [$\gamma = 0°$]	55.6	19.0	28.9	19.0	2746	1951
Beam 4 [$\gamma = 5.5°$]	67.7	19.0				

Table 4. Output beam parameters for the 4 beams reflected from the LSM, for minimum, zero and maximum poloidal angle α (Deg). Beam waists and their locations after LSM are in mm.

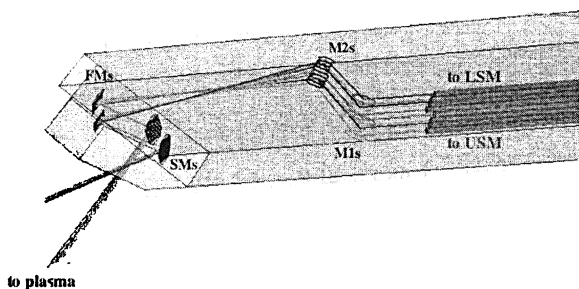| LSM	α	β	w_{0POL}	w_{0TOR}	z_{0POL}	z_{0TOR}
Beam 5 [$\gamma = -5.5°$]	23.6	18.6				
Beam 5 [$\gamma = 0°$]	35.2	19.3	21.1	21.0	2198	2190
Beam 5 [$\gamma = 5.5°$]	46.8	19.5				
Beam 6 [$\gamma = -5.5°$]	23.6	17.7				
Beam 6 [$\gamma = 0°$]	34.9	18.4	21.1	21.0	2194	2186
Beam 6 [$\gamma = 5.5°$]	46.6	18.6				
Beam 7 [$\gamma = -5.5°$]	23.5	16.9				
Beam 7 [$\gamma = 0°$]	34.9	17.6	21.1	21.0	2194	2186
Beam 7 [$\gamma = 5.5°$]	46 4	17.8				
Beam 8 [$\gamma = -5.5°$]	23.3	16.0				
Beam 8 [$\gamma = 0°$]	34.7	16.7	21.1	21.0	2198	2190
Beam 8 [$\gamma = 5.5°$]	46.5	17.0				

Fig. 5. The full QO design. The 8 beamlines for upper and lower row are shown. The dimensions of the two focusing mirrors (FMs) and of the two steering mirrors (SMs) are only indicative.

Conclusions

With equivalent physics performances (in terms of launching angles, proper focusing into the plasma and astigmatism of the beams) the launchers with or without mitre bends still differ in terms of other aspects such as design complexity, transmission efficiency, flexibility and overall cost per port. Even not fully engineered, a full quasi-optical launcher is preferable for cost, power capability and adaptability to possible future adjustments of beam size, astigmatism, trajectory, that may be required by mechanics or physics.

This work has been carried out in within the framework of the European Fusion Development Agreement (task TW6-TPHE-ECHULB1). The views and opinions expressed herein do not necessarily reflect those of the European Commission.

References

1. *Henderson M. A. et al.* Nucl. Fusion *48* 054013 (2008).
2. *Ramponi G. et al* Fusion Science and Technology **52** (2007)
3   *Balakin A. A. et al.* Nucl Fusion *48* 065003 (2008).
4. *Ramponi G. et al.* Nucl. Fusion **48** 054012 (2008).
5   *Poli E et al* Proc 14th Joint Workshop on Electron Cyclotron Emission and Electron Cyclotron Resonance Heating, Santorini, Greece, 2006, pages 301—305
6   *Moro A. et al* Fusion Science and Technology **52** (2007).

NUMERICAL ANALYSIS OF THE W7-X ECRH TRANSMISSION LINE

G. Michel[1], W. Kasparek[2]

[1] Max-Planck-Institut für Plasmaphysik, TI Greifswald, EURATOM Ass. Greifswald, Germany
[2] Universität Stuttgart, Institut für Plasmaforschung Stuttgart, Germany

Quasi-optical transmission lines with a complicated three-dimensional geometry and many mirrors are difficult to model numerically with general purpose codes. They are challenged by the size, the large number and the complicated arrangement of the mirrors. In the following a method and computer implementation are presented, which address these issues and use the W7-X ECRH transmission line as an example.

Introduction

The design of quasi-optical transmission lines is usually based on the ABCD matrix formalism for Gaussian beams [1]. The design basis is a well-defined Gaussian input beam. However, a gyrotron output beam is usually not perfectly Gaussian. In addition the mirrors produce mode conversion and diffraction losses. In order to model these phenomena and the effect of tolerances and misalignments, a numerical analysis is desirable. In the case of the W7-X ECRH transmission line [4] there is the additional challenge that there are more than hundred mirrors which partly extend over hundreds of wavelengths (multi-beam mirrors) in a complicated 3D arrangement.
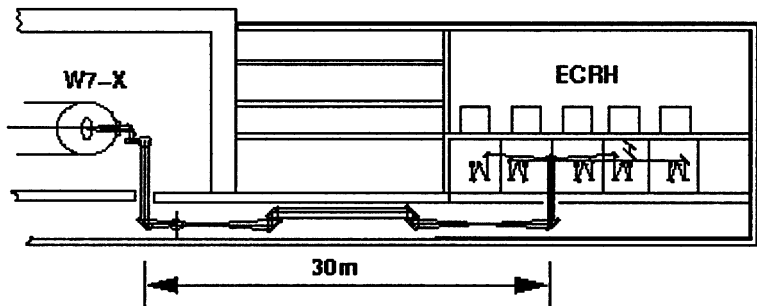
Fig. 1. ECRH transmission line for 5 gyrotrons

In Fig. 1 we can identify the five single-beam transmission lines which consist mainly of the beam matching optics and the polarizers. Finally they are combined into the multi-beam waveguide. The multi-beam waveguide is a Gaussian telescope which reproduces the entrance field pattern at the exit plane. The entrance pattern is five individual beams, therefore we have the same beams also in the exit plane where they can be separated and redirected into the torus. W7-X has two of these transmission lines.

The modeling of such a large and complicated mirror setup is difficult to handle for computer codes, which usually make use of the plane wave decomposition in conjunction with the FFT to propagate paraxial beams. In addition, the plane wave decomposition is not very accurate for mirrors with a large tilt angle, as it only applies to apertures which are perpendicular to the optical axis. Classical EM codes can not be used as the structures are too large compared to the wavelength where geometrical optics or Fraunhofer diffraction are too inaccurate.

Mathematical Background

The field propagator which is used can be seen as a generalized plane wave decomposition and solves the scalar Helmholtz equation in the wavenumber domain [2]. It (back)propagates the field between two plane apertures with arbitrary orientation in a global coordinate system. An aperture is represented by the $z = 0$ plane of its local coordinate system. If the position of the target has a positive z-component in the local coordinate system of the source and the position of the source has a negative z-component in the local coordinate system of the target, then a forward propagation is performed. In the opposite case, a backward propagation is carried out. I.e. all waves pass the aperture from the negative-z half space to the positive-z half space. So there is only one operator which distinguishes automatically between forward and backward propagation [2]:

$$U_t\left(k_{x,y}\right) = \frac{1}{k_z} U_s\left(\left(\mathbf{S}^\mathsf{T}\mathbf{T}\mathbf{k}\right)_{x,y}\right)\beta\left(\left(\mathbf{S}^\mathsf{T}\mathbf{T}\mathbf{k}\right)_z\right)e^{-j(\mathbf{T}\mathbf{k})_z d} \ . \tag{1}$$

Here, $e^{+j\omega t}$ time dependence is assumed and $k_z = \sqrt{k_0^2 - k_x^2 - k_y^2}$ holds. The subscripts of vectors refer to their respective components, U_t and U_s are the two-dimensional target and source distributions in the wavenumber domain, β is the ramp function, d is the distance between the apertures, the columns of the dyads $\mathbf{S}$ and $\mathbf{T}$ consist of the base vectors of the local coordinate systems of the source and target aperture within the global coordinate system. The transformation from the spatial domain to the wavenumber domain is carried out via the FFT which increases the computational speed significantly.

In order to be able to represent arbitrarily polarized wave beams, the field in the local $z = 0$ plane is represented by an Ansatz for the electric vector potential $\mathbf{F}(x,y,0) = u(x,y)\mathbf{F}_0$ where $\mathbf{F}_0$ is a constant complex vector and u is two-dimensional scalar function. Now the field calculations involve only scalar operations while the polarization state is preserved. If we took a constant vector for the electric or magnetic field, this Ansatz would not be correct because $\mathbf{E}$ and $\mathbf{H}$ must obey the Maxwell equations and hence the ratio of their components cannot be constant.

In order to produce the right polarization state after the reflection on a mirror or polarizer, we consider only the transformation of $\mathbf{F}_0$ for the plane wave which represents the "mass center" of U_t. For this plane wave we can write the definition of the electric vector potential in matrix form:

338

$$\mathbf{E_0}(\mathbf{r}) = -\nabla \times \mathbf{F_0}e^{-j\mathbf{k_0} \cdot \mathbf{r}} / \varepsilon_0 = \frac{-1}{\varepsilon_0} \begin{Bmatrix} 0 & k_z & -k_y \\ -k_z & 0 & k_x \\ k_y & -k_x & 0 \end{Bmatrix} \mathbf{F_0}e^{-j\mathbf{k_0} \cdot \mathbf{r}}. \qquad (2)$$

The incident and reflected electric field in the center of the mirror ($\mathbf{r} = \mathbf{0}$) can now be expressed in the form of (2). The boundary conditions on a perfect electric conductor define the sum of the incident and reflected electric field vectors. From a comparison of coefficients in this sum it is easy to see that the boundary conditions for $\mathbf{F}$ are identical to those of $\mathbf{H}$. Therefore, after a reflection on a flat mirror in the x-y-plane of the local coordinate system, only F_z has to be multiplied by -1.

For polarizers this procedure is a little bit more complicated. First the incident electric field is calculated by (2). The reflected electric field is calculated by multiplying the incident field with the 3D Jones-matrix [3]. Unfortunately, the matrix in (2) is of rank 2 and cannot be inverted in order to obtain $\mathbf{F_0}^{\text{refl}}$ from $\mathbf{E_0}^{\text{refl}}$. This is only natural because the definition of the vector potential leaves a gauge freedom which is used by the Lorenz or Coulomb gauge. Hence, in order to calculate $\mathbf{F_0}^{\text{refl}}$ from $\mathbf{E_0}^{\text{refl}}$ we must introduce a constraint. A reasonable assumption is $\mathbf{F_0}^{\text{refl}} \cdot \mathbf{k_0}^{\text{refl}} = 0$. This has the effect that there will be no cross-polarization in the outer regions of a beam. It can be enforced by transforming $\mathbf{E_0}$ to a coordinate system where $\mathbf{k}^{\text{refl}}$ has only a z-component and E_z is negligible or zero. Usually the z-axis of this coordinate system will be the connection from the center of the polarizer to the center of the next mirror. When we now enforce $F_{0z} = 0$ in this coordinate system, the matrix in (2) becomes a regular 2×2 matrix which can be inverted. The resulting vector $(F_{0x}, F_{0y}, 0)^T$ can now be transformed to the global coordinate system or to the local coordinate system of the next mirror or aperture.

Implementation

Complex geometries with many mirrors can best be handled by an object-oriented design. A GUI would be rather obstructive for complex geometries with hundreds of mirrors. Therefore the computer code is implemented in the form of a high-level programming language. It is an object-oriented extension to the command language Tcl/Tk which provides the basic scripting functionality. Mirrors, polarizers, vacuum windows and the like are instances of a class of type "aperture". The most important attributes of that class are a complex 2D field for the storage of u with dimensions according to the size of the aperture, a real 2D field for the storage of the power distribution on a window or the phase correction of a flat mirror, a complex 3D vector for the storage of $\mathbf{F_0}$ and a real 3×3 matrix for the storage of the dyad which maps the local coordinate system to the global one. The most prominent methods of that class are the setup of the attrib-

utes, methods for rotation and translation of the apertures, a method to calculate the (back)propagated field on another object of type aperture and a method which we call "toggle" which needs some explanation.

When an aperture serves as the target of a projection, the source must be located in its (local) negative half-space (see above). If it is a mirror, the reflected beam is directed in the negative half space as well which makes it impossible to turn that aperture into a source for the next aperture which is also located in the negative half-space. It is the purpose of the "toggle" operation to overcome this problem. It turns the aperture by 180° around its y-axis, it sets the orientation dyad accordingly and it exchanges $u(-x)$ and $u(x)$, such that the field distribution remains unchanged in the global coordinate system. The last operation is to multiply F_{0x} by -1 since the x-axis points now in the opposite direction. This is not done for F_{0z} because the boundary condition on a perfect electric conductor is automatically fulfilled by the rotation of the z-axis. In the case of a polarizer, the Jones-matrix must be applied instead as described above. If it is not a plane mirror or polarizer, the corresponding phase corrector must also be applied, but this is not part of the "toggle" operation.

The above methods are complemented by other methods for the calculation of diffraction losses, phase unwrapping or phase correction [2] and the like, such that they form a tool box for all required operations on the optical elements. This serves now as a language to describe a complex quasi-optical system with many elements similar to the textual description of scenes in 3D modelers. Iterative algorithms for phase reconstruction and mirror synthesis or Fox-Li iterations on quasi-optical resonators can be implemented in minutes. Due to the application of the FFT and the fact that only the scalar Helmholtz equation is solved, the interpreter is fast enough to do trial-and-error experiments and to optimize parameters manually.

Applications

The described code was used to model the ECRH transmission line of W7-X. A gyrotron beam travels along 19 mirrors and 2 polarizers, where 3 mirrors are internal mirrors of the gyrotron, 7 mirrors are multi-beam mirrors and 2 mirrors belong to the ECRH launcher in the plasma vessel. However, a more realistic scenario is to inject measured beams (measured amplitude + reconstructed phase) into the model to investigate the field pattern and the diffraction losses at any position in the transmission line. Calculations of an injected beam which was measured on the manufacturer's gyrotron test stand have shown that the non-Gaussian but paraxial content is not completely lost during the transmission due to the effective mirror diameter of four times the local radius of the Gaussian beam. Figure 2 below shows that the side lobes in the gyrotron window can still be recognized at the torus window. However, this is not an undesired behavior as the non-Gaussian content is still delivered to the plasma instead of being lost in the transmission line. The similarity of the figures is also a confirmation for the imaging properties of the quasi-confocal design of the system, yielding broadband transmission characteristics.
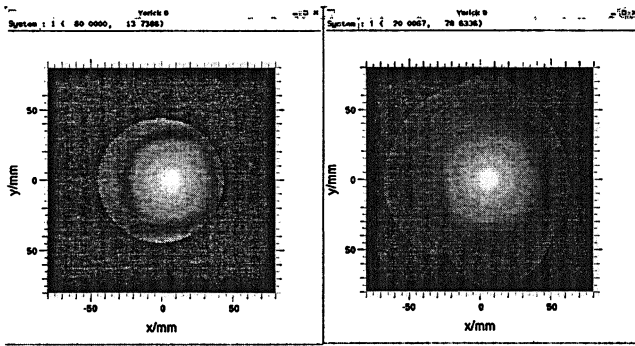
340

Fig. 2. Reconstructed beam at the gyrotron window (*left*) and at the torus window (*right*)

Another possible application would be the in-situ beam reconstruction where the field at any position can be calculated from infrared images of any three (not necessarily consecutive) mirror surfaces. As the IR camera looks perpendicularly onto the mirror it will not be hit by the microwave beam. This can be helpful in geometrically constrained areas and could be programmed in minutes. Note that there is no rectification of the infrared images required (it is even forbidden). We have also used this code to estimate the spill-over on subsequent mirrors, depending on a beam tilt caused by the thermal expansion of the gyrotron cavity during a longer pulse.

Summary

A method for the modeling of complicated quasi-optical transmission lines was developed. Measured or calculated fields can be tracked from the gyrotron cavity to the plasma. Algorithms for the phase retrieval or mirror synthesis can easily be implemented. The actual purpose of this development was the calculation of look-up tables for the control of the ECRH launchers of W7-X in conjunction with the polarizers such that the desired content of O- and X-mode polarization is produced, depending on the poloidal and toroidal launching angles. Other applications are the investigation of tolerances or mechanical drifts in the transmission line or to identify locations where the given beam pattern differs too much from the design beam (especially on vacuum windows).

References

1   *Goldsmith P. F* Quasioptical Systems, IEEE Press (1998).

2. *Michel G , Thumm M* Spectral Domain Techniques for Field Pattern Analysis and Synthesis, Surveys on Mathematics for Industry, vol 8, pp. 259–270, 1999

3   *Wagner D., Leuterer F* Broadband Polarizers for High-Power Multi-Frequency ECRH Systems, Int J of Infrared and MM-Waves, Vol. 26, No 2, 2005, pp. 163–172

4   *Erckmann V et al.* Electron cyclotron heating for W7-X: Physics and Technology, Fusion Sci Technol. 52(2007) 291–312.

CONCEPTUAL DESIGN OF THE LOWER HYBRID ADDITIONAL HEATING SYSTEM FOR FAST

F. Mirizzi, A. Cardinali, R. Cesario, L. Panaccione,
V. Pericoli Ridolfini, G. L. Ravera, A. A. Tuccillo

Associazione EURATOM-ENEA sulla Fusione, C. R. Frascati, Frascati (Rome), Italy

In the frame of the European Fusion Research Program (EFP), a new tokamak machine, the Fusion Advanced Studies Torus (FAST), has been proposed by the Italian Fusion Association as a Satellite Tokamak for the ITER program. FAST must investigate burning plasma relevant dynamics, associated with the presence of energetic ions and dominant electron heating, as well as advanced plasma operation regimes. The total additional RF heating power coupled to the FAST plasma is 40 MW of which 30 MW of ICRH at $f = 60 \div 90$ MHz, and 4 MW of ECRH at 170 GHz. For long pulse Advanced Tokamak (AT) scenarios, a 6 MW Lower Hybrid Current Drive (LHCD) system at 3.7 GHz will actively control the current profile.

Introduction

In order to demonstrate by the first half of this century that nuclear fusion is a safe and environmentally acceptable source of energy, the construction of a prototype reactor (DEMO) should start before the complete exploitation of ITER. To fulfill this ambitious objective, DEMO regimes of operations must be effectively demonstrated during the first ten years of operations of ITER.

The successful development of these regimes on ITER would be clearly difficult and expensive. Hence preliminary activities on smaller devices, with sufficient operational flexibility and able to investigate the peculiar physics of burning plasma conditions, are considered necessary.

FAST has been envisaged to fully accomplish the first three out of the seven missions established by the European Fusion Research Program (EFRP) [1]. Moreover missions 4 and 5 are consistent with FAST scientific rationale, while mission 6 and 7 are out of the scope of its conceptual design.

FAST: a satellite tokamak proposal

In the above frame the Italian Fusion Associations is proposing to the European scientific community the "Fusion Advanced Studies Torus" (FAST) (Fig. 1), a tokamak machine which main objective is to exploit the physics of burning plasmas.

The conceptual design of FAST [2] foresees an aspect ratio $R/a = 1.82/0.64$ (R and a in metres), a magnetic field up to 8 T and a plasma current $I_P = 2.0 \div 7.5$ MA. The average plasma density $<n_{20}>$ is in the range $1.3 \div 5.0$ m^{-3}, and the expected maximum electron temperature is $T_0 = 15$ keV with a $Q = 0.2 \div 3.0$.

These parameters would guarantee reliable operations in the reference H-mode scenario, and a good flexibility at Advanced Tokamak (AT) regimes in long pulse operations with reduced magnetic field and plasma current.

Following the recommendations of the EFRP, FAST will operate in Deuterium plasmas; to achieve burning plasmas conditions, plasma ions will be accelerated in the half-MeV range through an Ion Cyclotron Resonance Heating (ICRH) system (f = 60÷90 MHz) able to couple up to 30 MW of RF to the plasma. An Electron Cyclotron Resonance Heating (ECRH) system

Fig. 1. FAST Load Assembly Axonometric view

(f = 170 GHz) will provide enough power (P = 4 MW) for MHD control. This power will be also available for current profile control and electron heating. The active control of the current density profile is assigned to a Lower Hybrid Current Drive (LHCD) system that will allow the generation and sustenance of Advanced Regime scenarios at ITER-like plasma densities.
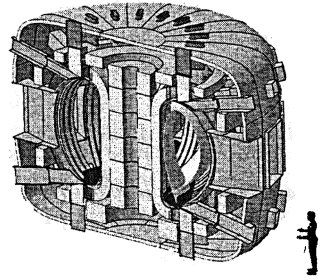
The LHCD system

The LHCD system is designed to couple a nominal RF power $P \geq 6$ MW at f = 3.7 GHz in pulsed regime (pulse length up to 160 s, equivalent to CW conditions). The frequency is mainly determined by existing high power RF generators, the TH-2103 klystron, rated for 500 kW/CW and 650 kW/10 s. A back up solution at a more efficient frequency of 5 GHz has been also studied; this alternative will be further developed if in the near future suitable RF sources will be available.

Assuming an estimated overall RF transmission loss of about 20%, at least 15 klystrons (total installed power P_{Tot} = 7.5 MW) will be used. Passive Active Multijunction (PAM) launchers [3] are envisaged to face the harsh plasma conditions expected in FAST and to assure an effective cooling of the antenna in long pulse operations and with heavy thermal loads.

A prototype PAM launcher has recently shown its good coupling performances on the Frascati Tokamak Upgrade (FTU) [4], [5].

To limit the RF losses in the Main Transmission Line (MTL), an oversized WR 650 rectangular waveguide (165.10 × 82.55 mm), carrying the fundamental TE_{10}, mode will be used. This waveguide has a nominal specific attenuation A = 4.84 × 10^{-3} dB/m at 3.7 GHz; by considering an average length of 40 m, the RF losses in the MTL are limited to 4.36%. The remaining 16% are mainly due to the launcher and to the other high power RF components. At the end of the MTL the RF power is split in four output rectangular waveguides (the WR 284 standard) by means of classical 3 dB hybrid couplers or equivalent devices. The

successive power splits, necessary to effectively feed the launcher, are made through E-plane bi-junctions.

The PAM launcher

The PAM for FAST is designed to launch a power spectrum with an $N_{\parallel peak} = 1.9$. At $f = 3.7$ GHz the vacuum wavelength is $\lambda_0 = 81.081$ mm and the phase constant $k_0 = 4.44°/$mm. To maximize the Multi-Junction (MJ) effect (reduction of the reflected power in the launcher and toward the generator) [6], a fixed phase shift $\varphi_0 = 270°$ between active waveguides on the same poloidal row has been set, thus the pitch between these waveguides result:

$$\delta = \frac{\varphi_0}{k_0 \cdot N_{//0}} = 32 \text{ mm.} \tag{1}$$

By considering a wall thickness $wt = 2$ mm to assure a good mechanical stiffness to the launcher, the same inner width of 14 mm has been assigned to both active and passive waveguides (Fig. 2).
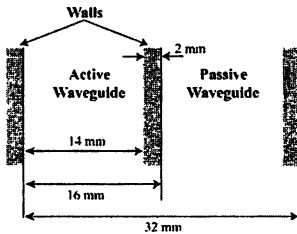

Fig. 2. Waveguides inner width

To limit the RF losses in the launcher, their inner height is set to $h_{WG} = 72.136$ mm (the height of the standard WR 284 rectangular waveguide). The cross section surface of each elementary waveguide is therefore about 0.001 m^2.
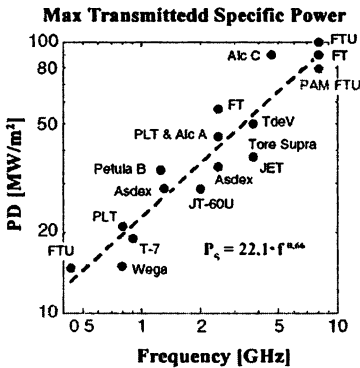

Fig. 3. Power density in existing LH experiments

Existing LHCD experiments (Fig. 3) suggest to limit the maximum power density at the launcher mouth to a safe value $D_{safe} \leq 30$ MW/m^2 already obtained in Tore Supra and JET (at $f = 3.7$ GHz, $D_{max} \approx 60$ MW/m^2 on the interpolating straight line in Fig. 3). Thus the 500 kW generated by a single klystron, reduced to $P_1 = 400$ kW at the launcher mouth because of the transmission losses, must be launched at least by:

344

$$N_{\min} = \frac{P_1}{D_{safe} \cdot S_1} = \frac{0.4}{30 \cdot 0.001} = 13.3 \qquad (2)$$

waveguides. Because, with a phase shift of 270°, the phase periodicity between active waveguides on the same row is 4, the 400 kW must be split in 16 waveguides (the minimum integer multiple of 4 greater than 13.3) arranged in four rows to form a PAM block (Fig. 4).

Each single row of 4 active waveguides, but including the 4 passive ones, is addressed as the PAM module. With this configuration the actual power density at the launcher mouth, in perfectly matched conditions (VSWR = 1:1), is:

$$D_{eff} = \frac{P_1}{N \cdot S_1} = \frac{0.4}{16 \cdot 0.001} = 25 \,\text{MW/m}^2 . \qquad (3)$$

The chosen power density limit of 30 MW/m^2 is reached with a VSWR = = 2.6:1; a total power reflection increases the power density to 50 MW/m^2, a value that, according to Fig. 3, can be still tolerated.
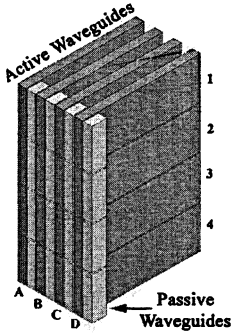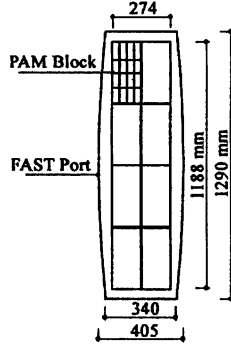

Fig. 4. The PAM block

Fig. 5. Port schematic and launcher layout

The launcher configuration depends on the cross-section dimension of the FAST's port (1290 × 405 mm at the horizontal middle plane), but the width is reduced to $W_P = 340$ mm at the upper and lower end planes (Fig. 5). The width of a PAM block is $W_{Blk} = 4 \times \delta + wt = 130$ mm, hence the maximum number of blocks in the poloidal direction is:

$$N_{Blk} = \text{Int}\left(W_P/W_{Blk}\right) = 2 \qquad (4)$$

where "Int" denotes the integer part of the result. The height of a PAM block is instead $h_{Blk} = 4 \times (h_{WG} + wt) = 288.55$ mm, so that a maximum of

$$N_{\max} = \text{Int}\left(h_{port}/h_{Blk}\right) = 4 \qquad (5)$$

blocks can be staked in toroidal direction.
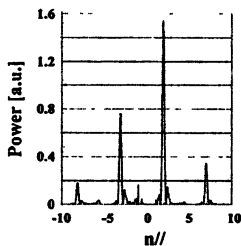
f=3.7GHz, φ=0°, n$_e$=6x10^7 m^{-3}

Fig. 6. Power Spectrum

As a consequence only a launcher composed by 8 PAM blocks, arranged in four toroidal rows and two poloidal columns (Fig. 5), can be allocated in a port and two ports are necessary to launch the required power. For symmetry reason both the launchers must be made by 8 blocks so that 16 klystrons must be used and the coupled power is increased up to 6.5 MW. The RF spectrum of the launcher is given in Fig. 6.

System configuration

The LHCD system is split in four independent modules (Fig. 7), each made by four klystrons (K) fed by a single High Voltage Power Supply (HVPS). Four Solid State Switches (S/S Sw) per module act as fast protection units for the klystrons.
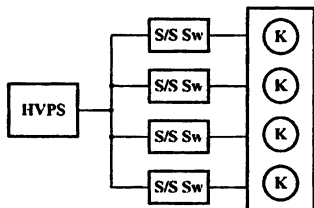

Fig. 7. Layout of a LHCD module

Given the nominal characteristics of the klystron (V_K = 60 kV, I_{Beam} = 20 A), the HVPS is dimensioned for an output voltage V_H = = 70 kVdc, to compensate the voltage drops along the high voltage feeding lines, and an output current I_H = 100 A to operate with a safety margin of 25%. The four klystrons of a module feed 2+2 PAM blocks belonging to same toroidal rows, so that a failure of whichever HVPS does not affect the coupling performance of the remaining rows of the two launchers.

The RF layout of the system is based on a high stability 3.7 GHz crystal controlled oscillator (XCO), which output feeds four primary lines (Fig. 8). Each
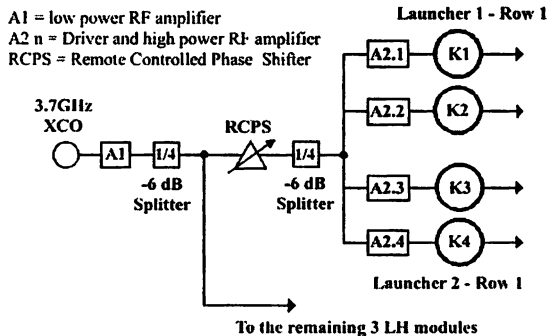
A1 = low power RF amplifier
A2 n = Driver and high power RF amplifier
RCPS = Remote Controlled Phase Shifter

Fig. 8. RF system layout

line in turn feeds the four klystrons pertaining to a launcher's row. The phase of each primary line is set by ¡a, suitable remote controlled phase shifter to opportunely fix the output phase of that row with reference to the remaining ones and thus to change the refraction index $n_\parallel$ of the whole launcher.

Conclusion

FAST, the new tokamak proposed by the Italian Association in the frame of the ITER programme, integrates in a single device many scenarios relevant for ITER/DEMO operations and will provide a unique opportunity to explore unexpected physics issues. FAST is a key facility for international collaboration and for training of young scientist in an ITER-scale device. The realization of FAST will involve an average project team, including other European Associations, of about 120 ppy. The construction time is estimated in 6 years following the design phase and the placement of the contracts for the long lead items.

Additional RF heating and current drive systems are essential for the full realisation of its scientific and technological objectives.

References

1. *EFDA-EFRP*, Positioning, Strategic outlook and need for infrastructure towards DEMO. Part II. Facilities. Input to the Facilities Review Panel. 6 May 2008. (EFDA Leaders, EFDA Associates and F4E).
2. *Italian Association on Fusion*: FAST, the Fusion Advanced Studies Torus, a proposal for a facility in support of the development of fusion energy. ENEA internal report, May 2008.
3. *Bibet Ph. et al.* Principle of a retroreflecting LH antenna. Conf. IAEA 1994: LHCD in ITER (IVA-LH)
4. *Mirizzi F. et al.* The test of a PAM launcher on FTU: the first step toward the LHCD launcher for ITER. Fus. Eng. Des. Vol. 74, Nov. 2005, 237–242.
5. *Pericoli V. Ridolfini et al.* LHCD and coupling experiments with an ITER-like PAM launcher on the FTU tokamak. Nucl. Fusion 45 (2005) 1085–1093.
6. *Moreau D et al.* Coupling of slow waves near the lower hybrid frequency in large tokamaks, CEA Internal Report EUR-CEA-FC-1246, 51-70, CEA Cadarache, 1983-84.

VACUUM COMPATIBLE QUASI-OPTICAL TRANSMISSION LINE WITH REMOTE STEERING LAUNCHER

B. K. Shukla and S. V. Kulkarni

Institute for Plasma Research BHAT, Gandhinagar, Gujarat (India) 382428

The idea of vacuum compatible quasi-optical (QO) transmission line with remote steering (RS) launcher is explored for ECRH systems in tokamak. The normal QO line consists of metallic mirrors (focusing as well as plane). The space requirement for QO line (from gyrotron to tokamak) is more. This is a problem for smaller as well as for large tokamaks. The use of remote steering antenna at the exit of QO line not only reduces the space requirement near the tokamak but also reduces the requirement of large number of mirrors to transfer the power from gyrotron to tokamak.

In RS launcher, the symmetric beam steering is achieved at a length L ($8a^2/\lambda$) of square-corrugated waveguide (SCW), where "a" is width of waveguide and "λ" is wavelength of microwave and at $L/2$ ($4a^2/\lambda$) anti-symmetric steering is achieved. The RS launcher can be selected as per the feasibility and space availability inside tokamak hall.

The existing QO lines are not vacuum compatible and need more maintenance. If QO lines are vacuum compatible, the chances of arc reduce and power-handling capability increases. The QO line alone requires more pumps to make it vacuum compatible, while QO line with RS launcher reduces the vacuum requirement significantly.

1. Introduction

A conventional transmission line for ECRH system consists of a matching optic unit, corrugated waveguides, bends, polariser, uptaper, bellows and an ultra high vacuum (UHV) compatible window figure 1. The circular corrugated waveguides are used to minimize the transmission loss in the line for a gaussian beam in HE_{11} mode. The conventional transmission lines are either pressurized or evacuated.
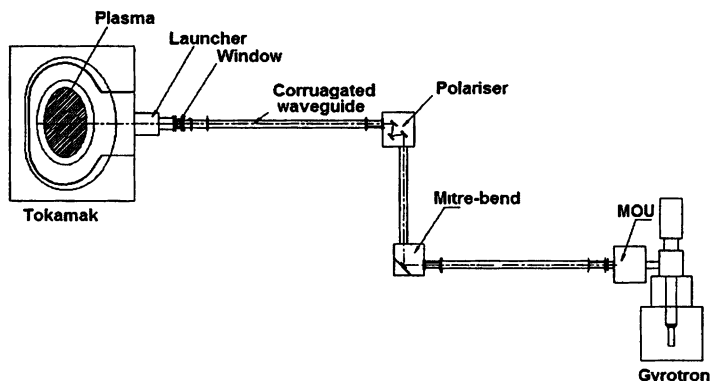

Fig. 1. Conventional transmission line for ECRH system

An alternate to this conventional transmission line could be mirror based quasi-optical (QO) transmission line. The QO lines are successfully installed in few tokamaks like TEXTOR and W7-X [1, 2, 3]. The normal QO line consists of profiled and plane mirrors which require more space inside the tokamak hall. The mirrors are mounted in free space and require periodic maintenance to avoid any arcing problem during the high power operation. The problem of maintenance of QO line can be minimized if the mirrors is mounted inside a vacuum compatible duct. But in this case the vacuum requirements will be more to make entire line compatible to high vacuum.

The use of remote steering (RS) launcher alongwith QO line may reduce such problems. The RS launcher is advantageous in several ways like; reduction in the space requirement near the tokamak, reduced vacuum requirement for vacuum compatible QO line, maintenance easy as number of mirrors is reduced and steering can be achieved remotely for current drive experiments.

2. Quasi-optical Transmission line

Since microwave beam emerges out from the gyrotron can propagate freely in space, an alternate transmission line can be designed without circular corrugated waveguide. A mirror based transmission line consisting of focusing and plane mirrors can be used to transmit the power from gyrotron to tokamak. The mirrors of the line can be designed based on quasi-optical gaussian beam theory. The focusing mirrors used in transmission line prevent the divergence of beam and reduce the size of transmission line. The mirrors at the end of transmission line near the tokamak can be used as launcher and required beam size can be achieved inside the tokamak.

The mirrors for the QO line can be designed using quasi-optical gaussian beam theory [4, 5, 6]. The mirrors size and profile can be estimated and it can be seen easily that at 140 GHz frequency, the 63.5 mm beam spreads to 300 mm after travelling to ~ 2.8 m (Fig. 2). Thus for QO line, the distance between two mirrors of size 500 × 300 mm would be around 5.5 m.
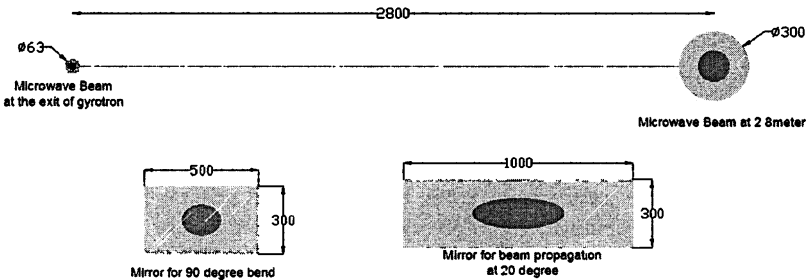

Fig. 2. Gaussian beam divergence and approximate size of mirrors for QO line

Thus for a transmission line of ~ 25 m long, around six to seven mirror will be required to transmit the power from gyrotron to tokamak as shown in the Fig. 3. The requirement of mirrors for MOU and polarizer (RFCU: RF conditioning unit) is same for both the transmission line conventional as well as QO line. Thus the mirror transmission line seems simpler and easy than the line based on circular corrugated waveguide.
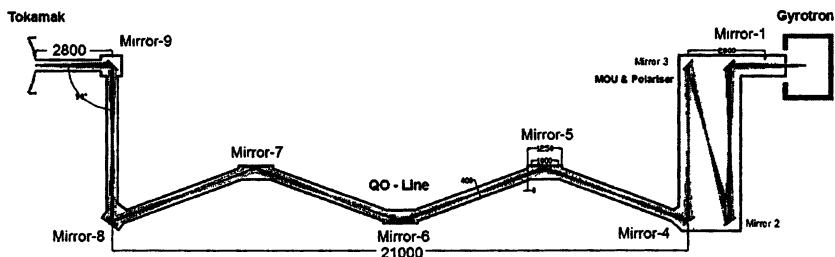

Fig. 3. Quasi-optical mirror transmission line

3. Anticipated problems with a quasi-optical transmission lines

Although the mirror transmission line seems simpler but it has certain problems related to its maintenance and requirement of space inside tokamak hall. The following problems can be anticipated with a quasi-optical transmission lines system:

- The mirrors of line are very big in size and need more space to mount.
- These lines are not vacuum compatible and need more maintenance.
- The connection of such line to the tokamak port may need bigger opening at radial port.
- Alignment of mirrors is a tedious job after every maintenance.

4. Hybrid transmission line system

The mirror based HV compatible transmission line requires large number of mirrors and more space for installation. In order to minimize the space requirement and number of mirrors in quasi-optical transmission line, the idea of remote steering can be used alongwith QO line. The schematic of hybrid transmission line (QO with RS launcher) is shown in Fig. 4.

The hybrid transmission line system would have another advantage that the mirrors inside or near the tokamak can be avoided and beam steering for ECCD experiments can be achieved remotely with RS launcher.

The remote steering launchers [7–11] are designed and tested for high power. The concept of steering of beam with square corrugated waveguide (SCW) is based on image characteristics of the waveguide. The symmetric and

anti-symmetric steering can be achieved with SCW. The square corrugated waveguide show symmetric steering at a length of $8a^2/\lambda$, where "a" is width of square corrugated waveguide and "λ" is wavelength of microwave and anti-symmetric at half-length i.e. $4a^2/\lambda$. The length of RS launcher can be decided as per the feasibility and available space inside the tokamak hall. The normal length of RS launcher at symmetric steering is several meters (around 12.5 m at 140 GHz frequency). Thus if total transmission line length is 25 m then using RS launcher and few mirrors of QO line, the power can be transmitted from gyrotron to tokamak as highlighted in Fig. 5. Thus the hybrid transmission line can be compact and simpler.
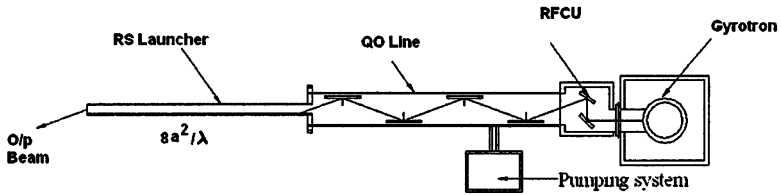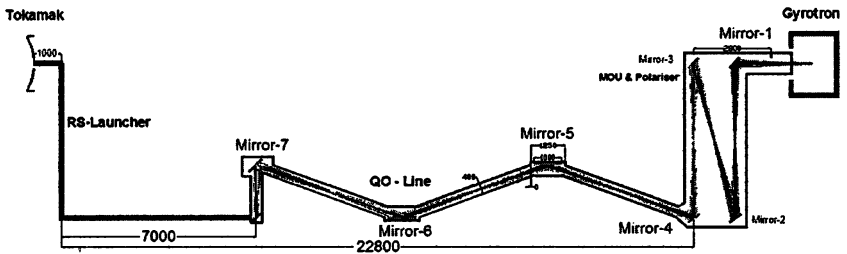

Fig. 4. Schematic of QO line with RS launcher

Fig. 5. QO line with RS launcher

This concept of mirror transmission line with square corrugated waveguide is not used in any tokamak but it may be useful for small tokamak as well as for bigger tokamak. For smaller tokamak antisymmetric RS launcher of $4a^2/\lambda$ length can be used, however for bigger transmission line RS launcher of $8a^2/\lambda$ length can be used. it requires very less space near the tokamak and installation is very simple. Thus for large tokamak, a big portion of transmission line will be from square corrugated waveguide (RS launcher) and mirror base QO transmission line could be small.

Another advantage of the hybrid line is that it needs smaller opening at the radial port of tokamak. Thus multiple remote steering launchers can be installed at one radial port and megawatts of power can be launched through hybrid transmission line system.

5. Option of vacuum compatible QO line

The vacuum compatible QO line will reduce the maintenance requirement and enhances the power handling capability. The chances of arc also reduce and improve overall system reliability. The design of the mirrors for the QO transmission line can be optimized. The entire mirrors can be mounted inside a metallic duct, which can be made vacuum compatible. Since ultra high vacuum is not required for the QO line, so pumping requirement is relatively small.

As shown in Fig. 4 and 5, for 20 m long transmission line with duct section size of 400×500 mm, only four turbomolecular pumps (TMPs) of speed 500 l/s will be needed to make entire line vacuum compatible (vacuum of $\sim 2 \times 10^{-4}$ mbar). For QO line with RS launcher, the volume and surface area reduce and hence pumping requirement also reduces significantly.

6. Summary

The mirror based quasi-optical transmission along with remote steering antenna can be used for ECRH systems in tokamaks. The combine use of QO line with RS launcher may be more advantageous as it requires less space near the tokamak. The installation of RS launcher will also be easy compared to mirror assembly near the tokamak. The length RS launcher (Symmetric or antisymmetric) can be decided as per the availability of space. The use of RS launcher reduces the number of mirror for QO line, which will reduce the maintenance of QO line. The entire transmission line (QO with RS launcher) can be evacuated easily as surface area and volume is reduced significantly with RS launcher. In this configuration, RS launcher will be a part of tokamak and mirror assembly to steer the beam will be in QO line. The window will be installed before the steering mirror. Since RS launchers are already tested for high power and QO lines are in use in some tokamaks and stellarators. This idea can be used as an alternate to conventional transmission line.

References

1   *Westerhof E.* Nucl. Fusion, **43**, 1371 (2003).
2.   *Kasparek W.* Fusion Engineering and Design, **74**, 243 (2005)
3   *Chirkov A V* Fusion Engineering and Design, **53**, 465 (2001)
4.   *Thumm M* Fusion Engg and Design, 28, 291–317 (1995)
5   *Vinogradov D. V.* International Journal of Infrared and Millimeter waves, vol 16, No. 11 (1995)
6.   *Crenn J. P* Applied Optics, vol. 24, No. 21 (1985)
7   *Moeller C. P.* Preprint for 23rd International conference on Infrared and millimeter waves, Colchester UK Sep 7–11 (1998).
8.   *Ohkubo K.* Fusion Engineering and Design, 65657–672 (2003)
9.   *Denisov G. G* Int. Journal of Infrared and millimeterwaves, vol. 22, No. 12, December (2001)
10   *Takahashi K* Fusion Engineering and Design, 65589–598 (2003).
11   *Ohkubo K* Fusion Engineering and Design, 26 325–333 (1995).

CRITICAL PROBLEMS IN PLASMA HEATING/CD IN LARGE FUSION DEVICES AND ITER

V. L. Vdovin

RRC Kurchatov Institute, Institute of Nuclear Fusion, Russia

We identify critical problems in Plasma Heating and Current Drive plasma-wave interaction physics and antennae concepts/technology for large fusion devices, including tokamaks, stellarators, mirror traps and constructing ITER for all major methods like ECRF, ICRF, NBI and LHH. Analysis is based on experiments in large machines like JET, JT-60, TOR SUPRA, LHD, middle and small tokamaks DIII-D, T-10, NSTX, etc., modelling with 3D ICRF and ECRF recently developed full wave PSTELION and STELEC codes, including mode conversion, 3D in-port antennae ANPORT and ANTRES3 codes and theoretical evaluations. Among identified problems are the role of Upper Hybrid resonance at fundamental harmonic (previously ignored in ECH/CD modelling), leading to power deposition broadening, important for NTM predictive suppression in ITER; Alfvenic type instabilities theoretically predicted and experimentally observed, together with power deposition-driven current profiles decoupling for NBI ITER-like operation regimes; principal problems with ICRF power coupling for multi loop individually fed resonant antennae (recently again confirmed in JET ICRF experiments [1]), loops inter coupled through weakly damped waves into plasma, and planned for ITER; antenna-plasma power coupling problem/theoretical predictive description with needed well controlled wave spectra for LHH method in large plasma-antenna gaps in big tokamaks and, especially, in ITER.

We outline identified problems resolution by: 1) elaborated ECRF full wave code modelling to decrease broadness of EC power deposition and proper EC power launcher(s) positions choice; 2) proposing High Frequency Fast Waves (HFFW) numerically modelled scheme for DIII-D and ITER, with commercially available 1 MW CW sources at 200 MHz, and waveguide type antennae, much more electrically strong, being as a back up for NBI method; 3) considering principally new approach for ICRH/CD method, especially in conditions of transient ELM activity, making use toroidally broad multi loop Travelling Wave Antenna (TWA) concept (prospective ITER design will be given; TWA consequently also uses previous magnetic loop antenna world theory/experiment experience), naturally incorporates antenna's loops inter coupling through a plasma (being principally unresolved problem for classical multi loop powerful antennae) with elegant control of antenna-plasma coupling through a small generator frequency change to properly control toroidal wave's spectrum during plasma edge density profile reconstruction; 4) developing new ITER-like ICRF scenarios at fundamental deuterium harmonic, partially recently explored on JET [1], and useful for non active ITER phase of operation

1. Ion Cyclotron Frequency range (ICRF).
ICRF Travelling Wave Antenna concept
for ITER and large machines

There are principal problems with ICRF power coupling for multi loop individually fed resonant antennae (recently again confirmed in JET ICRF experiments [1]) due to loops inter coupling through vacuum and weakly damped Fast Wave (FW) waves into plasma, especially severe for Current Drive (CD) mode, and designed for ITER. This is easy to understand looking on JET-EP ICRF 8 loops antenna design shown in Fig. 1.
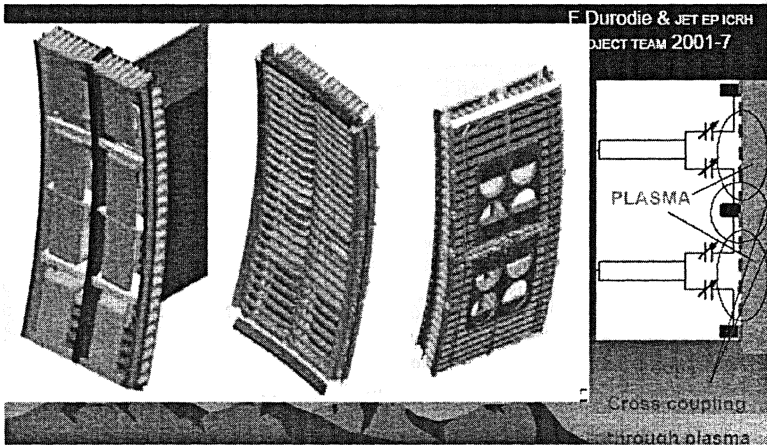
Fig. 1. JET-EP ICRF 8 loops antenna design

Each resonating loop is located in **individual conducting housing** (thus decreasing antenna power capability) and is supported by lumped capacitance. For ITER this approach doubles **simultaneously** resonating circuits number (16). Physically loops coupling through a plasma is unavoidable one thus leading to mismatching of an antenna, with respective problems to generator matching. Coupling with ELMy plasma creates additional problems. Matching of this type antenna is even more difficult one in CD mode $(0, \pi/2, \pi, 3/2\pi)$: loops radiate different RF power, and some loops start do not radiate but to receive RF power [3a].
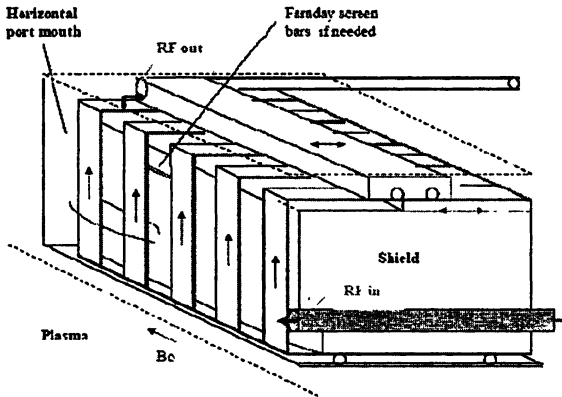

Fig. 2. Travelling Wave Antenna approach [2], with ITER-DEMO concept and theory developed in [3]

We propose to use qualitatively new Travelling Wave Antenna approach [2], with ITER-DEMO concept and theory developed in [3] displayed in Fig. 2. In TWA approach vacuum and plasma loop inter coupling is a positive effect, being

354

intrinsical requirement for proper antenna operation. ITER TWA concept of multi poloidal loop toroidal array supported by ridge waveguide (last one is an essential feature of this TWA concept providing needed wave dispersion and no need for lumped capacitances) [3].

This TW Antenna is integrated with neutron shield and has only· TWO coaxes: for input and output RF power. Antenna operates as follows: at upper frequency each loop resonates at half of vacuum wave length (Fig. 3). When generator frequency decreases the e.m. field is·pushed into ridge waveguide legs with simultaneous increase of toroidal wave length. Respectively e.m. wave more slowly decays in major radius direction thus still touching a plasma during ELM activity density profiles reconstruction. Simultaneously slowly radially decaying field start to touch "hump" of ridge waveguide, playing a "capacitance-like" role promoting e.m. wave pushing at reduced frequency to the ridge legs.
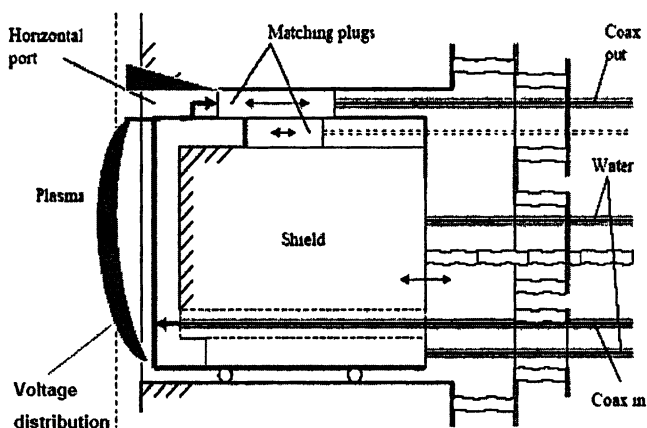

Fig. 3. Poloidal cross section of ITER advanced TW antenna

Thus we see that lower TWA frequency is simply cut off frequency of ridged waveguide because at cutoff there are no toroidal RF currents and the cuts (loops) at top of waveguide do not play a role. It means that TWA proposed is narrow frequency band one, band defined by legs length. Proper generator quick frequency sweep provides **constant** power coupling to potentially ELMy plasma. We stress that antenna poloidal loop geometry is exactly the same one as in past and now day ICRF experiments, so coupling antenna characteristics are the same one. Really TWA coupling is remarkably larger one because NO Faraday shield is needed and loops are located more closely to plasma. In principal it is possible to install "O-mode" like conducting bars directly between nearby loops, as indicated in Fig. 2.

We found a possibility to incorporate to this TW antenna a frequency broad band possibility installing at the top of the shield two horizontally moving match-

ing conducting plugs providing resonating loops lengths increasing. Thus this concept completely covers ICRF frequency band 40–80 MHz to support majority ITER H/CD scenarios. Antenna has possibility for radial movement for power coupling increase and matching with a generator.

Non absorbed during TWA toroidally propagating wave power comes through output coax and again is combined in proper phase with RF generator TWA's input power through outside machine recirculator. This is shown in Fig. 4. This recirculator is an extension of tested DIII-D recirculator for 4 loop individually loop fed ICRF antenna [4] with our extension of ferrite elements in 3 dB hybrids and phase shifters. These ferrite elements magnetization by outside low frequency solenoids is timely tracked in accordance with ELM activity process and generator needed frequency change to control appropriate toroidal wave slowdown.
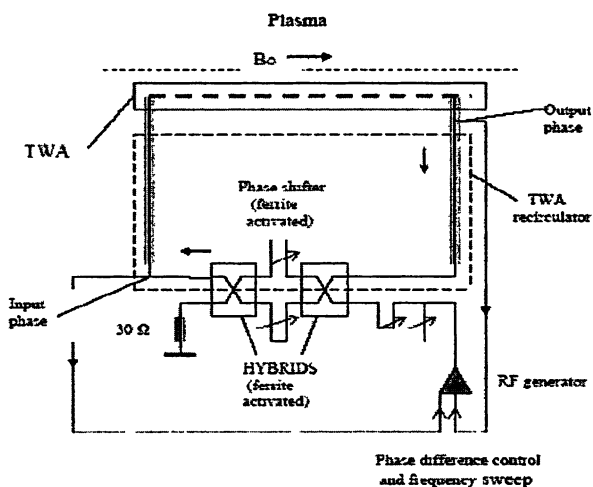

Fig. 4. Equatorial view of ITER TW antenna recirculator

The TW antenna was successfully tested on JFT-2M tokamak at 200 kW RF power [5] LHD stellarator has prepared Fish-bone like TWA antenna for electron CD goals (LHD web side). Screenless ICRF antenna was successfully operated on AUG tokamak with very similar plasma heating characteristics for screened antenna [6]. The code modelling is displayed in Fig. 5 for ITER tritium second harmonic F = 53 MHz D-T scenario and Faraday screen looks not to be needed.

The ICRF screen less "O-mode" antenna very inefficiently excites Fast Waves in ITER as shows STELION code comparison modelling for usual X-mode and O-mode antennae as is displayed by |E_psi| contour plots in Fig. 5.
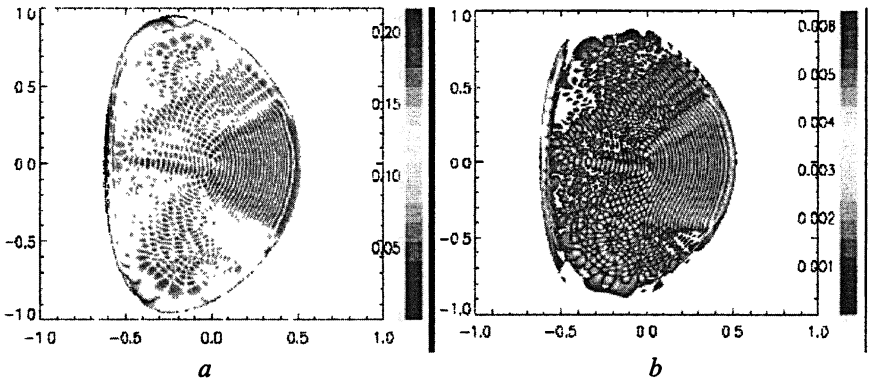
356

Fig. 5. |E_psi| contour plots for X-mode (*a*) and O-mode (*b*) antenna in ITER

2. Electron Cyclotron Frequency range 3D full wave updated code modelling at fundamental harmonic. Outstanding role of EB waves

Among identified problems in ECRF is the role of Upper Hybrid resonance at fundamental EC harmonic (previously ignored in ECH/CD ray tracing modelling) due to O-mode and X-mode coupling at fundamental [7] leading to power deposition broadening, important for NTM predictive suppression in ITER.

2.1. ECH full wave fundamental harmonic modelling in NSTX

Recently we have upgraded 3D ECH full wave STELEC code by proper addition far out off diagonal wave induced plasma response term which increased wave attenuation, as well known from ray tracing. Basic previous result on O-mode and X-mode coupling at fundamental harmonic in toroidal plasma was again confirmed just manifesting on important role of Electron Bernstein Waves (EBW), previously neglected in usual ECRF ray tracing modellings, including ITER , for O-mode antenna launch.

Well numerically resolved modelling of fundamental harmonic O-mode quasi perpendicular 2 MW outside launch in NSTX L-mode plasma is shown in Fig. 6 displaying |E_minus| EC wave 2D field.

The respective 2D power deposition to electrons is shown in Fig. 7. Main power absorption occurs at **right** resonance zone wing, while usual O-mode consideration at quasi perpendicular outside launch stress to power deposition at high magnetic field side due to relativistic effects involved. STELEC code results are another one due account to poloidal modes coupling, which broadens K_parallel spectrum, and huge amplitudes of EB waves approaching resonance zone.
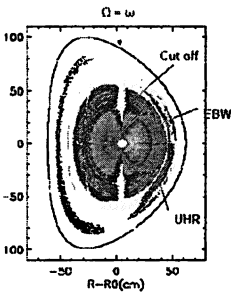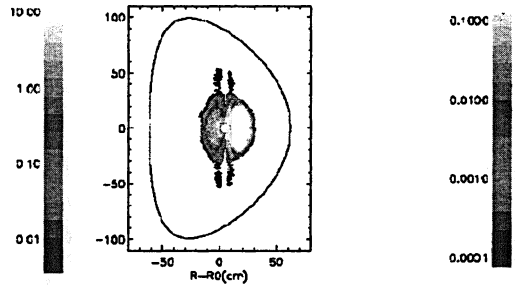
Fig. 6. |E_minus| EC wave 2D field

Fig. 7. 2D power deposition to electrons

Flux surface averaged power deposition is shown in Fig. 8. All these Figures confirm crucial role of EB waves. These waves have small group velocity at Upper Hybrid (UH) resonance and when approaching EC cyclotron resonance zone.
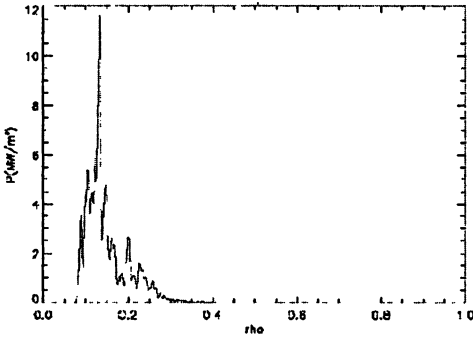

Fig. 8. Flux surface averaged power deposition to the electrons

Power deposition is broader one in compare with ray tracing and occurs in another space place.

EBW activity is crucial one at fundamental harmonic. Similar results were obtained for ITER making use similarity laws technique [7] for modelling at reduced frequencies. Outside quasi perpendicular O-mode ECH launch STELEC full wave code well resolved modelling shows: strong coupling to X-mode with respective mode conversion to small scale EBW. Large amplitude EB waves and strong modification of K_parallel spectrum provide power absorption on right side of resonant zone (contrary to usual analytic and ray tracing approach). This effect must be accounted in analysis of ECRF power deposition in large fusion machines and predictive ITER ECH/CD modeling. Huge EBW amplitudes can create poloidal sheared velocities particles streams, important for ITB creation.

2.2. ECRF second harmonic modelling

2.2.1. Second Harmonic ECH Scenarios in T-10

The majority of present tokamaks and stellarators operate at second harmonic and for not so large plasma densities the UHR is absent one. Second harmonic X-mode launch in T-10 is shown in Fig. 9a: |real(E_psi)|, at $N = 90$ ($N_{//}(0) =$

= 0.02), $F = 140$ GHz, $N_e(0) = 4.5 \cdot 10^{19}$ m^{-3}, $T_e(0) = 8.7$ kV, ($\alpha_n = 1$, $\alpha_T = 2$), $B_o = 2.5$ T, $I_p = 300$ kA (relativistic effects are included) and power deposition is displayed in Fig. 9b.
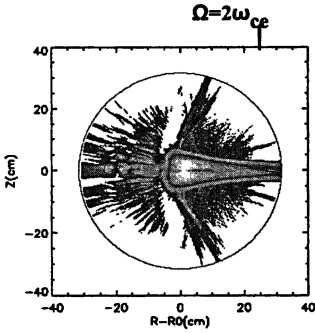

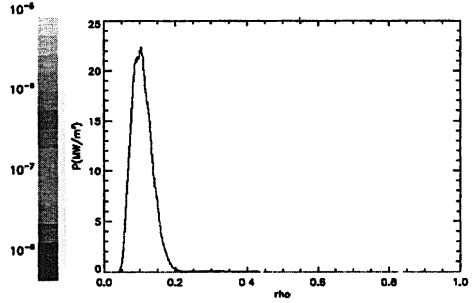**Fig. 9a.** |real(E_psi)| in T-10, $N_e(0) = 4.5 \cdot 10^{19}$ m^{-3}, $F = 140$ GHz

Fig. 9b. $P_e(\rho)$ in T-10, $\omega = 2\omega_{ce}$, $F = 140$ GHz

At plasma density $N_e(0) = 9 \cdot 10^{19}$ m^{-3} the diffraction is more strong one (Figs. 10a, 10b).
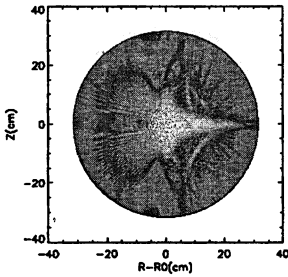
Fig. 10a. |real(E_psi)| in T-10, $N_e(0) = 9 \cdot 10^{19}$ m^{-3}
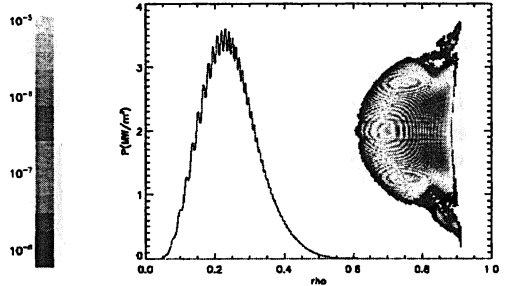
Fig. 10b. 1D&2D P_e in T-10, $N_e(0) = 9 \cdot 10^{19}$ m^{-3}

2.2.2. Second Harmonic ECH Scenarios in DIII-D at Oblique Launch

Second harmonic X-mode oblique 1 MW upper port launch in DIII-D **H-mode dense** plasma with elongation $\kappa = 1.65$, triangularity $\delta = 0.5$, $N = 160$ ($N_{//}(0) = 0.075$), $F = 60$ GHz, $T_{e0} = 6.55$ kV, $N_e(0) = 1.0 \cdot 10^{19}$ m^{-3}, $I_p = 360$ kA, $B_o = 0.95$ T, $q(0) = 1.1$, $q(a) = 5.4$ is displayed in Figs. 11a, 11b by |real(E_psi)| and |Im(E_z)| fields components. Radial power deposition calculated by STELEC for elliptically polarized Gaussian X-antenna is given by Fig. 12. One can see

two wave patterns propagation and absorption lobs. Standing wave structure, clearly seen on E_z contour plots, shows that the reflection and diffraction effects play a remarkable role in dense plasma H-mode scenario.
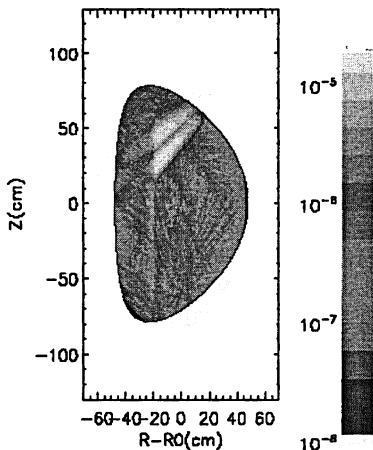
Fig. 11a. |real(E_psi)| in DIII-D at $2\omega_{ce}$
in H-mode plasma
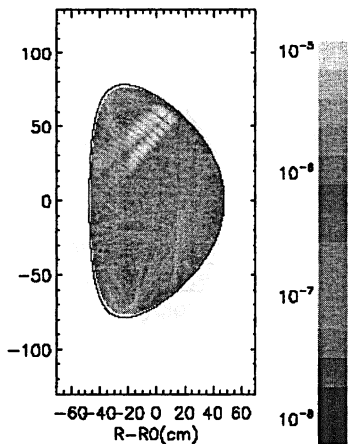
Fig. 11b. |Im(E_z)| in DIII-D at $2\omega_{ce}$
in H-mode plasma
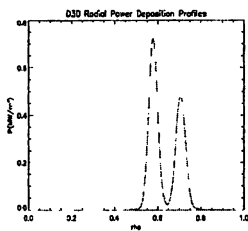
Fig. 12. $P_e(\rho)$ in DIII-D
calculated by STELEC
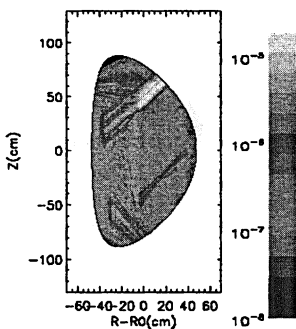
Fig. 12a. |real(E_psi)|
in DIII-D
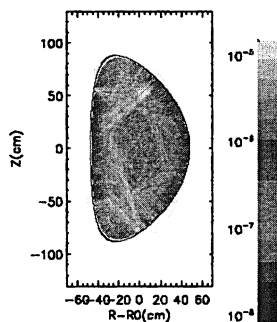
Fig. 12b. |Im(E_z)|
in DIII-D

In DIII-D **L-mode rare** plasma with $N_e(0) = 0.5 \cdot 10^{19}$ m^{-3} , $B_o = 1.05$ T, with smaller density gradients, the wave reflection plays a smaller role as displayed by Figs. 12a, 12b.

In DIII-D L-mode **dense** plasma with $N_e(0) = 2.0 \cdot 10^{19}$ m^{-3} ($N_e(0) \sim N_{cr}$) the diffraction and refraction effects are more pronounced as is demonstrated by |real(E_psi)| and |Im(E_z)| fields components in Figs. 13a, 13b. Radial power

360

deposition for this case is given by Fig. 14. One can see two wave patterns propagation and triple absorption lobs. Wing lobs are remarkably smaller ones. Behavior of parallel E_z contour plots shows that the O-mode more deeply propagates beyond second harmonic resonant zone with following multiple reflections from the walls.
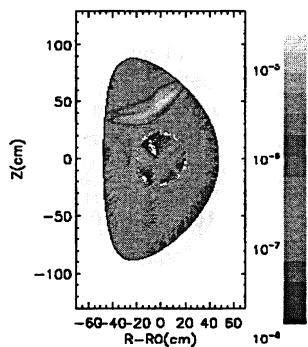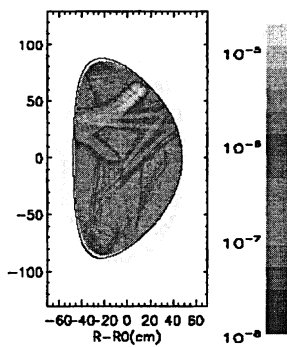
Fig. 13a. |real(E_psi)| in DIII-D at $N_e(0) = 2.0 \cdot 10^{19}$ m^{-3} **Fig. 13b.** |Im(E_z)| in DIII-D at $N_e(0) = 2.0 \cdot 10^{19}$ m^{-3} **Fig. 14.** $P_e(\rho)$ in DIII-D at $N_e(0) = 2.0 \cdot 10^{19}$ m^{-3}
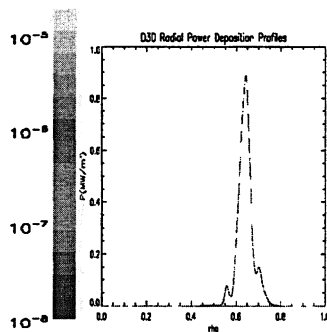
2.2.3. ECH Similarity Laws check for ITER

This was done for the ITER hydrogen phase of operation at twicely reduced magnetic field for scenario #2, i.e. at second harmonic X-mode outside launch from the upper port. at $B_o = 2.65$ T for $F = 5$, 10.1, 20.2 and 30.3 GHz with the gaussian beam divergence ±0.71° and $N_{//} = 0.09$ suitable for NTM suppression scenario. The 2D contour plots of electrical fields |Re(E_psi)| are given in Fig. 15 and displaying very similar wave pattern for all frequencies.

$$\Omega = 2\omega_{CE}$$
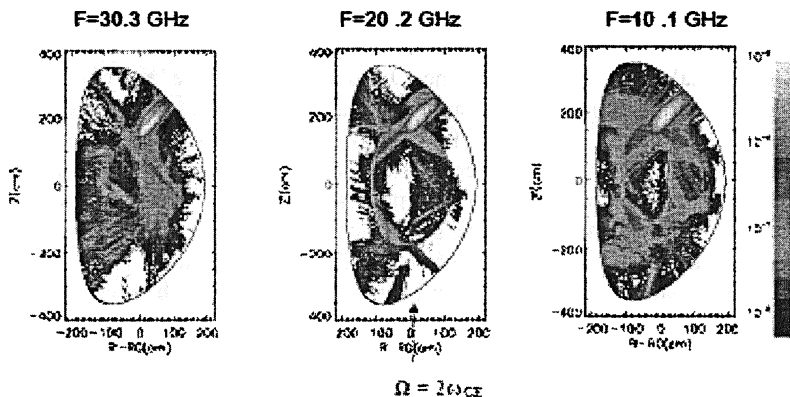
Fig. 15. Contour plots of |Re(E_psi)| for three frequencies in non active ITER

361

The respective flux surface averaged radial power deposition profiles are shown in Figs. 16a, 16b, 16c. They are also very similar and displaying well localized power deposition profiles in conditions of absence into plasma Upper Hybrid resonance. Thus ECH similarity Laws [1] are working well as shown for the frequency change up to factor ~6.
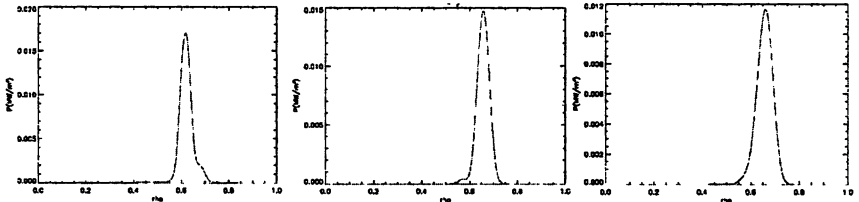
Fig. 16a. P_e in ITER at 30.3 GHz **Fig. 16b.** P_e at 20.2 GHz **Fig. 16c.** P_e at 10.1 GHz
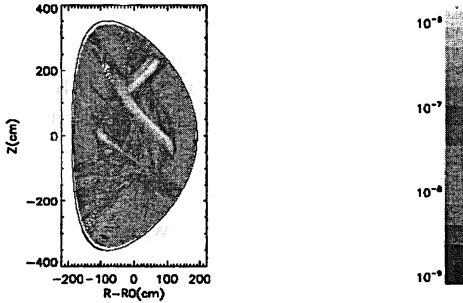
Fig. 17. $|Im(E\_z)|$ in ITER

Fig. 17 shows parallel electrical fields $|Im(E\_z)|$ at second harmonic in the ITER: The remarkable reflection from second harmonic resonance layer at 30.3 GHz is evident one (DIII-D earlier modelling has shown similar effect at 44 GHz [1]). This can influence the usual diagnostic EC emission interpretation based on WKB.

2.2.4. Conclusions on second harmonic modelling

In toroidal bounded plasmas the O-mode and X-mode are coupled ones through the space inhomogenity and boundary conditions even at second EC harmonic. This modes coupling effect in toroidal plasmas is weak one but important at the second harmonic scenarios in waves reflecting conducting chamber. In second harmonic scenarios the modes coupling is more weak one. Ray tracing/bi-tracing technique may be still used.

Second harmonic X-mode scenarios in T-10, DIII-D and ITER evidently show more broader power deposition profiles in compare with usual ray tracing ones at moderate plasma densities. At low densities the ray tracing approach still works. Refraction and diffraction effects in rare and dense plasmas were modelled for the T-10 and DIII-D tokamaks in circular and elongated magnetic configurations respectively.

Recent STELEC code modelling for non active ITER phase plasma in frequency range 5–30 GHz confirmed validity for the similarity laws use at reduced frequencies for large fusion machines.

3. HFFW CD in large machines and ITER

The JT-60U reported NNB CD experiments ($EB_{injB} = 340$ keV) in conditions modelling the ITER scenario ($VB_{BEAMB} \sim VB_{alfvenB}$) with unfavorable results [8], instabilities (waited from theory) have appeared and expelled energetic ions before their slow down to thermal energies. This information became even more worser with recent off-axis ASDEX NB CD experiments [9] which demonstrated NO any change in driven current PROFILE (JT-60U previously also reported similar results) thus manifesting on ions and current profiles decoupling.

In such situation High Frequency Fast wave CD (frequency ~ 10 cyclotron harmonics) may be a back up to substitute NBI in ITER/DEMO creating driven current peaked at HALF of plasma minor radius (goal of NNB) simply relying on large amount FW wave lengths over fusion reactor plasma minor radius, sufficient to provide single pass wave absorption at classical damping mechanisms on electrons.

The HFFW Current Drive, with efficiency comparable to EC and NBI methods, was demonstrated in DIII-D [10]. Active program on HFFW Current Drive experiments is underway at NSTX [11] (efficient electron heating without density rise, RF driven current ~100 kA, plasma internal inductance drop,). We modeled HFFW CD scenario with MRAYS code. Plasma and machine ITER parameters are close to present design weak negative steady state scenario #4

- Major radius, R 6.35 m
- Minor radius, a 1.85 m
- Plasma elongation, κ 1.97
- Plasma triangularity, δ 0.58
- Nominal plasma current, IB_{pB} 9 MA
- Toroidal field, BB_{0B} 5.3 T
  (at $R = 6.2$ m)
- MHD axis safety factor, qB_{oB} 3.44
- MHD safety factor, $qB_{\psi95B}$ 5.5

Plasma parameters of representative ITER scenario #4
- Central deuterium temperature TB_{DOB} 25.2 keV
- Central tritium temperature TB_{TOB} 25.2 keV
- Central electron temperature TB_{eOB} 24.4 keV
- Volume averaged electron temperature $< T_e >$ 10.5 keV
- Central electron density n_{e0} $7.27 \cdot 10^{19}$ m^{-3}
- Volume averaged density $< n_e >$ $6.74 \cdot 10^{19}$ m^{-3}
- Impurity fractions $fB_{HeB}, fB_{Be9B}, fB_{ArB}, fB_{AlphasB}$ 0.039, 0.02, 0.0035, 0.0056
- Effective Zeff   2.17
- RF power   20 MW

Power deposition to the electrons and driven current profiles for 3D STELION code modeling with single toroidal harmonic $N = 50$ at frequency 300 MHz are given in Fig. 18a, 18b.
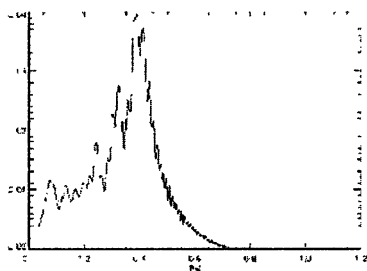
Fig. 18a. Electrons power deposition
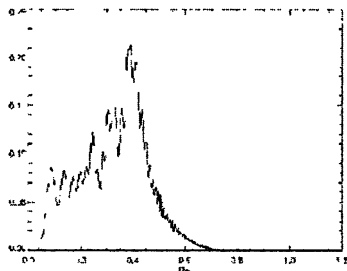
Fig. 18b. Driven current profile in ITER

The CD efficiency is high as 0.55 A/W/mP^{2P}. FW's absorption on Alphas cyclotron harmonics was not accounted in this modeling. Modeling together with Yu. V. Petrov with the multi rays MRAYS code [9, 10] with account to full multi loop antenna poloidal and toroidal spectrums in SS-Active ITER: 12 loops, $5\pi/8$ phasing ($NB_{\|maxB} = 3$) is displayed in Figs. 19a, 19b.
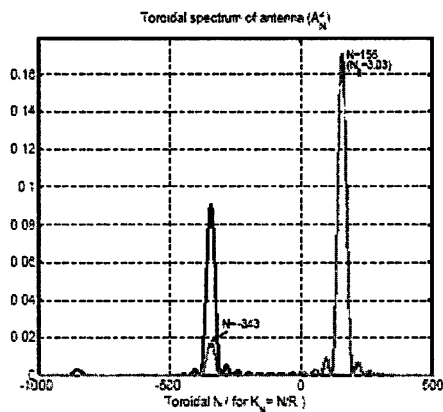
Fig. 19a. ITER antenna toroidal spectrum
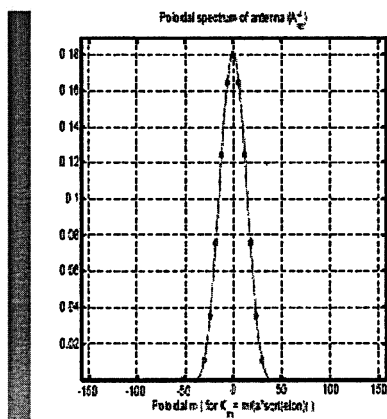
Fig. 19b. ITER antenna poloidal spectrum

Power deposition profiles and the profile of driven current at $NB_{\|maxB} = 3$ in ITER scenario #4 with 20 MW input power is displayed in Fig. 20 ($\gamma = 0.32$ A/W/MP^{2P}, MRAYS code, 990 rays).

Ray trajectories (each 3rd ray is shown) and contour lines showing power depositions to the electrons and ions are given in Fig. 21.
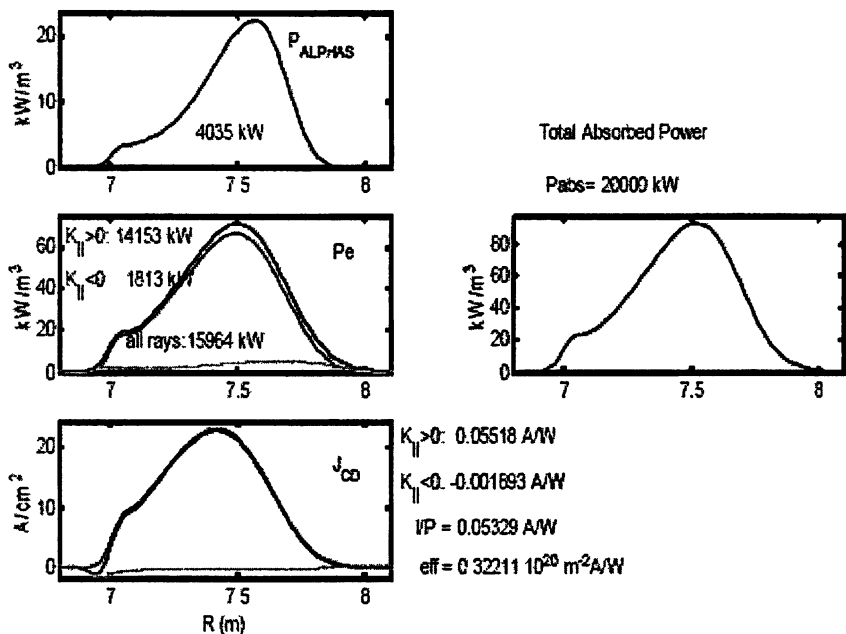
Fig. 20. Power deposition profiles to Alphas, electrons, plasma and driven current
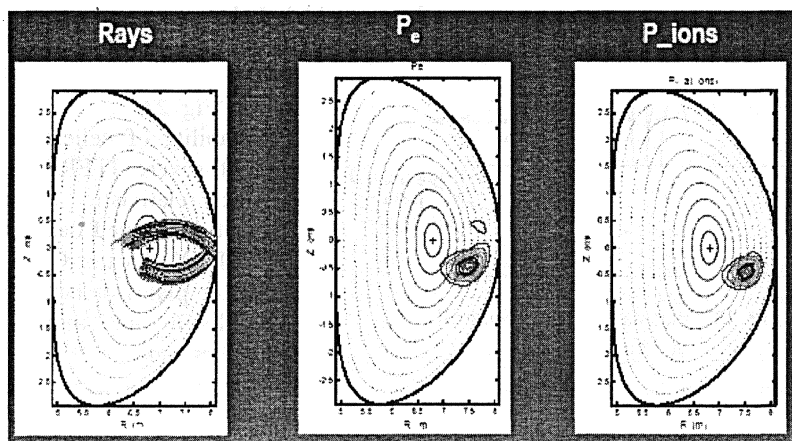
Fig. 21. Ray trajectories, 2D contour plots of power deposition to the electrons and ions

We propose for ITER/DEMO to use electrically strong Waveguide's slightly oversized narrow frequency band Travelling Wave Antenna radiating through the periodic holes in broader waveguide's side as sketched in Fig. 22.
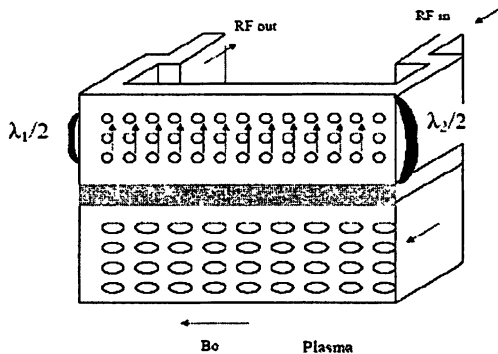
This antenna's toroidal wave slow down also is controlled by small frequency sweep – similar to above TWA ICRF antenna concept. There are commercially available CW sources 1 MW/tube at 200 MHz (EU accelerator developments [7]).

4. Low Hybrid Frequency range (LHH)

The projection of this method for the ITER must overcome several problems:

1) – coupling with main plasma through broad SOL region in ITER;

– "Plasma arm", appearing at plasma mouth in present LH CD experiments on Tore Supra and JET, must be properly modelled to predict correct toroidal LH wave spectrum near boundary of a bulk plasma needed for an integrated ITER modelling, Fig. 23.

2) Viability of delicate grill antenna at severe ITER/DEMO conditions: relativistic electron tail generation, played dangerous role in ASDEX, Alcator-C, JT-60 etc. Divertor plates damage, carbon/Be bloom due interaction with chamber wall.
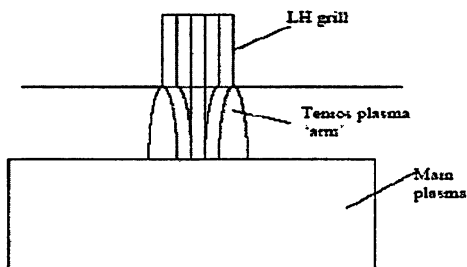
Fig. 23. "Plasma arm" between grill and bulk plasma

5. New far off axis Fast Wave CD scenario in non active ITER

There is a possibility to destroy usual FW central focussing adding to the hydrogen ITER plasma the He-4 (or He-3) minority ions of 1–3 % and matching the generator frequency to the fundamental ion cyclotron resonance. This mixture creates in a plasma the "cut off – singularity" pair, known as the ion-ion (i-i) hy-

brid resonance pair. The proposed (and natural) so called "heavy" minority scheme H(He-4) (minority ions – in brackets) keeps the cyclotron and i-i resonances behind of a cut off layer (being practically vertical one) – at the High Field Side (HFS) from a cut off. Fast Waves, propagating from an antenna, partly will be reflected from the cut off, partly will tunnel through the evanescent region and will be absorbed at the IC He-4 minority ions resonance. The reflected FW will be remarkably trapped between the cut off layer and vacuum chamber, at the LHS (Fig. 24 displays power deposition to electrons; ITER parameters are for the scenario #2). The amount of the wave power penetrated to the cyclotron resonance (to the HFS) depends on the minority ions amount and an antenna's toroidal number. Far off axis driven current profile in hydrogen plasma with addition 2.5 % of He-4 for frequency 38 MHz and wave toroidal number $N = 27$ is given by Fig. 25. Recommended action for the ITER ICRF system is a lower generator frequency to be 35 MHz.
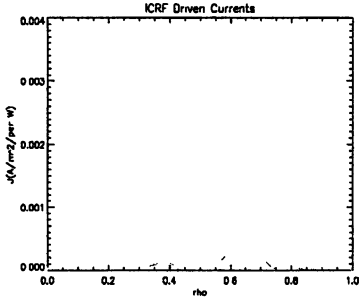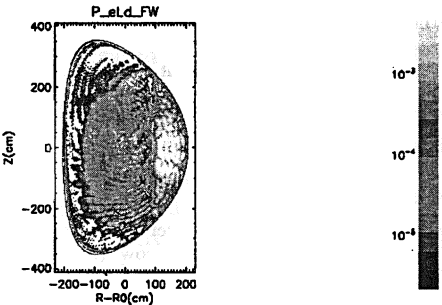
Fig. 24. 1 FW Power deposition to the electrons in non active ITER at 38 MHz

Fig. 25. Far off axis FW driven current profile in non active ITER at 38 MHz

Conclusions

A. ICRF

1) Advanced ICRF Travelling Wave Antenna, based on Multi loop array supported by ridge waveguide, was proposed. This is electrically strong, frequency broad band antenna: 40–80 MHz.

2) TW Antenna due to small frequency sweep keeps constant power coupling to ELMy plasma. It has only two coaxes and there are no lumped capacitances at all.

3) Power recirculator, located outside machine, is an essential element of proper antenna operation.

B. ECRH

1) 3D Full wave ECH STELEC code numerically well resolved modelling for NSTX tokamak supported our previous finding: O-mode and X-mode coupling in toroidal plasmas at fundamental EC harmonic.

367

2) Electron Bernstein waves play crucial role at O-mode antenna polarization (contrary to ray tracing) and lead to broader EC power deposition profiles. Last ones are located in another space positions in compare with usual ray tracing predictions.

3) This new role of huge amplitudes EB waves provides a possibility of particles velocity shear generation, important for ITB creation.

C. HFFW scheme being back up for NBI

1) To fulfill NBI role – CD creation in middle of minor ITER radius – we propose for ITER/DEMO new/old HFFW CD scheme (Kurchatov1960 – PPPL 2007 activity) operating at 200–300 MHz.

2) 3D antenna-plasma modelling shows RF current generation peaked in middle of plasma minor radius with CD efficiency about 0.3 A/W/mP^{2P}.

3) Wave guide type Travelling Wave antenna, surviving ELMy plasma activity with constant power coupling to plasma, was proposed.

4) The CW power sources at 200 MHz are commercially available ones.

D. Proposal of New far off axis Fast Wave CD scenario in non active ITER

Can be a second useful tool to drive off axis current by fast waves, at least in non active ITER phase, to support ITER advanced scenarios.

References

1. *Krasilnikov A. V. et al. JET team*, "Ion cyclotron resonance heating of jet deuterium plasma fundamental frequency", XXXIV Int. Conf. on Plasma Physics, Moscow (Zvenigorod), 12– 16 February 2007, Invited lecture, EU Task Force H Planning Meeting and EFDA Coordination Task Meeting, 16–20 April 2007, Castle Ringberg, Bavaria, Germany.

2. *Moeller C. P. et al.* AIP Conf. Proc. 289, 10th Top. Conf. on RF Power in Plasmas, Boston, p. 323, 1993.

3. *Vdovin V.* "Analysis of Travelling Wave Fast Wave ICRF antenna radiating from a recess in first Tokamak wall", ICPP-98 and 25PthP EPS Conf. on Plasma Physics and Contr. Fusion, P3 087, p. 1438 (Praha, 1998).

3a *Vdovin V., Kamenskij I.* Kurchatov Institute ITER Physics Design group report "ITER ICRF antennae impedance characteristic simulation", ITER Expert group meeting on ICRF antennae for ITER, May 1998, Oak Ridge, US.

4. *Phelps et al.* DIII-D report GA–A22574.

5 *Ogawa T. et al.* Nuclear Fusion, Vol. 41, p. 1767–1775.

6 *Noterdaeme J.-M. AUG team "Achievement of the H-Mode with a Screenless ICRF Antenna in ASDEX Upgrade"*, Radio Frequency Power in Plasmas (Palm Springs, CA, 1995), Vol. 355, (R Prater et al. eds), AIP Press (1996) 47–501.

7 *Vdovin V L.* "Role of Upper Hybrid resonance and diffraction effects at Electron Cyclotron Heating in tokamaks", Proceedings of 14th Joint Workshop on Electron Cyclotron Emission and Electron Cyclotron Resonance Heating, invited lecture, p. 323–333, 9–12 May 2006, Santorini island, Greece (Publisher: Heliotopos Conferences Ltd., Athens, Greece; ISBN: 960-89228-2-8, December 2006).

8. *Shinohara K. et al.* Nucl. Fusion 41 (2001) 603.

9. *Hobirk J. et al.* 30th EPS conference (St. Petersburg, 2003) O-4.1B.

10. *Prater R. et al.* Proc. of the 16th IAEA Fusion Energy Conf., Montreal, Canada, 1996, Vol. 3 (International Atomic Energy Agency, Vienna, 1997) p. 243.

11 *Hosea J et al* IAEA Lyon 2001 Conf ; *Swain D. W. et al* RF Topical, Oxnard 5/01.

ORDINARY AND EXTRAORDINARY WAVE COUPLING IN 2D-INHOMOGENEOUS PLASMAS: RECENT RESULTS

E. D. Gospodchikov, A. G. Shalashov, E. V. Suvorov

Institute of Applied Physics of Russian Academy of Sciences, Nizhniy Novgorod, Russia

Recently the theory of linear coupling between the ordinary (O) and extraordinary (X) electron cyclotron waves propagating in a vicinity of the critical (cut-off) plasma density has been generalized for two-dimensionally inhomogeneous plasma configurations, in particular with taking into account variation of a magnetic field on flux surfaces in tokamaks and stellarators. In the present communication some recent results in this theory are discussed.

Introduction

In recent years, interest in the linear mode coupling in smoothly inhomogeneous magnetized plasmas in electron cyclotron resonance frequency range has been increased appreciably in connection with high-frequency plasma heating and diagnostics in spherical tokamaks and optimized stellarators. Most of the theoretical results related to linear coupling of the electromagnetic ordinary (O) wave launched from the low field side to the slow extraordinary (X) wave in the vicinity the O mode cutoff surface (O-X mode coupling) have been studied within the one-dimensional approximation, in which plasma density and magnetic field were assumed to vary along one direction [1]. In this case, the propagation regions for the O and X waves are separated by a slab evanescent region defined by the following condition

$$\varepsilon_\parallel(\varepsilon_+ - N_\parallel^2) < 0, \quad \varepsilon_\parallel = 1 - \omega_{pe}^2/\omega^2, \quad \varepsilon_+ = 1 - \omega_{pe}^2/\omega \ \left(\omega + \omega_{ce}\right), \tag{1}$$

where ω, ω_{ce} and ω_{pe} being, correspondingly, the wave, electron cyclotron and plasma frequencies, and $N_\parallel = ck_\parallel/\omega$ being the wave refractive index parallel to the ambient magnetic field.

Recently it has been understood that the one-dimensional approximation may be insufficient to describe the O-X conversion in toroidal magnetic configurations, in which the density and magnetic field vary essentially differently resulting in intersection of the cutoff surfaces due to variation of a magnetic field on flux surfaces. Theory of the O-X coupling in a non-planar case has been developed in [2–8]. The theory is based on a new reference problem in which the linear interaction region is formed by intersection of two flat cutoff surfaces, see Fig. 1. Thus, a tokamak-like geometry has been reduced to the two-dimensionally inhomogeneous problem allowing the analytical solution when variation of the magnetic field direction is neglected. Reduction of a three-dimensionally inhomogeneous case to the reference two-dimensional geometry is discussed in detail

in [8]. Although obtained analytical solutions include both transformed and re-
flected waves, as a particular case it describe localized· quasi-optical beams ex-
hibiting perfect conversion with no reflection (that substitute an optimal plane
wave specific for the one-dimensional geometry). Such wave structures are ana-
lyzed in more detail in the present communication. In particular the optimal
beams may be realized with generalized Gaussian distributions with slow phase
modulation and astigmatism. Although this modulation is smooth enough to pro-
vide the aberration-free propagation of a paraxial beam, practical application of
such beams may face essential difficulties. At the same time, conversion effi-
ciency of not modulated Gaussian beams with plane phase fronts may be rather
high despite of not perfect character of transformation. Such beams can be easily
realized in a magnetic fusion experiment.
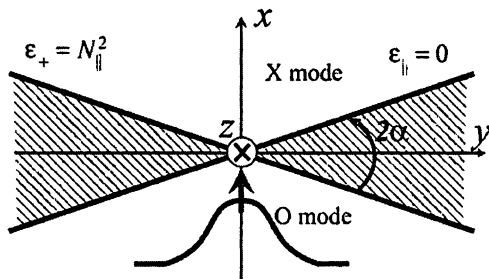
Fig. 1. The O-X transformation region in 2D geometry, where the plasma density and the magnetic field intensity vary in' the xy plane and the flat cutoff surfaces are assumed. The evanescent region for left-hand polarized waves is dashed. Adopted from [2].

Perfectly converted wave beams

Following [2], let us introduce a coordinate system in accordance with Fig. 1.
The z-axis is along the homogeneity direction, the y-axis is located inside the
evanescence region, and the x-axis is located in the propagation region of left-
hand polarized waves and is directed toward the higher plasma densities along
the bisector of the angle between the cutoff surfaces. Formally, the x-axis is di-
rected along the vector $\nabla\varepsilon_\parallel / |\nabla\varepsilon_\parallel| + \nabla\varepsilon_+ / |\nabla\varepsilon_+|$. Wave beam propagation in the
positive direction along the x-axis corresponds to the O-X mode conversion,
propagation in the opposite direction corresponds to the reverse process, namely
the X-O mode conversion. The origin of (x, y)-coordinates is chosen on the line
of intersection between the cutoff surfaces for a given $N_\parallel$.

Let us consider first a simplified case in which the external magnetic field is
oriented along the z-axis. In tokamak applications this is equivalent to neglecting
the poloidal component of the magnetic field and the curvature of a magnetic flux
surface (perfect conversion in presence of a poloidal magnetic field component is
analyzed in [7]), thus the two-dimensional inhomogeneity is fully attributed to
the variation of the toroidal magnetic field intensity on a flux surface within the
transformation region. There are two characteristic parameters of the model: the

angle 2α between the directions of $\nabla\varepsilon_+$ and $\nabla\varepsilon_\parallel$ and the characteristic length L_∇ of the coupling region defined as

$$L_\nabla = \sqrt{N_z}\left(2k_0^2|\nabla\varepsilon_+||\nabla\varepsilon_\parallel|\right)^{-1/4}. \tag{2}$$

Since the model under consideration is homogeneous along the z-axis, the longitudinal wave number $N_\parallel \equiv N_z$ is conserved as in the one-dimensional case. Accordingly, the general solution of the wave equation can be found as a convolution of partial solutions corresponded to a fixed wave number, with any finite weight function:

$$\mathbf{E}(x,y,z) = \int G(N_z')\mathbf{E}\left(x-\Delta x, y-\Delta y, z, N_z'\right)dN_z'. \tag{3}$$

Here Δx and Δy define the displacement of local coordinates corresponded to N_z' with respect to the laboratory coordinate system.

For the geometry shown in figure 1 there is a particular (optimal) wave field distribution in an incident beam that exhibits perfect mode conversion, i.e. pass through the transformation region with strictly zero reflection. In a smoothly inhomogeneous media this wave structure is defined by the following expression:

$$A(x,y,z,N_z) = C\exp\left(-\frac{ix^2\cos\alpha + y^2\sin|\alpha|}{2L_\nabla^2} + ik_0 N_z z\right), \tag{4}$$

see, e.g. [2]. Here A is amplitude of wave propagating in the positive directions with respect to the x-axis when $\alpha > 0$ and negative when $\alpha < 0$.

The optimal field distribution (4) is not limited in the z-direction. However, one can construct a limited distribution by summation of the optimal beams with different N_z. Indeed, substituting (4) into convolution (2), one may find the following general form of the perfectly transforming wave beam:

$$A(x,y,z) = A(x,y,z,N_z)\Phi(\zeta), \tag{5}$$

where $\Phi(\zeta) = \displaystyle\int_{-\infty}^{\infty} G(\Delta N_z)\exp(\zeta\Delta N_z - \eta\Delta N_z^2)d\Delta N_z.$

Here all non-trivial dependence on coordinates is expressed through the autonomous variable

$$\zeta = ik_0(-\sigma x + i\sigma y\,\mathrm{sign}\alpha + z), \quad \sigma = \sqrt{2|\nabla\varepsilon_\parallel|/|\nabla\varepsilon_+|},$$

while the constant coefficient $\eta = \sigma^2 k_0^2 L_\nabla^2 \exp(i|\alpha|)/\sin|2\alpha|$ affects only the characteristic scale of function $\Phi(\zeta)$.

As a practically universal example one may consider

$$\Phi = \exp(\zeta^2/2k_0^2 a_z^2). \tag{6}$$

Then, the perfectly transforming beam (12) takes a form of Gaussian distribution of general type with astigmatism and phase modulation:

$$A \sim \exp\left(-\frac{ix^2 \cos\alpha + y^2 \sin|\alpha|}{2L_\nabla^2} - \frac{(\sigma x - i\sigma y \ \mathrm{sign}\alpha - z)^2}{2a_z^2} + ik_0 N_z z \right). \quad (7)$$

Relation between orthogonal widths of this beam in the y- and z-directions, a_y and a_z, is given by

$$(a_y^2 - a_0^2)(a_z^2 - \sigma^2 a_0^2) = \sigma^2 a_0^4. \quad (8)$$

Here $a_0 = L_\nabla / \sqrt{\sin|\alpha|}$ corresponds to the width of the optimal distribution (4); parameter σ is always of the order of unity, $\sqrt{2} < \sigma < 2$. Equation (8) shows, that localization of the beam in the y-direction results in its widening in the z-direction. For more details see [7].

The maximum intensity $|A|^2$ of field distribution (7) lies on the straight line $\sigma x - z = 0$, $y = 0$. One may consider this line as a trajectory along which the beam propagates; more deep analysis shows that the wave power flux also propagates along this direction. The characteristic beam size in the direction transverse to the propagation direction is

$$a_\perp = \min(a_y, a_z / \sqrt{\sigma^2 + 1}) \sim a_0. \quad (9)$$

Outside the local region of linear interaction, the optimal beam may change due to diffraction and more complex plasma inhomogeneity than assumed in the present analysis. The parameters of the beam, widths and phase modulation, change on characteristic distance $k_0 a_\perp^2 \gg L_\nabla$.

Transformation efficiency for not focused Gaussian beams

From (6) it follows, that perfect O-X conversion may be realized with Gaussian beams by dedicated modulation of its phase fronts. Although this modulation is smooth enough to provide the aberration-free propagation of a paraxial beam, practical application of such beams may face essential difficulties. In this section we show, that transformation efficiency of Gaussian beams with plane phase fronts may be rather high, despite not perfect character of transformation.

Let us consider the two-dimensional Gaussian incident beam specified outside the linear interaction plane, $|x| \gg L_\nabla$, as

$$A_i = \exp[-(y - y_0)^2 / 2a_y^2 - z^2 / 2a_z^2 + ik_0 N_y y + ik_0 N_z z]. \quad (10)$$

The wave field distributions in the transformed and reflected beams corresponded to incident beam (10) have been studied in [3]. After passing the mode conversion region this beam restores the Gaussian form, although parameters of this form are modified. Below we analyze the corresponding transformation efficiency, i.e. the ratio of total power fluxes in the incident and passed through the

interaction region wave beams. An explicit expression for the transformation efficiency has been obtained in [6] in the following form:

$$T = \frac{\bar{a}_y a_y \left(1 + \tanh\left(\pi \tan\alpha\right)\right)}{a_y^2 + a_0^2 \tanh\left(\pi \tan|\alpha|\right)} \frac{a_z}{\bar{a}_z} \exp(-\phi), \tag{11}$$

$$\bar{a}_y^2 = a_0^2 \frac{a_y^2 + a_0^2 \tanh(\pi \tan|\alpha|)}{a_0^2 + a_y^2 \tanh(\pi \tan|\alpha|)}, \quad \bar{a}_z^2 = a_z^2 + \frac{\sigma^2 a_0^4}{a_y^2 + a_0^2 \coth\left(\pi \tan|\alpha|\right)}. \tag{12}$$

$\bar{a}_y$ and $\bar{a}_z$ denote the effective width in the y- and z-directions of the beam after passing the transformation region, $a_0 = L_\nabla / \sqrt{\sin|\alpha|}$ is the optimal beam width defined previously, and $\exp(-\phi)$ describes degradation of the transformation efficiency due to not optimal aiming, namely, not optimal beam propagation angle and a shift in the y-direction. Below we assume the optimal aiming, therefore $\exp(-\phi) = 1$.

The dependence of transformation efficiency (11) on the incident beam sizes is illustrated in Fig. 2. The transformation efficiency monotonously increases with a_z approaching its maximum value when the incident beam converges to optimal distribution (4) not localized in the z-direction: $T \to 1$, when $a_z \to \infty$. For constant a_z, there is a maximum of the transformation efficiency over a_y,

$$\hat{T} \equiv \max_{a_y} T = \frac{a_0^2 \exp\left(\pi \tan\alpha\right)}{\hat{a}_y^2 \cosh\left(\pi \tan|\alpha|\right) + a_0^2 \sinh\left(\pi \tan|\alpha|\right)}, \tag{13}$$

realized when $a_y^4 = \hat{a}_y^4 \equiv a_0^4 + \left(\sigma^2 a_0^6 / a_z^2\right) \tanh\left(\pi \tan|\alpha|\right)$.

It should be stressed here, that fairly good conversion efficiency may be achieved in modern toroidal systems even with not modulated Gaussian beams. Taking, for example, the typical parameters for the L-mode regime at the MAST spherical tokamak, $\omega / 2\pi = 28$ GHz, $\omega_{ce} / \omega \approx 0.35$, $\alpha \approx 2^\circ$ and $L_\nabla \approx 1$ cm in the vicinity of the transformation region [5]. Correspondingly, one might expect 90 % mode conversion for Gaussian beams with $a_y \approx a_0 \approx 5.7$ cm and $a_z \approx 4.9$ cm in case of favorable direction of beam propagation. Such beams are quite accessible in experimental conditions.
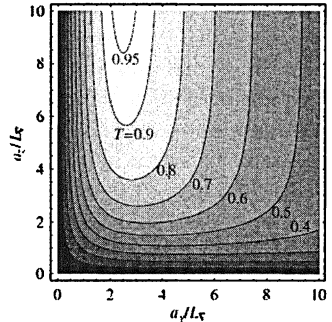
Fig. 2. Contour lines of O-X transformation coefficient of the Gaussian incident beam as a function of and for fixed angle between the cutoff surfaces and in case of optimal aiming.

373

Conclusions

Absence of a unique value for the parallel refractive index corresponding to the perfect O-X conversion is an essentially two-dimensional effect reflecting the fact that intersection of the cutoff surfaces does not vanish with moderate variation of $N_\parallel$. This allows synthesizing limited in both transverse directions paraxial wave beams that pass through the linear coupling region in the vicinity of the radiation cutoff without reflection. In particular, such optimal beams may be realized with generalized Gaussian distributions with slow phase modulation and astigmatism, that can be realized in a magnetic fusion experiment.

References

1. *Laqua H. P.* Plasma Phys. Control. Fusion 49, R1–42 (2007).
2. *Gospodchikov E. D. et al.* Plasma Phys. Control. Fus. 48,869 (2006).
3. *Shalashov A. G. et al.* JETP, 103, 480 (2006).
4. *Popov A. Yu., Piliya A. D.* Plasma Phys. Rep. 33 (2), 109 (2007).
5. *Popov A. Yu.* Plasma Phys. Control. Fusion 49, 1599 (2007).
6. *Gospodchikov E D. et al.* Fusion Sci. & Tech. 53, 261 (2008).
7. *Shalashov A. G. et al.* Plasma Phys. Control. Fusion, 50, 045005 (2008).
8. *Shalashov A G.,Gospodchikov E. D.* Phys Rev. E., 78, 065602 (2008).

ECRH SCENARIOS ON W7-X

N. B. Marushchenko[1], H. Maassberg[1], C. D. Beidler[1], V. Erckmann[1],
J. Geiger[1], H. P. Laqua[1], A. G. Shalashov[2], E. V. Suvorov[2], Yu. Turkin[1]
and W7-X Team

[1] Max-Planck-Institut für Plasmaphysik, EURATOM Association,
D-17491 Greifswald, Germany
[2] Institute of Applied Physics RAS, 603950 Nizhny Novgorod, Russia

The main ECRH scenarios for the W7-X Stellarator are described. Both X2 (low and moderate densities) and O2 scenarios (high density) have been checked. Since only the current drive is considered as a tool for compensating the residual plasma current and for controlling the edge rotational transform value, the efficiency of ECCD for all considered scenarios has been estimated.

Introduction

The W7-X stellarator is a large-scale device ($R_0 = 5.5$ m and $a = 0.53$ m) with superconducting coils and without an ohmic transformer. The main scientific objective is to demonstrate a good plasma confinement in steady state operation with reactor relevant parameters. The magnetic configuration (a low-shear configuration of Helias type [1] with five field periods) is quite flexible and well optimized with respect to low neoclassical transport and small bootstrap current. The "bean-shaped" plane corresponds to the maximum B region, where the strong toroidal curvature is located, whereas the minimum of B is in the "triangular" plane in the nearly straight part of the configuration. The toroidal mirror term, defined by the $m = 0$, $n = 1$ Fourier mode of $b = B/B_0$, i.e. the b_{01}-term, can be varied in a wide range, $-0.035 < b_{01} < 0.225$ [2]. For example, the configurations under investigations have $b_{01} = 0$ ("low-mirror"), $b_{01} = 0.043$ ("standard") and $b_{01} = 0.1$ ("high-mirror") on the axis in vacuum (the toroidal mirror term is reduced by the plasma pressure). The bootstrap current is minimized for the "high-mirror" configuration, whereas the neoclassical confinement is optimum in the "standard" configuration. The trapped-particle fraction on axis is also varied significantly from $f_{tr} = 0.02$ for "low-mirror" up to $f_{tr} = 0.45$ for 'high-mirror", and $f_{tr} = 0.3$ for the "standard" configuration (see [2] for more details).

The ECRH system is designed for continuous operation with a total injected power up to 10 MW at 140 GHz [3]. For low and moderate densities up to $n_e < 1.2 \cdot 10^{20}$ m^{-3}, the main heating scheme is low-field-side (LFS) launch of the RF beams at the 2nd harmonic of the extraordinary mode (X2 scenario). High-density regimes above the X2 cut-off density, from $1.2 \cdot 10^{20}$ m^{-3} to $2.0 \cdot 10^{20}$ m^{-3}, are accessible with the multipass scheme at the 2nd harmonic of the ordinary mode (O2 scenario). For heating of so-called over-dense plasma beyond the O2 cut-off density, the more sophisticated OXB scenario using electron Bernstein

waves is foreseen. Additionally, the multi-pass X3 scenario at 140 GHz and at 104 GHz with reduced magnetic field is under consideration. The main ports for RF power launch are situated near the "bean-shaped" plane, where the maximum of B is located. Apart from this, high-field-side (HFS) launch from one gyrotron with $P_{RF} = 1$ MW can be performed through the port near the "triangular" plane with the minimum of B and inverted ∇B.

The plasma current, I_p, affects the edge value of the rotational transform, $\Delta t = 1.2 \cdot 10^{-3} I_p$ [kA], which may exceed the required range for a proper island divertor operation without external field compensation [4]. The acceptable shift of the X-point, ΔZ [cm] $= 0.3 I_p$ [kA], is about few centimeters, and the net plasma current is limited by $|I_p| < 10$ kA [5]. Due to the absence of an ohmic transformer, electron cyclotron current drive (ECCD) will be used for compensating the bootstrap current and for a feedback control of the net plasma current. Since the ECCD efficiency is quite sensitive not only to the plasma parameters, but also to the magnetic configuration, it is important to estimate properly the range of ECCD values for the various magnetic configurations and to check its ability to counteract the residual bootstrap current. The effects of finite plasma pressure ($\beta > 0$) also play a significant role, especially in high-density scenarios, changing the deposition and current drive profiles. It can be seen in the Fig. 1a, where the change of the magnetic field along the major radius in the equatorial plane for different β-values is shown. Additionally, one can recognize in Fig. 1 (b–d) the difference in the RF power deposition location for X2 and O2 scenarios. In the following, the effects of finite β are only briefly discussed (when it is possible), just to indicate the tendency.
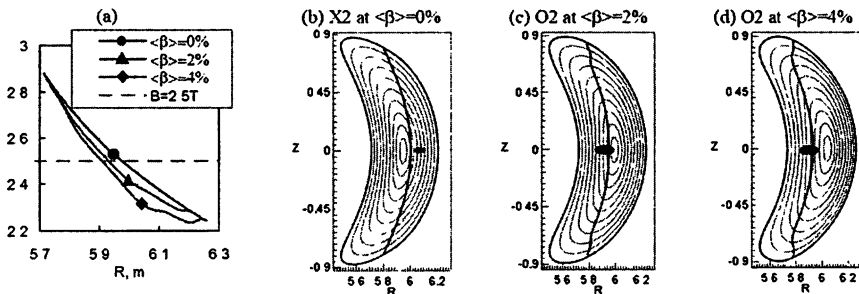
Fig. 1. B-field along major radius, magnetic axis positions are shown by markers (a). RZ cross-section in the "bean-shaped" plane with locations of the ECRH deposition for both X2 with $\langle\beta\rangle = 0$ (b) and O2 scenarios with $\langle\beta\rangle = 2$ % (c) and 4 % (d)

Numerical tools

The modeling has been performed with the ray-tracing code TRAVIS [6, 7] coupled self-consistently with a predictive 1D transport code [8]. The ray-tracing

code is developed for ECRH/ECCD predictions in arbitrary 3D magnetic configurations. The tracing equations are based on the general Westerhof-Tokman Hamiltonian [9] in weakly relativistic formulation, while for absorption the fully-relativistic model is applied (see, e.g. [10]). In this work we analyze the ECCD scenarios for operating with the different magnetic configurations in the collisionless limit, which is more realistic for the W7-X conditions, especially for the regimes with moderate densities and high temperatures. Since the widely used "high-speed limit" approach is in general not qualified for the estimation of the ECCD efficiency [11] because of its applicability only for scenarios with sufficiently large launch angles in an optically thick plasma, the ECCD model is formulated with momentum conservation in electron-electron collisions [11–13], which is especially important and even mandatory for these scenarios, where mainly bulk electrons absorb the RF power. The predictive 1D transport code solves the set of non-linear equations for particle and energy balance, as well as for the radial electric field and the current diffusion. The magnetic configuration is still not self-consistent with the plasma pressure and current density profiles. Based on the experience of W7-AS [14], it is assumed, that neoclassical transport dominates in the plasma core, while the plasma periphery is described by anomalous transport. Neoclassical transport coefficients were precalculated by the DKES code [15] without momentum conservation, which may somewhat overestimate the bootstrap current.

Low and moderate densities: X2 scenario

From the experience of W7-AS operation [14], the X2-mode allows for a short start-up producing the plasma from the neutral gas with a short time delay of about a few milliseconds. The single-pass absorption of the X2-mode is so high that nearly 100% absorption can be expected. The deposition profile being defined by the Doppler broadening and relativistic effects (for oblique and quasi-perpendicular launch, respectively) is well localized and quite predictable. By changing the launch angle as well the magnetic field both on- and off-axis deposition profiles can be obtained. The range of predicted plasma temperatures is determined mainly by assumptions about the dominated transport. Two different transport models based on the tokamak like Lackner-Gottardi confinement scaling [16] and the neoclassical transport model give two limits for the plasma temperatures, a conservative and optimistic, respectively [3, 13]. For 10 MW total power deposited near axis, the neoclassical transport model predicts $T_e(0)$ values up to 25 keV for low density and about 10 keV near the cut-off density, while for the conservative model $T_e(0)$ does not exceed 10 keV even for low densities. Important is that the high T_e values were obtained due to the neoclassical "electron-root" feature [17] with strongly positive radial electric fields. This scenario can lead to collisional decoupling of electrons and ions, when $T_e/T_i > 3$. The density profile, that is kept constant in the calculations, also does not reflect properly the

"electron-root" feature (a possible RF pump-out is omitted), which may significantly change the shape of density profile. The appearance of RF-induced convective non-local flux [18] requires a much more complex modeling and is ignored in the 1D simulations.
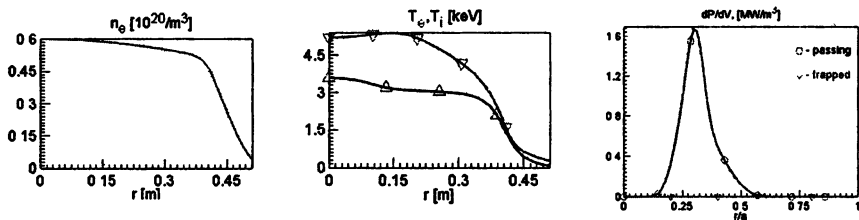

Fig. 2. X2 scenario with LFS launch of 5 RF beams 1 MW each; off-axis heating, $B = 2.53$ T; stored energy $W = 1.73$ MJ, confinement time $\tau_E = 0.35$ s. Left: density profile, $n_e(r_{\text{eff}})$, kept frozen in present calculation. Middle: temperature profiles, $T_e(r_{\text{eff}})$ (down triangles) and $T_i(r_{\text{eff}})$ (up triangles). Right: summarized deposition profile for 5 beams, $\Sigma dP_{\text{abs}}/dV$ with $\Sigma P_{\text{abs}} = 5$ MW.

As an example, we describe an X2 scenario with parameters suitable for transition to the O2 scenario. Since the plasma is optically gray for the O2-mode and the deposition profile is broader than for the X2-mode, plasma start-up with off-axis LFS deposition is required. The RF beams are launched from the LFS through the ports near the equatorial plane and directed to the corresponding mirrors installed on the inner wall for multi-pass O2 scenario. A scenario with only five beams is considered, which are injected in such a way that the current drive compensates the bootstrap current. The typical profiles of density, n_e, and temperature, $T_{e,i}$, together with the power deposition profile are shown in Fig. 2. The "electron-root" regime does not appear, and the radial electric field (not shown) is negative and small in the core. Both electron and ion temperatures are rather flat and ions are well collisionally coupled with electrons. Since the plasma is optically thick with respect to the X2-mode, $\tau_{X2} \gg 1$, and trapped electrons do not participate in absorption, the shape of the current drive profile (not shown) approximately coincides with the deposition profile. The obtained results confirm optimistic expectations for W7-X about ECRH with X2-mode as a very flexible and convenient scenario for all densities within the range of applicability.

High densities: O2 scenario

Because of very weak cyclotron absorption in low temperature plasmas ($\sim T_e^2$), the O2 scenarios cannot be used without preheating. In order to select the density range suitable for changing the RF wave polarization from X- to O-mode, the O2 scenario was simulated for different initial densities and temperatures. It was found that the O2 scenario does not have a thermal collapse if $n_e > 0.4 \cdot 10^{20}$ m^{-3}

and $T_e(0) > 0.5$ keV, and a steady-state with high temperature can be established. The change of polarization from X-. to O-mode has to be performed in the regime where both X2 and O2 scenarios can produce steady-state operation. As found in the simulations, the density range most suitable for changing the mode is $(0.8\div1.0) \cdot 10^{20}$ m^{-3} (for lower values, O2 single-pass absorption is too low and might increase the thermal load on the reflecting mirror; for higher values, the trajectory of the X2 beam becomes significantly influenced by refraction and thermal effects that also may lead to a potential danger for the inner wall). The RF beam after the first pass is reflected from the mirror installed on the inner wall, and after the second pass (from the HFS) from the metal wall. In simulations, we deem a scenario suitable if the beam power after the 3rd pass is less than 10% of the injected one (it is assumed that the remaining power is absorbed due to multiple reflections from the wall without any danger for the device).
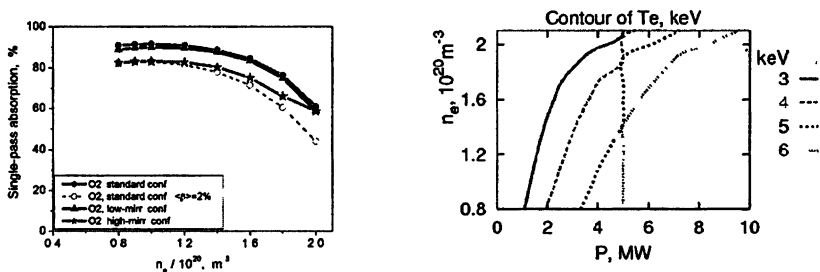
Fig. 3. *Left*: Density scan for O2-mode single-pass absorption. *Right*: Isolines of T_e on the operation diagram n_e vs P_{RF} (three passes calculated). The "standard" magnetic configuration is applied with $<\beta> = 0$ for $P_{RF} < 5$ MW and with $<\beta> = 2$ % for higher power.

In Fig. 3 (*left*), the single-pass absorption for the O2 scenario as a function of density is shown. The obtained values are sufficiently high for all magnetic configurations investigated, i.e. are about 70÷90 % for $n_e > 1.8 \cdot 10^{20}$ m^{-3}. It is important to mention here that single-pass absorption is reduced in comparison with vacuum configurations (compare the solid and dashed lines) due to the Shafranov shift and diamagnetic effects which shift the deposition profile in the HFS direction, reducing the optical depth. In the Fig. 3 (*right*), the isolines of central electron temperature as function of density and power are shown, from which one can conclude, that the high temperature regime ($T_e > 3$ keV) is reachable with the power starting from $P_{RF} = 1$ MW.

Plasma current control

The calculations were done for five different beams launched from the LFS with 1 MW power for each beam. Both X2 and O2 scenarios are modeled for the same launch conditions for three different magnetic configurations. As the RF-

beams in O2 scenarios must be directed onto the corresponding mirrors at the inner wall, the chosen direction is not optimal for ECCD in X2-mode. For the fairly low O2 single-pass absorption, three passes are calculated [19].

Let us consider first the moderate density range, $n_e < 10^{20}\,\text{m}^{-3}$, where both X2 and O2 scenarios can work. An increased field, $B = 2.562$ T, with a significant outward shift of the X2 power deposition (preventing the "electron-root" feature) allows for a central O2 power absorption. High central β, however, shifts the O2-absorption to the HFS.

In Fig. 4 (left), the X2 ECCD profiles, $j_{cd}(\rho)$, which summarize the contributions from all beams, are shown (the corresponding deposition profiles have a very similar shape). Negative ECCD is chosen since the bootstrap current is positive for these simulations. Due to very high optical thickness, the location of the deposition profile (ECCD as well) for the X2-mode is almost completely defined by the resonance location, and the Doppler broadening is mainly responsible for the width of the $j_{cd}(\rho)$ profile. For each configuration, the temperature dependence during the density scan is not strongly pronounced since T_e only varies slightly: for the "standard" configuration with n_e increased from 0.4 to $1.1 \cdot 10^{20}\,\text{m}^{-3}$, T_e is varied from 5.7 keV to 4.4 keV, respectively.
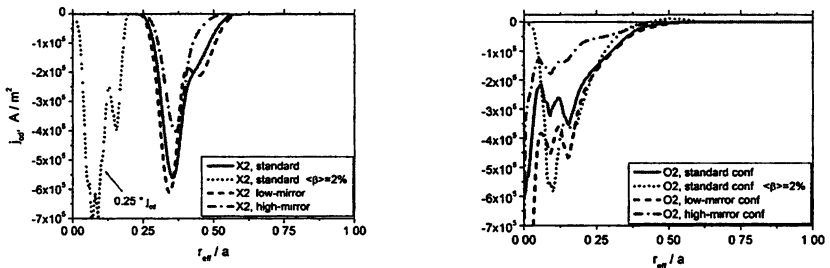
Fig. 4. Summarized ECCD profiles (5 beams 1 MW each) for the different configurations: "standard" (solid), "low-mirrors" (dash), and "high-mirrors" (dot-dash). Additionally, the case of $<\beta> = 2\,\%$ for the "standard" configuration is shown (dots). *Left* – X2 scenario, *right* – O2 scenario. For all cases, the density is the same, $n_e = 0.8 \cdot 10^{20}\,\text{m}^{-3}$.

Since the "standard" configuration is optimized for neoclassical confinement, the steady-state temperature obtained by transport simulation is highest in comparison with the "low-" and "high-mirror" configurations. On the other hand, due to the reduced trapped particle fraction, the parallel electric conductivity is high in the "low-mirror" configuration, which leads to an increase of ECCD. Nevertheless, due to the reduced confinement the temperature in the "low-mirror" configuration is for the same heating conditions also lower, and the decrease of f_{tr} is masked by a decrease of T_e. For the "high-mirror" configuration, with increased f_{tr} and decreased T_e, the ECCD efficiency is significantly reduced. For compari-

380

son, the case of the "standard" configuration with $<\beta> = 2\%$ is shown (see Fig. 4, dashed). One can see that the finite pressure leads to a fairly strong effect. The Shafranov shift combined with the diamagnetic effect leads to central X2 deposition (ECCD as well), making the appearance of the "electron-root" almost unavoidable.

The O2 scenario is more complicated. First of all, the plasma is optically "gray" and a significant part (up to 20 % or even more) of the power is absorbed during the second pass (third and fourth passes are of minor importance). The direct consequence of it is that electrons with $k_\parallel v_\parallel < 0$ are involved in cyclotron interaction with a current contribution of opposite sign, thus reducing $j_{cd}(\rho)$ in this point [12]. For the "standard" configuration with $<\beta> = 2\%$ this effect is most pronounced, and even positive values of $j_{cd}(\rho)$ appear (see Fig. 4, right, dashed). Although the RF beams are launched near the maximum of B ("bean-shaped" plane), trapped electrons are noticeably involved in the cyclotron inter-action, absorbing up to 10% of the power and reducing the ECCD. The absorption of the O2-mode ($\sim T_e^2$), is very sensitive to the shape of the T_e profile (the n_e profile is almost flat in the simulations). On the other hand, the T_e profile is defined mainly by the deposition profile. Due to this (positive) feedback, the resulting deposition profile (as well as ECCD) for scenarios with the resonance shifted to LFS are rather independent of density, and its shape is quite similar to those shown in Fig. 4 (*right*) for a quite broad range of densities (changing only the magnitude of $j_{cd}(\rho)$, which scales roughly as $1/n_e$).
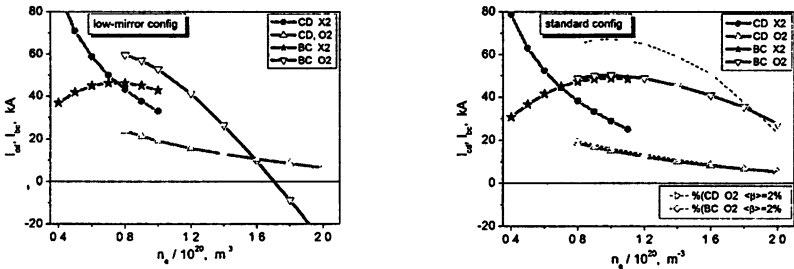
Fig. 5. Density scan for "low-mirror" and "standard" magnetic configurations. Both I_{cd} (circles for X2 and triangles for O2 scenarios) and I_{bc} (stars for X2 and rectangles for O2 scenarios, respectively) are shown.

In Fig. 5, the results of the density scan for the "low-mirror" and "standard" configurations are shown (since the bootstrap current is much lower for the "high-mirror" configuration up to acceptable level, it is omitted here). Following the theoretical predictions, the current drive for both X2- and O2-mode scales roughly as $1/n_e$. As expected, the current driven by the X2-mode is larger than that of the O2-mode for all tested configurations. There are two main factors

381

which lead to this jump of ECCD efficiency (from red circles to red triangles). First, due to a weaker cyclotron interaction the single-pass absorption of the O2-mode is less than 90 %, and the rest of the power is absorbed in the plasma periphery, where the temperature is low. Second, since the deposition profile is quite broad, the participation in the cyclotron interaction of both the electrons with $k_\| v_\| < 0$ and the trapped ones reduces the ECCD efficiency.

Even for the O2-launching conditions, the bootstrap current can be roughly compensated by X2-ECCD for the "high-mirror" and "low-mirror" configurations. For optimized X2-launching scenarios, however, the bootstrap current is completely compensated by the ECCD for all configurations under investigation. For O2 operation at high density, full current control is only obtained for the "high-mirror" configuration. Note that for the "standard" configuration with $\langle\beta\rangle = 2$ %, the bootstrap current is increased, whereas the ECCD is almost unchanged.

Summary

Different ECRH/ECCD scenarios have been analyzed using the selfconsistently coupled ray-tracing and 1D transport codes. For the X2 scenario, suitable for low and moderate densities, $n_e < 1.2 \cdot 10^{20}$ m^{-3}, good confinement with high temperatures is predicted. Similar results are found also for the O2 multi-pass scenario, for higher densities, $n_e < 2.0 \cdot 10^{20}$ m^{-3}. The best density range for transition from X2- to O2-mode is $(0.8 \div 1.0 \cdot 10^{20}$ m^{-3}.

Moreover, the reachable values of ECCD were estimated for both X2 and O2 scenarios. In high-density operation at low ECRH power, the bootstrap current exceeds the maximum ECCD for the O2 scenario. Only the "high-mirror" configuration has a sufficiently small bootstrap current thus confirming the corresponding W7-X optimization criterion. For the "standard" configuration with improved neoclassical confinement, however, ECCD control of the bootstrap current is possible only for the X2 scenario. With full current control by ECCD, only a few skin-times (i.e. about 10 s) are necessary to obtain stationary conditions for optimum divertor operation.

High density scenarios might be important for the W7-X island divertor operation since fairly high separatrix densities are required. Consequently the O2 scenarios are expected to be important for longer discharges. For these conditions, however, only the "high mirror" configuration allows for complete bootstrap current control by ECCD. In particular for the "standard" configuration, another discharge scenario must be chosen. Here, the edge value of the rotational transform in the vacuum configuration can be reduced by the amount which is generated by difference of maximum ECCD and the bootstrap current in the final steady state. The evolution of the total plasma current scales on the L/R-time (i.e. several 10 s). Such a discharge scenario, however, is much more complex compared to the case of full ECCD control of the bootstrap current.

References

1. *Nuerenberg J. and Zille R* Phys. Letters **114A** 129 (1986).
2. *Geiger J., Maassberg H, Beidler C. D.* 35th EPS Conf. on Plasma Phys., Hersonissos, Crete, 9–13 July 2008.
3. *Erckmann V. et al* Fusion Sci. Technol. **52** 291 (2007).
4. *Koenig R et al* Plasma Phys. Control. Fusion **44** 2365 (2002).
5. *Werner A. et al.* Rev. Sci. Instrum. **79** 10F122 (2008)
6. *Marushchenko N. B. et al.* Proc. of 14th Joint Workshop on ECE and ECH, Santorini, Greece, May 9–12, 2006, http://www.hellasfusion gr/ec14/papers/26.pdf.
7 *Marushchenko N. B et al.* Proc. of 16th Toki Conference, Toki, Japan, December 5–8, 2006, http://www.jspf.or.jp/PFR/PFR_articles/pfr2007S1/pfr2007_02-S1129.html.
8. *Turkin Yu. et al.* Fusion Sci. and Technol. **50** 387 (2007).
9. *Tokman M. D., Westerhof E. and Gavrilova M A.* Plasma Phys. Control. Fusion **42** 91 (2000).
10 *Bornatici M. et al.* Nucl. Fusion **23** 1153 (1983).
11. *Marushchenko N. B et al.* Fusion Sci. and Technol., accepted for publication.
12. *Taguchi M.* Plasma Phys Control. Fusion, **31** 241 (1989).
13 *Romé M. et al.* Plasma Phys. Control. Fusion **40** 511 (1998).
14. *Hirsch M. et al.* Plasma Phys. Control. Fusion **50** 053001 (2008).
15. *van Rij W. I. and Hirshman S. P.* Phys. Fluids B1 563 (1989).
16. *Lackner K. and Gottardi N. A. O.* Nucl. Fusion **30** 767 (1990)
17. *Maassberg H. et al.* Phys. Plasmas **7** 295 (2000).
18. *Murakami S et al.* Nucl. Fusion **40** 693 (2000).
19 *Marushchenko N. B. et al* 34th EPS Conf. on Plasma Phys., Warsaw, 2–6 July 2007 ECA. ol. **31F**, P-5.129 (2007)
20. *Marushchenko N. B. et al.* Proc. of 17th Toki Conference, Toki, Japan, October 15–19, 2007, http://www.nifs.ac.jp/itc/itc17/file/PDF_proceedings/poster2/P2-068.pdf.

OPPORTUNITIES FOR PLASMA DIAGNOSTICS
IN FUSION DEVICES BY MEANS OF TERAHERTZ SOURCES

N. N. Skvortsova, G. M. Batanov, L. V. Kolik, D. V. Malakhov, K. A. Sarksyan,
A. E. Petrov, N. K. Kharchev, W. Kasparek[1], M. I. Petelin[2], E. P. Koposova[2],
V. E. Zapevalov[2], V. A. Vershkov[3], D. A. Shelukhin[3], K. Tanaka[4], S. Kubo[4]

A. M. Prokhorov General Physics Institute, Russian Academy of Sciences, Moscow, Russia
[1]Institut für Plasmaforschung, Universität Stuttgart, Germany
[2]Institute of Applied Physics, Russian Academy of Sciences, Nizhny Novgorod, Russia
[3]Nuclear Fusion Institute, Russian Research Centre Kurchatov Institute, Moscow, Russia
[4]National Institute for Fusion Science, Toki, Japan

In large toroidal plasma traps (tokamaks, stellarators) terahertz devices may be used for:
– interferometry and reflectometry of plasmas with densities about 10^{21} m^{-3} (such densities are already available in LHD and are expected in the divertor region of ITER),
– studies of short-wave (tens Debye lengths) plasma density fluctuations by collective scattering technique,
– studies of fast ions and α-particles by means of collective Thomson scattering.
These methods could be realized by using sub-millimeter wave ~ 10^{-2}–10 kW CW gyrotrons and quasi-optical systems composed of duplexers, multiplexers, notch filters etc.

1. Main reasons to apply Terahertz tools for diagnostics in plasma traps

1.1. Interferometry and reflectometry

As is known the interferometer and reflectometer microwave diagnostics are used in plasma density measurements and in monitoring the plasma profile position. In recent years high plasma densities have been achieved in toroidal magnetic confinement systems. Thus, the maximum density in LHD amounts to 10^{21} m^{-3} [1] and is about 10^{21} m^{-3} in the D-III tokamak in standard regimes [2]; a density of 10^{19}–10^{20} m^{-3} is expected in the divertor region of the ITER tokamak [3, 4]. As an example, Fig. 1*a* shows a density profile in LHD stellarator operating in diffusion barrier regime taken from the 2007 report. Figure 1*b* shows the frequency appropriate for microwave reflectometer measurements as a function of the critical density (in the reflection region). Using the D-III and LHD data on plasma density as an example, it is shown that the reflectometer frequencies fall within the subterahertz range.

As yet, such diagnostics are not completed with an appropriate radiation source. For example a diagnostics of microwave reflectometry planned in 1995 for controlling the plasma position in ITER divertor region [5] was deleted from the list of ITER diagnostics in the late 2007s for the lack of THz sources.

Necessity of passing to terahertz frequencies: measurements in high-density plasmas of existing tokamaks and stellarators, including divertors. The power required of CW subterahertz sources for such diagnostics is 0.1–1 W.
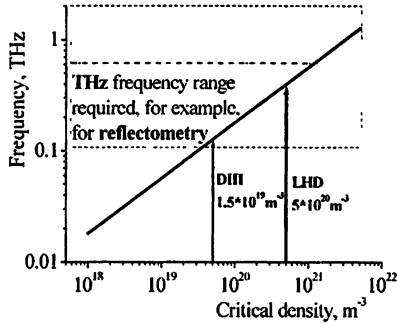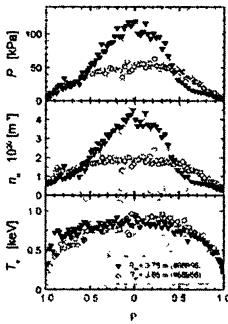
Fig. 1. *Left*: distributions of plasma parameters in LHD (where the central plot is the density distribution) in diffusion barrier regime (from the NIFS report [1]); *right*: microwave reflectometer frequency versus the critical plasma density (arrows indicate reflectometer frequencies for the D-III tokamak and the LHD stellarator).

1.2. Analysis of small-scale plasma turbulence and anomalous transport

It is the common knowledge that, if we have the parameter $\alpha = 1 / k_s \lambda_{De} > 1$ (k_s is the measured wavenumber, and λ_{De} is the Debye radius), we are then probing the collective behavior of the plasma. In the collective scattering diagnostics it is possible to measure oscillations that satisfy the Bragg relation: $|k_s| = 2|k_i| \sin(\Theta / 2)$, where k_i is the wave vector of the incident wave, and Θ is the angle between the incident and scattered waves.

Evidently, of prime interest are studies of small-scale fluctuations when the wavelength is close to the Debye radius. Figure 2 shows a diagram where the incident wave frequency is plotted versus the wavenumber of plasma fluctuations measured by back scattering technique. The measurable range of the wavenumbers of plasma fluctuations is shown by gray shade. As is seen from the diagram constructed for plasma parameters typical of tokamaks and stellarators (electron densities of 10^{19} m^{-3} and temperatures of 1 keV), small-scale fluctuations become accessible for observations when moving to subterahertz frequencies.
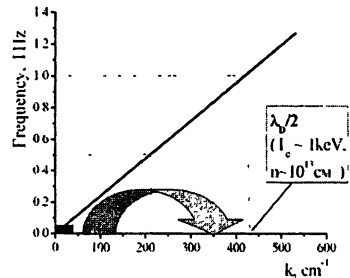

Fig. 2. Incident wave frequency versus the wavenumber of fluctuations measured by back scattering technique. A black rectangle shows the wavenumber range where measurements have already been conducted.

385

The frequency required of microwave sources increases with increasing plasma density and temperature. The power of CW subterahertz sources for such diagnostics is higher than that for interferometer measurements and amounts to 1–10 W. In this case, the requirements to measuring detectors may be greatly simplified.Investigations in the range $k_s < r_{De}$ by collective scattering of gyrotron radiation of operation frequency and its second harmonic are carried in L-2M and LHD (for more than 5 years) [6–9]. Features common to experiments:

1. As microwave sources for diagnostic, we used gyrotrons producing electron cyclotron heating in these devices;

2. Quasioptical transmission lines were used to transmit both the incident beam and the scattered signal.

Experiments were always conducted within the framework of specific research programs of L-2M and LHD devices, that is to say, without arrangement of any special conditions for operation of these diagnostics.

Table 1 lists wavenumbers of plasma density fluctuations in the central region of the plasma column, which were measured at the first and second harmonics of heating gyrotrons in these devices. Figure 3 shows the noise energy distribution ($k_s \sim 34.5\,\mathrm{cm^{-1}}$) over the plasma cross section in LHD [10] and a typical spectrum of plasma fluctuations with quasiharmonics ($k_s \sim 40\,\mathrm{cm^{-1}}$) measured in a high-temperature plasma in L-2M [11].

Table 1. Characteristic wavenumbers of plasma fluctuations measured from collective scattering of heating gyrotron radiation in L-2M and LHD

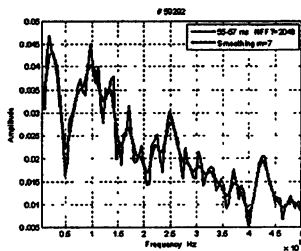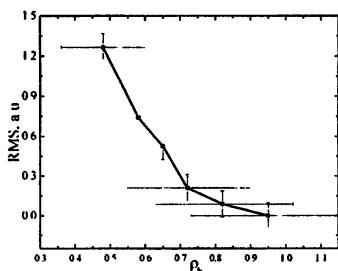| L-2M		LHD	
75 GHz (I harm.)	$k = 2$–$20\,\mathrm{cm^{-1}}$	82.7 GHz (I harm.)	$k = 30$–$34.5\,\mathrm{cm^{-1}}$
150 GHz (II harm.)	$k = 40\,\mathrm{cm^{-1}}$	84 GHz (I harm.)	$k = 34\,\mathrm{cm^{-1}}$

Fig. 3. Noise energy distribution ($k_s \sim 34.5\,\mathrm{cm^{-1}}$) over the plasma cross section in LHD (*left*); fourier spectrum (following the Welch algorithm) of fluctuations with quasiharmonics ($k_s \sim 40\,\mathrm{cm^{-1}}$) in L-2M (*right*)

1.3. Studies of collective Thomson scattering

The collective Thomson scattering (CTS) system is expected to be an efficient diagnostic tool for measuring thermal ions and fast ions. After successful experiments at the W-7AS, this diagnostic is being developed for a number of large devices [see, e.g., 12–14].

Note that the radiation from the real hot plasma represents a noisy signal of continuous Fourier spectra with non-Gaussian statistics. So, the probabilistic characteristics are critically important in interpreting received signals [15, 16]. For example, from a non-Gaussian histogram of scattered signal of gyrotron second harmonic it became possible to estimate the number of processes forming small-scale turbulence in the core plasma of the L-2M stellarator (Fig. 4).

Figure 5 illustrates a diagnostic system that will put into operation at the LHD. The hatching shows the propagation of the probing and scattered beams. Such a diagnostic requires a high gyrotron power of up to 10^5 W (change of gyrotron frequency spectrum also is necessary for considering [17]). Consequently, the CTS diagnostics should make use of gyrotrons with frequencies of up to 100 GHz (77 GHz in LHD, 90 GHz in TEXTOR, and 60 GHz is proposed for ITER). At the same time, a possibility to shift LHD plasma diagnostics to higher frequencies is being considered: the experience at 77 GHz is planned to be applied to a scheme based on a 400 GHz gyrotron [18].
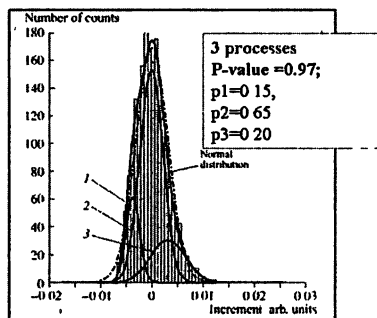
Fig. 4. Fit to a non-Gaussian histogram of scattered signal
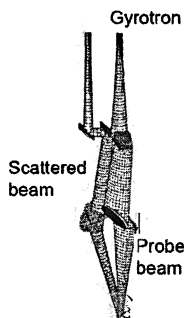
Fig. 5. Schematic of the collective Thomson scattering diagnostic for LHD (77-GHz)

2. THz diagnostics hardware

The dense plasma diagnostics (Fig. 6) needs
- THz sources of sufficiently high power,
- wave transmission, control and filtration systems,

proper methods of signal processing.

Fig. 6. Block diagram of terahertz plasma diagnostics

THz sources → Quasioptical transmission lines and systems → Techniques for signal processing
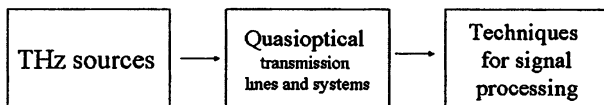
2.1. Gyrotrons

The dense plasma diagnostics requires microwave sources with frequencies 0.3–3 THz and average powers $1-10^5$ W. Such parameters have already been attained with free-electron lasers, but these sources are too large and costly, and so seem less attractive than gyrotrons. A 0.326 THz /1.5 kW CW second harmonic gyrotron was demonstrated by the Radiophysical Research Institute as early as in 1972 [19]. Recently the Institute of Applied Physics has tested a 1 THz / 1 kW fundamental gyrofrequency gyrotron in a pulsed solenoid [20] and constructed a 268 GHz / 20 W CW second harmonic gyrotron [21]. Broad-frequency-tunable, phase-locked, frequency-multiplication THz gyrotrons are being discussed.

However, presently, for the sub-THz plasma diagnostics, second harmonic CW gyrotrons operating in cryomagnets of relatively low magnetic fields (Table 2) seem most practical.

Table 2. Parameters of up-to-the-date subterahertz CW gyrotrons

Frequency, THz	Power, kW	Harmonic number	Voltage, kV	Reference
0.326	1.5	2	27	N. Zaitsev et al., JRTE, 1974
0.395	0.056	2	25	T. Idehara et al., IPMMW, 2007
0.460	0.008	2	13	R.Temkin et al., IEEE TPS, 2006

2.2. Quasioptical wave transmission and control components

To avoid the RF breakdown and reduce the RF absorption, electrodynamic components (mode converters, multiplexers, polarizers, diplexers etc.) for at the subterahertz band should be quasioptical. As a prototype, Fig. 7 shows a 140 GHz resonant diplexer [22, 23] used to combine beams from two ~1 MW gyrotrons and to switch, electronically, the combined beam from one channel to another (FADIS experiment, Greifswald, 2008). Such a device is planned, in particular, to combine the ECR heating with a notch filtering for a collective scattering diagnostics of a plasma [24]. In this case the whole plasma radiation, except of a narrow near-gyrotron band, is forwarded to the receiver of the plasma diagnostics unit.
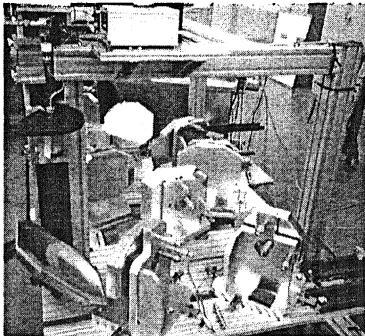
Fig. 7. 140 GHz resonant diplexer

Such a method might be used at the LHD, where the diplexer would have resonant frequency 77 GHz.

3. Diagnostics schemes and signal processing techniques

As both O-mode and X-mode waves propagate in the plasma, wave beams should be polarization controlled, and beam traces in the plasma should be calculated to determine the plasma structure in the region of interest.

For studying collective scattering to measure plasma density fluctuations and collective Thomson scattering to measure the ion distribution function at subterahertz frequencies, techniques similar to those used at L-2M, LHD, W7-AS and ASDEX can be used. Fig. 8 shows a simple quasi-optical reflectometric scheme based on multiplexing of 3–10 gyrotrons, each frequency modulated within 0.3–1 GHz.
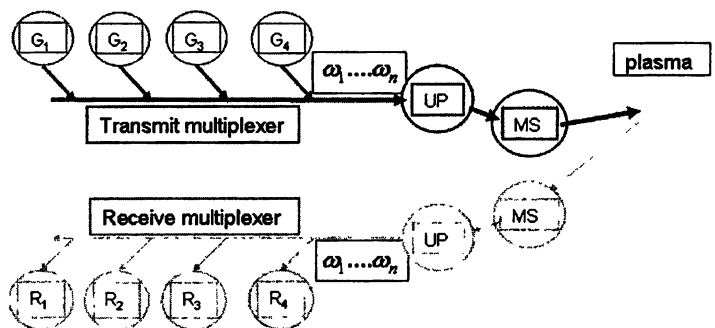
Fig. 8. A gyrotron based reflectometric scheme:
(UP) universal polarizer, (MS) mechanical scanner

4. Conclusions

In toroidal systems, including ITER, THz gyrotron based systems can be used for three types of plasma diagnostics listed in Table 3. CW powers necessary for plasma diagnostics can be estimated as follows:

- 0.1–1 W for reflectometry, interferometry, and scattering on long-wave fluctuations;
- 1–10 W for scattering on short-wave fluctuations;
- 10^2–10^4 W for diagnostic of fast ions, α-particles, and collective Thomson scattering.

Such powers can be provided with various modifications of gyrotrons (in particular, with gyrotrons operating at the second cyclotron harmonic).

Relevant
- quasi-optical wave transmission and control components,
- signal control and processing methods

can be developed basing on the present-day experience.

389

Table 3. Opportunities for plasma diagnostics
in ITER by means of terahertz sources [25]

Interferometry, radar interferometry and reflectometry	Collective scattering diagnostic (short-wave plasma density fluctuations)	Collective Thomson scattering diagnostic (fast ions and α-particles)
MHD, Disruption and Control Determination of control system requirements for diagnostics.	**Transport Physics** Encourage tests of simulation predictions via comparisons to measurements of turbulence characteristics, code-to-code comparisons and comparisons to transport scalings. **Steady State Operation and Energetic Particles** Study fast particles collective modes in low and reversed magnetic shear configurations: Identify key parameters. Perform theory-data comparison on damping and stability, including non-linear mode dynamics and fast particle transport.	**Diagnostics** Review requirements for measurements of neutron/a source profile and assessment of possible methods of measurement Develop methods of measuring the energy and density distribution of confined and escaping alphas

References

1. Annual Report of NIFS. October 2007. http://www.nifs.ac.jp/report/annrep07/index.html (2007).
2. *Rhodes T L et al.* Phys. Plasmas, 14, 056117 (2007)
3. *Vayakis G. et al.* Nuclear Fusion, 46 S836 (2006).
4 *Conway G. D.* Nuclear Fusion, 47, 1710 (2007).
5. *Manso M. et al* Diagnostics for experimental thermonuclear fusion reactors V. 2 Ed. P. E. Stott. P. 139. Plenum Press (1998).
6. *Batanov G M. et al* Pisma v JETF. 72, 250 (2000)
7. *Skvortsova N. N. et al* J. Plasma Fusion Res. SERIES, 5, 328 (2002).
8. *Batanov G. M. et al.* Plasma Phys. Reports, 29, 363 (2003).
9 *Batanov G M et al.* Plasma Phys Reports, 29, 1019 (2003)
10 *Kharchev N., Tanaka K. et al* 17th HTPD08. F25 (2008).
11 *Skvortsova N N. et al* The 35th IEEE ICOPS. 5E3 (2008).
12 *Suvorov E et al* Plasma Phys Controlled Fusion, 37, 1207 (1995).

13 *Bindslev H., Nielsen S. K. et al.* PRL 97, 205005 (2006).

14. *Nishiura M., Tanaka K. et al.* 17th conference HTBD08. F38 (2008).

15 *Korolev V. Yu and Skvortsova N. N.* (Eds) "Stochastic Models of Structural Plasma Turbulence". VSP, Leiden – Boston (2006).

16. *Korolev V. Yu., Skvortsova N. N.* // The systems and means of informatics / ed. I. A. Sokolov. 126 (2005).

17. *Batanov G M., Kolik L V. et al* Technical Physics, 46, 595 (2001).

18 *Idehara T et al.* The 35th IEEE ICOPS. 3B6 (2008).

19. *Zaitsev N et al.* JRTE (1974).

20. *Glyavin M Yu., Luchinin A. G.* 7 W. Strong Microwaves. S19 (2008).

21. *Zapevalov V. E et al.* 7 Workshop Strong Microwaves. S22 (2008).

22 *Erckmann V. et al.* Fusion Science and Technology, Vol. 55, pp. 23–30 (2009).

23. *Petelin M. et al.* AIP Conference Proc. Woodbury, NY. 304 (1998).

24. *Kasparek W. et al.* A fast switch, combiner and narrow-band filter for high-power millimetre wave beams, 2008 // Nucl. Fusion, 48 054010, pp. 1–9.

25. Progress in the ITER Physics Basis, Nuclear Fusion, 47 (2007).

SMALL SCALE INSTABILITIES AT HIGH POWER REB-PLASMA INTERACTION AS MECHANISM OF PLASMA HEARTING IN LONG SOLENOID (REVIEW OF INVESTIGATIONS)

A. V. Arzhannikov[1,2], A. B. Burdakov[1,2]

[1]Novosibirsk State University, Novosibirsk, Russia
[2]Budker Institute of Nuclear Physics SB RAS, Novosibirsk, Russia

We present short review of investigations on pumping of small scale turbulence in plasma by high power relativistic electron beam which are carried out at BINP SB RAS about thirty five years at experiments for plasma heating in a long solenoid Influence of key parameters determining an energy transfer from the beam to the plasma was investigated and this problem is discussed in this paper.

Introduction

One of the appropriate ways for obtaining plasma with parameters which are necessary for operation a fusion reactor as energy source, is to heat a plasma column in a long multi-mirror trap. The main idea of the process of plasma heating by a relativistic electron beam (REB) was given by Prof. D.D. Ryutov in the early 70th of past century [1]. Experiments were carried out in time period about thirty five years at various devices: INAR, GOL, INAR-2, GOL-M, and GOL-3 in Budker Institute of Nuclear Physics.

A key parameter taken into account in the pointed experiments is the ratio of e-beam density to plasma one since it fixes the growth rate of two-stream instability that is the base mechanism of energy transfer from the beam to plasma oscillations. Another important parameter determining the growth rate is the velocity spread of injected beam electrons. This parameter was varied by changing a thickness of the anode foil of an accelerator diode or geometry of a magnetically insulated diode with magnetic field strength. Next main parameter which has essential influence on beam-plasma interaction process, is the ratio of electron cyclotron frequency to the plasma Langmuir one; therefore this ratio has to limit an energy level and spectrum of turbulent Longmuir oscillations. As a result, it determines the energy transfer from the plasma oscillations to various groups of plasma electrons and, consequently, the final efficiency of energy transfer from e-beam to the plasma electrons. The energy level and the spectrum of the Langmuir oscillations also depend on the temperature of plasma electrons, and for changing this temperature we varied the time duration of beam injection into plasma column: from a few tens of nanoseconds up to ten microseconds. Taking into account local values of the parameters pointed above we discuss time behavior of the energy distribution function of beam and plasma electrons and the distribution of plasma energy content along the axis of the solenoids.

Experiments with beams of tens of nanoseconds duration

The first experiment was done by a group Dr. R.X. Kurtmulaev in 1971 [2]. Soon afterward, other group of Dr. V.S. Koidan started experiments at INAR device [3, 4]. These experiments were carried out with the following beam parameters: initial electron energy −1 MeV, beam current up to 25 kA, pulse duration −70 ns. Schematic drawing of the experiment is presented in Fig. 1. The beam was injected into plasma column (diameter 8 cm and length 230 cm) which plasma density was varied from 10^{12} cm^{-3} up to 10^{16} cm^{-3}. Plasma was located in strong longitudinal magnetic field of mirror configuration with induction up to 2.5 T in a uniform section and up to 4.2 T in the mirrors. Beam current density could be varied by changing the beam diameter at the same beam current.
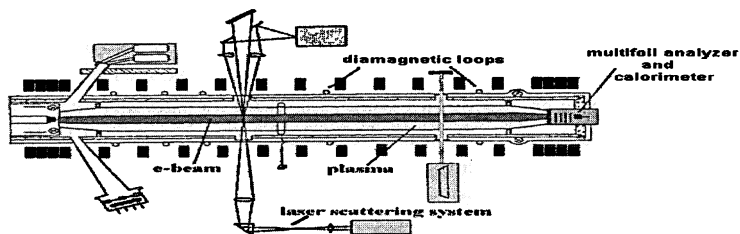
Fig. 1. Schematic of INAR experiments

In experiments on measuring of the beam current neutralization [5] we used the beam with the current 10 kA and the beam diameter 2 cm. The beam was injected into the plasma through titanium foil with the thickness of 50 μm and had the beam angular spread about 25°. Varying of the plasma density from short to short we measured a return plasma current outside of the beam cross-section and a total current in the plasma column cross-section during beam injection. Experiments showed that only, if the plasma density excided the value $2 \cdot 10^{14}$ cm^{-3} the entire plasma return current was concentrated inside of the beam cross-section and there was no current outside of it. Analyses of the experimental result showed that a reason of this limitation of the plasma density is connected with anomalous strong decreasing a plasma conductivity in the beam cross-section due to an excitation of both the Buneman and ion-sound instabilities when the plasma electron current velocity become larger than the electron thermal velocity.

In a series of experiments on energy transfer from REB to the plasma for the case of total beam current compensation by the plasma return current we used two variants of the injected beam: with the current density −1 kA/cm^{-2} (electron density −2 · 10^{11} cm^{-3}) and −5 kA/cm^{-2} (−10^{12} cm^{-3}). The beam was injected through the titanium foil, 6 μm thick, the magnetic field was 4.2 T in the diode. This provided a small angular spread of the relativistic electrons less than 0.15 rad at entrance to the plasma. Beam energy loses in the plasma was meas-

ured by a calorimeter and by a multifoil analyzer of energy distribution function. Dependence of beam energy deposition over the plasma column was measured by diamagnetic loops. Measurements showed that the most effective energy transfer from the beam to the plasma occurs near the entrance of the beam and the interaction efficiency decreases as the beam propagates through the plasma column [6, 7]. Distribution of a transverse pressure (nT) of the heated plasma over the axes (the coordinate z) of the plasma column follows approximately a dependency law $nT(z) = nT_0\, x(1 + z/l)^{\alpha}$, where $nT_0 = nT(z = 0)$, l is a spatial scale of energy release and exponent α is negative. The experiment showed that the spatial scale $1 \sim 1$ cm and the exponent $\alpha = -3/4$ [8]. This strong gradient of the energy density in the plasma over the axis of device is conserved during time of the beam injection into plasma and then it decays. It means that the small-scale turbulence pumping by REB strongly depresses an electron thermo-conductivity along the magnetic field during passing the beam through the plasma.

As seen in Fig. 2, the energy release level (nT) decreases with the increase of plasma density, however, it is high enough up to the density $(4–7) \cdot 10^{15}$ cm^{-3} for the beam density 10^{12} cm^{-3}. When the beam has a lesser density $(2 \cdot 10^{11}$ cm$^{-3})$, the energy release character along the length of the plasma column remains the same, however, the absolute level become lower. The measurements show that the energy release grows at the decrease of the plasma density and then stops growing. At this plasma density the full compensation of the beam current by the plasma return current starts to break down. As it has been earlier established [5], the beam decompensation is due to the return current instability and, apparently, to the appearance of anomalous resistance in the plasma column. The anomalous resistance can lead to stabilization of the two-stream instability and, correspondingly, to limitation of the maximum energy deposition in the plasma. The behavior of the energy deposition into the plasma measured by diamagnetic loops, depending upon the plasma density, agrees with the calorimetric measurements of the total energy losses of the beam. The corresponding results are given in Fig. 2 for the beam density $n_b = 10^{12}$ cm^{-3}, as well. It is seen that with a decrease of plasma density the losses first grow and then at a plasma density $\sim 10^{15}$ cm^{-3} for the beam with $n_b = 10^{12}$ cm^{-3} this growth saturates. According to these measurements the maximum energy losses of the beam is about of 35 % (see [7]).
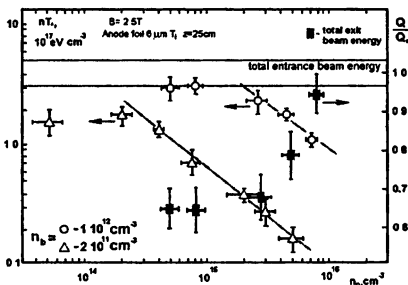
Fig. 2. Beam energy transfer to plasma with various density (INAR)

394

These results showing the high efficiency beam-plasma interaction were obtained in the case of small angular spread of the beam electrons. When we increased the beam angular spread by replacing the titanium foil of 6 μm thicknesses by other ones with large thickness the efficiency of energy transfer was dramatically decreased [6, 7]. Figure 3 demonstrates such results for the beam density $n_b = 2 \cdot 10^{11}$ cm^{-3} and the plasma density $n_p = 4 \cdot 10^{14}$ cm^{-3}.

Fig. 3. Efficiency as a function of beam angular spread (INAR)
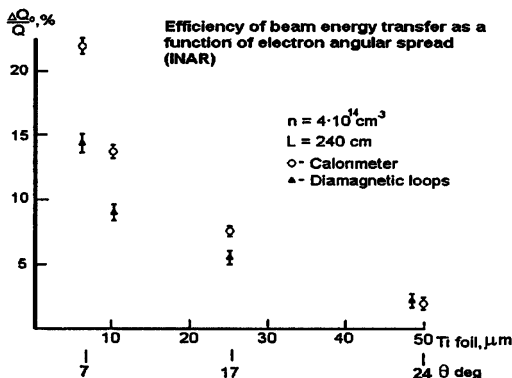
As a result of collective interactions, the distribution function of heated plasma electrons becomes essentially non-equilibrium one (see Fig. 4 and [9, 10]). At effective beam-plasma interaction conditions the major part of plasma electrons is heated up to average energies (temperature) of 1÷2 keV. In this case the spatial anisotropy of the electron distribution function is observed: the mean energy of electrons in the axial direction exceeds by several times the electron energy in the radial direction. These suprathermal electrons keep the major part of energy left by the beam in the plasma. In addition, the electron spectrum is non-Maxwellian and it extends up to energy of the heating beam [9, 10]. Energy distribution function of the electrons of the relativistic beam after interaction with plasma as soon as their angular

Fig. 4. Energy distributions function of the heated plasma electrons (INAR and GOL-M)
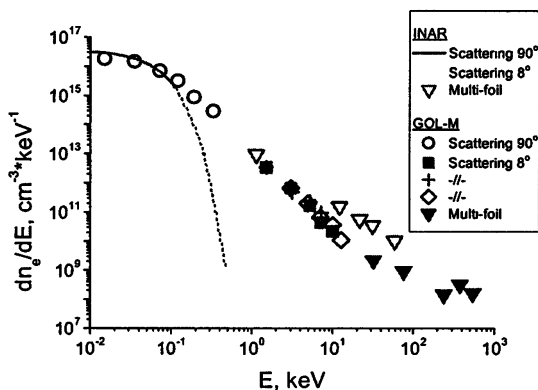
spread were measured in special series experiments at the INAR device [11]. These measurements showed that the comparative energy spread and the angular one had approximately the same value [9, 11] and this value agreed with the beam energy losses measured by the calorimeter.

Experiments at beam duration about ten microseconds

In order to increase the heated plasma parameters we had to increase an energy content of the heating beam by increasing its pulse duration at keeping other experimental conditions approximately on the same level that was done for tens nanosecond beams. On this purpose we created new electron accelerators with the beam current $30 \div 50$ kAs, the pulse duration $3 \div 10$ μs at the electron energy $0.7 \div 1.0$ MeV [12, 13]. First experiment at the GOL-3 facility on plasma heating at few microsecond pulse duration of the beam was curried out when the beam was generated by the accelerator U-3 with the beam energy content was about 70 kJ [14]. Than such experiment at the beam time duration about 10mcs and the beam energy content up to 180 kJ respectively was done by use other accelerator U-2 [15]. In these experiments we measured by diamagnetic loops the beam energy deposition along the axis of the plasma column and obtained that the distribution of specific plasma energy content was strongly non homogeneous as we had obtained earlier at the INAR device (see [16] and results in Fig. 5).
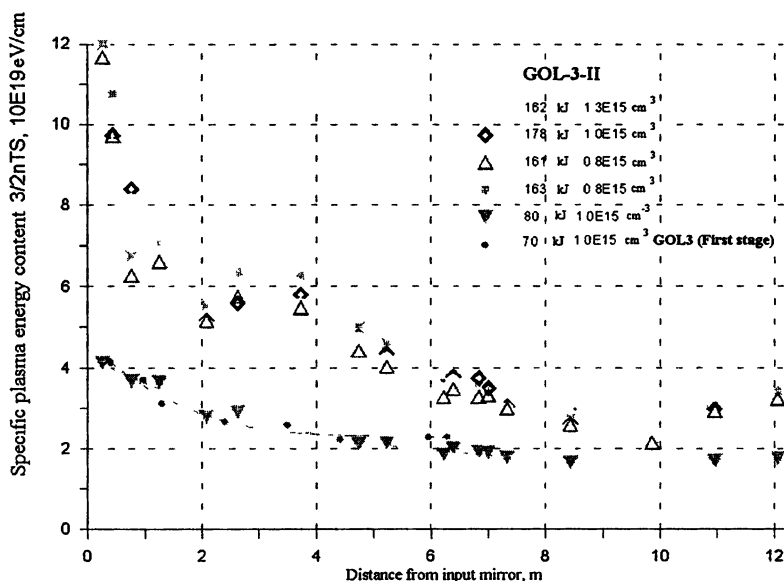

Fig. 5. Distribution of specific plasma energy content over the length of plasma column (GOL-3)

Since such high level gradient in the energy deposition was took place in time of the beam pulse duration (ten microsecond) when average energy of the heated plasma electrons was a few keV, we had to suppose that the high level of the small scale turbulent fluctuations in plasma generated by two-stream instability strongly depressed longitudinal thermoconductivity in plasma column. Existing of a high level Langmuir oscillation in plasma during all time of the E-beam injection demonstrates results of measurements of the energy distribution function of beam electrons after their passing through the plasma column by a special diagnostics – multi-foil analyzer. These results are presented in Fig. 6 for the time of 4 µs moment when the initial beam electron energy was 1 MeV, at the total beam duration was about 10 µs [16].
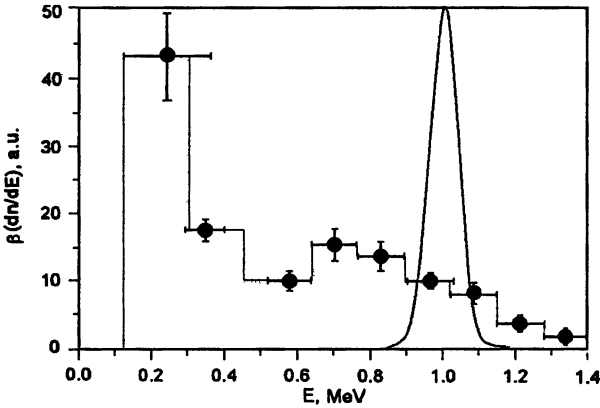
Fig. 6. Energy distribution function of beam electrons (GOL-3-II)

The energy distribution function of the beam electrons after passing through the plasma is drawn in Fig. 6 by a histogram. Initial beam energy spectrum must be narrower than it is shown by thin line in this Fig. 6. One can see that after passing through plasma column the electron energy spectrum becomes very wide and the average energy losses over all beam electrons are about 30 %. This percentage of the energy losses is very close to results obtain with ten nanoseconds beam.

Since two-stream instability transfers the beam energy through Langmuir oscillation to the plasma electrons that the high level of the gradient of energy deposition along the axis of the column means very high changing of the electron temperature over this coordinate with a small spatial scale. Such gradient of the electron temperature allowed us to realize a fast heating of ions by their acceleration as a result of the plasma motion along the axis under the gradient of plasma electrons pressure [17]. To investigate the mechanism of heating the plasma ions is a main goal of the experiments on beam-plasma interaction in long solenoids in this time.

Conclusion

As result of thirty years experiments on beam-plasma interaction the following regularities were clearly discovered:

- energy losses of a high current relativistic electron beam reach 30% in 1meter plasma column length at the beam-plasma interaction under two-stream instability;
- energy deposition of REB in plasma has strongly non-homogeneity over the axis of the column with a peak located near the beam entrance;
- both energy and angular spreads of the beam electrons increase approximately synchronous at the beam-plasma interaction under two-stream instability;
- strong Langmuir turbulent oscillations pumped by two-stream instability deliver the beam energy to the plasma electrons which obtain non-Maxwellian energy distribution function that extends up to energy of the heating beam;
- the turbulent plasma oscillations pumped due to passing of the beam, strongly (in few orders value) suppress longitudinal conductivity and thermoconductivity of the plasma as well.

References

1. *Breizman B. N. and Ryutov D. D.* Nucl. Fusion , 14, p. 873 (1974).
2. *Altyntsev A T. et al.* Plasma Phys. and Control. Nucl. Fusion Res., IAEA, Vienna, 2, p. 309, (1971).
3. *Koidan V. S. et al* Proc. 5th Europ. Conf. on Control. Fusion and Plasma Phys., Grenoble, 1, p. 161 (1972)
4. *Abrashitov Yu. I. et al.* Zh Eksp. Teor. Fiz., 66, p. 1324 / JETP, 39, 1974 p. 647 (1974).
5. *Arzhannikov A. V. and Koidan V. S.* Proc 12th Int Conf. on Phen. in Ion. Gases, Eindhoven,1, p. 278 (1975).
6. *Arzhannikov A. V et al.* Pis'ma v Zh. Eksp. Teor. Fiz., 27, 1978, p. 173 / JETP Lett , 27, p. 161 (1978).
7. *Arzhannikov A. V et al* Proc. 3rd Int. Conf. on High Power Electr. and Ion Beam, Novosibirsk, p. 29, (1979).
8. *Arzhannikov A V.* Kandidatskaya dissertatsiya. Novosibirsk, p. 106 (in Russian), (1980).
9. *Arzhannikov A V. et al.* Physica Scripta. Vol. T2/2, p. 303 (1982).
10. *Vyacheslavov L. N. et al.* JETP Letters, Vol. 75, No. 1, p. 41 (2002).
11. *Arzhannikov A. V. et al.* Proc. of XVI Inter. Conf. on Phenom.in Ionized Gases, Duesseldorfp. 348, (1983).
12. *Voropaev S G. et al.* Pis'ma v ZTF, v. 13, N 7, 431, (1987).
13. *Arzhannikov A. V. et al* Laser and Part. Beams, v. 7, part 1, p. 139 (1989).
14. *Burdakov A. V. et al.* JETP, 82, p. 1120 (1996).
15. *Agafonov M. A. et al.* Proc. 11th Int. Conf. on High Power Part. Beams, Prague, p 182 (1996).
16. *Arzhannikov A V et al* Transactıon of Fusion Techn , Vol. 35, N 1T, p. 112 (1999).
17. *Arzhannikov A V. et al* Transaction of Fus Scin. and Techn., Vol. 43, N 1T, p. 30 (2003).

QUASI-OPTICAL BEAMS IN INHOMOGENEOUS MAGNETIZED PLASMA

A. A. Balakin, M. A. Balakina, A. I. Smirnov

Institute of Applied Physics RAS, Nizhny Novgorod, Russia

The past decades have seen a considerable advance in the description of wave beam propagation in complex anisotropic and inhomogeneous media. The history of this process is many sided and includes both mainly theoretical works [1] and more practical attempts, for example, to formulate a complex geometrical optics [2–4]. The latter has initially been motivated by the needs to describe wave beam propagation and dissipation in plasmas, in particular, in the electron cyclotron range of frequencies. This ultimately led to the development of a number of numerical codes capable of the calculation of Gaussian beam propagation in cold inhomogeneous media. Two examples are the codes ECWGB [4] and TORBEAM [5]. The last few years have seen a remarkable revival of this field. The GRAY code [6] was developed on the basis of ECWGB, and represents some improvement of the latter. Attempts have been made to improve the TORBEAM code allowing the account of non-Gaussian beams [7–9]. Typically, these beam tracing codes are based on an expansion assuming the ordering of the different length scales as $L \gg w_{beam} \gg \lambda$, where L is the scale length on which plasma and wave properties vary, w_{beam} is the size across the wave beam, and λ the wave length. Generally, the first of these conditions is broken in the electron cyclotron resonance (ECR) layer. There has also been the suggestion to use the expansion of the wave beam in plane waves, to each of which a geometro-optical rays can be associated [10]. finally, numerical codes have been developed to solve the full wave equation directly for wave beam propagation in realistic configurations representative of magnetic confinement fusion [11, 12].

At the same time, the complexity of the problem poses various limitations to each of these newly developed codes. For example, the GRAY code cannot be applied to strongly focused beams in media with strong spatial dispersion nor near areas of caustics formation. The improvements of the TORBEAM code remain within the frame of the aberration free (AF) approximation. The geometro-optical (GO) code based on the plane wave, Fourier mode expansion [10] apparently encounters problems in strongly inhomogeneous media, when the curvature of the geometro-optical rays becomes comparable to the beam width. The full wave codes, finally, still suffer from limitations in computing speeds. In particular in the electron cyclotron range of frequencies, the scales of the plasma device and wave beam greatly exceed the wave length which makes full wave codes computationally extremely intensive: even on state of the art supercomputers a typical run may take several days. This virtually excludes the use of these codes for parametric scans in searches of optimal launch scenarios.

In order to improve on these efforts cited above, the current authors have developed a novel formulation of the wave beam propagation in magnetized plasmas [13–15]. Starting from the full wave equation for arbitrary anisotropic media, like warm plasma, and assuming slow variation of both the medium and the wave beam on the scale of a wavelength, a parabolic equation for the evolution of the wave beam amplitude profile has been formulated. This equation can be seen as a generalization to anisotropic media with spatial dispersion of the parabolic equation for wave propagation in isotropic media of Fock and Leontovich [16]. It is valid for wave beams of arbitrary shape. In the approach followed, the scalar amplitude can be used to reconstruct the vectorial wave field with high accuracy. On the basis of the resulting quasi-optical equations [13, 14] a new beam tracing code has been developed. The theoretical model and beam-tracing code allow to describe the wave beam propagation correctly both in the presence of strongly inhomogeneous dispersion and absorption as well as in media with strong spatial dispersion. In such regions most other codes [5, 6, 10] will fail. In the limit of homogeneous cold plasma the model [13, 14] naturally reduces to AF equations similar to those of Refs. [7, 8].

The quasi-optical equation for wave beams in an inhomogeneous medium can be obtained in different ways. first, assuming that the field structure is fixed, it is possible to derive equations for the beam parameters (such as the width, the centroid position, etc.) by the method of variation of an arbitrary constant [3]. Second, it is possible to apply the Leontovich method and then sequentially omit small terms in the equation for the field [13]. finally, in analogy with quantum mechanics, the quasi-optical equation can be derived heuristically by making the Schrödinger – Weyl replacement $p \to \nabla / i k_0$ in the Hamiltonian $H(r, p)$ for geometrical-optics rays [14].

The third approach applies naturally to linear homogeneous media with a spatial dispersion whose permittivity tensor has the form $\varepsilon_{ij} = \varepsilon_{ij}(k)$. In this case, applying the Fourier transformation to Maxwell's equations yields not a set of partial differential equations, but a set of algebraic equations

$$L_{ij}(k)\left[E_j(k)\right] = 0, \tag{1}$$

where $L_{ij} = \delta_{ij} k^2 - k_i k_j - k_0 \varepsilon_{ij}(k)$. The solution to these equations can readily be written in terms of the eigenvalues and eigenvectors of the matrix L_{ij}:

$$E_j(k) = e_j(k) \cdot U(k), \; H(k) \cdot U(k) = 0, \tag{2}$$

where $H = e_i^* L_{ij} e_j$ and e are the eigenvalues and eigenvectors (such that $e^2 = 1$) of the matrix $L_{ij}(k)$ of order n, respectively.

Applying the inverse Fourier transformation to solution (1) and (2), we obtain an equation for the scalar complex field amplitude U in the coordinate space:

$$\hat{H}(\nabla / i k_0)\left[U(r)\right] = 0. \tag{3}$$

With the help of the polarization operator e_j, the distribution of the vector electric field is expressed in terms of this amplitude as

$$E(r) = \hat{e}(\nabla / ik_0)\big[U(r)\big]. \tag{4}$$

The procedure of deriving quasi-optical equations (4) and (3) can be generalized to inhomogeneous media. Qualitatively, it can be done by introducing smooth dependence on coordinates into operators H and e. As result, equation (3) will have the form:

$$\hat{H}(r, \nabla / ik_0)\big[U(r)\big] = 0. \tag{5}$$

Such procedure is valid for regions far from the singular points or from the mode conversion points in smoothly inhomogeneous media. The formal condition for this is that the parameters of the medium should vary smoothly on a spatial scale on the order of the wavelength of the beat wave, $|k_n - k_m| L \gg 1$, where L is the characteristic inhomogeneity scale of the medium and k_n and k_m are the wave-numbers of the co-propagating modes. In what follows, we restrict ourselves to precisely this situation and consider the evolution of the wave beams whose width is much greater than their wavelength.

Eq. (5) in many cases, is simpler than the vector Maxwell's equations. Note that, in Eq. (5), we do not make any assumptions about the dependence of the operator H on the parameters. Although the operators r and p are non-commuting, they should obviously enter the combinations ensuring that the operator H is Hermitian for a non-absorbing medium. This problem will be considered in more detail later.

In smoothly inhomogeneous media, the wave beams are localized near a certain reference curve – the centroid ray $r_0(\tau)$ (where the parameter τ depends on the length of the arc). It is therefore reasonable to consider Eq. (5) in the immediate vicinity of the ray $r_0(\tau)$ rather than in the entire space. We pass over to the curvilinear orthogonal coordinate system associated with this ray $r = r_0(\tau) + g_1\xi_1 + g_2\xi_2$, where the unit vectors $g_i(\tau)$ ($i = 1, 2$) are perpendicular to the reference ray $r_0(\tau)$ and are displaced along it parallel to themselves (in the Levi-Civita's sense, $\dot{g}_i g_j = 0$), i.e., satisfy the equation

$$\dot{g}_i = -\big(g_i, l\big) l, \; l = \dot{r}_0 / |\dot{r}_0| \tag{6}$$

with l being a unit vector tangential to the curve $r_0(\tau)$. The Lamé coefficients for this curvilinear coordinate system are equal to

$$h_{ij} = \delta_{ij}, \; h_\tau = \chi(1 - \theta_i\xi_i), \; \theta_i = \big(g_i, l\big)/\chi, \; \chi = |\dot{r}_0|, \tag{7}$$

where θ is the curvature vector. From formulas (6) it follows, in particular, that the accompanying coordinate system uniquely identify the points in space only for $|\theta\xi| < 1$, i.e., at distances from the reference curve that are smaller than the local curvature radius $R = 1/|\theta|$.

401

We introduce the complex envelope of the wave beam field u by singling out the rapidly oscillating factor:

$$U = u(\xi, \tau) \exp\left(ik_0 \int \chi p_\tau d\tau + q(\tau)\xi\right), \tag{8}$$

where the functions $p_\tau(\tau)$ and $q(\tau) = g_1 q_1 + g_2 q_2$ are the longitudinal and transverse (with respect to the reference curve) components of the normalized wave vector at the point $r_0(\tau)$. In anisotropic media, unlike in isotropic ones, the transverse component q is nonzero because the group and phase velocities point in different directions.

Later, we focus only on the wave beams that evolve slowly along the reference ray. In this case, the equation can be greatly simplified by eliminating from consideration higher order derivatives of the amplitude u, such as $\partial^2 u / \partial \tau^2$ and higher. In fact, we consider wave beams with relatively narrow angular spectra in smoothly inhomogeneous media; this implies the conditions $1 \ll k_0 L$ and $1 \ll k_0 \Lambda$ (where L and Λ are the characteristic spatial scales on which the parameters of the medium and the field in the beam vary). One can obtain quasi-optical equation after expanding the equation in a series in $\partial / \partial \tau$ (as is done in the Taylor series expansion) and retain only the terms with the first derivative:

$$\frac{i}{k_0} \frac{\partial u}{\partial \tau} = \hat{H}_0[u], \quad \hat{H}_0 = \hat{H}\left(r_0(\tau) + \xi, p_0(\tau) + \frac{1}{ik_0} \frac{\partial}{\partial \xi} + \frac{\chi p_\tau + \dot{q}\xi}{h} l\right). \tag{9}$$

It should be emphasized that passing over to the curvilinear coordinate system in Eq. (9) is justified only for a small vicinity of the reference curve, i.e. for distances from it that are much less than its curvature radius. For larger distances, difficulties arise that are associated with the ambiguous identification of the coordinates of points in space.

Equation (9) is an evolutionary one and is commonly solved by various mesh methods or by the operator exponent method [13, 15]. The second way is more convenient because relatively long time steps can be used, which are independent of the number of mesh points (as in mesh methods) and are determined only by the specific features of the problem and by the diffraction and refraction scale lengths of the beam.

However, we have not yet answered a number of questions. In particular, how to choose the reference curve, how accurate are Eqs. (5) and (9), and how to pass over to the geometrical-optics approximation and to describe the propagation of Gaussian beams. To answer these questions, it is necessary to further expand Eq. (9) near the reference ray by additionally assuming that the transverse distribution of the wave beam field is sufficiently smooth and the maximum field amplitude is sufficiently small, $1 \ll k_0 a \ll k_0 L$ (where a is the characteristic beam width).

Let us specify the form of the operator H. Unfortunately, it is difficult to define the operator exactly even for a homogeneous cold magnetized plasma. On the other hand, the form of the operator may be guessed from heuristic considerations. In fact, for an inactive non-dissipative medium, the operator H should be

402

Hermitian. A consequence of the Hermitian nature of the operator is the conservation of the energy flux, which is the fundamental integral of the equation for the beam amplitude u. In addition, in the short-wavelength limit ($k_0 \to \infty$), the operator should pass over to the function $H(r, p)$. But these two conditions are obviously insufficient for specifying the operator H unambiguously.

Let us define the operator H in terms of its Taylor series expansion, as is usually done for conventional functions of several variables:

$$\hat{H} = \sum_{m,n} \frac{1}{m!n!} \frac{\partial^{m+n} H}{\partial x^m \partial p^n} \cdot \frac{\hat{x}^m \hat{p}^n + \hat{p}^n \hat{x}^m}{2}. \tag{10}$$

Here x and $p = \nabla / ik_0$ are meant Cartesian coordinates and the corresponding momenta (normalized wave-numbers), respectively. The geometrical-optics Hamiltonian, which is understood as a complex function of the coordinates and momenta. All the derivatives are taken at the reference ray $\{x_0, p_0\}$.

It should be noted that, for $\Im H = 0$, expansion (10) is the simplest representation of a Hermitian operator that gives the conventional Hamiltonian in the geometrical-optics approximation. The situation at hand is analogous to that in quantum mechanics, in which the problem arises of how the quantum equation can be unambiguously reconstructed from a given mechanical Hamiltonian in the general case. It turns out, however, that representation (10) leads to a correct equation in the AF approximation and leads to equations that differ from the exact ones by insignificant local (non-accumulative) preexponential factors [11] in the aberration orders.

The Hamiltonian in the form of expansion (10) is rather difficult to apply directly. But for magnetized plasmas in magnetic confinement systems, it is possible to choose a coordinate system in which the off-diagonal elements $\partial^{m+n} H / \partial x^m \partial p^n$ are small [15]. As a result, operator (10) is reduced to a form that can be conveniently used to solve the quasi-optical equation by the operator exponent method (see [14, 15] for details).

Rather general Eq. (9) is quite a complicated one. By expanding the operator H in Eq. (9) in Taylor series (10) in the small quantities ξ and $\partial u/\partial \xi$ and retaining terms up to the second order, we can reduce this equation to a parabolic form [13, 14]

$$0 = \frac{1}{ik_0} \frac{\partial u}{\partial \tau} - \frac{1}{2k_0^2} \frac{\partial^2 H}{\partial q_i \partial q_j} \frac{\partial^2 u}{\partial \xi_i \partial \xi_j} + \frac{1}{2} \frac{d^2 H}{d\xi_i d\xi_j} \xi_i \xi_j u +$$
$$+ \frac{1}{ik_0} \frac{d^2 H}{dq_i d\xi_j} \left(\xi_i \frac{\partial u}{\partial \xi_j} + \frac{\delta_{ij} u}{2} \right) + Hu + \frac{1}{ik_0} \frac{\partial H}{\partial q_i} \frac{\partial u}{\partial \xi_i} + \frac{dH}{d\xi_i} \xi_i u, \tag{11}$$

where $\partial/\partial q_i = g_i \, \partial/\partial p$ and total derivatives on ξ are equal to

$$\frac{d}{d\xi_i} = \frac{\partial}{\partial \xi_i} - \frac{1}{\chi} \frac{\partial \Re H}{\partial \xi_i} \frac{\partial}{\partial p_\tau}.$$

For a non-dissipative medium, we have $\Im H = 0$, so the last three terms in Eq. (11) vanish along the geometro-optical ray because of the vanishing of the first total derivatives: $\partial H/\partial q_i = 0$ by virtue of the choice of the coordinate system and $dH/d\xi_i = 0$ by virtue of the geometrical optics equations, $H = 0$, because there is no anti-Hermitian part in the Hamiltonian. For a dissipative medium, the last three terms in Eq. (11) are nonzero. They are determined by the anti-Hermitian part of the Hamiltonian and by its derivatives.

Equation (11) is called the AF equation, because it preserves the shape of the Gaussian beam (i.e., adds no aberrations to the beam shape). In [13, 14], this equation was considered quite thoroughly for a non-dissipative medium and relevant analytic solutions were obtained for the general case and for a number of particular cases. Equation (11) is also attractive for numerical simulations because the problem of solving it can be reduced to that of solving a set of ordinary differential equations and calculating the resulting integral convolution (for beams of arbitrary shape). However, for an arbitrary boundary field distribution at the point $\tau = 0$ the general solution of Eq. (11) also can be found [17]

$$u(\xi,\tau) = A\int u_k \exp ik_0 \left(\kappa_i\xi_i + \zeta_i k_i \right) - ik_0/2 \left(\sigma_{ij}\xi_i\xi_j + 2\beta_{ij}\xi_i k_j + \alpha_{ij}k_i k_j \right) dk, \quad (12)$$

where $u_k = \int u(\xi,0) \exp(ik_i\xi_i) d\xi$ is the Fourier spectrum of the initial field distribution over the transverse coordinates. The coefficients satisfy following equations

$$\frac{d\sigma_{ij}}{d\tau} = \frac{d^2 H}{d\xi_i d\xi_j} - \frac{d^2 H}{dq_m dq_n}\sigma_{mi}\sigma_{jn} + \frac{d^2 H}{d\xi_i dq_m}\sigma_{mj},$$

$$\frac{d\beta_{ij}}{d\tau} = \frac{d^2 H}{dq_m dq_n}\left(\sigma_{mi}\beta_{nj} + \sigma_{ni}\beta_{mj}\right) + \frac{d^2 H}{d\xi_i dq_m}\beta_{mj},$$

$$\frac{d\alpha_{ij}}{d\tau} = \frac{d^2 H}{dq_m dq_n}\beta_{mi}\beta_{nj},$$

$$\frac{d\kappa_i}{d\tau} = \frac{1}{2}\frac{d^2 H}{dq_m dq_n}\left(\kappa_m\sigma_{ni} + \kappa_n\sigma_{mi}\right) - \frac{d^2 H}{d\xi_i dq_m}\kappa_m + \frac{dH}{dq_m}\sigma_{mi} - \frac{dH}{d\xi_i},$$

$$\frac{d\zeta_i}{d\tau} = \frac{1}{2}\frac{d^2 H}{dq_m dq_n}\left(\beta_{ni}\kappa_m + \beta_{mi}\kappa_n\right) + \frac{dH}{dq_m}\beta_{mi},$$

$$\frac{dA}{d\tau} = \frac{A}{2}\left(\frac{d^2 H}{dq_m dq_n}\sigma_{mn} - \frac{d^2 H}{d\xi_m dq_n}\right) + ik_0\left(H + \frac{dH}{dq_m}\kappa_m + \frac{d^2 H}{dq_m dq_n}\kappa_m\kappa_n\right).$$

These equations should be supplemented with the initial conditions at the point $\tau = 0$ that ensure the identity transformation of the function into itself at this point: $\sigma_{ij} = 0$, $\beta_{ij} = \delta_{ij}$, $\alpha_{ij} = 0$, $\kappa_i = 0$, $\zeta_i = 0$.

In actual magnetic confinement devices, the transport along magnetic field lines is very fast, such that the plasma parameters are effectively constant on magnetic surfaces. Therefore, the average power deposition on a magnetic surface is the more relevant quantity. Magnetic surfaces are commonly identified by a dimensionless flux surface label $\rho(r)$, for example the square root of the normalized poloidal or toroidal flux. Generally $\rho = 1$ on the boundary of the plasma and $\rho = 0$ in the center. The power deposition on a given flux surface ρ_0, $P(\rho_0)$ can be determined as:

$$P_{QO}(\rho_0) = \frac{2k_0}{S(\rho_0)} \int u^* \Im H[u] \delta(\rho_0 - \rho(r)) dr + c.c., \qquad (13)$$

$$P_{AF}(\rho_0) = \frac{2k_0}{S(\rho_0)} \int \Im H(\tau) \cdot |u|^2 \delta(\rho_0 - \rho(r)) dr, \qquad (14)$$

where $S(\rho_0) = \int \delta(\rho_0 - \rho(r)) dr$, is the effective flux surface area. For the case of the AF approximation, the $\Im H(\tau)$ is the absorption coefficient from geometric optics evaluated on the central ray. This can lead to significant errors in the power deposition profile, when the direction of propagation is oblique to the ECR plane. In AF beam tracing codes as TORBEAM [5], this is corrected by defining ad hoc the coordinates ξ in the equation for the AF power deposition such that they span a plane parallel to the ECR plane.

We perform a set of calculations for ITER parameters to see if any difference between AF and full quasi-optical approaches. The plasma conditions for ITER are chosen according to the ITER reference scenario 2 [30, 31]. The magnetic equilibrium data and the relevant plasma profiles have been supplied by the ITER team and are identical to those used in the EC code benchmark published in [18]. The basic parameters of ITER scenario 2 are major radius 6.2 m, minor radius 2.01 m, magnetic field $B_\varphi = 5.3$ T, plasma current 15 MA, electron temperature on axis 25 keV, plasma density $1.02 \cdot 10^{20}$ m^{-3}. Full details on the ITER scenario 2 magnetic equilibrium and plasma profiles are provided in [18]. Positions and widths of power deposition are given in terms of the flux surface label which is defined as the square root of the normalized poloidal flux. We use parameters for the Upper Port ECRH launcher which is proposed to be used for NTM and sawtooth control. It consists of four launchers divided over different ports, each of which consists of an upper and a lower steering mirror (USM and LSM, respectively). The used dielectric tensor was tensor for a weakly relativistic plasma [19], because the plasma temperature in ITER is fairly high and, therefore, the behavior of the rays and wave beams depends sensitively on the thermal corrections.

To quantify the effects from the new physics on the objectives of the ITER ECRH Upper Port launcher, quasi-optical calculations have been performed for beams injected from each of the two mirrors and aimed at the $q = 3/2$ and $q = 2$ surfaces. In the case of the USM also calculations for beams aiming close to the
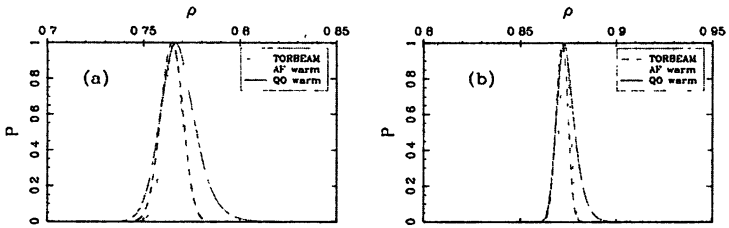
Fig. 1. Power deposition profiles for beams injected from the LSM in ITER. The figure shows the results for beams aiming at (*a*) the $q = 3/2$ and (*b*) the $q = 2$ surface
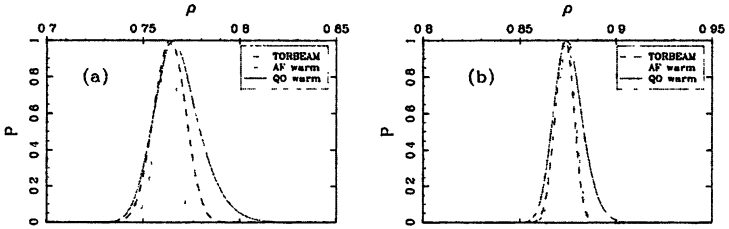

Fig. 2. Power deposition profiles for beams injected from the USM in ITER. The figure shows the results for beams aiming at (*a*) the $q = 3/2$ and (*b*) the $q = 2$ surface

$q = 1$ surface have been performed. The resulting power deposition profiles are shown in Fig. 1, 2. These deposition profiles are compared with those obtained from the TORBEAM code. In all cases a significant broadening of the quasi-optical power deposition profile as compared with the TORBEAM calculations is seen. This is expected to lead to a reduction of the achievable NTM or sawtooth figures of merit as typically $\eta_{NTM} \rightarrow 0.6\eta_{NTM}$ or $\eta_{sawtooth} \rightarrow 0.5\eta_{sawtooth}$. Also note that in the case of the more vertically oblique injection cases the TORBEAM profiles (see the table) are significantly wider than those obtained from the AF approximation.

	USM			LSM	
	$q = 1$	$q = 1.5$	$q = 2$	$q = 1.5$	$q = 2$
Broadening	1.38	1.53	1.63	1.71	1.61

This is due to the fact that the effect of the spatial inhomogeneity caused by the angle between the practically vertical ECR plane and the wave beam is partly taken into account in the power deposition calculation in TORBEAM by distributing the absorbed power in the vertical plane rather than in the plane perpendicular to the direction of propagation.

406

Summarizing

A quasi-optical description of wave beam propagation in anisotropic media has been developed generalizing the parabolic wave equation of Fock and Leontovich. The QO equation provides a proper description of the spatial and spectral inhomogeneity of absorption and their effects on beam propagation. Taking into account new effects show that current estimates of required power may be too optimistic by factor 1.6 for NTM to 2.0 for sawtooth control This will restrict the possible control scenarios for the present design of the ITER ECRH systems Further physics effects, not included yet in present day modeling, may broaden the deposition even more.

References

1. *Kravtsov Yu. A. and Orlov Yu. I.* 1990, Geometrical Optics of Inhomogeneous Media (Berlin-Heidelberg: Springer Verlag); Kravtsov Yu. A. Radiophys. Quantum Electron. **10**, 719 (1967).
2. *Mazzucato E* Phys. Fluids B, **1** 1855 (1989).
3. *Pereverzev G. V.* Rev. Plasma Phys. **19**, 1 (1996).
4. *Nowak S., Orefice A.* Phys. Fluids B **5**, 1945 (1993).
5. *Poli E., Peeters A. G., Pereverzev G. V.* Computer Physics Communication **136**, 90 (2001).
6. *Farina D.* IFP-CNR Internal Report FP 05/1 (2005), http://www.ifp.cnr.it/publications/2005/FP05-01.pdf.
7. *Pereverzev G. V.* Phys. Plasmas **5**, 3529 (1998).
8. *Poli E., Pereverzev G. V., Peeters A. G. and Bornatici M.* Fusion Eng. Des. **53**, 9 (2001).
9. *Tsironis C., Poli E., Pereverzev G. V* Phys. Plasmas **13**, 113304 (2006).
10. *Saveliev A. N. and Piliya A. D.* 30 EPS Conf. on Control. Fusion and Plasma Phys. ECA **27A** (2003), P-2.20.
11. *Vdovin V.* in Proc. 14th Joint Workshop on Electron Cyclotron Emission and Electron Cyclotron Heating, 9–12 May 2006, Santorini, Greece, p. 323 (2006).
12. *Irzak M. A. and Popov A. Yu* 34th Int. Conf. on Plasma Phys. and CF, February 12–16, 2007, Zvenigorod, p. 39.
13. *Balakin A. A., Balakina M. A., Permitin G. V., Smirnov A. I.* J. Physics D: Applied Physics, **40**, 4285 (2007).
14. *Balakin A. A., Balakina M. A., Permitin G. V., Smirnov A. I.* Plasma Phys. Reports **33**, 302 (2007)
15. *Balakin A. A , Balakina M. A., Westerhof E.* Nucl. Fusion, **48**, 065003 (2008).
16. *Fock V. A.* Electromagnetic diffraction and propagation problems, Pergamon (1965).
17. *Balakin A. A., Balakina M A., Permitin G. V., Smirnov A. I.* Plasma Phys. Reports **34**, 486 (2008).
18. *Prater R. et al.* Nucl. Fusion **48**, 035006 (2008).
19. *Shkarofsky I. P.* J. Plasma Phys. **35**, 319 (1986).

FLUCTUATIONS INFLUENCE ON EC POWER DEPOSITION

A A Balakin, M. A. Balakina, A. I. Smirnov

Institute of Applied Physics RAS, Nizhny Novgorod, Russia

The influence of medium inhomogeneities (plasma and magnetic field fluctuations) on wave beam propagation in an isotropic media has been investigated for a long time [1]. It is accepted, that this influence first of all perturbs the phase of the quasi-optical wave beam and later this perturbation results in the additional diffractional beam widening along the propagation trace. It is obvious, that the influence of a single large-scale (on the beam width) and small-scale fluctuations are weak enough. The first one leads only to the turn of the beam as a whole (like a prism). The small-scale fluctuations merely do not influence on the beam propagation since their effective cross-section is small. So, fluctuations with a size of the order of the beam width are most dangerous since they scatter the wave beam most effectively.

In comparison with optical or laser wave beams in plasma of installations with magnetic confinement traces of the wave beam propagation are relatively small – about 1 meter or 500–1000 wave-lengths. As a result, the beam diffraction caused by the phase variations (particularly, if these variations are localized not near the boundaries of the plasma volume) is relatively small and, as a rule, does not lead to remarkable modification of the beam or power deposition profiles. Really, numerical modulation shows that the plasma density fluctuation amplitude should be about 10% to become noticeable. Exactly with this fact, seemingly, the interest extinction to this problem is connected.

At the same time, in magnetized plasma a fundamentally another sort of inhomogeneities may take place. These are inhomogeneities of poloidal magnetic field flux. Despite the amplitude of these inhomogeneities may be small, their gradients (more exactly, second derivatives) may be remarkable. The danger of these fluctuations consists in that they change not the beam phase but exactly the beam profile. This variation occurs directly in inhomogeneity area and not along the propagation trace far from the inhomogeneity region.

The danger of inhomogeneities of such type is obvious, in particular, for aims of stabilization of MHD instabilities in tokamak and stellarator plasmas. Indeed, the usual way here is the local plasma heating near rational magnetic surfaces with $q = 1$, 3/2, 2. So, if there is an inhomogeneity of the magnetic flux on the beam propagation trace then the beam width increases immediately and the power deposition profile width increases correspondingly. Exactly to the problem of the medium parameter fluctuation influence on the wave beam propagation and absorption in magnetized plasma this work is devoted.

First of all we show some analytical solutions for beam envelop and later results of numerical solution will be presented. As usual, the analytical solution can be found only for some limit cases: in case of "shallow" fluctuation (which amplitude and corresponding influence are small) and in case of "wide" fluctuation which characteristic scale Δr is much larger than the beam width.

For simplicity we propose that fluctuation scale Δr is much smaller than the characteristic scale of the medium inhomogeneity. Then the geomertooptical

(GO) Hamiltonian in the medium without fluctuations H_0 don't depend on spatial coordinates:

$$H \approx H_0\left(p_0; u_0, v_0\right), \quad u_0, v_0 = \text{const}, \tag{1}$$

where p_0 is momentum in unperturbed media, v_0 is normalized plasma density, u_0 is normalized magnetic field. Here and further in this paragraph index "0" denotes values in the unperturbed medium. The corresponding values without index mean the same but in the medium with fluctuations.

The medium fluctuations lead to the appearance of the dependence on coordinates in Hamiltonian parameters:

$$v = v_0 + \delta v, \quad u = u_0 + \delta u, \quad \delta u = [\nabla \delta \psi \times e_\varphi]. \tag{2}$$

Here e_φ is the unity vector directed along the toroidal direction. Correspondingly, the form of Hamiltonian changes. At this, everything is more ore less clear for density fluctuations δv. If the fluctuation is shallow for density fluctuations $\delta v \ll 1$ then far from resonances Hamiltonian may be presented as

$$H \approx H_0 + C \delta v(r), \quad C = \partial H_0 / \partial v. \tag{3}$$

In the isotropic medium C is constant and the relation (3) becomes even simpler.

The case with the flux variations is more complicated, since not only amplitude of parameter u is changed but its orientation is changed too. As a consequence, the orientation of dielectric tensor axes varies also. To take this into account one should note that in magnetized plasma GO Hamiltonian depends on momentums in combinations $p^2 = |p|^2$, $p_u = (p \cdot u) = u\, p_\parallel$ and depends on magnetic field amplitude u. Then fluctuations δu will influence on both parameters. Again, assuming the flux variation as weak one $\delta u \ll u_0$ and far off the resonance one can formulate GO Hamiltonian in the form

$$H \approx H_0 + A \cdot (p \cdot \delta u) + B \cdot (\delta u \cdot u_0) + D \cdot (p \cdot \delta u)^2, \tag{4}$$

where the following notation introduced

$$A = \partial H / \partial p_u, \quad B = \partial H / \partial u, \quad D = 1/2 \cdot \partial^2 H / \partial p_u^2.$$

Now, we can find analytical solution for the beam field a in the area inside and after the fluctuation. Firstly, we consider the case of "shallow" fluctuation (fluctuation of small amplitude). Then the beam field may be found in GO approximation

$$\tilde{a} = a\left(r_0 + \delta r(r_0, t)\right) \cdot \exp\left(ik_0 \int \delta p(r, t) dl\right), \tag{5}$$

where the values δr and δp are determined by GO equations

$$\delta r = \int \partial \delta H / \partial p\, dt, \quad \delta p = \int \partial \delta H / \partial r\, dt = l \cdot \delta H / \chi, \quad \chi = |\partial H / \partial p|.$$

One can obtain well known result by applying (5) to (3):

$$\tilde{a} = a \cdot \exp\left(ik_0 \int C \delta v\, dl\right). \tag{6}$$

Here we take into account that the value δr is small, since far from resonances density fluctuations do not give essential contribution to the medium anisotropy. Eq (6) denote the known fact about the fluctuation influence as mostly a phase change for beam envelop.

In case with the flux fluctuations (4) the procedure becomes more complicated. Again

$$\delta p = l \cdot H / \chi = l / \chi \cdot (Ap + Bu_0, \delta u).$$

However, the integral phase change $\int \delta b dl = 0$ caused by the first order of the expansion over δu is equal to zero and the next order of expansion should be kept:

$$\delta p = Dl / \chi \cdot (p, \delta u)^2. \qquad (7)$$

Note, that the resulting phase change is always defocusing independently on the sign of the fluctuation amplitude δu! This is result of second order of smallness over δu and the magnetic field variation enters as it square.

At the same time, the value of δr differs essentially from the zero already in first order over parameter δu

$$\delta r \approx \int A \delta u dt \qquad (8)$$

and increases itself after the variation passing. This means that the beam phase front distortion should be relatively small. Nevertheless, its width may change itself sufficiently already on fluctuation scale. Here we are close to the limit of GO approximation applicability, where δr becomes of the order of the beam width w. In this case to find the exact solution one should use quasi-optical equation [2].

Another case when the analytical solution can be found is the case of "wide" fluctuation with scale much larger than the beam width. In this case we can use aberration-free approximation [3, 4]. The corresponding equation for the beam amplitude is

$$\frac{1}{ik_0} \frac{\partial a}{\partial t} = \frac{\alpha_{ij}}{2k_0^2} \frac{\partial^2 a}{\partial \xi_i \partial \xi_j} + \frac{\beta_{ij}}{ik_0} \left(\xi_i \frac{\partial a}{\partial \xi_j} + \frac{\delta_{ij} a}{2} \right) + \frac{\gamma_{ij}}{2} \xi_i \xi_j a + \frac{\eta_i}{ik_0} \frac{\partial a}{\partial \xi_i} + \rho_i \xi_i a.$$

Here ξ_i, ξ_j are accompanied coordinates transverse to the unperturbed reference ray. Note, that in general case linear terms (terms with η_i, ρ_i) are not zero and may lead to the beam deflection as a whole from the reference "unperturbed" ray. The coefficients of the equation are real and may be found as derivatives from GO Hamiltonian on the reference ray. The general solution of the equation is known for the general initial form of the wave beam [3, 4]. Here we shall consider the Gaussian beam

$$a(t, \xi) = a_0(t) \cdot \exp\left(-ik_0 / 2 \cdot \sigma_{ij} \xi_i \xi_j + ik_0 \cdot \kappa_i \xi_i \right) \qquad (9)$$

which coefficients satisfying the equations [4]

$$\dot{\sigma}_{ij} = \gamma_{ij} - \alpha_{mn} \sigma_{mi} \sigma_{jn} + \beta_{im} \sigma_{mj},$$

$$\dot{\kappa}_i = \alpha_{mn} \left(\kappa_m \sigma_{ni} + \kappa_n \sigma_{mi} \right) / 2 - \beta_{im} \kappa_m + \eta_m \sigma_{mi} - \rho_i, \qquad (10)$$

$$\dot{A} = A / 2 \cdot \left(\alpha_{mn} \sigma_{mn} - \beta_{mm} \right).$$

Coefficient σ_{ij} describes the complex beam width, κ_i is the position of mass center of the beam in momentum and coordinate spaces.

410

At the presence of fluctuations (3) or (4) the form of α, β and γ coefficients becomes essentially simpler. So, for the plasma density fluctuation (3) coefficients are equal to $\alpha'_{ij} = \partial^2 H_0 / \partial p_i \partial p_j$, $\beta_{ij} = 0$, $\gamma_{ij} = C \cdot \partial^2 \delta \nu / \partial \xi_i \partial \xi_j$, and for the flux fluctuation (4):

$$\alpha_{ij} = \partial^2 H_0 / \partial p_i \partial p_j, \quad \beta_{ij} = A \cdot \partial \delta u_j / \partial \xi_i, \quad \gamma_{ij} = D \cdot p_m p_n \cdot \partial^2 \delta u_m \delta u_n / \partial \xi_i \partial \xi_j.$$

The beam width variation is the most interest for the further investigation since it influences on the power deposition width immediately in real plasma heating experiments. In case of constant diagonal matrices α_{ij}, β_{ij} and γ_{ij} the solution of the equation (10) can be found analytically (let us for short turn matrix indexes down):

$$\sigma = \left(\left(\sqrt{4\alpha\gamma + \beta^2} + \beta \right) e^{\sqrt{4\alpha\gamma+\beta^2}\,(t+\zeta)} + \sqrt{4\alpha\gamma + \beta^2} - \beta \right) \Big/ 2\alpha \left(e^{\sqrt{4\alpha\gamma+\beta^2}\,(t+\zeta)} - 1 \right), \quad (11)$$

where the complex constant ζ can be found by the initial width σ^0.

Formula (11) is rather complicated at first sight, but it describes the basic important limiting cases. So, at $\beta = 0$ and $\gamma = 0$ one can get $\sigma = 1/2\,\alpha\,(t + \zeta)$, that corresponds to the usual diffraction law $w = w_0 \sqrt{1 + 4\alpha^2 t^2 / w_0^4}$ if one introduces the usual width in coordinate space $w = 1/\sqrt{3\sigma}$.

The case then the term with $\beta \sim \sqrt{\alpha\gamma}$ prevails will be the most interesting for us. In this case the expression for σ can be simplified:

$$\sigma = \frac{\beta / \alpha}{1 - e^{-\beta\,(t+\zeta)}} \Rightarrow 3\sigma \sim \frac{\beta / \alpha}{2\cosh\left(\beta \cdot |t + \zeta|\right)}. \quad (12)$$

From these formulas an important feature can be seen – the imaginary part of σ decreases exponentially along the trace. As a result, the beam width increases *exponentially fast* correspondingly. At $\beta < 0$ this follows directly from formula (12) – the σ value tends to zero as a whole, i.e. the beam exponentially spreads and its phase front becomes flat. At $\beta > 0$ only the imaginary part of σ decreases exponentially (and the beam spreads), but the phase front curvature comes to the constant value. It is obvious, that diffraction (term with α in the equation (10)) and the defocusing second order term with $\gamma > 0$ cannot stop this beam widening. As a consequence, the beam will widen so long as it will pass the fluctuation region (in reality $\beta = \beta(t)$ is a localized function) or applicability conditions of the aberration-free approximation will break, i.e. as long as the beam width will become of the order of fluctuation size!

Numerical simulation has been fulfilled for ITER [5] plasma parameters corresponding to the so called scenario 2. The launch conditions were selected from Upper Port ECRH launcher from upper steering mirror (USM). Results of numerical simulation in real conditions confirm in general the theoretically predicted features of the beam propagation in medium with fluctuations.

The typical evolution of the beam width is in agreement with theoretical prediction (Fig. 1). Thus, for $\eta > 0$ there is an abrupt, exponentially fast increase of the beam width with its further relatively smooth spreading. The effect increases with the fluctuation amplitude growth exponentially. For another inhomogeneity sign ($\eta < 0$) widening of the beam also takes place, but it is delayed slightly in compliance with formula (12). The further relatively slow beam spreading caused by perturbation of its phase front occurs practically equally independent of the amplitude η sign, as the theoretical model (7) predicted. The situation with density fluctuation δv also shows good correspondence with analytics. At this, the fluctuation may both focus and defocus the wave beam (Fig. 2) dependently on the η sign. This leads either to additional narrowing and further more remarkable widening of the beam or to its immediate spreading directly after the fluctuation passing. In both cases the beam widening acts only on long traces after the fluctuation position.
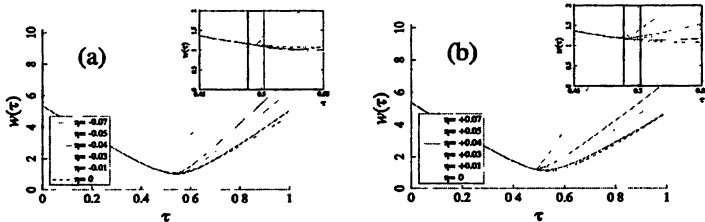
Fig. 1. The beam width change along the propagation trace at the flux fluctuation δu passing. Half-width of fluctuation is about 1 cm. Fluctuation amplitude η was both negative (*a*) and positive (*b*).
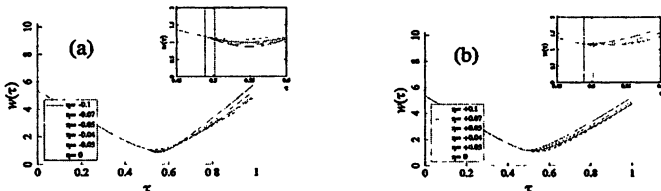

Fig. 2. The beam width change along the propagation trace at the density fluctuation δv passing. Half-width of fluctuation is about 1 cm. Fluctuation amplitude η was both negative (*a*) and positive (*b*).

As conclusion we can say that new type of fluctuations is found. There are fluctuations of anisotropy direction that correspond to fluctuation of magnetic flux. The analytical solution for wave beam amplitude is obtained in 2 limiting cases. Exponential fast beam broadening on the scale of flux fluctuation is demonstrated.

References

1   *Landau L. D., Lifshits E. M* Electrodynamics of Continuous Media, 2ed , Pergamon, 1984.
2. *Balakin A. A., Balakina M. A , Permitin G. V., Smirnov A. I.* Plasma Phys. Reports, **33**, 302 (2007).
3. *Balakin A A , Balakina M A , Permitin G. V., Smirnov A I* J. Physics D. Applied Physics **40**, 4285 (2007).
4   *Balakin A. A , Balakina M A , Permitin G. V., Smirnov A I.* Plas Phys. Rep., **34**, 533 (2008)
5   ITER Physics Basis Editors et al Nucl Fusion **39**, 2137 (1999), Editors of "Progress in the ITER Physics Basis" et al Nucl Fusion 47, S1 (2007)

2D FULL-WAVE MODELING OF O-X CONVERSION IN TOKAMAK PLASMAS

M. A. Irzak, A. Yu. Popov, A. N. Saveliev

A. F. Ioffe Physico-Technical Institute, 194021 St. Petersburg, Russia

The results of 2D full-wave modeling of O-X conversion by numerical solution of plasma wave equation in 2D inhomogeneous tokamak plasma are presented. The dependence of the conversion efficiency on the parameters of the launched wave beam is investigated. Comparison with recently developed analytical approach is made. One of the most important 2D effects is that conversion efficiency is different for the antenna positions above or below the equatorial plane.

O-X-B mode conversion scheme [1] has been widely discussed recently as it is the most promising candidate to provide auxiliary microwave electron heating and current drive in spherical tokamaks where conventional ECR heating schemes become impossible due to a high plasma density and a comparatively low magnetic field. O-X-B conversion efficiency is determined mainly by O-X conversion process near the O cut-off. An accurate account of 2D plasma inhomogeneity and of the realistic tokamak magnetic field geometry are required for correct estimation of the conversion efficiency. The analytical results obtained recently [2, 3] are somewhat contradictory and have a limited validity domain.

Here we present the results of 2D full-wave simulation of O-X conversion process based on the numerical solution of plasma wave equation in 2D inhomogeneous tokamak plasma [4]. A flux-bound reference system (ρ, θ, φ) – flux, poloidal and toroidal coordinates – was used with functions $\Delta(\rho)$ (Shafranov shift), $\lambda(\rho)$ (ellipticity) and $\gamma(\rho)$ (triangularity) describing the shape of the flux surfaces. The electric field was sought as a solution of the wave equation:

$$\nabla \times \nabla \times \mathbf{E} = \frac{\omega^2}{c^2} \varepsilon \mathbf{E}, \qquad (1)$$

where ε is the local dielectric tensor. Electric field was represented as a sum over toroidal and poloidal modes. Poloidal modes (m) are coupled due to the poloidal inhomogeneity, but toroidal modes (n) are not coupled so the solution was sought separately for each toroidal mode:

$$\mathbf{E}(\rho, \vartheta, \varphi) = e^{in\varphi} \sum_m e^{im\vartheta} \mathbf{E}(\rho). \qquad (2)$$

Tangential electric fields at the surface were imposed as a boundary condition. The wave equation (1) was solved by FEM technique similar to the one proposed by M. Brambilla [5]. Cyclotron damping was taken into account by introducing the electron plasma dispersion function Z in the appropriate tensor components. The finite Larmor radius effects, allowing to describe the Bernstein wave were not included in the model and the singularity at the UHR was avoided by introducing an artificial collision frequency.

In order to underline the 2D features of O-X conversion phenomenon a special plasma model was assumed – a hypothetical tokamak ($R_0 = 12$ cm, $a_0 = 8$ cm, $\lambda = 1.6$, $\gamma = 0.18$, $n_{e0} = 6 \cdot 10^{13}$ cm^{-3}, $I_p = 20$ kA, $B_0 = 10.7$ kGs) with a peaked density profile and a very low density at the outer half of the minor radius, so both cut-offs and UHR were shifted far from the wall. In most cases the frequency was 30 GHz.

We carried out the computations for a single toroidal mode $n = 60$ corresponding to the toroidal angle closest to the optimum (maximum conversion efficiency). The Gaussian transverse profile of the RF beam electric field was assumed (with the beam width 3 cm by e-fold level). The beam was launched from different positions in respect to the equatorial plane and at various elevation angles (see Fig. 1), which was modeled by choosing an appropriate poloidal spectrum of the boundary electric field. O and X cut-offs are marked by blue curves, ECR and UHR by green and purple curves, respectively. An example of 2D image map of the electric field (absolute value) in poloidal cross-section is shown in Fig. 2 (launch from position 4). Initially the beam has O-mode polarization, it propagates inside and is reflected from the cut-off, where part of the power is conversed to X-mode and absorbed at UHR (by collisions), and what is left in O-mode propagates back to the wall and is almost totally absorbed in the artificial damping layer placed along the wall in order to avoid numerous reflections.
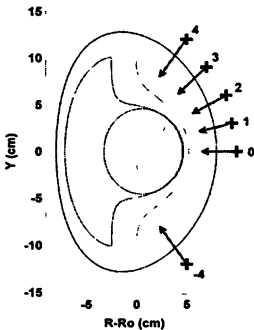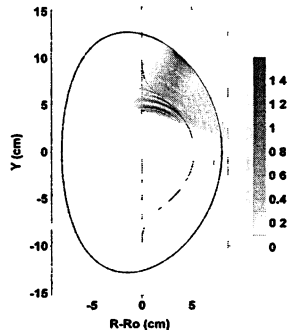

Fig. 1. RF power launching scheme

Fig. 2. 2D map of |E| (poloidal cross-section)

An important 2D effect is the dependence of the conversion efficiency on the direction of the toroidal magnetic field which was first discovered (analytically) in [2] and is discussed in details in [6]. In this work the conversion efficiency was defined as the ratio of RF power absorbed at the UHR surface over the power incident at the conversion region from the periphery. It is justified by the fact that the power absorbed at the UHR (by collisions) in the cold plasma model is exactly equal to the one that is transformed to the Bernstein wave in a hot plasma. In Fig. 3 RF power absorption near UHR is shown for two opposite directions of

the toroidal magnetic field B_φ. One can clearly see that the absorbed power (and hence, conversion efficiency) is much higher in the case $B_\varphi < 0$. It should be noted that in both cases the 2D patterns of the electric field in the poloidal cross-section look very similar.

A more detailed dependence of the O-X conversion efficiency on the beam starting position and elevation angle is shown in Fig. 4. For each starting position (R, Y) there is an optimum elevation angle; also the conversion efficiency is different for opposite magnetic field directions. While there is nearly no difference for the equatorial plane launch ($Y = 0$ cm), it is very pronounced for the starting positions far from this plane ($Y = 9$ and 12 cm). It should be noted that swapping B_φ direction has the same effect as flipping the launching position from above to below equatorial plane, or vice versa (i.e. $Y => -Y$).
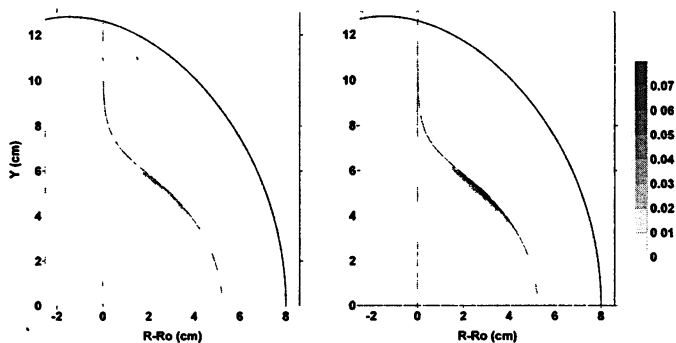
Fig. 3. Power deposition at UHR: *left* – $B_\varphi > 0$, *right* – $B_\varphi < 0$
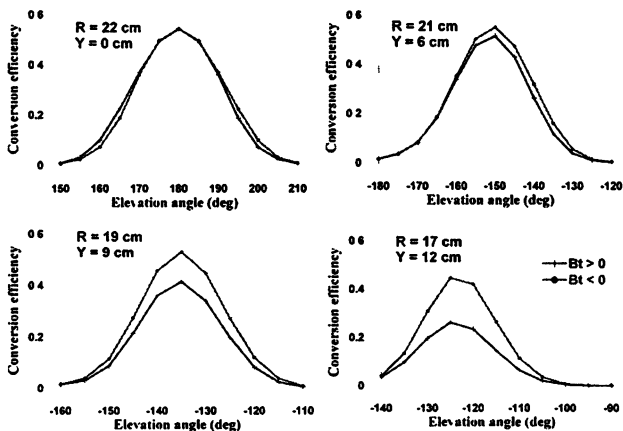

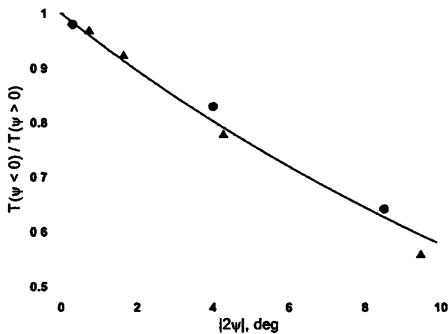**Fig. 4.** O-X conversion efficiency versus elevation angle

415

The ratio of conversion efficiencies T for opposite B_φ directions versus the angle ψ between X and O cut-offs is shown in Fig. 5 ($\psi = 0$ at the equatorial plane and $|\psi|$ increases as we move up or down from it). We compare numerical simulation results (dots for 15 GHz, triangles for 30 GHz) with analytical predictions [6] (solid curve) which appear to fit fairly close for both frequencies, even though analytical theory (which is still valid at 30 GHz) is no longer valid at 15 GHz.

Fig. 5. The ratio of conversion efficiencies T for opposite B_φ directions versus the angle between X and O cut-offs

However, the comparison of poloidal profiles of $|E_z|$ along a flux surface near the conversion region (Fig. 6 and 7) revealed that while there is a good correspondence between analytical (solid curve) and numerical (dashed curve) results at $f_0 = 30$ GHz, the profiles at $f_0 = 15$ GHz differ significantly.
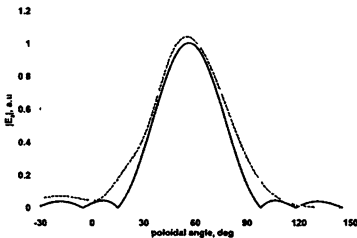
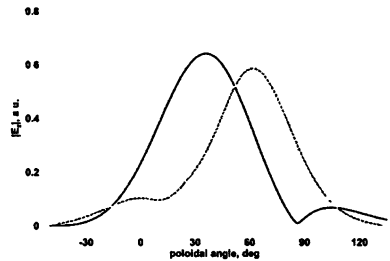**Fig. 6.** Poloidal profiles of $|E_z|$ for 30 GHz

Fig. 7. Poloidal profiles of $|E_z|$ for 15 GHz

Our modeling did not confirm the result of numerical simulation reported in [7] that the UHR plays an important role in RF power deposition when O-mode is launched at the fundamental harmonic and no conditions for effective O-X conversion are provided. This is illustrated by Fig. 8 and 9, corresponding to the O-mode launch from the LFS and HFS in FT-2 tokamak ($R_0 = 55$ cm, $a_0 = 8$ cm, $n_{e0} = 3 \cdot 10^{13}$ cm^{-3}, $B_0 = 21.4$ kGs, $f_0 = 60$ GHz, $N_\varphi = 0.5$). In both pictures $|E|$ is presented on the left and RF energy absorption on the right. In both cases no traces of O-mode absorption near UHR was detected. All RF power was absorbed in the damping layer at the wall opposite the launching position that was introduced in order to avoid multiple reflections from the wall which would complicate the picture.

Vertical profiles of $|E|$ at various R for HFS launch are shown in Fig. 10, where the numerical results are compared with beam-tracing modeling [8].
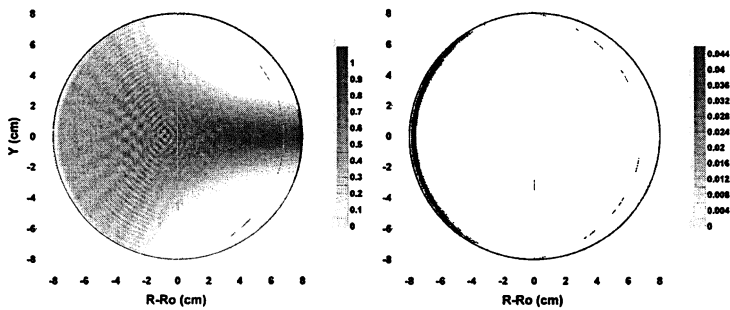
416

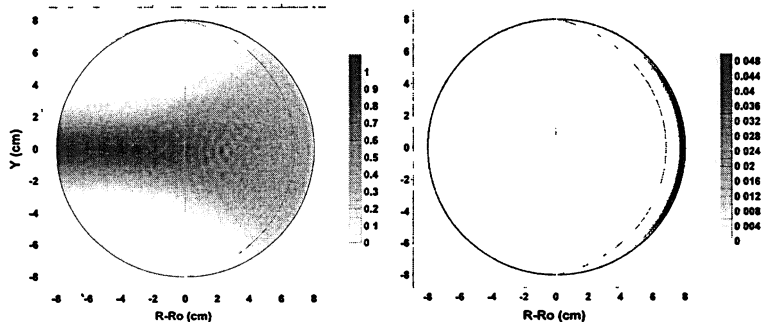**Fig. 8.** |E| (*left*) and power absorption (*right*). LFS launch

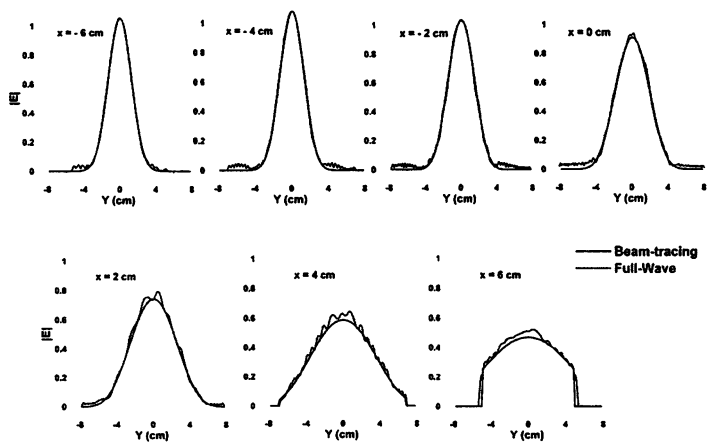**Fig. 9.** |E| (*left*) and power absorption (*right*). HFS launch

Fig. 10. Vertical profiles of |E| at various $x = R - R_0$

So, our modeling provides a good tool for optimizing O-X-B conversion scheme to be used for effective microwave heating, especially in spherical tokamaks where 2D effects might be important: in particular, the conversion efficiency appear to be different for the opposite directions of toroidal magnetic field (or for the antenna positions above or below the equatorial plane). This result is the first numerical confirmation of the effect predicted earlier by the 2D O-X conversion theory.

References

1. *Prienhalter J., Kopecky V.* J. Plasma Physics **10**, 1 (1973)
2. *Gospodchikov E. D , Shalashov A G., Suvorov E. V.* Plasma Phys. Control. Fusion **48**, 869 (2006).
3. *Popov A Yu , Piliya A. D.* Plasma Phys. Reports **33**, 109 (2007).
4   *Irzak M. A.* 30th EPS Conf. on Contr. Fusion and Plasma Phys., St. Petersburg, 2003 ECA **27A**, P-2 175.
5. *Brambilla M , Krücken T.* Nuclear Fusion, **28**, 10, 1813 (1988).
6. *Irzak M. A , Popov A. Y* Plasma Phys. Control. Fusion **50**, 2 (2008), ArtNo: #025003.
7. *Vdovin V L.* Proc. of 33rd EPS Conference on Plasma Phys , Rome, 2006 ECA **30I**, O-2 015.
8. *Saveliev A. N.* 30th EPS Conf. on Contr. Fusion and Plasma Phys , St. Petersburg, 2003 ECA **27A**, P-2.20.

RECENT RESULTS OF THE TJ-II EC HEATING SYSTEMS

J. M. Fontdecaba, A. Fernández, A. Tolkachev, A. Ros, A. Cappa,
J. M. García-Regaña and G. Catalán

Laboratorio Nacional de Fusión. EURATOM-CIEMAT Association, Madrid, Spain

The present heating systems of the TJ-II stellarator are Electron Cyclotron Resonance Heating (ECRH) and Neutral Beam Injection (NBI). The ECRH system is formed by two GYCOM 53.2 GHz gyrotrons with its corresponding quasi-optical transmission line. Each transmission line has 10 mirrors. In 2007 the gyrotrons high voltage power supply was changed. This new power supply increases the voltage output up to –80 kV and the output current up to 50 A. This upgrade has improved the performance of the gyrotrons and the reliability of the system. An Electron Bernstein Waves Heating (EBWH) system is being assembled. It uses a 28 GHz gyrotron. The power is transmitted by a 45 mm corrugated waveguide Inside the vacuum vessel there is a steerable mirror which permits to focus the beam to get the optimum transmission efficiency through the O-X conversion layer. The status of both EC systems, as well as some new diagnostics is presented.

Introduction

The TJ-II is a medium size heliac flexible stellarator ($R = 1.5$ m, $<a> \leq 0.2$m, $B_0 = 1$ T) [1] whose plasmas are created and heated by the microwaves launched by two 53.2 GHz gyrotrons (second harmonic X-mode). The power of the gyrotrons was only 200 kW each due to a limitation in the current of the high voltage power supply. The output voltage ripple was over 7 % and the microwave radiation was not stable. Moreover, spurious switch-offs occurred. In order to guarantee the reliability of the ECRH system and to improve the performance of the gyrotrons, a new HVPS has been commissioned.

The heating of high-beta plasmas is one of the main goals for TJ-II. The cut-off density for the 2nd harmonic X mode is reached as soon as NBI is switched on and no more ECRH power is absorbed at the plasma centre. This density is still low and, depending on the plasma conditions, radiative collapse may occur. Electron Bernstein waves (EBWs) are envisaged for having additional heating after NBI switch-on, thus easily avoiding the collapse. Besides this purpose, this heating method can also be very useful to perform kinetic studies on the plasma-wave interaction for the specific values of the EBW refractive index and field polarization. The EBWH system that is being put into operation is foreseen as a routinely heating system in the operation of the TJ-II.

New diagnostics have been developed. An IR camera is used to check the microwave beam shape in different places along the path from the gyrotrons to the vacuum vessel. Prior to the EBW heating experiments, the measurement of the thermal EBW emission from the plasma is being used to determine the mode-conversion efficiency and the optimum launch angle. Using reciprocity, the optimum launch angle of the heating wave can be determined by finding the optimum viewing angle that maximizes the thermal emission intensity in over-dense plasmas.

419

New ECRH high voltage power supply

A new high voltage power supply (HVPS) based on solid-state technology and high frequency commutation techniques, has been designed and manufactured by the company JEMA. The new unit reaches –80 kV and 50 A during a maximum pulse length of 1 s.

The new solution includes a matching transformer, which isolates the AC input and provides the DC current for the 12 pulses SCR rectifier. This rectifier generates stabilized 700 V continuous voltage and it consists of 2 stacks of thiristors. The DC bus is connected to 32 IGBT invertors, which operate at 2.7 kHz. The pulse width modulated output of each converter is connected to a high frequency transformer, which provides the main isolation from the low voltage to the high voltage side. The square waveform obtained at the secondary of each transformer is rectified by means of a diode bridge. The connection in series of the 64 diode bridges provides the required –80 kV d.c. at the output. In case of arcing in the gyrotrons the HVPS switches off in less than 5 μs, which limits the energy deposited in the gyrotrons and a crow-bar protection is not needed. The level of the output voltage ripple is 3 % peak to peak and it has been reduced to 1.3 % with an additional filter. All the functions of the HVPS are controlled by a central system based on a SIMATIC S7 PLC.

The HVPS was commissioned in May 2007 and it has been working in two TJ-II experimental campaigns. The reliability of the ECRH system has significantly increased. In approximately 2200 TJ-II shots, only 3 of them were lost due to a failure in the ECRH HVPS. 300 kW microwave power in each gyrotron has been achieved and the plasma parameters have been improved. Moreover, due to the decrease in the output voltage ripple, the frequency is more stable and the spectrum is narrower [2].

Electron Bernstein Waves Heating

Theoretical calculations have shown that the most suitable approach for launching EBWs in the TJ-II stellarator is via O-X-B mode conversion at the first harmonic (28 GHz), which is estimated to have good heating efficiency for central densities above $1.2 \cdot 10^{19}$ m^{-3} [3] . The beam/ray tracing code TRUBA has been used as basic tool for these calculations with weakly relativistic approximation. TRUBA is used to find both the optimum launching position, which ensures high centered absorbed power and the optimum structure of the beam [4]. EBCD calculations in the high velocity limit (using the Langevin equations approach) are being carried out [5].

The results of the optimization were used as an input for the design of the heating system. The power of the 28 GHz gyrotron is transmitted to the vacuum vessel by an oversized (45 mm diameter) corrugated waveguide and launched with the optimized beam parameters by a movable focusing mirror. To obtain the required polarisation to get maximum O-X conversion efficiency, two flat corru-

gated mirrors act as polarizers [6]. The main components of the waveguide: the launcher inside the vacuum vessel, the window, the DC break and both curvature bends have been installed and are ready for alignment. The polarizers and the matching ellipsoidal mirrors are also manufactured and installed. The 300 kW old gyrotron that was prepared for the experiment could not be conditioned and a new one with higher power: 500 kW is going to be purchased.

IR diagnostic

Preliminary measurements of the microwave beam have been carried out during the last experimental campaign. The experimental set-up consists of a target which is focused by a thermal camera. As during the experiments the entrance in the experimental hall is forbidden the camera is controlled via GPIB connection from a PC.

The images are treated in different ways in order to perform the analysis of the results. As the camera does not have a perpendicular view of the target the image must be deformed to transform it in a perpendicular image. Four resistances are installed in the target to help the geometrical transformations, knowing the distance between resistances the relation mm/pixel can be calculated. Before the beam shot some pictures are taken to use them to subtract the background heat from the beam image in the target.

When the images are ready, a program uses them to calculate the beam waist and the distance from the minimum waist. This program takes the images as input and with a recursive Nelder-Mead method [7] finds the wanted quantities. All these measurements have been done in different places of both lines showing a good agreement with the theoretical values. In the future this system will be upgraded and used to check the beam in the Bernstein heating line.

EBE diagnostic

A microwave emission measurement diagnostic has been installed in the TJ-II. The system uses the movable mirror of the heating system, a flat mirror attached to a section of corrugated waveguide, a glass focusing lens and a quad-ridge dual polarized microwave horn. The microwave emission from the plasma at 28 GHz is reflected from the steering mirror into the detection waveguide via the flat mirror. The emission is then focused into the horn via the glass mirror. The horn is aligned with the ridges oriented with the magnetic field such that one channel measures the emission with the electric field parallel to the magnetic field, while the other channel measures in the perpendicular direction.

The system was absolutely calibrated using a chopper wheel arrangement that alternated between the microwave absorbers at room temperature and liquid nitrogen.

Prior to the heating experiments, the measurements of the thermal EBW emission will be used to determine the mode-conversion efficiency and the opti-

mum launch angle. Using reciprocity, this angle of the heating wave can be determined by finding the optimum viewing angle that maximizes the thermal emission intensity in over-dense plasmas.

Preliminary measurements have been made. When the plasma is operated below the O-mode cut-off density, the time evolution of the 28 GHz is consistent with measuring oblique fundamental O-mode ECE. When the plasma is in overdense conditions with NBI, the emission is consistent with the measurement of B-X-O mode conversion [8].

Conclusion

The status of the EC systems has been presented. The ECRH system has improved its performance with the new high voltage power supply, the power of the gyrotrons can reach 600 kW, the frequency of the radiation is more stable and the failures in the TJ-II operation have been significantly reduced. The EBWH system has not been put into operation due to a failure in the gyrotron and a new one is going to be purchased. The transmission and launching components are installed and ready for alignment.

An IR camera has been used to check the shape of the microwave beam. The electron Bernstein emission diagnostic has been installed and preliminary measurements have been carried out.

References

1. *Sánchez J. et al* Nucl. Fusion **47** S677-S685 (2008).
2. *Fernández A. et al.* Performance of the ECRH system with the new –80 kV / 50 A high voltage power supply. Submitted and accepted in Fusion Engineering and Design.
3. *Castejón F. et al.* Nucl Fusion **48** 075011 (2008)
4. *Cappa A. et al* Summary of the EBW Theoretical Calculations in the TJ-II Stellarator, Proceedings of the 15th Joint Workshop on ECE and ECRH, Yosemite, CA, 2008
5. *García-Regaña J M. et al.* Linear estimation of Electron Bernstein Current Drive (EBCD) in inhomogeneous plasmas, Proceedings of the 35th EPS Plasma Physics Conference (2008).
6. *Fernández A. et al* Fusion Engineering and Design **74** 325-329 (2005)
7. *Lagarias J. C et al.* SIAM J. Optim **9** (1998) № 1 pp. 112–147.
8. *Caughman J. et al.* Submitted to Fusion Science and Technology.

COMPARATIVE ANALYSIS OF VACUUM FEEDTHROUGHS FOR THE ICRH SYSTEM FOR IGNITOR

F. Mirizzi

Associazione EURATOM-ENEA sulla Fusione, C.R. Frascati, Frascati (Rome), Italy

ICRH systems are widely used for the heating of thermonuclear plasmas in tokamaks. The RF power, in the 30–120 MHz range, is generally transmitted by coaxial cable. The transmission line is usually split in two main sections: the pressurized Main Transmission Line (MTL) and the Vacuum Transmission Line (VTL), connected to the launcher. The vacuum feedthrough, one of the most critical components of the system, assures the reliable separation between these two sections. Several types of feedthroughs, mainly differing on the form of the ceramic window, have been developed. The conscious choice of the proper window's shape for the feedthroughs of a given ICRH system must be the result of an accurate analysis.

Introduction

IGNITOR (Fig. 1) is a high field ($B = 13$ T), high density ($n_0 \approx 10^{21}$ m^{-3}) burning plasma experiment designed to achieve ignition conditions. It is characterized by compact dimensions ($R = 1.32$ m), relatively low aspect ratio ($R_0/a = 2.8$), considerable plasma cross section elongation and triangularity ($k = 1.83$, $d = 0.4$) and by a very high plasma current $I_P = 11$ MA. The calculated peak ignition temperature is about 11 keV for an energy confinement time $t_E = 0.6$ s. In IGNITOR, ignition conditions are mainly obtained by ohmic heating. Relatively low levels of additional RF power, when applied during the current ramp-up, can optimize the process of ignition. According to the latest proposed scaling [2], less than 5 MW are sufficient to access the H-mode regime. The compactness of IGNITOR and its high plasma density and magnetic field impose the use of a flexible Ion Cyclotron

Fig. 1. IGNITOR artist view

Resonance Heating (ICRH) system. The system is designed to couple a RF power up to 5 MW, in the 80–120 MHz frequency range, through 4 independent launchers, each made by 4 current straps, installed in 4 equatorial ports of the machine.
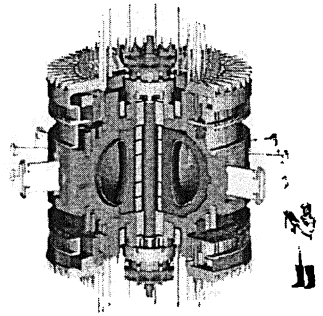
The system operates in pulsed regime (pulse length 4 s), and is powered by 8 high power (1 MW/CW) tetrodes. The power of each tetrode is transmitted through a Main Transmission Line (MTL), a pressurized 9 1/16" coaxial cable with characteristic impedance $Z_0 = 50$ Ω. At the end of the MTL the power is

split by a 3 dB hybrid coupler and transferred into two 6 1/8" coax cables ($Z_0 = 30\,\Omega$), which dimensions are more suitable for the IGNITOR ports.
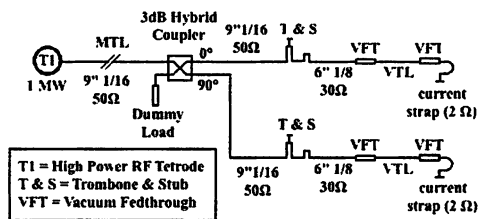

Fig. 2. ICRH unit schematic

The impedance matching between the two cables with different sizes is obtained through stubs and conventional "trombones", that assure also an exact 90° phase shift between the two output cables. Each output cable feeds, through a Vacuum Transmission Line (VTL), a current strap which equivalent impedance is about 2 Ω. The VTL is delimited by two vacuum feedthroughs: the first one at the connection with the pressurized MTL and the second one at the connection with the current strap. Figure 2 gives the principle schematic of an ICRH unit.

The vacuum feedthrough

The vacuum feedthrough is the most critical element of a VTL. It separates parts of coaxial cable at different inner pressures. The separating element is a

Fig. 3. Typical forms of ceramic windows: *a*) flat disk, *b*) corrugated disk, *c*) cylindrical, *d*) conical, *e*) JAERI type

ceramic window welded between the central conductor and the shield of the cable. The ceramic window must have sufficient mechanical robustness to withstand the pressure difference between its two faces and must be "transparent" to the RF, that is power reflection and power losses in the ceramic must be as low as possible. In addition it must withstand surface electrical stresses (the danger of arcing along the insulating surface is much larger than through the vacuum).
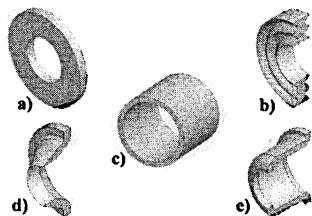
Several forms of windows have been used. All of them can be gathered in five typical forms (Fig. 3): flat and corrugated disk window, conical window, JAERI-type and cylindrical window.

Feedthrough analysis

The feedthrough for IGNITOR is rated for a nominal forward RF power of 400 kW and a maximum VSWR = 12:1. The electric field must be limited to 5 kV/cm. Its characteristics impedance is set to $Z_0 = 30\,\Omega$ to avoid power reflections at the interface with the coax cables. The cross section of the IGNITOR ports imposes to the inner radius of the shield of the coax cable

a maximum radius $b = 55$ mm. According to the general theory of the coax cable, to have $Z_0 = 30\ \Omega$ in the region where the dielectric is air/vacuum ($\mu_r = \varepsilon_r = 1$), the radius of the central conductor must be $a = b/1.65 = 33$ mm.

In the region interested by the ceramic window ($\varepsilon_r = 9.83$, $\mu_r = 1$) instead the ratio b/a must be accordingly changed. In this analysis "b" has been fixed to 55 mm throughout the feedthrough, while the value of "a" has been optimized in terms of scattering matrix for the lowest reflection coefficient (S_{11}) and the highest transmission coefficient (S_{12}).

Flat disk window

Flat disk windows have been successfully used in ASDEX and W7 AS. This window is very simple to realize and install, but the electric field is parallel to its surface, hence surface electrical discharges are greatly probable at high power level.

Anyhow the flat disk window has been examined to select the suitable shape of the connection between the two parts of the central conductor with different radius in order to limit the electric field in the connection region.

Three different shapes of connection have been considered: rounded, conical and cosinusoidal (Fig. 4). The analysis has shown insignificant differences between them in terms of reflection coefficient S_{11}. By considering instead the electric field in the connection region (Fig. 5), the best performances are obtained for the conical connection. This result has been considered independent from the shape of the windows and hence all the feedthroughs have been modelled with the conical connection.

Fig. 4. Connections between the two different sections of the central conductor. *a*) rounded, *b*) conical, *c*) cosinusoidal
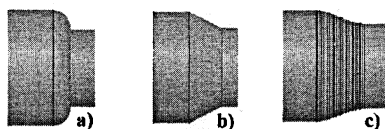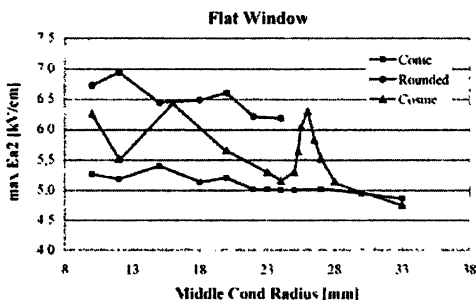

Fig. 5. *E*-field for different connections

425

The corrugated disk window

To overcome the intrinsic limitation of the flat disk window by lengthening the discharge path on the surface of the window, a feedthrough with corrugated disk window (CD) has been considered. In particular a cosinusoidal corrugation has been chosen because easy to draw and to realize. The minimum thickness of the window has been set to 10 mm to safely withstand the pressure gradient between its two faces, and the amplitude of the cosine varied from 0 (flat disk) to 5 mm. This amplitude influences the conductor radius in the window region, and hence the combination between these two parameters has been optimised for the lowest S_{11} (Fig. 6) that results to be better than -70 dB for the whole range of amplitudes considered.

The analysis shows that the strongest electric field occurs at the first corrugation from the central conductor. Its value depends on the corrugation amplitude (Fig. 7) and is lower than 5 kV/cm for an amplitude $D \leq 2.5$ mm. The related equivalent discharge length, given by the line integral of the cosinusoidal path, has a value of about 37 mm.
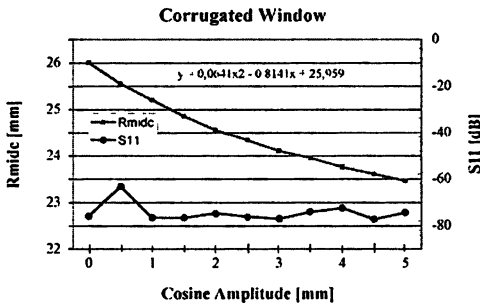

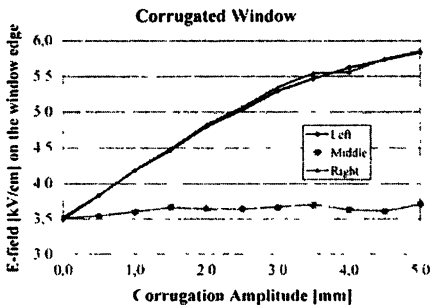**Fig. 6.** Optimisation of the corrugated disk window

Fig. 7. E-field around the window at $P = 400$ kW and VSWR $= 12.1$

The peak voltage inside the feedthrough for $P = 400$ kW and VSWR $= 12:1$ is 11.6 kV, thus the maximum E-field along the surface of the window is less than 3.1 kV/cm, a value that satisfies the technical specs of the feedthrough.

The conical window

The conical window assures a longer surface discharge path. The best performances of this window in term of the reflection ($S_{11} \approx -45$ dB) have been obtained for a radius of the central conductor in the window region of 25 mm. The maximum E-field is localized at the connection between the ceramic and the central conductor where its value overcomes 8 kV/cm (Fig. 8). This window hence has a high probability of arcing in that critical region.
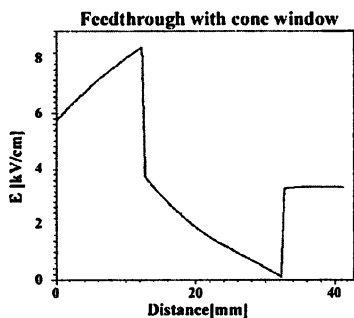

Fig. 8. E-field in the window region

JAERI type window

This window is a combination between a conical window and a cylindrical one Also in this case the feedthrough has been optimized for the minimum reflection and a value of $S_{11} = -54$ dB has been obtained for a radius of the central conductor in the window region of 27.5 mm.

The maximum electric field is localized in the window region; its value is dependent on the radius of the conductor in the window region (Fig. 9). In this region the electric field is always greater than 5 kV/cm and, in particular, for $R_{midc} = 27.5$ mm its value is $E \approx 7.5$ kV/cm.

This window needs a more accurate analysis to find better performances.
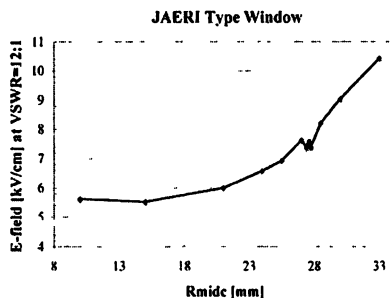

Fig. 9. E-field in the window region vs. Rmidc

Feedthrough performances comparison

The analysis has been concluded with a comparative analysis of the performances of all the examined windows. In particular the maximum electric field in the window region with $P = 400$ kW and VSWR = 12:1 is given in Fig. 10 as function of the radius of the central conductor in that region. From this figure it is evident that the two feedthroughs with disk window (flat and corrugated) have the lower value of electric field; the corrugated disk window must be preferred because of its longer electric discharge path.
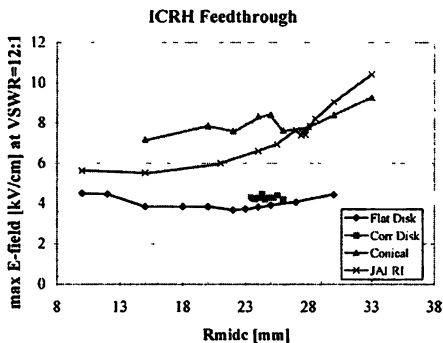
427

ICRH Feedthrough

Fig. 10. Max *E*-field in the window region

Conclusions

To select the most suitable vacuum feedthrough for the ICRH system for IGNITOR, an accurate analysis from the electric point of view has been carried out with the support of a FEM code. The analysis has considered the most common ceramic windows used in existing ICRH system. All of them have been optimized for the lowest reflection coefficient and generally an $S_{11} \leq 50$ dB has been obtained. Major differences have been instead evidenced for the maximum electric fields inside the feedthroughs, specifically in the window region where values in excess of 6 kV/cm have been computed for conical and JAERI type windows, while for disk windows these values are about 4 kV/cm. To conclude the analysis a feedthrough with corrugated disk window will be built and tested in real conditions to verify their promising computed characteristics.

References

1   *Coppi B et al.* Critical Physics Issues for Ignition Experiments, MIT RLE Report PTP 99/06 (1999)
2.   *Snipes J. A et al.* Plasma Phys Contr. Fusion **42**, 381 (2000)

TERAHERTZ- AND MICROWAVE-ASSISTED MATERIALS PROCESSING AND NANOTECHNOLOGIES

(including a broader range of microwave applications)

MICROWAVE SINTERING OF NANOSTRUCTURED CERAMICS

Yu. V. Bykov, K. I. Rybakov

Institute of Applied Physics RAS, Nizhny Novgorod, Russia

The worldwide interest in the development of fabrication methods of nanostructured ceramics and composites is based on their superior mechanical and functional properties. One of the main problems in the sintering of articles compacted from nanostructured powders is to achieve high final density of the material while retaining the structure on the nanoscale.

The sintering with the use of microwave heating is one of the promising methods of obtaining ceramic materials with a close-to-theoretical density and nanometer (< 100 nm) grain size. Microwaves are absorbed throughout the entire volume of the material undergoing processing, which makes it possible to achieve very high heating rates. However, experimental results suggest that fast heating alone is insufficient for limiting grain growth at the final stage of densification. The results achieved to date in the microwave sintering and joining of nanostructured ceramic materials suggest that the success-determining factor is the quality of the starting nanopowders and compacts.

The prospects of the use of methods aimed on efficient separation of the densification and grain growth processes, such as two-stage sintering, with microwave heating are discussed. Another promising route to obtaining dense nanostructured ceramic materials is simultaneous application of microwave heating and external pressure.

Introduction

Nanocrystalline solids are polycrystals, the crystal size of which is from several to tens nanometers, so that a significant part of volume is occupied by incoherent interfaces between crystals of different orientations. The atomic arrangements formed in the core of an interface are determined by the minimum energy in the potential field of two adjacent crystalline lattices on either side of the interface. These boundary conditions result in the atomic structures that cannot be formed elsewhere (e.g., in glasses or perfect crystals). This may lead to unusual optical, magnetic, electrical and mechanical properties of nanocrystalline solids. From the performance viewpoint, nanostructured materials are often defined as those exhibiting radically new properties associated with the nanostructure. This paper is limited mainly to structural nanoceramics whose mechanical properties differ greatly from those of conventional ceramics.

Ceramics are generally fabricated from powder materials by a high-temperature consolidation process called sintering. The sintering process relies on diffusion mass transport which is activated at high temperature. The driving force for sintering is capillary stresses arising due to the tendency of the system to minimize the free energy associated with the surface. There are different diffusion mechanisms involved in the sintering process: surface diffusion, grain boundary diffusion, and bulk diffusion. The densification of ceramic material during sintering is generally accompanied by concurrent grain growth via grain boundary migration.

.Usually ceramics are considered nanostructured when the average grain size is on the order of 100 nm or less. Although at a grain size of 100 nm grain boundaries still occupy an insignificant fraction of the volume, the presence of an increased number of grain boundaries influences certain properties of ceramics, both structural and functional. In particular, upon transition to the nanostructure, enhanced microhardness, fracture toughness, and plasticity are observed.

A polycrystalline material is stronger than a single crystal because the grain boundaries impede the motion of dislocations which is a primary mechanism of plastic deformation, and the number of grain boundaries increases as the grain size decreases. Numerous experiments have shown that the Hall–Petch relation, $\sigma_y = \sigma_0 + kd^{-1/2}$, that links the yield stress of a polycrystalline material, σ_y, with the grain size, d, is obeyed for grain sizes down to ~ 100 nm (here σ_0 is the yield stress of single crystal, and k is a material constant). A similar relation is valid for the hardness of polycrystalline material: $H = H_0 + kd^{-\beta}$, where H_0 is hardness of a single crystal and β is an exponent between 0 and 1. Due to strengthening and hardening caused by dislocations blocking, the nanocrystalline ceramics are considered as candidates for superhard materials applications. As for the grain size domain well below 100 nm, the validity of the Hall–Petch relation is not supported experimentally for it. Similarly, the hardness saturates or even decreases as the grain size goes below 100 nm [1].

The fracture toughness in conventional materials is based on the emission of lattice dislocations from crack tips. This mechanism becomes inefficient in ceramics as their grain size enters the nanometer domain. Instead, the fracture toughness of nanostructured ceramics is improved due to other mechanisms such as grain boundary sliding [2]. Clearly, this-process depends greatly on intergrain interfaces. For example, in a fully dense nanocrystalline composite, $Al_2O_3 - 10$ vol. % Nb, the fracture toughness increases by more than 250 % as compared with microcrystalline single-phase alumina while retaining the hardness [3].

The hardness and fracture toughness are the most important mechanical properties of ceramic materials for tribological applications. Without going into details of many mechanisms of wear in ceramics, it can be said that for all practical purposes, the tougher and the harder the ceramic, the better its wear resistance. It is worth noting that among structural ceramics, the only manufacturing sector that currently exhibits major growth is in tribological applications.

Another very important property of nanostructured ceramics from the practical point of view is enhanced plasticity. With conventional ceramics, finish machining operations account for a significant portion of the production costs and impair the ecology. Therefore, considerable attention has been given to both examining the mechanical properties of ceramics at elevated temperature and developing new superplastic forming techniques. The superplastic behaviour in ceramic materials was demonstrated in 1986 when Wakai and co-workers re-

ported tensile elongations of over 100 % in yttria-stabilized zirconia [4]. The superplastic deformation of fine-grained (average grain size of 300 nm) zirconia-based ceramics with tensile elongation to failure over 350 % was demonstrated in [5].

It may be argued that enhanced plasticity of nanocrystalline materials contradicts to their high hardness. However, the deformation mechanism can change with a decrease in the grain size, from the generation of dislocations to grain boundary sliding. The superplastic flow of dense nanocrystalline ceramics at strain rates considerably higher than in their conventional counterparts is a direct consequence of the added interfacial surfaces available for intergranular sliding. If the creep behaviour found in conventional materials is still valid in the nanometer range, then nanostructured ceramics can be deformed plastically at rates of industrial interest, which opens prospects of developing net shape production methods similar to those based on superplastic creep of metal alloys.

Among the distinctive features related to the functional properties of nanostructured ceramics are high ionic conductivity [6], low thermal diffusivity [7], higher I–V nonlinearity of varistor electroceramics [8], different photonic and electrical [9], ferro- and piezoelectric properties [10], etc.

An issue of crucial importance for production of nanostructured ceramics is the preparation of the starting powder material and powder compacts, the so-called green bodies. At present, nanopowders of different chemical composition produced by various methods are available. Depending on the production method, the powders differ in the average particle size, particle size distribution, and the degree of particle agglomeration. It has been proven experimentally in many research studies that in order to obtain fully dense nanostructured ceramics, one should choose monodisperse powder (i.e., with the narrowest particle size distribution) with minimum tendency to agglomeration. Generally, it is not possible to obtain nanoceramics from agglomerated powders or powders having a fraction of coarser particles, at least by pressureless sintering. Upon compaction such powders form an inhomogeneous structure with large pores surrounded by many particles. It has been shown from thermodynamic considerations [11–13] that a pore can only disappear during sintering if the number of particles surrounding it (called coordination number) does not exceed some critical value. Larger pores that are surrounded by many pores remain in the ceramic structure and can only be eliminated if their coordination number is reduced at the expense of grain growth. It was demonstrated in [14] using sintering of nanocrystalline TiO_2 as an example, that no matter how small are the crystallites inside the agglomerate, the size of agglomerates dictates the size of the interagglomerate pores and, ultimately, the densification behavior of the ceramic material.

In this connection, various sophisticated methods of nanopowder preparation are being developed, aiming on agglomeration prevention, as well as methods of de-agglomeration. In addition, promising results have been obtained with nanopowders compacted by advanced techniques to highest possible densities.

Microwave sintering: background

The use of microwave heating offers good prospects for the sintering of nanostructured ceramics. Due to volumetric nature of microwave heating, the heating rate is not limited by thermal conduction of the material undergoing processing, as well as by the thermal mass of the furnace. Numerous studies of the sintering of fine-grained ceramics have shown great benefits of fast microwave heating for rapid densification while preventing grain growth.

The volumetric energy deposition during microwave heating gives rise to the so-called inverse temperature distribution in the material, with the core hotter than the periphery. As a result, the open porosity remains in the periphery of the sintered product up to the later stages of sintering, which is favorable for the outflow of pores and faster densification. It is worth noting that the controllable non-uniformity of density in the microwave-sintered material can facilitate finish machining of the ceramic part. In addition, such a porosity structure is preferred for solid state synthesis processes, such as silicon nitride ceramics production by nitridation of silicon powder in nitrogen-rich atmosphere with subsequent sintering [15].

Other benefits of microwave processing include high energy efficiency (energy savings can reach 90 % in high-temperature processes because energy is not spent on heating massive furnace parts), heating selectivity that finds applications in the processing of composite materials and self-propagating synthesis, and enhancement of mass transport processes due to non-thermal effects of microwave electromagnetic field.

To date, most of research and pilot tests in microwave processing have been done using the power of standard microwave frequencies (2.45 or 0.915 GHz). Wider opportunities for a broad range of processes are opened by the use of the millimeter-wave radiation. The main advantages of exploiting the millimeter-wave energy for technological applications were formulated in [16]. The following factors appear to be of the greatest importance for the technologies based on processing of solid materials:

• most materials that are of interest for high-performance applications have higher capability of radiation absorption in the millimeter-wave range. Even materials usually considered as "transparent" for microwaves (pure Al_2O_3, BN, Si_3N_4) can be successfully heated by millimeter waves, without any additional means that have to be used at standard frequencies;

• the electromagnetic field distribution is more uniform in the applicators fed with millimeter-wave radiation. Much higher uniformity attributed to applicators with $L \gg \lambda$ (where L is the dimension of applicator and λ is the wavelength of radiation) results from a significant increase in a number of modes which can be excited simultaneously;

• it is easier to solve the heating instability ("thermal runaway") problem due to weaker dependence of the millimeter-wave absorptivity on temperature;

• high-intensity wave beams can be easily produced by focusing the millimeter-wave radiation in a spot of size on the order of λ^2. This makes it possible

to use such wave beams for local surface treatment of materials, similar to such techniques as infrared laser, electron beams, plasma flows, etc.

These considerations, along with other factors discussed in [16], are being proven today in the experimental research in millimeter-wave processing of materials.

Microwave sintering of oxide nanoceramics

There have been a number of papers on the microwave sintering of nanopowder compacts. Most of the research was undertaken in order to determine whether fast microwave heating could be a means of producing high-density nanocrystalline ceramics with no significant grain growth. One of the first experimental attempts was performed back in 1991 [17]. Titania nanopowder compacts with particle size ≤ 10 nm and initial packing density about 60 % were sintered using microwave (2.45 GHz) heating at a rate of 70 °C/min. The sintered ceramics had an average grain size (determined by TEM and XRD) of about 30 nm at a density of 92 %. In line with many experiments using conventional heating, abrupt grain growth started in nanopowder compacts as the density exceeded 90 %.

In an early effort of the IAP team [18], titania nanopowders with initial particle size of 30 nm were sintered using millimeter-wave (84 GHz) radiation at heating rates of 50–100 °C/min to a final density of 98–99 %. The average grain size of crystallites in the sintered samples, estimated by the XRD techniques, was over 300 nm. It should be noted that the microhardness of the microwave sintered samples was about 10 % higher than the microhardness of the samples sintered conventionally to the same values of density, being equal to the microhardness of the monocrystalline rutile.

Many research groups investigated the sintering of nanocrystalline alumina using microwave heating because the alumina-based ceramics are the most widely used structural ceramic material. The nanocrystalline alumina powder, produced by all methods of practical interest, comprises a mixture of the metastable polymorphic phases which transform at heating into the stable α-Al_2O_3 phase. It is well known from the studies of the conventional sintering of nanocrystalline alumina that a sequence of polymorphic transformations is accompanied by a sharp decrease in the surface area and by changes in the particle and pore morphology which adversely affects the sintering process making it difficult to obtain dense ceramics with fine microstructure. An attempt has been made in [19] to determine if the use of very fast microwave heating could enhance the densification of the nanocrystalline alumina while maintaining the nanostructure of the grains in the material. Although the heating rates of samples, compacted from powder with particle size in the 5–20 nm range, were over 250–300 °C/min, the dimensions of grains exceeded 1 μm even in the samples sintered to a density of only 89 % of the theoretical value.

Another approach based on the precise controllability of microwave heating was exploited in [20], where the samples for the study were compacted from the

same powder as in [19] produced by *Nanophase Technologies Corp.*, USA. The use of the millimeter-wave (30 GHz) power allowed easily controllable heating of nano-alumina compacts in a broad range of ramp-up rates without any susceptors. A characteristic feature of the microwave heating regimes was a slow ramp-up with the rate of 5–10 °C/min within the temperature range of the polymorphic phase transformations in Al_2O_3 (1000 °C $\leq T \leq$ 1200 °C), then rapid temperature increase (50 °C/min) without a hold at the maximum temperature of sintering. An example of the microwave heating regime is shown in Fig. 1.
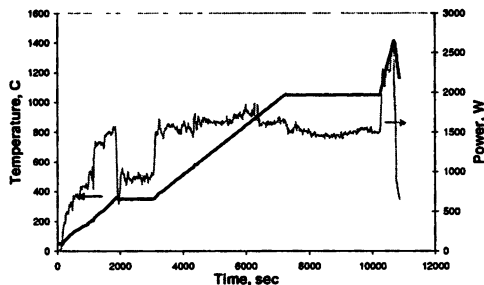
Fig. 1. Temperature-time schedule and millimeter-wave power recorded in an alumina nanoceramics sintering process

A beneficial effect of the annealing of transient Al_2O_3 phases at conventional heating was reported in [21]. An α-Al_2O_3 matrix of uniform porosity was the result of an annealing process (1020 °C for 10 hours) that enhanced densification considerably and reduced grain growth during the sintering stage.

The results of experiments on millimeter-wave sintering [20] are summarized in Table, and an AFM image of the microstructure is shown in Fig. 2.

Results of millimeter-wave sintering of alumina nanoceramics

Heating rate in the temperature range of polymorph transformation (°C/min)	T_{max} (°C)	Relative density	Average particle size by AFM (nm)	Crystallite size by XRD (nm)
50	1500	≤ 0.98	220 ± 60	85
5	1475	≤ 0.98	180 ± 60	81
5	1300	≤ 0.98	130 ± 30	80
10	1300	0.96	115 ± 35	73
7	1200	0.91	90 ± 25	63.5

Virtually fully dense pure Al_2O_3-ceramics with the grain size well below 100 nm was obtained in these experiments at a temperature of 1300 °C and zero hold time. It is worth noting that the effect of annealing of transient Al_2O_3-phases correlates with the results of the study of the dependence of both phase transformation and pore structure evolution in Al_2O_3 on the microwave intensity [22]. It has been found that microwave heating results in lowering the phase transformation temperature. The phase transformation rate and the rate of porosity reduction depended non-monotonically on the microwave electric field strength and reached its maximum when moderate-intensity microwaves were used for heating.
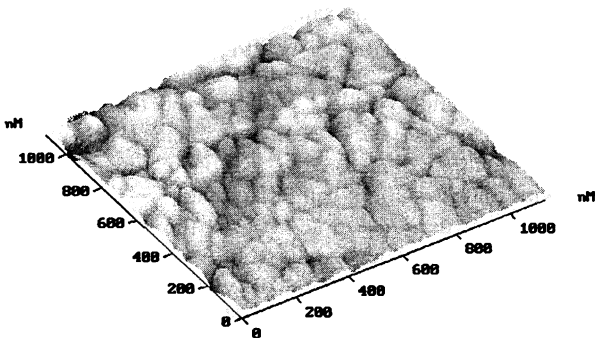
Fig. 2. AFM image of the microstructure of alumina nanoceramics

More recent results of the IAP team in the field of millimeter-wave sintering of nanoceramics can be found in a separate paper in these Proceedings [23]. In collaboration with the Institute of Electrophysics (Ekaterinburg, Russia) and Nizhny Novgorod State University, an experimental effort has been undertaken that combines production of nanopowders (Al_2O_3, ZrO_2, Y_2O_3) by wire explosion, magnetic dynamic compaction of the powders to elevated densities, rapid millimeter-wave sintering, and characterization of mechanical properties. The most interesting findings resulting from this effort are enhanced microhardness and wear resistance of the obtained ultrafine ceramic materials, and enhanced high-temperature creep rate demonstrated under millimeter-wave heating. It has been established in the creep studies that the activation energy of grain boundary diffusion is lower under microwave heating than the literature data collected from conventional heating experiments.

Yttria-stabilized zirconia is another ceramic material of great practical interest for structural and functional applications. The microstructural development during microwave sintering of nanocrystalline yttria-zirconia ceramics has been investigated in [24]. The relationships between density and grain size were studied to determine whether microwave heating altered the densification/grain-growth relationship and to compare the resultant properties and microstructure with the material sintered by a conventional constant-heating-rate process. The materials for the study were samples of 3 and 8 mol. % yttria-stabilized zirconia compacted from a powder with 22–27 nm particle size. Little grain growth was observed in both materials until densities over 96 % of the theoretical value were attained during conventional or microwave heating. After this point, the average grain size increased up to 300 nm and up to 3 μm in 3 and 8 mol. % yttria-stabilized zirconia, respectively. In 3 mol. % yttria-stabilized zirconia the grain growth was less during microwave sintering compared to conventional heating, but no difference was observed for 8 mol. % yttria-stabilized zirconia. The results of this study indicate once more that the mass transport processes responsible for densification depend greatly on the specific character of the interaction of mi-

437

crowave field with materials. At the same time, it should be noted that there is almost no data on the microwave dielectric properties of nanostructured powders. The difficulties in acquiring these data stem, in particular, from the very high specific surface area of nanocrystalline powders and their high absorbtivity of various impurities. Clearly, the lack of such data makes it difficult to develop the sintering processes which account for the specific features in the interaction of microwave field with polycrystalline solid materials.

The properties of powders play a key role in the sintering of nanoceramics. As shown in [25], both the particle size distribution and phase composition affect the results of microwave sintering. 3 mol. % yttria-stabilized zirconia ceramics was sintered from a 50 nm powder under 2.45 GHz heating at 1250 °C for 30 min up to a density over 97 % of the theoretical density with an average grain size of 140 nm.

In a more recent paper from FZK [26], yttria-stabilized zirconia with initial particle size of 37 mm was millimeter-wave (30 GHz) sintered at a low temperature of 1200 °C (heating rate 20 °C/min, zero hold time) to a final density of 99 %. The average grain size in the sintered samples was less than 100 nm. For comparison, conventional heating at a heating rate of 5 °C/min required sintering temperatures as high as 1300 °C with a hold time of 3 hours. This yielded ceramics with a final density of 98.5 % with an average grain size of 150–200 nm.

A related research direction is joining of ceramics. Dissimilar ceramics, such as Al_2O_3 and ZrO_2, cannot be joined directly because of the mismatch of the coefficients of thermal expansion, which gives rise to residual stresses that exceed the tensile strength of the ceramic materials. It has been demonstrated in [27] that the use of an interlayer sintered from a mixture of nanophase alumina and zirconia powders matches the coefficients of thermal expansion, reducing the stresses and thereby making it possible to obtain a crack-free joint between the ceramic parts. It is also believed that the enhanced ductility of the interlayer material also contributes by relieving a portion of the residual thermal stresses.

Promising methods of nanoceramics sintering with microwaves

The main problem that makes it difficult to obtain dense ceramics with the grain size in the nanometer domain is the grain growth that accompanies densification. Rapid pressureless sintering is not completely capable of overcoming this problem because grain boundary migration which is responsible for the grain growth is based on virtually the same diffusion micromechanisms as sintering. However, there is a certain difference in the kinetics of grain boundary diffusion and grain boundary migration. Grain boundary migration may involve an activation process that has a higher activation energy than grain boundary diffusion. Grain boundary migration can be severely hampered by the slow mobility of grain junctions as well as grain boundary/pore junctions at lower temperatures, the latter having a higher activation energy. This fact is exploited in the two-stage sintering method proposed in [28]. The two-stage process includes a rapid temperature rise to some maximum temperature value, T_1, required for sintering,

followed almost immediately by a drop down to some lower temperature, T_2, and then by a prolonged hold at this lower temperature (Fig. 3). This temperature drop "freezes" the grain boundary junction points and similar features in the microstructure, thereby stopping the grain growth process while allowing continued densification. The use of this method for microwave sintering of nanocrystalline ceramics can have a good potential due to a specific influence of the microwave field on the diffusion mass transport that has been confirmed by results of numerous experimental studies.
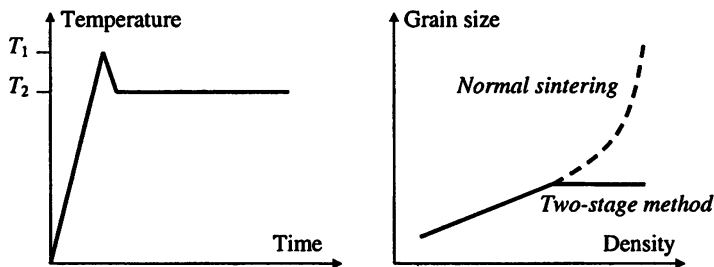
Fig. 3. Schematic temperature-time schedule and a sketchy dependence of grain size versus density for the two-stage sintering method, after [28]

There has been a first report of a use of the two-stage sintering method with microwave hybrid heating [29]. 3 % yttria-stabilized zirconia powder with an average particle size of 16 nm was used in this study. A proprietary wet chemical process was used to produce de-agglomerated nanosuspensions and to slip cast the samples. The two-stage microwave hybrid heating process had $T_1 = 1150$ °C (held for 6 seconds only) and $T_2 = 1000...1050$ °C. For comparison, conventional and one-stage heating processes were used.

It has been observed in [29] that the use of microwave hybrid heating has consistently resulted in a finer average grain size for a given final density compared to conventional heating. Moreover, the use of two-stage sintering does indeed seem to result in the ability to retain a very fine grain size, whilst achieving effectively full densification. With conventional heating rapid increase in grain growth began at densities of 90–95 %; achieving full density resulted in average grain sizes > 160 nm. However, the combination of microwave hybrid heating with the two-stage sintering technique clearly resulted in the ability to retain a final grain size in the range 60–80 nm whilst achieving densities in excess of 99 %.

Another promising line of research is pressure-assisted microwave sintering. The implementation of sintering under simultaneous action of microwave heating and applied pressure is a technically complicated problem, especially in the case of ceramics materials which need very high temperature for densification. A pressing device should possess both low microwave loss and high strength at a high processing temperature. The sintering of nanocrystalline powder compacts alleviates this problem, to some extent, due to a decrease in the temperature at which the mass transport is effectively activated. As opposed to the hot pressing

and related methods, which utilize very high pressures (above 1 GPa), first results obtained with microwave heating suggest that it is possible to use much lower pressures to obtain nanostructured ceramics. As reported in [30], the millimeter wave pressure sintering combined with non-equilibrium reaction milling made it possible to obtain full densification, via enhanced superplastic flow, of tetragonal $(ZrO_2–3mol\%Y_2O_3)_{62}(Al_2O_3)_{38}$ with the grain size 28 nm at a relatively low temperature of 1200 °C. In that work, the pressing device was made up of sintered coarse-grain alumina.

Similar experiments are underway at IAP. The pressing device is installed inside a large-size millimeter-wave cavity applicator, as shown in Fig. 4. In contrast to [30], the millimeter-wave radiation in this configuration is channeled to the ceramic sample via dielectric ceramic rods, which makes it possible to use the mold made of any material that retains its strength at high temperature, without regard to its dielectric properties.
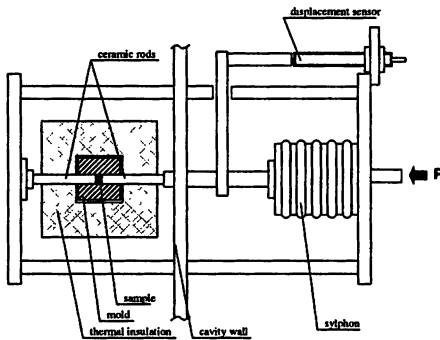
Fig. 4. Schematic of the setup for pressure-assisted microwave sintering [31]

Conclusions

• Nanostructured ceramic materials offer great benefits due to enhanced mechanical properties such as microhardness, as well as a range of functional properties.

• Nanostructured ceramics exhibit enhanced plasticity which facilitates finish machining, reduces the production costs and ecologic impact.

• The problem to solve is grain growth at high density.

• A necessary prerequisite to successful sintering of nanoceramics is high quality of the starting powder materials.

• The primary advantage of microwave heating in the sintering of nanoceramics is high heating rate.

• The focus of current research is on two-stage and pressure-assisted microwave sintering processes.

References

1. *Lu Ch., Mai Y.-W., Shen Y -G.* J. Mater. Sci. **41**, 937–950 (2006).
2. *Ovid'ko I. A , Skiba N. V., and Sheinerman A. G.* Physics of the Solid State, **50**, 1261–1265 (2008).
3. *Mishra R. S., Mukherjee A. K.* Mater. Sci. Eng. A, **301**, 97–101 (2001).
4. *Wakai F., Sakaguchi S., Matsuno Y.* Adv. Ceram. Mater. **1**, 259–263 (1986).
5. *Nieh T. G., McNally C. M., Wardsworth J.* Scripta Metallurg. **22**, 1297–1300 (1988).
6. *Heitjans P., Indris S.* J. Mater. Sci. **39**, 5091–5096 (2004).
7. *Vaben R., Stover D.* Mater. Sci. Eng. A, **301**, 59–68 (2001).
8. *Duran P., Capel F., Tartaj J., Moure C.* J. Am. Ceram. Soc. **84,** 1661–1668 (2001).
9. *Hosono H.* Int. J. Appl. Ceram. Technol. **1**, 106–118 (2004).
10. *Gruverman A., Kholkin A.* Rep. Progr. Phys. **69**, 2443–2474 (2006).
11. *Kingery W. D., Francois B.* // Sintering and Related Phenomena / ed. by G. C. Kuzcinski, N. A. Hooton and G. F. Gibbon. New York: Gordon and Breach Science Publishers, 1967. P. 471–498.
12. *Lange F. F.* J. Am Ceram. Soc. **67**, 83–89 (1984).
13. *Lange F. F. and Kellet B. J.* J. Am. Ceram. Soc. **72,** 725–734 and 735–741 (1989).
14. *Mayo M. J., Hague D. C., Chen D.-J.* Mater. Sci. Eng. A, **166**, 145–159 (1993).
15. *Kiggans J. O., Tiegs T. N.* Mat. Res. Soc. Symp. Proc. **269**, 285–290 (1992).
16. *Bykov Yu. V., Rybakov K. I., Semenov V. E.* J. Phys. D: Appl. Phys. **34**, R55–R75 (2001).
17. *Eastman J. A., Sickafus K. E., Katz J. D. et al.* Mat. Res. Soc Symp. Proc. **189**, 273–278 (1991).
18. *Bykov Yu., Eremeev A., Egorov S. et al.* Nanostructured Materials, **12**, 115–118 (1999).
19. *Freim J., McKittrick J., Katz J., Sickafus K.* Mat. Res. Soc. Symp. Proc. **347**, 525–530 (1994).
20. *Egorov S., Eremeev A., Sorokin A., Bykov Yu., Rachkovskii A., Poduretz A.* // Proc. X APAM Topical Seminar and III Conference "Materials of Siberia: Nanoscience and Technology". Novosibirsk, 2003. P. 162–163.
21. *Kao H.-Ch., Wei W.-Ch.* J. Am. Ceram. Soc. **83**, 362–368 (2000).
22. *Rybakov K. I., Eremeev A. G., Egorov S. V. et al.* Effect of variable-power microwave heating on phase transformations and pore structure evolution in nanostructured alumina // this volume.
23. *Egorov S. V., Eremeev A. G., Holoptsev V. V. et al.* Sintering and mechanical properties of ultrafine alumina ceramics under microwave heating // this volume.
24. *Nightingale S. A., Worner H. K., Dunne D. P.* J. Am. Ceram. Soc. **80**, 394–400 (1997).
25. *Vaidhyanathan B., Binner J. G. P., Liang Y.* // Proc. 9th Int. Conf. Microwave and RF Heating. Loughborough, UK, 2003. P. 63–66.
26. *Link G., Rhee S., Thumm M.* // Advances in Microwave and Radio Frequency Processing / ed. by M. Willert-Porada. 2006. P. 506–513.
27. *Bykov Yu. V., Egorov S. V., Eremeev A. G. et al.* // Synthesis, Functional Properties and Applications of Nanostructures. NATO Science Series II: Mathematics, Physics and Chemistry. Vol. **128** / ed. by T. Tsakalakos, I. A. Ovid'ko, A. K. Vasudevan. 2003. P. 413–426.
28. *Chen I -Wei and Wang X.-H.* Nature, **404**, 168–171 (2000)
29. *Binner J. G. P., Annapoorani K., Paul A. et al.* J. Europ. Ceram Soc. **28**, 973–977 (2008).
30. *Kimura H. and Yamazaki Y.* // Proc. Int. Microwave Power Institute 40th Annual Symposium. 2006. P. 52–55.
31. *Bykov Yu. V., Eremeev A. G., Egorov S. V. et al.* Russia patent application 2007139152 (2007).

ECR MULTICHARGED ION SOURCES
OF NEW GENERATION

G. Ciavola, S. Gammino, L. Celona

Istituto Nazionale di Fisica Nucleare – Laboratori Nazionali del Sud,
Catania, Italy

The Electron Cyclotron Resonance ion sources (ECRIS) have a significant number of applications either in the accelerator facilities, increasing the beam energy and intensity available from different types of accelerators, and in the industrial applications, making more efficient the industrial processes. Actually, the increasing cost for the construction of ion beams accelerators and the need of high current (mA level) of highly charged ions are the major reason for the development of new ECRIS, along with their ability to provide intense beams of highly charged heavy ions with high reliability, stability and low emittance. Such an achievement is important for any accelerator facility based on a linac or a cyclotron, and is particularly relevant for the future facilities (LHC and GSI in Europe, RIA in US, RIBF in Japan).

Even if it is difficult to obtain multi-mA current on each charge state, because the current is distributed over different charge states, the ECRIS present the advantage of a higher current and reproducibility than other ion sources and moreover they can work either in cw mode and in pulsed or afterglow mode, by maintaining their characteristics.

Following the roadmap defined by the Geller's scaling laws [1] and the High B mode concept [2], the evolution of ECRIS has been steady. The increase of current for highly charged ions in the period 1980–2005 has amounted to a factor 100 to 1000 (e.g. O^{7+} current increased from 2 to 600 eμA) Further remarkable increases are possible but they may be limited by technological problems and mA beams of highly charged heavy ions may be achieved only if the microwave coupling to plasma will be optimized, thus obtaining larger currents with power below 1kW/l. In this sense the availability of new schemes of microwave coupling is promising and it will permit to improve the density of warm electron population that is essential for ionization. The paper will also describe some critical point of the 3rd generation ECRIS yet in operation or under construction (including technological troubles and limits) and the scenario for future 4th generation ECRIS.

1. Introduction

The trend to higher frequency and to higher magnetic field is deemed to continue in order to have longer confinement time and higher plasma density, and finally higher beam currents and higher charge states, that are particularly important for heavy ion programmes and for nuclear physics with radioactive ion beams respectively. Such a trend is limited by the experimental evidence of hot electron population formation that becomes more important for high plasma density (i.e. for operational frequency of 28 GHz and higher) and for microwave power above 3 kW. Some recent experimental evidences have suggested to re-

442

consider the current model of ECRIS, that is largely based on the Geller's scaling laws: the extracted current strongly increases as the microwave frequency increases, but only the increase of mirror ratio permits to fully exploit the source capabilities, making effective the increase of electron density with frequency. A full description of the ECRIS standard model is given in [1, 2, 3].

More recently it was understood that a complex system like ECRIS plasma requires an accurate analysis of particle dynamics. In particular the energy transfer from the electromagnetic wave to the plasma electrons has to be investigated; microwave absorption, electron acceleration and heating, influence of electron dynamics on ion dynamics remain outside the current model of ECRIS and it is to be studied carefully in the next years.

As an example, no scaling laws have been put in evidence about the microwave power and the ECR heating process (ECRH), because the relation between the power and the magnetic field is not so simple. Some authors studied the RF coupling to the plasma in terms of the maximum power rate per unit volume and of its relationship with the beam intensity produced by different ECR ion sources but this approach is not satisfactory; only recently it was observed that the efficacy of the microwaves injection in the plasma is related to the geometry of injection plug and plasma chamber. In addition the technological limits imposed by this model (the confining magnetic field is close to the limits of technology nowadays) can be overcame only by means of a better understanding of plasma physics, in particular of the phenomenon that is at the basis of the ECR plasma creation, i.e. the ECR-heating.

Experiments at LNS and LBNL have shown that, instead of a monotonic increase of the extracted currents for higher mirror ratio, a remarkable decrease of such current occurs for very high mirror ratios. Such behaviour have been explained by considering the single electron dynamics, and the "regime transition" from gentle to strong magnetic field gradient. A first series of measurements of X-ray spectra on the 3rd generation ECRIS of Lawrence Berkeley National Laboratory named VENUS have shown a great amount of MeV electrons produced especially when the mirror ratio decrease, that is in good agreement with our clues. The presence of these electrons is detrimental for the cryostat and it is strictly necessary to reduce them to optimize the ECRIS operations.

Different "tricks" have been used in the past to improve the ECRIS performances, as the two frequency heating. Recently some technical solutions related to microwave injection have found their theoretical basis and this should be a step for new advancements in the field, linking the experimental results obtained in various experimental setups and with different microwave frequency and injection design. The possibility to operate with more than one frequency for plasma heating or by using broad microwave spectra may be extended, with the mixing of more frequencies to be used for plasma heating, of which at least one is provided by a broadband microwave generator (like a travelling wave tube, TWT) which allow to combine the frequency tuning and the multi-frequency heating.

2. Second and third generation ECRIS

The laws that regulate the ECRIS (Fig. 1) in terms of the plasma parameters are now quite clear. A number of experiments have demonstrated that a stable plasma is created in ECRIS if the magnetic trap field is $B/B_{ECR} > 2$ (the resonance field is 0.5 T for 14 GHz, 0.63 T for 18 GHz and 1 T for 28 GHz), which is called "High B mode condition" [2]. The magnetic field increase boosts either the electron density and the electron temperature, but other limits to the ionization of the highest charge states come from non–magnetohydrodynamical instabilities excited in plasmas and from the charge exchange process. Experiments have proven that when $B/B_{ECR} > 2$, a quiescent plasma with only few turbulences is obtained, resulting in an easy source tuning. The efficient coupling of microwave to the plasma should not be neglected, as the instabilities are emphasized by a bad microwave matching (it is common experience that unstable RF input turns out in a noisy plasma). In conclusion the increase of microwave power and frequency is necessary but not sufficient.
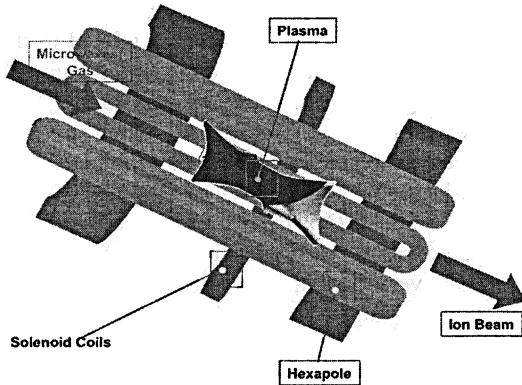
Fig. 1. A scheme of a typical ECRIS

The increase of the performances of ECRIS with magnetic field and frequency have been synthesized in the definition of ECRIS generations, where the 1st generation is based on 5–10 GHz sources with magnetic field around 0.5–1 T and total current below 1 mA; the 2nd generation is based on 14–18 GHz sources with magnetic field around 1–2 T and total current below 10 mA; the 3rd generation gathers 28–35 GHz sources with magnetic field around 3–5 T and total current above 20 mA. A perspective 4th generation ECRIS has been outlined operating at 56–75 GHz with magnetic field around 6–8 T and total current up to 50 mA.

As an example, let us discuss the results obtained with the SERSE source operating at 14, 18 and 28 GHz; it can be observed in Fig. 2 that the increase of frequency from 14 to 18 GHz increases also the current of Xe^{27+} of 50 %, while for 28 GHz operations, even in presence of modest levels of confinement, the

444

better microwave matching boosts the performances. The plot is given in terms of the B/B_{ECR} ratio. The 28 GHz curve in Fig. 2 does not show any saturation, then the capability to produce intense beams of highly charged ions was mainly limited by technological constraints, as the available magnetic field and the RF power that can be safely injected in the plasma chamber. It was also observed from the analysis of the spectra that a significant amount of very high charge states was produced, and the current of Xe^{38+} was typically increased by one order of magnitude with respect to 14 or 18 GHz operations. Similar increases of beam current for increasing B/B_{ECR} were observed more recently for the other source that is operating at 28 GHz, i.e. the VENUS source at LBNL in USA [4].
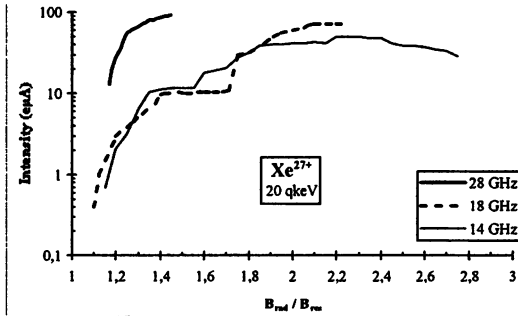
Fig. 2. Xe^{27+} currents extracted from the SERSE source for increasing frequency and magnetic field

A limit to the 'ad libitum' increase of beam currents of highly charged ions comes from the production of energetic electrons that reach an energy above the adiatic barrier, that is around 100 to 500 keV for the best ECRIS nowadays. Otherwise the electron leakage lowers the temperature so that the temperature of warm electrons T_e is far from the theoretical limit. A substantial improvement of the RF energy transfer may permit to set up a strong magnetic field gradient, because in this case even shorter time for the resonance crossing can be sufficient for the electron heating. The combined effect of strong gradient and high rf power may take to a better ionization process. The improvement of the microwave coupling to the plasma permits to get rid of the technological limits hereinafter described.

3. Technological limits

The design of 3rd generation ECRIS obliged to take into account some technical issues that are usually not evaluated for conventional ECRIS, either in terms of microwave power management and in terms of stray magnetic field. In fact strong magnets originates high stray fields which are detrimental for beam optics, for pumping system lifetime and mainly for the gyrotron normally used for power generation. Additionally the presence of intense x-ray fluxes generated

by the ECRIS plasma, observed by many experiments, can generate an unexpected heat load upon the thermal balance of the superconducting ECRIS cryostat, which is even heavier in the case of closed loop cryostat connected to a cryocooler setup.

The complexity and the cost of the modern ECR ion sources are then relevant with respect to the past; on the other way, a technological step forward to master the problems involved in the design, realization and routine operations of such type of sources is needed.

The first point concerns the design of the magnetic system for the axial and radial confinement: due to the high fields required the system consists of a set of superconductiong coils and hexapole which structure must be carefully designed and simulated with particular care to 3D stress analysis.

The high values of stray magnetic fields can cause problems to the pumping system and to the gyrotron. The stray field affects the formation of the beam emittance remarkably as it is seen in the Fig. 3, which shows a typical beam shape according to 3D simulations, and in Fig. 4 which shows the beam shape on a viewer located in the beamline.
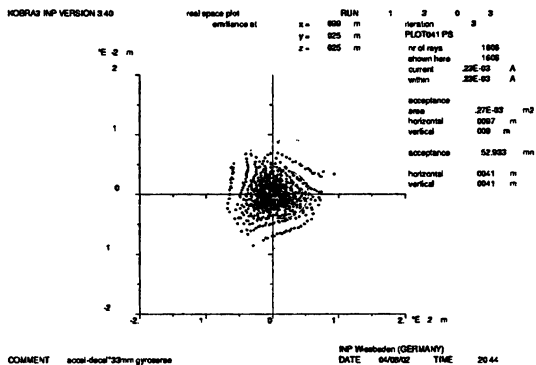
Fig. 3. Beam shape calculated with the KOBRA3D code
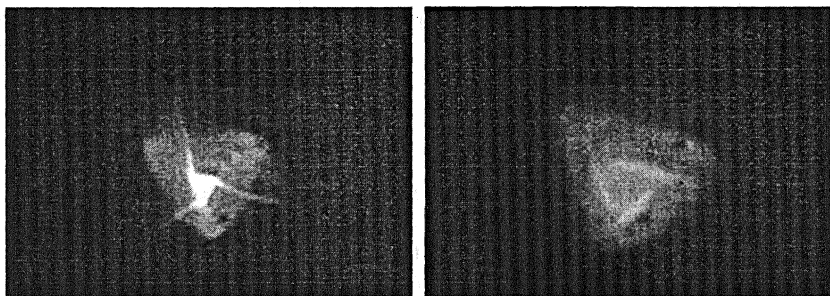
Fig. 4. Beam shape observed over a viewer located in the beamline, corresponding to operations with slightly separated frequencies

The insulator aging is also present, as the lifetime of the insulator located between the cryostat and the plasma chamber is one of the major parameters affecting the reliability of a superconducting ECR source.

4. Frequency tuning effects

Figure 4 shows that a minor change of frequency takes to relevant modification of the beam shape and current distribution in the space. A similar result was obtained either on the beam current measured over the Faraday cup by changing the frequency and it is described in Fig. 5.
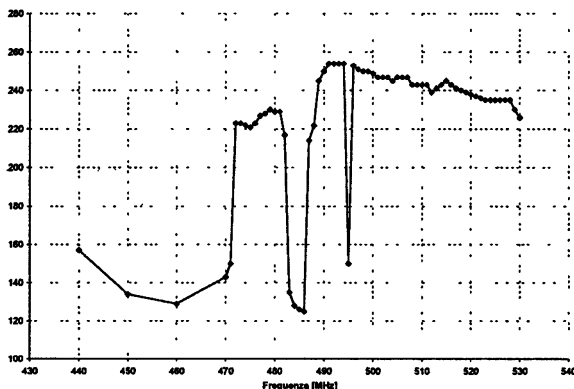
Fig. 5. Beam current vs. the frequency between 14.44 and 14.53 GHz

This effect that we called "frequency tuning effect" in 2005 can be explained roughly in the following terms: as the ECRIS plasma chamber is a multimode resonant cavity, when the microwave frequency increases, the number of excited mode increases too, so that the change of electromagnetic field pattern takes to a change of the beam distribution at the plasma meniscus, where the beam is created.

A little bit more complicated description was considered recently. The ECRIS behaviour and the plasma formation mechanism are strongly affected by frequency and power of the electromagnetic wave feeding the plasma chamber, that requires a careful study with up-to-date computer code. As a first approach to the study, a lossless empty cylindrical cavity (with the dimensions of the SERSE plasma chamber, i.e. 6.5 cm radius and 45 cm length) was considered, fed by a WR62 rectangular waveguide placed off axis on the cavity base and excited on the first mode. A discrete number of modes can exist inside the chamber, each characterized by its resonant frequency; the density of modes rises with the frequency.

The study of the formation of modes inside the multimodal cavity was experimentally verified [5] and the pictures in Fig. 6 help us to understand how the

frequency changes modify the electron energy and finally the ability to produce ions. In these figures the minima and maxima of the electric field in the plasma chamber section are given; it is evident that the presence of high accelerating field in the ECR resonance region permits a better transmission of energy between the microwave field and the electrons of the plasma, that is further affected by the field gradient in the same region. The increase of electron energy for the different modes may change by one order of magnitude with minor changes of frequency.

$TM_{6\ 3\ 19}$, f_{res} = 13994 593 MHz, E_{max} = 0 282 V/m
$TM_{5\ 4\ 4}$, f_{res} = 13995 993 MHz, E_{max} = 0 798 V/m
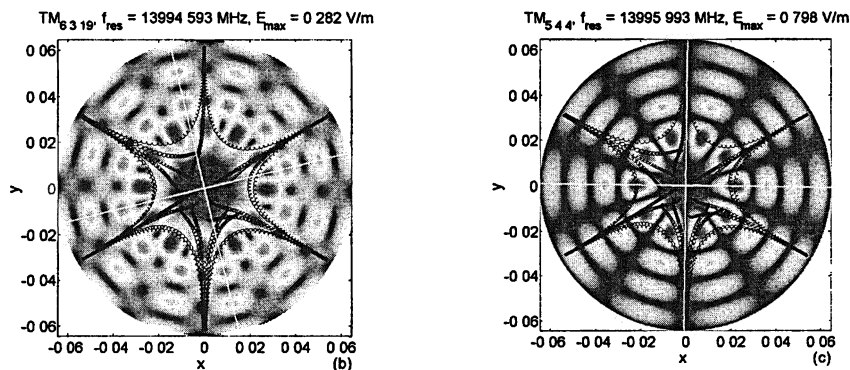
Fig. 6. Modulus of the electric field without the term $\{1/[1-(w/w_{n\ nr})^2]\}$ in the plane $z = L/2$ for modes close to 14 GHz. The star-shaped pattern represents the trajectory of an electron moving under the action of the magnetostatic field only

The electron dynamics is determined by the electromagnetic field pattern which in turns is modified by the electromagnetic field propagation. The electron cyclotron resonance heating (ECRH) and the ionization process was demonstrated to depend on the electromagnetic field distribution and on its value over the resonance surface.

5. MS-ECRIS and 3rd generation ECRIS

Different ECRIS that can be considered as 3rd generation ECRIS have been built in the last few years, some of them already working as the VENUS source of LBNL, which is the best ECRIS for highly charged ions [4], other in the commissioning phase. Between them, we will describe here the MS-ECRIS source [6], funded by the European Union in the framework of the EURONS JRA07-ISIBHI initiative, which magnetic trap has the highest design values to date, to get an optimum confinement for 28 GHz or higher frequency. Its design is open to be adapted to the major accelerators in Europe; the main parameters are given in table 1 and compared to the ones of the SERSE source, which is the parent project.

448

Table 1. Main features of MS-ECRIS

F	18 GHz	28 GHz
B_{radial}	1.55 T	2.7 T
B_{inj}	2.7 T	4.5 T
B_{ext}	1.6 T	3.2 T
$\Phi_{chamber}$	130 mm	180 mm
$L_{chamber}$	550 mm	650 mm
$\Phi_{cryostat}$	1000 mm	1100 mm
$L_{cryostat}$	1310 mm	1700 mm
V_{extr}	20–25 kV	40 to 60 kV
O^{8+}	~7 pµA	~20 to 50 pµA
Xe^{20+}	–	> 50 pµA
Pb^{27+}	–	> 40 pµA

With respect to SERSE it will have the advantage of a LHe-free cryostat (served by two 1.5 W cryocoolers) and of a much more complex plasma chamber, designed for 60 kV insulation, for the management of 10 kW microwave power and including also a X-ray tantalum shield to prevent the LHe boil-off experienced in previous experiments. As for the case of SERSE, particular care was given to the design of the hexapolar coils, not only in terms of stability versus quench, but also in terms of uniformity for different azimuth, which is important to avoid preferential loss paths for the electrons and to keep the plasma stable. The possibility to get a last closed ECR surface inside the plasma chamber with a value close to 3 T may permit even the coupling of higher frequency microwave generators, up to 37 GHz, or even 56 GHz, with a modest confinement. The design of MS-ECRIS (Fig. 7) has taken benefit of the experience with the SERSE source [7] and of the GyroSERSE project [8]. A description of the source design was presented in [9].
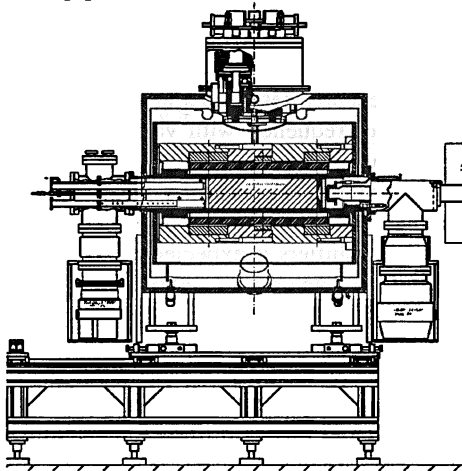
Fig. 7. A layout of MS-ECRIS with cryostat and support

The cryostat warm bore has a inner diameter of 202 mm, able to host a 180 mm plasma chamber. The plasma chamber size is relevant to increase the ion confinement time and finally the achievable charge states. Another key point is the magnets' reliability. The choice of small section wires (simple for the solenoid, ribbon-linked for the hexapole) permits to keep the current low for all the magnets (about 50 % of the critical current for the hexapole and 40 % for the solenoids). The quench detection system (QDS) is designed to switch off the magnets in case of a quench; cold diodes will keep a high level of safety. An additional heat load of 500 mW was considered to take into account the X-rays flux.

The microwave system will be based on a gyrotron (28 GHz–10 kW) followed by an arc detector, a bi-directional coupler and a mode filter before the TE_{02} to TE_{01} converter; then a 90° corrugated bend follows which avoids higher order mode excitation and also acts as an additional mode damper; a straight waveguide and a mechanical compensator takes close to the source where a dc break designed for 60 kV insulation is placed, followed by a watercooled vacuum window. The biased disk is located on the axis and the oven is placed on the lower part that is not much affected by electrons coming from the plasma. Room for plasma diagnostics is left on the right side, away from the plasma leakage path.

A 1000 l/s turbomolecular pump at the injection side and a 2000 l/s turbomolecular pump at the extraction side will be able to maintain the pressure in the order of 10^{-8} mbar. The extraction system consists of the plasma electrode, fixed to the chamber and cooled by contact with the wall, and of a movable system made by the puller and ground electrode that may be shifted over 80 mm, to optimize the watercooled puller position. Information on the other 3rd generation ECRIS are given in [10].

6. Future perspectives

The experiences described above and in [11] opened a new domain to the future experiments; we have recently designed a new system able to inject simultaneously different microwave frequency with variable phase, in order to verify experimentally the results of our simulations, stating that a further increase of performance of ECR ion sources is obtained when th plasma is excited by "Multi-Frequency Heating". These technique is not new but the availability of simulation tools and of phase shifters is expected to boost the improvements that are nowadays driven by the 'trial and error' method.

The preliminary results of our simulations show that a large increase of the electrons confinement is achieved through the so-called 'plug effect' and that will allow a strong increase of the beam current for the highly charged heavy ions that are interesting for the nuclear physics.

The use of phase shifters and traveling wave tube amplifiers (TWTA) is also expected to change the EEDF (electron energy distribution function) so that it is

essential to add in the next future a proper X-ray diagnostics, as it was done in the experiment on the study of the ECR heating with the VENUS source in Berkeley [12]. This will permit to act on the optimization of the EEDF and finally to get a significant increase of the extracted beam current, especially for the highest charge states. In the case of the VENUS source, the increase of highly charged ions current, described in table 2, was limited by the occurrence of X-rays generation and the related liquid Helium boil-off. We expect that a better coupling of microwave to the plasma may limit this phenomenon and permit to increase the current significantly.

In order to perform the multiple injection of microwaves into an ECR ion source, the use of different microwave generators each of them responsible to amplify a single component is ideally needed: the electromagnetic wave may be fed to the ion source through a single port, by means of an external mixer, or through different ports. Alternatively, the use of a single microwave generator and then of one microwave port for the amplification of the whole signal is viable.

Table 2. Highest current achieved for Kr and Xe during the LNS-LBNL experiment with the VENUS source in 2006 [12]

Kr	I [mA]	Xe	I [mA]
24^+	192	30^+	98
25^+	223	31^+	80
27^+	88	33^+	61
28^+	25	34^+	42
29^+	5	35^+	28
		36^+	19
		37^+	12
		38^+	7

Certainly the use of different microwave generators (klystron or TWTA) each one responsible of the amplification of a single frequency can permit to provide more power to the ECR plasma, but the external mixer should be able to withstand high power and will limit the number of microwaves that can be mixed to two or three for each microwave port. In all the cases we should take into account the different coupling for each microwave port (S parameter characterization) and for each frequency used.

Klystron or TWTA may be used with the only constraint that for the first type of generator features a bandwidth in the order of 80 MHz, while in the second case the bandwidth is at least in the order of 1 GHz.

Therefore, the choice to use a TWTA is certainly more appealing and consists to use only one generator to amplify the signal generated by different oscillators or frequency synthesizers.

An important point is the power control relative to each carrier; certainly the use of a high power klystron could overcome the problem but with the great constraint of a too small frequency bandwidth which can be studied. The use of a 1 kW broadband TWT, 18 GHz, could be the correct compromise.

A first attempt will be done soon with the hardware already present at LNS. A scheme of the apparatus is shown in Fig. 8.

Fig. 8. Simplified scheme of the proposed microwave injection system

The signal generators (DROs, Frequency synthesizers) provides the required frequencies f_1, f_2, ...,f_n; the relative phases φ_1, φ_2, ..., φ_n and amplitudes A_1, A_2, ..., A_n can be changed by means of frequency shifters and variable attenuators. The signals are then added and the resulting signal is amplified.

In order to operate at 28 GHz or above, the construction of a gyroTWT must be considered; while costs and schedule of such a device cannot be determined easily, an easy evaluation of the performance of a source driven by such machine can be achieved. For 28 GHz operation, the level of 0.5 or 0.7 mA produced for medium charge states of heavy ions was almost achieved. So we can expect to produce current of $2 \div 5$ mA over each charge state around 20+ for Xenon and 12+ for Argon, as the electron density is expected to increase by a factor four, and further improvements will be obtained by the higher available power and by the better microwave coupling.

While this kind of study is essential to have a fruitful operation with existing 2nd and 3rd generation and beyond, some preliminary studies have been carried out starting on the consideration that the effectiveness of the scaling laws and High B mode at 28 GHz suggests that no limitations to higher frequencies exist except for the availability of adequate magnets and RF generators. These consideration takes to the design of a $56 \div 60$ GHz "dream machine" ($B_{ECR} = 2$ T), with an axial field of 6 to 8 T and a radial field of 4 T [13].

A similar machine, with a modest confinement, can profit of the condition $I^{q+} \sim n_e/\tau_i$ if there is enough RF power to sustain a lossy plasma. By relaxing the trapping constraints, the lost electrons must be replaced by other electrons that should be heated in a short time (i.e. electric field at the resonance must be large).

The dream machines is anyway limited by the ability to reach such a high field that is not obtainable by means of NbTi superconducting wires magnets. High critical temperature superconductors are not a solution in the mid-term, as their stability and the possibility to permit industrial design is not yet established. Bi-2212 may be a solution for higher fields in the long term. MgB_2 is also a possible candidate and the research in the field is active because of the cheap investment necessary.

Nb_3Sn seems to be the best candidate, as it has increased the range of values attainable for accelerator magnets, e.g. for LHC dipoles the maximum field of 9.7 T for NbTi magnets was increased to 15.3 T. But on the other side, the B-minimum trap of an ECRIS is quite challenging in terms of the forces/stresses

452

containment and it is not evident that Nb_3Sn may be so robust and so flexible at the same time.

In summary, the feasibility of a 4th generation ECRIS magnetic system is highly questionable, so that further improvements on ECRIS performances may come rather from a better knowledge of microwave-plasma coupling in ECRIS devices than from a technological improvement.

Table 3. Specification of the broadband microwave amplifier

Parameter	Value
Center frequency	28 GHz
Bandwidth (–1 dB)	1 GHz
Minimum output power	10 kW
Maximum reflected power	2 kW
Operating mode	Continuous wave or pulsed

One of the solutions that we plan to adopt in the future is the use of an "ad-hoc" microwave generator, based on gyroTWT, which characteristics are summarized in table 3.

References

1   *Geller R et al.* The Grenoble ECRIS status 1987 and proposal for ECRIS scaling, Proc. 8th Int. workshop on ECR ion sources, East Lansing, NSCL report #MSUCP-47 (1987).

2. *Ciavola G., Gammino S.,* Rev. Sci. Instr. 63(4), 2881 (1992).

3. *Gammino S., Ciavola G* ECR ion sources and scaling laws, 14th Int. Conf. on Cyclotrons & Applications, Capetown, Sudafrica, World Scientific, Singapore, 377 (1995).

4. *Leitner D. et al.* Rev. Sci. Instr. 77, 03A302 (2006).

5. *Celona L et al.* On the observation of standing waves in cylindrical cavities filled by microwave discharge plasmas, Proc. 18th Workshop on ECR ion Sources, Chicago (2008), to be published.

6. *Ciavola G. et al.* Rev Sci. Instr 79, 02A326 (2008).

7. *Gammino S., Ciavola G.* Rev. Sci. Instr. 71(2), 631 (2000).

8. *Gammino S. et al.* GyroSERSE, a new superconducting ECRIS, Proc. 15th Int. workshop on ECR ion sources, Jyvaskyla, 17 (2002).

9. *Ciavola G et al* High Energy Physics and Nuclear Physics, 31(S1): 13 (2007)

10. *Celona L., Gammino S., Ciavola G.* Nucl Instr. & Meth B261, 1023 (2007).

11 *Gammino S. et al* IEEE Trans. on Plasma Science, 36, 1552 (2008).

12. *Gammino S. et al.* Highly charged ion production and X-ray measurements with the VENUS source at LBNL, LNS report 15.5.2007.

13 *Prestemon S et al* Design of a Nb_3Sn magnet for a 4th generation ECR ion source, Proc. Int. Conf on Applied Supercond., Chicago (2008), to be published.

453

NANO- AND MICROCRYSTALLINE DIAMOND GROWN IN MILLIMETER WAVE CVD REACTOR

A. L. Vikharev, A. M. Gorbachev, A. V. Kozlov,
D. B. Radishev, A. B. Muchnikov

Institute of Applied Physics RAS, Nizhny Novgorod, Russia

The paper reviews the results of investigations of nanocrystalline and microcrystalline diamond film deposition in novel microwave plasma-assisted CVD reactor based on 10 kW gyrotron operating at frequency 30 GHz. The growth rate of diamond films, their quality and morphology at wide variation of process parameters (methane concentration, gas pressure, substrate temperature, microwave power) in gas mixture Ar/H2/CH4 were investigated. For understanding of growth conditions the investigations of the plasma parameters (electron density and gas temperature) in this CVD reactor are presented.

1. Introduction

Diamond films growth using the method of microwave plasma-assisted chemical vapor deposition (MPACVD) is now becoming more and more widely used [1, 2]. In MPACVD reactors the plasma is maintained in H_2-CH_4 gas mixture by microwave radiation that has frequency of 2.45 GHz or 915 MHz [3–5]. In these resonance-type reactors high quality diamond films (having high thermal conductivity and well-faceted microcrystallines) are grown at a not high rate 1–2 micron per hour.

Many attempts have been made to deposit microcrystalline diamond (MCD) having high quality and high growth rate simultaneously. For this purpose the addition of argon to H_2-CH_4 feed gas was used [6–10]. It has been found that in Ar-H_2-CH_4 gas mixture there is the optimal Ar concentration when the growth rate of microcrystalline diamond is enhanced. In those experiments the increases of growth rates were 1.5–2 times in comparison with the use of the H_2-CH_4 feed gas due to the fact that the argon can effectively increase the electron density of the plasma [6, 7].

Recently high-electron-density plasma generated by the millimeter-wave radiation of gyrotron was also suggested for enhanced-growth-rate CVD [11]. Due to a higher frequency of the microwave radiation in the novel CVD reactor, the plasma produced near the substrate has higher electron density, and, correspondingly, higher density of radicals and atomic hydrogen, thus providing a higher rate of the diamond film growth as compared to the traditional plasma reactors with a microwave discharge at 2.45 GHz frequency.

In this paper the results of investigations of nanocrystalline and microcrystalline diamond film deposition in the millimeter wave plasma-assisted CVD reactor based on 10 kW gyrotron operating at frequency 30 GHz are presented. Microcrystalline diamond films were grown on silicon substrates with 60–75 mm diameter. The growth rate of diamond films, their quality and morphology at

wide variation of process parameters (gas pressure, substrate temperature, microwave power) in gas mixtures Ar-H_2-CH_4 were investigated. Diamond films were deposited for CH_4 concentrations (CH_4/H_2) between 1 % and 10 % and Ar concentrations (Ar/H_2+Ar) between 50 % and 75 %. The diamond quality was characterized using Raman Spectroscopy and Atomic Force Microscopy. For understanding of growth conditions the investigations of the plasma parameters (electron density and gas temperature) in the novel CVD reactor are presented.

2. Method of high-rate diamond growth

The growth rate of microcrystalline diamond film in MPACVD reactor is determined by the values of concentrations of carbon-containing radicals and hydrogen atoms near the substrate [2]. According to results obtained in the papers [12, 13], the growth rate G and relative defect density X_{def} (that determines film quality) may be estimated by the following formulae:

$$G \propto \frac{[CH_3]_{sur}[H]_{sur}}{3 \cdot 10^{15}\,cm^{-3} + [H]_{sur}}, \qquad X_{def} \propto \frac{G}{[H]_{sur}^2}. \qquad (1)$$

Here, $[H]_{sur}$ is the atomic hydrogen concentration and $[CH_3]_{sur}$ is the methyl concentration at the substrate surface. Often the gas-phase reaction, $CH_4 + H \leftrightarrow CH_3 + H_2$, is rapid and close to partial equilibrium [12], therefore the methyl concentration is coupled chemically to atomic hydrogen. Thus, the diamond film quality and growth rate are determined by density of atomic hydrogen at the substrate surface.

The main channel for dissociation of hydrogen molecules in MPACVD reactors, even at high temperatures of the gas ($T_g \sim 3000$–3200 K) is dissociation by an electron impact [14]. Therefore, an increase in the value of electron density, N_e, in the plasma of a CVD reactor should result in a higher density of atomic hydrogen.

The value of electron density N_e in the plasma maintained by the microwave field in resonance-type reactors [3–5] grows up to the point, at which the nonlinear effect of microwave field skinning starts to manifest itself. So, the characteristic dimension of the plasma at the substrate in a reactor is equal approximately to the depth of the skin layer. In the case of the parameters used traditionally in MPACVD reactors (gas temperature $T_g \sim 2700$–3000 K depending on the specific power absorbed into the plasma, and the initial pressure of the gas mixture 50–200 Torr) the density of the gas near the substrate corresponds to the minimum of the Pashen curve for maintenance of a continuous microwave discharge [15], at which the electron collision frequency is of the order of the wave frequency. Under the conditions when $\nu \geq \omega$ and $N_e \leq N_{c0}\nu/\omega$ the depth of the skin layer is equal to

$$\delta \approx 2(c/\omega)(N_{c0}/N_e)[(\omega^2 + \nu^2)/\omega\nu], \qquad (2)$$

where $N_{c0} = m\omega^2 / 4\pi e^2$ is the critical density, ω is the wave frequency, ν is the electron collision frequency with neutral particles, and m and e are mass and charge of electrons, respectively. At a fixed depth of the skin layer (e.g. for resonance-type reactors this value is of the order of $\delta = \delta_0 \approx 1 \div 2$ cm) from the above relation for δ we obtain that the value of electron density in the plasma is proportional to the frequency of the microwave radiation:

$$N_e \propto N_{c0}(c/\delta_0\omega)[(\omega^2 + \nu^2)/\omega\nu] \propto \omega. \tag{3}$$

Hence, the densities of both the electrons and radicals in non-equilibrium plasma of MPACVD reactors may be increased with an increase in the frequency of microwave power.

The above estimates show that the microwave radiation of shorter-wave bands (centimetre and millimetre wavelength bands) allow to obtain a higher electron density and a higher specific power absorbed into the plasma, correspondingly, higher density of radicals and atomic hydrogen than that used traditionally (decimetre wavelength band). It will provide a higher rate of the diamond film growth as compared to the traditional plasma reactors with a microwave discharge.

It should be mentioned that in resonance-type CVD reactor at frequency of 2.45 GHz the increasing the specific power in the plasma can be also obtain by the increasing the gas pressure (for a constant microwave radiation power) but it leads to a decrease in the discharge volume [16]. Nevertheless microcrystalline diamond synthesis at high rates was achieved in 2.45 GHz CVD reactor at high gas pressure and at small deposition area (less than 1 cm^2), Fig. 1 [17].
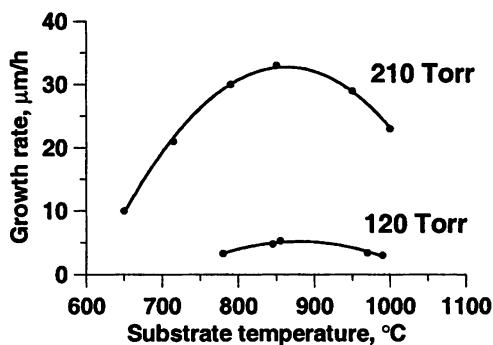
Fig. 1. Dependence of the growth rate of diamond film on the substrate temperature for a microwave radiation at frequency of 2.45 GHz, power of 3 kW and pressures 120 and 210 Torr

As it has been shown in paper [11], in the developed millimeter wave plasma-assisted CVD reactor based on gyrotron the high specific power in plasma can be obtained and consequently high rate diamond growth can be achieved over a larger area (more than 100 cm^2) in comparison with 2.45 GHz CVD reactor.

456

3. Millimeter wave plasma-assisted CVD reactor

Generation of the plasma over large area substrate using short-wave microwave radiation with higher frequency than 2.45 GHz can be realized only with the use of an electrodynamic system of the quasi-optical type. Figure 2 shows a general schematic diagram of the developed 30 GHz gyrotron-based system for diamond film deposition [11]. The steady-state microwave discharge is sustained in a region where four wave beams are intersecting under the substrate and where the area of enhanced field intensity is formed. In this system the four focusing mirrors (*1*) direct the microwave radiation into the area over the substrate (*5*), near which the plasma is maintained. In its turn, the radiation is transferred to mirrors (*1*) by means of the system of mirrors (*2*) and (*3*). Formation of four coherent beams takes place at the output from the oversized square waveguide (*4*) due to the effect of image multiplication during propagation of an electromagnetic wave [11]. The quasi-Gaussian beam is delivered to the input of waveguide (*4*) from an oversized circular waveguide with a corrugation surface (*7*). Such a waveguide provides propagation of an electromagnetic wave with the nearly Gaussian transverse distribution of the field. In its turn, the linearly polarized microwave radiation from the gyrotron (*9*) in the form of a Gaussian beam is sent to the input of this waveguide (*7*) by means of mirrors (*10*) and (*11*).

Fig. 2. Schematic diagrams of the gyrotron-based system and the plasma reactor: *1* – top focusing mirrors, *2* – bottom focusing mirrors, *3* – plane mirrors, *4* – wave beam spliter, *5* – substrate holder, *6* – discharge plasma, *7* – circular corrugated waveguide, *8* – mitre bend, *9* – gyrotron, *10* and *11* – mode converter into a Gaussian beam
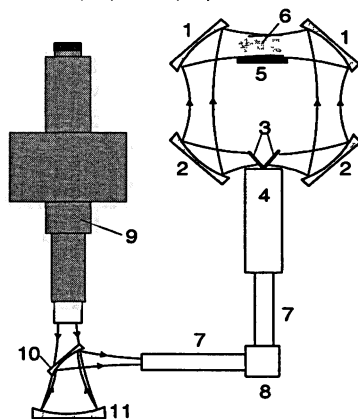
The investigation of diamond film deposition in the gas mixture Ar-H$_2$-CH$_4$ was carried out at wide variation of process parameters. It is well known that in the gas mixture Ar-H$_2$-CH$_4$ it is possible to grow microcrystalline (MCD) as well as nanocrystalline (NCD) diamond films by varying the content of argon in the mixture [18]. The influence of argon on the MCD growth is the greatest when the argon density ranges from 40 % to 75 % [6–10]. Therefore in our experiments the content of methane (CH$_4$/H$_2$) in the gas mixtures is varied in the range from 1 % to 10 %, and that of argon (Ar/H$_2$+Ar) from 50 % to 75 %, while the total gas flow was 400 sccm. The 30 GHz CVD reactor was operated across a range of

the gas pressure from 100–400 Torr and input microwave power from 4 to 10 kW. At all gas pressures the microwave discharge has a disk shape with a diameter equal to the substrate diameter and a thickness of 1.5–2 cm. Such a shape of the discharge makes it possible to achieve sufficiently high microwave energy input into the discharge plasma.

Diamond films were grown on 2 mm thick (100) oriented silicon with 60–75 mm diameter. The substrate temperature was measured by an optical pyrometer. Before deposition process the silicon substrates were mechanically seeded with a 2 μm diamond powder. Typical deposition times were 6–8 hours.

4. Results of diamond deposition in 30 GHz CVD reactor

Two series of experiments with the three-component gas mixture were performed [19]. In the first series, the methane content was changed while the Ar/H$_2$+Ar ratio was fixed. In the second series, the methane content (the CH$_4$/H$_2$ ratio) was fixed, and the argon content in the mixture varied. In these experiments, the substrate temperature was from 850 to 900 °C and the gas pressure was 150 Torr. Figure 3 shows microphotographs of the diamond films grown at different CH$_4$ concentrations and 50 % Ar concentration.

Microphotogragns shown in Fig. 3 demonstrate the changes in the surface morphology of the films with increasing the methane concentration. There is a narrow composition range CH$_4$/H$_2$ = 1.5–4.5 % in which MCD is grown. For CH$_4$ concentration below 1.5 % NCD is deposited. For CH$_4$ concentration above 4.5 % the ballas diamond (half-spherical polycrystalline diamond often termed as cauliflower) is observed.
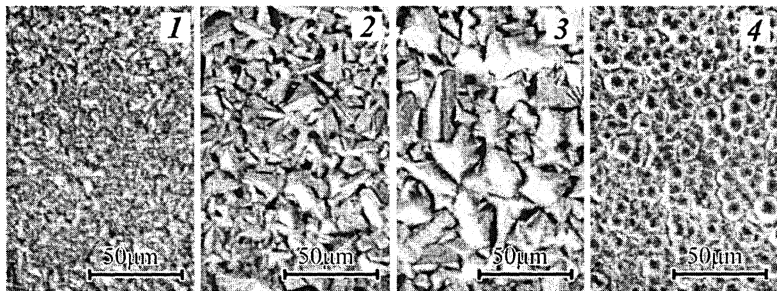
Fig. 3. Microphotographs of the surface of the as-grown diamond films deposited at 50 % Ar concentration and at various CH$_4$ concentration: *1* – 1 %, *2* – 2 %, *3* – 4 %, *4* – 5 %

For these deposited films the average growth rates were determined based on the data about the mass of the films under the assumption that the film thickness is equal across the substrate surface. The growth rate is compared with respect to the variation of the methane concentration in Fig. 4. It shows a linear increasing trend with increasing CH$_4$ concentration for MCD films.

Fig. 4. Variations of the growth rates of diamond films versus the CH_4 content at 50 % Ar concentration and pressure 150 Torr
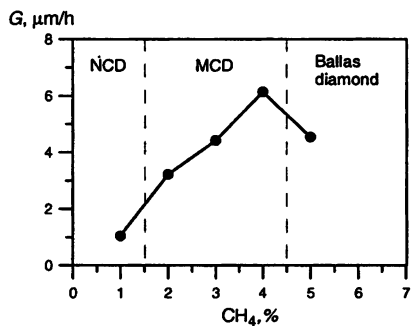
The second set of experiments was carried out varying the Ar concentration at defined value of CH_4/H_2 at which MCD is grown. It was found that the grain size of the microcrystalline films increases with decreasing of the Ar concentration in the gas mixture. Figure 5 shows the dependence of the growth rate of MCD films on the argon content in the gas mixture for two different concentrations of methane: 2 % and 4 %. As seen from the Figure, we observed an increase in the rate of the diamond film growth, as the argon content decreased and, correspondingly, the concentration of hydrogen in the working mixture increased. The increase in the growth rate was not accompanied with deterioration of the quality of the diamond film, as it was studied using Raman scattering spectra.
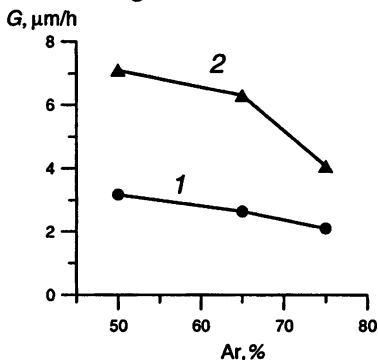
Fig. 5. Growth rate of MCD films versus Ar content at the CH_4 concentration: $1 - 2$ %, $2 - 4$ %, pressure 150 Torr.

The value of the gas pressure also influenced the rate of the MCD film growth significantly. Figure 6 shows the diamond film growth rate as a function of the methane content for two gas pressures and a 75 % concentration of argon. As seen from the Figure, a significant increase in the rate of the diamond film growth was observed for the same content of the gas mixture.

Having performed a series of experiments aimed at determining the optimal regimes for growing MCD films in the Ar-H_2-CH_4 mixture, we grew a disk of microcrystalline diamond 0.65 mm thick and 75 mm in diameter by making the reactor working continuously for 130 hours. The general view of the disk without the silicon substrate is shown in Fig. 7. As seen from the Figure, the diamond disk has good optical transparency and high homogeneity along its thickness. This made is possible to determine the average growth rate based on measuring the weight of the diamond disk. The linear rate of the growth of the diamond disk was 5 microns per hour.

459
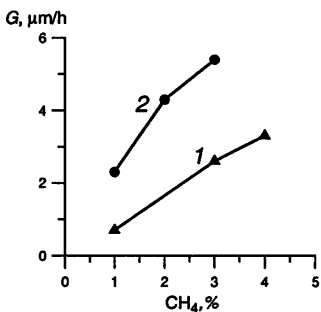
Fig. 6. Growth rate of MCD films versus CH₄ content at different pressure: 1 – 150, 2 – 200 Torr, 75 % Ar concentration.
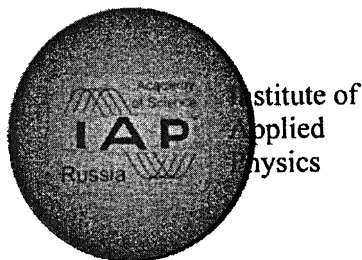
Fig. 7. Photograph of the free-standing diamond disk of 0.65 mm thickness and 75 mm in diameter from the nucleation side

The grown microcrystalline diamond disk was used to study the structure of the surface and the quality of the obtained diamond. Microphotographs of the surface and the spectrum of Raman scattering at the centre and near the edge of the disk are shown in Fig. 8. It is seen from the Raman spectrum that the disk contains insignificant amounts of the graphite phase.
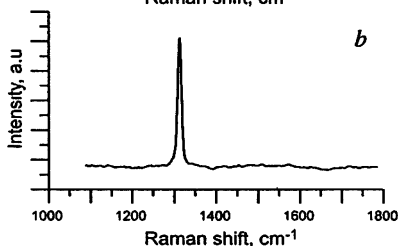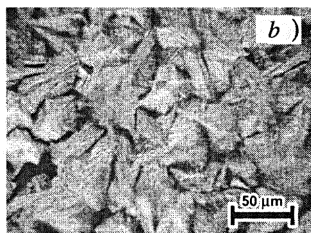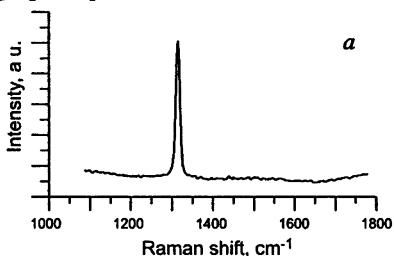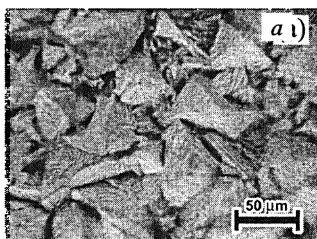
Fig. 8. Raman scattering spectra and microphotographs of the surface of diamond disk at the center (*a*) and at the periphery (*b*)

5. Plasma parameters in 30 GHz and 2.45 GHz CVD reactors

For understanding of high growth rate of MCD films the investigations of the plasma parameters (electron density and gas temperature) in millimeter wave plasma-assisted CVD reactor were made [19]. Gas kinetic temperature and electrons concentration and their dependence of external parameters – incident microwave power, operating pressure and gas mixture composition were studied by method of optical emission spectroscopy.

Light emitted from plasma is collected with a quartz short-focus lens and focused into a optical fiber. Emission is then delivered into Jobin Yvon FHR-1000 spectrometer, spectrum is acquired with thermoelectrically cooled Jobin Yvon CCD head connected to spectrometer, and recorded on a computer.

For measurements of kinetic gas temperature (T_g) in carbon-containing plasmas it is optimal for several reasons to use emission spectrum of $d^3\Pi_g \rightarrow a^3\Pi_u$ transition (Swan band) of C_2 radical, with well studied and easy to analyze rotational structure. To evaluate temperature from the spectrum, we perform fitting of experimental data with calculated spectrum. Necessary constants to calculate rotational spectrum of C_2 molecule were taken from [20, 21], instrumental profile of spectrometer, required for fitting, was measured using He-Ne laser and then approximated. Measurements of gas temperature were performed in gas mixture Ar-H_2-CH_4 at different external parameters. Dependence of gas temperature on gas pressure in this gas mixture is shown on Fig. 9.
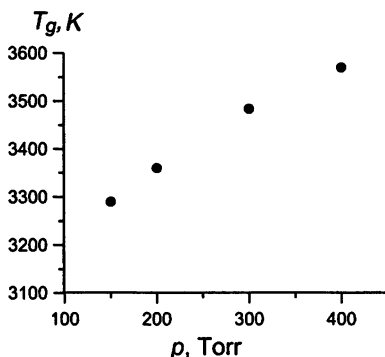
Fig. 9. Dependence of gas temperature (T_g) on gas pressure (p) at 65 % Ar, 2 % CH_4 concentrations and at 8 kW incident microwave power

In plasma-assisted 2.45 GHz CVD reactor gas temperature demonstrates another dependence´on gas pressure. Figure 10 shows how the experimental and calculated gas temperatures depend on the gas pressure in a continuous microwave discharge produced in a cavity at the frequency of 2.45 GHz. The calculations [22] were performed taking into account the energy losses due to hydrogen dissociation, the calculated gas temperature at high pressures is in a good agree-

461

ment with the experimental data. We can see that, this energy loss mechanism is so efficient that it limits the gas temperature at a level of 2500–2700 K.

Second parameter investigated in millimeter wave plasma-assisted CVD reactor was electron concentration [19]. To obtain electron concentration we utilize the effect of Stark broadening of Balmer series of atomic hydrogen emission lines (H_α, H_β, H_γ). Width of Stark broadening heavily depends on electron concentration, which allows evaluating electron concentration from measured spectral profiles of atomic hydrogen lines. Well known that experimentally measured spectral profiles are a convolution of three different profiles: Stark broadening profile, Doppler broadening profile, and an instrumental function of spectrometer. Therefore we evaluate electron concentration from experimental spectra using the following procedure.
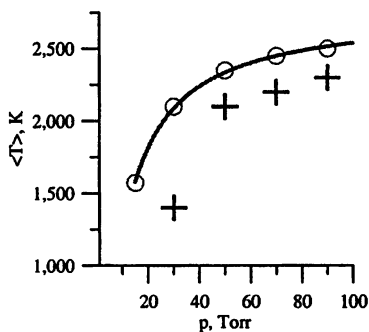
Fig. 10. Gas temperature vs. gas pressure in a continuous discharge at an absorbed microwave power of 1.5 kW: experimental data (+) and results of calculations (o)

First, the gas kinetic temperature was obtained from spectrum of C_2 Swan rotational distribution. Using this temperature, the Doppler broadening profile for given temperature was calculated [23]. Then, the instrumental profile for FHR-1000 spectrometer at given wavelength was approximated. After that, we use information presented in the paper [24] to generate Stark-broadened profiles for selected Balmer line using FWHA (full width half area) as the parameter for generation, numerically convolve this profile with Doppler profile and then with instrumental profile, and vary FWHA parameter until we find closest fit of the experimental data. After that, electron concentration is easily obtained from FWHA of Balmer line using plots and tables from [24]. We use FWHA instead of FWHM (full width half maximum), since according to [24] FWHA has much less dependence on electron temperature and heavy particle mass then FWHM, and therefore gives more accurate values for electron concentration.

Electron concentration measurements were performed in gas mixture Ar-H_2-CH_4 at different external parameters. Dependence of electron concentration on gas pressure in this gas mixture is shown on Fig. 11. It can be seen that the increase of gas pressure leads to increase of both gas temperature and electron concentration, possibly due to increase of specific power absorbed in plasma.

In plasma-assisted 2.45 GHz CVD reactor an electron concentration is sufficiently less than in millimeter wave plasma-assisted CVD reactor. The electron density in a continuous microwave discharge produced in a cavity at the frequency of 2.45 GHz was measured at moderate pressure 5–60 Torr using a millimeter wave open resonator technique [25]. Figure 12 shows the dependence of electron density on gas pressure for both hydrogen and the hydrogen-methane mixture discharges at an absorbed power of 400 W.
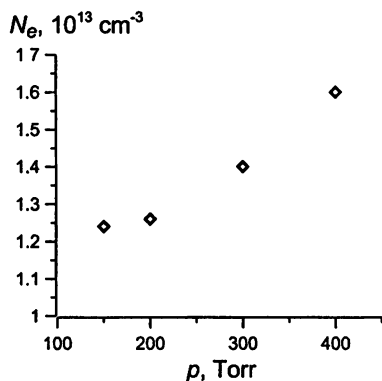
Fig. 11. Dependence of electron concentration (N_e) on gas pressure (p) at 65 % Ar, 2 % CH_4 concentrations and at 8 kW incident microwave power
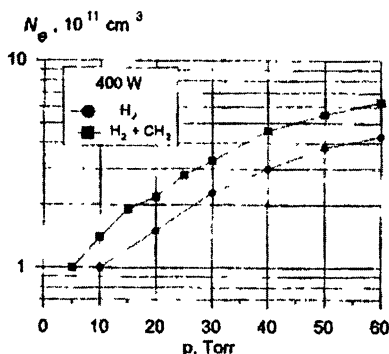
Fig. 12. Dependence of electron density on total gas pressure in hydrogen and in hydrogen-methane mixture at microwave power of 400 W

6. Conclusion

Application of non-equilibrium plasma with high electron density generated by microwaves with frequency that is much higher than frequency of 2.45 GHz is suggested for diamond deposition with high rates and over large area substrates simultaneously. In research plasma-assisted CVD reactor based on a 10 kW gyrotron operating at frequency 30 GHz the four crossing wave beams were used for maintaining a stable localized plasma layer over large area. The addition of argon to the H_2-CH_4 feed gas and the high-electron density plasma generated by the millimeter wave power were used to deposit high-quality microcrystalline diamond (MCD) films. For the Ar-H_2-CH_4 gas mixture, there is a range of gas content parameters, within which MCD films grow and have high quality and a high growth rate simultaneously.

When the gas mixture content is retained, the rate of the MCD film growth increases as the gas pressure grows within the range from 100 to 400 Torr in accordance with the strong growing dependence of the electron concentration on the gas pressure in the microwave discharge of a 30 GHz gyrotron-based CVD reactor.

In research 30 GHz CVD reactor microcrystalline diamond films were grown with deposition rate up to 15 micron per hour on silicon substrate of 60–75 mm in diameter. The optical transparent diamond disks were deposited at growth rates 5–10 micron per hour.

Acknowledgements

References

1. *Bachmann P. K. //* Prelas M. A , Popovici G , Bigelow L. K (Eds.), Handbook of Industrial Diamonds and Diamond Films, Marcel Dekker, New York, 1998. P. 821.
2. *Grotjohn T. A and Asmussen J. //* Asmussen J., Reinhard D. K. (Eds.), Diamond Films Handbook, Marcel Dekker, New York, 2001. P. 211.
3. *Asmussen J. //* High Density Plasma Sources / Ed. by O. A. Popov. Park Ridge, NJ: Noyes, 1995 P. 251.
4. *Funer M., Wild C., Koidl P.* Appl. Phys. Lett. 72, 1149 (1998)
5. *Besen M. M., Sevillano E., Smith D. K.* US Patent 5,556,475, Sep. 17, 1996.
6. *Zhu W., Inspektor A., Radzian A R., McKenna T., Messier R.* J. Appl. Phys. 68, 1489 (1990).
7. *Shih H. C., Sung C. P., Fan W. L., Hsu W. T.* Thin Solid Films, 232, 41 (1993).
8. *Zhou D., Gruen D. M., Qin L. C., McCauley T. G., Krauss A R.* J. Appl Phys. 84, 1981 (1998).
9. *Yang Tien-Syh, Lai Jir-Yon, Cheng Chia-Liang, Wong Ming-Show.* Diamond and Related Materials, 10, 2161 (2001).
10. *Han Young-Soo, Kim Yoon-Kee, Lee Jai-Young.* Thin Solid Films, 310, 39 (1997).
11. *Vikharev A. L., Gorbachev A. M., Kozlov A. V., Koldanov V. A., Litvak A. G., Ovechkin N. M., Radishev D. B., Bykov Yu. V., Caplan M.* Diamond and Related Materials, 15, 502 (2006)
12. *Goodwin D. G.* J. Appl. Phys. 74, 6888 and 6895 (1993)
13. *Goodwin D. K , Butler J. E. //* Handbook of Industrial Diamonds and Diamond Films / Ed. by M. A. Prelas, G. Popovici and L. K. Bigelow. New York; Basel; Hong Kong: Marcel Dekker, 1998. P. 527.
14. *Markelevich Yu. A., Rakhimov A. T., Suetin N. B.* Fizika Plazmy, 21, 921 (1995) (in Russian).
15. *Vikharev A. L., Ivanov O. A., Kuznetsov O. Yu., Stepanov A. N.* Sov. J. Plasma Phys. 13, 648 (1987).
16. *Vikharev A. L., Gorbachev A. M , Koldanov V. A., Radishev D. B.* Plasma Phys. Rep., 31, 376 (2005).
17. *Vikharev A. L., Gorbachev A. M., Vuchnikov A. B., Radishev D. B.* Radiophysics and Quantum Electronics, 50, 913 (2007).
18. *Gruen D. M.* Annu. Rev. Mater. Sci. 29, 211 (1999).
19. *Vikharev A. L., Gorbachev A. M., Kozlov A. V., Radishev D. B., Muchnikov A. V.* Diamond and Related Materials, 17, 1055 (2008).
20. *Prasad C. V. V., Bernath P. F.* Astrophysical Journal, 426, 812 (1994).
21. *Pellerin S , Musiol K , Motret O., Pokrzywka B., Chapelle J.* J. Phys. D Appl. Phys. 29, 2850 (1996).
22. *Koldanov V. A., Gorbachev A M., Vikharev A. L., Radishev D B* Plasma Phys. Rep. 31 (11), 965 (2005).
23. *Griem, Hans R* Spectral Line Broadening by Plasmas, 1974
24. *Gigosos M. A , Gonzalez M. A., Cardenoso V.* Spectrochimica Acta, Part B, 58, 1489 (2003).
25. *Grotjohn T. A., Asmussen J., Sivagnaname J., Story D., Vikharev A. L., Gorbachev A., Kolisko A.* Diamond and Related Materials, 9, 322 (2000).

MICROWAVE PLASMA-ASSISTED DIAMOND SYNTHESIS OVER LARGE AREAS AT HIGH RATES

T. Grotjohn[1,2], J. Asmussen[1,2], K. Hemawan[1], S. Zuo[1], D. K. Reinhard[1]

[1]Michigan State University, East Lansing, MI USA
[2]Fraunhofer Center for Coatings and Laser Applications, East Lansing, MI USA

The deposition conditions and reactor configuration for the uniform deposition of diamond across substrates with diameters of 25, 50, 75, 100, 150 and 200 mm in a microwave plasma-assisted diamond deposition process are presented. Reactor configurations operating a frequencies of 2.45 GHz and 915 MHz are studied. Types of diamond deposited include polycrystalline diamond, nanocrystalline diamond and single crystal diamond.

Introduction

Chemical vapor deposition (CVD) of diamond started by employing low power density microwave discharges/reactors (< 5 W/cm^3) that were operated at low pressures of 20–100 Torr and used input CH$_4$/H$_2$ gas mixtures that varied between 1–5 % [1, 2]. Diamond was grown with deposition rates that increased from less than a one μm/h at very low methane concentrations (< 1 %) to a maximum of a few μm/h as methane concentrations were increased to 5 %. However, high-quality films grew only under low methane input conditions (< 1 %) and as a result, diamond growth rates were very low; i.e $< \sim 1$ μm/h. During the mid 1990's and early 2000's several research groups [3–7] searched for improved diamond synthesis methods. Their experiments, which synthesized both polycrystalline and single crystal materials, utilized high power density (50–100 W/cm^3) microwave discharges operating at moderate pressures between 100–180 Torr. They found that (1) synthesis rates for both polycrystalline (PCD) and single crystalline diamond (SCD) were greatly increased and (2) the diamond quality was improved as the microwave discharge power density and process pressure were increased. In particular, good quality PCD was deposited at 4–10 μm/h [5–6] and SCD was produced at rates of 50–100 μm/h [3, 4].

Researchers now recognize [7–11] that growth rates can be increased by carrying out the deposition process above 100 Torr and by using high power density microwave discharges. It is now further speculated that by increasing the deposition pressure beyond 180 Torr and by increasing the discharge power density that the diamond growth rates can be increased considerably further while yielding high quality diamond. Thus, research groups around the world [10–14] are exploring new designs for higher pressure (> 180 Torr) and higher power density (> 150 W/cm^3) microwave plasma-assisted CVD (MPACVD) machines.

At high pressures above 100 Torr, microwave discharges in molecular gas mixtures like hydrogen have neutral gas temperatures in excess of 2500 K, contract and separate from the surrounding discharge chamber walls and they be-

come a non-uniform, intense and "arc like" discharge. Since pressure increases above 100 Torr can result in higher diamond deposition rates, it is advantageous to increase the pressure. Such increases in pressure result in gas temperature and discharge power density increases that produce a floating discharge with increased active radical plasma species that has the potential for increased growth rates. The formation of contracted and floating microwave discharges at high pressures, has been observed and studied in many experiments [15–17, 20]. These high pressure microwave discharges are thermally inhomogeneous with a hot central core and sharp thermal gradients exist between the discharge center and the surrounding walls. This inhomogeneous nature of the discharge can lead to diamond deposition rates that spatial vary across a substrate. The goal in a CVD diamond application is to control the size, the spatial location and the shape of this very hot, non-uniform discharge in such a manner to enable optimal CVD diamond synthesis. This is a formidable engineering challenge. The high pressure plasma reactors and experimental methods described below allow the spatial positioning and shaping of this thermally inhomogeneous, hot microwave discharge and thereby enable the optimization of the diamond CVD process at high pressure.

Here, we report the results of investigations that have the objective of experimentally evaluating MPCVD diamond synthesis at pressures of 70–240 Torr in both a 2.45 GHz system and a 915 MHz system with an emphasis on uniform deposition across substrates of various diameters. A specific focus is to find what size of deposition reactor and what pressure range is best to achieve uniform deposition across 25, 50, 75, 100, 150, and 200 mm diameter substrates. The experiments reported employ a specific reactor geometry [5, 6, 18, 19, 21] identified here as the microwave plasma cavity reactor (MPCR).

Experimental System
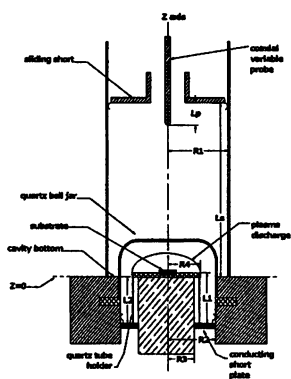
Fig. 1. Microwave plasma source reactor cross section

A cross sectional view of the MPCR is displayed in Fig. 1. It has a cylindrical structure that is axially aligned along the z-axis and the applicator geometry is φ symmetric about the z-axis. Microwave energy is introduced into the applicator via the length variable coaxial coupling probe that is located in the center of the length variable, "sliding short" top plate of the applicator. The applicator consists of two coupled cavities, i.e. a cylindrical cavity section ($z >$ 0) and a coaxial cavity section ($z <$ 0). The two cavities are coupled at the $z = 0$ plane which is also the cylindrical cavity bottom plane. The important dimensions and coordinates of the applicator are shown in Fig. 1. They are the

coupling probe depth, L_p, the cylindrical cavity length, L_s, the cylindrical cavity radius, R_1, the coaxial cavity radii R_2 and R_3, the molybdenum substrate holder radius R_4, and the coaxial cavity lengths L_1, and L_2. The substrate itself is located approximately at the $z = 0$ plane on top of the open end of the coaxial cavity on the molybdenum holder. Thus, the end of the center conductor of the coaxial cavity also serves as the substrate holder and is either thermally floating or cooled/heated to control the substrate temperature. The substrate is placed upon the molybdenum holder that is located on the top of the coaxial center conductor. The difference between L_1 and L_2, i.e. $L_1 - L_2$, identified as ΔL, is the distance that the top surface of the powered electrode or the substrate surface is above or below the cavity bottom plane $z = 0$.

In practice, the plasma loaded applicator is excited with the hybrid TM_{013} + + TEM_{001} electromagnetic mode. In order to achieve TM_{013} excitation in the open cylindrical section L_s must be adjusted to be very close to $3\lambda_g/2$, where λ_g is the guided wavelength of the TM_{01} cylinder waveguide mode. In order to achieve TEM_{001} excitation in the coaxial section, L_2 must be adjusted to approximately $\lambda_0/2$ where λ_0 is the free space wavelength. Typical discharge ignition starting lengths for process development are when L_1 and L_2 are equal to each other and are equal to $\lambda_0/2$. Then, ΔL is zero and the top of the substrate is even with the $z = 0$ plane. Typical starting lengths for the cylindrical section are $L_s \sim 3\lambda_g/2$ and the coupling probe depth $L_p \sim \lambda_g/4$.

The geometry of the reactor shown in Fig. 1 is a function of the following geometric variables L_s, L_p, L_1, L_2, R_1, R_2, R_3, and R_4. In general, when these geometric length variables are changed the electromagnetic fields and the electromagnetic focus in the local region above and around the $z = 0$ plane are controlled and altered. Similarly, when a microwave discharge or plasma is present, the discharge power density, the plasma shape and position can be altered by varying one or more of the geometric variables. Thus, the diamond synthesis process can also be changed, controlled and optimized by changes in the reactor geometry.

When the size and shape of the MPCR is varied, for example by changing the various reactor radii or lengths, the reactor can be optimized for a specific deposition process. In practice R_1 is determined primarily by the choice of the excitation frequency, and R_2 and R_3 are then determined by the specific process application, i.e., desired substrate size and operating pressure regime. For example, for low pressure, large area operation and low discharge power density R_2 and R_3 take on lengths that are slightly smaller than R_1. Typical reactor designs fix the applicator radii, and then during process optimization the electromagnetic field patterns and associated microwave discharge are modified by varying L_1, L_2, L_s and L_p as well as pressure and input microwave power. This is a multivariable optimization procedure that is initially performed by the operator during process development and after some experience it can also be performed automatically via a preprogrammed recipe. Since there are many variables, there are many pos-

sible shapes, positions, and intensities that the discharge can assume in the vicinity of the $z = 0$ plane. All of these are available for process optimization. Table 1 lists four MPCR reactor configurations and sizes that are considered in this paper.

Table 1. MPCR Reactor System Configurations

Reactor System	R_1, mm	R_2, mm	R_3, mm	R_4, mm
A: 2.45 GHz	89	70	41	51
B: 2.45 GHz	89	70	19	32
C: 915 MHz	300	150	95	120
D: 915 MHz	300	150	Thermal Floating	120

Early experimental investigations that used a MPCR (labeled reactor A in Table 1) employed a 2.45 GHz design and explored CVD diamond synthesis over the low to moderate synthesis pressure regime (60–160 Torr). These results have been reported in several publications [5, 6, 18, 19, 21]. The specific dimensions of this reactor are $R_1 = 89$ mm, $R_2 = 70$ mm, $R_3 = 41$ mm and $R_4 = 51$ mm. These dimensions were chosen to enable diamond synthesis over 50–75 mm substrate diameters while operating in the low to moderate pressure regime. At the low pressures of less than approximately 80 Torr the reactor is operated in a configuration that the substrate is thermally floating, i.e. the substrate holder is heated by the plasma discharge and no additional substrate cooling or heating is done. At the moderate pressures of 80–160 Torr, the substrate holder is actively cooled by the substrate cooler located below the substrate holder.

Reactor B in Table 1 is a redesign of the MPCR [24] to allow operation at higher discharge power densities and higher pressures. This redesign reduced the substrate holder radius R_4 to 32 mm and the coaxial cavity inner conductor radius R_3 was reduced to 19 mm. This modification focuses the electromagnetic energy on the reduced diameter substrate holder and increases the axial electric field intensity and the associated displacement current density at the location of the substrate surface. This redesign not only increases the plasma absorbed power density above the substrate but also facilitates operation at higher pressure. The electromagnetic field focus at and above the substrate is additionally controlled and varied during process development by length tuning L_1, L_2, L_s and L_p. When a discharge is present, this length tuning changes the electromagnetic field focus and in turn, changes the location and the shape of the plasma.

In reactor B, for example, L_s and L_p are adjusted to excite and match the TM$_{013}$ mode in the cylindrical section of the applicator; i.e. $L_s = 20.3$ cm and $L_p = 3.6$ cm. During process optimization, L_1 is held constant at 5.65 cm while L_2 is varied between 5.16 cm and 6.13 cm and thus ΔL varies between +0.48 cm and −0.48 cm about the $z = 0$ plane. As the substrate axial position is varied, the electromagnetic field intensity and spatial distribution also are altered in the local region of the discharge (i.e., around the $z = 0$ plane).

When the reactor geometry, substrate size and total gas flow rate are held fixed the deposition process is a function of input power, pressure, substrate temperature, and methane concentration. The major variables are the input power, pressure and substrate temperature. The relationship between these variables is nonlinear and the relationship between them can best be understood by experimentally measuring and plotting a set of operating curves [19]. Fig. 2 displays such a set of curves for reactor B [24] where the reactor geometry is held fixed at L_s = 20.5 cm, L_p = 3.5 cm, and L_2 = 6.13 cm and the total gas flow rate is 412 sccm with 3 % methane in hydrogen.

Fig. 2. Substrate temperature as a function of pressure and absorbed microwave power for reactor B [24]
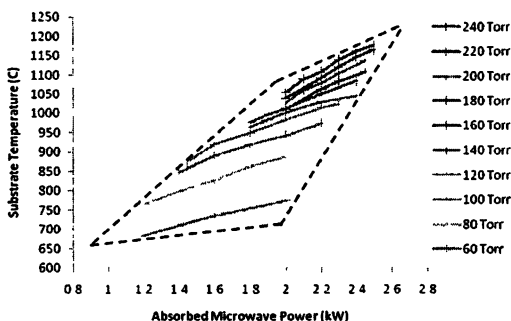
Each of the experimental curves in Fig. 2 is plotted for a constant pressure and the set of curves displays the variation of the substrate temperature versus input microwave power over the entire 60–240 Torr pressure regime. Only the safe and process useful operating data points are displayed in Fig. 2. The allowable operating regime is the area enclosed within the dashed line boundary. The enclosed region displays the acceptable experimental operating region for process operation and optimization. The left hand side of the parallelogram is determined by the minimum power required to generate a discharge of sufficient size to cover the substrate while the right side of the parallelogram is determined by the power that produces a plasma discharge that is so large that it starts or might start to interact with the discharge chamber walls. Thus, at each operating pressure the right hand side of the data points represents the approximate limit of the maximum input power at that pressure before reactor wall heating becomes a problem.

Several observations can be made from the curves of Fig. 2. First, as the pressure and input power increase the substrate temperature increases. At low pressures, the change in substrate temperature is less sensitive to input power changes than at high pressure; i.e. the slope of the constant pressure curves increases as pressure increases. However, the substrate temperature is more sensitive to pressure changes at low pressures than at high pressures. For a fixed reactor geometry the experimental synthesis is more sensitive to input power changes at high pressures than at lower pressures and thus at high pressures the input

469

power must be actively experimentally monitored to keep the process within the desired temperature deposition conditions.

Reactor C that operates at 915 MHz is a scaling of the 2.45 GHz reactor A to a larger size [22]. Most of the dimensions of reactor C are scaled in size by approximately the ratio of the frequencies. Reactor C operates with a substrate cooler on which sits the substrate holder and substrate. Reactor D is the same reactor as reactor C with the exception that the substrate holder and substrate are thermally floating, i.e. the substrate holder does not sit on the substrate cooler. Operating curves such as the one shown in Fig. 2 for a reactor B configuration can be created for each of the reactors A, C and D. Operating curves for reactor A were published earlier in [19].

Diamond Deposition Uniformity, Rate and Quality at High Pressures

Uniform growth of diamond film requires adjustment of the diamond deposition reactor to achieve an optimum plasma discharge shape and size. A good initial indication of such a discharge is the adjustment of the reactor to get good substrate temperature spatial uniformity. Obtaining uniform deposition often becomes more difficult at higher deposition pressures so in this section the operation/adjustment of reactor B, i.e. the reactor design for the higher operating pressures above 180 Torr, is described. Five reactor variables are adjusted to achieve temperature uniformity including the cavity length, the antenna length into the cavity, the height of the substrate holder, the length of the lower coaxial cavity section, and the design of the substrate holder. The adjustment of the cavity length and the antenna length determine not just the resonant microwave mode and reflected microwave power, but they also affect the shape and position of the plasma discharge. In operation the sliding short, antenna position, lower coaxial cavity length and substrate height position are adjusted to obtain a hemispherical shaped discharge that extends across the substrate with good contact between the plasma and substrate. The plasma is the source of heating for the substrate and the substrate temperature is determined by this heating and simultaneous cooling that occurs due to the water-cooled substrate holder that the substrate holder structure sits on. The electric field is φ symmetric for the utilized cavity mode resulting in a φ symmetric plasma discharge. The tuning process via the short position, antenna length, lower coaxial section length, and substrate height are adjusted so that the plasma discharge is as uniform radially as possible, but radial variations in plasma heat load to the substrate can not be totally tuned away. This results in radially non-uniform heating of a substrate by the plasma. To compensate for this a fifth reactor variable is addressed. Specifically, the substrate holder is designed to compensate for this radial gradient by removing more heat at the center of the substrate as compared to the edge.

As an example of reactor optimization, when reactor B is operating at a constant pressure within the allowable deposition region shown in Fig. 2 the reactor performance can be further optimized by length tuning the lower coaxial cavity.

Thus, within the allowable deposition region shown in Fig. 2, each curve can be modified by adjusting the coaxial cavity section of the applicator. When this is done, the electromagnetic focus is altered around the $z = 0$ region and the substrate also is moved changing its axial position from above to below the $z = 0$ plane. As the substrate position changes the position, size, shape and power density of the microwave discharge is also varied in a complex nonlinear fashion.

As the substrate position is lowered from a position above to a position below the $z = 0$ plane the discharge size and shape, its position with respect to the substrate changes, and the substrate temperature changes. Fig. 3 displays the variation of substrate temperature versus pressure as the substrate position is varied from above to below the $z = 0$ plane, i.e. ΔL varies from +4.9 mm to –4.9 mm. These curves demonstrate that at a constant pressure, the substrate temperature can vary more than 300 °C. For example as shown in Fig. 3, at 240 Torr as the substrate position is varied from +4.9 mm to –4.9 mm, the substrate temperature changes from 875 °C to 1175 °C. The substrate temperature increases as the substrate is lowered below the $z = 0$ plane. As the substrate is lowered, the discharge shape is changed, its volume is reduced and the discharge becomes more intense. These experiments clearly demonstrate the ability to alter the substrate temperature and the discharge position and power density as the lower section coaxial cavity size is changed. It should be emphasized that not all the data points shown in Fig. 3 yield a diamond deposition result that is spatially uniform. In practice a subset of the data points shown in Fig. 3 would yield useful uniformity results.
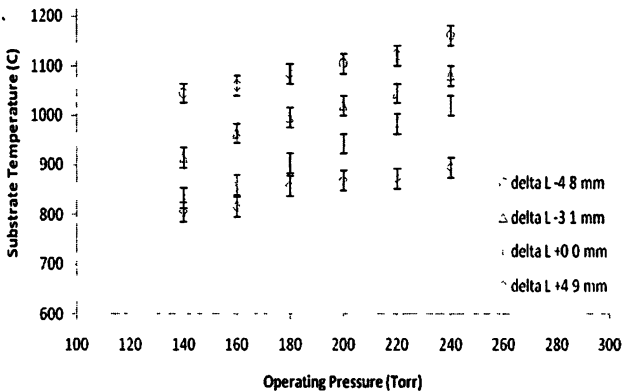
Fig. 3. Substrate temperature with different substrate positions ΔL versus operating pressures. The vertical bars represent the maximum/minimum variation of substrate temperature [24].

Diamond quality is determined in this paper from visual observations of the color and transparency of the freestanding films, and from the Raman spectrum of the diamond film. The freestanding PCD diamond films were produced by

removing the silicon substrate. This is done by placing the deposited film and substrate into a wet etching solution of nitric acid, ionized water, and hydrofluoric acid so that the silicon is etched away. In order to reduce the surface roughness and produce a smoother flat diamond surface some of the samples were polished and lapped prior to back etching. The Raman measurement system utilized 514 nm laser light to measure the diamond Raman signal FWHM at 1332 cm^{-1}. For reference, the Raman system measured a FWHM of 1.8 cm^{-1} for a single crystal sample. As an example of the diamond quality obtained in the diamond deposition reported in this work, Reactor A samples grown at conditions of 140 Torr and 1–1.5 % methane percentage in hydrogen showed Raman FWHM of 2.5 to 4.1 cm^{-1}. These samples also showed optical appearance of being white to slightly gray once they were back-etched off of the silicon. For purposes on this paper, good quality diamond is define as having a Raman signal FWHM of approximately 5 cm^{-1} or less and/or a color/transparency of white to light gray. This is not an absolute indication of diamond quality for a specific application, rather it is a definition of quality established for this paper as a relative indicator.

Each reactor configurations defined in Table 1 above has a pressure range of operation that has been used to get deposition across a specified substrate size. For example, in reactor A used to deposit diamond on 50 mm diameter silicon substrates, the pressure range investigated with uniform deposition achieved was 100–160 Torr. An example of the growth rate obtained for this pressure range averaged across the 50 mm substrate is shown in Fig. 4. The growth rate is seen to increase with both pressure increases and methane increases. Uniform deposition is defined for this paper as a variation in diamond thickness across the substrate being in a range of ±10 % from the average.
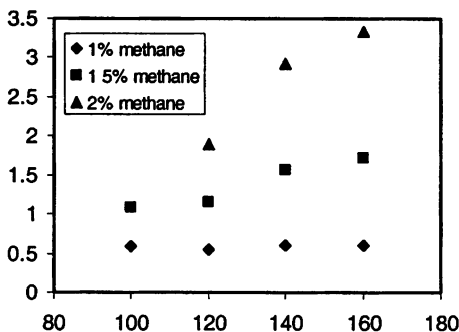
Fig. 4. Growth rate versus pressure for methane percentages of 1, 1.5 and 2 % in hydrogen for growth on 50 mm diameter substrates in reactor configuration A.

Diamond Deposition Uniformity Summary

For all four reactor configurations listed above in Table 1 experiments have been performed to obtain deposition uniformities of ±10 % or better across substrates of various sizes. The substrate uniformity is determined by measuring the grown diamond thickness at multiple points along two perpendicular lines that

pass through the center of the substrate and extend out to the outer diameter of the film. The results are summarized in Table 2. The data shown is for high quality diamond that is growth with a quality that gives white to a slightly gray color. Such films when removed from the silicon substrate and polished allow significant light to be seen through them. The table shows, for a given substrate size, what are the conditions that give high growth rates with high quality diamond. The general results are (1) uniformity is achieved over larger areas at low pressures, (2) high pressures yield higher growth rates, (3) for a given growth rate (or methane concentration in the feedgas) the quality is higher at higher pressures, and (4) the larger 915 MHz reactor can achieve uniformity over larger areas as compared to the smaller 2.45 GHz systems at the same pressure. In addition to the polycrystalline diamond growth, Table 2 also shows results for single crystal diamond grown on multiple diamond seeds (70 seeds) distributed across a substrate holder that had seeds over a circular region of approximately 100 mm diameter. Results are also shown for the larger 915 MHz reactor that demonstrate uniform deposition across 200 mm diameters for a argon gas based nanocrystalline diamond deposition process. It should be caution that the results in Table 2 are those obtained to-date. Further optimization can be expected to result in improved growth rates and quality for a given substrate diameter.

Table 2. Growth conditions that achieve uniformity of ±10 %

Reactor System Configuration	Substrate Diameter	Diamond Deposition Process	Pressure Range	Growth Rate (for films that are white to slightly gray)
2.45 GHz – A	25 mm	Polycrystalline	180–240 Torr	3–14 μm/h for methane percentage from 2–5 %
2.45 GHz – B	50 mm	Polycrystalline	120–160 Torr	0.5–3 μm/h for methane percentages of 1–2 %
2.45 GHz – B	75 mm	Polycrystalline	100–120 Torr	1–2 μm/h with methane percentages of 1–2 % [19]
915 MHz – C	100 mm	Polycrystalline	110–120 Torr	1–2 μm/h with methane percentage of 2 %
915 MHz – C	100 mm holder	70 single crystal seeds on substrate holder	125 Torr	14–21 μm/h with small amount of nitrogen in the feedgas [23]
915 MHz – D	150 mm	Polycrystalline	40–70 Torr	0.3–0.4 mm/h [22] See note
915 MHz – D	200 mm	Nanocrystalline	75 Torr	0.03–0.18 mm/h [22] (Argon based discharge with added methane and H_2) See note

Note: No quality measurements were performed on these diamond films deposited in reactor configuration D.

References

1. *Kamo M , Yurimuto H., Sato Y.* Appl. Surf. Sci. 33/44, 553 (1988)
2. *Teraji T.* Phys. Stat. Sol.(a) 203, 3324-3357 (2006).
3. *McCauley T. S., Vohra Y. K.* Appl. Physics. Lett. 66, 1486 (1995).
4. *Yan C.-S , Vohra Y. K., Mao H.-K., Hemley R L.* Proc. Natl. Acad. Sci. U. S. A. 99, 12523 (2002).
5. *Kuo K P., Asmussen J* Diamond Relat. Mater. 6, 1097 (1997).
6. *Kahler U.* Microwave Plasma Diamond Film Growth, Diplomarbeit Thesis, Michigan State University and Gesamthochschule Wuppertal, 1997.
7. *Mokuno Y., Chayahara A., Soda Y., Horino Y., Fujimori N.* Diamond Relat. Mater. 14, 1743 (2005).
8. *Tallaire A., Acharda J., Silvaa F., Sussmanna R. S., Gicquel A.* Diamond Relat. Mater. 14, 249 (2005).
9. *Sternschulte H., Bauer T., Schreck M., Stritzker B* Diamond Relat. Mater. 15, 542 (2006).
10. *Yamada H., Mokuno Y., Chayahara A , Horino Y., Shikata S.* Diamond Relat. Mater. 16, 576 (2007).
11. *Yamada H , Chayahara A., Mokuno Y., Shikata S.* Diamond Relat. Mater. 17, 1062 (2008).
12. *Yamada H., Chayahara A., Mokuno Y., Horino Y., Shikata S.* Diamond Relat. Mater. 15, 1389 (2006).
13. *Asmussen J.* Keynote paper 11, presented at the 2nd Conference on New Diamond and Nano Carbons, 2008, May 26–29th, Taipei, Taiwan; *Hemawan K. W., Grotjohn T. A., Reinhard D. K., Asmussen J.*, invited paper presented at ICOPS 2008, Karlsruhe, Germany, June, 2008.
14. *Silva F., Hassouni K., Gicquel A., Bonnin X.*, paper presented at the International Workshop on Strong Microwaves, Aug. 2008.
15. *Asmussen J., Mallavarpu R., Hamann J. R., Park H. C.* Proceed. IEEE, 62, 109 (1974).
16. *Mallavarpu R., Hawley M. C., Asmussen J.* IEEE Trans. On Plasma Sci. PS-6, 341 (1978).
17. *Kapitza P. L.* Soviet Physics JETP, 30, 973 (1970).
18. *Kuo K. P.* Ph. D. Dissertation, Michigan State University, 1997.
19. *Zuo S. S., Yaran M. K., Grotjohn T. A., Reinhard D. K., Asmussen J.* Diamond Relat. Mater. 17, 300 (2008).
20. *Whitehair S., Asmussen J.* J. Propulsion and Power, 3, 136–144 (1987).
21. *Asmussen J., Reinhard D. K.* Diamond Films Handbook, Chapter 7, Marcel Dekker, New York, 2002.
22. *King D., Yaran M. K., Schuelke T., Grotjohn T. A., Reinhard D. K., Asmussen J.* Diamond and Related Materials, 17, 520–524 (2008)
23. *Asmussen J., Grotjohn T. A., Schuelke T., Becker M., Yaran M., King D., Wicklein S., Reinhard D. K.* Appl. Physics Lett. 93, 031502-1 (2008).
24. *Hemawan K. W., Grotjohn T. A., Reinhard D. K., Asmussen J.*, to be published.

CYCLOTRON RESONANCE MASER
DRIVEN BY PLASMA MAGNETIC COMPRESSION

A. G. Shalashov and S. V. Golubev

Institute of Applied Physics RAS, Nizhny Novgorod, Russia

A new source of pulsed high-power electromagnetic radiation based on adiabatic magnetic compression of non-equilibrium plasma confined in a mirror magnetic configuration is proposed. Conditions are investigated at which the magnetic compression is accompanied by accumulation of significant energy in a hot anisotropic electron tail with subsequent release of this energy as a pulse of coherent electromagnetic radiation due to development of the kinetic instabilities of fast extraordinary waves under the of electron-cyclotron resonance conditions. The possibilities of creating THz radiation sources of multi-megawatt power level are discussed.

Introduction

The capabilities of modern vacuum electronic devices with respect to accumulation of energy in an "active substance" and control of the duration of resultant electromagnetic radiation are constrained by the interaction time of an electron beam with the radiation limited by the beam transit through a resonator. As was first noted in [1], using nonequilibrium plasma as the active substance opens new possibilities for long-lasting accumulation of energy in a resonator volume with subsequent release of this energy in the form of a short pulse of electromagnetic radiation. Energy may be effectively pumped by a magnetic field smoothly increasing in time (magnetic compression) resulting in formation of nonequilibrium energetic tails in the electron distribution function in which the transverse to the magnetic field momentum prevails over the longitudinal one. The energy of fast electrons may be released as coherent maser electromagnetic radiation due to development of electron cyclotron (EC) instabilities caused by the anisotropy of the electron distribution function. The radiation frequency is defined by the magnetic field strength at the moment when the instability develops, and therefore can be varied in wide limits.

Realization of such regimes in a plasma device faces essential difficulties because the accumulation time of energetic electrons exceeds by many orders of magnitude the instability growth times, what causes a premature release of the energy before it is accumulated. This essentially limits the radiated power and energy of electromagnetic waves propagating along the ambient magnetic field in dense plasma, the case studied in the pioneer work [1]. These difficulties were discussed in [2] and partially overcame in [3], where a new regime of generation was proposed based on excitation of oblique waves in rarefied plasma. It was found that development of the cyclotron instabilities may be refrained by dense background plasma, what has been confirmed by a laboratory experiment on de-

tecting the cyclotron instabilities on a decay phase of a pulsed ECR discharge in a mirror trap [4, 5].

These results open good prospects for development of a new class of extremely powerful sources of pulsed electromagnetic radiation, in particular, in the terahertz (THz) frequency range poorly mastered by classic vacuum electronics devices [6]. In THz range, few megawatt power level may be obtained with a typical ECR discharge plasma with density about 10^{13} cm^{-3}; further power increase up to GW level is possible by using more dense plasma [3]. Expected power greatly exceeds the record values achieved in free electron lasers in a single pulse [6, 7]; however, magnetic compression does not allow generation of pulses with high repetition rate, thus the average radiated power will be much lower than obtained in a free electron laser. Confining magnetic field in the discussed source should be raised up to about 40 T within a millisecond time; such fields have been already achieved, e.g. in THz-gyrotrons [8] and in large volume pulsed solenoids [9]. Besides, generation of electromagnetic radiation in laboratory experiments have much in common with the operation of natural cyclotron masers, see e.g. [10]. Thus, the proposed new mechanism of triggering the electromagnetic radiation may be of interest for interpreting of peculiar processes related to auroral kilometric radiation of Earth ionosphere, decametric radiation of Jupiter, and Solar flares.

The present paper extends works [2–5]. We study a case when magnetic compression of plasma confined in a simple mirror trap is accompanied by a significant accumulation of energy in a hot electron component. The stored energy is released during the loss cone instability of the fast extraordinary wave propagating obliquely to the magnetic field just above the fundamental EC harmonic. A peculiar feature of this instability is that its threshold is affected by the low-frequency cutoff, thus in a weakly relativistic case the instability may develop only in sufficiently rarefied plasma satisfying the following condition:

$$\omega_p^2 / \omega_c^2 \ll 1 - \omega_c / \omega \sim \beta^2,$$

$$\beta = \upsilon / c \qquad\qquad (1)$$

with ω_p, ω_c, and ω being the plasma Langmuir, electron cyclotron (in the center of a trap), and radiation frequencies, and β being the ratio of average velocity of the energetic electrons to the speed of light [2, 3, 11]. Note that during magnetic compression ω_p^2 / ω_c^2 decreases faster than $1/B$, where B is the magnetic field strength. A radiation source based on this principle may work as follows:

- Two-component plasma is produced in a mirror trap by an external source, e.g. by ECR discharge, then the source is switched-off.
- Confining magnetic field is increased in time resulting in energy pump into the hot electron component. The instability does not develop due to presence of the dense background plasma providing $\omega_p^2 / \omega_c^2 \gg \beta^2$.

476

- Simultaneously the background plasma decays since it is not supported by an external source; below we assume that this process is governed by gas-dynamic losses.
- Maser instability of the fast extraordinary wave develops once condition (1) becomes valid.

Different aspects of realization of such a device, which we call a plasma magneto-compressional maser, are discussed below. We found that the instability of the extraordinary wave is very sensitive to variations of ω_p^2 / ω_c^2 in the vicinity of the threshold, what provides fast instability "switching on" and high average power in the resulting electromagnetic pulse. In some sense, this process is similar to generation of giant pulses in lasers [12]. However, development of parasitic instabilities limited the maximum radiated power and the range of plasma parameters in a magneto-compressional maser.

Adiabatic magnetic compression

Let us consider a magnetic trap that confines a two-component plasma consisting of a fairly dense, cold, equilibrium plasma with density N_e and electron temperature T_e and the anisotropic admixture of hot electrons with density N_h and average energy T_h. We shall be interested in the case when wave dispersion properties are determined by the background plasma, $N_e \gg N_h$, and energy is stored in hot but weakly relativistic electrons,

$$N_e T_e \ll N_h T_h \ll N_h m_e c^2 .$$

The most effective energy pump to hot electrons is realized when the magnetic field increases adiabatically slow compared to the cyclotron oscillations, but fast compared to particle collisions and radiation damping, thus the latter two effects may be neglected,

$$\nu_h, \nu_r \ll \nu_B \ll \omega_c, \ \nu_B = d \ln B / dt, \ \nu_r \sim 2 e^2 \omega_c^2 [\beta_\perp^2] / 3 m_e c^3 .$$

Here ν_B is the rate of magnetic field increase, ν_h is the rate of Coulomb collisions of hot electrons with background plasma, ν_r is the loss rate due to cyclotron radiation. Let us assume that fast electrons are not lost from a trap during the compression before the development of the instability. In a regime of collisionless confinement this is provided by condition $\nu_h \ll \nu_B \ln \sigma$, where $\sigma = \max B / \min B$ is the mirror ratio of a trap. With these assumptions, evolution of a distribution function of hot electrons is defined by conservation of two adiabatic invariants of motion:

$$v_\perp^2 / B \quad \text{and} \quad \oint v_\| dl ,$$

where $\upsilon_\perp$ and $\upsilon_\parallel$ denote transverse and longitudinal components of the velocity with respect to the magnetic field; the latter integral is calculated over a bounce-oscillation with the total particle energy kept constant [13]. For example, assuming a parabolic profile of the magnetic field, $B(t,l) = B(t)\max(1+(\sigma-1)l^2/L_B^2,\sigma)$, where l and L_B are the coordinates along the field line and the half-length of a trap correspondingly, one obtains that $\upsilon_\perp \propto B^{1/2}$ and $\upsilon_\parallel \propto B^{1/4}$ in the trap center [3].

Let us consider an anisotropic Maxwellian distribution function with a loss cone. At the trap center such distribution may be defined as

$$f(\upsilon_\perp,\upsilon_\parallel) = \frac{N_h}{\pi^{3/2}\mu\, w_\perp^2 w_\parallel}\exp\left(-\frac{\upsilon_\perp^2}{w_\perp^2}-\frac{\upsilon_\parallel^2}{w_\parallel^2}\right)\Theta(\alpha), \qquad (2)$$

see Fig. 1. Here $w_\perp$ and $w_\parallel$ are the transverse and longitudinal thermal velocities of hot electrons; $\alpha = \arccos(\upsilon_\parallel/\upsilon)$ is the pitch-angle; $\Theta(\alpha)$ defines a part of a velocity space in which there are no hot electrons, this function equals to unity in the range $\alpha_* < \alpha < \pi-\alpha_*$ and smoothly goes to zero outside with a scale $\Delta\alpha_* \ll \alpha_*$; and $\mu = (1+(w_\parallel^2/w_\perp^2)\tan^2\alpha_*)^{-1/2}$. Initially, the boundary α_* coincides with the loss cone from a trap, and the width of transition region is determined by collisions: $\Delta\alpha_* > (\nu_h L_B/\upsilon_\parallel)^{1/2}$.
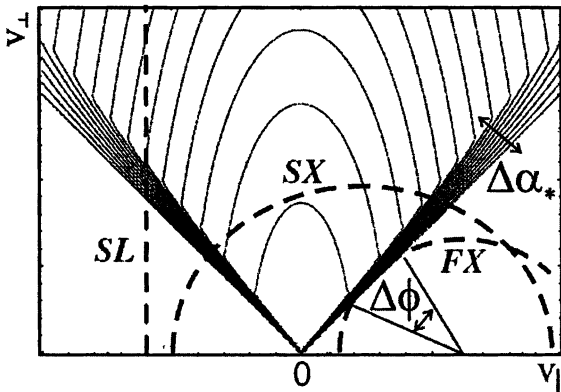
Fig. 1. Isolines of the distribution function (2) and curves of the EC resonance corresponding to fast oblique (FX), slow quasi-transverse (SX), and slow longitudinal (SL) waves

For the parabolic profile of a magnetic field, parameters of the distribution function (2) change during magnetic compression under the following laws:

$$N_h = b^{5/4}N_{h0}, \quad w_\perp = b^{1/2}w_{\perp 0}, \quad w_\parallel = b^{1/4}w_{\parallel 0}^2,$$
$$\tan^4\alpha_* = b/(\sigma_0-1), \quad \mu = \mu_0. \qquad (3)$$

Here, index 0 denotes the beginning of compression, and $b \equiv B(t)/B_0$.

Let us consider evolution of the background plasma during the magnetic compression. For the plasma parameters of a magneto-compressional maser it is reasonable to assume that the dense bulk plasma confined in the gas-dynamic regime in which particles leave a trap with the ion-acoustic velocity $\upsilon_a \approx \sqrt{T_e / m_i}$. The magnetic compression begins immediately after switching off a source supporting initial plasma. Then the evolution of the bulk electron density and temperature may be calculated within the standard approach based on balance equations [2, 3, 5]:

$$\begin{cases} dN_e / dt = (\frac{5}{2}\nu_B - \nu_{gd})N_e - \alpha_r T_e^{-9/2} N_e^3 \\ \frac{3}{2}d(N_e T_e)/ dt = (\frac{5}{2}\nu_B - \nu_{gd} \ln\sqrt{\frac{m_i}{m_e}})N_e T_e - P_{loss} \end{cases} \quad (4)$$

Here, terms with ν_B and $\nu_{gd} \approx \upsilon_a / L_B \sigma$ consider accordingly magnetic compression and gas-dynamic losses of particles and energy, α_r is the collisional (three-body) recombination rate, P_{loss} accounts for other channels of energy losses (cyclotron radiation, bremsstrahlung) insignificant in cases presented below. Depending on the initial conditions, the bulk density and temperature may either monotonously decrease (plasma decay), or pass through a maximum (plasma compression).

Kinetic instabilities of the electron distribution function

Instabilities of distribution function of energetic electrons against excitation of cyclotron waves during magnetic compression have been considered in [1–3]. In the present context, most important is the loss cone instability of the fast extraordinary wave propagating at a sufficient angle to the magnetic field above the fundamental EC harmonic. This instability has a maximum growth rate when the curve of relativistic cyclotron resonance condition,

$$\omega - k_\parallel \upsilon_\parallel = \omega_c \sqrt{1-\beta^2} \, ,$$

is tangent to the region where $\partial f / \partial \upsilon_\perp > 0$ and lies inside the region where there are no resonant particles [11]; see Fig. 1. Then, the frequency and the propagation direction of the most unstable waves are unambiguously defined by the coordinates υ_* and α_* of the tangency point as

$$\omega / \omega_c = 1 + \upsilon_*^2 / 2c^2, \quad k_\parallel c / \omega = \upsilon_* /(c \cos\alpha_*) \, . \quad (5)$$

Using the technique of Melrose et al. [11] for the distribution function (2), one obtains the following growth rate of the fast extraordinary mode at the fundamental harmonic [3]:

479

$$\gamma_{\text{FX1}} \approx \omega_c \frac{\sqrt{\pi}}{2} \frac{N_h}{N_e} \frac{\mu^4 \sin^2 \alpha_*}{\cos^4 \alpha_*} \frac{w_\parallel^4}{w_\perp^2 c^2} \frac{\Delta\phi}{\Delta\alpha_*} \Phi(\xi), \quad \Phi(\xi) = \xi^5 e^{-\xi^2}. \quad (6)$$

Here $\xi = v_* \cos\alpha_* / \mu w_\parallel$ defines the radiation frequency and propagation direction according to Eqs. (5), and $\Delta\phi/\Delta\alpha_* \approx 2(2\cot\alpha_* / \Delta\alpha_*)^{1/2}$ is explained in Fig. 1. Equation (6) is obtained for $\omega_p^2 / \omega_c^2 \gg w_\parallel^4 / c^4$, the limit corresponded to a group velocity being much less then c. In the presence of a dense background plasma, only the waves with $\omega - \omega_c > \omega_p^2 / \omega_c^2$ (here $\omega_p^2 / \omega_c^2 \ll 1$ is assumed) can propagate due to a radiation cutoff near ω_c. According to Eqs. (5), this is equivalent to the following restriction in Eq. (6):

$$\xi > \omega_p / \omega_p^*, \qquad \omega_p^* = \omega_c \mu w_\parallel / \sqrt{2} c \cos\alpha_*.$$

With this constrain, the maximum growth rate over the frequency is proportional to $\Phi(\omega_p / \omega_p^*)$ when $\omega_p / \omega_p^* > \sqrt{5/2}$, i.e. it vanishes exponentially fast with plasma density increase; therefore, the instability may develop only in a sufficiently rarefied plasma when $\omega_p / \omega_p^* < \sqrt{5/2}$.

The central frequency and the propagation direction of the radiated pulse are $\omega \approx \omega_c + \omega_p^2 / \omega_c$ and $k_\parallel \approx \sqrt{2}\omega_p / c\cos\alpha_*$. Note, that the quasi-linear relaxation of the unstable distribution function may result in broadening of a frequency-angular spectrum of the radiation; the analysis of such process is beyond the scope of this work.

The oblique fast extraordinary wave at the fundamental harmonic (FX1) is not the only unstable electromagnetic mode considered. Other potentially unstable modes are the fast oblique wave at the second harmonic (FX2), the slow waves, also known as Z-modes, propagating quasi-transverse (SX1) and along (SL1) the magnetic field at the fundamental harmonic [14]; all other modes are less pronounced in rarefied weakly relativistic plasmas [15]. Growth rates of SX1, SL1, and FX2 modes were analyzed in [2]. These growth rates are not influenced by the plasma cutoff, thus they are smoothly dependent on plasma parameters. If one of these instabilities develops before the FX1 instability, an electromagnetic pulse of smaller power would be generated which we consider as a parasitic effect to be avoided. Some insight in the physics involved is given by resonant lines corresponding to different types of instabilities shown in Fig. 1. The SL1 instability is excited under the non-relativistic Doppler condition due to the temperature anisotropy $A = w_\perp^2 / w_\parallel^2 > 1$, therefore suppression of this instability requires a restriction of the maximal anisotropy of hot particles [$\gamma_{\text{SL1}} / \gamma_{\text{FX1}} \propto A^2$]. The SX1 instability is excited under the relativistic resonance

condition with negligible Doppler shift, so in a weakly relativistic case it is less pronounced than the FX1 instability, as well as the FX2 instability $[\gamma_{SX1}/\gamma_{FX1} \propto A^2 w_\perp^4/c^4, \quad \gamma_{FX2}/\gamma_{FX1} \propto w_\parallel^2/c^2]$. Nevertheless these spurious modes may be excited when the FX1 mode is suppressed by the cutoff. This situation may be avoided by reducing the ratio $\gamma/\delta \propto N_h/N_e^2$.

Power and duration of the radiated electromagnetic pulse

The possibility of fast actuation makes the instability of the fast oblique extraordinary wave the most attractive from the standpoint of power increase in the electromagnetic pulse. Indeed, assuming that in the vicinity of the instability threshold defined by condition $<\gamma>=<\delta>$ evolution of the wave energy may be approximately described by

$$dE_w/dt = <\gamma - \delta> \approx \dot{\gamma}\ t\ E_w(1 - E_w/E_w^{max}),$$

one obtains that the pulse duration may be estimated as $\tau_w \approx 1/\sqrt{\dot{\gamma}}$ [2, 3]. Here $\delta \approx \nu_e$ is the damping rate defined by absorption of waves by the background plasma with the collision frequency ν_e; $\dot{\gamma} = d<\gamma-\delta>/dt$ is the rate of variation of the averaged instability growth rate;

$$<...> = \tau_{gr}^{-1}\int ...\ \upsilon_{gr}^{-1}dl \quad \text{and} \quad \tau_{gr} = \int \upsilon_{gr}^{-1}dl$$

denote averaging over the interaction volume and the time of pulse propagation (with the group velocity) through the interaction volume.

In a particular case of the FX1 wave instability described by growth rate (6), which is exponentially dependent of the plasma density, one obtains $\dot{\gamma} \approx d\gamma_{FX1}/dt \propto \dot{N}_e + \dot{N}_h$ and, correspondingly,

$$1/\tau_w^2 \approx \left(<\delta>/\omega_p^{*2}\right)\left(\omega_{pe}^2/\tau_e + \omega_{ph}^2/\tau_h\right). \tag{7}$$

Here ω_{pe}, and ω_{ph} are the plasma frequencies corresponded to the bulk and hot electrons, τ_e and τ_h are the confinement times of the bulk and hot electrons inside a loss cone, all quantities are calculated at the instability threshold defined by condition

$$<\gamma_{FX1}(\omega_p/\omega_p^*)>=<\delta>. \tag{8}$$

The lower limit of the confinement time of fast electrons is defined by free electron escape from a trap, the upper limit is defined by ambipolar flowing (the flux of fast electrons is compensated by the ion flux), and the bulk electron life-time if defined by gas-dynamic losses:

$$L/w_\parallel < \tau_h < L/w_\parallel\sqrt{N_h m_i/N_e m_e}, \quad \tau_e \approx 1/\nu_{gd}.$$

481

Note that typically $\tau_h \ll \tau_e$, so the pulse duration (7) may be affected by fast density variation of hot electrons even though the its fraction is small. Equation (7) is valid when τ_w is much less then evolution times of the background plasma and the ambient magnetic field. A sufficient condition for fast actuation of the FX1 instability is

$$< \gamma_{FX1} |_{\xi^2=5/2} >>>< \delta >,$$

this inequality may be easily satisfied in laboratory conditions.

Due to interaction with waves resonant electrons lose mostly transverse momentum and moves to a loss cone in velocity space. This process occurs on a time-scale $\sim 1/< \gamma >$, which is much faster than the consequent escape of the fast particle from a loss cone. The energy and power of the electromagnetic pulse may be estimated as

$$E_w \approx \eta \; VN_h T_\perp, \qquad P_w = E_w/\tau_w,$$

where $VN_h T_\perp$ is the total energy stored in cyclotron rotation of fast electrons and η is the efficiency of wave excitation. The generation efficiency may be found as $\eta = \Delta W / N_h T_\perp$ where ΔW is the total energy that electrons loss during the quasi-linear relaxation. The maximum efficiency corresponds to the case of rapid losses of fast electrons, $\tau_h \ll \tau_w$. In this case the loss-cone is empty, and an electron with initial velocity $(\upsilon_\perp, \upsilon_\parallel)$ escapes from a trap when its velocity becomes $(\upsilon_\parallel \tan\alpha_*, \upsilon_\parallel)$. For the distribution function (2) this corresponds to the energy losses:

$$\Delta W = \int\limits_{-\infty}^{\infty} d\upsilon_\parallel \int\limits_{\upsilon_\parallel \tan\alpha_*}^{\infty} 2\pi\upsilon_\perp d\upsilon_\perp \frac{m_e(\upsilon_\perp^2 - \upsilon_\parallel^2 \tan^2\alpha_*)}{2} \qquad f = \frac{m_e(w_\perp^2 - w_\parallel^2 \tan^2\alpha_*)}{2}.$$

This equation results in the following estimation for the efficiency

$$\eta \approx 1 - z, \qquad z = w_\parallel^2 \tan^2\alpha_* / w_\perp^2 = T_\parallel /T_\perp (\sigma - 1), \qquad \tau_h \ll \tau_w.$$

Note that z is constant during the magnetic compression. One can see that $\eta \approx 100\,\%$ when $T_\perp \gg T_\parallel$.

However, condition $\tau_h \ll \tau_w$ implies too strong limitations on parameters of laboratory plasma. Thus, it is meaningful to consider the opposite case of slow losses of fast electrons. When there are no losses, the quasi-linear relaxation results (at the final stage) in plateau formation over the perpendicular velocities. Conservation of number of resonant particles and continuity of the distribution function lead to the following equation valid for each $\upsilon_\parallel$:

$$\int\limits_{\upsilon_\parallel \tan\alpha_*}^{\upsilon_*} 2\pi\upsilon_\perp d\upsilon_\perp f(\upsilon_\perp, \upsilon_\parallel) = \int\limits_{0}^{\upsilon_*} 2\pi\upsilon_\perp d\upsilon_\perp f(\upsilon_*, \upsilon_\parallel).$$

This equation unambiguously defines width v_* and height $f(v_*, v_\parallel)$ of the plateau for a given initial distribution function $f(v_\perp, v_\parallel)$. The energy difference between the initial and final distribution functions is given by

$$\Delta W = \int_{-\infty}^{\infty} dv_\parallel \left(\int_{v_\parallel \tan\alpha_*}^{v_*} 2\pi v_\perp dv_\perp \frac{m_e v_\perp^2}{2} f(v_\perp, v_\parallel) - \int_{0}^{v_*} 2\pi v_\perp dv_\perp \frac{m_e v_\perp^2}{2} f(v_*, v_\parallel) \right).$$

Substituting the distribution function (2) into two latter equations, after some algebra one may obtain the following expression for the efficiency:

$$\eta \approx \frac{\sqrt{1+z}}{2\sqrt{\pi z}} \int_{0}^{\infty} \frac{x^3 (1+x)^{1/z-1} \exp(-x - x/z)}{\sqrt{x - \ln(x+1)}} dx < 13\%, \quad \tau_h \gg \tau_w.$$

More accurate calculation of the generation efficiency may be performed basing on space-averaged quasi-linear equations that describe self-consistent evolution of the distribution function of hot electrons and the spectrum of excited waves, see e.g. [16].

Towards a high power source of single pulse THz radiation

The balance equations together with the estimations of the instability growth rates and the parameters of the resulting electromagnetic radiation allow searching and optimization of the regimes of magnetic compression. Although this problem may be studied analytically (with some limitations), below we demonstrate several examples obtained numerically and optimized for generation of electromagnetic radiation in the THz frequency range. The optimization procedure was as follows. First, the compression rate bulk plasma confinement was adjusted such that the threshold of the FX1 instability is achieved at a desired frequency. Second, parameters of hot plasma were found that allowed to avoid development of the spurious instabilities. Third, the radiation power and efficiency were maximized by tuning the compression degree, the energy and confinement of the hot plasma. Then the iteration repeats.

The first example corresponds to initial plasma with the bulk density $\sim 10^{13}$ cm^{-3}, the hot electron density $\sim 10^{11}$ cm^{-3} and energy ~ 1 keV typical of ECR discharge in a mirror trap produced by gyrotron radiation [5]. A rather large trap volume (about 6 liters) is assumed having in mind best achievements of high-field large-aperture pulsed solenoids [9]. Evolutions of averaged growth and damping rates for the instabilities considered above during the plasma compression are shown in Fig. 2. All important plasma parameters are specified in the caption. Generation of coherent maser radiation starts once the threshold (8) is exceeded. Initial parameters are chosen such that the threshold of the FX1 instability is achieved first. By this moment (240 μs) the magnetic field increases by 25 times up to 33 T, and the free energy accumulated in the hot electrons (6.4 J) is radiated as an

electromagnetic pulse with duration about 50 ns, frequency 920 GHz, spectral width about 2 GHz, energy 0.3–6 J and average power 6–120 MW. The latter estimates differ from what was published before in [2, 3] due to more deep treatment of the generation efficiency in the present paper. In particular, we found a big uncertainly in power and energy of the radiated pulse (the generation efficiency varies from 5 % to 90 %) related to uncertainty in the confinement time of exhausted fast electrons inside a loss cone, the matter that needs further investigations.
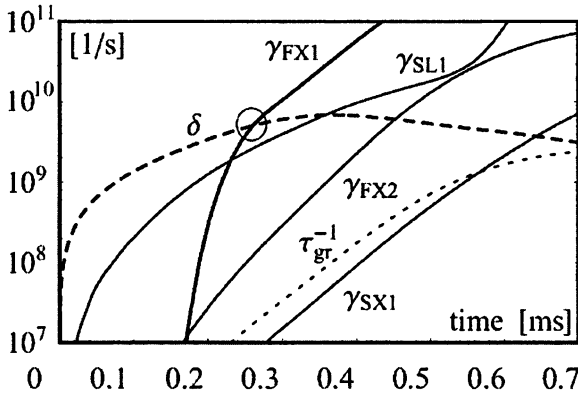
Fig. 2. Evolution of averaged growth rates of the FX1, FX2, SX1, SL1 modes, damping rate $< \delta >$ and inverse group time $1/\tau_{gr}$ during compression of argon plasma (large trap, ECR plasma). The magnetic field varies as $B = (1 + \nu_1 t) B_0$ with $\nu_1 = 10^5$ s^{-1}. Before the compression $N_e = 1.6 \cdot 10^{13}$ cm^{-3}, $N_h = 1.6 \cdot 10^{11}$ cm^{-3}, $T_e = 10$ eV, $T_\parallel = 110$ eV, $T_\perp = 1$ keV, $B_0 = 1.3$ T, $\sigma_0 = 4.3$, $L_B = 10$ cm, radius of a plasma cord 10 cm; at the threshold of the FX1 instability (marked by a circle) $N_e = 1.6 \cdot 10^{14}$ cm^{-3}, $N_h = 4.3 \cdot 10^{12}$ cm^{-3}, $T_e = 0.7$ eV, $T_\parallel = 0.6$ keV, $T_\perp = 27$ keV, $B = 32.8$ T. Discharge is in argon plasma.

The radiation power may be further increased by raising the hot electron density. This is demonstrated in Fig. 3 that corresponds to extreme values of the hot electron density 10^{13} cm^{-3}, the bulk density is adopted so that $N_e > N_h$ when the instability develops, all other parameters remain close to the previous example. The plasma is still magnetized for both components, $N_e T_e$, $N_h T_h \gg B^2/4\pi$ and the hot electron density is limited by two conditions: the FX1 instability should arise first, and the electromagnetic pulse should be long enough to provide acceptable generation efficiency (about 10 %). At the FX1 instability threshold (by moment 190 μs) the magnetic field increases by 20 times, and an electromagnetic pulse is radiated with duration 10 ns, frequency 904 GHz, spectral width about 5 GHz, total energy 30 J, and average power 3 GW.
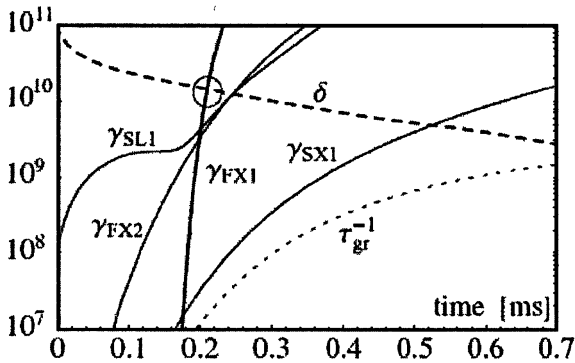
Fig. 3. The same as Fig. 2, but for more dense plasma. Before compression $N_e = 10^{16}$ cm^{-3}, $N_h = 10^{13}$ cm^{-3}, $T_{\parallel} = 400$ eV, $B_0 = 1.6$ T, all other parameters are the same as in Fig. 2; at the threshold $N_e = 5.2 \cdot 10^{14}$ cm^{-3}, $N_e = 2.2 \cdot 10^{14}$ cm^{-3}, $T_e = 0.7$ eV, $T_{\parallel} = 1.8$ keV, $T\perp = 22$ keV, $B = 32.3$ T.

With the last example shown in Fig. 4 we demonstrate the abilities of the magneto-compressional maser realized in a small volume solenoid (about 30 cm^3) similar to that has been already used in the THz gyrotron [8]. Again we consider a typical ECR discharge plasma with parameters close to the example in Fig. 2. At the FX1 instability threshold (by moment 200 μs) the magnetic field increases by 27 times, and an electromagnetic pulse is radiated with duration 40 ns, frequency 970 GHz, spectral width about 1 GHz, total energy 2 mJ, and average power 50 kW.
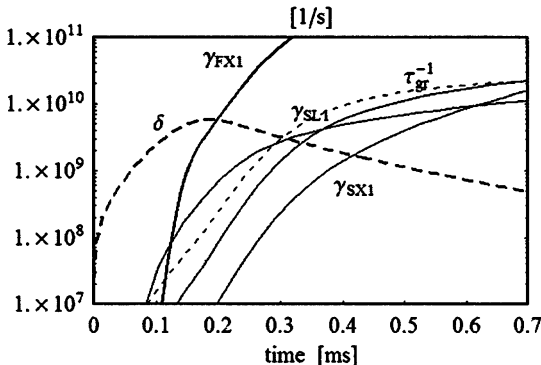
Fig. 4. The same as Fig. 2, but for compact trap. Before the compression $T_{\parallel} = 450$ eV, $B_0 = 1.6$ T, $\sigma_0 = 5$, $L_B = 5$ cm, radius of a plasma cord 1 cm, all other parameters are the same as in Fig. 2; at the threshold $N_e = 3.3 \cdot 10^{13}$ cm^{-3}, $N_h = 3.4 \cdot 10^{12}$ cm^{-3}, $T_e = 0.2$ eV, $T_{\parallel} = 0.45$ keV, $T\perp = 21$ keV, $B = 35.1$ T.

485

Note, that the optimized regimes may be realized more easily (in a broader parameter range, such as initial density, temperatures, compression rate etc) in a short trap. Magnetic compression in such trap is accompanied by acceleration in both transverse and longitudinal directions, what results in a sufficiently slower growth of the temperature anisotropy of fast electrons (e.g. $A \propto B^{1/2}$ for a parabolic magnetic field), as compared to the case of a long quasi-homogeneous trap (with $A \propto B$) studied in [2]. Low anisotropy is favorable both for development of the FX1 instability, and, more important, for suppression of the parasitic SL1 instability limited operational capabilities in [2].

ECR discharge seems to be the most suitable solution for producing the plasma with a bulk density below 10^{14} cm^{-3}. The number of fast electrons and their energy may be controlled by varying the location of EC resonance and the gas puff. Methods for creation of the more dense two-component plasma need further investigation.

Let us make few remarks on the applicability of our approach. Local approximation for growth rates is valid when gyrophase detuning due to inhomogeneity of the magnetic field along the field line is small on the distance of phase detuning due to the relativistic resonance shift; for the parabolic field it results in condition $L_B \gg \lambda \beta_{\parallel} / \beta^3 \sim 1$ mm for the parameters used, $\lambda = 2\pi c / \omega$. In principle, the efficiency of generation may reduce due to perpendicular non-uniformities, but they could be avoided or diminished by a proper trap design. The amplification length for the above examples is less but comparable to the trap size. Thus, an external resonator may be required to extract all available free energy like in laser systems. Although the main saturation mechanism is due to quasi-linear degradation, in the regime of multi-GW pulse generation, pondermotive non-linearities could affect the background plasma dispersion and the electromagnetic pulse generation.

Preliminary experimental evidences

As was already mentioned in Introduction, suppression of EC instabilities in a mirror axisymmetric magnetic trap by a bulk plasma has been recently demonstrated experimentally [4, 5]. In this experiment, intense short-pulse (a duration ~ 5 μs) quasi-periodic (a period 150–200 μs) emissions of fast electrons and synchronous electromagnetic radiation have been observed with about 1 ms delay after the end of a microwave pulse supporting the initial non-equilibrium plasma, see Fig. 5. Parameters of the initial plasma were $N_e \sim 10^{13}$ cm^{-3}, $N_h \sim 5 \cdot 10^{10}$ cm^{-3}, $T_e \sim 300$ eV, $T_h \sim 10$ keV. The burst emissions have been explained as the development of kinetic instabilities of the extraordinary waves with the threshold affected both by the absorption in the background plasma and by the transparency of the plasma layer. During ECR discharge such instabilities are depressed by the

dense plasma; the development of instabilities becomes possible only in suffi-
ciently low-density plasma at the late phase of plasma decay when condition (1)
is fulfilled.

gyrotron   decay of a bulk plasma

500 µs/grad
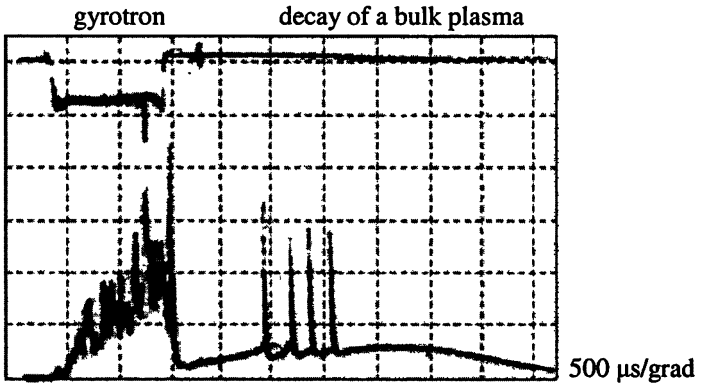
Fig. 5. Oscillogram of the envelope of the gyrotron pulse supporting the microwave dis-
charge in nitrogen (upper ray) and the signal from the pin diode detecting precipitations of
fast electrons from the magnetic trap (lower ray). Adopted from Ref. [4].

Conclusions

Magnetic compression of plasma confined in a mirror magnetic trap may be
accompanied by accumulation of significant energy in a hot anisotropic electron
tail with the subsequent release of this energy as a pulse of coherent broadband
electromagnetic radiation. We show that the radiation power may be substantially
increased when maser instability occurs above the fundamental cyclotron har-
monic due to the cut-off effect of the fast extraordinary waves. In particular, this
mechanism provides a unique possibility of creating THz radiation sources of
multi-megawatt power level.

The aim of the present paper is to demonstrate the basic idea of a magneto-
compressional maser operating in the THz range. Therefore we are limited by a
qualitative analysis. More accurate treatment requires further development of the
theory including modeling based on numerical solution of a bounce-averaged
quasi-linear kinetic equation and "ordering" of a parameter space to find more
rigorous optimization procedure of confinement regimes. There are still not
solved problems in physics:

- What source of initial plasma should be used and how to control its parame-
  ters? (ECR discharge provides plasma up to 10^{14} cm^{-3}.)
- What factors determine the life-time of exhausted fast electrons inside a loss-
  cone, and how to reduce this time?
- What design may be proposed for external cavity & radiation output?

Besides, the same generation principle may be used in a device based on the magnetic compression of a plasma flow propagating in a spatially inhomogeneous magnetic field towards a magnetic mirror. Such systems are characterized by "horse shoe" distribution functions of hot electrons and considered now as the most likely model of auroral kilometric radiation [10, 17]. This motivates interest to investigation of EC instabilities driven in such systems in laboratory conditions [18]. However, present day experiments are based on using of compensated electron beams, rather than a two-component plasma flow; the role of background plasma has been investigated neither experimentally, nor theoretically. However, using plasma instead of an electron beam would greatly increase the density of emitting electrons. Also, interaction of weakly magnetized ions and strongly magnetized electrons in such system may result in formation of ambipolar (due to charge separation) electric field that accelerates electrons up to ion energies. Our preliminary calculations show that the longitudinal ion flow may drag magnetized electrons to the higher magnetic field; as a result a substantial part of the ion kinetic energy transfers to the gyromotion of hot electrons. This effect is very favorable for creating the radiation source which would provide a high-repetition rate, opposite to the device studied in the present paper.

References

1. *Gaponov-Grekhov A. V., Glagolev V. M., Trakhtengerts V. Yu.* Sov. Phys. JETP **53**, 114 (1981).
2. *Golubev S. V., Shalashov A. G.* JETP Lett. **86**, 91 (2007).
3. *Golubev S. V., Shalashov A. G.* Phys. Rev. Lett. **99**, 205002 (2007).
4. *Shalashov A. G., Vodopyanov A. V.* et al. JETP Letters **84**, 314 (2006).
5. *Vodopyanov A. V., Golubev S. V., Demekhov A. G. et al.* JETP **104**, 330 (2007).
6. *Bratman V. L., Suvorov E. V.* // Strong Microwaves in Plasmas (2006) / edited by A. G. Litvak. Nizhny Novgorod: IAP RAS, 2006. Vol. 1. P. 76.
7. *Bolotin V. P. et al.* // Proceedings of the 26th Int. Free Electron Lasers Conference and 11th FEL Users Workshop. Trieste, Italy, 2004. P. 226.
8. *Glyavin M. Yu , Luchinin A. G., Golubyatnikov G. Yu.* Phys. Rev. Lett. **100**, 015101 (2008).
9 e.g. see http://www.magnet.fsu.edu.
10. *Speirs D. C. et al.* Plasma Phys. Control. Fusion, **50**, 074011 (2008).
11. *Melrose D. B., Dulk G. A.* Astrophys. J. **259**, 844 (1982), Hewitt R. G. et al. Aust. J. Phys. **35**, 447 (1982); Wu C. S. Space Sci. Rev. **41**, 215 (1985).
12. *Khanin Ya. I.* Fundamentals of laser dynamics. Cambridge International Science Publishing Ltd , Cambridge, 2006.
13. *Killeen J., Kerbel G. D., McCoy M G., Mirin A. A.* Computational methods for kinetic models of magnetically confined plasmas. NY: Springer-Verlag, 1986.
14. *Zheleznyakov V. V.* Radiation in Astrophysical Plasmas. Kluwer Ac. Pub., 1996.
15. *Mikhailovskii A. B.* Theory of Plasma Instabilities. Vol. 1. Consultants Bureau, New York, 1974
16. *Bespalov P. A., Trakhtengerts V. Yu.* The Alfven Masers [in Russian]. Gorki: Inst. Prikl. Fiz. of Akad. Nauk USSR, 1986.
17. *Bingham R*., *Cairns R. A* Phys. Plasmas, **7**, 3089 (2000), Vorgul I., Cairns R. A., Bingham R. Phys. Plasmas, **12**, 122903 (2005); Speirs D. C. et al. J. Plas. Phys. **71**, 665 (2005).
18. *McConville S. L. et al.* Plasma Phys. Control. Fusion, **50**, 074010 (2008).

PROSPECTS OF HIGH-POWER MILLIMETER-WAVE RADAR

A. A. Tolkachev, B. A. Levitan, M. I. Petelin[1]

JSC "Radio Physics", Moscow, Russia
[1]Institute of Applied Physics, Nizhny Novgorod, Russia

The paper discusses various aspects of past, present and possible high-power MMW radar: general block diagrams, high power amplifiers, multiplexers, duplexers, monopulse configurations, passive-active phased arrays and signal processing techniques.

Advantages, difficulties and natural applications of MMW radar

If the carrier frequency f enlarges, capabilities of radar systems are known [1–3] to grow up:
- according to the formula

$$\theta \sim \frac{\lambda}{D},\qquad(1)$$

where $\lambda = c/f$ is the wavelength and c is the light velocity, the frequency enhancement reduces the beam width θ for a fixed antenna diameter D or reduces the antenna diameter D at a fixed angle resolution θ;
- if the signal bandwidth B is proportional to the carrier frequency f, the frequency enhancement reduces the target range uncertainty

$$\Delta r \sim \frac{c}{2B};\qquad(2)$$

- according to the formula

$$\Delta f = 2\frac{v_r}{c}f,\qquad(3)$$

where v_r is the radial projection of the target velocity, the Doppler frequency shift Δf is proportional to the carrier frequency f.

However, in spite of the above attractions, penetration of the radar into the millimeter wave (MMW) band has been relatively slow, owing to 1) a relatively high absorption of millimeter waves by the atmosphere and 2) a strong scattering of millimeter waves by rains and snows.

Nevertheless, for some applications, the above limitations are tolerable [4]. Near the Earth surface, stationary and mobile MMW radar systems can be used for weather monitoring, tracking small moving targets, collision avoidance etc. Relevant low power phased arrays can be composed of solid state elements. Medium power "semi-active" arrays can be fed by ~10%-bandwidth TWTs or gyroTWTs; distributed reflectors or lenses composed of semiconductor or ferrite phase shifters can perform agile ±45° wave beam scanning and multi-target tracking within tens kilometers coverage range [5] (to combine the high range resolution with the broad-angle scanning, time delays between sections of the phased array should be agile controlled [3, 4]).

The highest MMW powers are needed for satellite imaging and space debris detection. Of course, this kind of ground based radar is weather dependent, and to reduce the atmospheric absorption, elevation angles should be over 20 degrees.

Up to the date experience with MMW radar of the highest powers

A combination of Ka-band and W-band radars was operating since 1983 at Kwajalien (USA) [6]. The Ka-band transmitter was based on two 50 kW pulsed TWTs made by the Varian. ~1 m^2 RCS targets were detected and tracked at distances up to 2000 km.

The 34 GHz radar "Ruza" [7] (Fig. 1) put into operation by the Research Institute "Radio Physics" (USSR) in 1989 had a ~1 MW pulse/ 0.02 duty transmitter with the final cascade based on gyroklystrons. The antenna had a mechanical hemispheric coverage. Within a conical sector about 1°, the beam formed by 120 radiators was steered electronically by ferrite phase shifters. The radar performance was passive on transmit and active on receive. Satellites were tracked at distances up to 2000 km. When a satellite-like object reentered the atmosphere, the radar saw not only the maim body, but its plasma tail as well (Fig. 2).
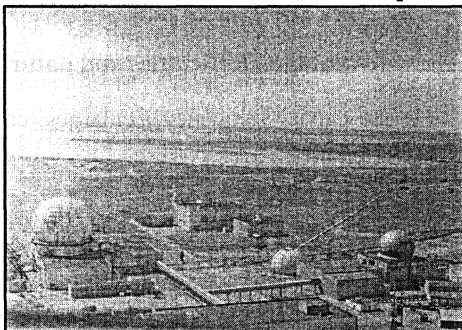
Fig. 1. A combination of X-band ("Argun", *left*) and Ka-band ("Ruza", *right*) radar systems at a Kazakhstan site
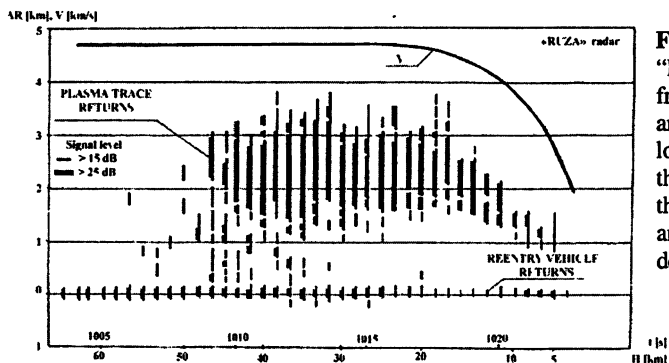
Fig. 2. Records of the "Ruza" radar. Returns from a reentry vehicle are followed with a long plasma tail under the condition that both the vehicle velocity and the atmosphere density are high enough.

The W-band "Warloc" radar operable since 1999 at the NRL (USA) has a 700 MHz band transmitter based on a 100 kW pulse/0.1 duty gyroklystron [8]. The system efficiently functions as a cloud radar studying wave refraction and scattering by the atmosphere.

490

High power MMW radar projects

With account of the previous experience, a MMW radar system aimed for
- detection of space debris and near-Earth asteroids,
- imaging of satellites,

needs ~1–10 MW radiated pulse power at ~0.1 duty. A relevant radar transmitter would have the final cascade composed of gyroklystrons or gyrotwystrons. Penultimate RF amplification would be performed with medium power vacuum tubes, for instance, EIKs [9]. Low power cascades of the transmitter would be based on solid state RF amplifiers. A sufficiently broad band for a high range resolution (2) can be provided with multiplexing [10–12] (Fig. 3).
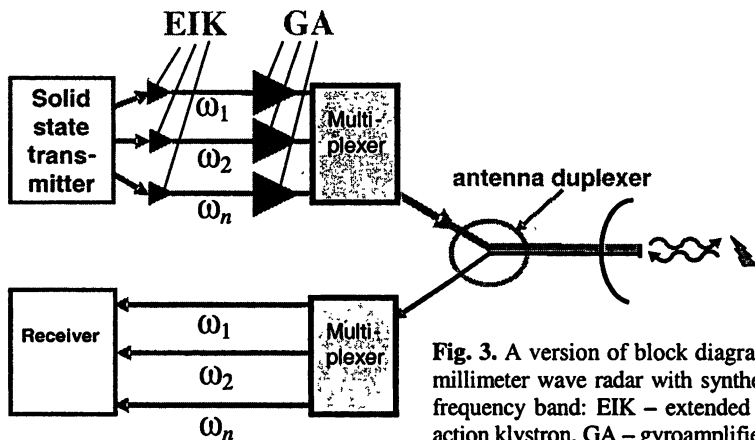
Fig. 3. A version of block diagram for millimeter wave radar with synthesized frequency band: EIK – extended interaction klystron, GA – gyroamplifier.

Presently, there are two projects of the sort:
- the "HUSIR" (Haystack Ultra Wideband Satellite Imaging Radar) [13] being developed by the MIT Lincoln Lab,
- the "Suffah" [14], an Uzbekistan-Russian complex, planned to combine functions of a MMW radio telescope and a MMW radar.

Wave transmission and control systems of such radars are assumed to be composed of oversized, quasi-optical components. If the elementary channel bandwidth is considerably less than 1 %, the signal multiplexing can be performed with a chain of resonant diplexers [11]. If the elementary channel bandwidth is not less than ~1 %, the signal multiplexing can be performed with a dispersive Littrow grating [12]. To compensate 1) the atmosphere fluctuations and 2) dips between central frequencies of neighboring sub-bands, an adaptive algorithm with an adaptive spectrum regularizer can bee used [11]*.

To operate at a megawatt MMW power with a single transmit-receive Cassegrain antenna, a relevant breakdown-proof duplexer is expedient to be com-

---

* Quasi-optical multiplexers may be used in multi-channel deep-space communication systems as well [17].

posed of metallic gratings [10, 15, 16]. By analogy with a number of practical radar systems (for instance, the RUZA) the duplexer would include

• a polarization separator and
• a polarizer.

An experimental W-band duplexer [16] (Fig. 4) tested at a low power level has provided the transmit-receive isolation –45 dB; the transmission loss did not exceed –0.1 dB within ~10 % frequency bandwidth.
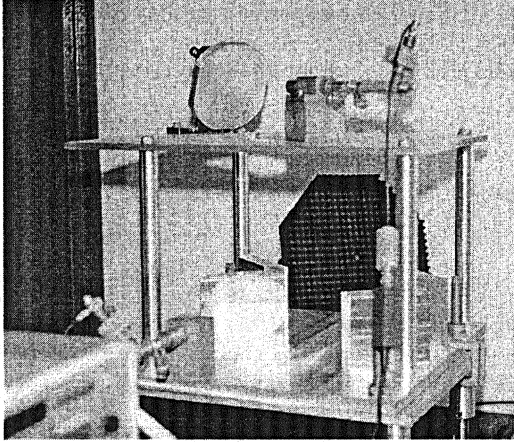
Fig. 4. An experimental duplexer with central frequency 94 GHz

A moving target may be tracked by the simplest mechanically steered mirror type antenna with quasi-optical monopulse matching to transmit-receive units (Fig. 5). More complicated multi-mirror configurations (Fig. 6) might provide additional opportunities to analyze target structures.
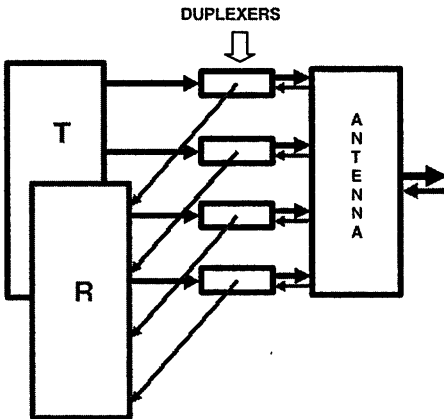
Fig. 5. A block diagram of radar with monopulse matching of antenna to transmitter and receiver. Both the transmitter (T) and the receiver (R) are assumed to be of a synthesized frequency band.

492
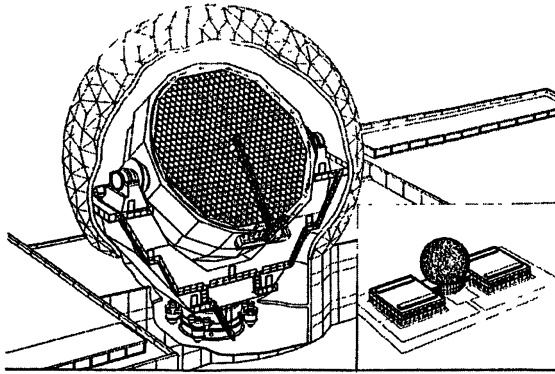
Fig. 6. An artistic view of a multi-module antenna system with controlled shaping of the beam pattern

References

1. *Skolnik M.* Introduction to Radar Systems, McGraw-Hill (2001)
2. *Barton D.* Modern Radar System Analysis, Artech House (1988).
3. *Brookner E.* Practical phased-array systems, ISBN 0-89006-563-2 (1997).
4. *Tolkachev A., Yegorov E., Shishlov A.* Quasi-optical Control of Intense Microwave Transmission / Ed. J. Hirshfield and M. Petelin. NATO science Series. Springer, 2005. P. 353–370.
5. *Korchemkin Y., Denisenko V., Milevsky N., Fedorov V.* Ibid., 165–175.
6. *Abouzahra M., Avent R.* JEEE Antennas and Propagation Magazine, **36**, 2 (1994).
7. *Tolkachev A., Levitan B., Solovjev G. et al.* IEEE Aerospace and Electronic Systems Magazine, **15**, No.7, 25–31 (2000).
8. *Linde G., Ngo M., Danly B, Cheung W., Gregers-Hansen V.* IEEE Trans. Aerospace and Electronic Systems, **44**, No. 3, 1102–1117 (2008).
9. *Steer B., Roitman A., Horoyski P. et al.* Abstr. of Workshop "Strong Microwaves: Sources and Applications". Nizhny Novgorod, 2008. P. 133.
10. *Petelin M., Caryotakis G., Tolkachev A. et al.* AIP Conference "High Energy Density Microwaves", Pajaro Dunes, California, Proc. 474, 304–315 / Ed. Robert M. Phillips. Woodbury, New York, 1998.
11. *Petelin M., Caryotakis G., Postoenko Yu. et al.* Quasi-optical Control of Intense Microwave Transmission / Ed. J. Hirshfield and M. Petelin. NATO science Series. Springer, 2005. P. 353–370.
12. *Koposova E., Petelin M.* Radiofizika, **32**, No. 9, 1178–1181 (1989).
13. *Usoff J.* Proc. IEEE Radar Conference, Boston, 2007. P. 7–22.
14. http://radioastron.ru/index.php.
15. *Hirshfield J., Kolchin P., Kuzikov S., Petelin M.* Digest of 25th Int. Conf. on Infrared and Millimeter Waves, Beijing, 2000 P. 405–406.
16. *Petelin M., Salin M., Shchegolkov D., Zaitsev N., Erckmann V., Hirshfield J., Kasparek W.* Proc. of IEEE Conference IVEC 2008. P. 87–88 (2008).
17. *Kodis M., Abraham D., Morabito D.* AIP Conf. Proc. 691 / Ed. S. Gold and G. Nusinovich. 2003. P. 47–53.

MILLIMETER WAVE AMPLIFIERS OF MEDIUM POWER

B. Steer, A. Roitman, P. Horoyski, M. Hyttinen, D. Berry

Communications & Power Industries Canada Inc., Georgetown, Ontario, Canada

This paper reviews the technology and demonstrated capability of mmW and THz Extended Interaction Klystrons at CPI Canada. It discusses design and manufacturing concepts stating design modifications to enhance power and bandwidth capability and extending operating frequency into the THz region.

Many of today's and future applications, such as communications, active denial, atmospheric sensing and near-object analysis, require RF sources producing microwave power of several watts to several kilowatts in the millimeter and submillimeter frequency range. The Extended Interaction Klystron (EIK) is one of the few readily available devices capable of providing the required performance.

Introduction

Since the 1970s CPI has developed and manufactured a series of millimeter-wavelength Extended Interaction Klystron amplifiers and oscillators. These devices are based on conventional vacuum electronics technology, which have consistently produced state-of-the-art performance.

The EIK has multiple interaction gaps in each cavity, raising cavity impedance, thus offsetting a significant difficulty when scaling VEDs to mmW frequencies. EIKs currently operate from 18 to 280 GHz but have performance projected up to 700 GHz as summarized in the chart below.

Achieved EIK Performance		
Frequency	Pulsed Power	Average Power
35 GHz	3500 W	1200 W
95 GHz	3000 W	400 W
140 GHz	400 W	50 W
220 GHz	50 W	6 W
Projected Performance		
350 GHz	20 W	1 W
450 GHz	10 W	0.5 W
700 GHz	2 W	0.1 W

The EIK is an optimum blend between the klystron and coupled-cavity TWT technologies achieving high peak power, efficiency, bandwidth and reliability at

millimeter and sub-millimeter frequencies. The multi-gap RF circuit has a simple, rugged geometry characterized by high impedance. Thus supporting efficient modulation and energy exchange between the RF field and electron beam over a broad instantaneous bandwidth. High gain produces a short interaction circuit allowing for a single-period permanent magnet. The result is a well-focused electron beam in a light-weight package.

Design and Construction Features of EIKs

Standard single gap klystrons are not capable of maintaining optimum cavity impedance at the frequencies above 15–18 GHz. This is due to two major factors: the reduction in cavity R/Q and the necessity of using electron beams with lower conductance. The EIK uses multiple gaps to achieve high cavity impedance with corresponding improvement in output power, efficiency and bandwidth. At the same time, due to lower beam currents and higher cavity losses, introduction of multiple gaps within a single cavity does not compromise RF stability at millimeter frequencies. Re-distribution of RF power across multiple gaps reduces risks of multipacting and RF arcing. Various electronic and electrodymanic methods for selective mode suppression provide conditions for good RF stability.

The sketch shows 2 cavities containing interaction gaps distributed along the electron beam.
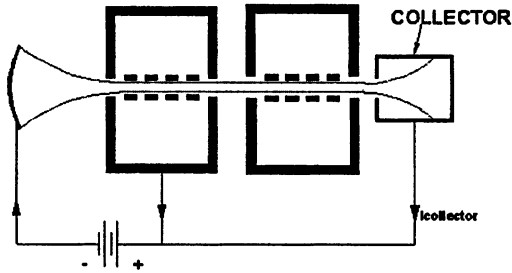
Electrons are emitted from the thermionic dispenser cathode; a high convergence electron gun accelerates and focuses the electron beam through an aperture in the anode. Beyond the anode, the beam, confined by a permanent magnetic field, passes through a beam tunnel in the center of a series of cavities. Each cavity represents a short piece of the resonant slow-wave structure (SWS) based on a ladder-circuit geometry. The number of SWS periods is selected to satisfy the conditions of RF stability and efficient beam modulation. When the electron beam enters the output cavity, the RF current magnitude exceeds the DC beam current by 40 %. Approximately 70 % of the microwave energy generated in output cavity is coupled to the waveguide. The spent electron beam then leaves the circuit and is recovered in the depressed collector.

495

Simplified Assembly of an EIK
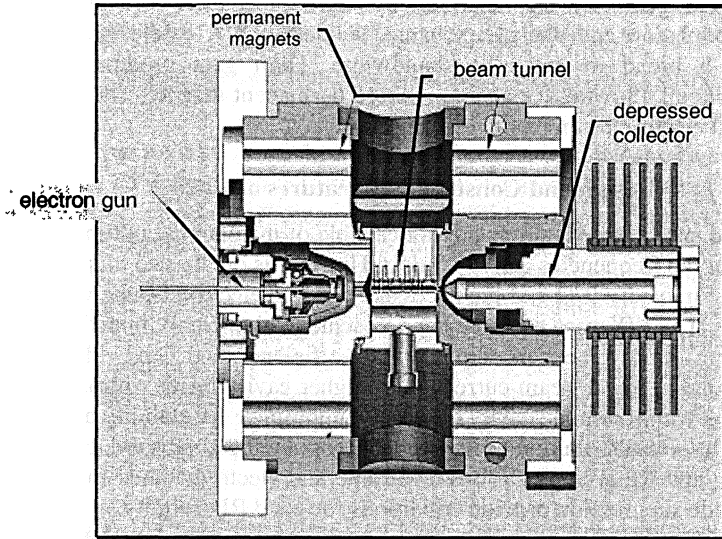
Pulsed and CW EIK Applications
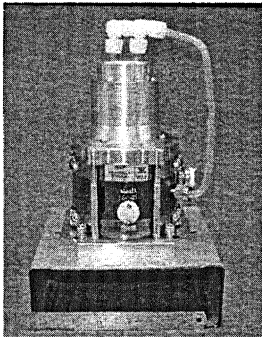
6 inches

EIKs are medium power compact mmW devices capable of providing RF power at frequencies starting at 17 GHz, 4 kW and going up to 700 GHz, 2 watts peak. Pulsed and CW EIKs have been developed, to meet a diverse spectrum of applications, including satellite communications, radar, ESR, plasma research, and RFI testing. An exhaustive survey of all the established uses of EIK devices is beyond the scope of this paper; instead, we will highlight applications at W-band, which is an area of particular interest to commercial, military, and scientific communities.

The importance of W-band radar to the study of the upper atmosphere and cloud physics is well recognized. EIK-based radar systems have been used for over a decade by a wide range of groups around the world to obtain fine-scale cloud information. W-band radars fill the gap between lidars which are subject to severe attenuation in thick cloud layers, and low-frequency precipitation radars (X-band) which will penetrate the most severe thunderstorms and are not as sensitive to clouds. The requirements for cloud radars are very stringent requiring high sensitivity (> –25 dBZ at 10 km) and wide dynamic range of received signal strengths (90 dB or more). Polarization observations are used to differentiate ice particles from water droplets, and dual frequencies are employed to characterize cloud particle sizes (typically the scat-

tering is quantified by comparing 95 GHz Doppler spectra to those collected at 35 GHz, which also allows the relationship between particle size and velocity to be measured). Current generation cloud radars utilize a pencil beam antenna which is either fixed or mechanically scanned. For these narrow-band transmitters (< 300 MHz bandwidth), a standard W-band EIK offers 1.5 kW peak power, 10 % duty cycle, air, liquid, or conduction cooling, in a package weighing less than 6.5 kg. The EIK enables the construction of compact, efficient radars for use in ground, airborne, and spaceborne applications. An image of the liquid-cooled configuration is shown below. For future radar systems utilizing an electronic scanning antenna, CPI has developed a W-band EIK which provides 2 GHz bandwidth with a peak power of 1 kW.

Another application of W-band radar is for imaging and classification of spaceborne objects. Ground-based systems typically require hundreds of kilowatts of peak power to obtain sufficient power "on target", and would utilize a fast-wave device such as a gyroklystron. For these systems, an EIK could serve as an intermediate power amplifier, since the input drive requirements for the gyroklystron would be far in excess of that available from solid-state sources. A space-based radar for debris detection has been proposed, in which case the EIK would serve as the final power amplifier.

W-band radars have also been studied for use in missile tracking and guidance systems, although no systems have been fielded to-date. The EIK provides kilowatts of peak RF power from a compact and electrically efficient package making it ideally suited for such uses. For identification, tracking, and guidance applications, the duty cycle requirements are typically higher than those for cloud radars; W-band EIKs have been provided at 10 % duty cycle, and are capable of even greater duty cycles.

An active area of development for W-band transmitters is in directed energy, non-lethal weaponry. This application requires high average power at 95 GHz with no bandwidth requirement. Both CW and pulsed power EIKs are suitable for this application; 200 W has been demonstrated with a CW EIK, and 400 W average power has been achieved with a pulsed EIK. Kilowatt power levels from an EIK are possible with further development effort.

EIK-based instrumentation amplifiers have been developed to provide end-users with a "turn-key" source of medium power at millimeter-wave frequencies. These units are self-contained cabinets which include the EIK, power supply, cooling system, automatic protection systems, calibrated power monitoring, with front panel and remote computer control capability. These products are attractive to users who require medium power RF sources but are not experienced in constructing millimeter-wave test sets.

EIK for Space-borne Applications

Various space missions require high-resolution radars and altimeters. These instruments operate at millimeter frequencies and require high-transmitted power with sufficient power handling capability to overcome propagation losses. The EIK is a readily available device capable of providing the required performance.

To address space-borne applications, starting in the 1990s CPI Canada began development of space flight EIKs. Modifications included packaging, electrical insulation; space approved materials, improved depressed collector, cooling configuration, cathode and electron gun design for long life and reduced electrical stress. The first W-band space qualified EIK was developed for NASA's Cloud-Sat mission. Its Cloud Profiling Radar (CPR) provides cross-sectional views of clouds with information on their thickness, altitude, water and ice content. The 94 GHz radar is 1000 times more sensitive at profiling clouds than existing weather radars. The satellite was launched in April 2006; the CPR has been in continuous operation since June 2, 2006. On-orbit performance is in a good agreement with the design predictions.

More Ku-, Ka-band and W-band EIKs are currently under development for the EarthCARE, CoReH2O missions and for a variety of space-borne precipitation and Topo-mapping radars. Specification requirements range from 800 W at 0.5 % duty cycle for the rain radar to 3 kW, 30 % duty cycle for a deep space mission topo-mapping radar. For these applications CPI developed a highly efficient and compact Ka-band EIK based on the platform of the W-band space-qualified model. These EIKs share the same beam-optics and packaging, and operate with the same Power Supply. Using this design approach space heritage is maintained, reducing development and delivery time. Further improvement in electron gun design has increased expected lifetime of space-borne EIKs to over 35,000 hours at W-band and 50,000 hours at Ka-band.

Ka- and W-band space-borne EIKs
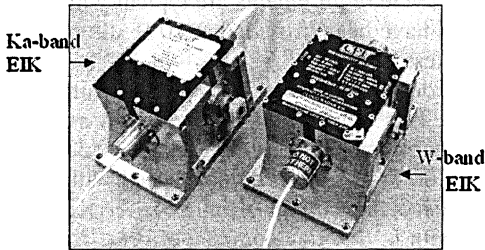
Conclusion

EIK technology from CPI Canada has a proven track record for over 30 years. EIKs are capable of providing mmW & THz radiation at low voltages, in a compact high efficiency package. CPI Canada continues to lead in the development and realisation of medium power mmW and THz sources for applicaions where quality and reliability are prioritised.

References

1. *Roitman A. et al.* "Extended Interaction Klystrons for Space-borne Applications", 6th IEEE International Vacuum Electronics Conference 2005, April 20–22, pp. 217–218.
2. *Roitman A , Horoyski P., Hyttinen M , Berry D , Steer B* "Extended Interaction Klystrons for Submillimeter Applications", 7th IEEE International Vacuum Electronics Conference 2006, April 25–27, p. 191.

IR SPECTROSCOPY DIAGNOSTICS
FOR MICROWAVE PROCESSING

G. Link[1], St. Heissler[2], W. Faubel[2], P. G. Weidler[2], M. Thumm[1,3]

[1] Forschungszentrum Karlsruhe, IHM, Germany
[2] Forschungszentrum Karlsruhe, ITC-WGT, Germany
[3] University of Karlsruhe, IHE, Germany

FTIR (Fourier Transformation Infrared) spectroscopy was applied for investigations on microwave processing of clay minerals. Therefore a standard waveguide resonator has been combined with a FTIR spectrometer. Using this instrument in-situ transmission and emission spectroscopy was performed during microwave processing of kaolinite and aragonite. This allows getting direct information about phase transformations or chemical reactions within the materials as function of temperature. Furthermore by measuring spectra with and without microwave irradiation investigations of microwave specific effects within the processed materials will be possible.

Introduction

In various fields of materials processing high power microwave technology faces growing interest. Although the process of development from first scientific investigations into an up-scaled and reliable industrial production line sometimes is a rather long way, several microwave processes were implemented in industry very successfully. Beside the procedural benefit of direct volumetric heating very often a reduction of processing temperature or processing time has been reported when microwave processing is compared to standard processes using conventional methods for heating. Very often those phenomenological differences in process parameters are explained by microwave specific effects based on microwave enhanced diffusion or microwave enhanced chemical reactions or are based on a selective microwave heating. This argumentation usually relies on the comparison of temperature measurements in different heating systems. Since within the materials the inherent temperature profiles of conventional heating and microwave heating are different and since precise temperature measurement in a microwave environment is far from trivial, such conclusion are very often a matter of criticism. In order to overcome the problem of potential misinterpretation of such microwave specific effects any other information from the process could be useful.

Therefore an infrared (IR) spectrometer has been combined with a microwave device that allows in-situ IR spectroscopy during microwave processing of different materials. IR spectroscopy has been widely used in research and industry for quality control, analytical and dynamic measurements for various organic and inorganic materials as for example semiconductors or clay minerals. The spectrometer applied is a Fourier-Transform Infrared (FTIR) spectrometer. It is a versatile instrument that can be used for measurements in transmission and in emission modus as well as for Fourier-Transform (FT) Raman spectroscopy.

Such IR spectra contain information about the vibrational states within the materials. Due to this material's specific information such spectroscopic methods can be used to monitor structural changes, phase transformations or chemical reactions during microwave materials processing. But the main motivation behind these efforts is to investigate if any direct influence of microwaves onto such materials specific IR spectra can be discovered. This would increase the insight into the microwave materials interaction and may help to understand microwave specific effects.

Experimental

Experimental Set-Up

A scheme of the experimental set-up for in-situ FTIR spectroscopy is shown in Fig. 1. Based on a standard WR340 aluminum waveguide a TE_{103} single-mode resonator has been build up including two cut-off sections on two opposite sites of the waveguide. A FTIR spectrometer of the type IF66S from the Bruker Company, Germany has been adapted to the microwave system. Therefore in case of transmission spectroscopy the IR beam is coupled out of the spectrometer and is focused to the sample by an elliptical mirror with 150 mm in focal length. The sample is placed in the center of the waveguide resonator (see Fig. 1 and 2) in the maximum of the electric field. That part of the beam transmitted through the sample is finally focused to a Mercury Cadmium Telluride (MCT) detector cooled by liquid nitrogen. The detector is sensitive in the mid infrared region from 600 to 4000 wavenumbers (corresponding to wavelengths from 16.7 to 2.5 μm). The IR source used for transmission measurements was a globar, which is a silicon carbide rod electrically heated up to 1000 to 1650 °C showing a emission spectrum similar to that of a Planck radiator.
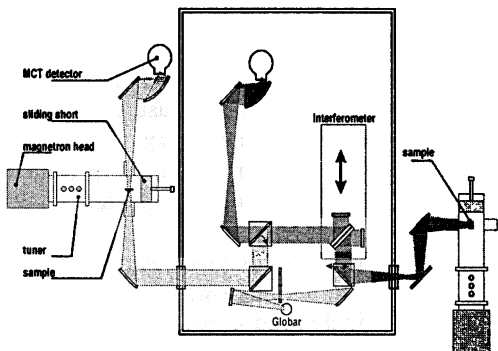
Fig. 1. Scheme of the FTIR spectrometer set-up for transmission (light grey path of rays) and emission (dark grey path of rays) measurement in combination with a single-mode microwave waveguide resonator
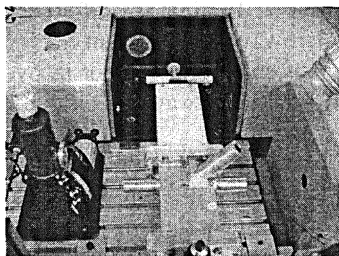
Fig. 2. Photography of the microwave resonator in the beam of the FTIR spectrometer in transmission modus

In case of emission spectroscopy the microwave processed sample itself acts as the IR source. Therefore an input hole on the backside of the spectrometer is used. The IR radiation of the sample has been coupled into the spectrometer via an elliptical and a subsequent plane mirror. In front of the IR coupling hole an adjustable iris was used which allows limiting the IR radiation on the MCT detector (Model MCT D315) to avoid signal saturation in case of high temperatures. In order to reduce the absorption bands coming from CO_2 and water vapor usually present in the atmosphere, the whole course of the IR beam was covered and continuously purged with dry air.

Sample preparation

For measurements of transmission spectra the powder materials under test were mixed in low concentrations of about 1 to 2 weight % with KBr powder. In order to produce a transparent sample these powder mixtures were pressed to pellets in a laboratory press using a pressure of 10 tons. The dimensions of so preserved pellets are 13 mm in diameter and about 1 mm in thickness. A background spectrum was obtained by measuring a pure KBr pellet.

In case of emission spectroscopy sample preparation is more complex, since the thickness of the sample is a critical parameter for the quality of the emission spectrum. Ideally the sample thickness of solid materials should be in the range of some μm only. With increasing sample thickness, the intensities of the emission bands will increase but continuously lose spectral contrast and the spectra more and more resemble a black-body. Furthermore the emission bands may be inverted or split due to reabsorption of emission bands from the hot bulk material in the cooler one near the surface [1], a temperature profile which is very typical for microwave processed samples.

Thus optimization of sample preparation for emission spectroscopy is a still ongoing task. Some first results have been obtained by using a bulk SiC sample with a sputtered gold layer on the surface facing the IR spectrometer. Thereafter a thin cover of the test material was applied to the metal layer by dropping an alcoholic suspension to the surface. After evaporation of the alcoholic phase a thin powder layer of the test material was left.

Results and discussions

In first experiments IR transmission spectra were recorded at ambient temperatures with a kaolinite sample type DSK50 from the Dorfner Company, Germany. Therefore microwave power was switched on for 1 or 2 seconds, sufficiently long to measure 3 to 4 interferograms used to calculate the IR spectrum and sufficiently short to avoid significant sample heating. Thereafter another spectrum was recorded while the microwave power was switched off. This procedure was repeated 10 times. Then the average spectra for both conditions (microwave on and off) were compared in accordance to the experimental approach, published by M. Vala and J. Szczepanski [2].

501

Figure 3 gives the resulting transmission spectrum when the kaolinite sample was exposed to microwave radiation (grey line) as well as the magnified difference to the spectrum without microwave irradiation (black line). Some but not all of the absorption bands typical for kaolinite can be distinguished in the difference spectrum as well. This indicates that the influence of microwave is different for different absorption bands. While the bands at the wavenumbers 3697, 3620 and 914 cm^{-1} can be assigned to vibrational states of hydroxyl groups the bands at 1114, 1033 and 1006 cm^{-1}, respectively correspond to SiO vibrations. This indicates to some extend a selective microwave interaction with the hydroxyl groups what may help to understand the enhanced dehydroxylation process into the amorphous meta-kaolinite, as it was reported elsewhere [3].
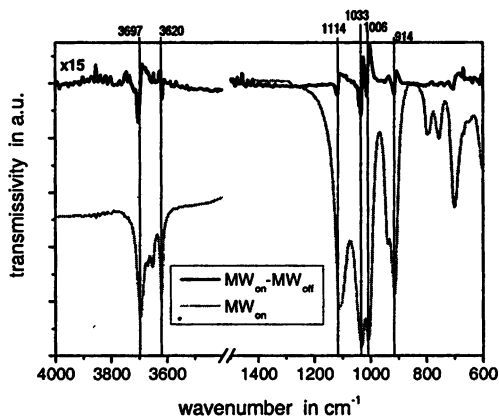
Fig. 3. FTIR transmission spectrum of kaolinite at room temperature under microwave irradiation (grey), and enlarged difference spectrum to the non-irradiated state (black)

To overcome the problem of temperature limitation due to lack of transmissivity if the sample was heated to temperatures above 100 °C, investigations in emission mode have been started. Figures 4 and 5 present emission spectra for kaolinite and aragonite, respectively, at temperatures starting from 300 °C up to 700 °C. Although the signal to noise ratio is by far not as good as for transmission measurements, phase transformations in the materials can be clearly observed. The dehydroxylation process in kaolinite can be clearly recognized as a disappearance of the hydroxyl bands at about 3600–3700 cm^{-1} at about 600 °C. The formation of the meta-kaolinite which coincides with the dehydroxylation process can be observed as a broadening of the band at about 1100 cm^{-1} which then merges into the band at 1000 cm^{-1} [4].

In the case of aragonite (see Fig. 5), which is the orthorhombic modification of calcium carbonate, at about 500 °C a phase change to the trigonal modification can be recognized by the disappearance of the band at 1075 cm^{-1} and a band shift of the bands in the range of 860 to 870 cm^{-1} [4]. At 700 °C the decomposition process of the carbonate into CaO and CO$_2$ can be concluded from the appearance of a strong absorption band at about 670 cm^{-1} that can be assigned to CO$_2$.
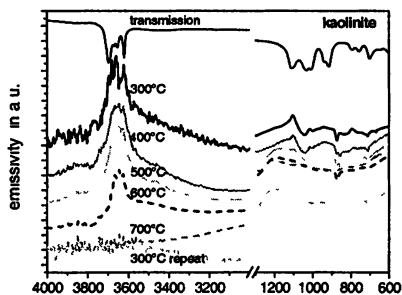
Fig. 4. FTIR emission spectra of kaolinite at different temperatures
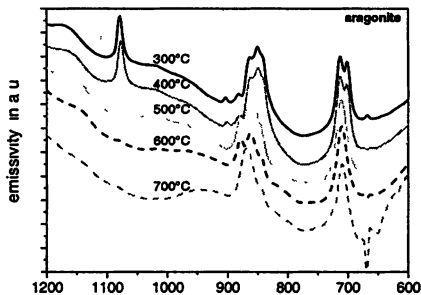
Fig. 5. FTIR emission spectra of aragonite at different temperatures

Conclusions and Outlook

A FTIR spectrometer has been adapted to a single-mode 2.45 GHz waveguide resonator, to investigate variation of transmission and emission spectra during microwave processing of different clay minerals. Transmission spectra at ambient temperature indicate some difference with microwave irradiation compared to a spectrum without microwave irradiation. By emission spectroscopy phase transformations in kaolinite and aragonite could be measured. If the still poor signal-to-noise ratio can be further improved, investigation of the direct influence of the microwave radiation to the emission bands as it was found in case of the transmission spectroscopy will be conducted. Furthermore in a next step Raman spectroscopy will be applied, which has the potential for a phase selective temperature measurement on a microscopic scale as already demonstrated by S. Vaucher and coworkers [5].

References

1. *Mink J.* Infrared Emission Spectroscopy // in Handbook of Vibrational Spectroscopy. Vol. 2 / eds. Chalmers J. M., Griffiths P. R. John Wiley & Sons Ltd. 2002. P. 1194.
2. *Vala M., Szczepanski J.* A microwave effect: Molecular level microwave study of water vapour // Ceramic Transactions. Vol. 80: Microwaves: Theory and Application in Materials Processing IV / editors D. E. Clark, W. H. Sutton, D. A. Lewis, 1997. P. 107–114.
3. *Link G., Hauser-Fuhlberg M., Janek M., Nüesch R., Takayama S., Thumm M., Weisenburger A.* High temperature processing of powders using millimeter-waves // Conf. Proc. of the 4th World Congress on Microwave and Radio Frequency Applications, Austin, Tex., November 7–12, 2004, New York. N. Y.: AIChE, 2005. P 54.
4. *Vassallo A. M., Cole-Clarke P A., Pang L. S K., Palmisano A. J.* Infrared Emission Spectroscopy of Coal Minerals and their Thermal Transformation // Applied Spectroscopy. 1992. Vol. 46, № 1. P. 73–78.
5. *Vaucher S., Catala-Civera J.-M., Sarua A, Pomeroy J., Kuball M.* Phase selectivity of microwave heating evidenced by Raman spectroscopy // Journal of Applied Physics. 2006. Vol. 99. P. 113505.

SINTERING AND MECHANICAL PROPERTIES OF ULTRAFINE ALUMINA CERAMICS UNDER MICROWAVE HEATING

S. V. Egorov, A. G. Eremeev, V. V. Kholoptsev, I. V. Plotnikov,
A. A. Sorokin, Yu. V. Bykov, Yu. A. Kotov[1], V. V. Ivanov[1],
V. N. Chuvil'deev[2], M. Yu. Gryaznov[2], S. V. Shotin[2]

Institute of Applied Physics, Russian Academy of Sciences,
Nizhny Novgorod, Russia
[1] Institute of Electrophysics, Ural Division of Russian Academy of Sciences,
Ekaterinburg, Russia
[2] Nizhny Novgorod State University, Nizhny Novgorod, Russia

Alumina-based ceramics with various additives, compacted from nanosize oxide particles, were sintered under microwave heating on the gyrotron system operating at the frequency of 24 GHz. The samples of 97–98 % density and average grain size in the range of 0.35–0.55 μm were sintered at temperatures of 1350–1450 °C with 2–15 min holding time. The microhardness and fracture toughness of ceramics were measured.

Uniaxial compression of the sintered samples under microwave heating was studied. The observed deformation rates were up to $2 \cdot 10^{-4}$ s^{-1} at temperatures up to 1400 °C and the applied pressure up to 80 MPa. The apparent activation energy for compressive deformation of alumina-based ceramics under microwave heating was determined. The influence of the temperature and duration of deformation on the mechanical properties of the samples are discussed.

Introduction

The great interest in the nanocrystalline structural materials originates from their unique mechanical properties. The enhanced hardness, strength, plasticity, wear resistance are among the properties of the most practical importance. The development of a manufacturing technology for nanostructured ceramics includes three major lines: synthesis of nanosize powders, compaction of articles and densification of the material to high density. Fabrication of nanopowders by electrical explosion of wires is one of the most promising methods due to its high productivity [1]. A necessary condition of obtaining fully dense nanostructured ceramics is high and uniform density of compacts produced from non-agglomerated nanopowders. High quality compacts of simple geometrical forms can be obtained by the method of magnetic dynamic pressing developed at the Institute of Electrophysics [2]. The technological challenge is densification of compacts to high final density while retaining the nanostructure of grains in the material. The sintering of compacts under microwave heating shows good prospects for this goal. The reduction in the thermal stresses resulting from the uniform volumetric absorption of the microwave energy allows heating at high rates which can restrict the grain growth at densification.

504

The results of the study of microwave sintering and plastic deformation of alumina-based ceramics under microwave heating are reported in this paper, as well as their microstructure and mechanical properties.

Experiment

The nanosize powders Al_2O_3, ZrO_2, $(AlMg)_2O_3$ and Y_2O_3 produced by the Institute of Electrophysics were used in this work. Al_2O_3, ZrO_2, and $(AlMg)_2O_3$ powder were fabricated by the wire explosion method, and Y_2O_3 powder by a method of a CO_2-laser evaporation of a target [3]. The median particle diameter, determined by the Sherrer method, was in the 15–45 nm range; the BET specific surface area was in the range from 55 to 85 m^2/g. Appropriate amounts of Al_2O_3, ZrO_2 and Y_2O_3 powders were mixed with isopropyl alcohol in an ultrasonic dispenser and dried to form uniform mixtures of the following compositions: Al_2O_3+8 wt.% ZrO_2, Al_2O_3+8 wt.% (97 mol.% ZrO_2+3 mol.% Y_2O_3) and ZrO_2+3 mol.% Y_2O_3.

The powders and powder mixtures were compacted at the Institute of Electrophysics by method of uniaxial magnetic dynamic pressing into pellets of 15 or 30 mm diameter, 3.0 mm thickness and a green density in the range of 68–73 % of the theoretical density.

The green samples were sintered in a gyrotron-based system operating at a frequency of 24 GHz with available microwave power up to 6 kW [4]. The green samples were placed in the center of a fused quartz crucible filled with granulated alumina powder for thermal insulation. The temperature of samples was measured by a $Pt – Pt$-Rh thermocouple. The sintering was performed in air. The microwave power control system controlled the heating process according to a preset temperature-time schedule. The rate of heating was 30 °C/min, and the cooling rate was 15 °C/min. The density of the sintered samples was measured by the Archimedes method.

The microwave sintered ceramics of compositions $(AlMg)_2O_3$ and Al_2O_3–8 wt.% ZrO_2 (3 % Y_2O_3) were tested for compressive plastic deformation under microwave heating. The cylinders, 2.2 mm in diameter and 3.0 mm in height, were cut from the pellets sintered to a density of 97–98 % of the theoretical value (ρ_{th}). A uniaxial pressing device for applying a pressure to the cylinders at temperatures up to 1500 °C was introduced into the microwave applicator of the gyrotron system. The device was equipped with a displacement sensor; the accuracy of linear shrinkage measurements was ±2.5 μm. For the deformation studies the cylinders were heated at a rate of 10 °C/min up to the prescribed temperature in the range 1200–1400 °C, and then the pressure in the range 20–80 MPa was applied to them.

The microstructure of the polished and annealed surfaces of the samples was studied by SEM using the *SUPRA 50VP* and *JEOL-6490LV*. The average grain size was determined by the method of random lines intersections. The mechani-

cal properties of the samples, such as the microhardness, H_μ, and fracture toughness, K_{1C}, as a function of the parameters of the sintering and deformation processes (temperature, duration, and the applied pressure) were investigated using the *Nanotest 600 (Micromaterials Ltd)* and *Duramin-2 (Struers)* instruments.

Results and discussion

Listed in Table are the relative final densities of the sintered samples, the regimes of their sintering, the microhardness H_μ, and the fracture toughness. From the published data is known that for ceramic materials of the same compositions but compacted from micron and sumicron size powders the typical temperature of sintering is about 1550–1600 °C and holding time ~ 60 min, which differ considerably from the corresponding values observed in this study. However, practically the same final densities have been obtained when the compacts used in this study were sintered under conventional heating in similar regimes [5]. This similarity of the results suggests that observed improvement in sintering ensues largely from high activity and sinterability of the nanosize powders used in the experiments.

Regimes of sintering, the relative final density (ρ/ρ_{th}), microhardness (H_μ), and fracture toughness (K_{1C}) of the sintered samples

Composition	Regime, T(°C)×t(min)	ρ/ρ_{th}, %	H_μ, GPa	K_{1C}, MPa·m$^{1/2}$
Al_2O_3	1450×2	97.2	20.7	5.15
$(AlMg)_2O_3$	1450×5	97.8	18.3	3.8
Al_2O_3 (8 % ZrO_2)	1450×15	97.6	20.4	4.3
Al_2O_3 [8 % (97 % ZrO_2 + + 3 % Y_2O_3)]	1450×5	98.2	19.6	5.75
ZrO_2 (3 % Y_2O_3)	1350×5	96.7	11.4	4.8

As follows from the study of the microstructure, the average grain size in the sintered ceramics was in the range 0.35–0.55 μm. The fine microstructure of the sintered materials leads to an enhancement in the fracture toughness by 15–20 % as compared with a value typical for the ceramics of the same composition but sintered conventionally from sub-micron powders.

The wear resistance of the sintered $(AlMg)_2O_3$ ceramics was determined in the process of dry cutting of steel counterparts. The triangular prisms were cut from the sintered samples. The steel cylindrical counterparts were hardened to the values of 45 and 62 HRC (Rockwell C Hardness). The wear rate was defined as [6]

$$k = \frac{m_0 - m}{\rho L P},$$

where m_0 and m are the starting and final mass of the sample, respectively, ρ is its density, L is the length of the cutting track, P is the cutting force. The wear

506

rate at dry cutting ranged from $2 \cdot 10^{-7}$ to $3 \cdot 10^{-7}$ mm^3/(mN), and met the requirements for ceramic workpieces used in tribological applications (the wear rate in the soft mode should be less than 10^{-6} mm^3/(mN) [7]).

The dependencies of the deformation rates on the stress for sintered $(AlMg)_2O_3$ and Al_2O_3–8 wt. % ZrO_2 (3 % Y_2O_3) ceramic samples are shown in Fig. 1 on a log-log scale for two fixed temperatures.
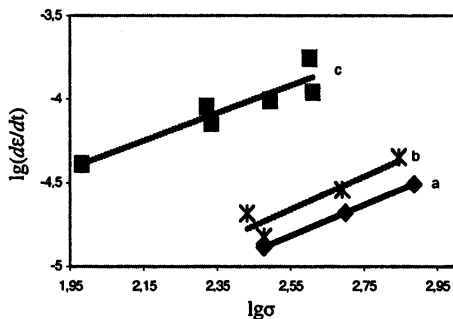
Fig. 1. Deformation rate vs. stress for compression of samples under microwave heating: *a)* Al_2O_3–8 wt. % ZrO_2 (3 % Y_2O_3) ceramics at 1300 °C, *b)* $(AlMg)_2O_3$ ceramics at 1300 °C, *c)* Al_2O_3–8 wt. % ZrO_2 (3 % Y_2O_3) ceramics at 1400 °C

The rate of deformation depends on the temperature and stress applied to a polycrystalline material as [8]:

$$d\varepsilon/dt = A \, (\sigma^{\,n} / d^{\,p}) \, \exp(-Q / RT), \qquad (1)$$

where $d\varepsilon/dt$ is the rate of deformation, A is a constant coefficient, σ is the applied stress, d is the grain size, Q is the activation energy, R is the universal gas constant, and T is the temperature. To determine the activation energy of plastic deformation under microwave heating, the samples were subjected to a constant pressure of 60 MPa while the temperature was increased stepwise from 1200 °C to 1400 °C with a step of 50 °C.

From the results presented in Fig. 1 it follows that the stress exponent $n \approx 1$ for both materials. The exponent p can be determined based on the deformation rate data and the results of microstucture analysis as [9]

$$p = -\left[\frac{\ln(\dot{\varepsilon}_{\hat{e}} / \dot{\varepsilon}_0)}{\ln(d_{\hat{e}} / d_0)} \right]_{\sigma, T}, \qquad (2)$$

where $\dot{\varepsilon}_0$ and $\dot{\varepsilon}_{\hat{e}}$ are the deformation rates at the start and the end of compression, d_0 and d_{e} are the grain sizes before and after deformation, respectively. The analysis of the experimental data gives $p \leq 3$ for both materials, and the activation energies of plastic deformation, Q, are 435 kJ/mol for Al_2O_3–8 wt. % ZrO_2 (3 % Y_2O_3) ceramics and 330 kJ/mol for $(AlMg)_2O_3$ ceramics.

507

It is known that the creep deformation with the rate described by Eq. (1) with $n = 1$ and $p = 3$ in alumina-based ceramics is controlled by grain boundary diffusion [8, 10]. The obtained values of the activation energy are in a reasonable agreement with the activation energy of grain-boundary diffusion of O^{-2} in pure alumina which is equal to 380 kJ/mol [11]. However, numerous experimental results demonstrated significant increase in the activation energy of plastic deformation at conventional heating of alumina ceramics doped with MgO and ZrO_2 [12, 13]. The additives, in amounts comparable with those used in this work, led to an increase in the activation energy of plastic deformation up to 500–600 kJ/mol in Al_2O_3 (add. MgO) ceramics and up to 600–800 kJ/mol in Al_2O_3 (add. ZrO_2) ceramics. The observed reduction in the activation energies discussed above suggests that microwave heating enhances the mass transport along grain boundaries compared to conventional heating. This is in agreement with the ponderomotive model of non-thermal microwave effect on mass transport [14].

The maximal deformation rate was above 10^{-4} s^{-1} in both ceramics at a temperature of 1400 °C and stress of 60 MPa, and the compressive strain exceeded 70 %. The mechanical properties were studied for the samples deformed to high strain. It follows from the obtained data that the mechanical properties deteriorate in highly deformed samples, depending on the temperature and duration of the process. An analysis of the data demonstrates that the temperature is a stronger factor influencing the mechanical properties than the duration of deformation. The samples deformed at 1300 °C even for a long time retain satisfactory mechanical properties. On the other hand, even not-so-long deformation at 1400 °C leaves the microhardness of materials unchanged but results in a significant reduction in fracture toughness. The decrease in fracture toughness is evidently caused by both the grain growth at high-temperature deformation and cavitation, as revealed by the electron microscopy study of the microstructure of the deformed samples.

References

1. *Kotov Yu. A. et al.* J. of Nanoparticle Research, **5**, 539 (2003).
2. *Ivanov V. et al.* Key Engineering Materials, **132–136**, 400 (1997).
3. *Ivanov M. et al.* Adv. Sci. and Technology, **45**, 291 (2006).
4. *Bykov Yu. et al.* IEEE Trans. on Plasma Science, **32**, 67 (2004).
5. *Kaigorodov A. S et al.* Science of Sintering, **37**, 35 (2005).
6. *Kerkwijk B. et al.* Adv. Eng. Mater. **1**, 69 (1999)
7. *Rainforce W. M.* J. Mater. Sci. **39**, 6705 (2004).
8. *Coble R. L.* J. Appl. Phys. **34**, 1679 (1963).
9. *Bernard-Granger G. et al.* J. Mater. Sci. **42**, 2807 (2007)
10. *Chokshi A. H.* J. Europ. Ceram. Soc. **22**, 2469 (2002).
11. *Frost H. J., Ashby M. F.* Deformation – mechanism maps: the plasticity and creep in metals and ceramics, Pergamon Pr. (1982)
12. *Lakki A. et al.* J. Am. Ceram. Soc. **82**, 2181 (1999).
13. *Wakai F., Nagano T, Iga T.* J. Am Ceram. Soc. **80**, 2361 (1997).
14. *Rybakov K. I., Semenov V. E.* Phys. Rev. B **52**, 3030 (1995).

TRANSPARENT Nd:Y$_2$O$_3$-CERAMICS
BY MILLIMETER-WAVE SINTERING

S. V. Egorov, V. V. Kholoptsev, A. A. Sorokin, Yu. V. Bykov, V. V. Osipov[1],
M. G. Ivanov[1], V. V. Platonov[1], A. S. Kaygorodov[1]

Institute of Applied Physics, Russian Academy of Sciences, Nizhny Novgorod, Russia
[1] Institute of Electrophysics, Ural Division of Russian Academy of Sciences,
Ekaterinburg, Russia

The results of millimeter-wave sintering of Nd:Y$_2$O$_3$ optical ceramics are presented. Weakly agglomerated powders of composition 1–3 at.% Nd:Y$_2$O$_3$ with the average size of particles about 20 nm were produced by pulsed CO$_2$ laser evaporation of the target prepared from a proper mixture of commercial Nd$_2$O$_3$ and Y$_2$O$_3$ powders. Green bodies with density of up to 70 % of the theoretical value were compacted by method of magnetic pulse pressing. The sintering of samples at various rates of heating, sintering temperatures, hold times and residual air pressure of 10 Pa was performed on a gyrotron system for microwave processing of materials, operating at a frequency of 24 GHz with a maximum power of up to 5 kW. Optically transparent ceramic samples were obtained by sintering at temperatures in the range of 1750–1900 °C and holding time from 2 to 20 hours. The porosity, estimated from the electron microscopy study, was about 15–30 vol. ppm. The transmittance of 3 at. % Nd:Y$_2$O$_3$ polished samples with thickness of 1.1 mm was about 82 % at the wavelength of 1.06 μm, and the optical loss coefficient was 0.045 cm^{-1}.

Introduction

At present, various optically transparent ceramics are widely developed for many applications, such as lamp envelopes, laser windows, high-strength armors. In recent years, great interest was attracted to the development of a new variety of transparent ceramic materials, the so-called laser ceramics. Laser ceramics are fully dense host materials with cubic crystalline structure, such as yttrium-aluminum garnet (YAG) or Y$_2$O$_3$, doped with lasing rare-earth elements, usually Nd, Yb, Er, etc. as laser active ions. Although the first Nd:ThO$_2$-Y$_2$O$_3$ ceramics, transparent enough for solid-state laser operation, has been demonstrated as early as in the 1970s [1, 2], a breakthrough in the fabrication of laser ceramics was achieved in the middle of the 1990s, when the processing routes for the synthesis of a new class of ceramic materials have been developed owing mainly to efforts of Japanese researchers. Larger gain from higher rare-earth dopant concentrations, the potential for composite configuration, cost-effective fabrication of large-size articles distinguish laser ceramics advantageously from single crystals and make them a unique candidate for high energy applications. The power of continuous wave Nd:YAG ceramic lasers reached 1.46 kW in 2002 [3] and is now approaching tens of kilowatts.

Two advantageous approaches to the fabrication of large-size optically transparent Nd:YAG ceramic articles by solid state sintering have been developed by Ikesue et al. [4] and then by Lu et al. [5]. The methods have made it possible to obtain polycrystalline ceramics with minimal optical loss, which originate primarily from pores, second phases, grain boundary impurities, compositional gradients, and lattice imperfections that cause local deviations of the refraction index. It has been found that a necessary prerequisite for the fabrication of high-quality optical ceramics is the use of green bodies with high uniform density, compacted from high-purity nanosize non-agglomerated powders. Major efforts have been focused on the synthesis of powders and powder compacts having the required properties. Pore-free ceramics with optical properties closely approximating those of single crystals were obtained by the sintering of powder compacts at a temperature of 1750–1850 °C for 20 hours in resistive furnaces under a vacuum of $1.3 \cdot 10^{-3}$ Pa.

The use of microwave heating for the fabrication of optically transparent ceramics is appealing because this method is free of high-temperature resistive heaters that cause pollution of materials. Microwave sintering eliminates the necessity to perform the sintering at high vacuum. In addition, the inverse temperature distribution that exists within the body under volumetric microwave heating is favorable for elimination of porosity [6]. Few studies on microwave sintering of optical ceramics have been undertaken to this date. The synthesis of undoped YAG powder and sintering of compacts with the use of microwave power of 2.45 GHz was described in [7], where 45 % optical transmission at a 520 nm wave-length was achieved in a 0.86 nm thick pellet. The authors of [8] reported on the sintering of YAG- and Y_2O_3-based ceramics for laser applications using the microwave power at a frequency of 83 GHz. The sintered samples with density over 99 % were translucent but not with transparency needed for lasing.

This paper reports the results of the research on the fabrication of Nd:Y_2O_3 ceramics using a laser-evaporation method for the production of powder and a 24 GHz gyrotron-based technological system for microwave sintering. A combination of these two techniques has a good potential for large-scale production of large-size articles for solid-state lasers.

Experimental

The details of the fabrication of powders and compacts for sintering are described elsewhere [9]. The nanosize powders were produced by pulse CO_2 laser evaporation of a ceramic target compacted from a proper mixture of commercial Nd_2O_3 and Y_2O_3 powders with grain size 5–10 μm and purity on the order of 99.99 %. The targets were evaporated in air environment in the regime of CO_2 laser operation optimized for the synthesis of nanosize powders. The major fraction of powder (93–97 wt. %) consisting of spherical particles with an average size of 10 nm and size distribution in the range from 2 to 40 nm was

separated by sedimentation in isopropyl alcohol. X-ray diffraction analysis has shown a monoclinic γ–Y_2O_3 phase of the produced powder with neodymium ions included in the Y_2O_3 crystalline lattice. The samples of 15–32 mm in diameter and 1.5–2.5 mm thick were compacted by uniaxial magnetic pulse pressing [10] of the powder at pressure of 0.5 and 1.5 GPa to the density of 50 % and 72 % of the density of the Y_2O_3 monoclinic crystalline phase, respectively. To remove organic inclusions and for relaxation of residual stresses the compacts were annealed in air for 1–5 hours at a temperature of 900–1300 °C.

The green samples were sintered in a gyrotron-based system operating at a frequency of 24 GHz with available microwave power up to 6 kW [11]. The vacuum-proof working chamber of the system was 40 cm in inner diameter and 60 cm in length. The chamber was evacuated before the start of microwave heating and all experiments were performed at a residual air pressure of about 10 Pa. The green samples were placed in the center of a fused quartz crucible filled with granulated Y_2O_3 (99.95 %) powder for thermal insulation, as shown in Fig. 1.
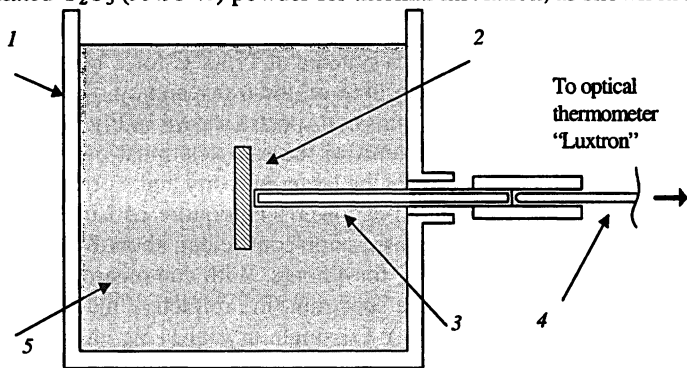
Fig. 1. Schematic view of a sample (2) in the fused quartz crucible (1) filled with Y_2O_3 powder (5): 3 – sapphire light pipe, 4 – sapphire sensor

The temperature of samples was measured by an optical thermometer "Luxtron", model M10. To prevent contamination of the samples and to avoid uncertainty in the measurements caused by possible damage of the sapphire sensor of the thermometer at high processing temperatures, the sensor was attached to a sapphire light-pipe whose other end was located at a 0.5 mm distance from the sample. The temperature measurements were calibrated up to 1800 °C in separate runs by the readings of the Pt – Pt-Rh thermocouple whose head touched the back side of the sample. The accuracy of the temperature measurements was about 1 % at the holding stage of sintering.

The computer-controlled heating of samples was carried out in various temperature-time regimes. The ramp-up rate varied from 3 to 10 °C/min, the temperature of sintering from 1750 to 1900 °C and the holding time varied from 2 to 20 hours. Upon completion of a preset temperature-time regime, the

511

microwave power was automatically switched off and the samples cooled down together with thermal insulation. The rate of cooling was over 25 °C/min during cooling down to 1400 °C.

Both surfaces of the sintered samples were mirror-polished with a diamond paste to the thickness of about 1.2 mm. The optical transmittance spectrum of each specimen was measured within the wavelength region from 400 to 1000 nm using a CF2000 spectrophotometer. Additionally, the coefficient of extinction at the wavelength of 1.06 µm was measured for some samples. The microstructure after sintering was studied by scanning electron microscopy (SUPRA 50 VP). The average grain size and porosity were estimated from the analysis of microstructure images.

Results

All samples sintered at temperatures over 1750 °C were optically transparent. A coefficient of extinction K less than 1 cm^{-1} and a porosity of about 20 vol. ppm were achieved even in the samples sintered at 1750 °C for 2 hours. The effect of sintering temperature and holding time on the transparency of 3 at. % Nd:Y$_2$O$_3$ samples is illustrated by the transmission spectra shown in Fig. 2. The difference between the transmission coefficients of the samples, most evident in the range of small wavelengths resulted from the larger porosity and, correspondingly, light scattering in the samples sintered at lower temperature and in shorter sintering time. The highest value of the transmission coefficient, about 82 %, was obtained for the sample sintered at 1900 °C for 4 hours. With due regard to Fresnel loss in the measurement of transmittance spectrum (the refractive index n = 1.91 at the wavelength λ = 1.07 µm for an Y$_2$O$_3$ single crystal [12]), this value gives the extinction coefficient K equal to 0.05 cm^{-1} at a wavelength of 1 µm, which agrees well with the value of 0.045 cm^{-1} measured at 1.07 µm. Further increase in the holding time up to 8 hours at a temperature of 1900 °C did not result in the increase in the optical transmission at a wavelength near 1 µm.
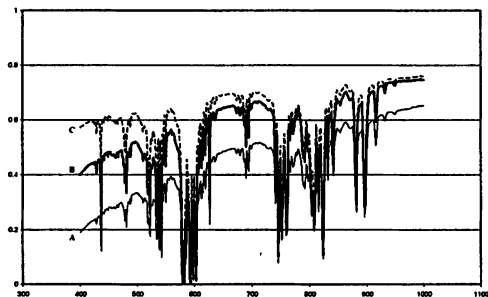
Fig. 2. The optical transmittance spectrum of the samples sintered at a temperature of 1750 °C for 3 hours (A), 1780 °C for 3 hours (B) and the sample sintered at a temperature of 1800 °C for 20 hours (C)

The sintered samples were polished and then thermally etched in air at a temperature 1400 °C for 2 hours to reveal the grain structure. The average grain

size was about 8 μm in the sample sintered at 1750 °C for 3 hours. The average grain size, observed on the polished face surface, increased to 50 μm in the sample sintered at 1770 °C for 6 hours. However, the average size of grains of about 15 μm was evident from SEM observation of the unpolished lateral side of this sample, which is equivalent to observation of its fracture. It remains unclear why the smaller size grain structure is not revealed by thermal etching. The presence of two fractions of grains significantly different in the average size is characteristic also for the samples sintered at higher temperatures and for a longer time.

The achieved level of optical transparency in 3 at. % $Nd:Y_2O_3$ ceramics is sufficient to test the sintered samples in experiments on lasing. At present such experiments are underway.

References

1. *Greskovich C., Wood K. N.* "Fabrication of transparent ThO_2-doped Y_2O_3", Am. Ceram. Soc. Bull. **52**, 473 (1973).
2. *Greskovich C., Chernoch J. P.* "Polycrystalline ceramic lasers", J. Appl. Phys. **44**, 4599 (1973).
3. *Ueda K., Lu J., Takaichi K., Yagi H., Yanagitani T. and Kaminskii A.* "Nd-doped ceramic YAG lasers and their future", The Review of Laser Eng. **31**, 465 (2003).
4. *Ikesue A., Kinoshita T., Kamata K., Yoshida K.* "Fabrication and optical properties of high-performance polycrystalline Nd:YAG ceramics for solid-state laser", J. Am. Cearm. Soc. **78**, 1033 (1995).
5. *Lu J., Song J., Prabhu M., Xu J., Ueda K. et al.* "High-power $Nd:Y_3Al_5O_{12}$ ceramic laser", Jpn. J. Appl. Phys. **39**, L1048 (2000).
6. *Janney M. F., Kimrey H. D.* "Diffusion-controlled processes in microwave fired oxide ceramics", Mat. Res. Soc. Symp. Proceedings, **189**, 215 (1991).
7. *Panneerselvam M., Subanna G. N., Rao K. J.* "Translucent yttrium aluminum garnet: Microwave-assisted route to synthesis and processing", J. Mater. Res. **16**, 2273 (2001).
8. *Fliflet A. W., Hornstein M., Gold S. H., Khan M., Imam M. A.* "Sintering ceramic laser materials with a high power 83 GHz beam", Book of Abstracts, 2008 IEEE Intern. Vacuum Electronics Conf. Monterey, CA, USA, p. 291 (2008).
9. *Bagaev S., Osipov V., Ivanov M. et al.* "Highly transparent $Nd^{3+}:Y_2O_3$ ceramics", Fotonika, № 5, 24 (2007) [in Russian].
10. *Ivanov V., Paranin S., Nozdrin A.* "Principles of pulsed compaction of ceramic nano-sized powders", Key Engineering Materials, **132–136**, 400 (1997).
11. *Bykov Yu., Eremeev A., Glyavin M. et al.* "24–84 GHz gyrotron systems for technological microwave applications", IEEE Transactions on Plasma Science, **32**, 67 (2004).
12. *Kaminskii A. A.* Laser crystals. Moscow: Nauka, 1975. P. 256.

REGULATED MICROWAVE HEATING
OF CERAMIC CYLINDER

P. V. Kozlov, E. B. Kulumbaev, V. M. Lelevkin

Kyrgyz-Russian Slavic University, Bishkek, Kyrgyz Republic

A theoretical model of microwave heating of an extensive ceramic cylinder in a chamber with cooled and heat-insulated walls is described. Numerical and analytical calculations of the heating characteristics of ceramic cylinder made of aluminum oxide in electromagnetic field have been carried out for the cases of constant or linearly growing input power of microwave radiation.

It has been shown [1, 2] that the thermal state of a ceramic cylinder made of aluminum oxide is characterized by the axial temperature T_{max}, which is determined by the input power of microwave radiation Q_n. The stability of the thermal states of the ceramic cylinder is determined on the basis of physical temperature fluctuations.

In this paper an analysis of the stability of stationary thermal states is carried out. The character of thermal relaxation of ceramic material at constant or linearly growing microwave input power, and the temporal dependence of the cylinder heating characteristics are addressed. The possibility of the control over the heating process is accessed taking into account the non-stationary thermal processes.

Model. Non-steady heating of an extensive ceramic cylinder (r, φ, z) due to power dissipation of the input radial electromagnetic wave with components $\vec{E}(0;\ 0;\ E_z = E(r))\exp(i\omega t)$, $\vec{H}(0;\ H_\varphi = H(r);\ 0)\exp(i\omega t)$ and conductive heat exchange of the cylinder with the surrounding air.

Equations. The description of the microwave heating process of ceramic articles is carried out on the basis of the non-stationary equation of energy balance and wave equation solution:

$$\rho_c C_p \frac{\partial T}{\partial t} = \frac{1}{r}\frac{\partial}{\partial r}\left(r\lambda\frac{\partial T}{\partial r}\right) + \frac{1}{2}\varepsilon_i\omega\varepsilon_0 EE^*, \quad \frac{1}{r}\frac{d}{dr}\left(r\frac{dE}{dr}\right) + k_0^2\left(\varepsilon_r - i\varepsilon_i\right)E = 0.$$

The initial and boundary conditions for T and E are imposed in the computation domain $0 \leq r \leq R$:

$$t = 0,\ 0 \leq r \leq R : T = T^0(r),\quad E = E^0(r);$$

$$t > 0,\ r = 0 : dT/dr = 0;\ dE/dr = 0;\ r = R : T = T_R;\ E = E_R(t).$$

The continuity of temperature and thermal flow is conserved on the surface cylinder – gaseous medium in the microwave chamber, and the value $E_R(t)$ is determined by the specified input power of electromagnetic field per unit length of the cylinder, $Q_r(t)$.

Numerical solution. The system of equations is discretized by the method of control volume using implicit approach [2]. Discrete analogs are linearized with regard to corrections to dependent variables and are solved iteratively at each time step with the use of Gaussian elimination method and under-relaxation. As an external parameter of the electrodynamic problem, the time dependence of the power in the input radial electromagnetic wave, $Q_r(t)$, or of the axial temperature of the ceramic cylinder, $T_0(t)$ is set by the method described in [2].

Results. The numerical calculation of the microwave heating process of the ceramic cylinder of radius $R_c = 15$ mm made of aluminum oxide in stationary air is carried out at atmospheric pressure, $R = 50$ mm, microwave frequency $f = 30$ and 130 GHz. The coefficients ρ_c, C_p, λ, $\varepsilon_r = \mathrm{Re}\,\varepsilon$, $\varepsilon_i = \mathrm{Im}\,\varepsilon$ are taken from the same sources as in [2].

As follows from the calculation results (Fig. 1), the character of the distributions $T(r,t_k)$, $E(r,t_k)$ at each instant of time t_k corresponds qualitatively to the stationary thermal states of the ceramic cylinder [1, Fig. 3]. Quantitatively, more noticeable temperature gradients in the cylinder cross section, as compared to the stationary case, and consecutive temporal changes of the electric field strength are observed.
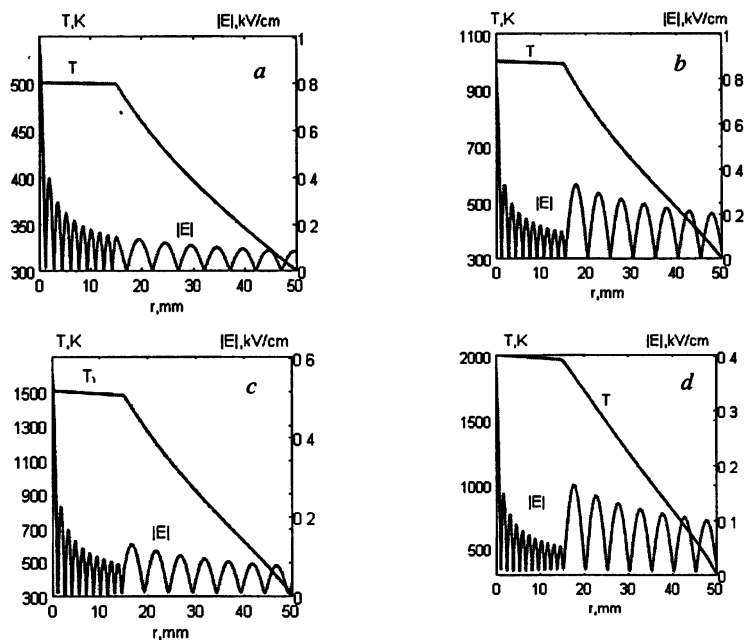
Fig. 1. Temperature and electric field strength in the ceramic cylinder: $t = 0.11$ h (*a*); 0.35 h (*b*); 0.60 h (*c*); 0.85 h (*d*)

Threshold and irregular character of microwave heating. During the microwave heating of the ceramic cylinder heating from $T^0(r) = T_R = 300$ K, $Q_n = 4$ kW/m ($Q_n < Q_B$, $t > 5$ h) the heating rate dT_{max}/dt (Fig. 2) becomes nearly zero, and the axial temperature value (Fig. 3a, dashed line) is settled corresponding to the stationary dependence $T_{max}(Q_n)$ on the branch AB [1, Fig. 3]. For the heating up to temperature greater than the maximum temperature T_B on the stable lower branch AB it is necessary that $Q_n > Q_B$ (Fig. 3a, dotted line). It can be seen that the temporal non-uniformity of the process becomes apparent upon heating up to 2000 K. At $t > 17$ h the heating rate dT_{max}/dt

Fig. 2. Axial temperature vs. time depending upon the initial thermal state of the ceramic cylinder. T_{S1}, T_{S2}, T_{NS} are the temperatures of the steady (dash-dot) and unsteady (dashed line) stationary states.

grows because of a sharp increase in the dissipated power. The reflection coefficient of the electromagnetic wave decreases by almost 9 times (Fig. 3b, dotted line). Let us consider the threshold character of microwave heating showing the
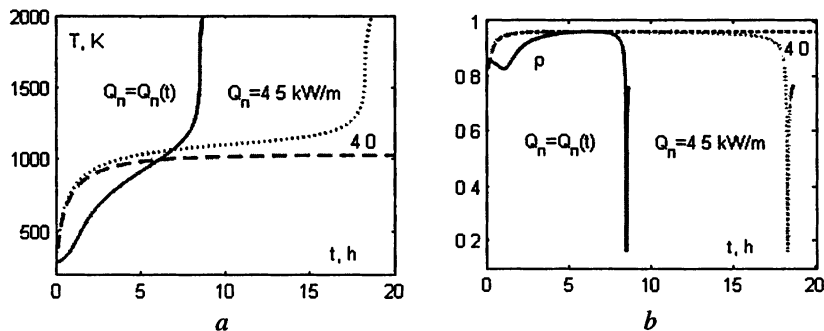
Fig. 3. Axial temperature of ceramic cylinder (a) and reflection coefficient (b) vs. time: $Q_n = 4.0$ kW/m (dashed curve); 4.5 (dotted curve); $Q_n(t) = 4.5t/t_0$ (solid curve), $t_0 = 5$ h

thermal state of the ceramic cylinder in the plane (Q_n, T_{max}) using the following time dependence of the input microwave power:

$$Q_n(t) = Q_0(t/t_0), \; t/t_0 < 1;$$

$$Q_n(t) = Q_0, \; t/t_0 \geq 1.$$

516

The temporal dependences of axial temperature and reflection coefficient (Fig. 4) at $f = 130$ GHz with $Q_n = 4.5$ kW/m are markedly different from the results at $f = 30$ GHz (Fig. 3). A "resonant" character of the number of time intervals, at which abrupt changes of reflection coefficient value occur, is observed. Synchronously with the decrease in ρ, the axial temperature increases rapidly; then it may go down as the reflection coefficient grows. With the given time dependence of the input microwave power the non-monotonic character of the dependence $T_{max}(t)$ is conserved for the heating times up to 1.7 h.
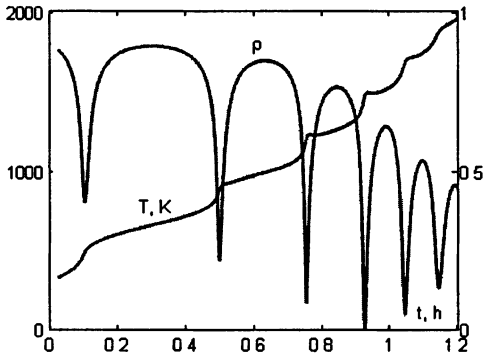
Fig. 4. Axial temperature of ceramic cylinder and reflection coefficient of microwave radiation vs. time: $f = 130$ GHz, $Q_n = 4.5$ kW/m

Specified regime of heating. As an example, the calculation (Fig. 5) of the heating dynamics of the ceramic cylinder up to $T_0 = 2000$ K for $f = 30$ and 130 GHz is carried out for the case of linear growth of the axial temperature in a chamber with cooled and heat-insulated walls:

$$T_0(t) = T_R + (T_0 - T_R) \cdot t / t_0 . \tag{1}$$

Fig. 5. Input power of microwave radiation and the reflection coefficient, calculated at the given axial temperature (3) $T_0 = 2000$ K; $t_0 = 5$ h, vs. time: $f = 30$ GHz (a, c); 130 (b, d) in the heating regime with cooled (a, b) and heat-insulated walls (c, d)

517
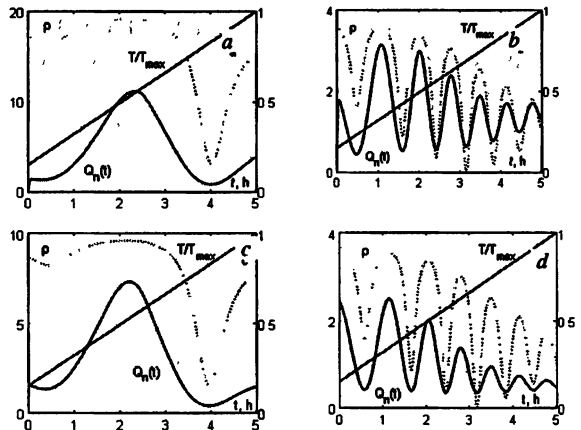
The mathematical model is simplified noticeably in the case of cylinder microwave heating with heat-insulated (adiabatic) walls. As a result of weak temperature change in the cylinder cross section (Fig. 1) we can neglect the contribution of heat conduction flux into the energy balance equation. For the acceleration of heating process the size of microwave chamber should be reduced or at the same chamber sizes it is necessary to pack the ceramic cylinder in a material with low thermal conductivity (analog of "adiabatic" walls) and "transparent" for electromagnetic radiation ($\lambda \approx 0$, $\varepsilon_i \approx 0$). Then the axial temperature of the ceramic cylinder can be found by a simple energy equation

$$\rho_c C_p \frac{dT_0}{dt} = \frac{\eta Q_r}{\pi R_c^2}\,, \qquad (2)$$

where η is the electromagnetic radiation absorption coefficient of the ceramic material. For the extended cylinder, the reflection and absorption coefficients are calculated as [2]

$$\rho = \left| \frac{J_0(kR_c)H_1^{(1)}(k_0R_c) - \sqrt{\varepsilon_K}J_1(kR_c)H_0^{(1)}(k_0R_c)}{J_0(kR_c)H_1^{(2)}(k_0R_c) - \sqrt{\varepsilon_K}J_1(kR_c)H_0^{(2)}(k_0R_c)} \right|^2, \qquad \eta = 1 - \rho\,.$$

As follows from (2), to sustain the linear growth of the axial temperature (1) the microwave radiation power must change in time as:

$$Q_n(t) = \pi R_c^2 (T_0 - T_R)/\eta\ t_0\,.$$

As follows from the calculations results (Fig. 5), the linear growth $T_0(t)$ during the microwave heating of ceramic cylinder is achieved by non-linear changes in $Q_n(t)$, η, ρ_c, C_p, having a complex character in time and temperature. It should be noted that the trajectory showing the thermal state of the ceramic cylinder resembles qualitatively the nonlinear curves of stationary conditions [1]. A comparison of the trajectories representing points [1] and temporal dependences $Q_n(t)$ (Fig. 5) for $f = 30$ and 130 GHz shows that from the energy point of view the application of high-frequency electromagnetic fields is profitable for ceramic material heating. The heating regime with "adiabatic" walls requires lesser microwave power expenditure for a specified heating time up to a required temperature, or provides a reduced heating time at a fixed input power of electromagnetic radiation.

References

1. *Kozlov P. V., Kulumbaev E. B., Lelevkin V. M.* Strong Microwaves in Plasmas. Nizhny Novgorod: Institute of Applied Physics, 2006. Vol. 2. P. 709–714.
2. Modeling and technology of ceramic obtaining on the base of silicon / ed. by V. M. Lelevkin, O. N. Kanygina. Bishkek· Kyrgyz-Russian Slavic University, 2008.

EFFECT OF VARIABLE-POWER MICROWAVE HEATING ON PHASE TRANSFORMATIONS AND PORE STRUCTURE EVOLUTION IN NANOSTRUCTURED ALUMINA

K. I. Rybakov, A. G. Eremeev, S. V. Egorov, Yu. V. Bykov,
I. Otto[1], Z. Pajkic[1], and M. Willert-Porada[1]

Institute of Applied Physics, Russian Academy of Sciences, Nizhny Novgorod, Russia
[1] Universität Bayreuth, Bayreuth, Germany

The microwave effect on phase transformation and pore structure evolution has been characterized quantitatively as a function of microwave intensity. The process rates have been demonstrated to depend non-monotonically on the microwave intensity, suggesting that there is more than one micromechanism of microwave influence on these phenomena.

Introduction

High-temperature microwave processing of ceramic materials is a promising area of research. In addition to technological benefits, an issue that has been attracting much research interest is the influence of microwave electromagnetic radiation on the fundamental processes occurring in the solids during processing. There have been a number of papers comparing the processes in solids subjected to microwave and conventional heating. The objective of this study is to characterize the dependence of phase transformation and pore structure evolution in nanostructured alumina on the intensity of microwave radiation.

Variation of the microwave intensity was achieved by changing thermal insulation conditions. Using this method, samples heated to the same temperature but at different microwave power levels were obtained. In addition, conventional heating of samples in identical regimes was also used for comparison.

Experimental

The samples for this study were prepared at the Institute of Electrophysics, Ekaterinburg, Russia, from nanosize alumina powder produced by the wire explosion method [1]. The specific surface area of the powder was 64 ± 1 m²/g, the average particle size 17.5 nm, and the phase content was $\gamma - 70$ % and $\delta - 30$ %. The samples used for porosity measurements contained 1.1 % Mg. The nanopowder samples were densified by magnetic dynamic compaction at a peak pressure of 1.5...1.8 GPa [2] to a density of about 64...68 % of the theoretical value.

Microwave heating was performed using a 24 GHz / 5 kW gyrotron system for microwave processing of materials [3]. The gyrotron output power was regulated automatically to implement the prescribed temperature-time schedule using an unsheathed Pt /Pt-Rh thermocouple as the temperature sensor. The accuracy of thermocouple measurements was checked using a pre-calibrated Accufiber Opti-

cal Fiber Thermometer (*Luxtron Inc.*, USA) equipped with a sapphire optical sensing probe.

To study the phase transformation sequence $\gamma \rightarrow \delta/\delta^* \rightarrow \theta \rightarrow \alpha$ [4], the samples were heated to 950...1100 °C (heating rate 10 °C / min, hold time 50 min), and for the pore structure evolution study – to 500...1000 °C (heating rate 7 °C / min, zero hold time). The quantitative phase analysis was performed by Rietveld refinement of the XRD spectra of the annealed samples [5]. The spectra calculated using the structure data of five alumina phases, γ, δ, δ^*, θ, and α, were fitted to the spectra obtained by XRD. In addition to the weight content of each phase, the refined parameters were unit cell dimensions, peak width, peak shape, extinction and preferred orientation parameters.

The porosity measurements were accomplished by nitrogen porosimetry methods. The pore area was determined by BET, and the distributions of pores over sizes were obtained by the BJH method.

Results

The results of quantitative phase analysis accomplished by Rietveld refinement are listed in Table.

Phase content vs. annealing temperature and microwave electric field strength

Temperature, °C	Microwave E-field, V/cm	Phase content, wt. %				
		γ	δ	δ^*	θ	α
950	conventional	68.6	22.1	5.4	4.0	-
	219	57.1	30.3	5.1	3.5	4.0
	300	61.5	14.4	7.5	11.9	4.7
1000	conventional	58.0	19.5	5.8	13.4	3.3
	176	43.9	14.9	4.0	8.4	28.8
	500	68.0	15.8	5.4	5.8	5.0
1050	conventional	7.4	16.8	11.0	9.3	55.5
	183	12.3	-	15.5	4.5	67.7
	420	9.9	3.3	13.7	10.0	63.1
1100	conventional	0.8	-	0.1	1.5	97.7
	217	-	-	-	-	100.0
	483	-	-	-	-	100.0

The analysis of the results suggests that the rate of the phase transformation process depends on the methods of heating, and for microwave heating – on the microwave intensity. In particular, shown in fig. 1 is the weight content of the α phase as a function of the microwave electric field strength, E. At each temperature microwave heating enhances the phase transformation process in comparison to conventional heating. Furthermore, the extent of phase transformation depends on the microwave intensity. What is most unexpected, this dependence occurs to be not monotonic but exhibiting a maximum. This suggests that there are at least

two micromechanisms of microwave non-thermal effect on new phase nuclei formation and growth which act at different microwave power levels [6].

In the porosimetry studies, the high-to-low microwave power ratio obtained by varying thermal insulation varied from 4.4 to 7.1. The results of BET pore surface area measurements are shown in Fig. 2. It can be seen that the evolution of porosity proceeds in different ways under conventional and microwave heating. The rapid decrease of BET surface area observed under conventional heating at 700 °C, followed by a subsequent increase, is most probably explained by rotation and rearrangement of the nanopowder particles, which affects the accessibility of their surface for nitrogen. By contrast, under microwave heating the pore volume decreases uniformly along the entire pore size distribution, which suggests that microwave heating inhibits the pore coalescence process [7].
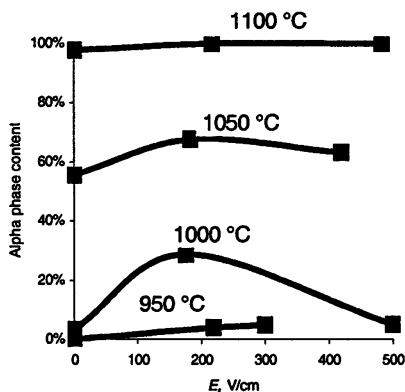
Fig. 1. Weight content of α–Al_2O_3 vs. the estimated microwave electric field strength. $E = 0$ means conventional heating.
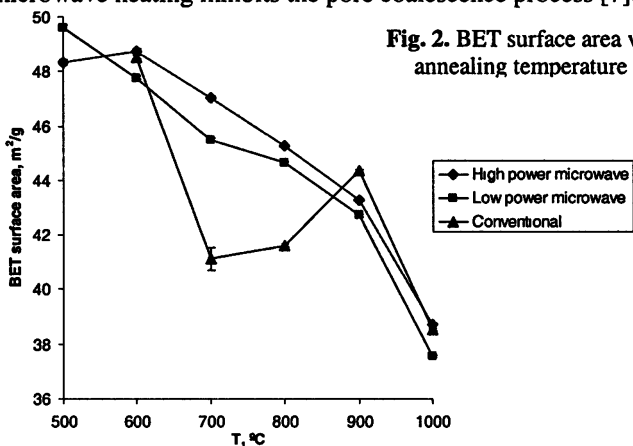
Fig. 2. BET surface area vs. annealing temperature

A comparison between high- and low-power microwave annealing processes demonstrates that similar to the phase transformation, the pore closure proceeds at a higher rate under low-power microwave heating than under high power.

Figure 3 shows pore volume vs. size distributions for the samples heated by three heating methods to a low temperature of 600 °C. It can be seen that the distribution obtained for high-power microwave heating is the closest to the distribu-

tion of an as-compacted (green) sample. The samples heated conventionally and by low-power microwaves exhibit a greater extent of small-size pore elimination.

Figure 4 shows similar distributions for the samples annealed at the highest temperature, 1000 °C. The sample annealed by low-power microwave exhibits the lowest porosity in the small-size region compared to the samples annealed conventionally and by high-power microwaves.
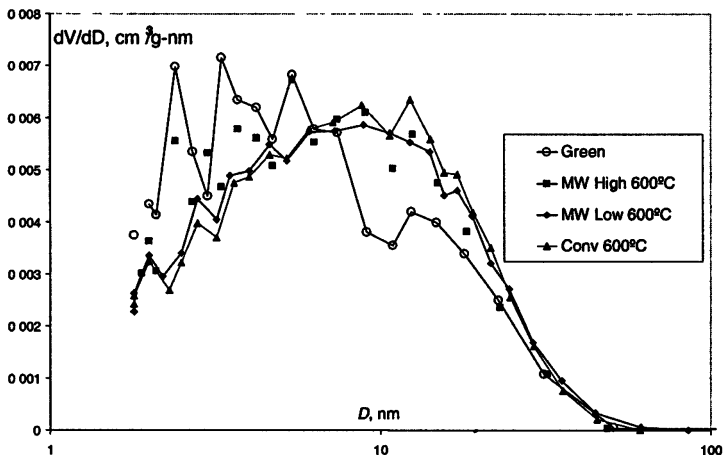
Fig. 3. Pore volume vs. size distributions for samples heated by three methods to 600 °C: high-power microwave heating (MW High), low-power microwave heating (MW Low), conventional heating (Conv), and for initial sample (Green).
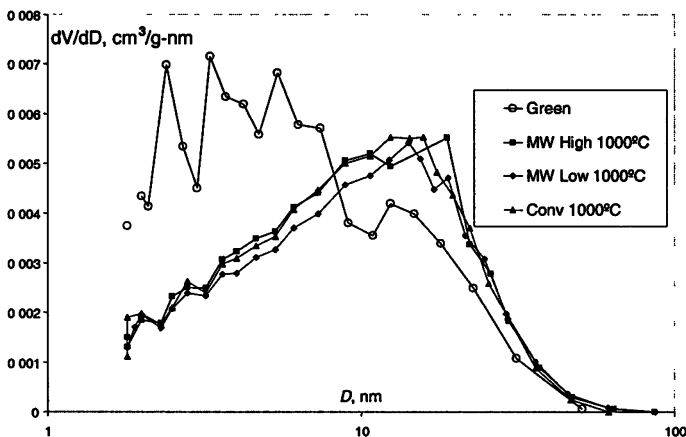
Fig. 4. Pore volume vs. size distributions for samples heated by three methods to 1000 °C: high-power microwave heating (MW High), low-power microwave heating (MW Low), conventional heating (Conv), and for initial sample (Green).

Conclusion

The effect of microwave field on phase transformations and pore structure evolution in nanostructured alumina has been characterized quantitatively. It has been found that microwave heating results in lowering the phase transformation temperature. The phase transformation rate depends non-monotonically on the microwave electric field strength and reaches its maximum when moderate-intensity microwaves are used for heating. A similar non-monotonic intensity dependence has been observed for the rate of porosity reduction under micro-wave heating. In addition, significant difference in the nature of the pore structure evolution process under conventional and microwave heating has been observed.

Acknowledgement

References

1. *Kotov Yu. A.* J. Nanoparticle Research, **5**, 539 (2003).
2. *Ivanov V., Paranin S. and Nozdrin A.* Key Engineering Materials, **132–136**, 400 (1997).
3. *Bykov Yu. V. et al.* IEEE Trans. on Plasma Science, **32**, 67 (2004).
4. *Levin I. and Brandon D.* J. Am. Ceram. Soc., **81**, 1995 (1998).
5. The Rietveld method / ed by R. A. Young. Oxford University Press, 1993.
6. *Rybakov K. I et al.* J. Phys. D: Appl. Phys., **41**, 102008 (2008).
7. *Willert-Porada M.* Microwaves: Theory and Application in Materials Processing IV. / ed. by D. E. Clark et al. (Ceramic Transactions, Vol. **80**, The American Ceramic Society, 1997), p. 153.

EXPERIMENTS ON APPLICATION OF HIGH POWER MICROWAVE RADIATION TO BIOMEDICINE USING MICRO- AND NANOPARTICLES

S. P. Besedin[1], A. K. Kaminsky, O. V. Komova, E. A. Krasavin,
I. A. Krjachko, E. A. Perelstein, S. N. Sedykh, V. N. Shaljapin,
N. L. Shmakova, S. I. Tjutjunnikov

Joint Institute for Nuclear Research, Dubna, Moscow region, Russia
[1] Russian Scientific Center "Kurchatov Institute", Moscow, Russia

High pulsed power microwave radiation gives new possibilities in the biomedicine, particularly to cancer cell damage study. Cooperative influence of microwaves and conducting micro- or nanoparticles provides local and selective action of microwaves on cancer cells. First results of JINR successful experiment are reported on cancer cells being killed with the help of high power microwaves propagating through the thin gold layer. The microwave source was the JINR free electron maser with the power of 20 MW and frequency of 30 GHz. The microwave fluence was about 1 J/cm^2 during cell irradiation, number of pulses was 300–1000. In the culture medium there are the cancer cells located on an object glass near the golden layer. The cell disruption was observed through 30–60 minutes after irradiation. The cells leaved the glass in the form of large conglomerates. Through 12 hours there were no irradiated cancer cells on the object glass. The preliminary study of processes leading to cancer cell damages were performed to estimate the perspective of such technique.

Introduction

An injection of the conducting micro- and nanoparticles into a tumor tissue and their subsequent local heating by electromagnetic radiation is now one of the promising directions in the targeted cancer therapy. Quasi-continuous heating regime using long-wave radiation acts like a well-known hyperthermia. Experiments were done with using a visible and infrared laser radiation to heat the gold clusters by the surface plasmon resonance [1]. The possibility was demonstrated to induce a mechanical damage of cells by explosion of carbon nano-tubes by a pulse of electromagnetic radiation [2]. In all these experiments, the specific problems are the selectivity in destruction of the cells and toxicity of the used nanoparticles.

In molecular biology, the first successful experiments were done on heating the metal nanoclusters attached to deoxyribonucleic acid (DNA) molecules by the eddy currents induced by the electromagnetic waves in a decimeter range of wave lengths [3].

In contrast to the foregoing experiments which have been carried out at rather low intensity of electromagnetic radiation pulse and its long duration, the use of high-power short pulse radiation opens the new opportunities for perform-

ing experiments on destruction the tumor cells and for further experiments in medical physics [4].

The use of conducting micro- and nanoparticles in combination with radiation in a cm range of wave-lengths allows intensifying the destruction of tumor cells locally and selectively. At the high power of radiation and with the special selection of metal particles shapes, they can become the centers of electron emission.

Obviously, at high concentration of the particles entered into biological substance, it is possible to initiate the damages at molecular level caused by ionization loss of electrons.

In this article, the first results are briefly presented of the successful experiment on damaging the tumor cells by injection the gold clusters from the thin gold films with a high-power short pulse of electromagnetic radiation at the frequency of 30 GHz. The experiment has been done in the Joint Institute for Nuclear Research, Dubna.

Experimental setup

The 20 MW 30 GHz Free-electron maser (FEM) oscillator has been developed by collaboration of Joint Institute for Nuclear research with Institute of Applied Physics RAS. It uses an electron beam of induction accelerator LIU-3000 with current of 250 A, electron energy of 0.8 MeV, pulse duration of 250 ns and repetition rate of 0.5 Hz [5].

The layout of experiment on irradiation of biological objects is presented in Fig. 1. After extraction into the atmosphere the microwave radiation is directed to 45° reflecting plate and then is focused by Teflon lens, above which the object is located. The cross-section diameter of the wave beam can be varied from 5 cm to 1 cm by changing the height of the object above the lens, taking into account that the maximal wave density is close to the air breakdown value ~ 1 MW/cm^2. Typically the cells culture has been placed into the Petri cups over the lavsan film with full- or partial coating with metal nanolayer and then covered by food solution (Fig. 1, *right*).
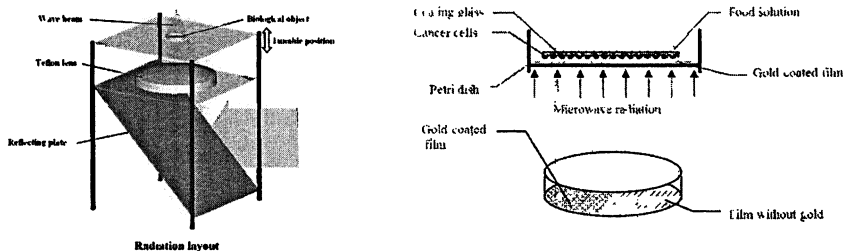
Fig. 1. The layouts of the experimental setup for irradiation of biological objects with gold-coated baking film

The aluminum filings fixed on plexiglass plate are used to control the size and position of the wave beam. Each metal particle is the center of air discharge under the high-power microwave radiation, so the shape of the light spot corresponds to the most intensive part of the wave beam.

Methodological experiments

Starting point of our experiments was the very intensive heating of the sub-millimeter metal fillings in the high-power wave. The spectral measurements of different sorts of the filling showed the fingerprint spectral lines of the metal used as well as the lines of molecular nitrogen. Our estimation of the filling surface temperature using thermal spectrum is 6000 °C. It exceeds the melting temperature of all the metals.

We have carried out the series of experiments on irradiation the 20 micron lavsan film covered by the gold with thickness of 50 nanometers. The samples have been irradiated in the air, in the oil and in thin layer of the water between the gold-coated film and covering film. The last layout is very similar to the condition of the biological experiment. In all cases the exposition of 500 pulses was enough to the partial destruction of gold layer. But the character of the damages differs dramatically depending on the condition of the experiment (compare Fig. 2 and Fig. 3). 3D investigations of covering films by atomic force microscope and confocal microscope showed the micron- and submicron particles penetrating into the cover film at few microns. We guess that the gold particles removed from the coating layer have rather big velocity caused by the action of the intense electromagnetic field. Another possibility is the high temperature of removed micro- and nanoparticles which is enough to partially melt the covering film. We hope in both cases it is possible to use these gold particles as a "weapon" against the cancer cells if the covering film will be replaced by the cell culture. In the first situation the cells can be destroyed by mechanical impact, in the second – by local heating.
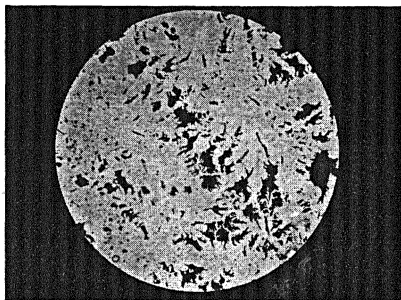
Fig. 2. Gold-coated lavsan film after irradiation in the oil
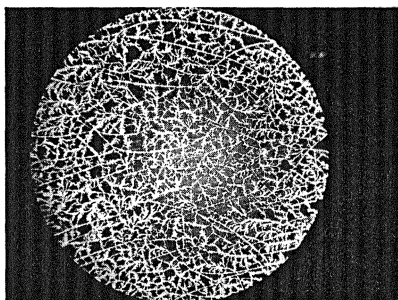
Fig. 3. Gold-coated lavsan film after irradiation in the thin water layer

Experiments on the cancer cells irradiation

The RF transport line is rather short, so our samples are simultaneously irradiated by the electromagnetic wave and bremsstrahlung. We have fulfilled control experiments to be sure that the bremsstrahlung dose is harmless for cells. The result was that the 500 pulses is safe dose.

In experiments we used an asynchronous population of carcinoma cells dairy human gland of a line cal 51, taking place in a logarithmic growth phase. Cells cultivated in DMEM environment with addition of 10 % fetal serum and 2 mmol/l glutamin in the incubator at 37 °C and atmosphere of 5 % CO_2. Cells were dispersed on cover glasses in plastic Petri dish with diameter of 35 mm in the number of 350000 cells on a cup, 48 hours prior to the before irradiation or of 700000 cells on a cup for 24 hours, so that to the beginning of experiment on cover glasses the equal cellular monolayer was formed.

Right after influence by the microwave radiation the glasses were overturned with monolayer upwards. After 30–60 minutes optical measurements were carried out, using the inverted microscope. Then samples were placed in an incubator for the further cultivation within 12 hours and again optical measurements were carried out, and then preparations were fixed and painted using the standard technique. In 30–60 min after irradiation it was observed interphase destruction of cells that was shown in partial exfoliation cells from the glass as large conglomerates. In 12 hours one can see the sites where cells are completely absent on these samples (Fig. 4).
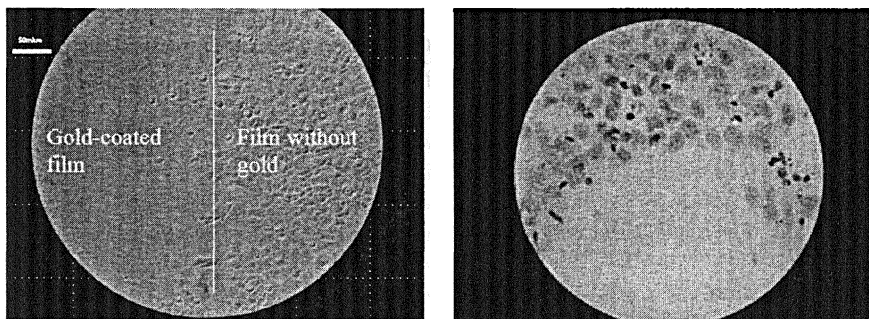
Fig. 4. Microphotographs of the cancer cell samples taking in 60 minutes after irradiation (*left*) and after 12 hours (*right*)

The cells fixing and painting by dye after 15 hours after irradiation has revealed the large number of pyknotic cells on edges of sites where cells completely were lost. Probably, it is the evidence of the delayed destruction of the cells which have received the smaller damages in comparison with cells died right after microwave radiation influence.

Conclusion

The first experiments carried out at JINR have shown that it is possible to destruct cancer cells under the action by the short pulses of high-power electromagnetic radiation. The further research should be directed on investigating of the physical phenomena resulting in defeat of cells. As a result of work it is supposed to determine optimal conditions of irradiation and parameters of nanostructures entered in biological tissues for the subsequent experimental and practical applications.

References

1. *Govorov A. O., Richardson H. H.* Generating heat with metal nanoparticles // Nanotoday. 2007. Vol. 2, № 1. P. 30.
2. *Panchapakesan B., Lu S., Sivakumar K. et al.* Single-Wall Carbon Nanotube Nanobomb Agents for Killing Breast Cancer Cells // NanoBiotechnology. 2005. Vol. 1. P. 133.
3. *Hamad-Schifferli K., Schwartz J. J., Santos A. T. et al.* Remote electronic control DNA hibridization through inductive coopling to an attached metal nanocrystal antenna // Nature. 2002. Vol. 415, № 10. P. 152.
4. *Bol'shakov M. A , Bugaev S. P., Elchaninov A. A. et al.* Effect of repetitive HPM pulses on some biological objects // Proc. of the 1st Intern. Congress on Radiation Physics, High Current Electronics, and Modification of Materials. Tomsk, Russia, 2000. Vol. 2. P. 514–518.
5. *Elzhov A. V., Ginzburg N. S., Kaminsky A. K. et al.* Test facility for investigation of heating of 30 GHz accelerating structure imitator for the CLIC project // Nuclear Instruments and Methods in Physics Research. 2004. Vol. A528. P. 225–230.

GENERATION OF TERAHERTZ RADIATION BY INTENSE FEMTOSECOND PULSES

E. V. Suvorov, M. I. Bakunov[1], R. A. Akhmedzhanov, D. A. Fadeev,
I. E. Ilyakov, V. A. Mironov, B. V. Shishkin, S. B. Bodrov, A. N. Stepanov

Institute of Applied Physics, Russian Academy of Sciences,
Nizhny Novgorod, Russia
[1] Nizhny Novgorod State University

A brief survey of IAP activity is presented in the field of THz radiation generation by intense femtosecond pulses using a specialized facility – laser system "Spitfire" capable to produce 2.5 mJ pulses of 50 fs duration at the wavelength 780 nm with the repetition rate 1 kHz with the optical beam aperture about 1 cm. Laser spark as a source of THz radiation is investigated using three main schemes of plasma production: (i) focusing of femtosecond pulses by usual parabolic lenses; (ii) axicon discharge in which the ionization front moving with super-light velocity is the source of Cherenkov THz radiation [2, 3]; and (iii) ionization by the combination of fundamental and second harmonic optical radiation, which looks at present as one of the most promising schemes for THz radiation generation [4]. A sophisticated sandwich scheme is proposed and tested on the base of Si-LiNbO3-Si structure in which group velocity of optical radiation exceeds the phase velocity of THz radiation in adjacent Si prism. According to measurements it allows to reach the record efficiency for transformation of optical pulse energy to the energy of THz radiation. A structure of theoretical block for modeling performed experiments is briefly described.

Introduction

In recent years the interest to the generation and applications of terahertz radiation grew greatly. In chemistry it can be used to investigate a compound molecules. The response to wideband action gives information about the structure of large organic molecules with variety of vibration lines in terahertz range. The terahertz waves can be used for imaging in biology, medicine and security. One of the problems of terahertz waves applications is the strong absorption by water vapor in air. So it is desirable to produce the terahertz waves in the vicinity of the object under investigation.

A lot of different groups develops terahertz sources of different types. Here we present preliminary results on THz pulse generation by means of fs laser radiation from modern facility constructed in IAP RAS and appropriate for optoelectronics investigations.

Experimental setup

The heart of experimental setup for investigation of THz radiateongeneration using nonlinearities in various media is the Ti:Sa regenerative amplifier system (Spectra-Physics Spitfire Pro XP), which provides ~ 50 fs laser pulses at 780 nm, with a maximum pulse energy of 2.5 mJ and a repetition rate of 1 kHz.

Two types of detection systems were used for investigation of generated THz pulses. The first type used for investigation of THz pulse waveform was based on traditional electro-optical sampling technique [1] with ZnTe plate (see Fig. 1). Due to dispersion of ZnTe in THz frequency range its temporal resolution is limited; in our case this limitation corresponds to approximately 3 THz.
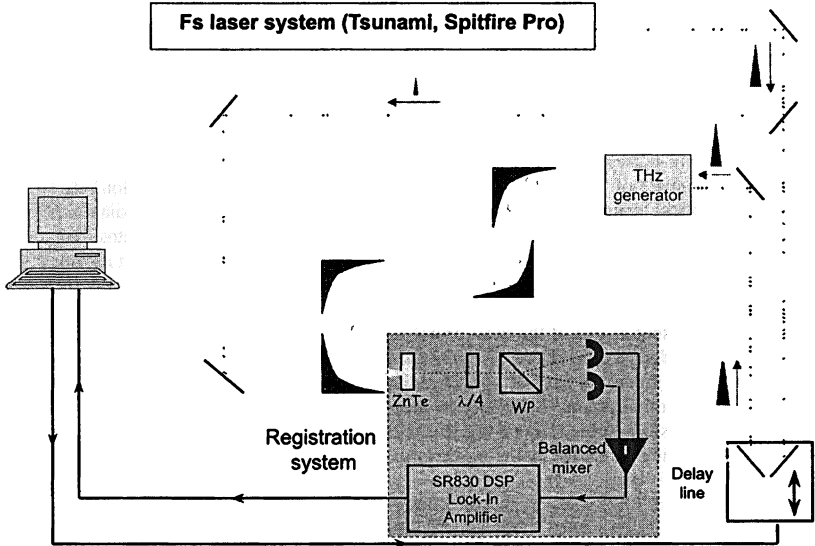
Fig. 1. The experimental setup for electro optic measurements

In the detection system of the second type the InSb bolometer was used for measuring the energy of THz pulses and the radiation pattern (see Fig. 1a). The radiation pattern was measured using the opaque screen with the round hole in it, movable in both directions transverse to the propagation direction of THz beam. Additionally the wired polarizer allowed to investigate direction and degree of linear polarization both integrated over the whole THz beam and over its part penetrating through the hole in the screen.
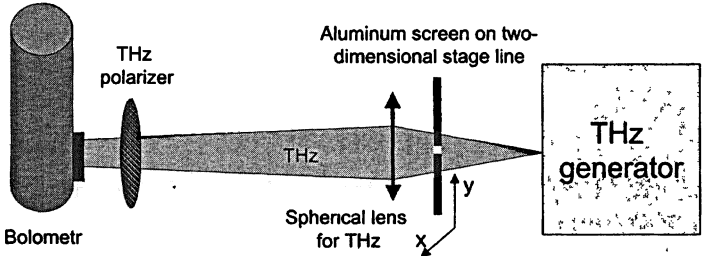
Fig. 1a. Detection system for bolometric measurements

The generation block has been changed optionally to investigate different mechanisms of THz radiation generation. The main part of our investigations was aimed to the generation of THz pulses in a laser spark produced by focusing of fs laser radiation. Three types of THz generators based on a laser spark are presented in Fig. 2. Two types of focusing systems were used: the axicon lens (with 15° focal angle) and a set of conventional parabolic lenses (with 80, 120 and 400 mm focal lengths). BBO crystal was optionally used to perform experiments with bi-chromatic pumping pulse which provided under definite conditions a rather high generation efficiency. There was also the possibility to apply a dc electric field across the laser spark by means of two specially designed electrodes.
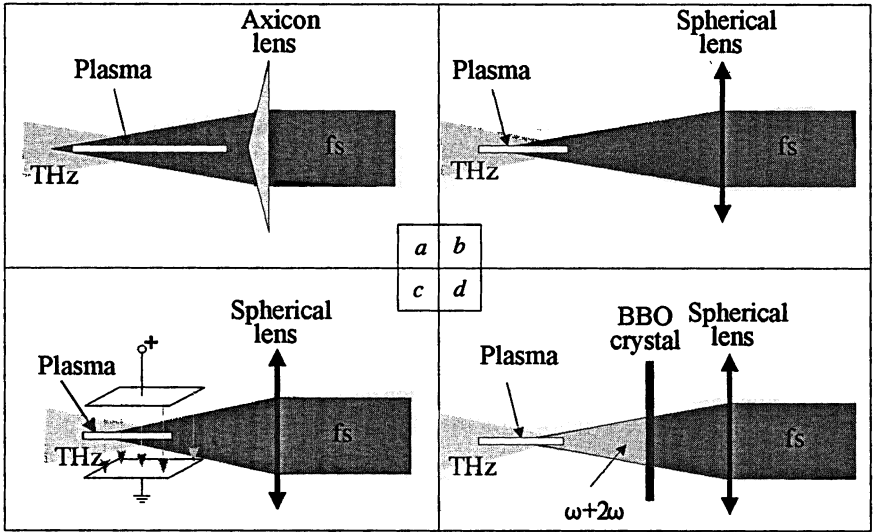
Fig. 2. Schemes of THz radiation generation in a laser spark: *a* – generation under conditions of axicon focusing of fs pulses, *b* – the same with the focusing by conventional (parabolic) lenses, *c* – generation in presence of external electric field, *d* – bi-chromatic generation scheme

Experimental results from axicon discharge

The original part of investigation THz generation mechanism in a laser spark is related to axicon discharge as proposed in [2, 3]. Fig. 3 demonstrates the waveform of generated THz pulses and corresponding spectrum obtained with the classical sampling technique using electro-optical ZnTe crystal in which THz radiation being focused by external mirrors to EO crystal together with probe laser pulses with varying shot-to-shot delay produce in principle both the wave-

form and the spectrum of THz pulses. The radiation pattern and polarization distribution under condition of zero external dc electric field are presented in Fig. 4.
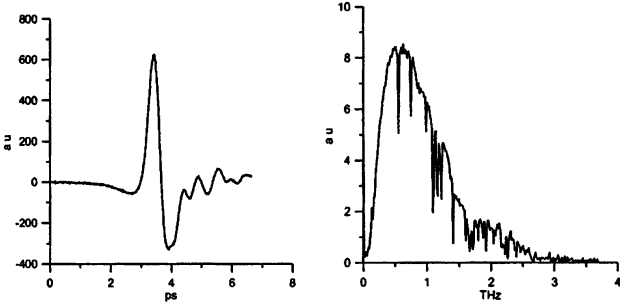
Fig. 3. Typical waveform and spectrum of THz pulse generated by axicon discharge
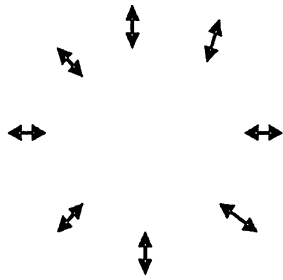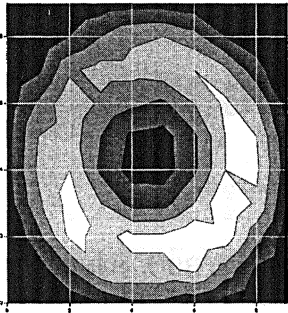
Fig. 4. Radiation pattern and polarization distribution in THz radiation from axicon discharge

Maximum of THz field intensity is concentrated in the vicinity of Cherenkov cone, while its polarization is linear and radially directed in the intensity maximum. Such kind of polarization distribution may result from both longitudinal (with respect to discharge axis) radiating current and from axially symmetric distribution of radial currents. The measured polarization distribution implies great uncertainty into results of EO diagnostics because in the case of absolute axial symmetry the response from the detector should be zero. This means that both waveforms and spectra are registered only due to some misalignment of the whole system, and the absolute values of registered field cannot be used for estimations of generation efficiency. Additional confirmation is not very high reproducibility of EO measurement results. Applying of the external dc electric field up to 15 kV/cm resulted in not very much essential increase (occasionally by 1.5–2 times) in THz pulse amplitude. This means that intrinsic electric fields originating in a plasma are significantly higher.

Theoretical modeling of gas break-down and accompanying generation of low-frequency currents demonstrated that more probably the source of THZ ra-

diation is related to axisymmetrical radial currents produced by plasma oscillations excited due to the ponderomotive force from fs light beam.

Experimental results from a laser spark produced by the focusing of fs radiation by conventional (parabolic) lenses

In this section the results will be mainly presented which were obtained by other groups (see e.g. [4–9]; so they may be considered as their additional check and confirmation with natural minor difference in some details. Fig. 5 represents radiation patterns and polarization distributions for THz radiation from laser sparks, produced by focusing of fs radiation by parabolic lenses with different focal distances.

For the case of focusing by parabolic lenses the radiation patterns and polarization distributions demonstrate qualitatively different behavior depending on the focusing length (Fig. 5). For shortest focal length (80 mm) under investigation the radiation pattern is cylindrically symmetrical, bell-shaped with maximum at the THz beam axis. Moreover, no preferable linear polarization was detected over the whole cross-section of THz beam. For the intermediate focal lengths (120 mm) the radiation pattern also possesses cylindrical symmetry but with well pronounced minimum in forward direction. The polarization is in this case the same as for axicon focusing. In the case of the largest focal length (400 mm) the radiation pattern has two maxima symmetrically situated with respect to the direction of laser pulse polarization vector. The polarization in that case is mainly transverse to the optical pulse polarization direction. Both radiation pattern and polarization distribution are typical of the case in which radiating current distribution corresponds to the quadrupole-type resonance plasma oscillations of plasma column.
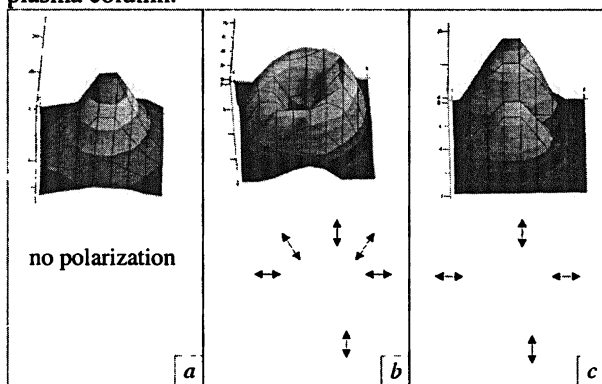
Fig. 5. The radiation patterns (top) and polarization distributions (bottom) of THz radiation from a laser spark with conventional (parabolic lens) focusing: *a)* $F = 80$ mm, *b)* $F = 120$ mm, *c)* $F = 400$ mm.

Small admixture of the second harmonic in the optical pulse produces essential increase of generated THz pulse energy, e.g. 10 % addition of the second harmonics with the polarization transverse to that of the first harmonics results in

the increase more than by three orders of magnitude in the energy of THz pulses. The well-known oscillating dependence of generation efficiency on the phase shift between optical fields of the first and second harmonics has been observed.

For the bi-chromatic mechanism of generation the radiation patterns are cylindrically symmetrical and bell-shaped, but for short focal length the plateau-shaped structure in the radiation pattern for THz pulses has been observed (Fig. 6). Polarization of generated THz pulses is linear and parallel to the polarization of the second harmonics.

F = 80 mm   F = 400 mm
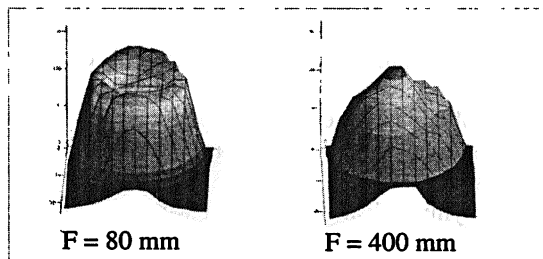
Fig. 6. The radiation patterns of THz radiation from a laser spark produced by bi-chromatic optical pulses

Implying external dc electric field parallel to the polarization direction of optical pulse also results in significant increase of THz pulse energy. For example, for the maximum dc field strength about 15 kV/cm (close to the break-down threshold in the atmosphere) THz pulse energy is increased by approximately two orders of magnitude independent of dc field direction with respect to polarization direction of optical radiation. Polarization of generated THz radiation in this case is parallel to the direction of dc electric field.

Fig. 7 demonstrates comparative dependences of THz pulse energy generated in the optical spark on the energy of optical pulses focused by parabolic lens ($F = 120$ mm) for monochromatic fs radiation (a), bi-chromatic fs radiation with the optimal positioning and orientation of I-type BBO crystal (b) and for monochromatic discharge in a 15 kV/cm dc electric field region (c). No definite signs of saturation have been observed in these plots.

a) parabolic lens   b) parabolic lens + BBO   c) parabolic lens + dc electric field
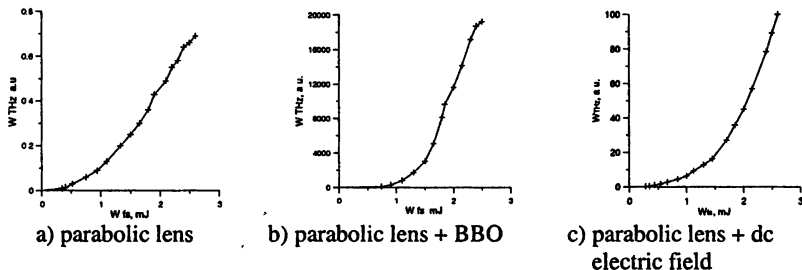
Fig. 7. Dependences of THz pulse energy on the energy of optical pulses with parabolic lens focusing: a – monochromatic fs radiation, b – bi-chromatic fs radiation, c – monochromatic fs radiation and dc electric field

The energies of THz pulses obtained from axicon discharge are in the same value region as for the case "a", but with more pronounced threshold and more steep dependence on the energy of THz pulses. Additional measurements performed for a circular polarization of optical pulses give strong evidence in favor of tunnel ionization mechanism – the same values of THz pulse energy are obtained with approximately double intensity of optical radiation with circular polarization.

Efficient solid-state source of THz pulses

The main part of setup, which is shown in Fig. 8, is the sandwich-like structure. It consists of a substrate BK7 glass, a slab of nonlinear medium (LiNbO$_3$) and a prism with low terahertz absorption. The laser pulse is focused into a nonlinear slab (which forms 1D waveguide for optical radiation) by cylindrical lens, thus forming in a slab road-like optical structure about 1 cm length and limited in transverse direction by the width of non-linear crystal layer (30 or 50 μm). The group velocity of light pulse inside the layer is higher than phase velocity of THz radiation in silicon prism and of order of that in BK7 glass. Under such conditions nonlinear low frequency polarization excited in nonlinear crystal by fs optical pulse is a source of Cherenkov radiation in Si prism which has a cut at the angle, transverse to the front of THz radiation for its best matching with vacuum.
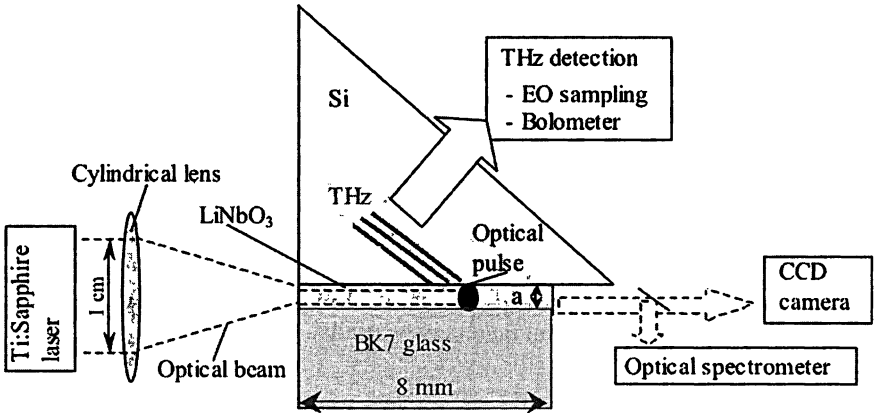
Fig. 8. Block-diagram of experimental set-up for THz pulse generation using sandwich-like structure

Absolute calibration of InSb bolometer allowed direct measurements of THz radiation generation efficiency, defined as the ratio of the energy of THz pulse to that of the optical pulse. The record efficiency of THz radiation generation ($\approx 10^{-3}$)

was obtained for both structures (the thickness 30 and 50 μm) at optical power density about 300 GW/cm^2 for 200 fs optical pulses, while for short pulses (50 fs) it has been reached only in a "fat" structure with optical power density about 500 GW/cm^2. Theoretical evaluation of the efficiency, performed for 200 fs optical pulses with power density 100 GW/cm^2 in 30 μm structure, gives the value $2 \cdot 10^{-3}$ which is by factor 3 higher than experimentally observed (more details of theoretical calculation for symmetrical structure are presented in [10]). The structure investigated, being combined with fiber fs laser, has a good prospect to be the basis of compact source of THz radiation.

Theoretical block for modeling of THz radiation generation in a laser spark

Theoretical block includes three separate problems which may be treated more or less independently. The first step is the modeling of nonlinear focusing of laser pulse, accompanied by neutral gas break-down and plasma column formation. The weak plasma oscillations at THz frequencies can be neglected, energy losses of optical radiation are rather small and for approximate model the only process included is the refraction of optical pulses on plasma. The rough self-consistent model includes the Schroedinger equation for complex amplitude E_i of optical pulse

$$2ik_0 \frac{\partial E_i}{\partial z} + \frac{1}{r} \frac{\partial}{\partial r}\left(r \frac{\partial E_i}{\partial r} \right) = -\frac{4\pi e^2}{c^2 m} n E_i, \tag{1}$$

and the Keldysh ionization rate law

$$\frac{\partial n}{\partial \tau} = 8\omega_H n_0 \exp\left(-\frac{2E_H}{3|E|} \right), \tag{2}$$

where τ is the co-moving time $(\tau = t - z/c)$; ω_H, E_H are atomic constants, E is the instant value of electric field in optical pulse, n is the plasma density and n_0 is the density of neutrals, e, m and c are electron charge and mass and light velocity in vacuum correspondingly. To take into account dispersion a bit more complicated equation for optical field may be used:

$$\frac{2}{c} \frac{\partial^2 E_i}{\partial z \partial \tau} + \frac{1}{r} \frac{\partial}{\partial r}\left(r \frac{\partial E_i}{\partial r} \right) = -\frac{4\pi e^2}{c^2 m} n E_i. \tag{3}$$

Eq. (1) is applicable for parabolic lens focusing with small values of initial laser pulse intensity, while Eq. (3) should be used for axicon focusing to obtain correct superlight velocity in the first approximation over focusing angle and for large intensities of fs pulses with focusing by parabolic lenses. Both of field equations (1) and (3) are written in the scalar approximation for the case of axial symmetry in the field and plasma density distributions. In the case of bi-

536

chromatic optical radiation electric fields for every harmonics are described by Eq. (1) (or Eq. (3)), and the sum of electric field of both harmonics enters into Eq. (2) for plasma density. In real calculations in Eq. (2) the values averaged over the period of optical pulse were used, where $|E|$ in exponential is substituted by modulus of complex amplitude $|E_i|$ which enter in Eqs. (1), (3) with modification of multiplier before exponential taken from [11]. Some results of self-consistent calculations are presented in the paper T-21 of this volume.

The next step of theoretical analysis is the modeling of plasma oscillation excitation. The simplified model written in the electrostatic approximation includes hydrodynamic equations for electron component and Poisson equation for electrostatic potential:

$$\frac{\partial \rho}{\partial \tau} = \operatorname{div} \mathbf{j}_{\perp} \, , \tag{4}$$

$$\frac{\partial \mathbf{j}_{\perp}}{\partial \tau} + \frac{e^2}{m} n \nabla_{\perp} \varphi = \mathbf{S} \, , \tag{5}$$

$$\Delta_{\perp} \varphi = 4\pi\rho \, , \tag{6}$$

where the source term $\mathbf{S}$ may include the action of a dc electric field, combined action of the first and the second harmonics (see paper T-21 of this volume), pondero-motive force from non-uniform optical beam (see [12]) or arbitrary their combination. Eqs. (4)–(6) are written in a quasi-cylindrical approximation, in which dependence on z co-ordinate is purely parametric.

The final stage of theoretical modeling is the calculation of THz field, radiated by low frequency currents following from (4)–(6), which in the "far" region define both radiation pattern and polarization distribution in generated THz pulses (for axi-symmetric example see [12]).

Conclusions

Contemporary facility based on advanced femtosecond laser system appropriate for investigations in optoelectronics has been put into operation in the Institute of Applied Physics (Russian Academy of Sciences).

Experimental investigations have been performed on plasma assisted generation of coherent THz pulses in a laser spark produced by focusing of fs optical radiation in the atmosphere air. Some previously reported results have been confirmed like essential increase of generation efficiency due to applying to the spark region of a dc electric field, or by adding of small admixture of the second harmonics into the optical radiation; this is also concerns the oscillating dependence of generation efficiency on the phase shift between optical fields of the first and the second harmonics. New results have been obtained on the radiation patterns of THz pulses generated under various conditions and on polarization distributions in the cross-section of THz beams, as well as on THz radiation from axicon discharge.

537

The initial step in the theoretical block formation has been done for modeling of plasma creation in a laser spark, nonlinear production of low frequency currents in it and subsequent generation of THz pulses. Up to now theoretical modeling is unable to explain the whole rich variety of experimental results and this is a challenge task for future.

Solid-state sandwich-like structure for generation of THz radiation using fs optical pulses has been designed, manufactured and tested in experiments. The best result demonstrated a record generation efficiency about 10^{-3}, which is the ratio of THz pulse energy to the energy of generating optical pulse.

Acknowledgement

References

1. *Wu Q. and Zhang X.-C.* Appl. Phys. Lett. **67**, 2523 (1995).
2. *Golubev S. V., Suvorov E. V., Shalashov A. G.* JETP Letters, **79**, 361 (2004).
3. *Gildenburg V. B., Vedenskii N V.* PRL, **98**, 245002 (2007).
4. *Cook D. J. and Hochstrasser R. M.* Opt. Lett. **25**, 16, 1210 (2000).
5. *Kress M., Loffler T , Eden S , Thomson M. and Roskos H G.* Opt. Lett. **29**, 1120 (2004).
6. *Bartel T., Gaal P., Reimann K., Woerner M., and Elsaesser T.* Opt. Lett. **30**, 2805 (2005).
7. *Zhong H., Karpowicz N., and Zhang X.-C.* Appl. Phys. Lett. **88**, 261103 (2006).
8. *D'Amico C., Houard A., Franko M., Prade B. and Mysyrovicz A.* PRL, **98**, 235002 (2007).
9. *Houard A., Liu Y., Prade B., Tikhonchuk V. T. and Mysyrovicz A* PRL, **100**, 255006 (2008).
10 *Bodrov S. B , Bakunov M. I. and Hangyo M.* Journ. Of Appl. Phys. **104**, 093105 (2008).
11. *Popov V. S.* Phys.-Usp. **47**, 855–885 (2004).
12. *Akhmedzhanov R. A , Ilyakov I. E., Mironov V. A., Suvorov E. V., Fadeev D A. and Shishkin B. V.* JETP Letters, **88**, 569 (2008).

TERAHERTZ EMISSION FROM LASER-INDUCED AIR PLASMA WITH THE SECOND HARMONIC OF THE PUMP FREQUENCY

R. A. Akhmedzhanov, D. A. Fadeev, I. E. Ilyakov, V. A. Mironov, B. V. Shishkin

Institute of Applied Physics, Russian Academy of Sciences,
Nizhny Novgorod, Russia

The nature of terahertz generation under conditions of bichromatic short laser pulse focusing in ambient air during the breakdown process is investigated theoretically and experimentally.

At present time the intensive researches of effective terahertz sources are performing. In recent years, efficient terahertz radiation of ultra-short THz pulses has been observed under the conditions when a short laser pulse, consisting of the fundamental frequency and its second harmonic, is focusing in the air. The four-wave mixing process is considered to be a possible mechanism of the generation in the plasma [1–4]. Here the investigation of the nature of terahertz emission, and fourwave mixing constant χ_3 ([1–4]) is performed.

Experiment

The experimental setup scheme and its description can be found in [5]. So we will discuss the obtained results below.

In the Fig. 1 the results obtained on the first experimental setup are shown. The radiation pattern displays the forward character of THz radiation with a divergence angle (FWHM) of about 20°. For the shorter focal lengths the plateau-shaped structure of emission pattern is typical. The THz energy dependence on laser pulse energy has the threshold character. For the higher energies (2.5 mJ) of pumping optic pulse the effect of satiation of THz energy can be also pointed out. The waveform of output THz signal is shown in Fig. 2, *a*. It's shape was the same for different pumping pulse energies and focal lengths. The oscillations behind the THz signal are considered to be connected with absorption and dispersion on water vapour [1–4]. The output signal frequency set is extended to 3 THz. In the fig. 2, *b* the dependence between maximum THz field and BBO position (phase ϕ between the fundamental and the second harmonic) is shown.

There is an equidistant set of BBO positions, where no THz generation occurs, but the dependence is not periodical due to nonlinear nature of second harmonic generation. Thus, for the shorter distances between the spark and BBO crystal the amplitude rises. The Fig. 2, *c* presents the waveforms of generated THz signal for different phases ϕ. It is well seen that the phase of THz signal changes according to the phase of the second harmonic.
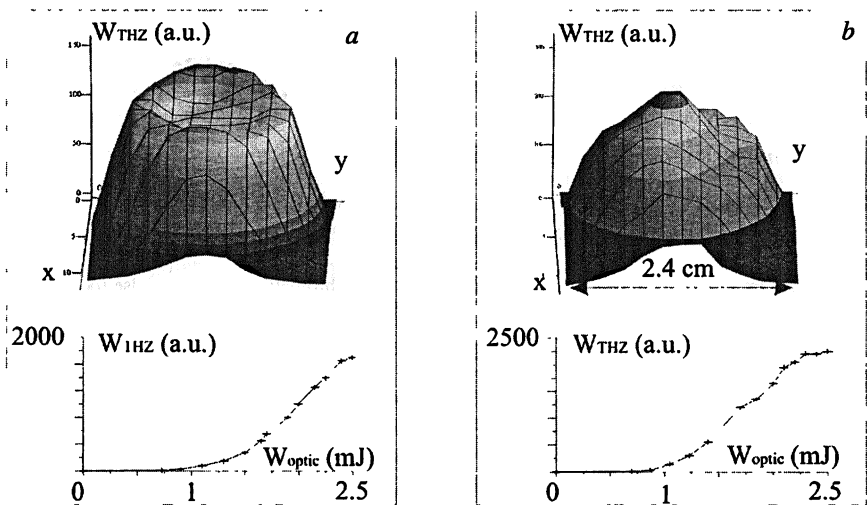
Fig. 1. Radiation pattern for different lenses: a – 80 mm lens, b – 400 mm lens, and the dependence between THz pulse energy and pumping pulse energy.
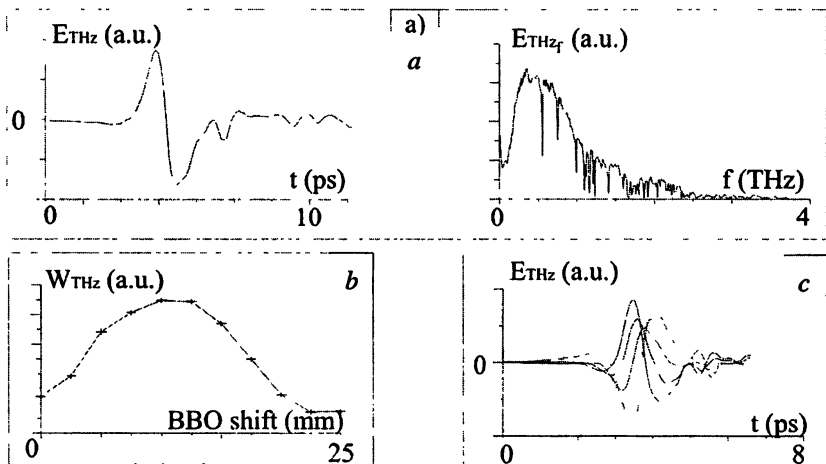
Fig. 2. Waveform and spectrum of generated emission (*a*), dependence of output THz energy phase ϕ (*b*), THz waveforms for different phases ϕ (*c*).

Theory

The theory describing the reported processes could be divided into three logical parts. The first is the nonlinear focusing of pumping laser beam under the conditions of break down of ambient air. The second problem under consideration is studying of the plasma wake oscillations in the column created

during the process of breakdown. The third problem is the calculation of far field radiated by the plasma oscillations. The first problem can be considered as detached because of a great interval of frequencies, which separates the optic pulse and the process on THz frequencies, which are under interest. Another problem is the analytic estimations for the source of plasma oscillations.

To describe the process of ionization ($n_i(\tau)$) the Keldysh law was used. For the complex amplitude of the first E_1 and the second E_2 harmonics couple of Schroedinger equations were used (see [5]).

In this approach the complex amplitude of the second harmonic was considered to be much smaller than the fundamental one. The presented model describes refraction of laser pulse on plasma. Due to this effect the density of plasma and intensity of laser pulse field become satiated with simultaneous formation of plateau in the transverse structure of plasma column (see Fig. 3). Although the second harmonic pulse refracts weaker due to its higher central frequency.
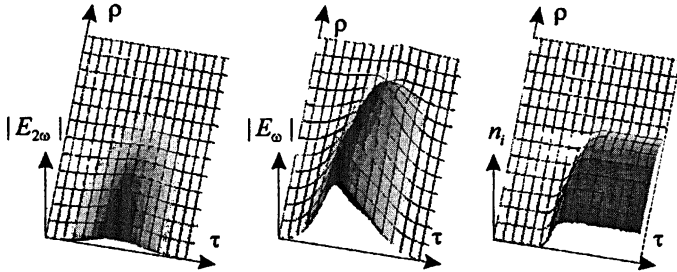
Fig. 3. The snapshots E_1, E_2, n_i, in dependence on cylindrical coordinate ρ and co-moving time τ at some section z

The next process is plasma oscillations excited during the ionization. The system of hydrodynamic and electrostatic equations was used to describe this process (see [5]). In this work we considered the part of $\mathbf{S}$ term $\mathbf{S} \propto \overline{n_i \mathbf{E}}^T$, which describes the bichromatic THz generation only (here $\mathbf{E}$ is the optic electric field vector). In the fig. 4, a the snapshots of charge density in transverse plane is presented for different co-moving times τ in some cross section z. As it could be seen from the definition for $\mathbf{S}$ it excites the dipole type of oscillations. The simple model of two uniformly charged cylinders gives the oscillation frequency of such a system equal to $\omega_p/\sqrt{2}$, where ω_p is plasma frequency. The developed model agrees with this result. As it could be seen from fig. 4, b, which presents the waveform of dipole momentum $\iint \mathbf{r} \rho \, d^2 \mathbf{r}_\perp$, for the oscillations under consideration, the dipole momentum fades, but no dissipative mechanisms were included in the model. This effect is supposed to be concerned

541

with mixing of the oscillations on different frequencies caused by non-uniform plasma distribution in transverse plane.
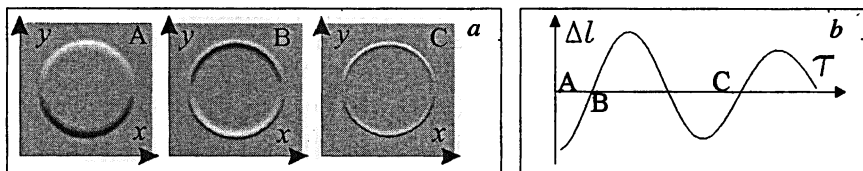
Fig. 4. The snapshots of charge density in transverse plane (*a*) the waveform of dipole momentum (*b*). Letters A, B, C on fig. *a* correspond to times on fig. *b*.

The far terahertz field was calculated basing on Maxwell equations with prescribed electric current, which had been counted from hydrodynamic-electrostatic model discussed above. Using this approach one could obtain the next formulas for electric field strength:

$$\mathbf{E} = \frac{4\pi i k_0}{cR} \left[\mathbf{n}[\mathbf{n} \times \mathbf{x_0}] \right] e^{ik_0 R} \tilde{f}\left(\omega, k_0\left(1 - \cos\theta\right)\right),$$

where $\tilde{f}(\omega, k) = \iint \iint j_x(\tau, r) d^2 \vec{r}_\perp \exp\left(i\omega\tau + i\left(k - k_{THz}\right)z\right) d\omega\, dz$ is the radiating momentum spatio-temporal spectrum. Here $\mathbf{x_0}$ is the direction of source vector $\mathbf{S}$, $\mathbf{n} = \mathbf{R}/R$ is the vector of direction from radiating object to the observation point, R is the is the distance, θ is the longitudinal angle. Supposing the next type of prescribed radiating momentum:

$$j(\tau, z) = e^{-\frac{z^2}{L^2}} e^{-\frac{\tau^2}{T^2}} \left(\cos\left(\omega_{THz}\left(\tau - V \cdot z/c\right)\right) + \cos\left(\omega_{THz}\left(\tau + V \cdot z/c\right)\right) \right),$$

where V – parameter corresponds to modulation of efficacy of plasma excitation. It could happen under the conditions when during the propagation the first and the second harmonic laser pulses loses its synchronization [4]. L is the length of the process (spark length), T is the duration of the plasma oscillation in each cross section. For each of two terms of previous expression the radiation pattern could be plotted. In the Fig. 5 one could see the radiation pattern for different combinations of parameters V and L.
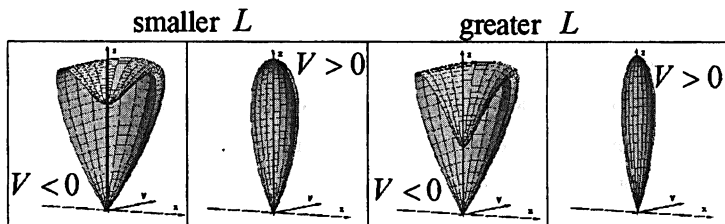
Fig. 5. Radiation patterns for different sources

542

To avoid the calculations with high time resolution including optic oscillations of electrons while the laser pulse takes effect the analytic research for plasma oscillations source force was developed. For parallel polarized pulses of the first and the second harmonics two mechanisms including the mixing fundamental frequencies ($\overline{n_{i\,\omega}E_\omega}$) and the second ones ($\overline{n_{i\,2\omega}E_{2\omega}}$) were considered. For transverse polarized pulses the only second harmonics mixing takes effect on average due to absence of odd harmonics in ionization rate waveform. To perform the averaging procedure one could estimate the appropriate Fourier components of ionization rate in assumption of monochromatic laser pulses. The result of this procedure is quite cumbersome so it is presented in Fig. 6 in the graphic form. Fig. 6, a presents the dependence of source on amplitude of second harmonic and in the fig. 6, b the dependence of source on phase between fundamental and second harmonic is presented.
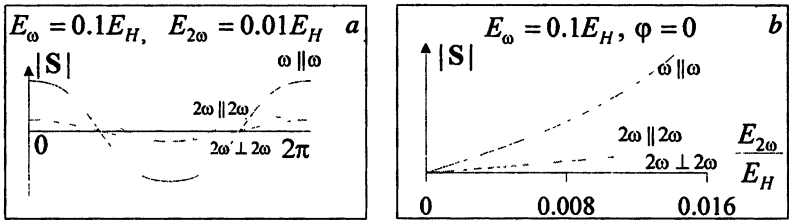
Fig. 6. The dependence of S on phase ϕ (a) and second harmonic strength (b) for three different mechanisms marked as $\omega \| \omega$, $2\omega \| 2\omega$, $2\omega \perp \omega$.
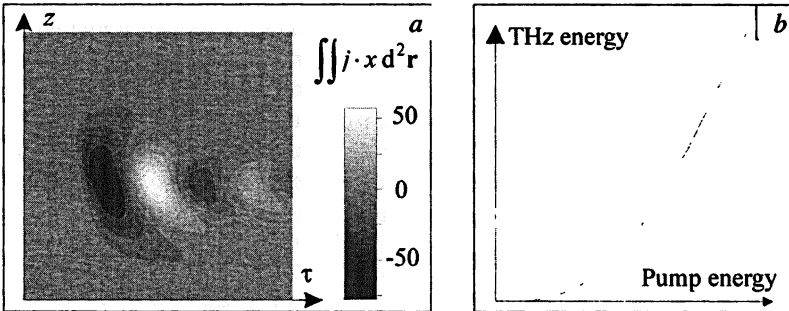
Fig. 7. The radiating momentum in dependence on co-moving time τ and z (a), the dependence of THz pulse energy on Pumping pulse energy (b).

Applying the mentioned stages of the analysis all together one could obtain the far terahertz field. In the Fig. 7, a the radiating momentum depending on z and τ coordinates is presented. The full modeling was performed for the comparatively small input pump amplitudes so the resulting pattern was not correct because of small dimensions of spark. But the common tendency of the

process is displayed. In the Fig. 7, *b* the energy of THz field depending on pumping pulse energy is presented. The satiation of the curve growth is caused by effect of refraction of pumping pulse on plasma that has been mentioned above.

Conclusion

In this work there were obtained some experimental results of THz waves generation in the process of breakdown of ambient air by the bichromatic laser pulse. The radiation pattern, polarization and energy were investigated in dependence of pumping laser pulse amplitude and phase shift between first and second harmonics for different focusing conditions (two focusing lenses). The theoretical model was developed and numerically investigated. Some of results that are typical for bichromatic scheme were obtained analytically. The analytical model was used to increase the efficiency of numerical approach. The first approach of electrostatic investigation of plasma oscillations is planned to be replaced by modeling of Maxwell equations for slow processes.

References

1. *Cook D. J. and Hochstrasser R. M.* Opt. Lett. **25**, 16, 1210 (2000).
2. *Kress M., Loffler T., Eden S., Thomson M., and Roskos H. G.* Opt. Lett., **29**, 1120 (2004).
3. *Bartel T., Gaal P., Reimann K., Woerner M., and Elsaesser T.* Opt. Lett., **30**, 2805 (2005).
4. *Zhong H., Karpowicz N., and Zhang X.-C.* Appl. Phys. Lett., **88**, 261103 (2006).
5. *Suvorov E. V. et al.* In this volume, p. 529–538

TERAHERTZ EMISSION FROM SUPERLUMINOUS IONIZATION FRONT CREATED IN AIR BY AXICON-FOCUSED LASER PULSES

V. A. Kostin, N. V. Vvedenskii

Institute of Applied Physics, Russian Academy of Sciences, Nizhny Novgorod, Russia

The long plasma channel created in air by an axicon-focused femtosecond laser pulse is a rather promising source of broadband THz emission having a narrow radiation pattern and a controllable spectrum. The emission is caused by excitation of a current pulse by the ponderomotive force behind the laser-produced superluminous ionization front. An unanticipated fact is that the frequency corresponding to the maximum of the THz spectrum is determined by the electron collision frequency and is almost independent of the maximum plasma density. The results obtained from the self-consistent theoretical model based on exact Maxwell's equations agree very well with the experiment.

Currently, great attention is given to the phenomenon of THz waves generation caused by gas ionization with intense femtosecond laser pulses [1–11]. Here, one can speak about the schemes of both *self-induced* generation, when the emitting THz currents in the plasma are excited by the field of an ionizing laser pulse [1–5], and *forced* generation, when the pumping is done by some external field [6–11]. This can be a static [6, 7, 9, 10] or microwave [8] electric field, or the field of the second harmonic of a laser pulse [11]. The authors of Refs. [2, 3, 10] studied the schemes of both *self-induced* and *forced* THz emission from a long plasma channel formed in a gas during filamentation of a femtosecond laser pulse. The use of a long laser filament producing radiation with a sufficiently narrow radiation pattern is rather attractive for solving an important problem of transmitting THz waves over long distances [3, 10].

In this paper, we present the results of studying THz waves generation by another method of forming a long plasma channel in air. This method is based on axicon focusing of femtosecond laser pulses [4, 5, 7–9, 12]. Laser beams refracted by an axicon (conical lens) converge to the symmetry axis z at a small angle θ. A so-called Bessel beam is formed near the axis and propagates without divergence along z with the superluminous velocity which is equal approximately to the phase velocity $V_{ph} = c/\cos\theta$, where c is the speed of light. The transverse electric field, which exceeds the longitudinal one significantly, is proportional to the Bessel function $J_0(r\omega_L\sin\theta/c)$, where r is the distance to the z axis, and ω_L is the carrier frequency. When the beam field ionizes the air, the superluminous ionization front propagates in it with the velocity $V_{if} = V_{ph}$, and a long quasi-cylindrical plasma channel is formed with the length $L \sim b/\tan\theta$, where b is the radius of the laser beam at the lens entrance. The channel radius is $a \sim c/\omega_L\sin\theta$ and the maximum plasma density is $N_{max} \sim N_{cL}\sin^2\theta$, where $N_{cL} = m\omega_L^2/4\pi e^2$ is the critical density, and e and m are electron charge and mass, respectively. The

laser field accelerates newly freed electrons on the ionization front and excites a current pulse behind it. Since the current pulse runs with the velocity $V_{if} = c/\cos\theta > c$, and its characteristic length is much shorter than L, this current radiates forward at the angle θ to the z axis.

Such a scheme of *self-induced* THz waves generation due to axicon focusing of short laser pulses was proposed earlier in Ref. [4] and was realized in the experiment described in Ref. [5]. The radiation pattern and polarization of the THz waves, which were measured in the experiment [5], are an indication of the ponderomotively-driven mechanism of THz current excitation in the plasma. The ponderomotive force forms axially symmetric current density on the ionization front. This current density has radial and longitudinal (parallel to z) components and excites symmetric *transverse magnetic* leaky waves in the formed plasma cylinder. For great r, both the radial component E_r of the electric field and the azimuthal component H_φ of the magnetic field exceed the longitudinal component E_z significantly due to smallness of the angle θ.

The spectrum of the THz radiation obtained in the experiment [5] is unexpected and, at a glance, inexplicable. Here, the plasma frequency can be very high, higher than 10^{14} s^{-1}, therefore one cannot explain the spectrum with the maximum at a frequency of about 0.7 THz by the oscillations at the plasma frequency, as it is frequently done. The value of f_{THz} cannot be related to the reciprocal duration of the laser pulse either, since the duration is very short. To explain the results of the experiment [5], we develop a self-consistent approach based on solving the exact Maxwell equations. As it will be shown in what follows, the value of f_{THz} is weakly dependent on the plasma frequency, but is determined by the effective collision frequency of electrons with heavy particles, which depends on the gas pressure and electron temperature. For the air at atmospheric pressure and the electron temperature $T_e \sim 10$ eV, which corresponds to the laser intensity $I_L \sim 5 \cdot 10^{14}$ W/cm^2 in the experiment [5], the collision frequency of electrons both with ions and with neutrals is $\nu \sim 5 \cdot 10^{12}$ s^{-1} [2, 3, 10].

In our theoretical model, we base our consideration on solving exact Maxwell's equations for self-consistent electric $\mathbf{E}$ and magnetic $\mathbf{H}$ fields in combination with the equation for the electron current density $\mathbf{j}$ in cold *nonrelativistic* plasma [2, 4, 8],

$$\frac{\partial \mathbf{j}}{\partial t} + \nu \mathbf{j} = \frac{\omega_p^2}{4\pi}\mathbf{E}, \tag{1}$$

where $\omega_p = (4\pi N e^2/m)^{1/2}$ is the electron plasma frequency, and N is the plasma density. We suppose that plasma density and all electromagnetic-field components in cylindrical coordinates depend only on r and $\xi = t - z/V_{if}$, where $V_{if} = c/\cos\theta > c$. We seek the solution of Maxwell's equations and equation (1) in the domain $\xi > 0$ by setting the initial conditions on the ionization front for $\xi = 0$. These conditions are the axially symmetric current density distribution $\mathbf{j}_0 = j_{0r}(r)\mathbf{r}_0 + j_{0z}(r)\mathbf{z}_0$, which is created by the ponderomotive force of the laser

pulse, and zero values of the fields **E** and **H**. By setting zero initial conditions for the fields, we assume actually that the condition of $f_{THz}\tau_p \ll 1$ is fulfilled and, hence, we can neglect the polarization response of the plasma at the THz frequency, which emerges during the time of the laser pulse action [4, 8, 9]. The boundary conditions for the fields are the radiation conditions for $r \to \infty$.

We solve Maxwell's equations and equation (1) by applying the Laplace transform with respect to ξ. Since for $\xi < 0$ the fields **E** and **H** are equal to zero, their Laplace transforms coincide with their Fourier spectra: $\{E_\omega, H_\omega\} = \int_{-\infty}^{\infty} \{E, H\} e^{i\omega\xi} d\xi$ for $q = -i\omega$. Here, q and ω are the Laplace and Fourier variables, respectively. The system of equations obtained after the Laplace transform is reduced to the equation for the Fourier spectrum $E_{z\omega}(r)$ of the longitudinal electric field $E_z(r,\xi)$,

$$\frac{1}{r}\frac{\partial}{\partial r}\left[\frac{\varepsilon r}{\kappa^2}\frac{\partial E_{z\omega}}{\partial r}\right] + \varepsilon E_{z\omega} = \frac{4\pi}{\omega + i\nu}\left[\frac{i}{rV_{if}}\frac{\partial}{\partial r}\frac{rj_{0r}}{\kappa^2} + \frac{j_{0z}}{\omega}\right], \quad (2)$$

where $\varepsilon(r) = 1 - \omega_p^2(r)/(\omega^2 + i\nu\omega)$ is the complex permittivity of the plasma, and $\kappa^2(r) = \omega^2(\varepsilon(r) - \cos^2\theta)/c^2$ is the complex transverse wave number squared.

First, we solve equation (2) analytically for the case of a uniform plasma cylinder with a sharp boundary assuming that $N = N_0$ for $r \le a$ and $N = 0$ for $r \ge a$. The solution at the plasma boundary, for $r = a$,

$$E_{z\omega}(a) = \frac{4\pi}{a^2\left(\omega^2 + i\nu\nu\right)J_0\left(\kappa_p a\right)\Delta} \times$$

$$\times \int r'\left[\frac{i\omega}{\kappa_p V_{if}}J_1\left(\kappa_p r'\right)j_{0r}\left(r'\right) + J_0\left(\kappa_p r'\right)j_{0z}\left(r'\right)\right]dr', \quad (3)$$

$$\Delta = \frac{\varepsilon_0}{\kappa_p a}\frac{J_1\left(\kappa_p a\right)}{J_0\left(\kappa_p a\right)} - \frac{1}{\kappa_\nu a}\frac{H_1^{(1)}\left(\kappa_\nu a\right)}{H_0^{(1)}\left(\kappa_\nu a\right)}, \quad (4)$$

where J_0, J_1 and $H_0^{(1)}$, $H_1^{(1)}$ are the Bessel functions of the first and third kind, respectively, ε_0 is the value of ε for $N = N_0$, and $\kappa_p = \omega(\varepsilon_0 - \cos^2\theta)^{1/2}/c$ and $\kappa_\nu = \omega\sin\theta/c$ are the values of the transverse wave number in plasma and vacuum, respectively. The spectrum of the field in vacuum, for $r > a$, is expressed in terms of the boundary solution as follows: $E_{z\omega}(r) = E_{z\omega}(a)H_0^{(1)}(\kappa_\nu r)/H_0^{(1)}(\kappa_\nu a)$.

For $a \ll c/\omega_p$, equations (3) and (4) allow one to obtain simple expressions for the radiation spectrum (i.e., the spectrum of electromagnetic fields far from the cylinder, for $|\kappa_\nu|r \gg 1$) at relatively low frequencies $|\omega| \ll \omega_p/\sin\theta$. If the collision frequency is not too low and satisfies the condition $(a\omega_p\sin\theta/c)^2 \ln[c/a\nu\sin\theta] \ll 1$, which is always fulfilled rather conservatively in reality, the radiation spectrum is

547

$$|H_{\varphi\omega}|^2 = \frac{|E_{z\omega}|^2}{\sin^2\theta} = \frac{|E_{r\omega}|^2}{\cos^2\theta} = \frac{2\pi I_0^2 \sin\theta}{c^3 r} \frac{|\omega|}{\omega^2 + \nu^2}. \tag{5}$$

Here $I_0 = 2\pi\int_0^a rj_{0z}dr$ is the total initial longitudinal current. As seen from formula (5), the radiation in the low-frequency (THz) domain is caused by the longitudinal component of the ponderomotive force, and the frequency $\omega_{THz} = 2\pi f_{THz}$ that corresponds to the spectrum maximum is equal to the electron collision frequency ν. The width of the spectrum is also approximately equal to it.

Now, we will use equation (5) to estimate the order of magnitude of the emitted THz energy $W_{THz} \sim rLc\nu|E_{z\omega}(\nu)||H_{\varphi\omega}(\nu)| = \pi I_0^2 L\sin^2\theta/c^2$. The longitudinal current generated by the ponderomotive force [2] and the current density are evaluated as follows: $I_0 \sim j_{0z}\pi a^2 \sim j_{0z}\pi c^2/\omega_L^2 \sin^2\theta$ and $j_{0z} \sim eN_0\Phi_{pi}/mV_{if}$, where Φ_{pi} is the characteristic value of the ponderomotive potential, at which the main part of free electrons is created on the ionization front. Assuming that the energy of the laser pulse is $W_L \sim I_L\tau_p Lc/\omega_L$ [12], we evaluate the efficiency η of the optical-to-THz conversion,

$$\eta = \frac{W_{THz}}{W_L} \sim \frac{1}{\omega_L\tau_p} \frac{1}{\tan^2\theta} \left(\frac{N_0}{N_{cL}}\right)^2 \frac{\Phi_{pi}^2}{mc^2\Phi_{pmax}} \tag{6}$$

where $\Phi_{pmax} = 2\pi e I_L/mc\omega_L^2$ is the maximum ponderomotive potential in the laser pulse.

The above regularities are confirmed by the results simulating numerically the dynamics of the field and plasma during ionization of the ambient air by axicon-focused laser pulses, as well as by experimental results [5]. In the numerical simulations, the formulas for the ionization rate of nitrogen and oxygen are used [13]. The calculations are performed in a wide range of pulse durations (30 fs $\leq \tau_p \leq$ 100 fs), laser pulse energies (0.5 mJ $\leq W_L \leq$ 5 mJ), focusing angles (3° $\leq \theta \leq$ 15°), and electron collision frequencies (10^{12} s^{-1} $\leq \nu \leq 10^{13}$ s^{-1}). The characteristic diameter of the plasma and the value of maximum plasma density are strongly dependent on τ_p, W_L, and θ. However, the spectrum of the THz radiation, which was found numerically, depends weakly on these parameters and its shape is close to that yielded by equation (5). In numerical calculations, a weak maximum is frequently also observed in the radiation spectrum at a frequency of about $1/\tau_p$, which is equal to several THz, although it is not observed in the experiment [5]. Figure 1 shows the results of numerical calculations compared with the experimental results [5]. As it can be seen, the spectrum and efficiency of the THz emission obtained by calculation and experimentally agree well with each other.
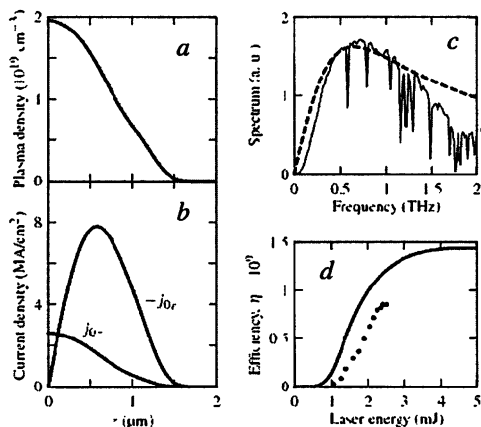
Fig. 1. Calculated profiles of (*a*) the plasma density $N(r)$ and (*b*) the current density j(*r*), which are generated on the superluminous ionization front by a laser pulse focused in ambient air by an axicon lens. In the calculations, the values of parameters corresponding to the experiment [5] are used: duration $\tau_p = 50$ fs, energy $W_L = 2.5$ mJ, focusing angle $\theta = 7°$, and collision frequency $\nu \sim 5 \cdot 10^{12}$ s^{-1}; (*c*) pectra of THz radiation, calculated (dashed line) and obtained experimentally [5] (solid line); (*d*) dependences of the efficiency of THz emission on the laser pulse energy, calculated (solid line) and obtained experimentally (dots, arbitrary units), for fixed values of other parameters.

References

1. *Hamster H. et al* Phys. Rev. Lett. **71**, 2725 (1993).
2. *Sprangle P. et al.* Phys. Rev. E, **69**, 066415 (2004).
3. *D'Amico C. et al.* Phys. Rev. Lett. **98**, 235002 (2007)
4. *Gildenburg V. B., Vvedenskii N. V.* Phys. Rev. Lett. **98**, 245002 (2007).
5. *Akhmedzhanov R. A. et al* JETP Lett. **88**, 569 (2008).
6. *Löffler T., Jacob F., Roskos H. G.* Appl. Phys. Lett. **77**, 453 (2000).
7. *Golubev S. V., Suvorov E. V., Shalashov A. G* JETP Lett. **79**, 361 (2004).
8. *Bystrov A. M., Vvedenskii N. V., Gildenburg V. B* JETP Lett. **82**, 753 (2005).
9. *Kostin V. A , Vvedenskii N V.* Czech. J. Phys. **56**, B587 (2006).
10. *Houard A. et al* Phys Rev. Lett **100**, 255006 (2008), *Liu Y. et al.* Appl. Phys. Lett. **93**, 051108 (2008).
11. *Xie X , Dai J., Zhang X.-C.* Phys. Rev. Lett **96**, 075005 (2006); *Kim K. Y. et al.* Nature Photonics, **2**, 605 (2008).
12. *Babin A. A. et al.* Phys. Usp. **42**, 74 (1999); *Vvedenskii N. V., Gildenburg V. B.* JETP Lett. **76**, 380 (2002); *Alexeev I., Kim K Y., Milchberg H. M* Phys Rev. Lett. **88**, 073901 (2002); *Kompanets V. O. et al.* Quantum Electron. **36**, 821 (2006); *Polesana P. et al.* Phys. Rev. A, **77**, 043814 (2008).
13 *Popov V. S.* Phys. Usp. **47**, 855 (2004).

PLANAR WAVEGUIDING SYSTEMS
BASED ON RESONANT METAMATERIALS

N. V. Ilin, I. G. Kondratiev, A. I. Smirnov

Institute of Applied Physics of RAS, Nizhniy Novgorod, Russia

This paper is devoted to detailed research of an opportunity to use modern metamaterials for an efficient guiding of electromagnetic waves of various ranges (mainly: giga- and terahertz). The following basic questions are considered: the true surface waves [1] guided boundary of the metamaterial; the surface waves guided by layers of a metamaterial.

In this paper we will study slow, spatially localized electromagnetic waves in layered structures of anisotropic metamaterial. Special attention will be focused on *true surface waves* at the metamaterial-vacuum interface. These waves are characterized by degeneration, when the same value of frequency corresponds to an infinite number of modes with arbitrary slowing down. We will also analyse in detail slow surface waves guided by a plane layer of metamaterial and lattices of resonance microelements. We will show that such systems can guide both forward and backward waves.

Specifically, we will speak about media that are described in the macroscopic approximation by the following permittivity and permeability tensors (of the type of a "uniaxial crystal"):

$$\hat{\varepsilon} = \begin{pmatrix} \varepsilon_{xx} = \varepsilon_\wedge & 0 & 0 \\ 0 & \varepsilon_{yy} = \varepsilon_P & 0 \\ 0 & 0 & \varepsilon_{zz} = \varepsilon_P \end{pmatrix}, \quad \hat{\mu} = \begin{pmatrix} \mu_{xx} = \mu_\perp & 0 & 0 \\ 0 & \mu_{yy} = \mu_\parallel & 0 \\ 0 & 0 & \mu_{zz} = \mu_\parallel \end{pmatrix}. (1)$$

Modern metamaterials are based on resonance elements. Therefore, neglecting losses, the frequency dependences of tensor components (1) have resonance character:

$$\varepsilon_{\perp,\parallel} = 1 - \frac{\omega_{p\perp,\parallel}^2}{\omega^2 - \omega_{\varepsilon\perp,\parallel}^2}, \quad \mu_{\perp,\parallel} = 1 - \frac{\omega_{m\perp,\parallel}^2}{\omega^2 - \omega_{\mu\perp,\parallel}^2}, \tag{2}$$

where ω is the frequency of the process, and $\omega_{p\perp,\parallel}$, $\omega_{\varepsilon\perp,\parallel}$, $\omega_{m\perp,\parallel}$, $\omega_{\mu\perp,\parallel}$ are characteristics of the metamaterial structural elements.

The "metamaterial – vacuum" interface

Let "metamaterial – vacuum" interface coincide with the plane $x = 0$: for $x > 0$ we have metamaterial, and for $x < 0$ vacuum. Let us seek solutions of Maxwell's equation in the form of a *true surface wave (exponentially pressed to the x = 0 plane on both its sides)* propagating along the z-axis:

TM mode:

$$x < 0 : \begin{cases} H_y = A \exp(\eta x) \exp(-ihz + i\omega t), \\ E_x = A \dfrac{ch}{\omega} \exp(\eta x) \exp(-ihz + i\omega t), \ \eta^2 = h^2 - \dfrac{\omega^2}{c^2}, \\ E_z = -iA \dfrac{c\eta}{\omega} \exp(\eta x) \exp(-ihz + i\omega t), \end{cases}$$

(3)

$$x > 0 : \begin{cases} H_y = B \exp(-\tilde{\eta} x) \exp(-ihz + i\omega t), \\ E_x = B \dfrac{ch}{\omega \varepsilon_\perp} \exp(-\tilde{\eta} x) \exp(-ihz + i\omega t), \ \dfrac{\tilde{\eta}^2}{\varepsilon_\parallel} = \dfrac{h^2}{\varepsilon_\perp} - \dfrac{\omega^2}{c^2} \mu_\parallel, \\ E_z = iB \dfrac{c\tilde{\eta}}{\omega \varepsilon_\parallel} \exp(-\tilde{\eta} x) \exp(-ihz + i\omega t). \end{cases}$$

For TE modes expressions have the same view with regard to duality principle. In these expressions h is the mode propagation constant, η and $\tilde{\eta}$ characterize the extent of its "being pressed" to the boundary, correspondingly, from the side of vacuum and metamaterial, c is the speed of light, and A and B are arbitrary constants. Meeting the boundary conditions of continuity of tangential components of the electric and magnetic fields, after simple transformations we obtain the following dispersion equations:

TM mode:

$$\sqrt{h^2 - \frac{\omega^2}{c^2}} = -\frac{1}{\varepsilon_\parallel} \sqrt{\varepsilon_\parallel \left(\frac{h^2}{\varepsilon_\perp} - \frac{\omega^2}{c^2} \mu_\parallel \right)},$$

(4a)

TE mode:

$$\sqrt{h^2 - \frac{\omega^2}{c^2}} = -\frac{1}{\mu_\parallel} \sqrt{\mu_\parallel \left(\frac{h^2}{\mu_\perp} - \frac{\omega^2}{c^2} \varepsilon_\parallel \right)}.$$

(4b)

It is clear from (4a, 4b) that true surface waves exist only for $\varepsilon_\parallel < 0$ (TM mode) and $\mu_\parallel < 0$ (TE mode). We will consider TM modes for isotropic metamaterial, as according to the duality principle, for TE modes it will be sufficient to exchange places ε and μ. Assuming $\varepsilon(\omega) < 0$, we will rewrite (4a) in the form:

$$h = \frac{\omega}{c} \sqrt{\frac{\varepsilon^2 - \varepsilon\mu}{\varepsilon^2 - 1}},$$

(5)

that is more convenient for analysis. For true surface waves, the conditions $h > \omega/c$, $h > \dfrac{\omega}{c} \sqrt{\varepsilon\mu}$ must be fulfilled, which according to (5) is possible only when:

$$1) \; \varepsilon < -1, \; \varepsilon\mu < 1 \qquad \text{or} \qquad 2) \; -1 < \varepsilon < 0, \; \varepsilon\mu > 1. \qquad (6)$$

Analogously, surface TE modes at the boundary of a "left-handed" metamaterial can exist only when

$$1) \; \mu < -1, \; \varepsilon\mu < 1 \qquad \text{or} \qquad 2) \; -1 < \mu < 0, \; \varepsilon\mu > 1. \qquad (7)$$

The requirements (6) and (7) are never fulfilled simultaneously or, in other words, surface TM and TE waves cannot propagate at the same frequencies simultaneously. Clearly, in the case of a "left-handed" metamaterial, the studied surface waves are a) *forward* if $\varepsilon < -1$, $\varepsilon\mu < 1$ (TM mode) or $\mu < -1$, $\varepsilon\mu < 1$ (TE mode), and b) *backward* when $-1 < \varepsilon < 0$, $\varepsilon\mu > 1$ (TM mode) and $-1 < \mu < 0$, $\varepsilon\mu > 1$ (TE mode). We remind that surface waves at the plasma–vacuum interface are always *forward*.

In the degenerate limiting case $\varepsilon(\omega) = \mu(\omega) = -1$ ($\varepsilon(\omega)\mu(\omega) = 1$), the dispersion relations (4a) and (4b) are fulfilled automatically for both TM and TE modes and arbitrary value of propagation constant h. If we compare energy fluxes in metamaterial and in vacuum, they will be equal in absolute magnitude and will have opposite directions. As a result, the total energy flux in all surface waves, as well as their group velocities are equal to zero.

The dependence of slowing down $\gamma = h/k_0$ on relative frequency detuning $\delta\omega = \omega/\omega_p$ is plotted in Fig. 1 for surface waves in metamaterial with

$$\varepsilon = 1 - \frac{\omega_p^2}{\omega^2}, \quad \mu = 1 - \frac{F\omega^2}{\omega^2 - \omega_m^2}, \qquad (8)$$

where $F = 0.56$. The choice of parameters is dictated by practical realization [2]. In Figure 1 we show the evolution of dispersion curves for different values of parameter ω_m for the metamaterial (8):

$$\left(\frac{\omega_m}{\omega_p}\right)_1 = 0.4, \; \left(\frac{\omega_m}{\omega_p}\right)_2 = 0.5, \; \left(\frac{\omega_m}{\omega_p}\right)_3 = 0.6, \; \left(\frac{\omega_m}{\omega_p}\right)_4 = 0.7, \; \left(\frac{\omega_m}{\omega_p}\right)_5 = 0.8,$$
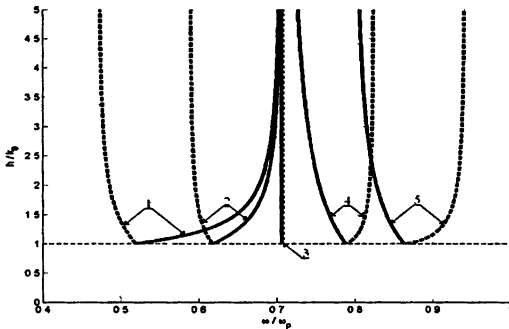
Fig. 1. Frequency dependence of slowing down (h/k_0) of surface TM and TE waves at the vacuum-metamaterial interface (TM waves – heavy solid line, TE waves – heavy dotted line) for five values of frequency ω_m.

552

that have been selected so that the conditions $\varepsilon = -1$, $\mu = -1$, $\varepsilon\mu = 1$ could be satisfied successively with the variation of frequency. When $\omega_m /\omega_p = 0.6$ both permittivity and permeability become equal to minus unity ($\varepsilon = -1$, $\mu = -1$) at the same frequency. The dispersion curve in this case degenerates into a vertical line $\omega = $ const, and the total energy flux and group velocity turn to zero.

Modes of plane waveguide made of metamaterial

Applied problems are always concerned with spatially bounded waveguiding systems, a simplest one-dimensional example of which is a plane layer of a medium. The presence of the second interface may significantly affect the structure and dispersive characteristics of the surface waves guided by the layer.

Let a metamaterial having thickness $2d$ be in vacuum. We will consider a wave traveling along the z-axis. The x-axis will be oriented across the layer; the y-coordinate is of no importance in this case. On the basis of the results presented in the previous sections, we can readily obtain dispersion relations for surface waves exponentially decaying in the regions $|x| > 0$ with increasing distance from the interface. Two variants of wave field behaviour are possible inside the layer at $|x| < d$. These are exponential behaviour (a slow wave in metamaterial) or oscillatory behaviour (a fast wave in metamaterial). In the first case, we will speak about a mode formed by two interacting true surface waves each of which is guided by its own interface. In the second case, mode existence, like in a conventional dielectric waveguide, is associated with the effect of complete reflection. When dispersion equations are derived without restriction of generality, one can assume that the wave in a layer is formed by two interacting natural surface waves.

Meeting the boundary conditions of the continuity of tangential components of electric and magnetic field intensities we can find dispersion relations for surface waves

TM mode:

$$\eta = -\frac{\tilde{\eta}}{\varepsilon_\parallel}\tanh^{\pm 1}\left(\tilde{\eta}d\right), \quad \begin{array}{l} \eta^2 = h^2 - \frac{\omega^2}{c^2} \\ \tilde{\eta}^2 = \varepsilon_\parallel\left(\frac{h^2}{\varepsilon_\perp} - \frac{\omega^2}{c^2}\mu_\parallel\right) \end{array}, \tag{9a}$$

TE mode:

$$\eta = -\frac{\tilde{\eta}}{\mu_\parallel}\tanh^{\pm 1}\left(\tilde{\eta}d\right), \quad \begin{array}{l} \eta^2 = h^2 - \frac{\omega^2}{c^2} \\ \tilde{\eta}^2 = \mu_\parallel\left(\frac{h^2}{\mu_\perp} - \frac{\omega^2}{c^2}\varepsilon_\parallel\right) \end{array}. \tag{9b}$$

In these equations the "plus" sign corresponds to symmetric modes, and "minus" to antisymmetric ones. By substituting $i\tilde{\eta}$ for $\tilde{\eta}$ we obtain from (9) dispersion equations for surface waves based on the effect of complete internal reflection.

In view to format of paper we show properties of isotropic metamaterial layer for symmetric and antisymmetric TM modes for $\omega_m/\omega_p = 0.6$. The value of parameter $\omega_m/\omega_p = 0.6$ corresponds to degeneration of true surface waves (see Fig. 1). Its characteristic feature is that the plane boundary separating two half-spaces filled by metamaterial and vacuum maintains at the same frequency an infinite number of waves with arbitrary slowing down and polarization.

One can see from Fig. 2 that the interaction between natural surface waves localized at different interfaces eliminates degeneration of both symmetric and antisymmetric surface waves. The less the layer thickness, the larger the frequency interval of their existence is.
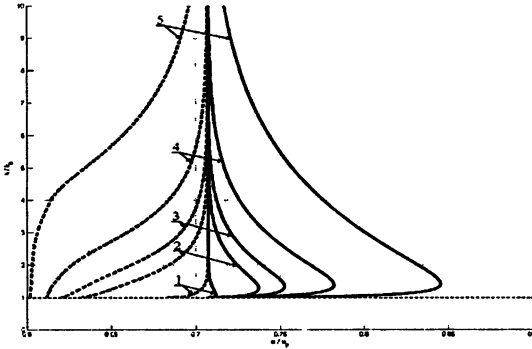
Fig. 2. Frequency dependence of slowing down (h/k_0) of symmetric (heavy lines) and antisymmetric (dotted lines) waves in a layer of metamaterial for five different layer thicknesses (($\omega_p d)/c = 3; 1; 0.75; 0.5; 0.25$).

Note that "removal" of degeneration for symmetric modes results in simultaneous appearance of two surface waves, forward and backward at the same frequency. The forward wave is less slowed down than the backward. The antisymmetric mode is always forward in this case.

Conclusion

To conclude, the presented analysis covers almost completely all possible structures of symmetric and antisymmetric surface modes of a plane layer of isotropic and anisotropic metamaterial. By varying layer thickness and parameters of resonance elements of which metamaterial consists one can obtain both forward and backward waves and control their slowing down.

References

1. *Ilin N. V., Kondratiev I. G and Smirnov A. I.* True surface waves guided by metamaterials // Bulletin of the Russian Academy of Sciences: Physics. 2008. Vol. 72, No. 1. P. 118–122.
2. *Shadrivov I V., Sukhorukov A. A. and Kivshar Y. S.* Phys. Rev. E, **67**, 057602 (2003).

MODELING OF HIGH PRESSURE MICROWAVE PLASMA REACTORS FOR THE GROWTH OF HIGH PURITY CVD DIAMOND FILMS IN THE HIGH GROWTH RATE REGIME

F. Silva, K. Hassouni, G. Lombardi, X. Bonnin, A. Gicquel

LIMHP, Université Paris 13, CNRS; Institut Galilée,
99 avenue Jean-Baptiste Clément, 93430 Villetaneuse, France

Because of its exceptional properties, CVD diamond is the ultimate material for high power electronics working at high voltage and high frequency. However, its industrial use will require processes yielding adequate growth rates, surface areas and quality. The only CVD diamond growth processes currently able to provide such high purity and high growth rate films are microwave plasma-assisted processes, which can produce the large amounts of atomic hydrogen required for growth.

We will show how a 1D plasma model describing the complete physico-chemistry of an H_2/CH_4 diamond deposition plasma has evidenced the roles of the microwave power density and the working pressure on the production of key growth species such as H and CH_3. The usable deposit area is directly dependent on the size and homogeneity of the plasma. However, the maximum discharge size is mainly dictated by the cavity geometry.

In this work we will show that our method for plasma reactor design, based on careful electromagnetic modeling of the microwave cavity and coupling system, as well as a self-consistent plasma model, has allowed us to build plasma reactors working stably, at very high power density and with large plasma sizes.

Introduction

The significant progress made on CVD diamond synthesis these last few years, notably with respect to purity and crystalline defects content [1–5], has generated new interest in this material for a large number of applications. However, CVD diamond production at high growth rates and on large areas remains a critical prerequisite for industrial usage. In that respect, reactor performance plays an essential role.

The first part of this paper will be dedicated to the influence of the deposition process parameters and more particularly the microwave power density on the production rate of deposition species and CVD diamond growth. From these results, a certain number of recommendations can be made to obtain simultaneously large growth rates and high film quality. The second part of this paper will concern itself with the design of plasma reactors in our laboratory, based on microwave engineering and plasma modelling. A detailed methodology will be presented, which allowed us to develop microwave plasma reactors which can operate in a very stable fashion even at very high power density, without leading to overheating of the reactor walls and other sensitive parts, such as the quartz window.

CVD diamond growth: mechanisms and key parameters

CVD diamond growth is a complex process difficult to describe accurately in a full way. Indeed, it is necessary to detail the gas composition just in front of the

growing surface, to describe the surface kinetics including adsorption-desorption, abstraction and diffusion phenomena on a complex evolving surface, made up of steps and terraces and subject to reconstruction processes. No model from the literature fully describes the complexity of CVD diamond growth, but certain simplified approaches do provide an understanding of the influence of some deposition process parameters.

The growth model proposed by Harris and Goodwin [6–8] describes the growth of CVD diamond in a very simple way, with only 2 species, H and CH_3, and 5 reactions (see below). The diamond growth proceeds by incorporation of growth units made of methyl radicals. This incorporation follows the creation of open sites available for growth (denoted Cd^*) through a series of abstraction reactions of the hydrogen atoms adsorbed with atoms from the gas phase. The CH_3 radicals which will occupy those sites must undergo these abstraction reactions so as to become fully integrated in the diamond lattice. From this simplified kinetic scheme, where some of the fundamental roles of atomic hydrogen come forth, it is possible to derive an expression for the growth rate $G_{\{100\}}$ of $\{100\}$ diamond planes which depends on the H and CH_3 surface concentrations (Eq. 1).

$$\begin{cases} Cd-H+H \xrightarrow{k1} Cd^*+H_2 & (R_1) \\ Cd^*+H \xrightarrow{k2} Cd-H & (R_2) \\ Cd^*+CH_3 \underset{k4}{\overset{k3}{\rightleftharpoons}} Cd-CH_3 & (R_3) \\ Cd-CH_3+H \xrightarrow{k5} Cd-CH_2^*+H_2 & (R_4) \\ Cd-CH_2^*+H \xrightarrow{k6} Cd-Cd-H+H_2 & (R_5) \end{cases} \qquad G_{\{100\}} = k_3 \frac{n_s}{n_d} \left(\frac{k_1}{k_1+k_2} \right) \frac{[CH_3]_s[H]_s}{\dfrac{k_4}{k_5}+[H]_s} \quad (1)$$
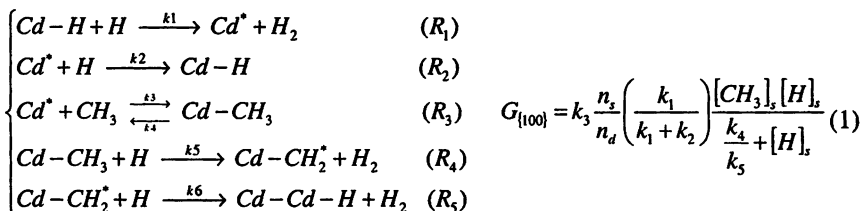
In order to determine the influence of the deposition parameters (pressure, microwave power, methane concentration) on CVD diamond growth, we have used plasma models developed in-house to compute the gas phase concentrations of H and CH_3 as a function of these variables. The first model is a 2D self-consistent plasma model [9, 10] which accurately describes all the physico-chemical phenomena taking place in a pure hydrogen microwave plasma (electromagnetism, energy transfer, chemistry, and transport). This plasma code takes into account the reactor geometry, and yields the spatial distribution of all relevant quantities such as atomic hydrogen and electron densities, gas and electron temperatures, and microwave power density.

Figure 1 shows the evolution of gas and electron temperatures, as well as atomic hydrogen density, in our laboratory reactor (previously described in [3]), as the working pressure varies from 50 to 300 mbar. The microwave power has been adjusted for each pressure so as to maintain a constant plasma volume. One sees that the electron temperature drops from 15 000 to 10 000 K within this pressure range because of the increase in collision frequency. In parallel, the gas temperature in the plasma center goes from 2200 to 3600 K for the same reason. If one considers the contributions of the different reactions to the H production

rate, one sees that, at low pressure, H is mainly produced by direct electronic impact dissociation ($e^- + H_2 \rightarrow e^- + 2H$) while it is mainly produced by thermal dissociation of H_2 molecules ($H_2 + H \rightarrow 3H$) at high pressure (cf. Fig. 2a). This result links the large increase in atomic hydrogen density at high pressure to the gas temperature rise of more than 1400 K.

Concerning CH_3 production, we used a 1D code describing the complex chemistry of a hydrogen/methane plasma including 28 species and 130 reactions [11]. This model accepts as input the process control parameters and the microwave power density profile obtained from the self-consistent plasma model.

Figure 2b shows that CH_3 production at low pressure takes place in the plasma bulk and is governed by H (through the reaction $CH_3 + H + M \leftrightarrows CH_4 + M$, M being a third body). At high pressure, CH_3 production is still controlled by H (through the reaction $CH_4 + H \leftrightarrows CH_3 + H_2$) but occurs only very close to the surface. In fact, CH_3 production is also regulated by the gas temperature as seen from the profiles in Fig. 2c. CH_3 is only produced if the gas temperature remains within a range going from 1200 to 2200 K. Consequently, the methyl radicals will be produced in larger quantities and closer to the surface as the working pressure increases.

For our reactor, one can trace the evolution of the operating point where CVD diamond growth occurs in a $[H]$-$[CH_3]$ process map, initially introduced by Goodwin [8]. This diagram, represented in Fig. 3, contains lines of constant growth rate (cf. Eq. 1) and also lines of iso-quality, corresponding in fact to sp_2 defect iso-density lines.
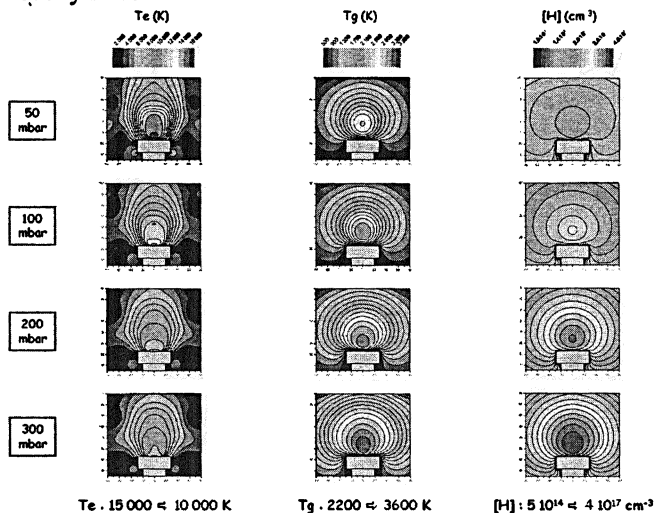
Fig. 1. From left to right, spatial distribution of electron temperature, gas temperature, and atomic hydrogen density for a pure hydrogen plasma ignited inside the LIMHP reactor [3], for different working pressures, obtained from our self-consistent plasma model.

This process map locates the different diamond deposition processes. From our modeling results, it is possible to follow the operating point for our deposition process as a function of working pressure and methane concentration. For a methane content of 1 % in the gas phase, with the pressure ranging from 50 to 300 mbar, the atomic hydrogen concentration at the surface increases by 3 orders of magnitude while the CH_3 concentration is multiplied by 10, leading to a growth rate of some 10 μm/h at 300 mbar. It is also seen that increasing the methane concentration at high pressure can increase significantly the growth rate without compromising film quality.

The upper limit for methane concentration is given by the nucleation of soot particles in the gas phase, which occurs in our process for methane content of 10 % and above. The process map shows all the advantages of working at the highest possible pressure to increase simultaneously the growth rate and the film quality. In this way, we could obtain high purity films grown at high pressure with a growth rate exceeding 70 μm/h [12].
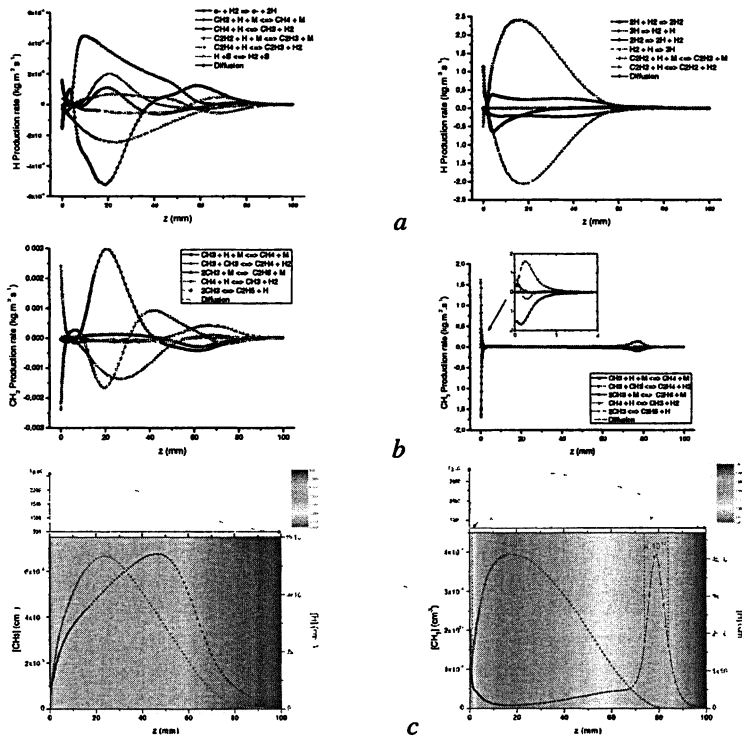
Fig. 2. Axial balance of (*a*) atomic hydrogen and (*b*) CH_3 radicals, for working pressures of 50 mbar (*left*) and 300 mbar (*right*), derived from the 1D H_2/CH_4 model. The corresponding density and gas temperature profiles are shown in the bottom panels (*c*).

However, the use of high power density plasmas often leads to a pronounced heating of the reactor metallic walls and damage to the quartz window enclosing the reduced pressure zone inside the reactor. The reactor must therefore be carefully designed to provide stable work process conditions over long deposition times at high microwave power density.

Microwave plasma reactors design methodology

Contrary to most materials deposited by plasma assisted CVD, diamond deposition occurs at relatively high pressures. For this reason, diffusion phenomena are less important and it becomes necessary to produce the plasma (and therefore the associated high electric field region) near the substrate. Moreover, the high gas temperatures and large thermal conductivity of hydrogen imply large heat fluxes onto the reactor walls which must be handled. Hence, resonant electromagnetic cavities with an appropriate field structure are used for the construction of diamond deposition microwave plasma reactors.
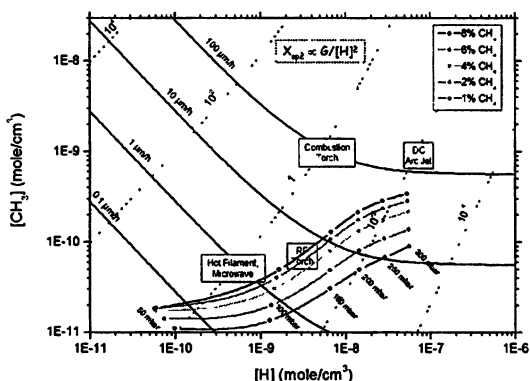
Fig. 3. Process map in [CH₃]-[H] space showing the operating ranges of the main CVD diamond growth processes. The evolution of the operating point of the LIMHP reactor as a function of working pressure (from 50 to 300 mbar) and methane concentration (from 1 to 8 %) has been added.

One of the first advantages to this type of cavity comes from the resonance phenomenon itself. Indeed, when an electromagnetic cavity is excited at its resonant frequency (which depends on geometry and dielectric content), it produces a much higher electric field, thus providing easier plasma ignition. But the main advantage of a resonant cavity is the electric field structure, which can be judiciously chosen to promote a high electric field region, located at the plasma ignition area, without using electrodes. The skill in designing plasma reactors resides in matching the electric field structure from the selected resonant mode so as to locally reinforce the field strength in front of the substrate and obtain the largest

and most homogeneous high field strength region possible. An additional difficulty is due to the presence of the plasma load which perturbs the cavity tuning and which must be taken into account from the start. We will come back later to the challenge of anticipating the cavity mismatch due to the plasma, particularly at high pressure.

There are two resonance mode types, TE and TM, depending whether the electric or magnetic field, respectively, is orthogonal to the cavity axis. Without going into further detail of the electric field structure of the different mode types, one can easily show that only TM_{0mn} modes yield perfectly axisymmetrical plasmas. The main design steps, from a purely electromagnetic standpoint, of a resonant cavity microwave plasma reactor, can be summarized as follows: (i) choice of the resonant mode with an appropriate electric field structure, (ii) choice of the coupling structure (which can be either electric or magnetic), and (iii) choice of the dielectric window (shape and location), generally in quartz, to enclose the reduced pressure zone and confine the useful plasma zone. Figure 4 shows the steps of this designing principle for the bell jar type reactor initially constructed at Michigan State University [13]. The TM_{012} resonant mode was chosen for this device. The cavity is excited by an antenna located at the top, where the upper lobe of maximum electric field lies. The reduced pressure zone is delimited by a quartz bell jar which surrounds the lower maximum field lobe of the cavity.

| a | b | c | d |
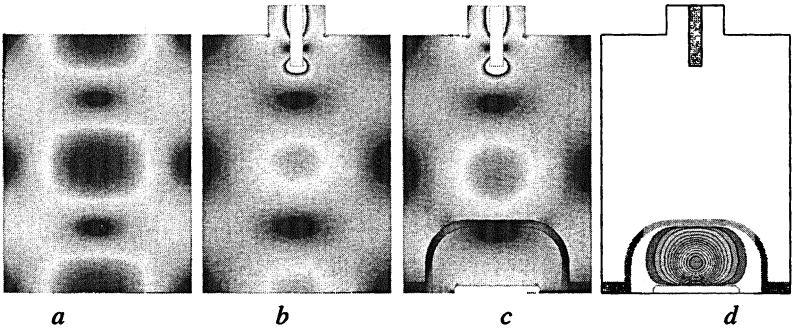
Fig. 4. Different design steps for a microwave plasma reactor (example of the MSU set-up [13]) : (a) choice of the cavity mode (TM_{012}), (b) introduction of the MW coupling system, (c) introduction of the dielectric window (quartz bell jar), (d) modeling of a pure H_2 plasma at 200 mbar obtained with our self-consistent model

One can see how the field structure evolves as different reactor elements are introduced into the cavity. It is thus also necessary to ensure that the final configuration (i.e. with all elements included) still presents a sharp resonance at the microwave generator excitation frequency, here 2.45 GHz. Fig. 4d shows a modeling of the plasma (atomic hydrogen density at 200 mbar), for this type of reactor, as computed from our self-consistent plasma model. Because the reactor dimensions (as deduced from the literature) could only be known approximately, this simulation is only given here for illustrative purposes. Our first LIMHP reac-

tor was designed in 1990, following the same principles. It is also a bell jar type reactor with a TM_{023} cavity mode as shown in Fig. 5.
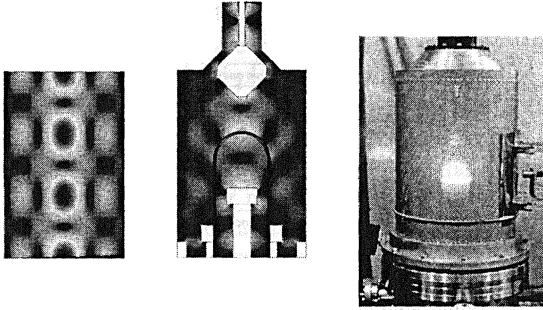
Fig. 5. LIMHP bell jar reactor designed in 1990: *(left)* TM_{023} cavity mode; *(center)* electric field distribution inside the coupled cavity with its substrate holder and quartz bell jar; *(right)* photograph of an H_2 plasma at 25 mbar and 600 W power

We did not then have the numerical tools available to us now and therefore this reactor was tuned semi-empirically, through a relatively long and fastidious trial and error process. We find a good correlation between the electric field structure in the empty cavity and the plasma shape obtained at low pressure (25 mbar), when the plasma load is not yet a strong perturbation to the cavity behavior. However, when we increase the microwave power density, the cavity tuning becomes more and more difficult to achieve and the reflected power, partially compensated through an impedance matching system, causes more and more pronounced heating of all the metallic walls, as shown by the thermal imaging in Fig. 6. This heating, which becomes detrimental for pressures above 150 mbar, is partially linked to the cavity detuning due the plasma load which had not been anticipated during the reactor design. We have since developed a methodology aiming to refine the microwave design of plasma reactors in order to facilitate stable operation for long deposition times at high power density. This method is detailed in Fig. 7.
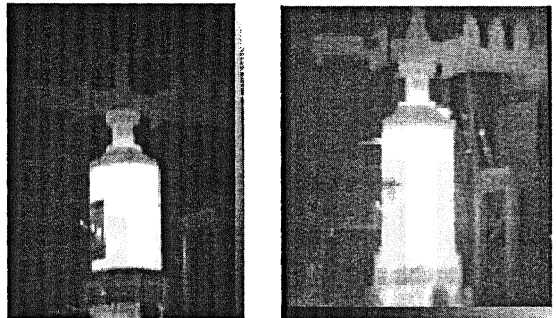
Fig. 6. Thermal imaging of the bell jar reactor from Fig. 5, working respectively at 50 mbar *(left)* and 200 mbar *(right)* pressures. The highest temperature recorded at 200 mbar lies above 60 °C.

561
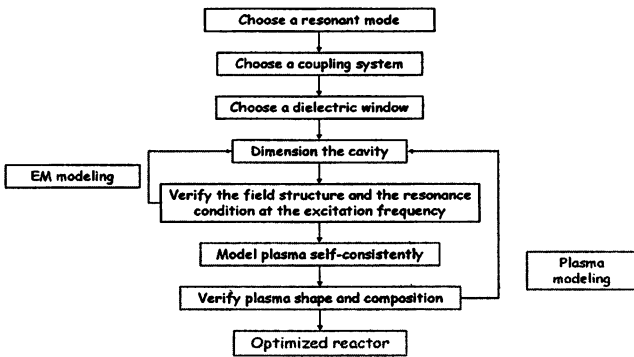
Fig. 7. Design and optimization methodology for MW plasma reactors used at LIMHP, relying on electromagnetic modeling coupled to self-consistent plasma modeling

After having chosen the resonance mode, the coupling structure, and the dielectric window, one proceeds with the cavity dimensioning with the help of an electromagnetic solver in order to get a cavity resonant at 2.45 GHz, while ensuring a large high electric field zone in front of the substrate holder. One then solves for the plasma inside this cavity, with the help of our self-consistent model, yielding the shape and composition of the plasma, as well as the cavity detuning. If the results are unsatisfactory, the cavity dimensions are modified accordingly and the process is repeated. This optimization is made with a high power density (i.e. high pressure) plasma in mind, since correcting for detuning at low power density is usually not a problem. We have recently undertaken such an optimization procedure on our first generation LIMHP bell jar reactor, in order to be able to use the reactor at higher power density.

To achieve higher power operation, we have increased the diameter of the quartz bell jar to move the quartz walls away from the plasma and modified the cavity geometry to obtain a higher power density plasma with a better radial homogeneity. The results shown in Fig. 8 confirm that the homogeneous plasma shape obtained experimentally is in perfect agreement with our self-consistent model predictions. This new bell jar reactor, which demonstrated excellent performance at working pressures in excess of 200 mbar as well as good handling of heat fluxes to the walls, is now commercially available through the PLASSYS Company.
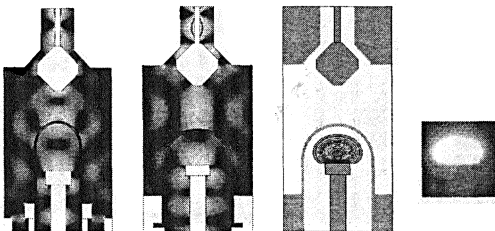
Fig. 8. Optimization of the first generation LIMHP bell jar reactor, following Fig. 7. (3 left panels). The plasma shape coming from the self-consistent model is in perfect agreement with the experimental results (rightmost panel; pressure: 200 mbar).

Conclusion

In this work, we have shown the importance of working at high pressure to obtain both high growth rates and high film quality. High density, large area, plasmas require optimization of the electric field structure inside the cavity through careful electromagnetic and plasma modeling. Moreover, important heat fluxes to the walls linked to the use of a high power density plasma require efficient cooling of sensitive reactor components and optimization of the microwave coupling structure as well as the shape and location of the dielectric window inside the cavity. The substrate holder must also be carefully designed to provide precise control of the surface temperature, which becomes particularly challenging at high pressure.

References

1. *Isberg J., Hammersberg J. et al.* Science, **297**, 1670 (2002).
2. *Kasu M., Kobayashi N.* Diam. & Relat. Mat. **12**, 413 (2003).
3. *Achard J., Silva F. et al.* J. Phys. D, **40**, 6175 (2007).
4. *Gaukroger M. P., Martineau P. M. et al.* Diam. & Relat. Mat. **17**, 262 (2008).
5. *Silva F., Achard J. et al.* Diam. & Relat. Mat. **17**, 1067 (2008).
6. *Harris S. J.* Applied Physics Letters, **56**, 2298 (1990).
7. *Harris S. J., Goodwin D. G.* J. Phys. Chem. **97**, 23 (1993).
8. *Goodwin D. G.* J. Appl. Phys. **74**, 6888 (1993).
9. *Hassouni K., Grotjohn T. A. et al.* J. Appl. Phys. **86**, 134 (1999).
10. *Hagelaar G. J. M., Hassouni K. et al.* J. Appl. Phys. **96**, 1819 (2004).
11. *Lombardi G., Hassouni K. et al.* J. Appl. Phys. **98**, 053303 (2005).
12. *Silva F., Achard J. et al.* Diam. & Relat. Mat. (2009). [Submitted].
13. Patent 5,311,103 / Asmussen J., Zhang J.; 1994.

SYNTHESIS OF ULTRANANOCRYSTALLINE DIAMOND FILMS IN MICROWAVE PLASMA

G. Ralchenko, A. V. Saveliev, I. I. Vlasov, A. V. Khomich[1],
A. F. Popovich, L. Ostrovskaya[2], S. N. Dub[2], V. I. Konov

A. M. Prokhorov General Physics Institute RAS, Moscow, Russia
[1] Institute of Radio Engineering and Electronics RAS, Fryazino, Russia
[2] Institute for Superhard Materials NASU, Kiev, Ukraine

Thin ultrananocrystalline diamond (UNCD) films are produced by chemical vapor deposition in microwave plasma (2.45 GHz) using $CH_4/H_2/Ar$ mixtures with low hydrogen content. The material was characterized by UV-IR optical absorption, Raman and photoluminescence spectroscopy, SEM, TEM, AFM. The effect of doping of the UNCD with nitrogen is studied. The data on thermal conductivity, elastic properties, optical absorption, and wetting of the films are surveyed.

Introduction

Growth of polycrystalline diamond films and wafers by chemical vapor deposition (CVD) becomes currently a commercial technology [1, 2] that allows production of diamonds with size much larger that it's possible with conventional high pressure – high temperature technique. The most perfect diamond films, with properties approaching to those for the best natural single crystals [2, 3], are grown at reasonable rates by microwave plasma assisted CVD (MPCVD), since the "clean" plasma at high pressures (of the order of 100 Torr) can be realized. The polycrystalline diamond films are deposited commonly using CH_4-H_2 gas mixtures with a small fraction (few percents) of methane. Noble gases like Ar can also be added in substantial amount, while keeping H_2 the dominated component [3]. The typical grain size is tens microns for the films of hundred microns thickness.

A special type of diamond films – ultrananocrystalline diamond (UNCD) with grain size as small as 2–10 nm can be grown in an Ar-CH_4-H_2 environment with reduced (or even zero) H_2 content [4–6]. Under these specific conditions in Ar-rich plasma the diamond grains keep nanoscale size independent on film thickness owing to extremely high secondary nucleation rate. The UNCD films form smooth, ultrathin, hermetic, superhard, low friction, low-field electron emission, biocompatible, chemically resistant coatings [7, 8], all this making them interesting for applications in microelectromechanics, tribology, biomedicine. Moreover, the UNCD films grown with nitrogen (N_2) added in high amounts in gas phase become electroconductive [9], thus the nitrogenated UNCD are promising for applications in electronics [10] and electrochemistry [11]. Grain boundaries (GB) play important role in UNCD structure and properties since the atoms on GB constituent an appreciable amount of the material. Here

we describe deposition, structure and properties of insulating and conductive (nitrogenated) UNCD films produced in microwave plasma.

Experimental details

The UNCD films were deposited in a MPCVD reactor (5 kW, 2.45 GHz) in Ar/CH$_4$/H$_2$/N$_2$ mixtures (Fig. 1) [5]. The percentages of CH$_4$ (2 %) and H$_2$ (5 %) in the gas mixture were constant, while nitrogen N$_2$ was added in concentration varied from 0 % to 30 % by partly replacing Ar to keep the total gas flow constant at 500 sccm. Other deposition parameters were as follows: pressure 90 Torr, microwave power 2.3 kW, substrate temperature 800 °C, deposition time 40 min – 11 hours. The substrates were mirror-polished Si 10 × 10 × 0.5 mm plates, which were seeded before deposition process with nanodiamond particles (produced by a detonation technique, nominal size 4–6 nm) by treatment in an ultrasonic bath with a nodiamond suspension in alcohol.
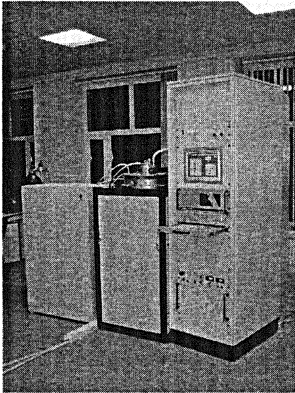
Fig. 1. MPCVD reactor for diamond deposition
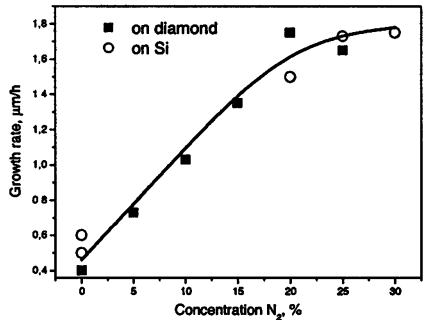
Fig. 2. Growth rate of UNCD films on Si and polycrystalline diamond substrates vs N$_2$ gas added into plasma

For optical absorption measurements the UNCD films were grown on transparent polycrystalline CVD diamond (PCD) substrates produced in the same CVD reactor using 2 % CH$_4$ – 98 % H$_2$ process gas mixture. The PCD substrates 3.5 × 5.0 × 0.4 mm (grain size 60–90 μm) were polished to surface roughness $R_a <$ 10 nm. No seeding was used in this case since the UNCD layer formed epitaxially. The thickness of as-grown films was measured either by viewing sample's cross-section with electron scanning microscopy (SEM), or by direct measurement with an optical interferometer ZYGO (NewView5000) of a step between a (unseeded) Cu mask on PCD and the film formed.

565

Surface topography was characterized with an atomic force microscope (AFM) Ultra Objective (Carl Zeiss). Raman analysis of the carbon phases in was performed with a Dilor XY Raman spectrometer using the 413.1 nm line of a Kr^+ laser for excitation, and UV LabRAM HR spectrometer with scattering excitation at 244 nm. Thermal diffusivity was measured at room temperature using a laser flash technique [6, 12]. For this aim 10–11 μm thick UNCD membranes of 5 mm diameter were prepared by selective-area etching of Si substrate.

Results

The deposition rate of undoped films (no N_2 was added in gas) is (0.5 ± 0.1) μm/h, increasing linearly to 1.6 μm/h with amount of N_2 added, up to 20 %, and showing a plateau at higher doping (Fig. 2). Typically two-hour deposition runs were used to prepare the samples for further analysis. The films are quite smooth: on Si substrates they exhibit a globular morphology (globule size of 50 nm to 1700 nm) and low surface roughness (R_a = 16–50 nm) as imaged with AFM. Even lower roughness R_a = 5–28 nm was measured on UNCD grown on PCD substrates (Fig. 4).
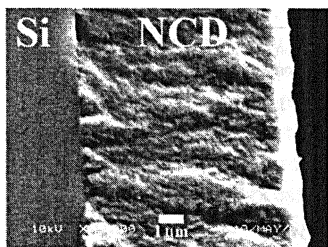
Fig. 3. Cross-section SEM image of 8.5 μm thick UNCD film (grown adding 15 % N_2 in gas) on Si substrate
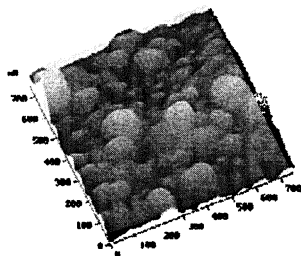
Fig. 4. AFM topography of UNCD film on polished diamond substrate. Image size 0.8 × 0.8 μm, surface roughness R_a = 4.7 nm.

The film structure is subjected to dramatic changes when N_2 is added in plasma in large amounts (> 20 %), according to SEM examination (Fig. 5). While ≈ 20 nm granules form in undoped UNCD, randomly oriented nanowires, up to 400 nm long, are seen on the surface of nitrogenated films. The fine structure of the diamond nanograins and nanowires was revealed in more details with transmission electron microscopy (TEM). Almost spherical diamond grains as small as 2–5 were observed in the undoped films, while diamond nanowires (DNW), often assembled in bundles (Fig. 6), are seen in nitrogen-doped samples. The nanowires have a cylindrical diamond core of 5–6 nm diameter, easily identified by (111) diamond planes with interdistance of d_{111} = 0.206 nm (Fig. 6). The DNWs grow along the [110] direction (identified from electron diffraction) with the (111) planes parallel to the growth direction [13].

566
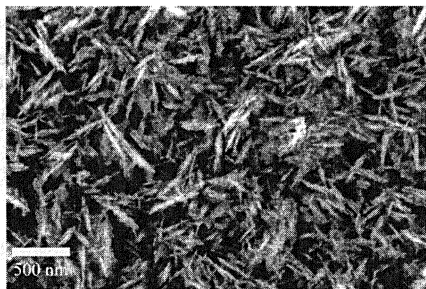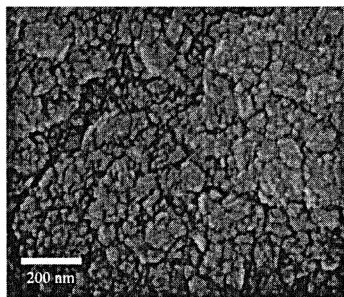
Fig. 5. SEM images of UNCD films grown on Si: without adding N_2 (*left*), and with adding 30%N_2 in gas (*right*). Note appearance of nanowires in the nitrogen "doped" film.

The DNW are always surrounded with a graphitic shell (Fig. 6), which thickness can vary from a few nm to more than 5 nm. It is this shell, composed also of a-C and trans-polyacetylene [6, 14], provides high electrical conductivity (resistivity $\rho < 10^{-2}$ $\Omega \cdot$ cm) of the N-doped UNCD [15], while the undoped films show $\rho \sim 10^{10}$ $\Omega \cdot$ cm [6, 9].
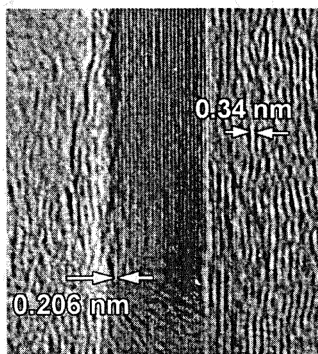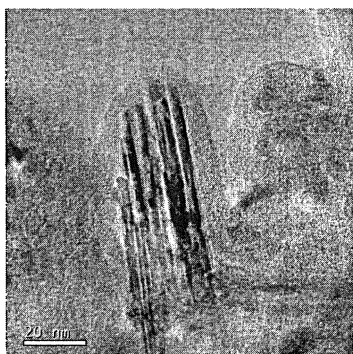
Fig. 6. TEM images of UNCD grown with 25%N_2 added in gas: *left* – a bundle of seven DNWs; *right* – individual DNW enveloped in graphite shell. Arrows indicate interplane distances for diamond and graphite lattices.

Raman spectra excited at 413 nm wavelength are shown in Fig. 7a for undoped (0% N_2) and four N-doped samples. For the undoped film the following phases can be identified from specific spectral features: diamond with the peak at 1335.7 cm^{-1}; sp^2-bonded carbon (disordered graphite) with D and G peaks at 1350 cm^{-1} and 1550 cm^{-1}; and trans-polyacetylene (t-PA) with two peaks at 1157 cm^{-1} and 1539 cm^{-1}. With N_2 addition the intensities of diamond and t-PA Raman peaks decrease relative to G band, indicating that the nitrogen stimulates an increase in sp^2 phase content (predominantly on grain boundaries). However, since

567

the diamond peak is very weak on the background of sp² phase signal upon Raman scattering in the visible, it's advantageous to use UV excitation with photon energy approaching to diamond band gap. The UV Raman spectra (Fig. 7*b*) clearly show the presence of diamond phase and sp²-bonded carbon ("G" band) in all samples, for any nitrogen doping level. The G peak narrowing and shift to 1580 cm⁻¹ with N_2 addition in gas indicate a partial transition of amorphous carbon to graphite structure.
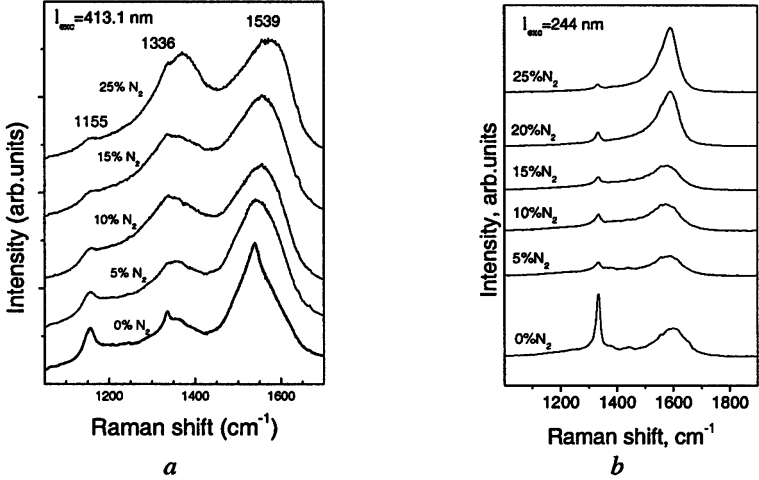
Fig. 7. Raman spectra for UNCD films grown at different N_2 concentration added in plasma as measured at excitation wavelengths in the visible (413 nm) and ultraviolet (244 nm) range

Elastic properties of UNCD have been evaluated using nanoindentation measurements with Nano Indenter-II apparatus (MTS Systems) under load of 1 mN and 5 mN. The highest hardness $H = 30$ GPa is achieved for undoped UNCD. The hardness monotonically decreases with adding N_2 in plasma (Fig. 8*a*), this reflects the increase of sp² carbon content in the films. Young's modulus shows non-monotonic behavior (Fig. 8*b*) with the maximum of $E = 350$ GPa for the sample produced at 10 % N_2 in plasma. There is a large scattering in the results due to composite (nonuniform) film structure, and possible presence of nanovoids. We note, that a revision of these data might be needed in view of rough surface (sticking nonowires) of heavily doped films.

The measured thermal diffusivity (D) at room temperature for UNCD films produced with different N_2 amount added in plasma is shown in Fig. 9 [6]. The highest diffusivity $D = 0.056$–0.07 cm²/s is determined for undoped sample, it gradually decreases with doping level down to 0.034 cm²/s for 25 % N_2 film. The thermal conductivity K was calculated as $K = D\rho C$, where $\rho = 3.51$ g/cm³ and

$C = 0.511$ J / (g · K) are the mass density and specific heat of single crystal diamond. We find $K = (0.12 \pm 0.02)$ W / (cm · K) for undoped UNCD, that value reducing further with doping to ~ 0.06 W / (cm · K) for 25 % N_2 film. The UNCD thermal conductivity is two orders of magnitude lower than that for single crystal diamond of PCD (10–20 W / (cm · K)). A monotonic increase of thermal conductivity with temperature in the range of $T = 80$–400 K was observed [16], similar to behavior of disordered materials. Yet, the K value is an order of magnitude higher compared to amorphous diamond-like carbon films, including t-aC films with high sp³/sp² bonding ratio [16]. The estimated phonon free pass in the UNCD films $L_{ph} = 0.7$–1.7 nm is less than the grain size, and it's comparable with grain boundary thickness.

a b
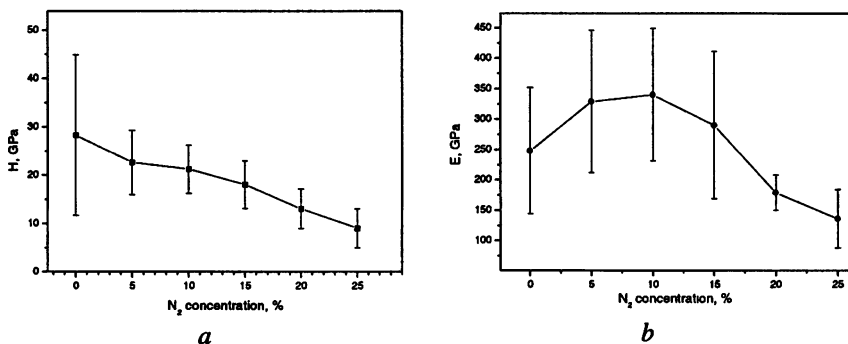
Fig. 8. Hardness H and Young's modulus E of UNCD films grown with different N_2 concentration in plasma.
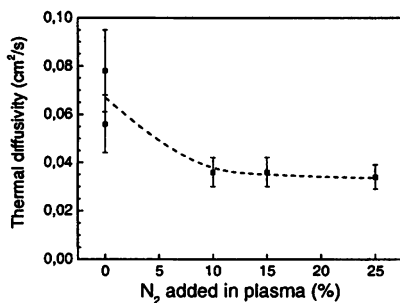
Fig. 9. Thermal diffusivity at room temperature for nitrogen doped UNCD films as measured by a laser flash technique

Absorption coefficient, α, in the visible is $(0.4$–$4) \cdot 10^4$ cm⁻¹ (at λ = 500 nm) [6], that is 3–4 orders of magnitude higher than for polycrystalline CVD diamond. The absorption increases with nitrogen doping, thus indicating an accumulation of graphitic component. Similar tendency is observed in IR optical transmission spectra which show progressive film darkening and transparency loss with doping (Fig. 10).

569
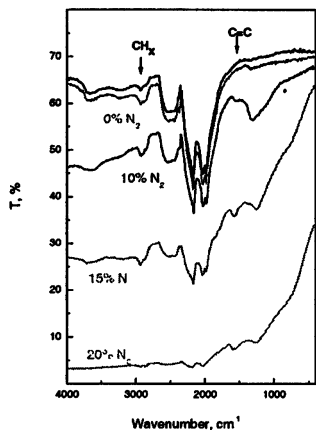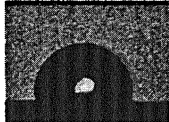
Fig. 10. IR optical transmission for UNCD films grown on diamond substrates at different N_2 contents in gas

UNCD as many other carbon materials are biocompatible, so nanocrystalline diamond films are of interest for use in biomedicine, e.g. coatings on implants. Wettability of these coatings is important parameter. The advancing contact angle θ for UNCD was measured by a sessile-drop method for distilled water in air at room temperature [17]. Other samples studied for comparison were a polished natural type IIa octahedral diamond single crystal (SC) of 6 mm in size, and natural monocrystalline graphite of (0001) orientation (freshly cleaved chips). Naturally oxidized and hydrogenated (treated in H_2 microwave plasma at 600 °C for 5 min) diamond surfaces were tested [18].

The contact angle θ for both oxidized SC diamond and UNCD are lower compared to that for graphite (Table), oxygen-related functional groups making the surface hydrophilic. After hydrogenation the contact angle for undoped UNCD films increased to $106 \pm 3°$ (corresponding to surface energy $\sigma = 50$ mJ/m^2), that's higher than for H-terminated SC diamond ($\theta = 92°$). Both surfaces become more passive than graphite basal plane. In contrast, oxygen treatment resulted in almost complete wetting ($\theta = 5°$) for UNCD surface, but not for SC diamond. The wetting behaviour of nanostructured films can be considered taking into account the relief features on nanoscale [18] using the Cassie–Baxter equation for heterophase nanoporous surfaces. Thus, the UNCD wettability and surface energy can be easily varied in very board range simply by making the surface H-terminated or O-terminated.

Measured contact angle θ for water on naturally oxidized and hydrogenated single crystal diamond, undoped UNCD and graphite, with corresponding photo of the contacting drop

Surface state	Diamond, (111) plane	UNCD (undoped)	Graphite, (0001) plane
Naturally oxidized	$42 \pm 2°$	$73 \pm 3°$	$85 \pm 2°$
Hydrogen plasma-treated	$93 \pm 2°$	$106 \pm 3°$	*n/a*

Acknowledgements

References

1. Low-Pressure Synthetic Diamond: manufacturing and Applications / Ed. by B. Dischler and C. Wild. Springer, Berlin, 1998.
2. Element Six: www.e6.com.
3. *Isberg J. et al.* Science, **297**, 1670 (2002).
4. *Gruen D. M.* Annu. Rev. Mater. Sci. **29**, 211 (1999).
5. *Konov V. I, Smolin A. A., Ralchenko V. G. et al.* Diamond Relat. Mater. **4**, 1073 (1995).
6. *Ralchenko V., Pimenov S., Konov V. et al.* Diamond Relat. Mater. **16**, 2067 (2007).
7. *Krauss A. R., Auciello O., Gruen D. M. et al.* Diamond Relat. Mater. **10**, 1952 (2001).
8. *Carlisle J. A., Auciello O.* Interface. **12**, 28 (2003).
9. *Bhattacharyya S., Auciello O., Birrell J. et al.* Appl. Phys. Lett. **79**, 1441 (2001).
10. *Williams O. A.* Semicond. Sci. Technol. **21**, R49 (2006).
11. *Pleskov Yu. V., Krotova M. D., Saveliev A. V. et al.* Diamond Relat. Mater. **16**, 2114 (2007).
12. *Vlasov A., Ralchenko V., Gordeev S. et al.* Diamond Relat. Mater. **9**, 1104 (2000).
13. *Vlasov I. I., Lebedev O. I., Ralchenko V. G. et al.* Adv. Mater. **19**, 4058 (2007).
14. *Vlasov I. I., Ralchenko V. G., Goovaerts E. et al.* Phys. Stat. Sol. (a) **203**, 3028 (2006).
15. *Arenal R., Bruno P., Miller D. J. et al.* Phys. Rev. B, **75**, 195431 (2007).
16. *Liu W. L., Shamsa M., Calizo I. et al.* Appl. Phys. Lett. **89**, 171915 (2006).
17. *Ostrovskaya L., Perevertailo V. M., Ralchenko V. et al.* Diamond Relat. Mater. **16**, 2109 (2007).
18. *Ostrovskaya L., Perevertailo V. M., Ralchenko V. G. et al.* J. Nanoscience and Nanotechnology [in press].

EFFECT OF HIGH MICROWAVE SPECIFIC POWER ON MPACVD GROWTH OF SINGLE CRYSTALLINE DIAMOND LAYERS

A. L. Vikharev, A. M. Gorbachev, A. B. Muchnikov, D. B. Radishev

Institute of Applied Physics RAS, Nizhny Novgorod, Russian Federation

Homoepitaxial growth of single crystalline diamond layers by microwave plasma chemical vapor deposition in a 2.45 GHz MPACVD reactor was investigated. Special efforts were made to reach high specific power conditions in the resonator type CVD reactor. Effect of microwave specific power on growth rate and diamond properties was studied. The results of homoepitaxial single crystalline diamond films growth for different specific power were presented. Properties of synthesized single crystalline diamond layers were studied using Raman and X-ray diffraction spectroscopy, SEM, AFM and optical microscopy.

Introduction

Currently, production of single-crystal diamond from the gas phase in chemical vapor deposition (CVD) reactors is studied intensively. This material combines such unique properties as highest thermal conductivity and transparency in a wide wavelength range, high carrier mobility, high electric strength, radiation resistance, and great hardness. Single-crystal diamonds (SCD) are already widely used in practice, as the basis for the development of ionizing-radiation detectors, micro-electro-mechanical systems, field effect transistors, heat sinks, surface acoustic wave filters and other applications [1].

For microwave plasma assisted CVD (MPACVD) reactors, one of the ways to increase the deposition rate and reduce the density of defects in the deposited diamond films is increasing the microwave specific power (microwave power density – MWPD) into the plasma [2–4]. Here, MWPD is understood as the microwave power absorbed in a unit volume of the gas-discharge plasma. Several methods of changing MWPD are known, e.g. 1) by varying the gas pressure, 2) by varying the microwave power together with the pressure, and 3) by changing the field structure in the CVD reactor. All these methods were used in practice by several research groups in order to increase the MWPD into plasma during the SCD deposition [5–7]. However, it has not been studied yet, whether the *method* of achieving high MWPD or only the *values* of the MWPD determine the properties of SCD.

This work was aimed at studying the influence of the MWPD into discharge plasmas on the growth rate and parameters of high-quality SCD films in an MPACVD reactor. The paper presents the results of simulating numerically a microwave discharge in the MPACVD reactor for various geometries of the substrate holder and MWPD. The configuration of the substrate holder, which ensures high MWPD, has been tested experimentally. The results of homoepitaxial SCD films growth for different MWPDs are presented. The properties of the ob-

tained SCD layers were studied by the Raman and X-ray spectroscopy, as well as the methods of optical microscopy, AFM and SEM.

Experimental setup

The MPACVD reactor used in the experiments is described comprehensively in, e.g. [8]. A quartz dome, in which a microwave discharge was ignited in the $H_2 + CH_4$ gas mixture, was placed in a cylindrical cavity excited by a 2.45 GHz magnetron at the TM_{013} mode. The discharge plasma was maintained over a substrate, on whose surface the diamond film was synthesized. The substrate temperature was measured with an MIKRON M67S infrared pyrometer.

The method of the field structure modification in the resonance cavity of the MPACVD reactor was used to increase the MWPD (while the pressure, gas mixture content and microwave power stayed identical), i.e. a local strengthening of the field was produced, which resulted in contraction of the plasma volume [9]. The experiments were performed at a pressure of 120 Torr with: a) standard (flat) geometry of the substrate holder (flat holder), and b) a substrate holder of the trapezoid form (trapezoid holder), see Fig. 1.

Fig. 1. Results of calculating the MWPD into the plasma as a function of the pressure for two different forms of the substrate holder: flat holder and trapezoid holder.
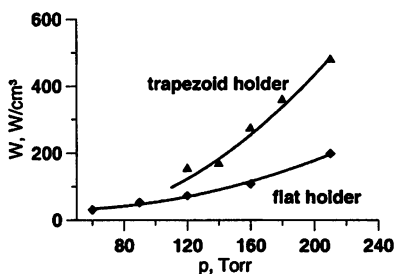
SCD layers were deposited on single-crystal high-pressure high temperature (HPHT) diamond substrates synthesized in HPHT apparatus (TISNCM, Troitsk). Single-crystal diamond type Ib substrates measuring $2.5 \times 2.5 \times 0.3$ mm, with plane (100) oriented perpendicularly to the growth direction, were used in the experiments. The diamond film growth rate was measured by two methods: by the mass gain and by the change in sample height (measured in the growth direction).

Results and discussion

Figure 1 shows calculated dependence of the MWPD on the pressure for the flat and trapezoid holders. Field distributions and the MWPD were calculated by using the self-consistent two-dimensional model of a microwave discharge in hydrogen, which was specified in [10]. Calculations show that in a wide pressure range, the MWPD for the configuration with the trapezoid holder is higher than that for the flat one.

Table shows parameters of depositing three SCD layers. All samples were deposited at the same gas pressure (120 Torr) and the same substrate temperature. However, the MWPD was different due to the change in the substrate holder configuration. Sample 1 and sample 2 were deposited from the gas mixture with equal methane content of 4 %, but with different MWPD (80 and 150 W/cm^2, respectively). The deposition of sample 2 and sample 3 was performed with the same geometry of the substrate holder and equal specific energy contributions, whereas methane content was different: 4 % and 8 %, respectively.

Results of depositing single-crystal diamond films in different regimes

Sample #	Pressure, Torr	Substrate holder	MWPD, W/cm^3	Methane content, %	Layer thickness, μm	Growth rate, μm/h
1	120	Flat	80	4	80	5
2	120	trapezoid	150	4	75	1.5
3	120	trapezoid	150	8	100	5

Figure 2 shows optical images of SCD samples after they have been deposited on seed crystals. It is seen that all SCD layers grew to be transparent, and the surfaces of sample 1 and sample 2 are macroscopically smooth, whereas the surface of sample 2 has etch pits, which are easily visible by an atomic force microscope (AFM), Fig. 3a. Note that the typical diameters of the etch pits range from 2 to 50 μm, Fig. 3b.

a b c
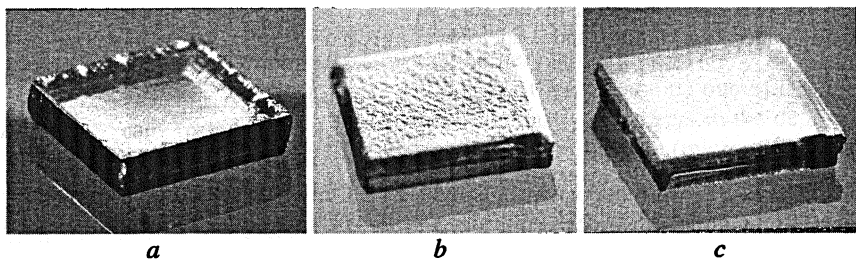
Fig. 2. Photos of the samples after the deposition process: sample 1 (a), sample 2 (b), and sample 3 (c)

As seen from Table, the growth rate of sample 1 (5 μm/h) is higher than that of sample 2 (1.5 μm/h), although these samples were deposited with the same percentage of methane content, 4 %. Apparently, when sample 2 was produced, i.e. the MWPD was higher and amounted to 150 W/cm^3, high density of hydrogen atoms was achieved, and they etched carbon atoms from the diamond surface [11]. Note that this supposition was mentioned in [6, 12–13]. However, our result contradicts the results of [2], where it was stated that the growth rate increased from 3 to 8.5 μm/h as the MWPD grew from 75 to 130 W/cm^3 and the substrate temperature and methane content stayed constant (850 °C and 4 %, respectively). Apparently, the increase in the MWPD in [2] occurred due an increase in the gas

pressure, which resulted in an increase in not only the gas temperature [8], but also the density of hydrogen atoms and the CH_3 radical (gas-phase precursor of diamond). In our case, the MWPD was increased by changing the substrate holder configuration (while retaining the constant gas pressure), which resulted in higher density of hydrogen atoms that etched carbon atoms off the diamond surface efficiently. However, this issue requires further investigation and, first of all, measurements of densities of active radicals. Evidently, the change in gas dynamics due to a modified internal configuration of the reactor also plays a part here.

Note that in the case of sample 1 deposition, the gas phase contained a small admixture of nitrogen having leaked into the vacuum chamber (diagnosed indirectly by IR absorption in sample 1 in the region of 1130 cm^{-1} [14]).

When depositing sample 2 and sample 3, there were no leakages into the vacuum chamber, and the IR absorption method did not reveal nitrogen in those samples (i.e., nitrogen density in the samples was less than the lowest detection limit of the instruments, namely, 1 ppm). It is known that nitrogen affects the diamond film growth rate [6], therefore, despite the low density of nitrogen in sample 1, the growth rate for sample 1 could be somewhat lower under the same conditions, but without nitrogen.
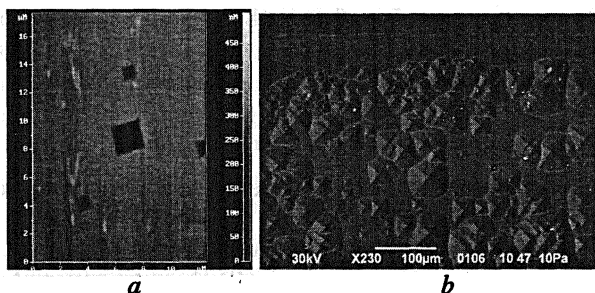
Fig. 3. AFM (*a*) and SEM (*b*) images of sample 2 surface

For sample 3, the growth rate was higher compared with sample 2, which was a result of the increase in the methane content in the gas mixture. However, the quality in this case did not deteriorate, see Fig. 4. FWHM of Raman peaks for sample 2 and sample 3 were 2.0 and 2.1 cm^{-1}, respectively. In the Raman spectrum, Fig. 4*a*, there are no peaks corresponding to photoluminescence at the N-V defects (in the region of 2100 cm^{-1}, in our case), which is an indication of low density of nitrogen in the deposited samples.

As seen from Fig. 4*b*, the (400) peak of X-ray diffraction is rather narrow (FWHM = 0.02°), although asymmetric, which can suggest the existence of a blocked structure of the deposited layer. However, the same asymmetric peak was observed for the substrates, on which the samples were grown, which prompts suggestions that the blocked structure of the deposited layers is a result of blocks in the structure of the seed crystals.

575
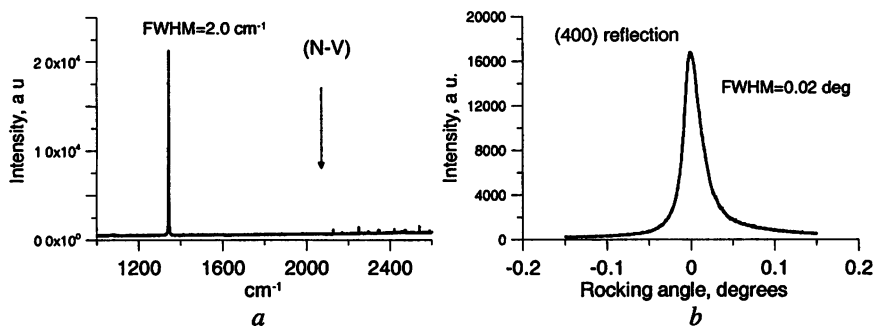
Fig. 4. Raman spectra from sample 2 (*a*) and high-resolution X-Ray diffraction rocking curve from sample 3 (*b*)

Conclusions

High microwave power density makes it possible to increase the methane content in the gas phase during MPACVD synthesis of SCD films. Thus, the growth rate could be enhanced without degradation of SCD quality.

SCD layers were grown at 5 μm/h growth rate with a low level of impurities. The synthesized samples' quality is identical to those seen in high-quality natural diamond (FWHM of Raman peak is 2 cm^{-1}).

Acknowledgements

References

1. *Kohn E. et al.* J. Phys. D: Appl. Phys. **34**, R77 (2001).
2. *Achard J. et al.* J. Cryst. Growth. **284**, 396 (2005).
3. *Findeling-Dufour C. et al.* Diamond Relat. Mater. **4**, 429 (1995).
4. *Silva F. et al.* Diamond Relat Mater. **5**, 338 (1996).
5. *Mokuno Y. et al.* Diam. Rel. Mater. **15**, 455 (2006).
6. *Achard J. et al.* J. Phys. D: Appl. Phys. **40**, 6175 (2007).
7. *Hemley R J. et al.* U. S. Patent No. 6,858,078 (2005).
8. *Vikharev A. L. et al.* Plas. Phys. Rep. **31**, 338 (2005).
9. *Yamada H. et al.* Jpn. J. Appl. Phys. **45**, 8177 (2006).
10. *Koldanov V. A. et al.* Plas. Phys. Rep. **31**, 965 (2005).
11. *Battaile C. C. et al.* J. Chem. Phys. **111**, 4291 (1999).
12. *Sternschulte H. et al.* Diamond Relat. Mater. **15**, 542 (2006).
13. *Gorbachev A. M. et al.* Plasma Phys. Rep. **33**, 871 (2007).
14 *Davies G.* Physica B, **273/274**, 15 (1999).

DEPOSITION OF THE NATURAL AND ISOTOPIC MODIFIED SILICON FILMS BY PECVD METHOD – FIRST RESULTS

V. A. Koldanov, P. G. Sennikov, S. V. Golubev, M. V. Starodubtsev, D. A. Pryakhin[1], V. I. Shashkin[1]

Institute of Applied Physics RAS, Nizhny Novgorod, Russia
[1] Institute for Physics of Microstructures RAS, Nizhny Novgorod, Russia

Results of the study of inductive-coupled RF discharge plasmas at a prototype of an experimental setup for PECVD silicon films depositions are presented. The first results of silicon films depositions with the help of a commercial PlasmaLab reactor are discussed.

The results of preliminary investigations of natural and isotopic-modified nano-crystalline silicon films grown by plasma enhanced chemical vapor deposition method (PECVD method) are presented. These studies are motivated by the unique physical properties of nano-crystalline natural silicon films and isotopic-modified silicon [1]. The silicon tetra-fluoride (SiF_4) is used as the source of silicon with mixture of hydrogen on several reasons. Nowadays there exist powerful methods for production, purification and isotopic enrichment of silicon tetra-fluoride. It is important that SiF_4 is less hazard in contrast with traditionally used in semiconductor industry silane (SiH_4). Besides, it has been shown [2] that the fluorine created in such a discharge changes the structure and morphology of silicon films significantly due to selective etching of amorphous phase of silicon.

Works on development of isotopic-modified silicon films technology are being conducted in two directions both at the Institute of Applied Physics (IAP) and at the Institute for Physics of Microstructures (IPM).

A new setup is being developed in IAP RAS. One of the main requirements for this setup is minimal level of losses of high-expensive enriched silicon tetra-fluoride precursor and dilution of produced isotopic-modified silicon. To get over this technological problem the helicon type of discharge (inductively-coupled RF discharge with static external magnetic field) will be used as a plasma source. Helicon discharge is characterized by an extremely high plasma density (up to 10^{13} cm^{-3}) at a low gas pressure. The external magnetic field provides the possibility of suppressing of plasma losses on the vacuum chamber walls. Magnetic insulation of plasma improves the isotopic and chemical purity of silicon films.

At the same time the preliminary experiments of silicon films growth are performed in IPM RAS at a commercial PlasmaLab setup (manufactured by Oxford Instruments). The experiments have been performed in a combined inductive-capacitive coupled RF discharge with RF power level up to 300 W in gas mixture $SiF_4 + H_2$. The main object of these experiments was the study of some important features of the deposition process that could be used by design of a new special setup for isotopic-modified silicon films deposition.

Study of the inductively-coupled RF discharge

The preliminary experiments have been performed on a prototype setup (Fig. 1). Special RF generator (13.56 MHz frequency) with maximal power 7 kW has been used as a power source. The main purpose of these experiments was to determine the dependence of the plasma parameters vs. input parameters (gas pressure and composition, RF power level, external magnetic field intensity etc.). The measurements have been carried out at a pulsed regime at RF power level of about 2–3 kW and pulse duration of about 1 ms.
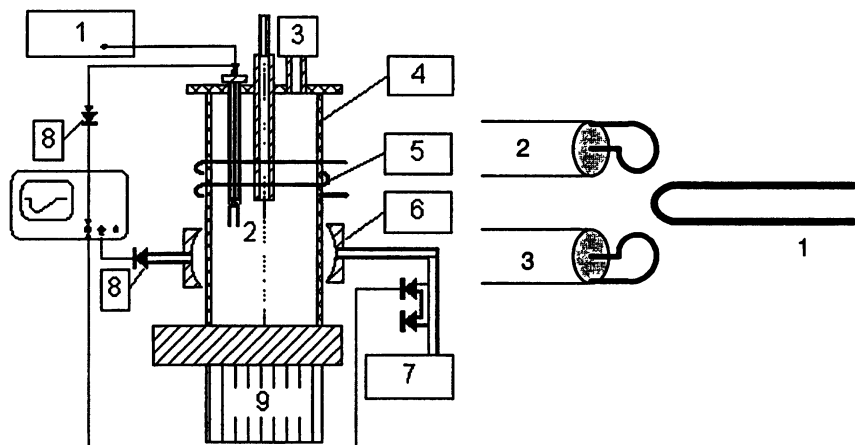
Fig. 1. Scheme of the experimental setup: *1, 7* – microwave generators, *2* – microwave probe, *3* – vacuum-gauge, *4* – discharge tube, *5* – RF inductor, *6* – quasi-optical resonator, *8* – microwave detectors, *9* – pump

Fig. 2. Scheme of the microwave probe: *1* – quarter-wavelength double line resonator, *2, 3* – input and output lines

The plasma density has been measured after the end of RF pulse in afterglow mode with the help of two independent contact and non-contact methods. In our opinion, combination of these two types of plasma diagnostic enables us to obtain the reliable data.

The first method is based on quarter-wavelength microwave probe (Fig. 2). This method is a contact one, but in the case of low gas pressure and high rate of diffusion the spatial distribution of plasma is practically undisturbed and electron concentration can be calculated from resonance frequency shift with the help of the following expression [3]:

$$N_e \approx \frac{\pi \cdot m_e}{e^2} \left(f_{res}^2 - f_0^2 \right), \qquad (1)$$

where $f_0 = 6.1$ GHz – resonance frequency of the probe without plasma.

The second method, which is a non-contact one, is a quasi-optical microwave resonator method. In the case of uniform plasma distribution the plasma density is proportional to the shift of resonance frequencies of quasi-optical resonator:

$$N_e \approx 2 \cdot N_C \frac{L_{res}}{L_{plasma}} \frac{\Delta f}{f_q}, \qquad (2)$$

where N_C – critical plasma density, L_{res} – distance between mirrors, L_{plasma} – plasma thickness, Δf – resonance frequency shift.

Frequency dependence of the signal from quasi-optical microwave resonator without plasma is presented at Fig. 3. The presence of plasma shifts this dependence. In the case of fixed excitation frequency, one may observe several maximums correlated with different resonant plasma densities (Fig. 4).
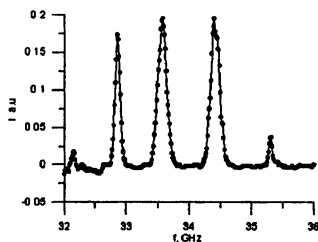
Fig. 3. Signal from quasi-optical resonator without plasma vs. Frequency
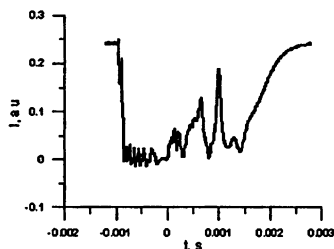
Fig. 4. Typical oscillogram of the signal from quasi-optical resonator (at tuned to the "resonance"). Gas – argon at pressure 0.01 Torr, frequency 34.5 GHz.

Typical decay of air plasma after the end of RF pulse is shown in Fig. 5. Analysis of these curves shows that at our experimental conditions plasma decay is determined by both recombination and diffusion processes. As the result, the dependence of plasma density and coefficients of recombination and diffusion vs. pressure has been found. Plasma density in air is found to be about 10^{12} cm^{-3} over all the working range of pressures (Fig. 6). The density of argon plasma is much higher and close to 10^{13} cm^{-3} as the result of lower breakdown field in argon in contrast with the one in air [4].
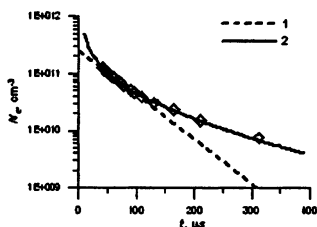
Fig. 5. The typical decay of plasma in air. Symbols – experiments, lines – approximations in assumed of diffusion (1) and combined (diffusion plus recombination) mechanism of electron losses.
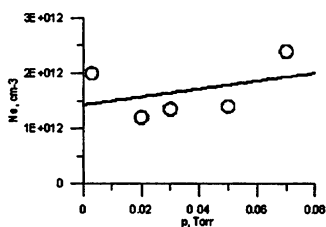
Fig. 6. Dependence of the plasma density at the end of RF pulse vs. air pressure.

The values of recombination and diffusion coefficients (Fig. 7) are close to well-known data [4]. But these dependences vs. pressure are much slower than usual for gas discharge.
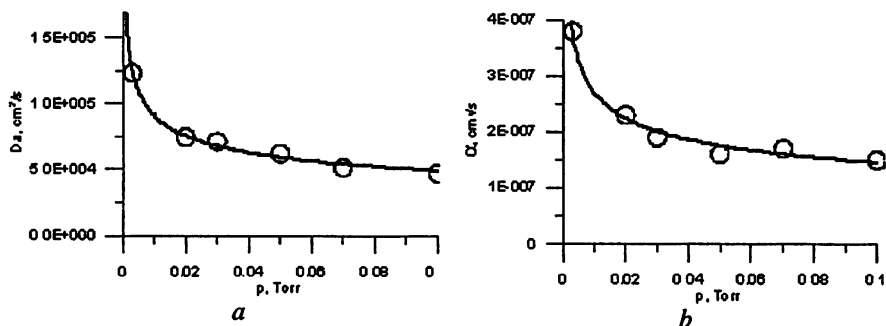
Fig. 7. Dependence of diffusion (*a*) and recombination (*b*) coefficients vs. air pressure

It's important to note, that according to these experimental results, the external magnetic field of up to 200 Gs does not change the plasma parameters significantly. Now we can't explain this effect. Actually it means that we have to use the stronger magnetic fields in future reactor for silicon films deposition.

Deposition of silicon films using RF discharge

The experiments on silicon films deposition have been performed in Institute for Physics of Microstructures at the PlasmaLab setup. This is a commercial setup for plasma deposition and etching with two types of plasma sources: capacitively coupled (CC) and inductively coupled (IC) discharges (with RF power of up to 300 W each), which could be used separately or simultaneously, at pressure of gas mixture up to 50 mTorr.

These experiments show silicon films growth with rate of 1–2 μm per hour in inductively coupled mode of discharge over the wide range of parameters on different substrates. The photo of silicon film grown on silicon substrate and atomic force microscope image of this film are shown in Fig. 8. When combined regime of plasma production is used (i.e. when both CC and IC discharges are used simultaneously), the growth rate decreases greatly with the increase of power of capacitively coupled source. When the power of CC discharge is higher then some critical value (of about 10 W), deposition process turns into etching because of intensive ion bombardment of the substrate surface.

The analysis of these films by the methods of Raman scattering (Fig. 9), X-ray diffractions and AFM images shows that these films consist of nanocrystals with typical crystal size of about 3–4 nm.

580
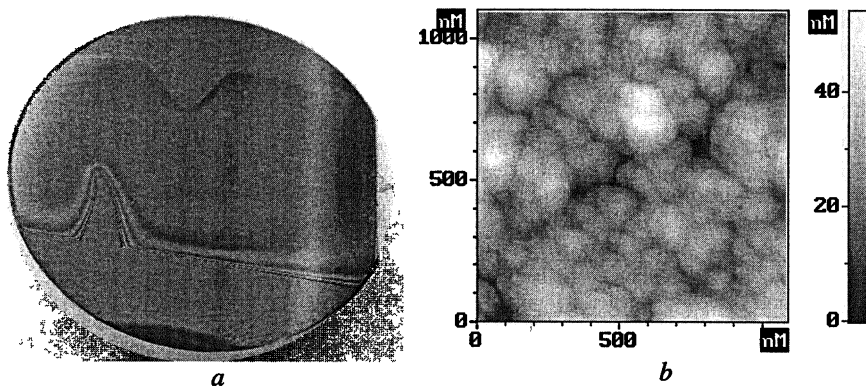
Fig. 8. Photo (*a*) and AFM image (*b*) of Si film growth in PlasmaLab
setup at RF power of 300 W
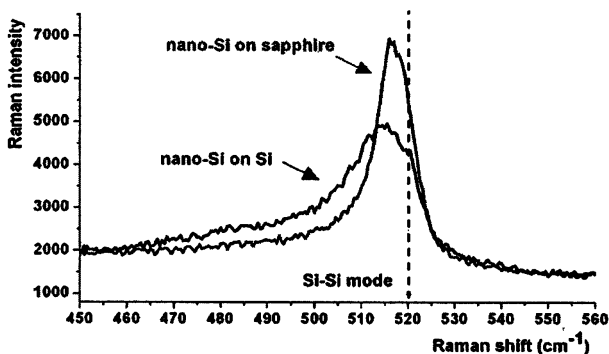
Fig. 9. Raman scattering for silicon films grown in PlasmaLab setup at RF power
of 300 W on the sapphire and silicon substrates

References

1. *Karaiskaj D., Thewalt M. L. W., Ruf T., Cordona M., Pohl H.-J., Devjatych G. G., Sennikov P. G., Rieman H.* Physical Review Letters, **86**, 6010 (2001).
2. *Bruno G., Capezzuto P., Cicala G.* J. Appl. Phys. **69**, 7256 (1991).
3. *Stenzel R. L.* Rev. Sci. Instr. **47**, 603 (1976).
4. *Raizer Yu. P.* Gas Discharge Physics. Moscow: Nauka, 1987.

SHADOW PROJECTION MILLIMETER-WAVE IMAGING USING VISIBLE CONTINUUM FROM A SLAB OF THE Cs-Xe DC DISCHARGE

M. S. Gitlin, V. V. Golovanov, A. I. Tsvetkov, and V. V. Zelenogorsky

Institute of Applied Physics, Russian Academy of Sciences,
Nizhny Novgorod, Russia

A slab of the positive column of the Cs-Xe DC discharge has been used as a 2-D sensor for real-time shadow projection millimeter-wave (MMW) imaging. MMW images are converted into visible images using the visible continuum from the plasma slab. Real-time shadow projection MMW images of test objects have been successfully obtained using 35.4 GHz millimeter waves for object illumination.

Introduction

Imaging and sensing with millimeter waves attracts attention due to many important scientific, biomedical, security, and industrial applications [1–4]. Millimeter-wave (MMW) radiation can penetrate through many materials, such as paper, plastic, wood, ceramic, and etc., therefore MMW imaging systems have some advantage for testing and evaluation over optical and infrared systems, even though they have less spatial resolution. MMW radiation is non-ionizing and so, is not a hazard to biological objects, as is the case with X-rays. MMW imaging also has some advantages compared to THz imaging [3, 5]: first, there is lower atmospheric absorption and scattering in millimeter-wave region, and second, many mature types of MMW sources and components are available.

In active-mode millimeter-wave imaging systems a transmitter is used for object illumination [1–4]. A 2-D array of millimeter-wave receivers can be applied for real-time record the MMW images. This allows achieving high frame rates, but 2-D imaging arrays are complex systems and their cost is too high for many applications [1]. Besides, active images obtained using 2-D arrays have rather poor quality, because of element-to-element gain and sensitivity variations, and big element-to-element spacing. The shortcomings of the 2-D imaging array technique make the development of other real-time imaging methods a challenging task.

Millimeter-wave imaging using a Cs-Xe DC discharge

Recently we developed a new technique for time-resolved imaging of the spatial distribution of the MMW intensity using visible continuum (VC) from a slab of the positive column (PC) of a Cs-Xe DC discharge [6]. The concept of this technique is based on the effect of the increase in the intensity of the e-Xe bremsstrahlung continuum in the visible region, when the electrons in the posi-

tive column of a Cs-Xe DC discharge are heated by millimeter waves [7]. By means of this technique, MMW images are converted into visible images, thus allowing conventional charged coupled device (CCD) cameras to acquire images at a rapid rate. This imaging technique has high energy flux sensitivity (about 10 μJ/cm^2 in Ka-band), microsecond temporal resolution, and spatial resolution 2–3 mm. Such a broad-band technique has been successfully applied to measure the field pattern at the output of Ka-, F-, and D-band MMW sources and antennas [6, 8, 9]. In this paper, we applied the discharge technique for active MMW imaging using the shadow projection method.

Experimental setup

The experimental setup (top view) is shown schematically in Fig. 1. A sealed discharge tube (DT) was used to generate the slab of the positive column of the Cs-Xe DC discharge [6]. A hollow rectangular parallelepiped glued from fused quartz plates was located in the middle of the tube. Two square quartz windows (1) with apertures 10 × 10 cm and a thickness 0.65 cm were set at a distance of 2 cm between their internal surfaces. Two plane anodes (2) and two heated cathodes (3) were placed in glass cylinders. The glass cylinders were glued to the quartz cell. The discharge tube was filled with 45 Torr xenon. To obtain the required density of cesium vapor, the discharge tube was heated in an oven (4). The oven had two quartz windows. Millimeter wave imaging experiments were performed for a discharge current of 1.5 A and a tube temperature of 95 °C. Under
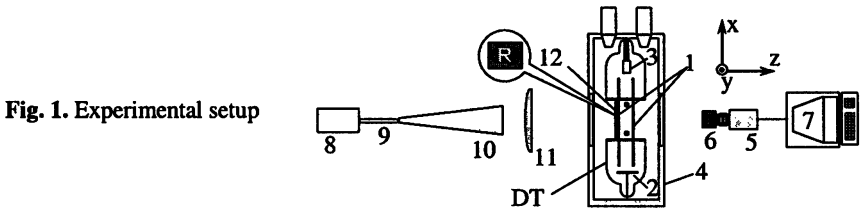
Fig. 1. Experimental setup

these conditions, the PC of the Cs-Xe discharge had the shape of a spatially uniform slab which filled the entire tube aperture 10 × 8 cm. The spatial distribution of VC intensity was recorded by a black and white CCD camera (5). The CCD camera exposure time was 1 ms. An optical filter (6) rejecting atomic emission lines was mounted on the camera lens. The data from the CCD camera were processed with a computer (7). Millimeter waves were generated by a 35.4 GHz magnetron (8) with its maximum output power of 20 W. The MMW pulse length was about 10 ms. The repetition rate of MMW pulses was 12.5 Hz. A rectangular waveguide (9) was used to feed the millimeter waves to the pyramidal horn antenna (10). The MMW beam was collimated using a plane-convex Teflon lens (11) 20 cm in diameter, with the focal length about 65 cm. The width (FWHM)

of the quasi-Gaussian beam in the region of the plasma slab was about 7 cm. The MMW intensity in the center of the beam was approximately 0.5 W/cm^2. The electric field polarization was along the y axis (see Fig. 1). The test object (12) was placed nearby the window of the discharge tube.

Experimental results

Amplitude and phase objects were used as test objects to evaluate the imaging system. At first static objects were imaged. Letters from "SMSA 08" and "IAP RAS" acronyms cut out in aluminum foil were used as amplitude test objects. The height of the letters was 50 mm. The width of the rectangular strips transparent for MMWs was 12 mm. The foils were pasted on cardboard sheets. The images of the VC intensity variation caused by the effect of the MMWs transmitted through slits are shown in Fig. 2. Since the variation of VC intensity $\Delta I(x,y)$ was directly proportional to the intensity of the MMWs $W(x,y)$ in the plasma slab (for $W < 1$ W/cm^2), the images represented 2-D distribution of the
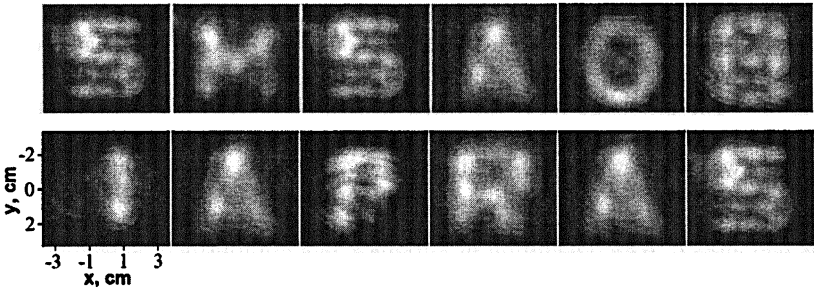
Fig. 2. MMW transmission images of letters from "SMSA 08" and "IAP RAS" acronyms cut out in aluminum foil.

MMW intensity behind the object [6]. The effect of electron heat conduction blurred the images slightly. Obtained images of the letters were distorted by the diffraction because the plasma slab was located in the Fresnel region, where the quasi-plane waves transmitted through the cuts progressively become cylindrical waves [10]. Nevertheless, all letters can be easily recognized. Fig. 3a shows the image of letter "E" cut out of aluminum foil and glued to a cardboard. The height of the letter was 50 mm, its width was 45 mm. The width of the foil strips was 10 mm. The image of this opaque object was clear enough.
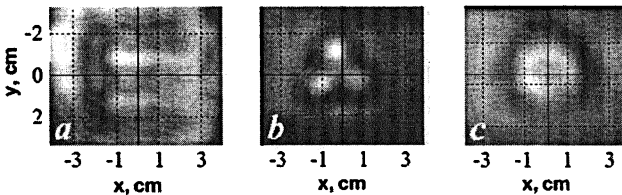
Fig. 3. MMW transmission images of static amplitude and phase objects

584

The phase objects were made of dielectric materials having low MMW absorption. In Fig. 3b the MMW transmission image of three Septogal pellets (cough-lozenge made by JADRAN, Croatia) is shown. The pellets were disks 16 mm in diameter and their thickness was about 3.5 mm. The pellets were arranged as a trefoil and placed inside an envelope. The three pellets were clearly visible in the MMW image (see Fig. 3b), although their diameter exceeded the wavelength by less than two times. Figure 3c shows MMW transmission image of an agate pendant in envelope. The pendent was a disk of 40 mm in diameter, and its thickness was about 3 mm. These experiments demonstrated that one could use the imaging technique for fast post office and custom inspection of gems and chemicals including illicit drugs hidden in packages and envelopes. In Fig. 4 MMW transmission image (a) and a photograph (b) of a pumice-stone in the shape of a fish are shown. The thickness of the pumice fish was 18 mm. The MMW transmission image of the phase object demonstrated the edge contrast enhancement (see Figs. 3c and 4a). There is a deep minimum of the intensity at the boundary of the object image. The minimum occurred between bright maxima of the intensity. The edge contrast enhancement phenomenon arose from MMW edge-diffraction by a transparent object, which produced the additional phase shift for the wave passing through it [11].
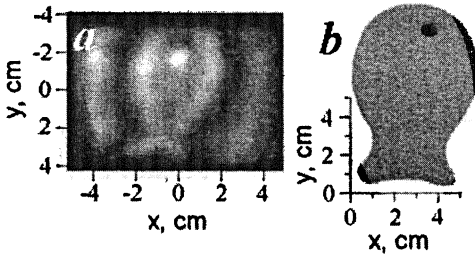
Fig. 4. MMW transmission image (a) and a photograph (b) of a pumice-stone in the shape of a fish

We have demonstrated that the technique can provide real-time imaging as well. In particular, we imaged oscillation of a pendulum. In Fig. 5 a continuity of MMW transmission images of pendulum motion obtained during a half of the oscillation period is shown. The pendulum was a Teflon ring suspended by thread about 15 cm long. The outer ring diameter was 25 mm, the inner ring di-
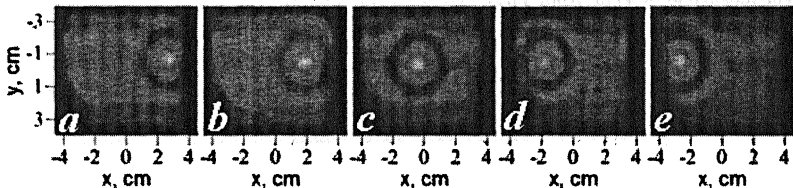
Fig. 5. Continuity of MMW transmission images of pendulum motion

585

ameter was 13 mm, and its thickness was 8 mm. The ring acted as three-zone phase mask which focused the MMW beam in the near-field in the focal spot about wavelength in diameter (see Fig. 5). The pendulum oscillation period was equal to about 0.8 s.

We imaged how a glass tube filled with water was emptied (see Fig. 6). The outer tube diameter was 8 mm, the inner diameter was 6 mm. The tube filled with water was opaque for MMWs (see Fig. 6a). When we opened a discharge cock located at the foot of the tube (outside the aperture) the water began to flow out of the tube. Fig. 6b – show how a glass tube was being emptied and becoming transparent for MMWs. The water poured out the tube for about 1 s. In Fig. 6e, the MMW transmission image of the empty tube is shown. Because of the considerable difference in the refractive indexes of glass and air, the boundaries of the tube are well-defined in Fig. 6e.
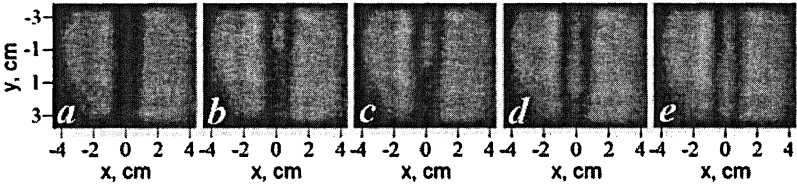
Fig. 6. MMW transmission movie how a glass tube filled with water is being emptied

Conclusion

We have developed video-rate active millimeter-wave imaging system. A slab of the positive column of the Cs-Xe DC discharge has been used as a time-resolved 2-D sensor for millimeter-waves. MMW images are converted into visible images using the visible continuum from the plasma slab. Shadow projection MMW images of amplitude and phase objects have been successfully obtained using Ka-band moderate-power millimeter waves for object illumination. It has been demonstrated that the technique can be used for single-shot security screening, as well as for real-time imaging of transient processes.

References

1. *Bolomey J. Ch.* IEEE Trans. on Microwave Theory Tech. **37**, 2109 (1989)
2. *Watabe K. et al.* IEEE Trans. on Microwave Theory Tech. **51**, 1512 (2003).
3. *Appleby R., Wallace H B.* IEEE Trans. on Antennas Propag. **55**, 2944 (2007).
4. *Volkov L. V. et al* Digest of the 27th Int. Conf. on IRMMW, San Diego, 155 (2002).
5. *Dem'yanenko M. A. et al.* Appl. Phys. Lett. **92**, 13116 (2008).
6. *Abubakirov I. E., Gitlin M. S. et al.* Radiophys. Quantum Electron. **46**, 722 (2003).
7. *Gitlin M. S., Spivakov A. G.* Tech. Phys. Lett. **33**, 205 (2007).
8. *Gitlin M. S., Glyavin M. Yu. et al.* IEEE Trans. on Plasma Sci. **33**, 380 (2005).
9. *Bratman V. L. et al.* Digest of the Joint 31st Int. Conf. on IRMMW and 14th Int. Conf. Terahertz Electronics, Shanghai, China, 297 (2006).
10. *Laybrous S. et al.* IEEE Antenn. Propag. Mag. **37**, 50 (2005).
11. *Anokhov S. P.* J. Opt. Soc. Am. A. **24**, 2493 (2007)

GASDYNAMIC ECR SOURCES
OF MULTICHARGED IONS

V. G. Zorin, A. F. Bokhanov, S. V. Golubev, I. V. Izotov, D. A. Mansfeld,
S. V. Razin, A. V. Sidorov, V. A. Skalyga, and A. V. Vodopyanov

Institute of Applied Physics RAS, Nizhny Novgorod, Russia

A new type of pulsed sources of multicharged ions (MCI), namely, a gasdynamic ECR source is proposed. Its main difference from the classical ECR ion sources is a different, quasi-gasdynamic regime of plasma confinement in a magnetic trap. Plasma was produced and heated by radiation of a pulsed gyrotrons with the frequencies of 37.5 and 75 GHz in magnetic traps of various configurations. Plasma confinement in quasi-gasdynamic regime under such conditions was studied. Present paper demonstrates that with such a confinement regime it is possible to generate multicharged ions and create intense (more than 1 A/cm^2) ion fluxes through the trap plugs. Creation of intense plasma fluxes allows one to extract high-current MCI beams of high brightness. Transverse homogeneity of a plasma flux makes it possible to use a multi-aperture extraction system for the formation of broad intense MCI beams. MCI beams with current up to 150 mA and normalized emittance lower than 1 π·mm·mrad were produced. Comparison of results of calculations and data of experiments shows that they are in a good agreement, which allows us to predict creation of a new type of ECR source.

Introduction

The recent experimental and theoretical research carried out at the Institute of Applied Physics (IAP RAS, Nizhniy Novgorod, Russia) resulted in development of a new type of pulsed ECR sources of multicharged ions – gasdynamic ECR ion sources (ReGIS). It will be demonstrated that such sources are capable of generating high-current and high-brightness ion beams with a moderate ion charge.

The ideas underlying development of such sources were borrowed from fields of classical ECR sources of multicharged ions (we will refer to them as to the Geller ECR ion sources (GECRIS)) [1], as well as from investigations of fusion mirror traps (FMT) [2]. The ReGISs differ from the Geller sources by the mechanism of plasma confinement in a magnetic trap. It is the quasi-gasdynamic mechanism [3] similar to that used in FMT. The principal distinction from FMT is strong nonequilibrium of confined plasma (the temperature of the electrons is much higher than the temperature of the ions), which is typical of GECRIS.

ReGIS principals

A possibility of realizing two different (classical and quasi-gasdynamic) regimes of confinement of nonequilibrium plasma in open magnetic traps at powerful ECR heating by millimeter wave radiation was demonstrated in [3]. The great

majority of modern ECR sources of MCI operates in the regime of classical plasma confinement in a trap. Ion confinement in this case is determined by ambipolar potential distribution in the trap [4]. In a mirror trap, electrons get into a loss cone either as a result of collisions with ions or with each other, or due to quasi-linear diffusion in velocity space due to intense ECR heating [5]. Realization of two regimes of plasma confinement (classical and quasi-gasdynamic regimes of plasma confinement) was observed in experiments [3]. The quasi-gasdynamic one is realized when plasma density is high enough. The mechanism of plasma confinement in a trap changes for the values of the plasma density such that the velocity at which the loss cone is filled in by electrons is higher than the maximum velocity of plasma escape from the trap. The loss cone is filled in, the electrons are confined in the trap by ambipolar potential, and plasma losses are determined by gasdynamic ejection of ions. This regime of confinement of non-equilibrium plasma with filled loss cone is called a quasi-gasdynamic regime. The transition to this regime of plasma confinement is inevitable when its density is increased [6]. The plane of plasma parameters divided into characteristic regions for the two regimes of plasma confinement with characteristic regions for classical and gasdynamic ECR ion sources is presented in Fig. 1.
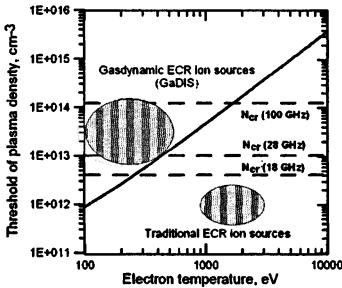
Fig. 1. The border between the two regimes of plasma confinement
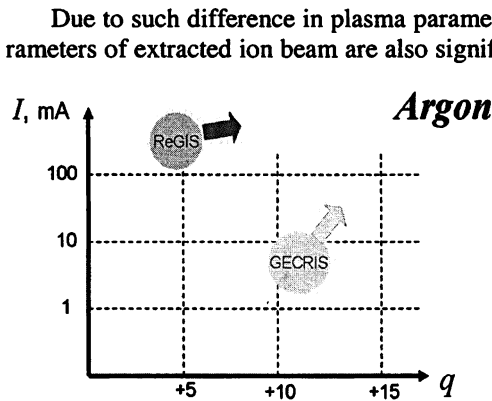
Due to such difference in plasma parameters inside the source the output parameters of extracted ion beam are also significantly different. In Fig. 2 the characteristic regions of ion beam parameters in classical and gasdynamic sources together with the tendencies of such devices development are shown. It is quite obvious that such data demonstrates the principle contrast between two type of the ECR ion sources.

Fig. 2

In quasi-gasdynamic regime plasma life time for a simple mirror trap can be roughly de-

588

termined as

$$\tau = \frac{R \cdot L}{2 \cdot V_s},$$

where R is the mirror ratio and L is the length of the trap and V_s is the ion-sound velocity. Thus, in the quasi-gasdynamic regime plasma lifetime is determined only by ion-sound velocity and geometry of the trap and does not depend on plasma density. Due to this plasma confinement parameter ($N_e \cdot \tau$) can be increased by enlargement of the trap size (trap length) and creation of plasma with higher density. For increasing of plasma density it is necessary to apply MW radiation with higher frequency. Effectiveness of both approaches was demonstrated in our experiments.

Deformation of ion charge state distribution due to modifying of the trap length, which lead in accord with (5) to a change in the confinement time, shown in Fig. 3.
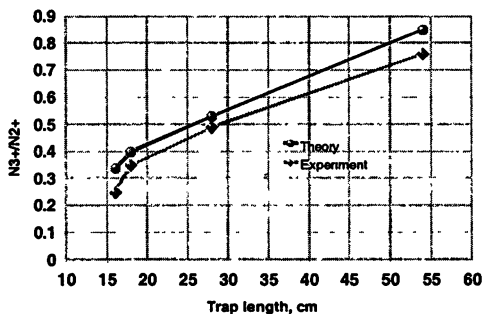
Fig. 3. The ratio of N ions with charge +3 and +2 *versus* the effective trap length (calculation and experiment)

In Fig. 4 the results of experiments for two frequencies of heating MW radiation (37.5 and 75 GHz) in helium are shown.
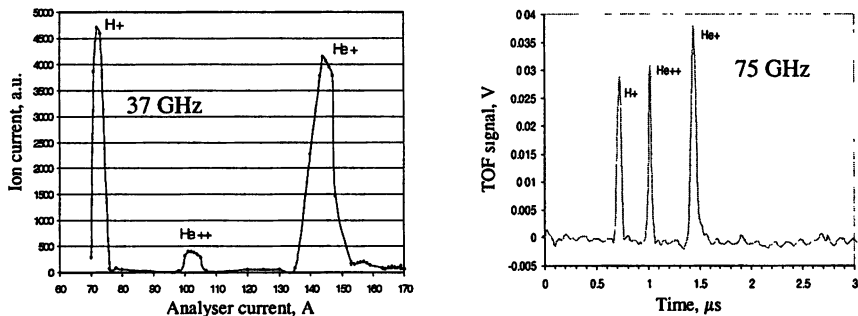
Fig. 4. Helium charge state distributions for 37.5 GHz (upper one) and 75 GHz

Ion beam current and emittance

The latest experiments were performed with multi-aperture extraction system, which is shown in Fig. 5.
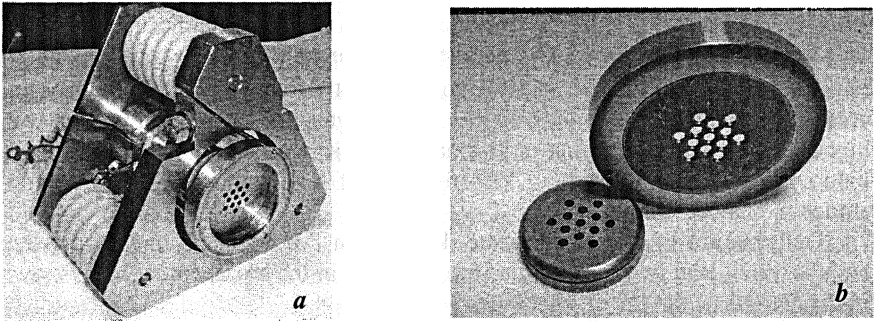
Fig. 5. 13-aperture extractor (photo). *a*) General view; the holes in plasma electrode can be seen at foreground. *b*) Electrodes of the extractor.

The 13-aperture extractor has been optimized; the beam current at the extraction system exit (Faraday cup current) and puller current have been measured as a function of the extraction voltage. The ion beam emittance has been measured at the extracting voltage equal to 30 kV.

The ion beam current (Faraday cup current) of 160 mA has been obtained at 30 kV extracting voltage (Fig. 6), 85 kW gyrotron microwave power and 1.6 T magnetic field in trap plugs (with cusp magnetic configuration), puller current being near 100 mA. In these experiments the extractor was placed 21 cm off the magnetic trap plug, distance between electrodes being 9 mm.
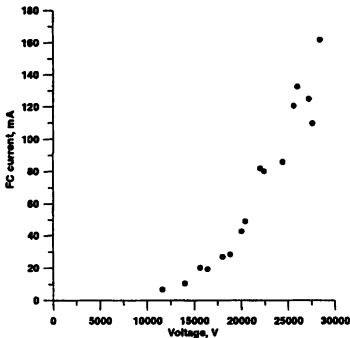
Fig. 6. Ion beam current (Faraday cup current) versus extracting voltage in 13-aperture extractor. Nitrogen is used as working gas.

The emittance of the obtained ion beam was measured with use of 'pepper-pot' screen and scintillator. Analysis of experimental data has demonstrated that normalized emittance of the beam is equal to 0.9 $\pi \cdot$mm$\cdot$mrad (for 30 kV extracting voltage).

Acknowledgments

References

1. *Geller R.* Electron Cyclotron Resonance Ion Sources and ECR Plasmas. UK, London, Institute of Physics Publishing, 1996.
2. *Dimov G. I., Ivanov A. A., Koidan V. S., Kruglyakov E. P.* 28th EPS Conference on Controlled Fusion and Plasma Physics, 18–22 June 2001, Funchal, Madeira, Portugal. Contributions ECA, 25A, 461–464 (2001).
3. *Vodopyanov A., Golubev S., Zorin V., Razin S., Shilov M.* Tech. Phys. Let. 25, (7); 588–589 (1999).
4. *Pastukhov V. P.* Nucl. Fusion, 14 (3), 68 (1974).
5. *Suvorov E. V., Tokman M. D.* Sov. J. Plasma Phys. 15, 540 (1989).
6. *Semenov V., Skalyga V., Smirnov A., Zorin V.* Rev. of Sci. Instr., 73(2); 635–637 (2002).

OPTIMIZATION OF GASDYNAMIC ECR ION SOURCES

I. V. Izotov, V. A. Skalyga, V. G. Zorin

Institute of Applied Physics of Russian Academy of Sciences,
Nizhny Novgorod, Russia

The present work is a continuation of the study of ECR gasdynamic ion sources (ReGIS). The main difference of these sources from classical Geller ECR ion sources is the use of the quasi-gasdynamic regime of plasma confinement in magnetic traps, which allows extracting of an ion beam of very high total current from plasma over 100 mA at a moderate average charge [1]. Conditions of gasdynamic confinement realization are analyzed in present work. Model described in [2] augmented with a superadiabatic effect [3] is used for it. A border between classical and gasdynamic confinement of non equilibrium plasma in a mirror trap was found within "Initial neutrals density – Microwave power" variables. Optimization of ReGIS for a certain application is demonstrated.

Introduction

In certain applications (e.g. F.A.I.R. [4]) classical Geller ECR ion sources can't be used due to low total ion current extracted from the magnetic trap of the ion source. One can find a solution in using of a gasdynamic ECR ion source, which is able to produce ion beams with total current over 100 mA [1]. Presented work is dedicated to methods of optimization of gasdynamic ion sources in order to fit predefined demands. A condition of realization of gasdynamic confinement and a boundary between classical and gasdynamic confinement of non equilibrium plasma confined in a mirror trap was found within "Initial neutrals density – Microwave power" variables.

Difference in plasma confinement regimes

Two confinement regimes for plasma in a mirror trap are described in detail in [3]. Here the main theses are mentioned only. The object of an examination is stationary held plasma inside a magnetic trap of an ion source. Transversal losses of the plasma and MHD instabilities aren't taken into account. One can determine two regions on Electron Energy – Electron Density (EVDF) plane (Fig. 1) in that case. One region corresponds to the case EVDF is fully isotropic; another accordingly – EVDF is anisotropic. Plasma confinement is certainly different inside two regions. Area of anisotropic VDF corresponds to classical confinement. It conforms to low plasma density, the main mechanism of
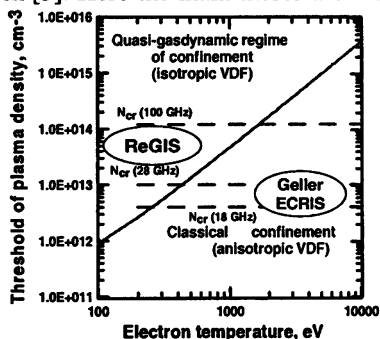
Fig. 1. Electron Energy – Electron Density plane

plasma losses is the electron scattering into the loss-cone with characteristic time

$$\tau_c = \ln(R/\nu_{ei}), \qquad (1)$$

where R is the mirror ratio and ν_{ei} is the electron-ion collision rate. All these properties are common for classical Geller's ECRIS.

With the increasing of plasma density isotropization of the EVDF occurs due to high collision rate. Loss cone is filled, plasma losses are determined by gas-dynamic flow outside the trap with characteristic time

$$\tau_g = L_{eff}/V_{is}, \qquad (2)$$

where L_{eff} is an effective magnetic trap length and V_{is} is ion-sound velocity. That mechanism of plasma confinement is used in so-called ReGIS (Resonance gas-dynamic ion source).

Theoretical model

The model used for numerical simulations consist of simple ionization balance equations and was described in detail in [2, 3]:

$$
\begin{cases}
\dfrac{dN_i}{dt} = (k_{i-1,i}N_{i-1} - k_{i,i+1}N_i) \cdot N_e - \dfrac{N_i}{\tau_i} \quad \text{Ions} \\[2mm]
\dfrac{dN_e}{dt} = N_e \sum_{i=0}^{n-1} k_{i,i+1}N_i - \dfrac{N_e}{\tau_e} \quad \text{Electrons} \\[2mm]
\dfrac{dN_0}{dt} = I(t) - k_{0,1}N_0 N_e \quad \text{Neutrals} \\[2mm]
\dfrac{1}{\tau_e} = \dfrac{1}{N_e} \sum_{i=1}^{n} \dfrac{iN_i}{\tau_i} \quad \text{Condition of quasi-neutrality} \\[2mm]
\dfrac{3}{2} \cdot \dfrac{d(N_e \cdot T_e)}{dt} = \dfrac{P}{L} - \dfrac{N_e}{\tau_e} \cdot (T_e + \varphi_0) - \sum_{i=0}^{n-1} k_{i,i+1} \cdot N_e \cdot N_i \cdot E_i \quad \text{Balance of energy} \\[2mm]
k = <\sigma v> = \dfrac{\int F(\varepsilon)\sigma(\varepsilon)v(\varepsilon)d\varepsilon}{\int F(\varepsilon)d\varepsilon} \quad \text{Ionization rate}
\end{cases}
\qquad (3)
$$

One of the main goals while projecting a new ion source is to determine the confinement regime would be realized, therefore, which possible ion current could be achieved depending on initial parameters.

Figure 2 represents results of simulation of realized confinement regime depending on initial microwave (MW) intensity and neutral gas density. Simulations were made for Argon, effective trap length $L_{eff} = 20$ cm. One can easily determine which regime of confinement would be realized with the help of such simulation without estimating average electron energy and density for steady state.

Simulation results of total current density and average electron energy on steady state made for different initial neutral gas density are shown in Fig. 3. One can see ion source producing high current density in the gasdynamic regime of plasma confinement (to the right from vertical line) with moderate electron energy enough for MCI formation.

593
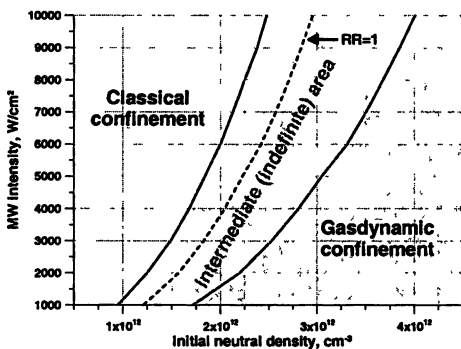
Fig. 2. MW intensity – Initial neutral density plane. Parameters of simulation: gas – Argon, L_{eff} = 20 cm, MW frequency – 37 GHz.
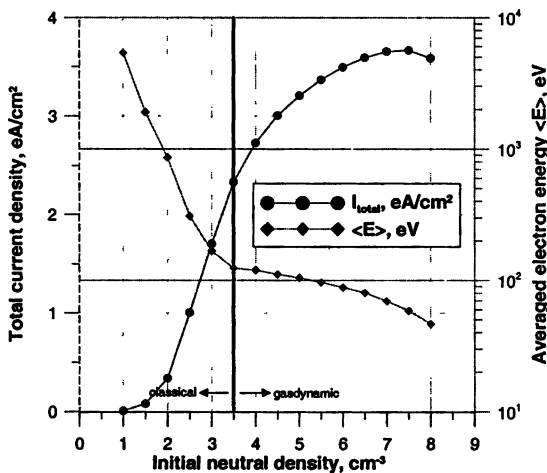
Fig. 3. Total current density and average electron energy vs initial density of Nitrogen. Parameters of simulation: L_{eff} = 20 cm, MW intencity – 1 kW/cm^2, MW frequency – 37 GHz .

Optimization of ReGIS for F.A.I.R.

The following part of present work is dedicated to the optimization of ReGIS to fulfill all requirements of F.A.I.R. (Facility of Antiproton and Ion Research) project hosted at GSI [4]. This accelerating facility planned to be build in a several years can operate all types of ions from protons to Uranium; however the

594

best transmission factor is reached for ions with mass-to-charge ratio close to 8 (e.g. Ar^{5+}, Xe^{15+}, U^{28+}).

Besides mass-to-charge ratio, ion beam must fulfill some additional requirements as a total current close to 100 mA and low emittance. These were achieved on an experimental setup SMIS'37 at IAP [1], therefore ion beam mass-to-charge ratio only is discussed further.

The most efficient way to get the best performance on certain ion with desired mass-to-charge ratio is to form an ion beam with maxima on desired charge state. Figure 4a represents results of simulation of steady-state Ar^{5+}/Ar^{4+} current ratio vs MW intencity, Fig. 4b represents a dependence of Ar^{5+}/Ar^{4+} current ratio on effective length of the magnetic trap, and Fig. 4c shows the CSD with the maxima on Ar^{5+} (corresponding MW intensity and L_{eff} are marked with circles in Fig. 4a and 4b).
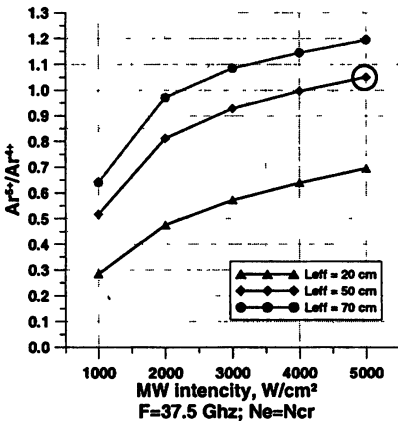
Fig. 4a. Ar^{5+}/Ar^{4+} current ratio vs MW intencity for different effective length
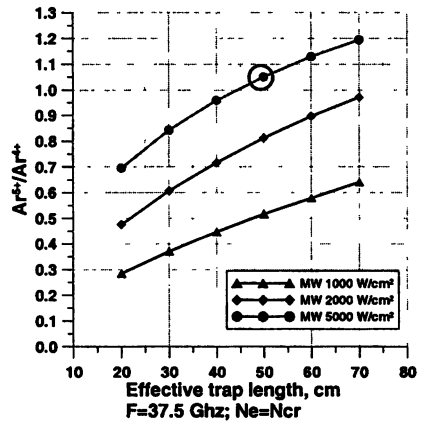
Fig. 4b. Ar^{5+}/Ar^{4+} current ratio vs effective length for different MW intencity
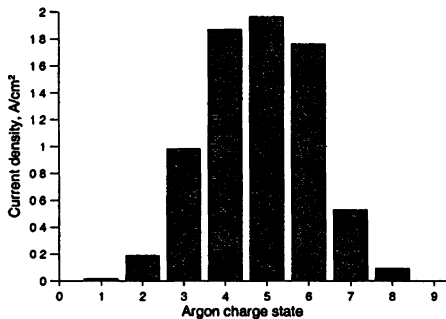
Fig. 4c. Argon Charge State Distribution

595

One can see the ability to tune the ReGIS for an efficient production of Ar^{5+} with adjusting a MW intensity and effective trap length.

Conclusion

Developed model is able to predict experimental results and helps to optimize real input parameters of the experimental setup (such as MW intensity and neutral gas density, parameters of a mirror trap) of a gas-dynamic multi-charged ion source for specific application. The use of the numerical code can help while developing a new source to determine its parameters in order to fulfill predefined requirements.

References

1. *Sidorov A., Dorf M., Zorin V., Izotov I., Razin S., Skalyga V., Roßbach J., Spädtke P., Balabaev A* Review of Scientific Instruments, 79, 02A317 (2008).
2. *Golubev S. V, Izotov I. V., Razin S. V., Skalyga V. A., Vodopyanov A. V., Zorin V. G.* Multicharged Ion Generation in Plasma Created by Millimeter Waves and Confined in a CUSP Magnetic Trap. // Transactions of Fusion Science and Technology. 2005. V. 47, № 1T, fuste 8. P. 345–347.
3. *Skalyga V., Zorin V., Izotov V., Sidorov A., Lamy T., Sortais P, Thuillier T.* Gas Breakdown in ECR ion Source // Review of Scientific Instruments. 2006. V. 77, № 3. P 03A325-1 – 03A325-3.
4. http.//www.gsi.de/fair/index_e.html.

ON SOME FEATURES OF THE AFTERGLOW OPERATION OF ELECTRON CYCLOTRON RESONANCE ION SOURCES

A. Efremov, V. Mironov, T. Nakagawa[1], Y. Higurashi[1], M. Kidera[1] and Y. Yano[1]

Joint Institute for Nuclear Research, Dubna, Moscow Reg., Russia
[1] RIKEN, Wako, Japan

Currents to the biased electrode were measured during the afterglow operation of the 18-GHz RIKEN Electron Cyclotron Resonance Ions Source. No increase in the electron currents was observed at the initial period of afterglow process indicating that "unplugging" of electrons does not trigger the increase in the extracted ionic currents during the afterglow. Alternative explanations for the effect are discussed briefly.

Extracted currents of the highly charged ions from the Electron Cyclotron Resonance Ion Sources (ECRIS) can be boosted for a short period of time by switching off the plasma heating with microwaves [1]. This so-called afterglow effect is known for a long time already [2] and is used for injection of ions into the accelerator facilities at GSI and CERN. It is supposed [3] that the effect is due to the increased losses of electrons from ECR plasma followed by a fast release of ions. Electrons in the ECR plasmas are heated by microwaves perpendicular to the magnetic field mostly and are confined by the mirror magnetic field. When the heating is off, the plugging effect for the high-energy electrons disappears; electrons start to escape the trap, which results in cancellation of the "potential dip" inside the ECRIS plasma and expulsion of the ions.

To get a deeper insight into the physics of the afterglow operation of ECRIS, we have measured [4] the electric currents to the biased electrode upon termination of the microwave heating in the 18-GHz RIKEN ECRIS. It was found that afterglow pulse is not triggered by the electron losses from ECRIS plasma.

I. Experimental set-up

The detailed description of the 18-GHz RIKEN source can be found elsewhere [5]. During the present experiments, the source ran in the optimized mixture of xenon (highly enriched with ^{136}Xe isotope) and oxygen gases. The microwave power was kept constant at 500 W throughout all measurements; extraction voltage was 10 kV. The source was equipped with the disk-shaped biased electrode, with the disk diameter of 12 mm and adjustable axial position. The extracted currents of highly charged xenon ions were maximized when the electrode was positioned close to the maximum of magnetic field at the microwave injection side of the source and the electrode bias was –40 V. Up to 50 μA of the Xe^{21+} dc currents were measured in these conditions, and the charge state distribution of xenon ion currents was peaked at (19–21)+ charge states. In the afterglow mode of operation, amplitude of the Xe^{21+} pulse reached 100 μA; steady afterglow operation with maximized amplitudes was achieved with the heating-

on period of 50 ms and heating-off period of 15 ms. For the time-resolved measurements, the ionic currents were collected with a Faraday cup after the analyzing magnet, amplified and recorded by a digital oscilloscope.

In parallel to the measurements of the extracted ion currents, currents to the biased electrode were registered. For this, power supply unit of the biased electrode circuit was grounded through a 600 Ω resistor; voltage drop at the resistor was digitized by a flash-ADC mounted at the high-voltage platform. Data from the ADC were transmitted to a computer via a fiber-optics communication channel to be analyzed off-line.

II. Results and discussion

Depending on the source tuning, two modes of the afterglow operation were clearly distinguished. The first mode was characterized by a smooth and steady afterglow pulse shape, whereas for the second mode, sharp discontinuities were observed in ionic pulse at the decay period. Transition between two modes was done by tuning the gas pressure and microwave power mostly, but it was also found that a small positive voltage at the biased electrode allows achieving the smooth pulse shapes with the relatively small decrease in the pulse amplitude. Generally, dc currents and afterglow pulses reacted to the changes in the bias voltage differently: while both currents reached their maxima at bias of around −40 V, decrease in the absolute value of bias voltage below the optimum value and setting the bias voltage positive suppressed the dc currents more remarkably than the afterglow ones.

The shape of the extracted Xe^{21+} ion pulses is shown in Fig. 1 for the source running in the smooth afterglow mode. The vertical scale is 25 μA per division, time scale is 1 ms. Zero level of the extracted current is indicated by the black box left to the picture. The lower trace shows the moment when the microwave power was switched off.
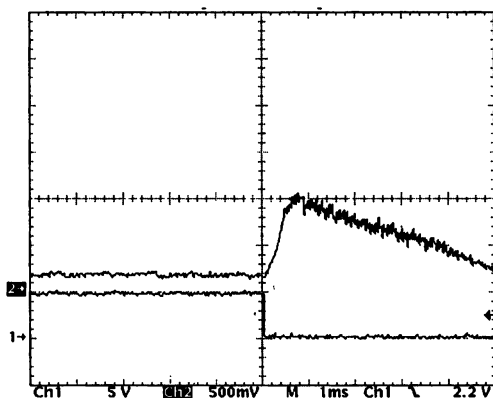
Fig. 1. Afterglow pulse shapes for the Xe^{21+} ions with the biased electrode voltage of +20 V

Electric current to the biased electrode was recorded in parallel to the extracted ion pulses in the same conditions as presented in Fig. 1. This current is shown in Fig. 2. Negative values at the graph correspond to an excess of the electron fluxes to the electrode. The microwave heating was switched off at 0 ms. At the moment of afterglow triggering, no increase of the electron currents to the biased electrode is observed; contrary, electron currents immediately start to decrease and go to the saturated non-zero level in 1–2 ms. Short bursts of the electron currents were detected at the stage of the microwave heating, but they disappeared in the afterglow. These peaks are of 1–2 μs duration and were attributed to be caused by the whistler instability elsewhere [6].

Fig. 2. Currents to the biased electrode for the electrode voltage of +20 V
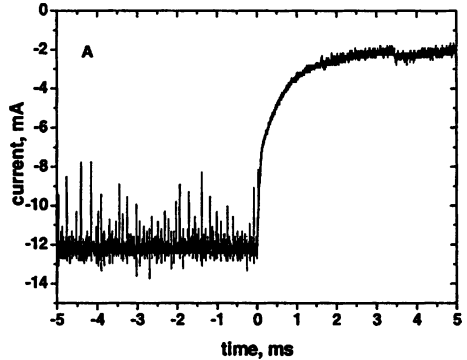
With the negative voltage at the biased electrode, current to the electrode is mostly due to the collected ions. Fig. 3 shows such the afterglow current for the bias of –50 V for the source tuned to produce the smooth afterglow shapes. The sharp peak in the ion current is observed, with the duration of around 0.5 ms and the amplitude of up to 1 mA.

Fig. 3. Currents to the biased electrode for the electrode voltage of –50 V
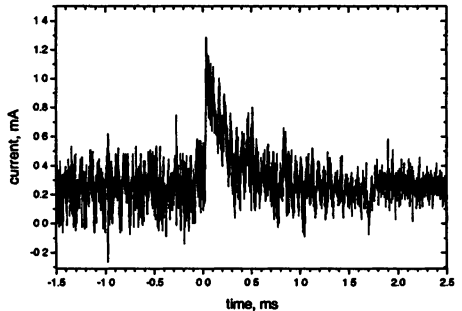
No increased electron fluxes that may trigger the main afterglow pulse in ECRIS were detected by measuring the electric currents to the biased electrode. Such the increased electron losses are observed only in the late stages of the afterglow in correlation with the drops in the extracted ion currents and with the

increased ionic currents to the biased electrode. This indicates that either the additional electron fluxes are directed in such the way that they do not hit the biased electrode, or that the "unplugging" of electrons is of no significance at all and some other physical processes are responsible for initiating the fast releases of ions upon termination of the microwave heating. Let us note here that the biased electrode is located such that the most of the magnetic field lines from the ECR zone intercepts it; electron losses trough the extraction aperture are blocked by the extraction voltage of +10 kV. So, we conclude that if the unplugged electrons are not collected by the biased electrode, then the whole plugged electron population is located outside the ECR zone and off-axis, which would be surprising.

It is experimentally proved elsewhere [7] that there is a substantial population of cold electrons in the ECRIS plasma with temperature of around 5–10 eV. Ion temperature is lower and estimated [8] to be below 1 eV. When the heating is off, the electron temperature goes down due to electron-ion collisions and termination of diffusion of electrons in the velocity space caused by interaction with microwaves. The drop in the electron temperature will result in a movement of the plasma sheath away from the extraction area. Such the movement of the sheath is observed in the plasma immersion ion implantation (PIII) technique [9].

Almost the same dynamics may be observed during the afterglow period of ECRIS operation, when the electron expulsion from the negatively biased extraction area and biased electrode is now caused by a drop in the electron temperature, not by increase in the bias voltage. Plasma meniscus is pushed inside the source chamber so fast that the ions stay at place due to their inertia, and the ions are extracted much more efficiently until the sheath relaxation occurs.

Other consequence of the electron cooling is an increase in the ion temperature. Ions are heated due to electron-ion collisions [10] with the rate:

$$\frac{dT_i}{dt} = \nu_{ei}(T_e - T_i), \tag{1}$$

where T_i and T_e are the ion and electron temperatures, and ν_{ei} is the electron-ion collision frequency. The collision frequency ν_{ei} depends on the electron temperature as following:

$$\nu_{ei} = 3.2 \cdot 10^{-9} \frac{Z^2 \lambda n_e}{\mu T_e^{3/2}} \, [\text{s}^{-1}], \tag{2}$$

where Z is the ion charge state, λ is the Coulomb logarithm, n_e is the electron density and μ is the ion mass in atomic units. The ion heating rate is inversely proportional to the square root of the electron temperature.

Upon termination of the microwave heating, electron temperature start to decrease, electron-ion collision frequency goes up and ions are heated faster until they do reach the thermal equilibrium with the cold population of electrons in ECRIS plasma. The increase in the ion temperature results in the rapid increase in the ion losses from the plasma and in a generation of the afterglow pulse,

whatever is the ion confinement mechanism. This is however in some contradiction with the observed very fast rise time of ion currents to the biased disk (around 100 μs), since the ion heating can not be immediate and depends on a level of the electron temperature drop and on the plasma density. Nevertheless, the additional ion heating can be important and contribute to the afterglow effect at the certain stages of the process.

Both scenarios are consistent with the observed drop in the electron currents to the biased electrode during the afterglow and can explain the experimentally observed differences [11] in the decay rates of the afterglow pulses for the different charge states. Also, the observed increase in the afterglow amplitude with asymmetric microwave timing [12] can be explained in the terms of a proper preparation of the cold electron population before switching the microwave heating off.

References

1. *Geller R.* ECR Ion Sources and ECR Plasmas (IOP, Bristol, 1996), pp. 412.
2. *Melin G. et al.* Rev. Sci. Instrum. **61**, 236 (1990).
3. *Sortais P.* Rev. Sci. Instrum. **63**, 2801 (1992).
4. *Nakagawa T. et al.* Proc. of the Workshop on the Production of Intense Beams of Highly Charged Ions (PIBHI), Conference Proceedings of SIF, Bologna, v. 72 (2001).
5. *Nakagawa T. et al.* Proc. 5th European Particle Accelerator Conf. IOP, Bristol, 1996, p. 1478.
6. *Garner R. C et al* Phys. Rev. Lett. **59**, 1821 (1987)
7. *Bibinov N. K. et al.* Plasma Sources Sci. Technol. **14**, 109 (2005).
8. *Melin G. et al.* J. Appl. Phys. **86**, 4772 (1999).
9. *Lieberman M. A. and Lichtenberg A. J.* Principles of Plasma Discharges and Materials Processing, Wiley, New York, 1994.
10. *Huba J. D.* NRL Plasma Formulary, NRL/PU/6790-04-477 (2004).
11. *Langbein K.* Rev. Sci. Instrum. **67**, 1334 (1996).
12. *Tinschert K. et al.* Rev. Sci. Instrum. 75, 1407 (2004).

ACHIEVEMENTS OF THE FORWARD SCATTER RADAR

A. B. Blyakhman, A. V. Samarin, A. G. Ryndyk[1], A. V. Myakinkov[1]

Nizhny Novgorod Research Radiotechnical Institute, Nizhny Novgorod, Russia
[1] State Technical University of Nizhny Novgorod, Nizhy Novgorod, Russia

Introduction

Bistatic radars based on the principle of forward scattering, or forward scattering radars, are designed to detect and track targets moving in the narrow region stretched along the base line, which connects the transmit and receive sides. In this region, the RCS of targets increases sharply due to the so called forward scatter effect. The topology of FSR is shown in Fig. 1, where Tr is a transmit position, Re is a receive position, x, y, z are Cartesian coordinates, with the origin corresponding to the phase centre of the receiving antenna, b is the base of the system, Tg is a target, $\vec{V}$ is a target velocity vector, φ is the angle of trajectory inclination towards the base line in the horizontal plane, β_B is a bistatic angle, α is a target azimuth and β is its elevation.
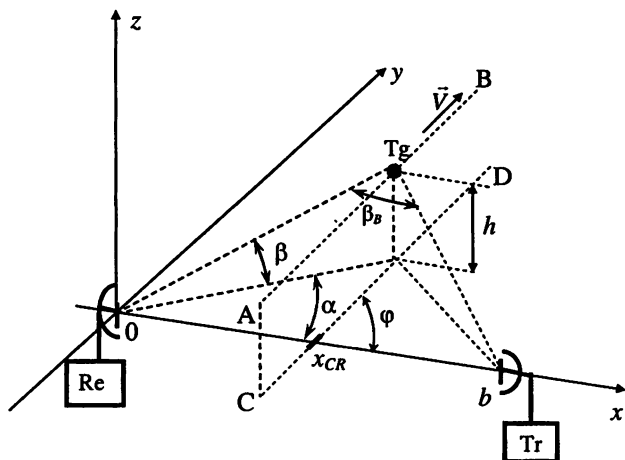
Fig. 1. Topology of FSR and model of target motion in FSR

1. Forward Scatter Radar Cross Section

The targets with the dimensions comparable and bigger to the wavelength have both shadow and self scattering fields that are separated in space. The shadow field is concentrated in the narrow solid angle near $\beta_B = 180°$, and is called the forward scattering field. In general, in this region the self scattering

field is much weaker than the shadow field. Because of this, analyzing the scattering field in the FS region, allows us to neglect the effect of the currents on the surface of the target, i.e. to consider a real target to be an absolute black body. Similarly, considering a scattering field at moderate β_B, we can neglect the shadow field. Hence, in an approximation of physical optics, the FS field is not dependent upon the three-dimensional shape of the target and is completely determined by the target shadow contour as well, as the field of the absolute black body.

For a quantitative assessment of FS RCS we can use Babinet's principle. According to this principle, the diffraction pattern from an opaque body is identical to that from a hole of the same size and shape, except for the overall forward beam intensity. The field arising from the incident wave diffraction on the opening, coincides (to within a sign) with the shadow field of the initial screen [1–4].

Let us consider shadow field, $\vec{E}_{SH}$, in the distant receiving point for the case when the incident wave is plane. This field corresponds to the radiation field of a planar cophasal aperture, which is perpendicular to the direction of the incident wave propagation. Aperture form is defined by the projection of the target shadow contour onto the plane, which is perpendicular to the direction of propagation of the incident wave.

Fig. 2 shows the cophasal aperture, A_{SH}, which forms the shadow field in the distant receiving point Re. In Fig. 2, $\vec{\rho}$ is radius-vector of an arbitrary point M of the aperture, A_{SH}; $\vec{r}_0$ is a unit vector oriented towards the receive side; x, y, z are Cartesian coordinates with an origin in the conditional centre of the aperture; θ_x, θ_y are arguments of direction cosines of unit vector $\vec{r}_0$, $\vec{R} = \{R_x, R_y, R_z\}$ is the radius-vector of the receiving point, and R_x, R_y, R_z are projections of vector $\vec{R}$. Hence, assuming that aperture A_{SH} presents the target while point Re presents the phase centre of the receiving antenna, magnitude $R = |\vec{R}|$ of vector $\vec{R}$ presents the target range.
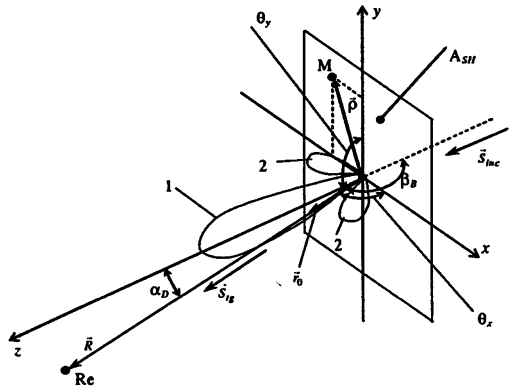
Fig. 2. Creation of cophasal aperture shadow field at distant point

603

In view of the "radiating" aperture, A_{SH}, the target FS RCS for a distant receiving point at bistatic angles, close to 180°, is determined by the following expression:

$$\sigma_F(\vec{r}_0) = 4\pi R^2 \left(|E_{SH}|^2 \big/ |E_{inc}|^2 \right) = \frac{4\pi}{\lambda^2} \left| \int_{A_r} \exp[j(2\pi/\lambda)\vec{\rho}\vec{r}_0] dS \right|^2, \qquad (1)$$

where E_{SH} is the electric field intensity of the shadow field, λ is the wave length of the transmitter; dS is the surface element of the cophasal aperture.

It follows from Equation (1) that when $\vec{r}_0 \perp \vec{\rho}$, FS RCS reaches the maximum. As it is seen from Fig. 2, in this case $\beta_B = 180°$ or $\alpha_D = 0$. Considering FS RCS as function of diffraction angle $\sigma_F = \sigma_F(\alpha_D)$, we obtain

$$\sigma_F(0) = 4\pi(S_A/\lambda)^2, \qquad (2)$$

where S_A is the area of aperture, A_{SH}. For clarity we shall present Equation (2) as $\sigma_F(0) = G_A S_A$, where $G_A = 4\pi S_A / \lambda^2$ is the directive gain of the cophasal aperture A_{SH} with an area, S_A. Thus, the FS RCS $\sigma_F(0)$ is larger than the geometrical square of the aperture A_{SH} in G_A times. If $S_A \gg \lambda^2$ then $G_A \gg 1$, and hence $\sigma_F(0) \gg S_A$. As a result the FS RCS happens to be much larger than the monostatic RCS. For example, for an ideally conductive full-sphere of radius, $r_S = 20\lambda$, the monostatic RCS and BRCS (at $\beta_B < 140...150°$) is $\sigma_0 = \sigma_B = S_A = \pi r_S^2 = 400\pi\lambda^2$. According to Equation (2), the FS RCS is $\sigma_F(0) = 4\pi(\pi r_S^2/\lambda)^2 = 64\pi^3 \cdot 10^4 \lambda^2$. Therefore, $\sigma_F(0)$ is $1600\pi^2$ times or by 42 dB bigger than σ_0.

The sharp increase in the magnitude of the target RCS in the FS region is called the forward scatter effect. This effect makes it possible to improve the power budget of the radar. It is very important to mention here that it is impossible to reduce the target's FS RCS by applying anti-radar coating or using other measures, which are used to reduce the monostatic RCS. Moving on to scattering on the ideally conducting bodies, it is known that applying even ideally absorbent coating on the metallic body, it is possible to reduce the value of its total scattered power by only 3 dB [1].

However the values of FS RCS σ_F, determined by Equation (2), hold true only in the narrow sector around the FSR base line. The directional pattern of the considered cophasal aperture usually has a lobe structure. In Fig. 2 the main and side lobes are marked by *1* and *2* correspondingly. So, in terms of directional pattern structure, deviation of bistatic angle β_B from 180° or deviation of diffraction angle, α_D, from zero should not be more than half the width of the main lobe of the directional pattern of the "radiating" aperture, A_{SH}. As we know, its half power level width is $\Delta\theta \approx \lambda/l_A$ in radians, where l_A is a linear aperture size. For

example, for $r_s = 20\lambda$ sphere, FS RCS decreases by 3 dB when α_D deviates from zero only by $\pm 0.75°$.

Nevertheless, an essential gain in RCS may remain in the side lobe region of the directional pattern of the aperture, A_{SH}, leading to the excess of $\sigma_F(\alpha_D)$ over σ_0. This gain can be evaluated. In [2, 4] a simple method of the approximate calculation of an integral defined by Equation (1) is considered. The upper and the lower bounds of the cophasal aperture are approximated by piecewise-linear segments, as illustrated by Fig. 3.
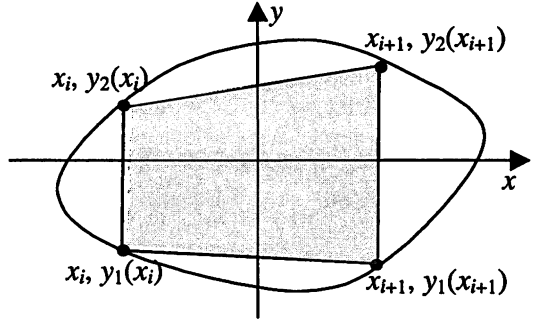
Fig. 3. Approximating segment in the form of trapezium

The integral in Equation (1) is then evaluated as the sum of integrals by the separate aperture segments, approximated by trapeziums. The final analytic expression for the evaluation of FS RCS takes the form:

$$\sigma_F(\alpha_h, \alpha_v) = \frac{4\pi}{\lambda^2}\left|\frac{-1}{k_w^2 \alpha_v}\sum_{i=1}^{N}(I_{1i} - I_{2i})\right|^2,$$

$$I_{1i} = \frac{1}{\alpha_h + \alpha_v b_1}\exp[jk_w\alpha_v a_1] \times$$
$$\times\{\exp\{jk_w[\alpha_h x_{i+1} + \alpha_v(y_1(x_{i+1}) - y_1(x_i))]\} - \exp[jk_w x_i\alpha_h]\},$$

$$I_{2i} = \frac{1}{\alpha_h + \alpha_v b_2}\exp[jk_w\alpha_v a_2] \times$$
$$\times\{\exp\{jk_w[\alpha_h x_{i+1} + \alpha_v(y_2(x_{i+1}) - y_2(x_i))]\} - \exp[jk_w x_i\alpha_h]\},\tag{3}$$

$$a_1 = y_1(x_i),$$
$$b_1 = \frac{y_1(x_{i+1}) - y_1(x_i)}{x_{i+1} - x_i},$$
$$a_2 = y_2(x_i),$$
$$b_2 = \frac{y_2(x_{i+1}) - y_2(x_i)}{x_{i+1} - x_i}.$$

The amplitude of the target return taken at the current time instance is proportional to the square root of the current target RCS. Then, the signal-to-noise ratio is proportional to the amplitude of target return. Thus, we can experimentally estimate FS RCS and compare the results with the results of theoretical calculation. The corresponding experimental diagrams are shown in Fig. 4 in comparison with the theoretically calculated diagrams.
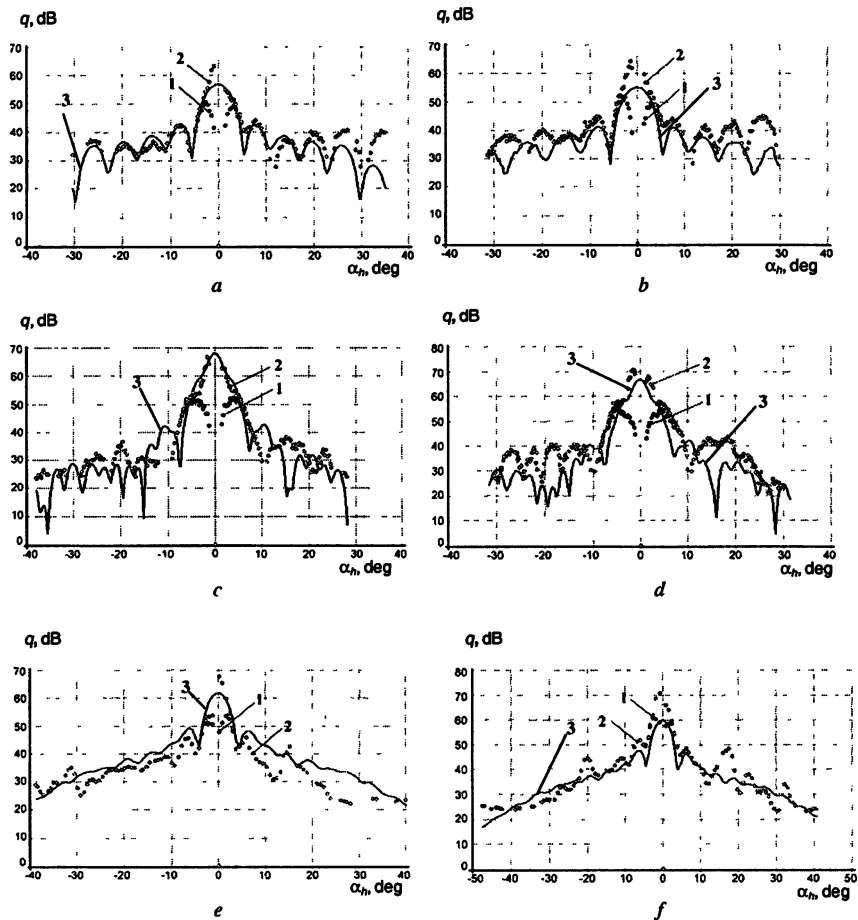
Fig. 4. SNR measurement and calculation results ($P_T = 1$ W): for Yak-52 airplane flying at an altitude of 100 m (*a*), 200 m (*b*); for Mi-2 helicopter flying at an altitude of 100 m (*c*), 200 m (*d*); for L-29 jet airplane flying at an altitude of 100 m (*e*), 200 m (*f*); *1, 2* – measurement results, *3* – theoretical calculation results

A comparison of theoretical and experimental data demonstrates good agreement between theory and experiment. It is seen from Fig. 4 that a certain

606

discrepancy in the form of side lobes between the theoretical and experiment dependences could be present. This is caused by a number of factors. Firstly, when calculating FS RCS, it is very difficult to accurately take into account the shape of the target shadow contour for all aspect angles. Secondly, the receiving antenna directional pattern side lobes form affects the form of experimental curves. Also, GPS data indicate that the air target did not maintain the assigned flight altitude. This leads to considerable change in the gains of the receiving and transmitting antennas due to ground influence.

However, theoretical and experimental results for the main lobe of FS RCS are practically the same, as well as the envelopes of side lobes in the range of diffraction angles up to 30...40°.

It is known that within the frequency range of FSR, the value of monostatic RCS is 0.4...0.7 m^2 for a Yak-52 light aircraft, 2...3 m^2 for a Mi-2 helicopter and 0.6...1 m^2 for an L-29 small-sized jet. Thus, the full-scale experiments proved an increase of 3–4 orders in the FS RCS of different targets in comparison to their monostatic RCS due to the forward scatter effect.

2. Experimental FSR

The block diagram of the experimental FSR is presented in Fig. 5.
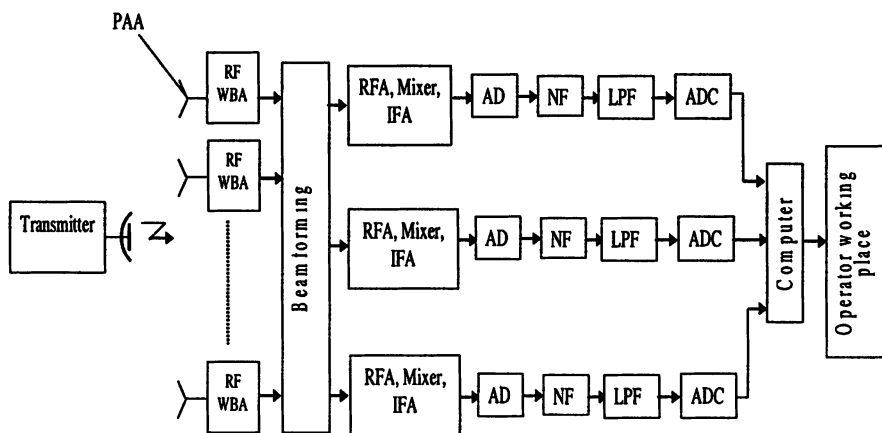
Fig. 5. Experimental FSR block diagram

In Fig. 5 PAA is the phased array antenna, RFA is the RF amplifier, RF WBA is the RF wide-band amplifier, IFA is the intermediate-frequency (IF) amplifier, AD is the amplitude detector, NF is the notch filter, LPF is the low-pass filter and ADC is the analogue-to-digital converter.

The transmitter was implemented on the basis of a standard 400 MHz radio station with a power output of about 6 W. Thus, the transmitted signal of FSR is

607

a continuous narrow-band quasiharmonic waveform. The antenna of the radio station (Fig. 6) was mounted on a mast at a height of 20...25 m and formed a single beam with a −3 dB width of 60° and 40° in the azimuth and elevation planes respectively. Due to losses in the feeder, the radiated microwave power level was 1÷2 W.

The antennas of the transmitter/receiver post are presented in Fig. 7. The receiving antenna was mounted on a similar mast at a height of 25–30 m. It was a planar phased array [5] with dimensions of about 5 × 2.5 m. The directional pattern of the antenna had three azimuth-plane partial beams with a −3 dB width of approximately 12° in the azimuth plane and 20° in the elevation plane.
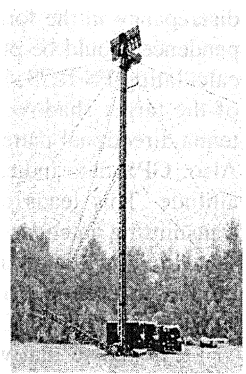
Fig. 6. Transmit/receive post
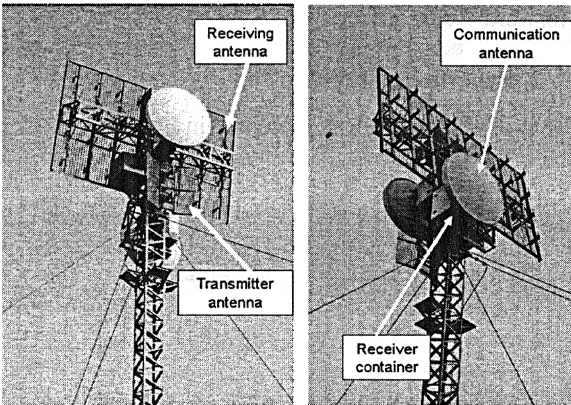
Fig. 7. Antennas of the transmit/receive post

The partial beam patterns measured in the experiment are given in Fig. 8. The numbers of beams *1*, *2* and *3* are shown. The small container behind the antenna curtain accommodates the RF parts of the receiving channels corresponding to the partial beams. These are located immediately on the antenna to mini-
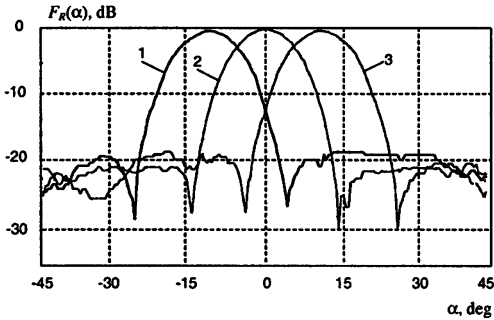
Fig. 8. Partial beams of receiving antenna directional pattern in azimuth plane

608

mize the loss inherent in the forming of partial channels and the loss in the feeders, which conduct the echo signal received on the antenna beams to the processing equipment.

It is seen from Fig. 7 that the antenna curtain has a tilt of about 10° in the vertical plane, which corresponds roughly to half the beamwidth in the elevation plane. The antenna tilt makes it possible to maximize the coverage of the radar in the vertical plane and to minimize the level of the underlying surface clutter, preserving the capability for detection of low-flying objects.

The subsequent analogue and digital processing of the echo signals is carried out by the equipment accommodated inside the cabin (Fig. 9).

a b
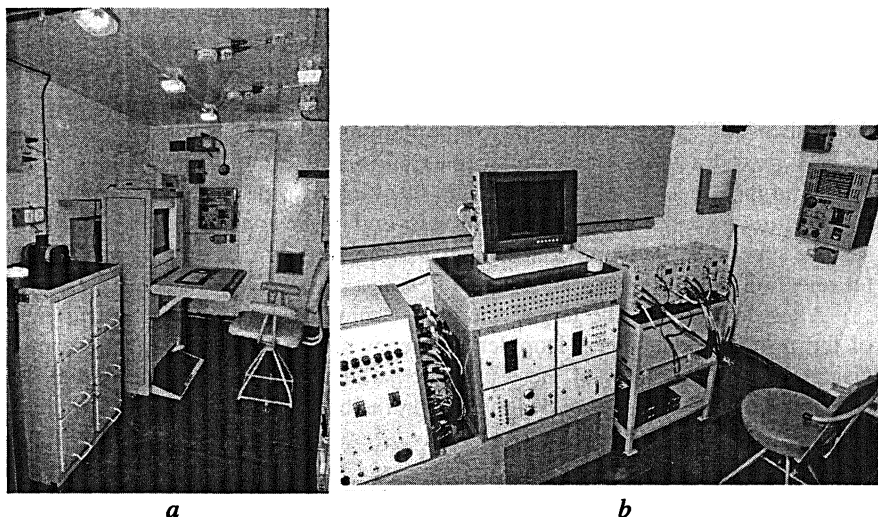
Fig. 9. Data processing equipment: a – at the operator position; b – at the transmitter/receiver post

Time processing is identical in the receiving channels of three partial beams and includes amplification, amplitude detection of signals, clutter rejection and coherent integration of the useful Doppler signal. In the presence of a powerful direct transmitter signal (by 30–60 dB stronger than target return), amplitude detectors perform synchronous detection of target return. Thus, non-linear distortions of Doppler signal are absent. This circumstance is essential since it determines the possibility of further optimal time processing (coherent integration of Doppler signal) and optimal space processing (measuring target return AOA). The linear processing requirement leads to the necessity of a high dynamic range of the receiving channels. This is required to avoid saturation in the receiving channels in the presence of a direct signal. In our case, the dynamic range was as high as 60 dB.

After amplitude detection, notch filters are used to suppress the constant component caused by the presence of a direct transmitter signal. Also, low-pass filters are used to exclude spectral foldover after the sampling. The processes at LPF outputs are converted into a digital code by ADC. In the pilot radar, a 10-bit ADC was implemented with a sampling rate of 500 Hz. The bit capacity in the ADC is governed by the dynamic range of the receiving channel. Since a large constant component caused by the strong direct signal is suppressed by NF, ADC dynamic range requirement is significantly reduced. So, the considered 10-bit conversion is appropriate. The requirement of the sampling rate is defined by the maximal Doppler frequency shift of the target return. In our case, the selected sampling rate was appropriate for the targets flying at near-sonic speeds.

Digital codes from the receiving channels of the beams were entered on the computer. The following tasks were performed by means of a regular computer. Firstly, multi-channel filtering in the Doppler frequency domain was realized on the basis of FFT processing [5]. Previous Hamming weighting was used. The use of FFT provides target echo signal integration with simultaneous clutter rejection. The most beneficial conditions for this kind of processing are achieved by transmitting a continuous harmonic waveform. For the analysis of the underlying surface spectrum, the Doppler spectrum analyzer was connected prior to the clutter rejection stage.

After detection of the target return spectrum components, the measurement of the primary parameters (Doppler frequency shift and AOA) was performed. Using the measurements of these primary parameters, the trajectory parameters were estimated via an iterative algorithm on the basis of the maximum likelihood method.

3. Coverage of FSR

Let us estimate a detection coverage area of FSR for the case when the echo signal from a moving target is received against the background of the receiver's thermal noise and reflections from the underlying surface. Coverage is defined as a region of space where detection probability, D, is not less than certain defined value while the false alarm rate, F, does not exceed the assigned value.

The coverage calculation is based on the radar equation for a bistatic system [6, 7]:

$$Q = \frac{P_S}{P_0} = \frac{P_T G_T G_R \lambda^2 \eta F_T^2(\alpha,\beta) F_R^2(\alpha,\beta)}{(2\pi)^3 P_0 R_T^2 R_R^2} \alpha_B(\alpha_v, \alpha_h) . \quad (4)$$

In Equation (4) P_S is the scattered signal power at the receive side; P_0 is the power corresponding to the threshold signal; $Q = P_S/P_0$ is the excess of the received signal over a threshold signal; P_T is the average transmitter power; G_T and G_R are the gains of the transmitting and the receiving antennas; λ is the wavelength; η is the generalized loss; $\sigma_B(\alpha_v, \alpha_h)$ is the target bistatic RCS as a func-

tion of diffraction angles in the vertical (α_v) and horizontal (α_h) planes; F_T (α, β) and F_R (α, β) are the directional patterns of the transmitting and the receiving antennas which include possible deformation due to the surface reflections; R_T and R_R are the transmitter-target range and the target-receiver range.

The false alarm rate, F, is determined by the total number of resolution cells, N_{RC}, in the observation space. $F \cong 1/N_{RC}$ for the case of not more than one false alarm in the observation space, and $N_{RC} \gg 1$. If the observation is performed in a time interval, T, in the azimuth sector, $\Delta\alpha$, and in range of the Doppler frequency shift, Δf, then the total number of independent resolution cells $N_{RC} = n_T \cdot n_\alpha \cdot n_f$, where n_T, n_α and n_f are numbers of resolution cells in domains of time, azimuth and Doppler frequency. We shall estimate the order of magnitude for these factors.

To solve the problem of constructing a coverage diagram, the threshold value of the signal-to-noise ratio (SNR) for a given false alarm rate requires determination. An example of a coverage calculation for FSR is given below for the following set of parameters: $P_T = 6$ W, $G_T = 11$ dB, $G_R = 23$ dB, (transmission loss) $\eta_T = -2$ dB, (reception loss) $\eta_R = -1.5$ dB, $n_0 = 1.2 \cdot 10^{-20}$ W, $\lambda = 0.714$ m. Target had been presented by Mi-2 helicopter. It was very interesting to compare results of theoretical calculation of FSR coverage with the experimental results. Fig. 10 illustrates shows this comparison.
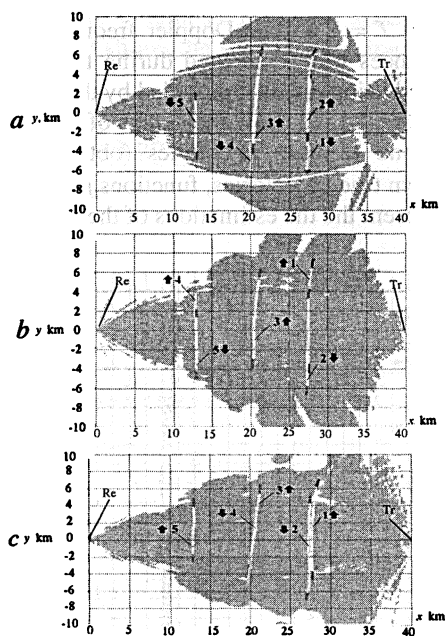
Fig. 10. Coverage estimation results for Mi-2 helicopter ($P_T = 1$ W) Flight altitudes: 100 m (*a*), 500 m (*b*), 1000 m (*c*). *1–5* are numbers of flight paths

611

Experimental estimations of FSR coverage were obtained in the following way. Using GPS data and measurements of target return amplitude, the experimental dependences of SNR upon the target plane coordinates for different target trajectories were obtained. The target was assumed to be inside FSR coverage until the measured SNR exceeded the assigned threshold. Segments of target trajectories satisfying this condition are shown in Fig. 10 as light paths on the grey background corresponding to the theoretical FSR coverage. Theoretical coverage was evaluated correspondingly to (4). Digits *1–5* are the numbers of paths, while the arrows show the directions of target motion along the trajectories. The presented results demonstrate that theory is in good agreement with experiment.

4. Tracking of the targets

In the considered FSR, the target trajectory parameters (Cartesian coordinates and their derivatives) are determined using the measurements of the primary parameters (target return Doppler frequency shift and AOA). The accuracy of the primary measurements determines the accuracy of target tracking.

In experimental FSR, air target trajectories were estimated using the iterative algorithm on the basis of the maximum likelihood method [8, 9]. A first approximation of the trajectory parameter vector was obtained from the first six primary measurements. The primary measurement interval was assigned to be equal $T = 1$ s. The Doppler frequency shift and angle of arrival measurement variances were estimated during target tracking. The true trajectories were obtained using the data provided by the onboard GPS equipment.

Fig. 11, 12 show the results of a target tracking experiment. Dotted lines correspond to true trajectories (obtained using on-board GPS equipment). For known true trajectories, functions $f_D(y)$ and $\alpha(y)$ have been calculated. Solid lines represent the the estimations of the coordinates obtained experimentally.
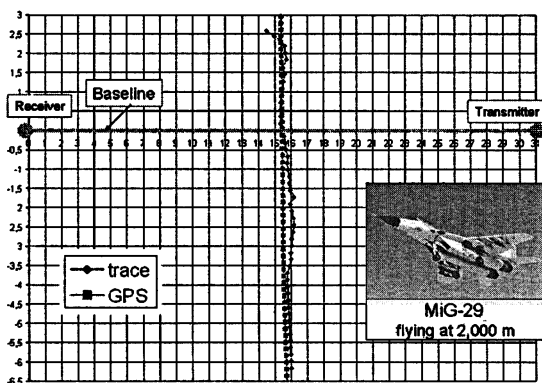
Fig. 11. Results of tracking experiment with MiG-29, altitude $h = 2000$ m

612
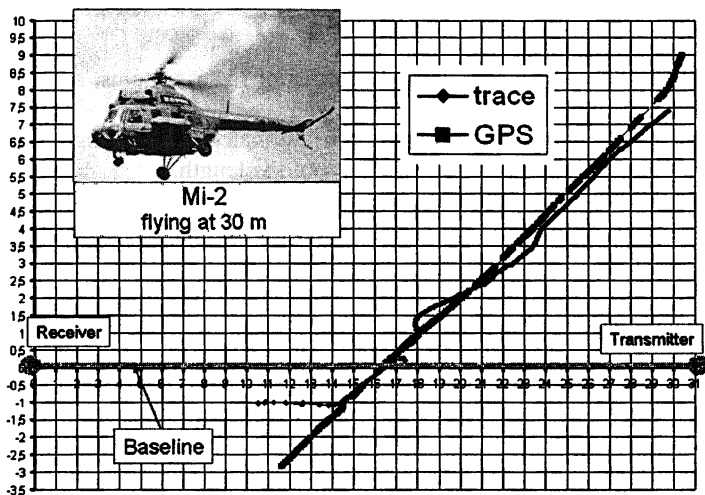
Fig. 12. Results of tracking experiments for Mi-2 helicopter, altitude $H = 30$ m

Thus, the experiment validated the suitability of the maximum likelihood algorithm for establishing trajectory parameters with sufficient accuracy in real time. Also, FSR is able to track several targets simultaneously. This statement also had been proved with a experiment. Fig. 13 shows the simultaneous tracking of five targets (all targets were Mig-29).
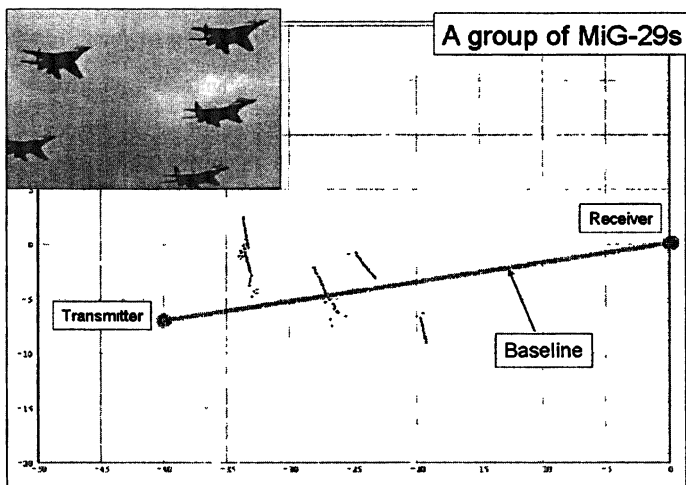
Fig. 13. Simultaneous tracking of five targets (Mig-29)

613

Conclusion

The full-scale experimental studies of FSR show:

CW FSR has the main traditional functions of radar systems, such as target detection and tracking.

The size and shape of FSR coverage were estimated, whose length is equal to the base length, while the width reaches 30 % of the length.

Target FS RCS increases by 30...50 dB in FS region in comparison with its equivalent monostatic counterpart and depends only on the shape of the object's shadow contour.

The developed algorithms for the measurement of trajectory parameters ensure real-time target tracking.

References

1. *Ufimcev P. Y.* Black Bodies and Shadow Radiation // Radiotekhnika i elektronika. 1989. Vol. 35, № 12. P. 2519–2527.
2. *Chernyak V. S.* Fundamentals of Multisite Radar Systems. Gordon and Breach Scientific Publishers, Netherlands (1998).
3. *Chapursky V. V.* Forward Scattering Inverse Hologram Spectrum and Complex Object Radar Cross Section Calculation // Izvestia vuzov. Radioelectronika. 1989. Vol. 32, № 7. P. 75–77.
4. *Blyakhman A. B., Runova I. A.* Forward Scattering Radiolocation Bistatic RCS and Target Detection // Proceedings of the IEEE Radar Conference. Waltham, Massachusetts, April 20–22. 1999. P. 203–208.
5. *Blyakhman A. B., Myakinkov A. V., Ryndyk A. G.* Phased Antenna Arrays in Bistatic Forward Scattering Radar System. Progress in Electromagnetics Research Symposium Proceedings // Boston, Massachusetts, July 1. 2002. P. 163.
6. *Skolnik M. I.* Radar Handbook. Second Edition. New York: McGraw-Hill, 1990.
7. *Willis N. I.* Bistatic Radar. Silver Spring: Technology Service Corporation. 1995.
8. *Blyakhman A. B., Myakinkov A. V., Ryndyk A. G.* Tracking Algorithm for Three-dimensional Bistatic Forward Scattering Radar with Weighting of Primary Measurements // Proceedings of 2nd European Radar Conference. Paris, 2005. P. 153–156.
9. *Blyakhman A. B., Myakinkov A. V., Ryndyk A. G.* Algorithm of Target Tracking for Three-dimensional Bistatic Forward Scattering Radar // Proceedings of IV International Radar Symposium, Warsaw, Poland, May 17–21. 2004. P. 309–324.

APPLICATION AND RECENT RESULTS ON PHYSICS OF ELECTRODE MICROWAVE DISCHARGE

Yu. A. Lebedev, A. V. Tatarinov, V. A. Shakhatov, I. L. Epstein

A. V. Topchiev Institute of Petrochemical Synthesis RAS,
Moscow, Russia

The first paper on the electrode microwave discharge (EMD) appeared in 1996. Presently many problems of EMD physics and application have already been solved. Several examples of EMD application are discussed: diamond growth, deposition of CN_x films and nanotubes, deposition of metal films (Cu, Al), deposition of TiN and TiO_2 films, generation of $O_2(a^1\Delta)$, and EMD as the plasma cathode. Recent results of modeling of strongly non-uniform electrode microwave plasma showed that a layer of space charge can be generated at the point of sudden increase of total ionization rate.

1. Introduction

Intensive study of the electrode microwave discharge (EMD) started in 1996 [1]. We call the discharge EMD if the plasma is ignited near the tip of powered electrode/antenna and luminous plasma region is less than dimensions of discharge chamber. The EMD turns into the ordinary discharge mode at smaller distances between the electrodes. The EMD discharge is interesting due to its distinctive features and promising applications.

Distinctive EMD features are: extremely low maintaining discharge power (1–2 W), wide range of operation pressures; generation of compact plasma structures; generation of plasma active particles in large vessels; generation of plasma in the chosen point of space (localization of plasma region), the area of plasma region is controlled by the electrode shape; generation of plasma active particles near the treated surface. Physical properties of the EMD are reviewed in [2, 3]. Several examples of EMD application are reviewed in this paper.

2. Application of the EMD

The EMD gives the possibility: to study and realize the plasma chemical processes, to intensify physical-chemical processes in gas phase, including the process of burning, to study the interaction of plasma with solids, to study the behavior of solids surrounded by plasma with gas flows, to study of interaction of plasma structures with gas flows. It is necessary to mention some obvious disadvantages of the EMD which can be important in research perspectives of this type of discharge. Considerable non-uniformity of plasma leads to low spatial homogeneity of plasma surface processing. We also indicate low level of plasma absorbed power.

2.1. Diamond growth

The EMD have been used for diamond growth and deposition of diamond-like films [1, 4, 5]. Process is held at pressure 15 Torr in the mixture $H_2 + (1–10 \%)$ CH_4 with stainless steel electrode [1, 4] and at pressure 20 Torr in the mixture $H_2 + 0.4 \% \ CH_2$ with graphite electrode [5]. Several results are shown in Fig. 1, 2 [4]. Deposition is made on silicon wafers at temperature of 1000 °C. It is known that the quality of deposit is increased with adding of oxygen and this is illustrated by curves 1 and 2 in figure 2. Deposition rate was of 1 μm/h. Method of electron spectroscopy for chemical analysis showed no traces of the products of electrode erosion in plasma-treated substrates in experiments on the diamond growth [1, 4].

The EMD is strongly nonuniform system and the deposition rate depends both on the distance of substrate from the electrode (d_0) and the distance from the center of the substrate. Experimental deposition rates can be approximated as $K(r) \approx \alpha(d_0^2 + x^2)^{-1}$ where r is the distance from the point on the substrate from the center of plasma ball [5]. It is important that deposit on the substrate was observed also outside the luminous plasma ball.
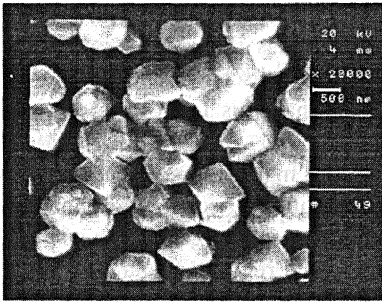
Fig. 1. Microphotograph of substrate after deposition [4]
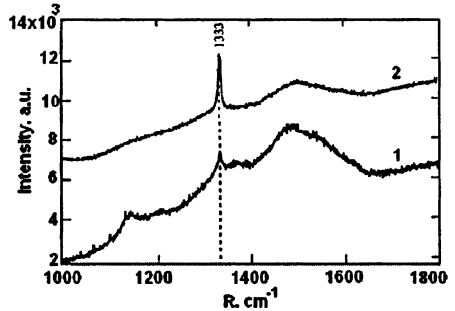
Fig. 2. Raman spectra of deposits: 1 – 400 sccm H_2 + 16 sccm CH_4, 2 – 400 sccm H_2 + 16 sccm CH_4 + 1 sccm O_2 [4]

There are three methods to increase the size of homogeneously treated surface: the first lies in using of lower field frequency; the second one lies in using the discharge system with several electrodes [28]; the third lies in using the dilative conical electrode (Fig. 3).
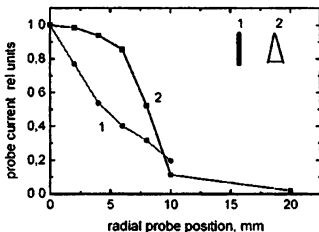
Fig. 3. Double probe ion saturation current in hydrogen EMD with cylindrical and conical electrodes in the plane of measurements is placed at the distance of 5 mm below the tip of the electrode and perpendicular to its axis [6].

2.2. Coating deposition

The EMD with graphite electrode in the mixture 0.9 Torr H_2 + 0.1 Torr CH_4 has been used for deposition of nanotubes on heated Ni substrate at incident power of 250 W [7]. The density of deposit was nonhomogeneous over the substrate surface.

The possibility of deposition of CN_x-films in the mixture of N_2 and C_2H_2 at pressure 1 Torr (power consumption 2–40 W) on silicon, glass, Al, paper and polymer films have been demonstrated in [8]. The temperature of substrates is varied between 30 and 700 °C. The deposit is nonuniform, the highest thickness is observed under the electrode. Coatings on silicon wafers have the columnar structure and columns are oriented perpendicular to the surface. The tops of vertical columns are seen in Fig. 4 along with few columns deliberately placed on the surface for illustration.
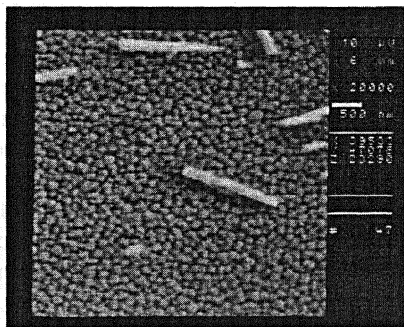
Fig. 4. Microphotograph of silicon substrate after CN-film deposition [8]

Melting of Cu and Al electrodes at high microwave power have been used for deposition of Cu and Al films on Pyrex and stainless steel substrates in hydrogen plasma. The deposit includes the droplets of metals [8]. Mixtures of hydrogen with nitrogen or oxygen have been used for deposition of TiN and TiO_2 films on stainless steel substrates [8].

2.3. The EMD as a source of $O_2(a^1\Delta)$

The process of $O_2(a^1\Delta)$ generation has been tested for the EMD on the base of 1D quasi-static model for oxygen discharge at different pressures [9]. Several results are presented in Fig. 5. At pressure of 1 Torr the calculated concentration of $O_2(a^1\Delta)$ is close to the theoretical limit (25 %) and radial distribution of concentrations is close to homogeneous. Increase of pressure leads to the reduction of the concentration and its homogeneity becomes worse.
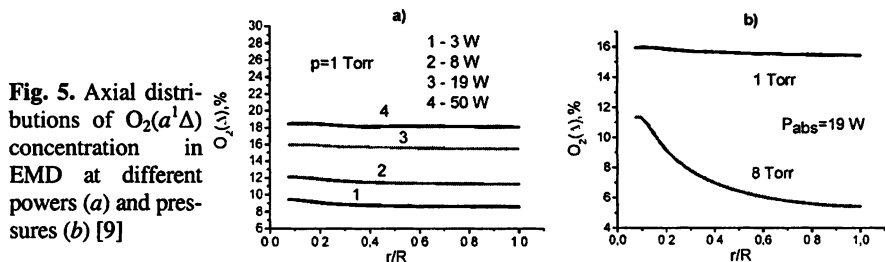
Fig. 5. Axial distributions of $O_2(a^1\Delta)$ concentration in EMD at different powers (*a*) and pressures (*b*) [9]

617

2.4. The EMD as a plasma cathode

The behavior of the EMD in external static field and the DC voltage-current characteristics of EMD have been studied in [10] (see Fig. 6). It was shown that the dark space of the discharge is a conductive medium. The DC current grows with microwave power at constant pressure and falls with pressure at constant power. In the range of voltages shown in Fig. 6 the EMD does not change its structure. At higher positive DC voltages with respect to the chamber the DC current increases in two orders of magnitude and a secondary surface discharge (non-self-sustained) appears near the walls of the chamber. The magnitudes of these voltages are not enough for generation of ordinary DC discharge. At high negative electrode voltage the EMD can extinguish. The EMD plays the role of plasma cathode. Thus the low power microwave source and external DC voltage can activate the medium in large volume and gives a possibility to process the internal surface of details with large dimensions. The danger of wall atomization is small because the secondary surface discharge is low voltage and non-self-sustained.
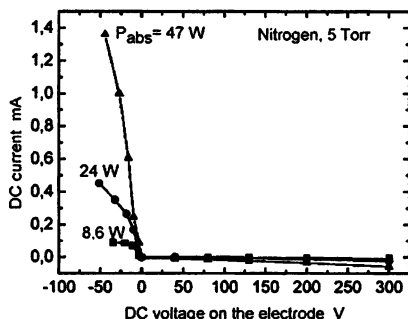
Fig. 6. Experimental DC voltage-current characteristics of the nitrogen EMD at different powers [10]
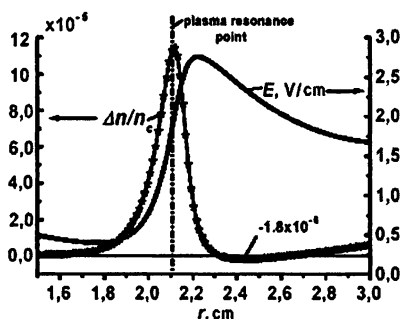
Fig. 7. Calculated layer of charge separation and the static field E in the region of plasma resonance

3. Generation of layers of charge separation

Recent simulations showed that charged layers can be created in the plasma with sudden increase of the electric field and ionization rate. One-dimensional quasi-static model for a stationary microwave nitrogen discharge inside spherically symmetric system of electrodes has been used. The model consists of the microwave field equation in quasi-static approximation, the Poisson equation, the balance equations which describe the kinetics of charged (e, N_2^+, N_4^+) and neutral ($N_2(A^3\sum_u^+)$, $N_2(B^3\Pi_g)$, $N_2(C^3\Pi_u)$, $N_2(a'^1\sum_u^-)$) plasma components, time-independent homogeneous Boltzmann equation for electrons obtained in the two-term approximation. The kinetic scheme involves the direct electron impact ioni-

zation, step and associative ionization, volume and wall recombination of charged and neutral particles, ion-molecular reactions, excitation and de-excitation processes for molecules. Processes with vibrationally excited molecules are accounted for by using the well-known analytical expression for the vibrational distribution function (VDF) obtained in the diffusion approximation.

This condition is satisfied in strongly non-uniform microwave discharge in the plasma resonance region (Fig. 7). Charge separation ($\Delta n = (\Sigma N_i^+ - n_e)$) induces the static electric field and this can be considered as one of the possible reasons of sharp external boundary of the EMD.

4. Summary

Nonequilibrium electrode microwave discharge attracts the interest both because of its unique physical peculiarities and promising applications. This type of discharge is a representative of strongly nonuniform discharges and thus combines the properties of quite different discharges. Physical processes in EMD are different in various regions of the discharge. Plasma content (excited and charged particles) is also different. This discharge can be attributed to the class of "self-sustained-non-self-sustained" discharges. EMD can be effectively used in plasma chemistry for treatment of surfaces, coatings deposition or as plasma cathode. The search of new applications of the EMD is a subject for further studying.

Acknowledgements

References

1. *Bardos L., Barankova H., Lebedev Yu. A., Berg S., Nyberg T.* Proc. 7th European Conf. on Diamond, Diamond-like and Related Materials, Tours, France, 4.1 (1996).
2. *Lebedev Yu. A., Epstein I. L., Tatarinov A. V., Shakhatov V. A.* Journal of Physics: Conference Series, 44, 30 (2006).
3. *Lebedev Yu. A., Epstein I L., Tatarinov A. V., Shakhatov V. A.* J. Phys. D: Appl. Phys. 41, 194001 (2008).
4. *Bardos L., Barankova H., Lebedev Yu. A., Nyberg T., Berg S.* Diamond and Related Materials 6, 224 (1997).
5. *Taniyama N., Kudo M., Matsumoto O., Kawarada H.* Jpn J. Appl. Phys. 40, L698 (2001).
6. *Bardos L., Lebedev Yu. A* Plasma Phys. Reports, 24, 956 (1998).
7. *Eto A., Kimura S., Kando M.* Microwave Discharges: Fundamentals and Application. Ed A. Ohl. Greifswald, INP, 65 (2003).
8. *Bardos L., Barankova H., Lebedev Yu. A.* 42nd Ann. Conf. of Soc. of Vac. Coaters, Chicago, IL, Proc. SVC TC, paper E-7 (1999).
9. *Lebedev Yu. A., Tatarinov A. V., Epstein I L.* High Temp. 46, 645 (2008).
10. *Lebedev Yu. A., Tatarinov A. V., Epstein I. L.* High Temp. 45, 283 (2007).

STRONG MICROWAVE ABSORPTION
BY A FILAMENTARY MICROWAVE DISCHARGE
EXITED ON A DIELECTRIC SURFACE

V. A. Ivanov, A. S. Sakharov, M. E. Konyzhev

A. M. Prokhorov General Physics Institute
Russian Academy of Sciences, Moscow, Russia

Excitation of microwave discharges by pulsed microwave radiation (0.7–2 MW, 1.95 GHz, 3 μs) on dielectric surfaces in vacuum was studied experimentally. It is found that, in the stage of microwave breakdown (which lasts for ~0.1 μs), up to 70 % of the incident microwave power is absorbed by a dense plasma filament with a diameter of ~0.1 mm, an electron density of $2 \cdot 10^{18}$ cm^{-3}, and an electron temperature of 1.5–2 eV. An electrodynamic model is constructed that accounts for the absorption and scattering of the microwave field by the filament, as well as for reflections of the scattered radiation from the waveguide walls. It is shown that the plasma of a filamentary discharge with the above parameters can absorb up to 70 % of the incident microwave power, which agrees well with the experimental data.

Experiment

The present study was motivated by the problem of microwave breakdowns on the surfaces of dielectric materials and subsequent destruction of dielectrics in their interaction with the discharge plasma.

A scheme of the experiment is shown in Fig. 1. The sample (a 0.2×1×6-cm NaCl or quartz crystal with a deposited polymethylmethacrylate stripe) was placed in the second antinode of the standing H_{10} mode ($f_0 = 1.95$ GHz, $\lambda_0 = c/f_0 \approx 15.4$ cm)
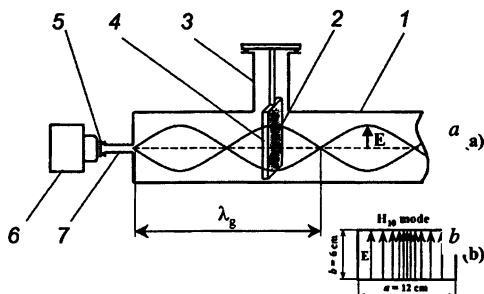
Fig. 1. (*a*) Arrangement of the sample in the waveguide (side view): *1* – evacuated waveguide, *2* – microwave plasma, *3* – 24-mm-diameter circular below-cutoff waveguide, *4* – dielectric sample, *5* – sealed optical window, *6* – photo camera, and *7* – 10-mm-diameter circular below-cutoff waveguide (the free-space wavelength is $\lambda_0 = 15.4$ cm, and the waveguide wavelength is $\lambda_g = \lambda_0/(1 - (\lambda_0/2a)^2)^{1/2} \approx 20$ cm); (*b*) waveguide cross section

of a short-circuit rectangular waveguide with the width $a = 12$ cm and height $b = 6$ cm. The residual gas pressure was $\sim 10^{-6}$ Torr. The incident pulsed microwave power was 0.7–2 MW. The diagnostic techniques included (i) balance measurements of the microwave power in the waveguide, (ii) plasma density measurements based on the Stark broadening of hydrogen spectral lines, and (iii) analysis of erosion tracks on the sample surface.

After the microwave power was switched on, a discharge was exited on the sample surface [1]. Three stages could be distinguished in the discharge evolution (see Fig. 2): (i) feebly glowing secondary-electron-emission microwave discharge, (ii) filamentary microwave discharge, and (iii) flare microwave discharge. The maximum microwave absorption (up to 60–70 %) was achieved in the stage of filamentary discharge (Fig. 3, $t \approx 1.25$ μs). The plasma electron density in the filament was estimated from the broadening of the hydrogen H_α line and was found to be in the range $n_e \approx 7 \cdot 10^{17} - 2 \cdot 10^{18}$ cm^{-3} [2]. The electron temperature was estimated to be in the range 1.5–2 eV. The discharge produced a 6-cm-long erosion track with a width of ~ 100 μm on the sample surface.
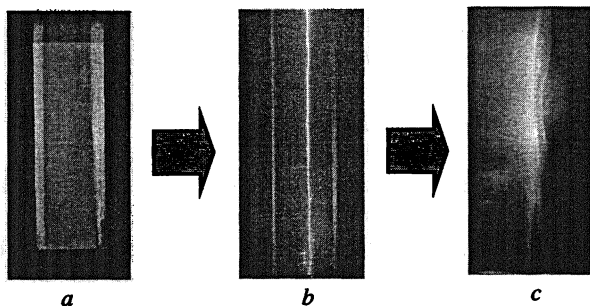
Fig. 2. Three stages of the electrodeless microwave discharge excited by pulsed microwave radiation on the surface of a solid dielectric in vacuum: a – secondary-electron-emission microwave discharge (1000-fold light amplification); b – surface microwave breakdown–filamentary microwave discharge (no light amplification); c – flare microwave discharge (fivefold light amplification)
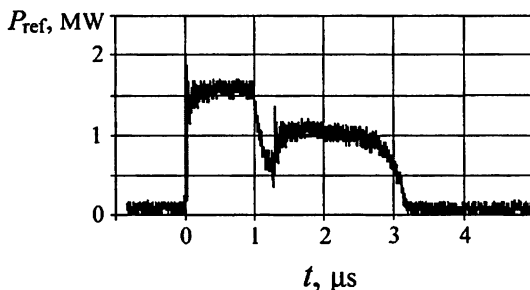
Fig. 3. Oscilloscope trace of the reflected microwave power P_{ref}. The incident power in the 3-μs-long rectangular microwave pulse is $P_{inc} = 1.5$ MW.

621

Theory

The coefficient of absorption of microwave radiation by a thin plasma filament ($k_0 r_0 \ll 1$, where r_0 is the filament radius, $k_0 = \omega_0/c = 2\pi/\lambda_0$, $\omega_0 = 2\pi f_0$) in a rectangular waveguide was calculated as follows. Let us first consider a thin cylindrical plasma filament in free space. Let the filament be placed in an external field $\frac{1}{2}(E_{ext}\exp(-i\omega_0 t) + \text{c.c.})$ directed along the filament axis [3]. The microwave power per unit length absorbed by such a filament (in CGSE units) is

$$p_{abs} = \frac{1}{2}|E_{ext}|^2(\text{Re}Z - \pi k_0/c)/|Z|^2, \qquad (1)$$

where $Z \equiv E_{ext}/I$ is the filament impedance (per unit length) and I is the complex amplitude of the electric current excited in the plasma filament. When the filament radius is on the order or less than the skin depth ($k_0^2 r_0^2 |\varepsilon| \le 1$, where ε is the plasma permittivity), the impedance Z can be represented as

$$Z \cong Z_0 + Z_{self}, \qquad (2)$$

where $Z_0 = (\pi k_0/c)(1 + (2i/\pi)\ln(0.89 k_0 r_0))$ is the impedance of a perfectly conducting cylinder, $Z_{self} = (2\pi\int\sigma ds)^{-1}$ is the self-impedance of the plasma filament, and $\sigma \equiv (i\omega_0/4\pi)(1 - \varepsilon)$ is the complex plasma conductivity.

The plasma filament not only absorbs, but also scatters radiation. The scattered power, $p_{sc} = (\pi k_0/2c)|E_{ext}|^2/|Z|^2$, is emitted in the form of an expanding cylindrical wave,

$$E_{sc} = -\frac{1}{2}(\pi k_0/2c)(I\, H_0^{(1)}(k_0 r)\exp(-i\omega_0 t) + \text{c.c.}), \qquad (3)$$

where $H_0^{(1)}$ is the zero-order Hankel function of the first kind.

Let us now consider a plasma filament placed in the second antinode of the standing H_{10} mode of a short-circuit rectangular waveguide, $x = 0$, $z = 3\lambda_g/4$, where $\lambda_g = \lambda_0/\cos\theta = \lambda_0/(1-(\lambda_0/2a)^2)^{1/2}$ is the waveguide wavelength (Fig. 4).
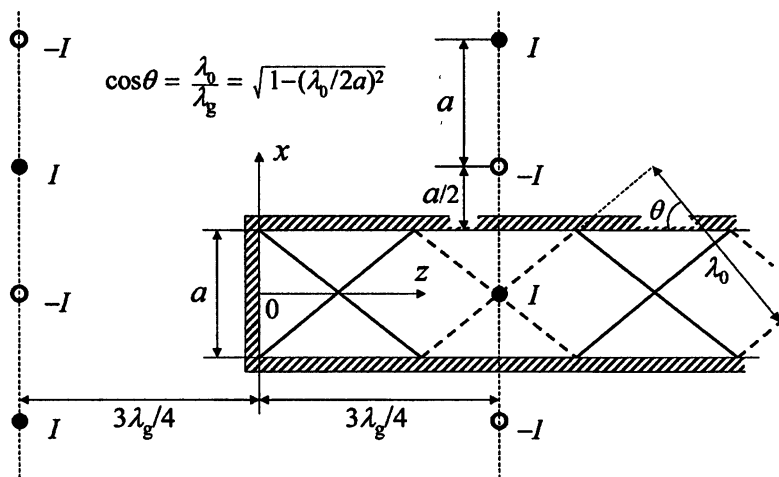
Fig. 4. Equivalent scheme of microwave–plasma interaction in a waveguide (top view)

Note that the results obtained do not depend on the number of the wave antinode. We assume that the filament length is equal to the waveguide height b. The field E_{ext} acting on the filament is the sum of the field of the standing wave in an empty waveguide, $E_g = \frac{1}{2}(2E_0\exp(-i\omega_0 t) + c.c.)$ (where E_0 is the field amplitude of the propagating H_{10} mode), and the field E_{ref} of the scattered wave, which has undergone multiple reflections from the waveguide walls. These reflections can be taken into account by introducing two vertical rows of filament images with alternating current directions, $\pm I$ (Fig. 4). The total field produced by the emitting plasma filament and its images satisfies the boundary condition $E_y = 0$ on the waveguide walls.

Then, the total field of the reflected waves is $E_{ref} = \Sigma E_{sc}(n, m)$, where summation is performed over both rows ($m = +1, -1$) and over images ($-\infty < n < +\infty$) in each rows (except for the filament itself). Since the scattered fields $E_{sc}(n, m)$ produced by the images of the plasma filament (see Eq. (3)) are proportional to the current I excited in the plasma filament, we can write $E_{ref} = Z_{ref}I$, where Z_{ref} is determined by the waveguide parameters and is independent of the parameters of the plasma filament. The real part of Z_{ref} is $\mathrm{Re}Z_{ref} = \pi k_0/c - (8k_0/c)\tan\theta$, while the imaginary part can be calculated numerically. Taking into account that the complex amplitude of the total field acting on the filament is $E_{ext} = 2E_0 + E_{ref}$ and $I = E_{ext}/Z$, we obtain

$$E_{ext} = 2ZE_0/(Z - Z_{ref}) . \qquad (4)$$

Substituting (4) into (1), we find that the total power absorbed by the plasma filament in the waveguide is

$$P_{abs} \equiv bp_{abs} = 2b|E_0|^2(\mathrm{Re}Z - \pi k_0/c)/|Z - Z_{ref}|^2 . \qquad (5)$$

The incident microwave power is $P_{inc} = ab(c/16\pi)|E_0|^2\cos\theta$. Hence, the coefficient of power absorption is

$$A \equiv P_{abs}/P_{inc} = (32k_0/c)(\mathrm{Re}Z - \pi k_0/c)/|Z - Z_{ref}|^2\tan\theta. \qquad (6)$$

For any dissipative medium ($\mathrm{Im}\varepsilon > 0$), absorption coefficient (6) is positive and is less than unity.

Let us make some estimates for our experimental parameters. For $a = 12$ cm and $\lambda_0 = 15.4$ cm, we find $Z_{ref} \approx -(\pi k_0/c)(1.13 + 0.53i)$. We calculated the absorption coefficient as a function of the parameter $k_0^2 r_0^2 \langle\varepsilon\rangle$ (where $\langle\varepsilon\rangle$ is the average value of the plasma permittivity within the filament) for a realistic value of the filament radius, $r_0 = 50$ μm (in this case, $k_0 r_0 \approx 2 \cdot 10^{-3}$ and $Z_0 \approx (\pi k_0/c)(1 - 4.04i)$). The results of calculations are presented in Fig. 5, where the left half-plane corresponds to plasma media ($\mathrm{Re}\varepsilon < 0$).

It is seen that, since $k_0^2 r_0^2 \ll 1$, appreciable absorption can be obtained only for very large values of $\langle\varepsilon\rangle$. Formally, total absorption ($A \doteq 1$) corresponds to the point $\mathrm{Re}\langle\varepsilon\rangle \approx 0.23/k_0^2 r_0^2$, $\mathrm{Im}\langle\varepsilon\rangle \approx 0.17k_0^2 r_0^2$, which, however, is unachievable for actual media. For a plasma filament, the maximum absorption coefficient, $A_{max} = 0.685$, is achieved at $\mathrm{Im}(k_0^2 r_0^2\langle\varepsilon\rangle) \approx 0.31 \gg \mathrm{Re}(k_0^2 r_0^2\langle\varepsilon\rangle)$, which corresponds to a dense collisional plasma: $\omega_{pe} \gg \nu_e \gg \omega_0$.
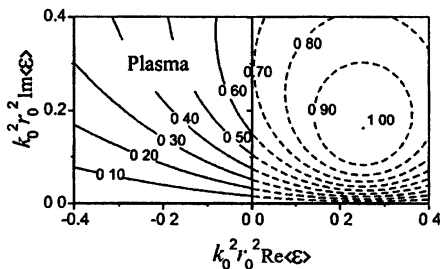
Fig. 5. Contour lines of the power absorption coefficient A in the (Re$<\varepsilon>$, Im$<\varepsilon>$) plane for $\lambda_0 = 15.4$ cm, $a = 12$ cm, $r_0 = 50$ μm ($k_0^2 r_0^2 \approx 4 \cdot 10^{-6}$)

Under our experimental conditions ($n_e \sim 10^{18}$ cm^{-3}, $T_e \approx 1.5$–2 eV), the characteristic path lengths of plasma particles (~0.03 μm) are much shorter than the filament diameter (~100 μm) and the characteristic time during which thermodynamic equilibrium is established in such a plasma (~0.15 ns) is mush shorter than the duration of the filamentary discharge (~50 ns). Therefore, the filamentary discharge plasma can be considered to be in thermodynamic equilibrium. It follows from the Saha formula that, in this case, the degree of ionization is fairly high, $n_0 \leq n_e$; i.e., the electron–ion collision frequency ($\nu_{ei} \sim 3 \cdot 10^{12}$ s^{-1}) is much higher than both the electron–neutron collision frequency ($\nu_{en} \leq 3 \cdot 10^{11}$ s^{-1}) and the microwave circular frequency ($\omega_0 = 1.23 \cdot 10^{10}$ s^{-1}), but much lower than the plasma electron frequency ($\omega_{pe} \sim 5 \cdot 10^{13}$ s^{-1}). Then, we have Im$\varepsilon \approx \omega_{pe}^2/\omega_0\nu_{ei} \approx$ $\approx 0.8 \cdot 10^5 >> $ Reε. For $r_0 \approx 50$ μm, this corresponds to Im($k_0^2 r_0^2 \varepsilon$) $\approx 0.3 >> $ $>> $ Re($k_0^2 r_0^2 \varepsilon$). Under these conditions, the absorption coefficient is close to its maximum value, $A_{max} \approx 0.7$, which agrees well with the experimental data.

Thus, strong microwave absorption by a thin plasma filament leads to a three-orders-of-magnitude increase ($A_{max}a/2r_0 \sim 10^3$) in the power flux density at the discharge location. This leads to local destruction of the dielectric surface in the form of a long narrow erosion track [1].

References

1. *Ivanov V. A., Konyzhev M. E.* Proc. Int. Workshop: Strong Microwaves in Plasmas / Ed. by A. G. Litvak. Nizhny Novgorod· IAP RAS, 2003. Vol. 2. P. 684.
2. *Ivanov V. A., Konyzhev M. E.* Proc. Int. Workshop: Strong Microwaves in Plasmas / Ed. by A. G. Litvak. Nizhny Novgorod: IAP RAS, 2006. Vol. 2. P. 784.
3. *Stratton J. A* Electromagnetic Theory Hoboken: Wiley, 2007.

EXPLORING MULTIPACTING THRESHOLD CHARACTERISTICS IN A RECTANGULAR WAVEGUIDE

A. G. Sazontov, V. A. Sazontov, and N. K. Vdovicheva[1]

Institute of Applied Physics RAS, Nizhny Novgorod, Russia
[1] Institute for Physics of Microstructures RAS, Nizhny Novgorod, Russia

The initiation of multipactor discharge in a rectangular waveguide has been studied taking into account the velocity spread of injected electrons. Special attention is focused on the case when part of the input RF power is reflected. For the situation considered we present the multipacting susceptibility diagram in the plane of reflecting coefficient and forward power. It has been found that this diagram has a continuous structure, in contrast to the discrete one predicted by the resonance theory.

The multipactor problem in waveguides has not received much attention in the literature: available analytical and numerical investigations on the subject of interest are essentially concentrated in a few works [1–5]. It is worth commenting that the majority of these papers were focused on a kinematic theory for the conditions of multipactor initiation. Thus, the kinematic considerations based on the constant emission velocity model led to the construction of multipacting band map bounding the power ranges in which multipactor is possible. In particular, according to the dynamic approach the discharge can occur only for a set of discrete multipacting barriers that are well separated. However, the discrete multipacting band structure predicted by numerical simulation is sharp contrast with that obtained in experiments [6] in which a continuous band structure is observed. Such a discrepancy can be explained taking into account the velocity spread of secondary electrons. In this context it should be noted that analysis of the effect of electron velocity spread was undertaken by Semenov et al. [5] who have employed Monte Carlo simulation and reported some preliminary results of statistical modeling.

In this paper, we present a statistical theory of multipactor discharge in a rectangular waveguide which allows one to obtain the multipacting threshold characteristics systematically.

Problem formulation

Consider a rectangular waveguide with broad dimension a and narrow dimension b (as shown in Fig. 1) in which the dominant mode TE_{01} is propagated. The vector-potential $\mathbf{A}(y, z, t)$ of the mode considered (depending on transverse coordinate y, propagation coordinate z and time t) has the form

$$\mathbf{A}(y,z,t) = -\mathbf{x}_0 A(\mathbf{r}_\perp,t), \qquad \mathbf{r}_\perp = (y,z);$$

$$A(\mathbf{r}_\perp,t) = \frac{E_0}{k} \cos\left(\frac{\pi y}{a}\right) \left[\cos(\omega t - h z) + R \cos(\omega t - h z)\right].$$

Here E_0 is the maximum electric field of the traveling wave, ω is the angular frequency, $k = \omega/c$ is the vacuum wave number (c is the velocity of light), $h = \sqrt{k^2 - (\pi/a)^2}$ is the propagation constant, R is the reflection coefficient, and $\mathbf{x_0}$ is unit vector of the x-axis.

The electromagnetic wave field components can be expressed via $\mathbf{A}(\mathbf{r_\perp},t)$ as

$$\mathbf{E}(\mathbf{r_\perp},t) = -\frac{1}{\tilde{n}}\frac{\partial \mathbf{A}(\mathbf{r_\perp},t)}{\partial t}, \qquad \mathbf{H}(\mathbf{r_\perp},t) = \mathrm{rot}\,\mathbf{A}(\mathbf{r_\perp},t).$$

Note that E_0 is related to the forward power P by: $P = \dfrac{cE_0^2 h}{16\pi k}\,ab.$
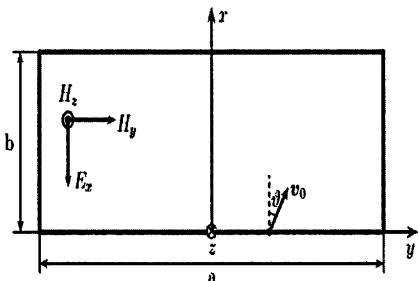
Fig. 1. Geometry of the problem

Let us assume that emission occurs at time t_0 from the bottom wall at $r_0 = (0, y_0, 0)$ with initial velocity $\mathbf{v_0}$ (directed at an angle ϑ with respect to the positive x-axis) and the impact occurs at the opposite broad wall at $x = b$. In general, the initial velocities $\mathbf{v_0}$ are random and are described by a given distribution function $f(\mathbf{v_0})$.

Below, the dependence of the secondary electron yield on the impact energy W_i is adopted from Vaughan's empirical formula

$$\sigma(w) = \sigma_m\left[w\exp(1-w)\right]^{k(w)}, \quad k(w) = \begin{cases} 0.62, & \text{if } w < 1, \\ 0.25, & \text{if } w > 1, \end{cases}$$

where $w = W_i/W_m$, σ_m is the maximum value of the secondary emission yield, and W_m is the impact energy which corresponds to σ_m.

Basic equations

At the initial stage (when the space charge effect can be ignored), the electron motion is described by the force equation

$$m\ddot{\mathbf{r}} = -e\left(\mathbf{E} + \frac{1}{c}[\mathbf{v}\times\mathbf{H}]\right), \qquad \mathbf{r} = (x, \mathbf{r_\perp}), \tag{1}$$

where m and $-e$ stand for electron mass and charge, respectively.
Equation (1) has an exact first integral

$$mv_x = mv_{0x} - \frac{e}{c}[A(\mathbf{r_\perp},t) - A_0], \quad A_0 = A(\mathbf{r_\perp},t)\big|_{t=t_0} \tag{2}$$

expressing the conservation law of the normal component of generalized momentum. With the use of (2) for $\mathbf{r_\perp}$ we get from (1):

626

$$m\ddot{\mathbf{r}}_\perp = -\frac{e^2}{2mc^2}\nabla_\perp[A(\mathbf{r}_\perp,t) - A_0 + \frac{mc}{e}v_{0x}]^2 . \tag{3}$$

To construct an approximate analytical solution of (3) we represent $\mathbf{r}_\perp(t)$ as a sum of slow and oscillating parts: $\mathbf{r}_\perp(t) \doteq \overline{\mathbf{r}}_\perp(t) + \tilde{\mathbf{r}}_\perp(t)$, where the overline denotes averaging over RF period As a result, for $\overline{\mathbf{r}}_\perp$ one obtains from (4):

$$m\ddot{\overline{\mathbf{r}}} = -\nabla U_{\text{eff}}(\overline{\mathbf{r}}_\perp), \tag{4}$$

where

$$U_{\text{eff}}(\overline{\mathbf{r}}_\perp) = \frac{e^2 E_0^2}{4m\omega^2}\cos^2\left(\frac{\pi \overline{y}}{a}\right)\left[1 + 2R\cos(2h\overline{z}) + R^2\right]$$

is an effective high-frequency potential and the quantity $-\nabla U_{\text{eff}}(\overline{\mathbf{r}}_\perp)$ represents the pondermotive or Miller force. For the considered geometry the transverse component of the corresponding force pushes the electrons from the center of the rectangular waveguide to the sidewalls. Hence, if the initial position y_0 or/and initial tangential velocity v_{0y} differ from zero, then the electron migrates to the sidewall after a few impacts where the electric field is zero and the multipactor cannot be developed. Thus, the action of tangential velocity components (together with RF magnetic field) leads to multipactor suppression.

In what follows we restrict ourselves to studying the 2D problem, assuming that the injected (at $z_0 = 0$) electrons have dominant v_{0x} and v_{0y} initial velocity components, and, thus, the action of the Miller force directed along the propagation coordinate z may be ignored.

For given values of E_0 (or P) and R equations (2) and (4) can be solved to compute the trajectories $x(t)$ and $y(t)$ of the emitted electrons. After some transit time t_i (defined as a smallest root of the transcendental equation $x(t_i) = b$) these electrons will interact with the opposite wall to produce secondaries.

Resonance theory: susceptibility diagrams

Before discussing the effects of random secondary emission velocities let us briefly describe the structure of susceptibility diagrams based on the resonance theory according to which the transit time between the impacts is odd number of half-periods of the RF field.

In the framework of the kinematic theory the multipactor is possible if secondary electron yield is greater than unity. The condition $\sigma = 1$ determines the multipactor region boundaries.

The multipacting band structure for 40.2 cm × 10.2 cm rectangular waveguide driven at 500 MHz is shown in Fig. 2 for 1D and 2D scenario, respectively.

This figure corresponds to secondary multipaction from the single initial launch location at the midline with a fixed emission energy of 3 eV. Comparison Fig. 2b with Fig. 2a shows a significant decrease of the number of possible zones: the action of tangential velocity components leads to the suppression of

627

multipactor development in the range of relatively low RF powers. However, in both cases the discharge can occur only for a set of discrete multipacting bands, each corresponding to a resonant condition of a specific order.
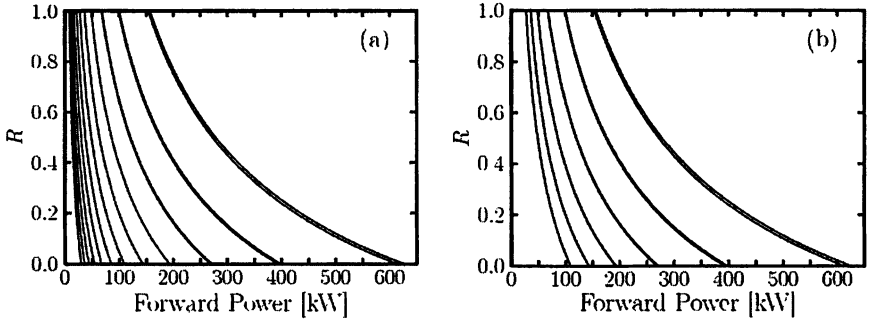
Fig. 2. Susceptibility diagram for 40.2 cm × 10.2 cm rectangular waveguide driven at 500 MHz with $\sigma_m = 1.7$, $W_m = 400$ eV for 1D case (a) and 2D case (b)

Threshold multipacting characteristics

In general, the initial velocities $\mathbf{v}_0$ are random, and the trajectory of the electron (emitted from location$(0, y_0)$ with launch phase $\varphi_0 = \omega t_0$) will intersect the opposite wall at a random horizontal coordinate y at some random instant $\tau = \omega(t_i - t_0)$. Hence, the problem reduces to evaluating the joint probability density of the arrival time and arrival position which we denote by $G(\tau, y \mid \varphi_0, y_0; P, R)$. The corresponding distribution function can be expressed in terms of $f(\mathbf{v}_0)$ by using the well known results from the statistical theory.

Knowledge of $G(\tau, y \mid \varphi_0, y_0; P, R)$ makes it possible to construct the general integral equation allowing prediction of the steady-state emission phase-position distribution and the threshold of multipactor growth:

$$f_{st}(\varphi_0, y_0) = \mu \int_{-a/2}^{a/2} dy_0' \int_0^{2\pi} K(\varphi_0, y_0 \mid \varphi_0', y_0'; P, R) f_{st}(\varphi_0', y_0') d\varphi_0', \quad \mu = \sigma_m,$$

$$K = G\left(\varphi_0 - \varphi_0', y_0 \mid \varphi_0', y_0'; P, R\right) \varsigma\left(\varphi_0, y_0 \mid \varphi_0', y_0'; P, R\right) \Theta(\varphi_0 - \varphi_0') + \quad (5)$$

$$+ \sum_{n=1}^{\infty} G\left(\varphi_0 - \varphi_0' + 2\pi n, y_0 \mid \varphi_0', y_0'; P, R\right) \varsigma\left(\varphi_0 + 2\pi n, y_0 \mid \varphi_0', y_0'; P, R\right),$$

where

$$\varsigma(\varphi_0, y_0 \mid \varphi_0', y_0'; R, P) = \left[w \exp(1 - w) \right]^{k(w)}, \quad w = w(\varphi_0 - \varphi_0', y_0 \mid \varphi_0', y_0'; P, R) \quad \text{and}$$

$\Theta(\varphi_0 - \varphi_0')$ stands for the step function.

628

For given parameters P and R, electron multipaction occurs when the maximum yield σ_m exceeds some threshold value (above which there is multipactor growth). From the mathematical point of view, the corresponding value coincides with the smallest characteristic value μ of the integral equation (5) (which depends on P and R). The condition $\min \mu(P, R) = \sigma_m$ determines the regions in the (P, R) plane in which multipactor is possible.

A multipacting map as provided by the statistical approach is depicted in Fig. 3. Here, the curve *1* corresponds to 1D scenario, and the curve *2* represents the results for 2D geometry in which the tangential components of the initial velocities are taken into account. (The mean emission energy was taken to be 3 eV.)

It is seen from this figure that the spread of initial velocities considerably changes the condition for multipactor initiation in comparison

Fig. 3. Multipactor region boundaries in the plane of (P, R) for 40.2 cm × 10.2 cm rectangular waveguide driven at 500 MHz with $\sigma_m = 1.99$, $W_m = 400$ eV.

with the resonance theory. For the given set of parameters the discharge development is possible in a wide enough range of RF powers. The latter conclusion is in a qualitative agreement with the experimental data reported by Geng et al. [6].

References

1. *Geng R. L. and Padamsee H. S.* Proc. 1999 Partical Accelerator Conf. New York, 429 (1999).
2. *Chojnacki E.* Phys. Rev. ST Accel. Beams, **3**, 032001 (2000).
3. *Geng R. L., Padamsee H. S., and Shemelin V.* Proc. 2001 Partical Accelerator Conf. Chicago, 1228 (2001).
4. *Shemelin V. D.* LNS Report SRF 010322-03. Cornell University, Ithaca (2001).
5. *Semenov V., Rakova E., Andersen D., Lisak M., and Puech J.* Phys Plasmas. **14**, 033501 (2007).
6. *Geng R. L., Goudket P., Carter R. G. et al.* Nucl. Instr. and Meth. Phys. Res. A. **538**, 189 (2005).

ANALYTICAL DESCRIPTION OF MULTIPACTOR BREAKDOWN IN A NARROW WAVEGUIDE IRIS

V. E. Semenov, E. I. Rakova, R. Udiljak[1], D. Anderson[1], M. Lisak[1], J. Puech[2]

Institute of Applied Physics, Nizhny Novgorod, Russia
[1]Chalmers University of Technology, Gothenburg, Sweden
[2]Centre National d'Etudes Spatiales, Toulouse, France

Multipactor breakdown in a single waveguide iris is analyzed within a 2D model for the electron motion and by using the quasi-static approximation for the rf field. The conformal mapping approach makes it possible to describe analytically the rf field structure in the iris. It is shown that using the complex variables of the conformal mapping one can obtain an explicit analytical form of the equations of electron motion, which allows developing a fast and accurate software for simulations of the multipactor in the iris. The simulation results are presented, discussed, and compared with experimental ones.

The waveguide iris represents a common microwave component which is often used in microwave systems for matching of different sections in waveguide transformers. A typical iris configuration consists of a step-like, short-length reduction of the waveguide height. As the rf electric field strength is enhanced in the iris and the gap height is small, there is a pronounced risk of having a multipactor discharge in this structure. Therefore an accurate prediction of the multipactor threshold in an iris is an important problem [1–3].

An important complication when simulating multipactor breakdown in a realistic iris is that the rf electric field in the iris depends, not only on the iris parameters, but also on the entire configuration of the rf circuit. Consequently the measured multipactor threshold in terms of transmitted power becomes sensitive to all parameters in the circuit. On the other hand, it is intuitively clear that in a sufficiently small iris, the spatial distribution of the microwave field as well as the multipactor threshold depends on the iris parameters only. To obtain this simpler situation, the multipactor problem should be separated from the electromagnetic one which is related to the entire microwave system and determines not only the field configuration but also its amplitude in the iris.

This strategy was first suggested in [2] where a step approximation of the microwave field was used in the iris gap (Fig. 1) and it was assumed that electrons are lost outside the gap. This model differs from the plane-parallel one only due to the finite length, a, of the iris gap which causes electron losses when the tangential component of the electron emission velocity is taken into account. The rate of electron losses was estimated in [2] on the basis of a combination of the resonance multipactor theory (used to describe the electron motion along the "y" coordinate) and the random walk theory (used to describe the shift of the electron trajectory along the "z" coordinate). To balance these losses, the value of the secondary emission yield, σ, has to exceed a certain threshold, γ, which depends on

the height to length ratio, h/a, and which is greater than unity:

$$\gamma \cong \exp\left\{\frac{\pi^2}{\eta\left(2\eta+\sqrt{2\pi^3}\right)}\right\}, \quad \eta = \frac{a}{V_T t_g}, \tag{1}$$

where V_T denotes the rms value of the tangential component of the electron emission velocity, t_g is the electron transit time between the plates and is equal to an odd number of half microwave periods (under multipactor resonance conditions). A decrease in the height to length ratio leads to an increase of the threshold value, γ, and consequently the multipactor threshold increases in terms of the rf voltage, U, applied to the iris. A similar increase has also been found in experiments [1], but for lower values of the height to length ratio as compared to the theoretical predictions based on the simple approximation used above.
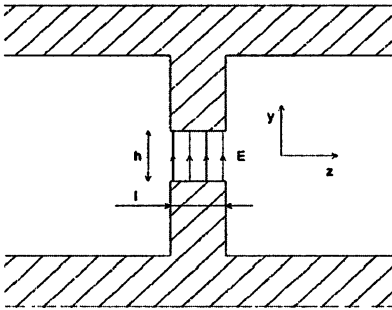
Fig. 1. The structure of the rf electric field in an iris in the step approximation.
Fig. 2. The 2D quasi-static model of an iris
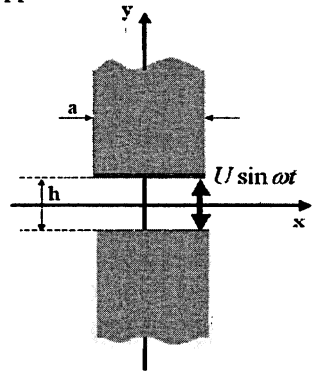
The theory presented above can be significantly improved by taking into account the non-uniformity of the rf field in the iris. The non-uniformity can be described using the quasi-static approximation when both the height and the length of the iris are small compared to the iris width and the rf wavelength. This approximation completely determines the configuration of the rf field in the vicinity around the iris whereas the other components of the entire rf circuit determine only the amplitude of this field or the amplitude, U, of the rf voltage applied to the iris (Fig. 2). The quasi-static rf electric field, $\vec{E}$, can be expressed in terms of an electric potential, ϕ, as $\vec{E} \cong -\nabla\phi \cdot \sin(\omega t)$. Specifically, within the 2D model of the iris, the potential $\phi = \phi(x, y)$ satisfies Laplace's equation

$$\nabla^2\phi \equiv \frac{\partial^2\phi}{\partial x^2} + \frac{\partial^2\phi}{\partial y^2} = 0, \tag{2}$$

631

with the boundary conditions $\phi = \pm U/2$ on the metal surfaces of the iris (upper plate + and lower plate −).

The solution of the above 2D electrostatic problem can be found by using the powerful method of conformal mapping [3]. Specifically, using this approach one finds that in the central part of any iris with a length to height ratio greater than approximately 0.5, the rf field structure is close to that between two parallel plates:

$$\phi(x,y) \cong U\left\{\frac{y}{h} - \frac{g}{2\pi}\sin\left(\frac{2\pi y}{h}\right)\cdot\cosh\left(\frac{2\pi x}{h}\right)\right\}, \tag{3}$$

inside a region where $2g\cosh(2\pi x/h) \ll 1$, and the parameter g is related to the iris length to height ratio approximately as

$$\frac{\pi a}{h} \cong \ln(1/g) - 2(1 - \ln 2) + O(g^2). \tag{4}$$

On the other hand, deviations of the field from the plane-parallel model increases exponentially close to the iris periphery and becomes significant outside the central part, i.e. for $|x| > (a/2) - (h/2\pi)$. This implies that the electron motion in the central part of the iris is governed essentially by a uniform rf field, as assumed in [2]. However, outside this region, the fringing field effect and the concomitant ponderomotive force, becomes important and an electron that is emitted here has a large probability to leave the iris without experiencing any collision with the iris walls. Thus, a reasonable approach is to determine the multipactor threshold by using the step approximation of the rf field, but in an iris with an effective iris length, $a_{eff} = a - (h/\pi)$ instead of the actual length a. The effective length is less than the actual iris length, which results in a shift of the step-like increases in the multipactor threshold towards lower values of the iris height-to-length ratio in complete agreement with the experimental data.

To avoid calculations of a great number of elliptical integrals associated with the conformal mapping it is attractive to derive the equations of electron motion in the variables of the conformal mapping which maps the actual iris geometry onto two parallel plates. For this purpose it is convenient to start with the complex form of these equations:

$$m\ddot{z} = e(d\Phi/dz)^* \cdot \sin(\omega t), \tag{5}$$

where $z = x + iy$ is complex coordinate, $\Phi(z)$ is the complex potential ($\phi(x,y) = \mathrm{Re}\{\Phi(z)\}$) and star denotes complex conjugate. Within the formalism of complex functions, the transformation of the time derivatives of z is given by

$$\dot{z} = \dot{\varsigma}\cdot\frac{dz}{d\varsigma}, \qquad \ddot{z} = \ddot{\varsigma}\cdot\frac{dz}{d\varsigma} + (\dot{\varsigma})^2\cdot\frac{d^2z}{d\varsigma^2}, \tag{6}$$

632

where $\varsigma \equiv \xi + i\eta = \varsigma(z)$ denotes a new complex coordinate related to the conformal mapping. Therefore Eq. (5) can be rewritten as

$$\ddot{\varsigma} - \left(\dot{\varsigma}\right)^2 \cdot \frac{g \sin(\varsigma)}{1 + g^2 + 2g \cos(\varsigma)} = \frac{e}{m} \frac{U \sin(\omega t)}{2\pi G^2} \cdot \left| \frac{1}{1 + g^2 + 2g \cos(\varsigma)} \right| , \qquad (7)$$

where the following expressions for the conformal mapping are substituted $\frac{dz}{d\varsigma} = iG\sqrt{1 + g^2 + 2g \cdot \cos(\varsigma)}$, $\frac{d^2z}{d\varsigma^2} = -\frac{dz}{d\varsigma} \cdot \frac{g \sin(\varsigma)}{1 + g^2 + 2g \cos(\varsigma)}$, and the parameter

G is related to the iris height, h, via $h = 2G\int_0^\pi \sqrt{1 + g^2 + 2g \cdot \cos(\alpha)} d\alpha$. Equation (7) contains only explicit analytical functions which makes it very convenient for numerical simulations.

Numerical simulations of the multipactor dynamics were carried out using a Monte-Carlo algorithm. In all simulations seed electrons were started in the middle of the bottom iris wall. The seed electrons were considered to be uniformly distributed over rf phases and direction of initial velocities whereas the value of the initial velocity was fixed. Each collision of an electron with an iris wall was assumed to generate secondary electrons and the dependence of the secondary emission yield on the electron impact energy was approximated by Vaughan's interpolation formula [4]:

$$\sigma = \sigma_{max} \left[\varepsilon \exp(1 - \varepsilon) \right]^{\nu(\varepsilon)} , \qquad (8)$$

where $\varepsilon = W_{im}/W_{max}$, $\nu(\varepsilon) = 0.62$ if $\varepsilon < 1$, $\nu(\varepsilon) = 0.25$ if $\varepsilon > 1$, W_{im} denotes impact electron energy, σ_{max} is the maximum value of the secondary emission yield, and W_{max} is the impact energy corresponding to this maximum. The evolution of the average electron number, N, in the iris gap (where $|\eta| < \ln(1/g)$) was followed and an exponential increase in time was considered as indicating multipactor build-up. For comparison multipactor simulations were also carried out using $g = 0$ (which corresponds to a uniform rf field) and using the same values of rf voltage, U, iris height, h, and parameters of the secondary emission (σ_{max}, W_{max}, and initial electron energy, W_0). In these simulations, the evolution of the average electron number was studied in gaps with different effective lengths ($|\eta| < a_{eff}$). In particular, infinite effective length ($a_{eff} \to \infty$) corresponds to the plane-parallel model, whereas the case $a_{eff} = a$ corresponds to the approximate iris model with uniform rf field, [2]. All models were found to give the same result when the iris length to height ratio was equal to or greater than 2. However, differences began to appear for decreasing length to height ratio and became significant when $a/h = 0.5$. In the latter case, the iris model with the

uniform rf field is not quite correct. However, it was found that the simple modification of this model, using the effective iris length, $a_{eff} = a - (h/\pi)$, instead of the actual length, a, gives quite good agreement with the exact calculations (see Fig. 3). An application of the iris model with uniform rf field and using the effective length, $a_{eff} = a - (h/\pi)$, was also shown to considerably improve the agreement between predictions and measured data for the multipactor threshold (Fig. 3).
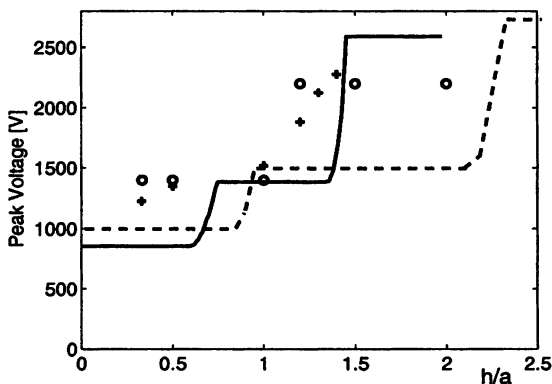
Fig. 3. The multipactor threshold as a function of the height to length ratio h/a. The dotted line corresponds to theoretical predictions (based on Eq. (1)) using the step approximation for the rf electric field in the iris gap. The solid line shows the corresponding results obtained using the effective iris length, $a_{eff} = a - h/\pi$, instead of the actual length, a. The circles represent results of exact numerical calculations using the conformal mapping approach. For comparison, measurement data from [1] are also included (+). The parameters used in the calculations are: iris height $h = 1.2$ mm, rf frequency $\omega/2\pi = 9.56$ GHz, electron initial energy $W_0 = 4$ eV, and for the secondary emission properties, $W_{max} = 519$ eV and $\sigma_{max} = 2.22$.

References

1. *Wolk D., Vicente C., Hartnagel H. L. et al.* Proc. of the 5th Int. Workshop on Multipactor, Corona and Passive Intermodulation in Space RF Hardware. Noordwijk. Holland, 2005. P. 93.
2. *Udiljak R., Anderson D., Lisak M. et al* IEEE Trans. Plasma Sci. 2007. Vol. 35. P. 388.
3. *Semenov V. E., Rakova E., Udiljak R., Anderson D., Lisak M., Puech J.* Phys. Plasmas. 2008. Vol. 15. P. 033501.
4. *Vaughan J. R. M.* IEEE Trans. Electron Devices. 1989. Vol. ED-36, № 9 P. 1963–1967.

INFLUENCE OF THE WAVEGUIDE CROSS-SECTION ON THE MULTIPACTOR THRESHOLD

V. Semenov, E. Rakova, N. Zharova, D. Anderson[1], M. Lisak[1], J. Puech[2]

Institute of Applied Physics of the Russian Academy of Science, Nizhny Novgorod, Russia
[1] Department of Radio and Space Science, Chalmers University of Technology, Goteborg, Sweden
[2] Centre National d'Etudes Spatiale, Toulouse, France

A comparative analysis has been done of the multipactor breakdown thresholds in waveguides with rectangular and wedge-shaped cross-sections respectively. An analysis demonstrates that a stationary electron trajectory exists in both geometries. However, this trajectory is shown to be unstable and small perturbations, e.g. due to a spread of the electron initial velocity, will give rise to electron losses to the waveguide walls and determine the multipactor breakdown threshold. Extensive numerical simulations have been carried out and show that the multipactor threshold for the two geometries are comparable, although slightly higher in the wedge-shaped waveguide than in the rectangular waveguide. Thus, no significant advantage from the point of view of multipactor mitigation is obtained by using wedge-shaped instead of classical rectangular waveguides.

In many high power microwave systems operating close to vacuum conditions, multipactor discharges are recognized as a serious problem. The basic physics of the multipactor phenomenon is comparatively well understood for the case of two infinite parallel plates with a homogeneous electric field between the plates. However, most realistic rf designs involve more complicated geometries, which introduces several complicating factors, in particular (i) finite transverse width of the device, (ii) inhomogeneous electric fields, and (iii) curved field lines. The physical understanding of the multipactor phenomenon in such cases is less well understood since these features introduce new physical effects that may significantly affect the multipactor breakdown threshold, viz. finite transverse width tends to cause electron losses by diffusion to the side walls, inhomogeneous electric fields give rise to the Miller force that pushes electrons out of regions with strong fields, and electron motion along curved field lines gives rise to a centrifugal force which make electrons migrate across the field lines.

Clearly, the rectangular waveguide geometry involves only the two first complications; the electric field lines are straight, but the field is symmetrically inhomogeneous around the center of the wide wall and the Miller force tends to push the electrons to the side walls. However, an electron trajectory that starts normal to the surface in the middle of the wide wall (where the Miller force vanishes) is stationary, it will not experience any shift to the side wall, and is potentially most dangerous for multipactor breakdown. It has been suggested that such dangerous trajectories can be avoided by using a wedge shaped waveguide, where the symmetry leading to the vanishing of the Miller force is avoided, and where consequently the multipactor threshold should be considerably higher than in the rectangular waveguide [1, 2].

However, these conclusions neglects the spread of the velocity of the secondary emitted electrons, which plays a very important role for the multipactor threshold, in particular for the higher order resonances [3]. This velocity spread may involve a spread in emission angle as well as in magnitude. A spread in emission angle has no effect on the breakdown threshold in the case of two infinite plane parallel plates, but becomes important in systems of finite transverse width and also as a mechanism for destabilizing stationary orbits. A detailed analysis of the problem of multipactor breakdown in rectangular waveguides was made in [4] where it was shown that the deviation of the electron trajectories from the line of symmetry increases exponentially in time. Consequently the electron losses increases and the correct multipactor breakdown condition becomes more demanding than that based on the stationary electron trajectory, in particular for the higher order resonances.

Although the existence of stationary electron trajectories are not as evident in the wedge-shaped waveguide geometry, it was shown analytically and numerically in [5] that a stationary orbit does indeed exist by considering the more intricate interplay between the Miller force and the centrifugal force on electrons moving along curved electric field lines. However, in analogy with the rectangular waveguide case, this trajectory is also unstable and any perturbation, e.g. caused by a spread of the electron emission velocities, will cause losses in a qualitatively similar way as in the rectangular waveguide.

The purpose of the present work is to summarize relevant results from the investigations reported in [4, 5] and to compare the breakdown predictions for rectangular and wedge-shaped waveguides having the same cross-sections and propagation constants.

It will be demonstrated analytically as well as by numerical simulations that when the important effect of a spread in the emission angles of the secondary electrons is taken into account, there is no qualitative difference between the two types of waveguides. It is found that the multipactor threshold in terms of the transmitted power is slightly higher in the wedge-shaped waveguide than in the rectangular waveguide. However, the main physical reason for this feature is simply that in the rectangular waveguide, the stationary electron orbit occurs at the location of the maximum electric field whereas in the wedge-shaped waveguide the corresponding orbit is located at a non-maximal electric field.

We will here give a short review of the main results concerning multipactor in rectangular waveguides as reported in [3]. Consider a rectangular waveguide of width, a, $(-a/2 \leq x \leq a/2)$ and height, b, $(0 \leq y \leq b)$. The rf electric field E (in the fundamental mode) is directed along the y axis and varies according to $E = E_0 \cos(k_\perp x)$. Neglecting a spread in the angles of secondary emitted electrons and considering only the stationary electron trajectory at $x = 0$, breakdown predictions can be obtained using classical multipactor theory between two parallel plates. However, such predictions are not in agreement with numerical simulation

results, see e.g. [6]. To remedy this unsatisfactory situation, a comprehensive analysis of different aspects of the multipactor dynamics was carried out in [3] where it was shown that the combination of a velocity spread and the Miller force plays a crucial role for the multipactor threshold, in particular for the higher order resonances.

The main result of the analysis made in [4] can be summarized as follows: the multipactor threshold in a rectangular waveguide can be calculated using the plane-parallel model, but the conventional velocity impact condition on the secondary emission coefficient $\left(\sigma(\varepsilon_i) > 1\right)$, where ε_i denotes the electron impact energy) must be replaced with a more restrictive condition $\sigma_{eff}(\varepsilon_i) > 1$ in terms of an effective secondary emission coefficient, σ_{eff} where $\sigma_{eff}(\varepsilon_i) = \sigma(\varepsilon_i)/\eta$ with the correction factor, η, being determined by the height-to-width ratio of the waveguide according to $\eta = \cosh\left(\pi b/\left(\sqrt{2}a\right)\right)$. This implies that in a waveguide with small height $\left(b << a\sqrt{2}/\pi\right)$, the breakdown threshold is close to that predicted by the plane parallel theory, provided the spread in emission velocity in the y-direction is taken into account. If this spread is not included, the classical plane parallel theory gives accurate results for the lowest order resonance mode only.

The geometry of the wedge-shaped waveguide with an opening angle, θ_0, and radii R_1 and $R_2(R_1 < R_2)$ is shown in Fig. 1. The vector potential determining
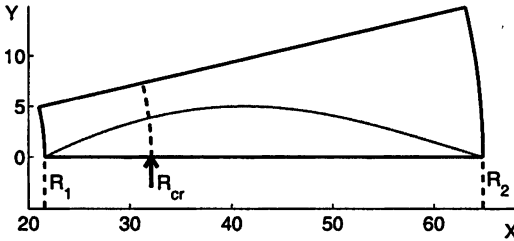
Fig. 1. Cross-section of the waveguide used in the multipactor simulations (wedge angle $\theta_0 = 0.23$, the inner and outer radii, $R_1 = 21.6$ cm and $R_2 = 64.8$ cm). The curved line shows the dependence of the rf electric field amplitude with radial coordinate. The arrow shows the launch position, $R_0 = R_{cr}$, for the trajectory that experiences zero radial shift for zero initial phase $\phi_0 = 0$.

the electric and magnetic fields can be expressed as $\mathbf{A} = A(r)\cos(\omega t)\mathbf{e}_\theta$, where $\mathbf{e}_\theta$ is the azimuthal unit vector in the cylindrical coordinate system and $A(r)$ can be expressed in terms of Bessel functions according to

$$A(r) = A_0 \left[\frac{J_1(k_\perp r)}{J_1(k_\perp R_1)} - \frac{N_1(k_\perp r)}{N_1(k_\perp R_1)} \right], \tag{1}$$

637

where the transverse wave number $k_\perp$ is determined as the smallest root of the equation $A(R_2) = 0$. A detailed analysis of the electron trajectories under the influence of the corresponding full Lorentz force was carried out in [4]. Separating the electron radial motion, $r(t)$, into a slowly varying drift motion, $R(t)$, and a small oscillating velocity component, $\rho(t)$, by writing $r(t) = R(t) + \rho(t)$, the evolution of the slowly varying drift motion could be obtained by averaging the equation of motion for the electron. This approach resulted in the following self consistent equation for the averaged motion, viz.

$$\frac{d^2R}{dt^2} = \frac{P_\theta^2}{m^2R^3} - \frac{1}{4}\frac{d}{dR}\left[\frac{eA(R)}{mc}\right]^2,$$ (2)

Where P_θ denotes the θ component of the canonical momentum, i.e.

$$P_\theta = mR_0V_0 + \frac{e}{c}R_0A(R_0)\cos\phi_0$$ (3)

and V_0 and R_0 denote the values of the emission velocity and radius respectively. Eq. (2) gives a clear physical picture of the interplay between the Miller force and the centrifugal force due to the curvature of the field lines. Clearly a stationary trajectory should exist when the Miller force balances the outward directed centrifugal force and the following condition is satisfied

$$\frac{P_\theta^2}{m^2R^3} = \frac{1}{4}\frac{d}{dR}\left[\frac{eA(R)}{mc}\right]^2.$$ (4)

This stationary trajectory must be located at a radius smaller than the one corresponding to the maximum field (where $dA(R)/dR = 0$, c.f. the rectangular case) since the Miller force now must be directed inwards.

Numerical calculations demonstrated that stationary trajectories exist for a radius R_{cr} which depends on the initial phase, ϕ_0. When the radius of emission, R_0, is larger than R_{cr}, the centrifugal force is stronger than the Miller force and the electron trajectory drifts outwards. In the opposite case, the Miller force dominates and the shift is inwards. This implies that the trajectory with zero radial shift is spatially unstable, completely analogous to the situation in the rectangular waveguide. However, an important difference with the rectangular case is that in the wedge-shaped waveguide, the launch position R_{cr} of the trapped trajectory depends on ϕ_0, which means that this trajectory is also unstable with respect to perturbations of the launch time. These predictions were confirmed by numerical solution of the exact equation of electron motion [5].

Thus, for both the rectangular and wedge shaped waveguides, the spatial instability of the trajectories of resonant electrons results in electron losses, which increase the multipactor threshold, but does not completely prevent the growth of the multipactor avalanche. Extensive numerical simulations, similar to that for the rectangular waveguide, was carried out also for the wedge-shaped waveguide

(including a spread in both emission velocity and emission angle) and compared to those for the rectangular waveguide where the width and the height were chosen so as to provide the same cross-sectional area and the same propagation constant of the fundamental mode as in the wedge-shaped waveguide. The result of these comparative simulations is summarized in Fig. 2, which shows that multipactor avalanche growth is indeed possible in the wedge-shaped waveguide, but the threshold in terms of transmitted power is slightly higher than in the equivalent rectangular waveguide. The physical explanation of this difference is the fact that in the rectangular waveguide, the position of the trapped electron trajectory coincides with that of the maximum amplitude of the rf electric field, whereas in the wedge-shaped waveguide, the position of the trapped trajectory is shifted with respect to the maximum of the rf field. Consequently, at the same power, the electric field amplitude at the position of the trapped trajectory is higher in the rectangular waveguide than in the wedge-shaped one.
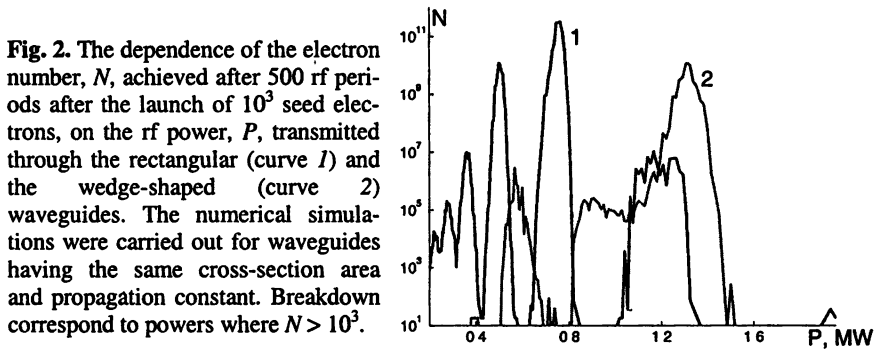
Fig. 2. The dependence of the electron number, N, achieved after 500 rf periods after the launch of 10^3 seed electrons, on the rf power, P, transmitted through the rectangular (curve 1) and the wedge-shaped (curve 2) waveguides. The numerical simulations were carried out for waveguides having the same cross-section area and propagation constant. Breakdown correspond to powers where $N > 10^3$.

References

1. *Chojnacki E.* Phys. Rev. ST Accel. Beams, **3**, 3, 032001(1–5) (2000).
2. *Gonzales J. H., Schmitt D., Raboso D., Hudalgo I., Esbert V. E. B., Martinez B. G.* Proc. 5th Int Workshop Multipactor, Corona and Passive Intermodulation Space RF Hardware, Noordwijk, The Netherlands, Sep. 12–14, 67–78 (2005).
3. *Sazontov A., Buyanova M., Semenov V, Rakova E., Vdovicheva V., Anderson D., Lisak M., Puech J., and Lapierre L.* Phys. Plasmas, **12**, 5, 053102(1–8) (2005).
4. *Semenov V. E., Rakova E. I., Anderson D., Lisak M., and Puech J.* Phys Plasmas, **14**, 3, 033501(1–8) (2007).
5. *Semenov V. E., Rakova E. I, Zharova N., Anderson D., Lisak M., and Puech J.* IEEE Trans. Plasma Science, **36**, 2, 488–493 (2008).
6. *Geng R. L., Goudket P., Carter R.G. et al.* Nucl. Instrum. Methods, Phys. Res. A, **538**, 1, 189–205 (2005).

MULTIPACTOR DISCHARGE ON A DIELECTRIC SURFACE IN MICROWAVE CAVITY

M. A. Lobaev, O. A. Ivanov, V. A. Isaev, A. L. Vikharev

Institute of Applied Physics, Nizhny Novgorod, Russia

Results of experimental study of multipactor discharge on dielectric in high-Q microwave resonator are presented. The influence of nonuniformity of microwave field near the dielectric surface and surface roughness on breakdown threshold has been determined.

Introduction

The multipactor discharge on a dielectric surface in vacuum is one of the main factors that affect operation of high-power microwave devices. The mechanism of multipactor formation is connected with the processes of secondary electron emission from the dielectric surface. Evolution of the discharge can be subdivided into two stages. The first one is formation of the multipactor proper, which leads to desorption of the gas from the surface. At the second stage, a microwave breakdown of the formed gas cloud occurs. The plasma that is generated in this process can destroy the dielectric surface and lead to a change in electrodynamic properties of microwave devices. Hence, studies of the conditions for occurrence and suppression of the multipactor are an important task in development of output windows in high-power microwave devices [1], accelerating dielectric structures for electron-positron colliders [2], and active compressors of microwave pulses [3]. This paper presents the results of studying experimentally the multipactor on a quartz surface under the conditions which are close to those existing in plasma switches of high-power microwave compressors [3].

Experimental setup

The multipactor was studied using the setup, the scheme of which is shown in Fig. 1.
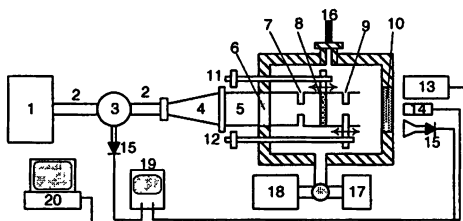
Fig. 1. Scheme of the experimental setup: *1* – magnetron, *2* – rectangular waveguide, *3* – circulator, *4* – mode converter, *5* – circular waveguide, *6* – microwave-transparent window, *7* – diaphragm, *8* – dielectric plate, *9* – movable diaphragm, *10* – dialectric window, *11* – window drive, *12* – diaphragm drive, *13* – spectrograph, *14* – photo multiplier, *15* – microwave detector, *16* – pressure controller, *17* – forevacuum pump, *18* – ion pump, *19* – oscilloscope, *20* – PC.

The setup was based on a cavity excited at a frequency of 9.4 GHz (the TE_{012} mode) and formed by a cylindrical waveguide 45 mm in diameter, which was bounded by to diaphragms. The diameter of the input diaphragm was $D_1 = 29$ mm, and that of the output diaphragm, $D_2 = 27$ mm. The loaded Q-factor of the cavity was $Q_L = 6000$, which ensured high electric-field intensities in the antinodes of the standing wave excited in the cavity even when the power produced by the microwave generator was low. The cavity was placed inside a vacuum chamber which was depressurized to the cavity $p \approx 10^{-6}$ Torr. A 9.15 mm thick quartz plate was placed in an antinode of the standing wave excited in the cavity. The thickness of the plate was chosen to be equal to a half-width of the wave in the cavity, therefore, the intensities of the electric field on the both sides of the plate were identical. The distance between the diaphragms (cavity length) and the position of the dielectric plate in the cavity could be varied from the outside by means of adjustors 11 and 12. The discharge was observed and optical measurements, performed through window 10. Pulses of the microwave radiation having the duration $\tau = 2$–6 μs and a power of up to 150 kV were sent to the cavity input through the mode converter, which formed the TE_{01} mode, and reflection-free vacuum window 6. The microwave power incident on, reflected from, and transmitted through the cavity was registered. The values of the electric field on the dielectric surface was determined from the measured microwave power allowing for the field structure in the cavity, which was calculated by the FDTD method [4], Fig. 2.

a b
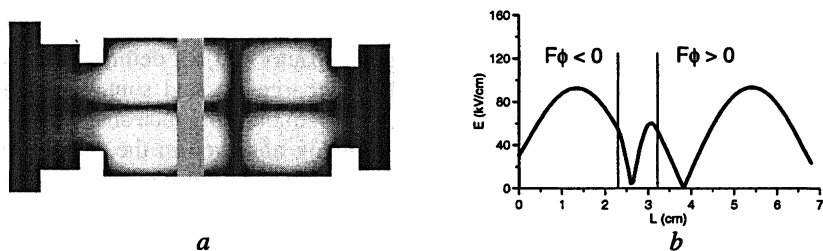
Fig. 2. Distribution of the field in the resonator (a) and the dependence of the amplitude of the mean-square field on the longitudinal coordinate (b). Incident power $P_i = 100$ kW.

Results of the experiment

The results of studying the multipactor in the setup operated in the traveling-wave-type regime are presented in [5]. To achieve this regime, we used linear tuning of the microwave generator frequency during a pulse. It was found that this regime made it possible to maintain high intensities of the electric field on the dielectric surface for a long time. As a result, the both stages of the multipactor were always observed in the experiment, which rendered this regime inconvenient to study the initial phase of the discharge thoroughly.

Therefore, in this work, we studied the multipactor in the regime, when the frequency of the microwave generator was constant. In this case, the occurrence of the multipactor resulted in fast detuning of the cavity and the decrease in the microwave field intensity to the values, at which the further growth of the electron avalanche stopped, and the intensity of the electric field was too low for a breakdown in the gas desorbed from the surface. The typical oscillograms of the signals in the cases of no discharge and the dielectric breakdown are shown in Fig. 3.

a) without discharge   b) with discharge
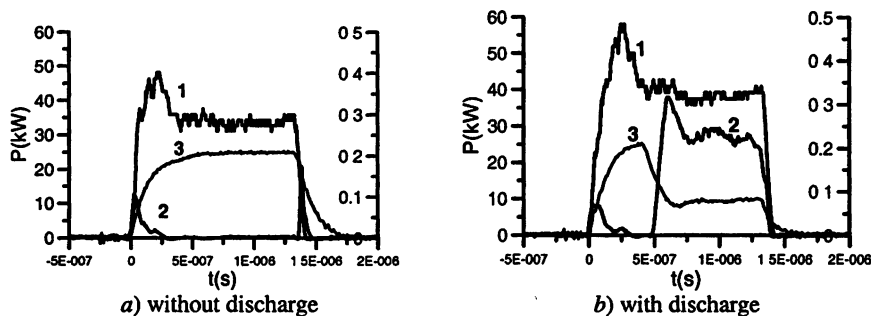
Fig. 3. Oscillogramms of the incident (*1*) reflected (*2*) and transmitted (*3*) microwave pulses

The characteristic time of discharge occurrence was determined from the durations of the fronts of the reflected and transmitted signals and did not exceed 100–150 ns, usually. The value of the electric field, at which the multipactor occurred, was (30 ± 3) kV/cm. The occurring multipactor did not detune the cavity completely. The density of electrons in the discharge reached some stationary level (Fig. 3*b*). Estimations show that the general amount of electrons in the discharge, which corresponded to the cavity detuning observed in the experiment, amounted to $N = 3\text{–}4 \cdot 10^9$. In this case, the electric field on the surface of quartz in the stationary state decreased to the values of $E_{st} = 10\text{–}12$ kV/cm. The oscillatory energy of electrons in such a field amounted to 25–35 eV. This value correlates well with the energy, after which the secondary emission ratio of quartz exceeds $E = 30$ eV. Thus, in the stationary state, the electric field decreased to the level, at which the emission avalanche did not develop again.

To understand the mechanism of the multipactor better, it is important to study the nature of the force that drives the electrons back to the dielectric surface. It is known that in a non-uniform microwave field, an electron is affected by the averaged ponderomotive force [7], which can act as the restoring force at the initial stage of the discharge and result in a discharge occurrence. The effect of microwave discharge nonuniformity on the multipactor threshold was studied by using polished quartz plates with different thicknesses: $d_1 = 2.3$ mm, $d_2 = 4.2$ mm, and $d_3 = 6.0$ mm. One surface of the plate was placed in a node of the standing wave, and different scenarios were realized on the other surface de-

pending on the thickness of the plate: ponderomotive force attracting electrons (d_1), no pondermotive force (d_2), no repulsive force (d_3). The longitudinal distribution of the root-mean-square electric field at the maximum of radial distribution for plates with different thicknesses is shown in Fig. 4.
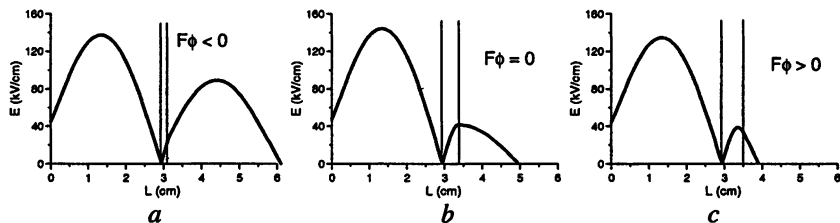
Fig. 4. Dependence of the amplitude of the mean-square field on the longitudinal coordinate. Incident power $P_i = 100$ kW. a) $d_1 = 2.3$ mm; b) $d_2 = 4.2$ mm; c) $d_3 = 6.0$ mm.

The threshold of the multipactor occurrence is shown in Fig. 5a as a function of the high-frequency E_ϕ potential for different plates. It is seen from the Figure that the ponderomotive force directed towards the dielectric surface decreases the breakdown threshold, whereas the opposite pondermotive force increases it. Note that the breakdown threshold was not achieved in the experiment with the d_3 plate, and the corresponding point in Fig. 5a marks the maximum field that the microwave source could produce.

In the next experiment, we studied the influence of a periodic ponderomotive force on the breakdown threshold. The half-wave quartz plate was placed at an antinode of the standing wave excited in the cavity, Fig. 2b.
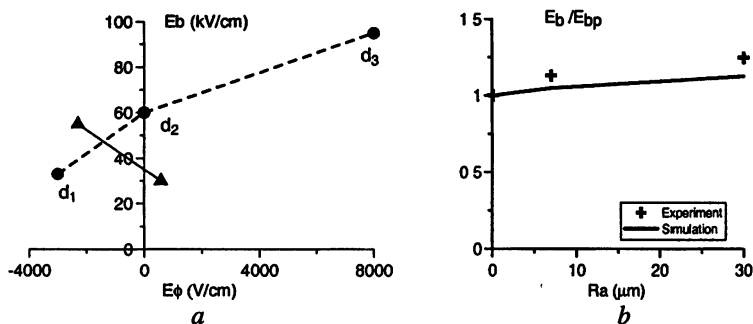
Fig. 5. a – Dependence of the breakdown threshold on gradient of radio – frequency potential: ● – plates with thicknesses d_1, d_2, d_3, ▲ – periodic ponderomotive force; b – Influence of surface roughness on breakdown threshold

The amplitudes of the electric fields at the both sides of the plate were equal, and the ponderomotive force attracted electrons on one side of the dielectric, and repelled them, on the other side. The dependence of the breakdown threshold on the gradient of the high-frequency potential for this plate is shown in Fig. 5a. It is

seen that despite the equal amplitudes of the electric microwave fields at the both sides of the plate, the threshold of the breakdown for the surface of the standing wave near the node turns out to be significantly lower. This difference can be explained as follows. In the presence of a spatially periodic ponderomotive force, the electrons having escaped from the dielectric surface pass through the node of the microwave field, reflect from the adjacent antinode, and come back to the surface initiating the multipactor.

In the experiment shown in Fig. 2b, we also studied the influence of the surface roughness on the value of the multipactor occurrence threshold. The roughness parameter R_a ranged from 0.1 to 30 μm. The results of the experiment are shown in Fig. 5b. The same Figure presents the results of calculating breakdown fields by using the model described in [6].

The value of the breakdown field in Fig. 5b is normalized with respect to the breakdown field amplitude E_{bp} = 30 kV/cm for a polished surface having roughness R_a = 0.1 μm. It follows from the Figure that the multipactor breakdown occurrence grows insignificantly as roughness increases.

Conclusion

In the result of the presented experiments, it was found that a change in the quartz surface roughness ranging from 0.1 to 30 μm does not affect the multipactor occurrence threshold significantly. On the contrary, the value and direction of the ponderomotive force on the dielectric surface was shown experimentally to influence significantly the breakdown threshold. The presence of the force repelling electrons from the surface makes the threshold signficantly higher, whereas the force attracting electrons lowers it. It was found that the multipactor threshold in a strongly non-uniform microwave field depends on the presence or absence of a spatially periodic field structure near the dielectric surface.

References

1. *Preist D. H., Talcott R. C.* IRE Trans. Electron Devices, 8, 243 (1961).
2. *Power J. G., Gay W., Gold S. H. et al.* Phis. Rev. Lett. 92, 164801-1 (2004).
3. *Ivanov O. A., Lobaev M. A., Vikharev A L., Gorbachev A. M.* Proceedings of the Conference "Physics of low temperature plasma", Petrozavodsk, 2, 139 (2004).
4. *Yee K. S.* IEEE Trans. Antennas Propagat, AP-14, 302 (1966).
5. *Ivanov O. A., Lobaev M. A., Vikharev A. L., Isaev V. A., Radishev D. B.* Proceedings of the 6th International Workshop "Strong microwaves in plasmas" / Ed. A. G. Litvak. Nizhny Novgorod, 2006. P. 793–798.
6. *Kishek R. A., Lau Y. Y.* Phys. Rev. Let. 80, 193 (1998).
7. *Gaponov A V., Miller M. A.* Sov. Phys. JETP, 7, 168 (1958).

DIFFERENT SATURATION REGIMES OF MULTIPACTOR BETWEEN TWO PARALLEL METAL PLATES

M. Buyanova[1], V. Semenov[1], D. Anderson[2], M. Lisak[2], J. Puech[3]

[1] Institute of Applied Physics, Russian Academy of Sciences, Nizhny Novgorod, Russia
[2] Chalmers University of Technology, Gothenburg, Sweden
[3] Centre National d'Etudes Spatiales, Toulouse, France

Saturation regimes of a multipactor between two parallel metal plates exposed to a given high frequency voltage are studied in detail both analytically and using numerical simulations. The number of electrons and the energy deposition on the surfaces at the saturation stage are determined depending on the value of the secondary emission yield (SEY) from the surfaces. Different regimes of multipactor saturation are found. It is shown that high SEY values give rise to the development of a single surface regime. This new regime becomes dominant at the saturation stage if the SEY value exceeds a certain threshold. As a result, the saturation level of the number of electrons and of the energy deposited on the surfaces by impacting electrons increase drastically.

In realistic conditions the space charge effect is a natural mechanism of multipactor suppression. Due to Coulomb repulsion between free electrons in a well-developed avalanche, the multipactor becomes defocused and further growth is stopped. An important result of this non-linear phenomenon is that the number of electrons and the energy deposited on the walls by impacting electrons per unit time reach certain saturation levels. A study of saturation levels is of particular interest if the operating parameters of the system are potentially dangerous from the multipactor point of view. In the present work, the saturation regimes of the two-surface multipactor between two metal surfaces are studied in detail with respect to its dependence on the SEY value.

The standard plane-parallel model exposed to a single carrier rf voltage is used and only normal components of the electrons motion are studied. The Coulomb repulsion between electrons in the avalanche is modeled using the concept of a thin charged layer and only classical resonant modes of the two-sided multipactor are studied. As suggested in [1], it is convenient to use the approach of normalized variables and express the classical resonance condition in terms of the normalized gap width:

$$\lambda = \pi k(\cos\phi_0 + v_0) + 2\sin\phi_0 , \qquad (1)$$

where $\omega = 2\pi f$ denotes rf angular frequency, $\lambda = \omega L/V_\omega$ normalized distance between the parallel planes (L is geometrical distance), $V_\omega = eU_0L/(m\omega)$ oscillatory velocity, m and e electron mass and charge respectively, U_0 rf voltage amplitude, $v_0 = V_0/V_\omega$ normalized initial velocity, and ϕ_0 initial phase of rf voltage. The odd number k represents the order of the mode and the electron gap-crossing time is equal to k rf half-cycles. The problem of resonance stability is of great impor-

tance since the phase focusing mechanism provides stability for the resonance and is the factor that counteracts the repulsion between the electrons and the spread over their emission velocities. Together these three factors determine the conditions for the saturation stage. The SEY value must be taken into account in the stability condition, c.f. [1], since secondary emission can partially compensate the electron losses caused by repulsion and defocusing.

Some general theoretical predictions concerning saturation levels can be made on the base of stability properties. First, high order classical modes are especially sensitive to disturbances caused by the space charge effect and reach saturation at lower levels of the number of particles and of the energy deposited on the surfaces per unit time. Second, for each particular resonance, a higher SEY value tends to sustain the electron avalanche growth by partial compensation of the electron loss. Consequently saturation does not occur until higher levels are reached. Moreover, in the case of high SEY values accompanied by a moderate spread over emission velocities some of the newly emitted electrons of the already well-developed avalanche can be forced back to their surface of emission. It is found that a single surface multipactor regime becomes possible if these electrons achieve appropriate impact phases and energies. The development of such a single surface regime was previously observed in experiments involving dielectric-loaded accelerating structures [2, 3] and also in numerical simulations carried out for a plane-parallel model with partial dielectric filling [4]. In these works the development of the single surface regime was attributed to the charging of the dielectric layer. In the present work, the change of the multipactor regime results from space charge effects only.

A Particle-in-Cell code was used for numerical experiments. Each test consisted of simulations of the motion of the electrons until the number of particles and the energy deposited on the surfaces by impacting electrons reached saturation. Most simulations were carried out using Vaughan's model [5] for the SEY (the approximation given by Eq. (2)) with varying maximum value σ_{max} and fixed energy W_{max} corresponding to the maximum of the SEY (and with varying values of the first cross over energy W_1, the minimum energy at which the SEY value is equal to unity):

$$\sigma = \sigma_{max}\left(w \cdot \exp(1-w)\right)^k, \quad w = (W - W_0)/(W_{max} - W_0),$$
$$k = 0.62, \text{ if } w \leq 1, \text{ otherwise } k = 0.25 \tag{2}$$
$$W \text{ is impact energy, } W_0 = 0\,\text{eV}, W_{max} = 350\,\text{eV}.$$

The rf voltage was kept fixed and corresponding to the following rf electric field parameters: $E_0 = 1.77 \cdot 10^5$ V/m, $f = 1$ GHz, $\phi_0 = 0$. Each surface area was 5 mm^2. A spread over the electron emission velocities $\Delta v_0 = \Delta V_0/V_\omega$ was included and the velocity distribution model was assumed Maxwellian (3) with $v_{0m} = 0.1$, $\Delta v_0 = 0.01$.

$$f(v_0) \propto \exp\left(-(v_0 - v_{0m})^2/(2\,\Delta v_0^2)\right). \tag{3}$$

The resulting saturation levels were analyzed and their dependence on σ_{max} was determined. In order to distinguish new regimes from the regular two-sided regime, each particle was followed to determine whether it impacts at its surface of emission or at the opposite surface. It was shown that near the saturation stage, multipactor development depends strongly on the SEY value (Fig. 1). For small SEY values, the saturation levels are relatively low and only increase slowly following the increase of the SEY value. This behaviour can be explained by the electron loss compensation effect. However, higher SEY values lead to a significant jump of the saturation levels, a behaviour associated with the realization of new multipactor regimes. Moreover, if the SEY value exceeds a certain threshold value, the saturation levels increase drastically, evidence of a qualitative change in the nature of the multipactor. Further increase of the SEY value leads to a smooth increase in the saturation level, which can be explained by the electron loss compensation mechanism in the new multipactor regime.
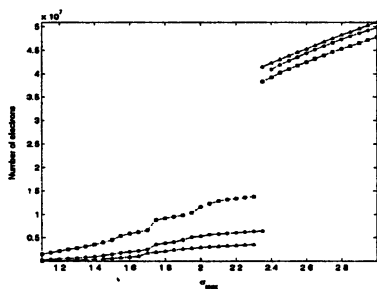
Fig. 1. Saturation levels for the number of electrons vs. σ_{max}. Lines marked with squares correspond to the classical mode k = 3 (λ = 10.37), those marked with circles to the mode k = 5 (λ = 17.28), and those marked with triangles to the classical mode k = 7 (λ = 24.19).
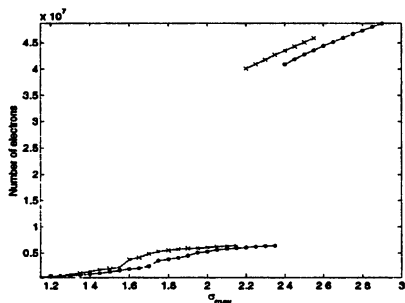
Fig. 2. Saturation levels of the number of electrons vs. σ_{max}. Lines marked with circles correspond to the SEY model (2). Lines marked with crosses correspond to the SEY model (4). Classical mode k = 5 (λ = 17.28).

Particular studies show that in the beginning of each test, irrespective of the SEY value, the multipactor develops as a regular two-sided multipactor process with all electron impacts occurring at the surface opposite to the emission surface (Fig. 3a, Fig. 3b). However, when approaching the saturation, the particular SEY value is important. If this value is small enough, the multipactor retains its two-sided character, but higher harmonics also appear (Fig. 4a, Fig. 4b). Nevertheless, for higher values of SEY, some of the higher harmonics may transform into the single surface regime, involving particles which return back to their surfaces of emission (Fig. 5a, Fig. 5b). The development of the single surface regime changes the saturation level: a first small jump of this level is obtained when the lowest single surface regime (with the electron flight time close to one rf cycle) appears (for the case shown in Fig. 5b, this regime corresponds to an electron flight time close to 10^{-9} seconds).

647
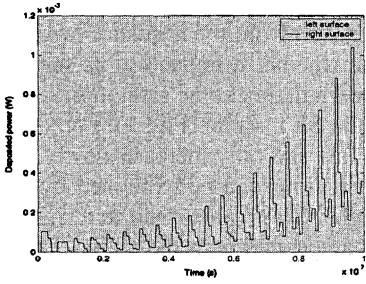
Fig. 3a. Energy deposited on surfaces per rf cycle at initial stage of multipactor. Classical mode $k = 5$. $\lambda = 17.28$, $\sigma_{max} = 1.1$.
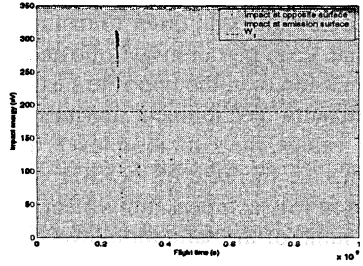
Fig. 3b. Impact energies and flight times for electrons crossing the gap (black) and returning to the emission surface (white) at 10^{-7} s after the start of the simulation. Classical mode $k = 5$, $\lambda = 17.28$, $\sigma_{max} = 1.1$.
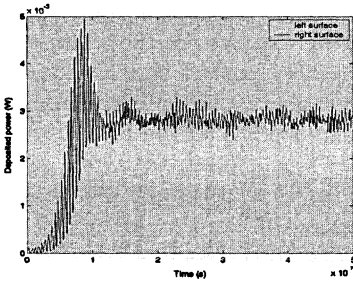
Fig. 4a. Energy deposited on surfaces per rf cycle at saturation stage. Classical mode $k = 5$. $\lambda = 17.28$, $\sigma_{max} = 1.2$.
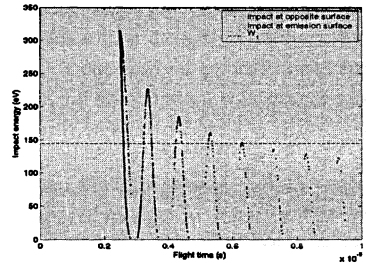
Fig. 4b. Impact energies and flight times for electrons crossing the gap (black) and returning to the emission surface (white) at $5 \cdot 10^{-7}$ s after the start of the simulation. Classical mode $k = 5$, $\lambda = 17.28$, $\sigma_{max} = 1.2$.
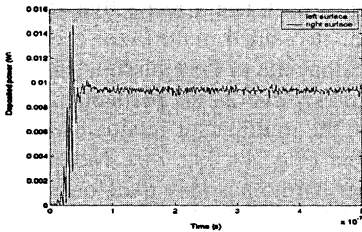
Fig. 5a. Energy deposited on surfaces per rf cycle at saturation stage. Classical mode $k = 5$. $\lambda = 17.28$, $\sigma_{max} = 1.75$.
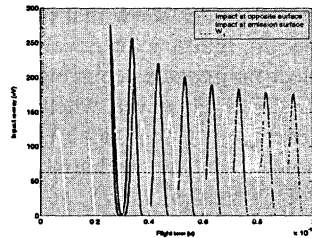
Fig. 5b. Impact energies and flight times for electrons crossing the gap (black) and returning to the emission surface (white) at $5 \cdot 10^{-7}$ s after the start of the simulation. Classical mode $k = 5$, $\lambda = 17.28$, $\sigma_{max} = 1.75$.

Finally, if the SEY value is high enough, the single surface regime, originating from a regular two-sided one under the action of strong space charge effects, become dominant at the saturation stage (Fig. 6a, Fig. 6b). The saturation levels then increase drastically. The lowest single surface regime becomes the dominating one since it develops faster than any of the other single surface regimes and faster also than any regular two-sided regime, the only exception being the first classical two-sided mode $k = 1$. The latter mode corresponds to an even shorter gap-crossing time and higher growth rate. It was found in numerical simulations that, independently of the SEY value, the classical two-sided mode $k = 1$ does not transform into a complete single surface regime.
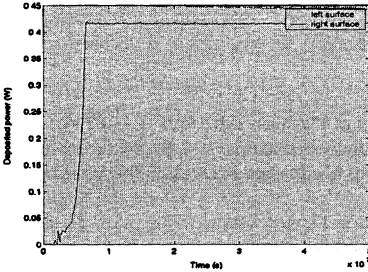
Fig. 6a. Energy deposited on surfaces per rf cycle at saturation stage. Classical mode $k = 5$. $\lambda = 17.28$, $\sigma_{max} = 2.45$.
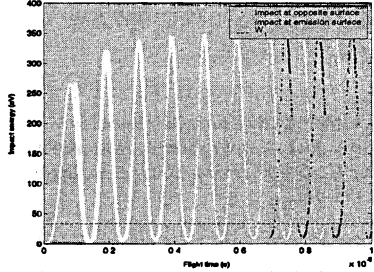
Fig. 6b. Impact energies and flight times for electrons crossing the gap (black) and returning to the emission surface (white) at $5 \cdot 10^{-7}$ s after the start of the simulation. Classical mode $k = 5$, $\lambda = 17.28$, $\sigma_{max} = 2.45$.

Some numerical simulations were also carried out using a step-wise SEY approximation model (4) (with varying σ_{max} and fixed W_1) in order to verify that it is the value of the SEY that determines the change in the multipactor nature.

$$\sigma = \begin{cases} \sigma_{max}, & \text{if } W_1 = 53\,\text{eV} < W < W_2 = 10000\,\text{eV}, \\ 0, & \text{otherwise.} \end{cases} \tag{4}$$

Unfortunately, theoretical analysis of the saturation stage can be carried out only for the limit cases of the regular two-sided and the pure single sided multipactor regime. In the first case, the analysis can be based on the stability properties of a resonant mode. In the second case, the analysis can be based on a study of the maximum value of the electric field produced by the electron cloud before the resonance condition is violated. In both cases, the SEY value must be taken into account. For the regular two-sided multipactor, as a first step, this can be done by using the stability condition suggested in [1]. However, an analysis based on a realistic SEY model is still a difficult problem. In addition, the uncertain geometry of the electron cloud significantly complicates such a study. Finally, the spread of the electron emission velocities is a crucially important factor and a quite difficult parameter to include in an analysis. Consequently, numerical

simulations give more reliable results than theoretical predictions when realistic systems are discussed.

The saturation regimes of the multipactor between two parallel metal plates are studied both theoretically and using numerical simulations. The electron number and the energy deposition on the surfaces at the saturation stage are determined as functions of the SEY value. High SEY values lead to development of single surface regimes at saturation. If the SEY value exceeds a certain threshold, the multipactor becomes mainly single-surface and the saturation levels increase sharply.

References

1. *Kryazhev A., Buyanova M., Semenov V. et al* Physics of Plasmas. 2002. Vol. 9. P. 4736.
2. *Power J. G., Gai W., Gold S. H. et al.* Physical Review Letters. 2004. Vol. 92, № 16. P. 164801.
3. *Jing C., Gai W., Power J. G. et al.* IEEE Transactions On Plasma Science. 2005. Vol. 33, № 4. P. 155–160.
4. *Torregrosa G., Coves A., Vicente C. P.* IEEE Electron Device Letters. 2006. Vol. 27, issue 7. P. 619–621.
5. *Vaughan J. R. M.* IEEE Trans. Electron Devices. 1989. Vol. 36. P. 1963–1967.

CONTENTS OF VOLUME 2

CURRENT DRIVE AND PLASMA HEATING BY MICROWAVES IN NUCLEAR FUSION DEVICES

TERAHERTZ- AND MICROWAVE-ASSISTED MATERIALS PROCESSING
AND NANOTECHNOLOGIES
(including a broader range of microwave applications)